PACIFIC EARTHQUAKE ENGINEERING RESEARCH CENTER

Earthquake Engineering for Resilient Communities:

2013 PEER Internship Program Research Report Collection

Heidi Tremayne, Editor
Stephen A. Mahin, Editor

Jorge Archbold Monterrosa
Shelly Dean
Curtis Fong
Elizabeth R. Jachens
David Lam
Mara Minner
Julia Pavicic
Lorena Rodriguez
Kelli Slaven
Jenny Taing
Matt Brosman
Katherine deLaveaga
Donovan Holder
Rakeeb Khan
Daniela Martinez Lopez
Geffen Oren
Melissa C. Quinonez
Sean E. Salazar
Vivian Steyert
Salvador Tena

PEER 2013/25
DECEMBER 2013

Earthquake Engineering for Resilient Communities:

2013 PEER Internship Program Research Report Collection

Heidi Tremayne, Editor

Stephen A. Mahin, Editor

Jorge Archbold Monterrosa
Matt Brosman
Shelley Dean
Katherine deLaveaga
Curtis Fong
Donovan Holder
Elizabeth R. Jachens
Rakeeb Khan
David Lam
Daniela Martinez Lopez
Mara Minner
Geffen Oren
Julia Pavicic
Melissa C. Quinonez
Lorena Rodriguez
Sean E. Salazar
Kelli Slaven
Vivian Steyert
Jenny Taing
Salvador Tena

PEER Report 2013/25
Pacific Earthquake Engineering Research Center
Headquarters at the University of California, Berkeley

December 2013

TABLE OF CONTENTS

INTRODUCTION

Recent earthquakes in the U.S. and around the world have repeatedly shown that earthquake resilience is essential to building and sustaining urban communities. Earthquake resilience will play an increasingly important role in the professions associated with earthquake hazard mitigation, thus there is a need to educate the next generation of these professionals. To address this need, the Pacific Earthquake Engineering Research Center (PEER) coordinates a summer internship program for undergraduate students that focuses on the theme of earthquake-resilient communities. With funding from the National Science Foundation (NSF), twenty interns from a variety of backgrounds and universities participated in the 2013 program.

The summer of 2013 represents the third year of funding from the National Science Foundation for this program. Since 2011, forty-three undergraduate students have conducted research with the support of a dedicated team of forty-nine faculty, post-doctoral, graduate student, and professional mentors. PEER students interns have come from 27 different universities, of which thirteen are primarily undergraduate serving institutions that have limited research opportunities in science, technology, engineering and math for their students. Forty percent of the interns have been women and 23% have been Hispanic or Latino. These statistics, gathered from program assessment surveys, show that PEER's Internship Program is actively serving a broad range of undergraduates interested in earthquake engineering and earthquake mitigation by exposing them to unique and meaningful research programs in an array of technical disciplines.

To show the importance of multidisciplinary cooperation and collaboration, PEER assigned each of the 2013 participating undergraduate interns with a project in one of the following disciplines: structural engineering, geotechnical engineering, risk analysis, urban planning, or public policy. The interns were matched with a combination of faculty, post-doctoral, graduate student, and professional mentors who help them complete a unique research project at one of the five partnering research sites for 2013: City and County of San Francisco, Stanford University, University of California Davis, University of Washington, and University of California Berkeley.

The addition of Stanford University in 2013 to the list of partnering organizations resulted from the involvement of several Stanford professors who were conducting experiments at the nees@berkeley Laboratory. Thus, the four Stanford interns were jointly hosted at Stanford University and the University of California, Berkeley.

Two students also participated in public policy projects through collaboration with the San Francisco City Administrator's Earthquake Safety Implementation Program (ESIP), under the guidance of Laurence Kornfield. These students utilized the newly created EPICENTER, a pop-up collaborative space for earthquake policy research and development in the City of San Francisco, to engage with design professionals, policy makers, and the community leaders during their research internship.

The 2013 interns are listed below in alphabetical order with their home university. PEER thanks the students for their energy, enthusiasm, and diligence throughout the ten-week internship.

- Jorge Archbold Monterrosa, Universidad del Norte, Columbia
- Matt Brosman, University of Florida
- Shelly Dean, Humboldt State University
- Katherine deLaveaga, University of California, Berkeley
- Curtis Fong, Stanford University
- Donovan Holder, University of Illinois at Urbana-Champaign
- Elizabeth Jachens, California State University, Chico
- Rakeeb Khan, California State University, Sacramento
- David Lam, University of California, Berkeley
- Daniela Martinez Lopez, Universidad del Norte, Columbia
- Mara Minner, University of California, Berkeley
- Geffen Oren, Stanford University
- Julia Pavicic, Gonzaga University
- Melissa Quinonez, University of California, Irvine
- Lorena Rodriguez, San Jose State University
- Sean Salazar, University of Arkansas
- Kelli Slaven, University of Washington
- Vivian Steyert, Harvey Mudd College
- Jenny Taing, University of California, Berkeley
- Salvador Tena, University of California, Davis

The number of participating faculty, post-doctoral, graduate student and professional mentors in 2013 was considerably higher than previous summers due to the large number of interns and the vast array of projects in which the interns participated. This gave the interns exposure to many different research projects, technical disciplines, and personal working styles. PEER extends its sincere thanks to the numerous participating mentors listed below. Without their superior dedication and time commitment, the PEER Internship Program would not be possible.

- California State University, Sacramento
  - Ben Fell
- City of San Francisco
  - Laurence Kornfield
- Stanford University
  - Greg Deierlein

- Eduardo Miranda
- Cristian Acevedo
- Ezra Jampole
- Scott Swenson

- University of California, Berkeley
  - Stephen Mahin
  - Jack Moehle
  - Carlos Arteta
  - Jiun-Wei Lai
  - Matt Schoettler
  - Barbara Simpson
- University of California, Davis
  - Ross Boulanger
  - Jason DeJong
  - Jay Lund
  - Nathan Burley
  - Mason Ghafghazi
  - Michael Gomez
  - Rui Hui
  - Christopher Krage
  - Ana Maria Parra
  - Adam Price
- University of Washington
  - Jeffrey Berman
  - Marc Eberhard
  - Dawn Lehman
  - Charles Roeder
  - John Stanton
  - Molly Johnson
  - Bryan Kennedy
  - Jeffrey Schaefer
  - Andy Sen
  - Dan Sloat
  - Max Taylor Stephens

During the ten-week summer research experience, each intern conducted a research project while also regularly engaging with the full intern cohort during weekly web-meetings to discuss and learn how each of their projects related to earthquake resiliency. Students learned how to conduct independent research and how to participate effectively as a member of a research team. Supplemental activities, including a two-day orientation program with multiple skill-building workshops and participation in a research poster session at the 2013 PEER Annual Meeting held as a part of the Northridge 20 Symposium (northridge20.org), were conducted to broaden the intern experience and inspire them to make future contributions to the field of earthquake engineering and related research.

As a final research deliverable, each intern was required to prepare a final research report. This PEER report, "Earthquake Engineering for Resilient Communities: 2013 PEER Internship Program Research Report Collection" is a compilation of the final research papers written by the 2013 interns. These reports follow this Introduction. A list of the institutions, projects, interns, and mentors is listed below:

University of Washington

- "Interface Strength between Roughened Precast Columns and Footing" was completed by interns Matt Brosman and David Lam under the supervision of the following mentors: Professors Marc Eberhard and John Stanton, and graduate students Bryan Kennedy and Jeffrey Schaefer.
- "Composite Action of Concrete Filled Tubes" was completed by intern Donovan Holder under the supervision of the following mentors: Professors Dawn Lehman and Charles Roeder, and graduate student Max Taylor Stephens.
- "Evaluation of the Optotrak System for Concentrically Braced Steel Frames" was completed by intern Kelli Slaven under the supervision of the following mentors: Professor Jeffrey Berman, and graduate students Molly Johnson, Dan Sloat, and Andy Sen.
- "Evaluating a Welded CFT-to-Cap-Beam Connection Detail" was completed by intern Vivian Steyert under the supervision of the following mentors: Professors Dawn Lehman and Charles Roeder, and graduate student Max Taylor Stephens.

University of California, Davis

- "Effect of Fines and Plasticity on Evaluating Sample Disturbance" was completed by intern Shelly Dean under the supervision of the following mentors: Professor Jason DeJong and graduate student Christopher Krage.
- "One-dimensional Compressibility of Intermediate Non-plastic Soil Mixtures" was completed by intern Sean Salazar under the supervision of the following mentors: Professors Jason DeJong and Ross Boulanger, and graduate students Ana Maria Parra and Adam Price.
- "Biostimulation of Native Ureolytic Bacteria for Biocementation of Sands" was completed by intern Salvador Tena under the supervision of the following mentors: Professor Jason DeJong and graduate student Michael Gomez.

- “Risk Analysis of Levee Failure: Optimization of levee height and crown width” was completed by intern Elizabeth Jachens under the supervision of the following mentors: Professor Jay Lund and graduate students Rui Hui and Nathan Burley.

University of California, Berkeley

- “Seismic Performance Assessment of Pre-1988 Steel Concentrically Braced Frames” was completed by intern Mara Minner under the supervision of the following mentors: Professor Stephen Mahin, post-doctoral researcher Jiun-Wei Lai, and graduate student Barbara Simpson.
- “Economic Loss Assessment for an Existing Tall Building” was completed by intern Melissa Quinonez under the supervision of the following mentors: Professor Stephen Mahin, post-doctoral researcher Matthew Schoettler and Jiun-Wei Lai.
- “Seismic Performance of an Existing Tall Steel Building” was completed by intern Lorena Rodriguez under the supervision of the following mentors: Professor Stephen Mahin, post-doctoral researcher Matthew Schoettler and Jiun-Wei Lai.
- “Performance of Concrete Shear Wall Boundary Elements under Pure Compression” was completed by intern Jorge Archbold Monterrosa under the supervision of the following mentors: Professor Jack Moehle and graduate student Carlos Arteta.
- “Exploring Adequate Layout for Ductile Behavior of Reinforced Concrete Shear Walls Boundary Elements in Compression” was completed by intern Daniela Martinez Lopez under the supervision of the following mentors: Professor Jack Moehle and graduate student Carlos Arteta.

City and County of San Francisco

- “Seismic Safety of San Francisco’s Private Schools” was completed by intern Julia Pavicic under the supervision of the following mentor: Laurence Kornfield.
- “Improving San Francisco’s Seismic Resiliency through Retrofits of Cripple Wall Homes” was completed by intern Jenny Taing under the supervision of the following mentor: Laurence Kornfield.

Stanford University

- “Torsion-Induced Sliding Displacement in Isolated Light-Frame Structures” was completed by intern Curtis Fong under the supervision of the following mentors: Professors Gregory Deierlein and Eduardo Miranda, and graduate student Ezra Jampole.
- “Sliding Base Isolation for Light-Frame Residential Housing” was completed by intern Katherine deLaveaga under the supervision of the following mentors: Professors Gregory Deierlein and Eduardo Miranda, and graduate student Ezra Jampole.

- “Evaluating the Bonding Properties of Various Construction Adhesives to Determine the Best Overall Product for the Light-Frame Unibody System” was completed by intern Rakeeb Khan under the supervision of the following mentors: Professors Gregory Deierlein, Ben Fell, and Eduardo Miranda, and graduate student Cristian Acevedo.
- “Modeling of Light-Frame Unibody Residential Buildings” was completed by intern Geffen Oren under the supervision of the following mentors: Professors Gregory Deierlein and Eduardo Miranda, and graduate student Scott Swenson.

Funding for the 2013 PEER Internship Program is provided by the National Science Foundation under Grant No. EEC-1063138, as a part of NSF’s Research Experiences for Undergraduate (REU) Program. Any opinions, findings and conclusions or recommendations expressed in this material are those of the author(s) and do not necessarily reflect the views of the National Science Foundation (NSF) or the Pacific Earthquake Engineering Research Center (PEER). For more information about the 2013 PEER Internship Program, visit: http://peer.berkeley.edu/education/summer_internship_program2013.html

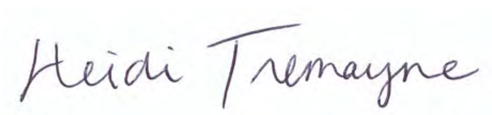

Heidi Tremayne
Outreach Director, PEER
PEER REU Coordinator

Stephen A. Mahin
Director, PEER
PEER REU Principal Investigator (PI)

1. Interface Strength between Roughened Precast Columns and Footing

Matt Brosman and David Lam

ABSTRACT

The socket connection is a column-to-footing connection created by placing a precast column into an excavation and then casting the footing concrete around the column. The column has an intentionally roughened surface in the region that is embedded into the foundation in order to increase the load transfer between column and footing. Tested at the University of Washington, this connection detail has proven to provide adequate strength under axial and lateral loading. However, the current method of roughening uses wooden strips in the formwork to create a saw-tooth shaped roughened surface, which is labor intensive and cannot be implemented on a column with a circular cross section. This report examines the implementation and performance of alternative methods of roughening that are intended to improve constructability while creating a roughened surface that provides adequate interfacial shear resistance to prevent push-through failure under axial loading.

1.1 INTRODUCTION

Currently in the U.S. there is a growing need for new highway bridge construction because of increasing traffic volumes and deteriorating transportation infrastructure. The construction of concrete bridges in seismic regions is conventionally done using cast-in-place components, but it can result in significant traffic delays because it requires numerous, sequential on-site construction procedures [Hieber et al. 2005]. This has stimulated the development of alternative construction methods intended to accelerate the construction process. In recent years, research has been done in developing bridge bent systems that incorporate precast components rather than cast-in-place components [Culmo 2009]. Precast construction allows components to be constructed in parallel, which has the potential to significantly minimize traffic disruptions, as well as improve work zone safety, reduce environmental impacts, improve constructability, increase quality of construction, and lower life-cycle costs [Hieber et al. 2005].

Precast concrete substructures (precast columns and cast-in-place foundations) have seldom been used in seismic regions due to design challenges concerning connection detailing.

Connections for precast systems are typically located at the beam–column and column–footing interfaces to facilitate fabrication and transportation; however, those locations experience high moments and large inelastic cyclic strain reversals during large earthquakes. As a result, designing connections that are both easy to assemble on-site and are robust enough to maintain structural integrity under seismic forces has proven to be challenging [Khaleghi 2010].

1.1.1 The Socket Connection Concept

Haraldsson et al. [2013] developed the current socket connection design for bridges in seismic regions. The construction sequence is illustrated in Figure 1.1. The column is first precast with intentional roughening on the surface that is later embedded in the cast-in-place footing. Then the column is positioned in the excavation, the footing reinforcement is placed around the column, and lastly the foundation is cast. Because no reinforcement crosses the interface, the resistance to vertical load relies solely on the shear friction created by the roughened column-to-footing interface.

Three specimens at 42% scale were tested at the University of Washington. It was concluded that under cyclic lateral loading, the connection performs as well as, or better than, a comparable cast-in-place connection if the footing depth is at least equal to the column diameter. Also, the connection can resist the maximum probable vertical load easily and without damage [Haraldsson et al. 2013].

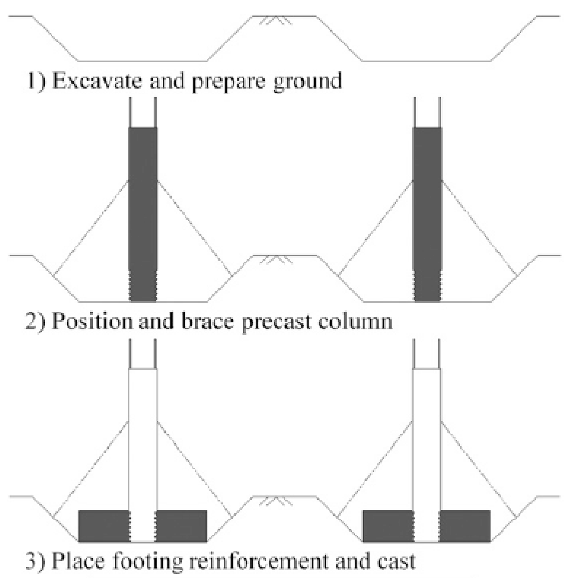

Figure 1.1 Construction sequence of socket connection [Haraldsson et al. 2013].

According to Marsh et al. [2011], the socket connection is the most promising precast connection for use in column-to-footing connections based on a series of criteria that includes: constructability, seismic performance, inspectability, durability, time saving potential, and technology readiness level. The main advantages that the socket connection has over a typical cast-in-place connection are constructability and time saving potential. A lack of protruding rebar across the column interface simplifies fabrication, handling, and transportation and provides good tolerances for erection on site. Also, prefabrication eliminates the need for time-consuming on-site activities such as formwork building, rebar placement, and concrete pours, which can result in an approximately 50% reduction in construction time [Marsh et al. 2011].

1.1.2 Current Implementation of the Socket Connection

The state of Washington has already implemented the precast column and socket connection system in a bridge carrying U.S. 12 over Interstate 5 (see Figure 1.2). Examination of the construction further reinforced the claim that the socket connection is relatively quick and easy to construct when compared to similar cast-in-place connection [Khaleghi et al. 2012]. Even though the current socket connection design has proven to be satisfactory in terms of constructability and seismic performance, improvements can be made to further minimize construction time and improve practicality.

The roughened surface at the column-to-footing interface in both the test specimens and the U.S.-12 bridge was achieved by attaching triangular timber strips onto sheets of plywood, forming a saw-tooth pattern, and then building formwork with an octagonal cross section (see Figure 1.3). The use of timber strips necessitates flat surfaces, so this portion of the column cannot have a circular cross section [Khaleghi et al. 2012]. Also, the process of cutting the timber strips and assembling the formwork is labor intensive. A simple way to form ridges on a curved surface would reduce labor costs and enable columns to have an arbitrary cross section.

Figure 1.2 Construction of the socket connection in the field [Khaleghi et al. 2012].

Figure 1.3 Saw-tooth pattern detail.

1.1.3 Research Objectives

The primary objectives of this research were the following:

- Develop novel methods of creating the roughened surface on a precast column that are constructible and allow for a column with an unrestricted cross section
- Conduct push through tests to determine the shear strength at the column-to-footing interface
- Determine the effectiveness of each roughening method based on strength and ease of implementation

1.2 EXPERIMENTAL METHODS

For the purpose of designing a specimen and facilitating experimental set-up, constructability and time constraint were major factors. Specimens were designed to simulate a column to footing socket connection as described by Haraldsson et al. [2013]. Special consideration was taken to ensure a push-through failure mode at the interface between the two surfaces, since previously tested large-scale specimens failed in the precast column section prior to shear sliding or punching shear failure. To fit within the constraints of the present study, the specimens had to be small-scale.

1.2.1 Geometry of Test Specimens

To mimic the on-site construction sequence, the specimens were constructed in two phases: the precast column phase and the cast-in-place footing phase. The design is shown in Figure 1.4. Precast columns measuring 4 in.×8 in. were cast, with surface roughening applied directly to the cylinders during the casting process. Cylinders were given a sulfur cap on one side to provide a flat testing surface, and were seated on a temporary 1.5-in. wooden shim in order to provide space to push through during testing. A 4-in.-diameter HDPE pipe was fitted to part of the outer surface of the precast cylinder in order to control the bonded length between the precast cylinder and cast-in-place foundation. This length must be regulated because it controls the size of the bonded area.

The cylinder was surrounded by a 12-in.-diameter concrete form-tube, cut to a height of 6 in. Two 10 in. rings of reinforcement, one in the bottom and one in the top of the foundation, were given 1 in. of cover from the foundation formwork. Prior to testing, a timber ring was secured to the bottom of the specimen in order to control the location of loading. See Figure 1.5 for a photograph of a specimen prior to casting.

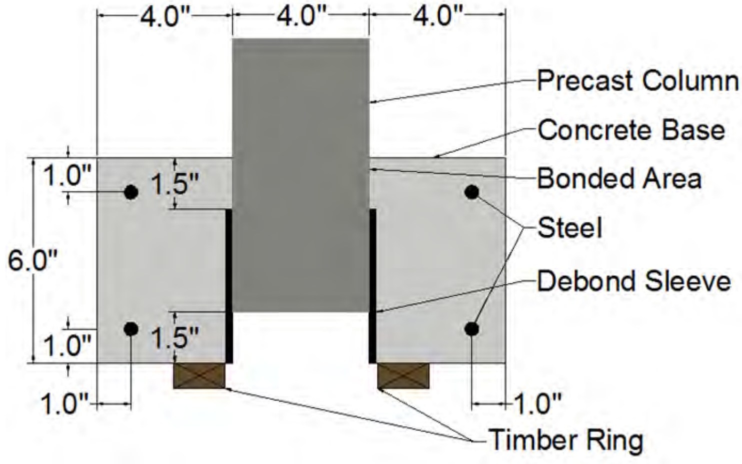

Figure 1.4 Model of test specimen.

Figure 1.5 Precast column in foundation formwork prior to casting.

1.2.2 Precast Column Construction Methods

Columns were cast using 4 in.×8 in. plastic cylinder molds. Surface roughening was applied prior to the casting of concrete directly to the cylinder mold. Two kinds of roughened surfaces were tested—a chemically roughened surface, and a mechanically roughened surface. For each type of roughened surface, two different finishes were to be achieved.

During casting, cylinders were vibrated on a vibrating table in two lifts. After the precasting process, cylinders were floated to a smooth finish, and allowed to cure overnight protected from moisture loss. After the cylinders were removed from the molds, a sulfur cap was created on one side of the column in order to provide a flat testing surface. Cylinders were then stored in the University of Washington Concrete Materials Lab fog room until the day of footing construction.

1.2.2.1 Smooth Cylinders

A smooth cylinder finish was tested in order to simulate a minimal realistic shear strength condition. The smooth cylinders were created by using 4 in.×8 in. plastic cylinder molds. The cylinders were cast, floated smooth, and sealed during curing. After curing, the cylinders were removed from their molds using compressed air and stored in the fog room until needed for testing.

1.2.2.2 Chemical Roughening Methods

The chemically roughened surface was created using in-mold cement retarder. Two different varieties of retarder were used, both manufactured by Architectural Concrete Chemicals, LLC, as part of the Altus Series of In-Form Retarders. One variety of the chemical retarder was "Exposed Finish Small Aggregate", designed to expose 3/8-in. aggregate. This retarder was referred to as "Coarse Retarder." The other variety of chemical retarder used was "Micro Finish Sand," designed to expose sand aggregate. This retarder was referred to as "Fine Retarder."

Both retarders were similar in consistency to an oil-based paint and were painted on the inside of the plastic cylinder molds (see Figure 1.6). An inch of unpainted region was left at the bottom of the cylinders, in order to preserve the integrity of the cylinder in the capping/loading region.

Cylinders were then cast, floated, and a plastic cap was placed on top to prevent moisture loss. Cylinders were left overnight for approximately 14 hours at the recommendation of the manufacturer and removed from their molds. Following the removal of molds, the cylinders were brushed evenly with a wire brush in order to loosen the retarded cement paste (see Figure 1.7). Additionally, the cylinders were uniformly rinsed with a water jet to remove trapped wet paste (see Figure 1.8). The process did not remove coarse aggregate.

Figure 1.6 Four in. x 8 in. plastic cylinder molds with coarse (yellow) and fine (blue) retarders painted on.

After the excess cement paste was removed, cylinders were given a sulfur cap on one end, and stored in the University of Washington Concrete Materials Lab fog room. A random sampling of void depths between aggregate were measured. Cylinders treated with the Coarse Retarder measured a nominal average depth of 0.079 in, while cylinders treated with the Fine Retarder measured a nominal average depth of 0.020 in., a ratio of approximately 4:1. Figures 1.9 and 1.10 are photos of the Coarse and Fine Retarder finishes, respectively.

Figure 1.7 Brushing off excess cement paste, revealing exposed aggregate surface.

Figure 1.8 Spraying off trapped excess cement paste.

Figure 1.9 Coarse Retarder finish.

Figure 1.10 Fine Retarder finish.

1.2.2.3 Mechanical Roughening Methods

Two methods were used to create a physically roughened surface using mechanical methods: a caulk and trowel finish and a plastic wire finish. Both were designed to roughly mimic the socket connection detail from Haraldsson et al. [2013] at the reduced scale used here. The large scale specimen had triangular roughening at a depth of 5/16 in. and a spacing of 5/8 in. The large scale columns were a diameter of 20 in., resulting in a scaling ratio of 5:1. Both roughening methods roughened the columns for approximately 6 in. of the 8 in. possible of column length, in order to preserve a clean surface for sulfur capping and loading.

The caulk and trowel approach was created by using a tile trowel with U-shaped grooves that measured 1/16 in. and were deep spaced 3/32 in. center-to-center. A line of caulk was spread throughout the interior of a plastic cylinder mold, and then the trowel was run through the interior to create a series of horizontal ridges (Figure 1.11). The caulk was then allowed to dry overnight prior to the casting of concrete. Following casting, the cylinders were removed and the excess caulk was removed from the ridges in the cylinder using an air hose (Figure 1.12). This method produced ridges of consistent spacing and depth. However, due to inconsistencies in the caulk, some of the roughening did not come out cleanly.

The plastic wire roughened precast cylinders were constructed using 0.095 in.-diameter weed trimmer line. The plastic wire was coiled edge to edge around a plastic tube of a smaller diameter than the plastic cylinder mold (Figure 1.13). The wire was then slipped into the interior of the plastic cylinder mold and the core tube was removed (Figure 1.14). The wire stayed in place without the use of adhesives. The surface created ridges that were nominally 0.0475 in. deep and 0.095 in. center-to-center. Following casting, the cylinders were demolded and the wire was carefully unwound (Figure 1.15). The resulting surface consisted of grooves mostly filled with cement paste. However, the finish underneath the flakey cement was uniform and had a slight roughness to it.

Figure 1.11 Caulk being applied to interior of concrete cylinder mold with trowel.

Figure 1.12 Caulk and trowel detail of cast cylinder prior to removal of excess caulk.

Figure 1.13 Plastic wire prior to placement in 4 in.×8 in. plastic cylinder mold.

Figure 1.14 **Plastic wire fitted into the interior of a concrete cylinder mold**

Figure 1.15 **Plastic wire mechanically roughened cylinder following removal of mold.**

1.2.3 Footing Construction Methods

Footings were constructed on a 20 in.×20 in. square of sanded and leveled 3/4-in.-thick plywood. The footing itself was formed using the plywood as its base, and a piece of 12 in. cardboard form-tube, cut to a height of 6 in., as the wall of the foundation. The form-tube was supported by a frame made from 2×6 wood sections. The frame was secured to the plywood base and secured to the form-tube using a single screw through the side of the tube. The location where the form-tube rested on the plywood was then caulked to prevent concrete seepage.

A 1.5-m high wooden shim was installed into the bottom of the plywood at the center of the form-tube, and was leveled. Ten-in. diameter steel hoops and $A_s = 0.232$ in.^{2} were placed 1 in. from the bottom and 1 in. from the top, secured by using rebar chairs and hanging, respectively. The steel hoops were anchored into the concrete using two hooks for each hoop. A footing prior to casting can be seen in Figure 1.16.

Prior to casting, the cylinder was fitted with a debonding sleeve around the bottom of the roughened region. The cylinder was then placed on the shim with the sleeve and then measured to ensure that it was level. After leveling, the debonding sleeve was caulked to the plywood. See Figure 1.17 to see foundation set-up prior to casting. After casting the base concrete, the top surface of the foundation was floated smooth (Figure 1.18). The concrete was covered with wet burlap as quickly as possible and was allowed to cure overnight. The burlap was continuously soaked until test day to prevent shrinkage cracking.

Figure 1.16 Footing set-up prior to casting.

Figure 1.17 Foundation set-up prior to casting.

Figure 1.18 A test specimen after casting and floating.

1.2.3.1 Monolithically Cast Specimen Construction

Two monolithically cast specimens were made using the same geometry as the other specimens. However, the column and footing were cast simultaneously, eliminating the precast element from the design. This was achieved by blocking off the wooden shim standoff (Figure 1.19), and installing a centered wooden top and extension to create the top of the footing and column shape, leaving a void beneath (Figure 1.20). The wooden top was created by taking a piece of plywood and cutting a 4 in. hole in the top. A piece of a plastic cylinder mold was then hot glued to the form to create the proper erected height above the interface for the column. The wooden top was centered and secured to the formwork.

Figure 1.19 Sealed void in monolithically cast specimen to allow push through.

Figure 1.20 Plywood top and column extension for monolithically cast specimen.

1.2.4 Instrumentation and Applied Loading

The installed instrumentation consisted of a load cell and linear displacement potentiometers.

1.2.4.1 Applied Loading

Load was applied axially by the 300 kip Baldwin Universal Loading Machine at the University of Washington Structural Laboratory (Figure 1.21). The load cell in the Baldwin machine is internal, and was monitored digitally. The load cell occupied channel 1 on the LabVIEW station.

1.2.4.2 Displacement Potentiometers

Two linear displacement potentiometers were utilized in order to track local displacement of the column. The potentiometers were calibrated to the LabVIEW station using the University of Washington's calibration station. The potentiometers had a range of 1.5 in., and were secured onto either side of the specimen's column portion with the plunger landing on the top surface of the foundation (See Figure 1.22). Displacement potentiometers were secured directly to the side of the column, with the plunger measuring displacement relative to the stationary base. Rubber bands and hot glue were used to secure the potentiometer in place (Figure 1.23). The potentiometers occupied channels 2 and 3 on the LabVIEW station.

Figure 1.21 300 kip Baldwin Universal Loading Machine with specimen in place.

Figure 1.22 Linear displacement potentiometer set-up.

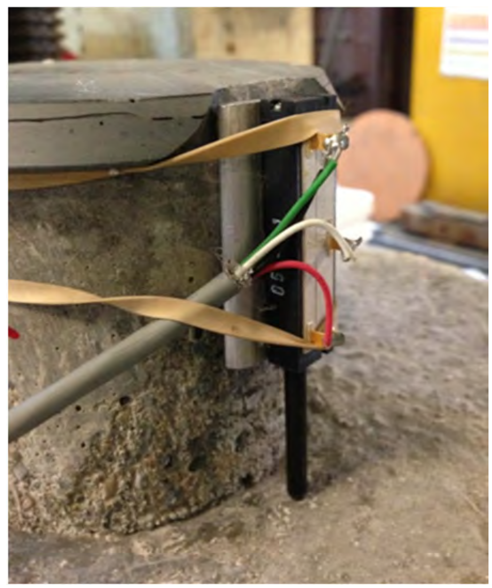

Figure 1.23 Detail of displacement potentiometer.

1.2.5 Testing Protocol

Specimens were loaded axially using the 300 kip Baldwin Universal Loading Machine until they reached a push-through displacement of 1 in. The specimens are loaded at a constant target load rate of 12 k/min, or 1 kip every 5 sec. Measurements were monitored and recorded by a LabVIEW station (Figure 1.24). The instrument board was supplied with a constant 10V power supply. Measurements were recorded every 0.10 sec in order to achieve an appropriate data density.

Figure 1.24 LabVIEW station and 300 kip Baldwin Universal Loading Machine.

The compressive strength of the base concrete was monitored over time in order to make sure that the true strength on test day was close to the target value. Test day strengths were obtained for both column and footing elements. Due to time constraints, most of the bases were tested aged less than 28 days. This was accounted for in the design, and the target strength was achieved. Table 1.1 shows the testing schedule as executed.

Table 1.1 Testing schedule.

Test Event No.	Number Tested	Description
1	3	Smooth finish, varying steel areas and bond lengths
2	4	Identical chemically roughened tests varying steel location
3	12	Chemically roughened cylinders with varying finishes, timber rings, and bond lengths
4	6	Mechanically roughened cylinders with varying finishes
5	1	Monolithically cast specimen
6	3	Smooth finish with updated testing configuration
7	3	~4500 psi base strength, with chemically roughened finish
8	3	~7000 psi base strength, with chemically roughened finish
9	1	Monolithically cast specimen with confined added to the cylinder
10	3	~4000 psi base strength, with chemically roughened finish and separate mix characteristics
11	3	~9000 psi base strength, with chemically roughened finish

1.3 MEASURED RESPONSE

1.3.1 Material Properties

The concrete columns and footings were made in the University of Washington Concrete Materials Laboratory. Column and footing specimens were cast simultaneously with 4 in.×8 in. test cylinders. These cylinders were subsequently stored in the fog room at the University of Washington Concrete Materials Laboratory until they were needed for testing.

1.3.1.1 Concrete

The concrete used to create the columns and footings used pea gravel as coarse aggregate, building sand as fine aggregate, Type I/II Portland cement, water, and in certain mixes, Rheobuild FC 3000 High Range Water Reducer. Appendix B lists the two mix designs.

Compressive tests were performed on both the column and footing concrete. The footings had target strength of 2500 psi in order to minimize forces and complete testing on schedule. A separate series, τ / f_c', was given a wide range of target base strengths, in order to quantify the relationship between concrete compressive strength and push-through shear strength. This relationship is used to provide a correction factor for shear strength among varying footing compressive strengths. Figure 1.25 shows a compressive strength test after its completion. The strength of the footings was monitored in order to conduct each test when the concrete compressive strength was as near as possible to the target compressive strength. When the target strength was achieved, the compressive strengths of the precast columns were subsequently tested and recorded. Table 1.2 provides a summary of the test day strengths of both columns and footings.

Figure 1.25 Concrete test cylinder after a compressive strength test.

Table 1.2 Concrete compressive strength of footings and columns on test day.

Specimen Set	Footing		Column	
	Compressive Strength (psi)	Age (days)	Compressive Strength (psi)	Age (days)
Smooth	2233	3	8820	14
Steel Configuration	2209	3	3636	8
Chemical	2290	4	4128	7
Mechanical	2743	3	4513	8
Monolithic	4169	10	4169	10
τ/f_c' 1	4516	1	9494	15
τ/f_c' 2	6986	2	9528	16
τ/f_c' 3	4017	11	9902	19
τ/f_c' 4	8947	9	10285	23
Smooth 2	2318	3	4335	30

1.3.1.2 Steel

The reinforcement used for the footings was 60 ksi, three-gauge AWG wire. The wire was delivered to site pre-coiled, a process that yields the steel in bending and cause strain hardening to occur. This process makes testing the steel unreliable because it yields as it re-straightens; however, tensile strength, ultimate strength, and elastic modulus values were obtained as can be seen in Table 1.3. Due to the unreliable nature of the results, the steel was conservatively assumed to be behaving with strength characteristics as defined by the manufacturer.

Table 1.3 Steel wire testing results.

Property	Strength
Tensile Strength	91.71 ksi
Ultimate Strength	102.35 ksi

1.3.2 Shear Stresses

Applied forces were monitored by the load cell in the 300-kip Baldwin Universal Loading Machine. The forces were then divided by the bonded area to calculate the average measured shear stress:

$$\tau = \frac{P}{\pi D L_b} \tag{1.1}$$

where τ is the shear stress (ksi), P is the measured force (kips), D is the diameter of column (in.), and L_b is the bonded length (in.).

As the applied load began its initial increase, residual displacements of up to 0.03 in. were measured. Following the peak shear stress, the measured shear stress generally expressed a steep decline, followed by a less steep linear decline as the column continued to push through the base. Measurements were recorded through at least 1 in. of push through, but are reported to 0.5 in. for clarity.

Results from the six different roughening and construction techniques are summarized in Figure 1.26 through Figure 1.31.

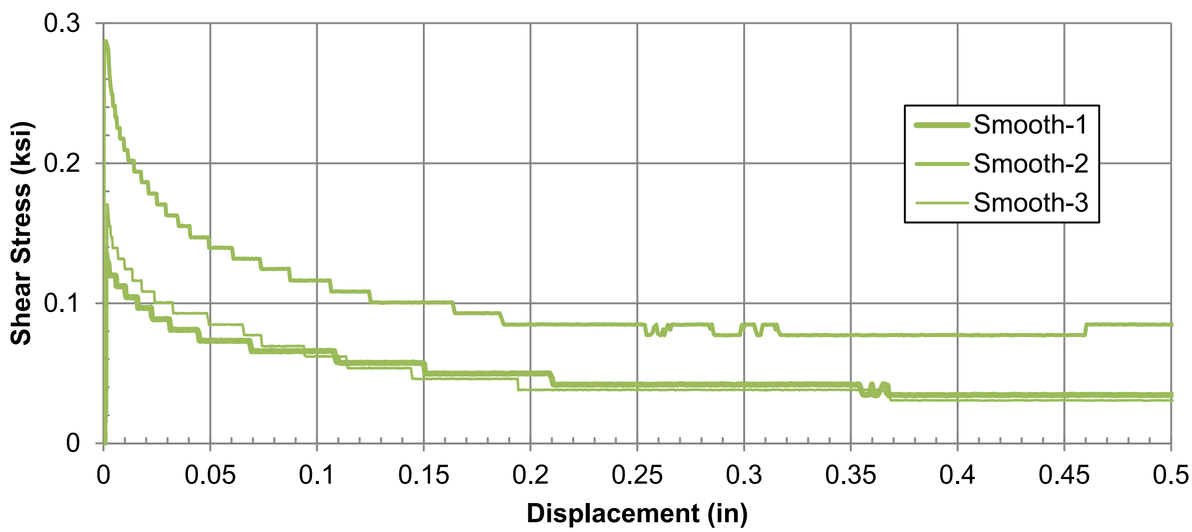

Figure 1.26 Shear stress versus displacement chart for nominally identical smooth specimens.

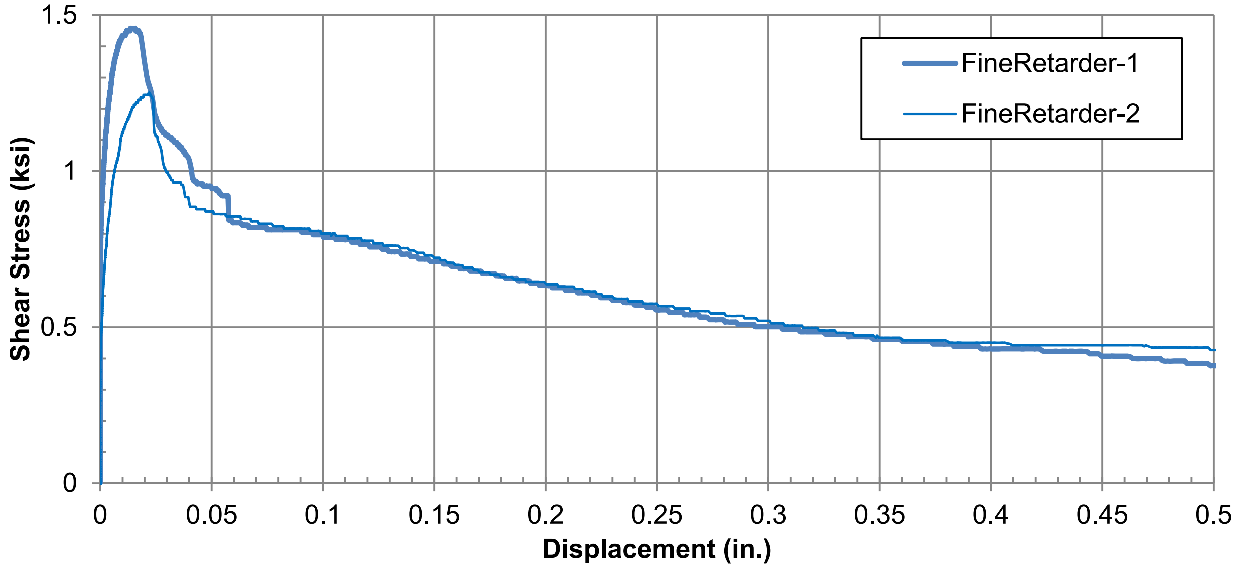

Figure 1.27 **Shear stress versus displacement chart for nominally identical fine retarder specimens.**

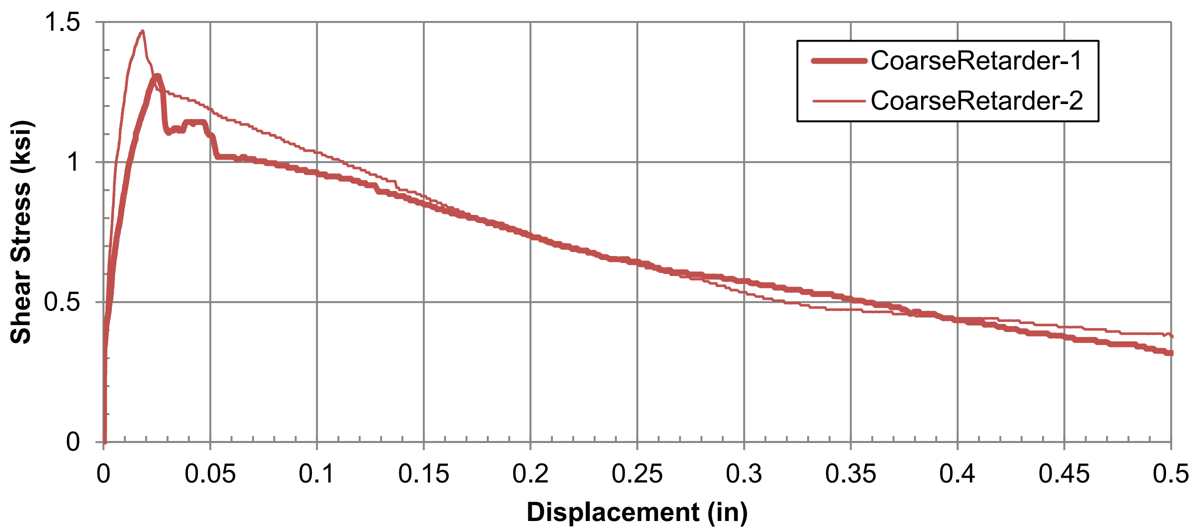

Figure 1.28 **Shear stress versus displacement chart for nominally identical coarse retarder specimens.**

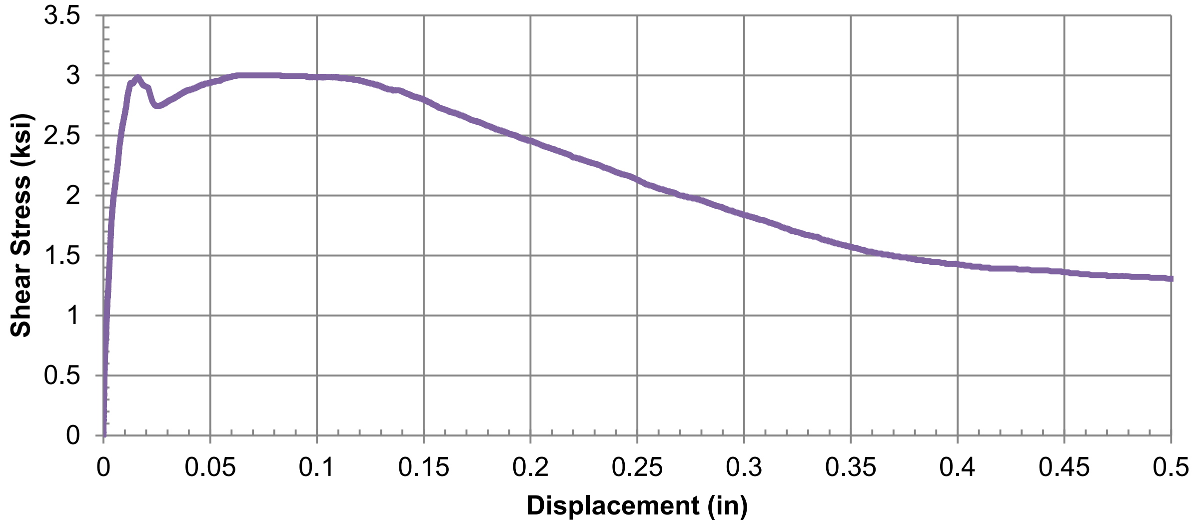

Figure 1.29 Shear stress versus displacement chart for monolithic specimen.

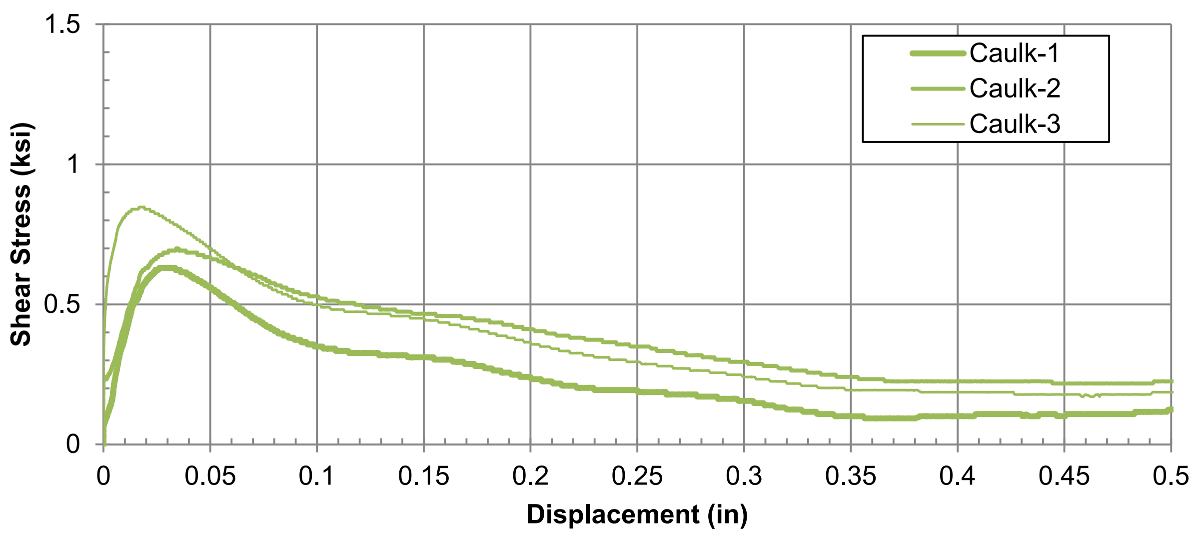

Figure 1.30 Shear stress vesus displacement chart for nominally identical caulk-comb mechanical roughening.

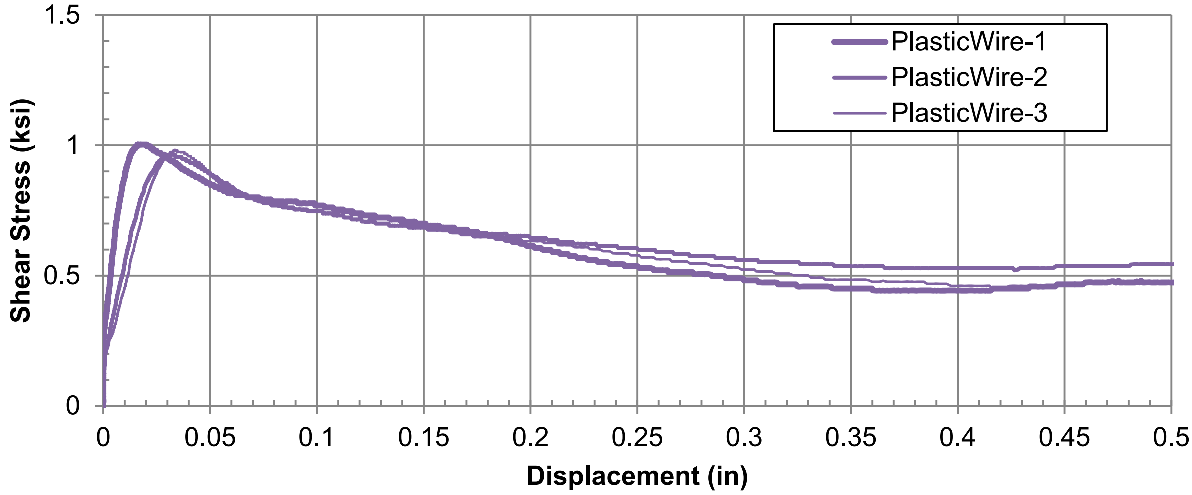

Figure 1.31 Shear stress versus displacement chart for nominally identical plastic wire mechanical roughening.

Shear stresses were reported at the peak and at 0.15 in. of slip in Figure 1.32. The peak shear measurement varied significantly between nominally identical samples and tended to be quite brittle; however, it serves as an indicator for the initial loss of bond among surrounding surfaces, and the presumed development of an internal crack plane.

The measurement at 0.15 in. of slip is included as well, as it is represents a push through of one tenth of the bonded length for samples of the standardized specimen design (L_b = 1.5 in.). In addition, 0.15 in. is 40% of the nominal coarse aggregate size of 3/8 in. Despite the relatively low angularity of pea gravel, it is presumed that protruding or revealed aggregate has engaged with the surrounding surface once slip has reached 0.15 in. Shear stress measurements also tended to cluster well near 0.15 in. of slip. Figure 1.32 charts the average measured shear stress for various roughening methods, with all other variables constant.

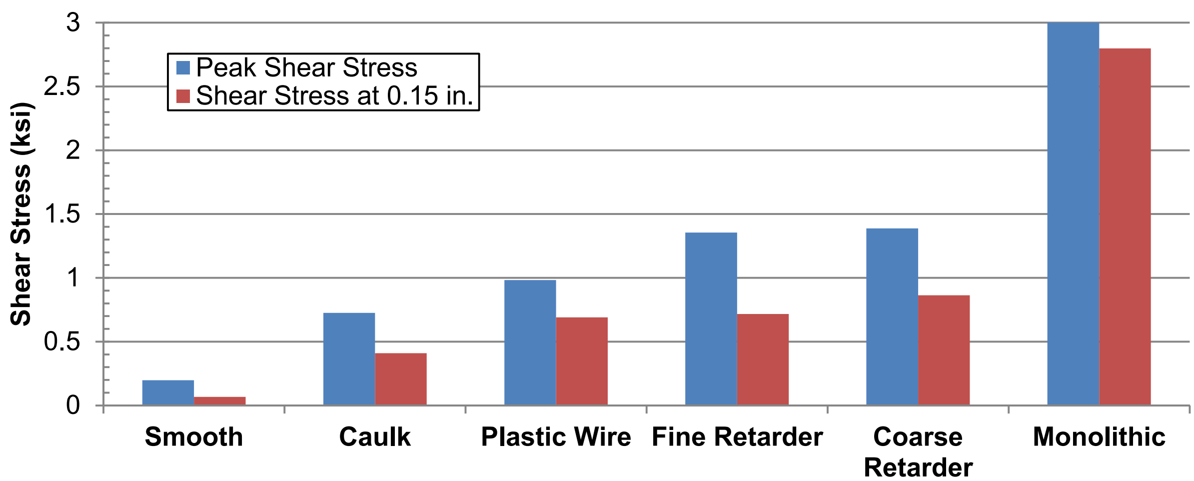

Figure 1.32 Measured shear stress plot for various roughening and construction conditions.

1.3.3 Observed Damage

Specimens were designed in order to force a push through failure while minimizing other damage. In cases where the load exceeded the compressive capacity of the cylinder prior to achieving adequate shear force to induce a push through failure, the cylinder was crushed, and the data was excluded.

1.3.3.1 Damage to Cylinder

Damage to the cylindrical precast columns was generally minimal. Specimens with the coarse chemical retarder roughening application sporadically lost individual pieces of coarse aggregate. This aggregate was initially above the column to footing interface, and was subsequently forced off of the surface of the column due to a short developed length between the piece of aggregate and the interior of the cylinder; see Figure 1.33.

Figure 1.33 Coarse retarder specimen with radial base cracking and forcibly loosened coarse aggregate caused via push-through.

1.3.3.2 Damage to Monolithically Cast Specimens

During monolithic testing, the resistance to push through and punching shear was significantly higher than in the composite specimens. During the first monolithically cast specimen test, the cylinder portion crushed prior to any push through failure. In order to reduce the likelihood of a concrete crushing failure in the column, the second monolithically cast specimen was tested with the column portion under confinement, forcing a push-through failure. This was achieved by placing a steel tube around the cylinder portion, and applying hydrostone on the interior of this region. A solid steel cylinder was then inserted into the tube to apply the axial force directly on the top of the cylinder portion of the specimen. A 1 in. gap was left below the steel tube and above the column to footing interface in order to allow for push-through to occur (see Figure 1.34).

After testing and achieving push through failure, the specimen was pulled apart and examined. It was determined that crushing occurred in the portion of the specimen that was pushing through the interior of the foundation region (Figure 1.35).

Figure 1.34 Second monolithically cast specimen prior to testing.

Figure 1.35 Crushed portion of monolithically cast specimen from foundation region.

1.3.3.3 Damage to Footing

The most significant damage to the specimens was in the form of radial cracking along the tops of the foundations (see Figure 1.36). They were attributed to hoop stresses induced in the foundation by the push-through process. The specimens were closely monitored visually and audibly for the occurrence of cracking. In cases where foundation cracking was observed, the cracks could be heard opening when the specimen reached the brittle peak and the column began to push through the bottom of the base. Cracking could also be heard sporadically as the column continued to push through. Cracks were measured and classified into categories of severity. Table 1.4 defines these categories, and Table 1.5 gives a summary of the types of cracking observed for each specimen variety.

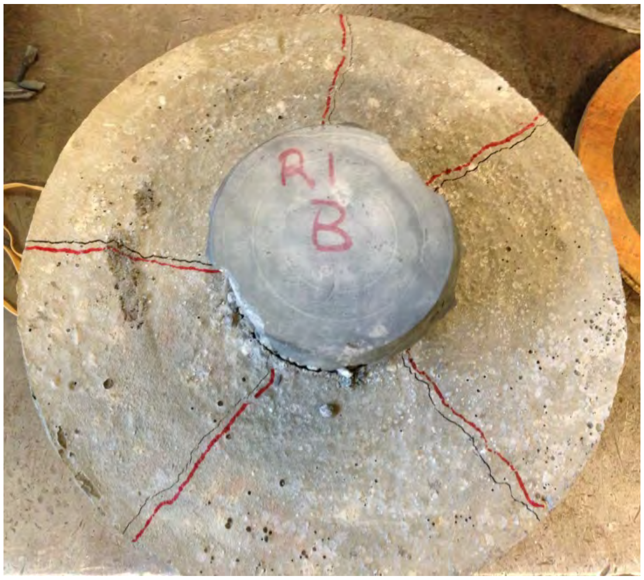

Figure 1.36 Radial cracking in foundation.

Table 1.4 Crack definitions.

Crack Type	Description
None	No cracking observed
Fine	Width < 0.07 in.
Moderate	0.07 in. ≤ width ≤ 0.09 in.
Significant	> 0.09 in.
Circumferential	Location of crack is along circumfrence of base

Table 1.5 Crack monitoring.

Specimen Type	Steel Configuration	Cracking Observed
Smooth	Bottom	Moderate cracking along top
Coarse Retarder	Bottom	Significant cracking along top
Fine Retarder	Bottom	Fine cracking along top
Coarse Retarder	Top and Bottom	Fine cracking along top
Fine Retarder	Top and Bottom	Fine cracking along top
Caulk and Trowel	Top and Bottom	No cracking observed
Plastic Wire	Top and Bottom	No cracking observed
Monolithically Cast	Top and Bottom	Significant cracking along top, significant circumferential compressive cracks
τ/f_c' 1	Top and Bottom	Moderate cracking along top
τ/f_c' 2	Top and Bottom	Moderate cracking along top
τ/f_c' 3	Top and Bottom	Moderate cracking along top
τ/f_c' 4	Top and Bottom	Moderate cracking along top
Smooth	Top and Bottom	No cracking observed

1.4 ANALYSIS OF MEASURED RESPONSE

In order to obtain a direct relationship between roughness and interfacial shear stress, variables that also affect shear stress needed to be identified and accounted for during specimen design and data analysis. In this section, the effect of base concrete strength, hoop steel reinforcement, bonded length, and support placement are determined before the effectiveness of the roughening methods is determined. The shear strengths are then compared to the current AASHTO shear friction provisions, and lastly, additional analysis is conducted to gain insight on shrinkage effects.

1.4.1 Effect of Hoop Steel Reinforcement

The initial specimen configuration was intended to have hoop steel 1 in. from the bottom of the foundation only as shown in Figure 1.37. A series of tests was conducted with smooth cylinders, 2 in. bond length, and variable steel area to determine if altering the amount of steel had any effect on the shear strength (see Table 1.6). They were tested at the start of the program, and served as pilot tests. However, they were the only tests in which the steel area was varied while other parameters were held constant.

Figure 1.37 Specimen with bottom steel only.

Table 1.6 shows that reducing the area of steel on the bottom resulted in a 5% increase in shear strength at the interface for a smooth specimen. This indicates that the bottom steel has little to no influence on shear strength. Additionally, while the specimen was being tested, moderately sized radial cracks formed on the upper surface of the foundation. This raised concern because the test specimen was designed to fail at the column-to-footing interface only, and this additional failure mode could potentially add inaccuracies to the shear stress data. As a result, an additional series of tests was conducted to investigate whether adding steel to the top of the foundation would provide enough confinement to inhibit radial crack formation as seen in Table 1.7.

Table 1.6 Shear stress at 0.15 in. displacement from varying area of bottom steel.

Area of Steel	Shear Stress (ksi) (smooth, 2-in. bond)
0.166 in.^{2}	0.250
0.232 in.^{2}	0.238

Table 1.7 Shear stress at 0.15 in. displacement from varying location and area of steel.

Location of Steel	Shear Stress (ksi) (Coarse Retarder, 3-in. bond)	Shear Stress (ksi) (Fine Retarder, 3-in. bond)
Bottom (0.232 in.^{2})	0.516	0.394
Top and Bottom (0.464 in.^{2})	>2.029	0.925

Adding hoop steel at the top of the foundation increased the shear strength by 135% in the specimen roughened with the fine retarder. Also, the specimen without top steel formed three moderate to significant radial cracks, while no cracking was observed in in the specimen with top steel. The presence of top steel proved to be necessary because it prevented moderate to significant cracks from forming in the foundation, thus preserving the desired failure mode. Without the top steel, the base tended to split at the top, which allowed the segments of the base to rotate outwards, away from the precast cylinder. The low shear strengths were attributed to this partial loss of contact at the column-to-footing interface.

The actual shear capacity could not be obtained in the specimen that was roughened with the course retarder and steel located at the top and bottom of the foundation because the cylinder failed in compression before it was able to push through the foundation. The value presented in Table 1.7 represents the axial capacity of the cylinder, which is less than the shear capacity of the interface.

1.4.2 Effect of Bonded Interface Length on Shear Stress

The purpose of investigating the behavior of specimens with different bond lengths was to ensure that the bonded region was large enough to incorporate a sufficient amount of roughened surface to yield accurate shear strength data, while maintaining an interface shear capacity that is below the axial capacity of the cylinder. If the length of the interface were to be comparable to the size of the aggregate, the number of pieces of aggregate providing interlock across the interface would be small, and might have to be counted individually, rather than simply evaluating the strength on an area basis. This concept provides an absolute minimum bonded length. If the distribution of shear stress along the bonded length (in the direction of loading) were not constant, then the bonded length might be expected to affect the average shear strength. The shear stresses corresponding to different bond length are presented in Table 1.8.

The specimens with a bonded length of 1.5 in. exhibited a shear strength that was 16.0% and 14.2% larger than the specimens with a 3 in. bonded length, respectively. This implies a nonlinear relationship between shear strength and bonded length. Contrary to expectations, the specimens with the larger bonded region produced more variable results than the specimens with the smaller bonded region. The average percent difference between identical specimens with a 3 in. bonded length was 18% while it was only 3% for the specimens with a 1.5 in. bonded length. Since the shorter bond length had a higher probability of failing in the desired manner along the shear interface and did not seem to exacerbate error, the remaining test specimens were constructed with a bond length of 1.5 in.

Table 1.8 Shear stress at 0.15 in. displacement from varying bonded length.

Bonded Length	Shear Stress (ksi) (Fine Retarder, Large Ring)	Shear Stress (ksi) (Fine Retarder, Small Ring)
1.5 in.	0.750	0.717
3 in.	0.646	0.628

1.4.3 Effect of Support Placement

In an effort to control the flow of forces, a timber ring was placed beneath each specimen during testing. By reducing the area of contact at the bottom surface between the specimen and the testing machine, the possible paths the force can take as it propagates through the specimen are limited. A series of tests were conducted utilizing a small ring (4.5 in. inner diameter, 7.5 in. outer diameter) placed beneath the test specimen and another with a large ring (8 in. inner diameter, 10 in. outer diameter). Figure 1.38 and Figure 1.39 show the small ring and large ring configurations. Table 1.9 shows the shear stresses obtained with the varying ring sizes.

The specimens with the large ring generally resulted in a slight increase in the shear stress. Altering the ring size had little to negligible effects on the shear strength, subsequent tests were conducted using the small timber ring.in order to minimize additional radial stress in the connection region.

Figure 1.38 Small timber ring support.

Figure 1.39 Large timber ring support.

Table 1.9 Shear stress at 0.15 in. displacement from varying ring size.

Ring Size	Shear Stress (ksi) (Coarse Retarder, 1.5-in. bond)	Shear Stress (ksi) (Fine Retarder, 1.5-in.bond)	Shear Stress (ksi) (Fine Retarder, 3 in.-bond)
Small Ring	0.863	0.717	0.628
Large Ring	0.999	0.750	0.646

1.4.4 Effect of Base Concrete Strength on Shear Stress

A series of tests was conducted on specimens with different base strengths while the remaining variables were kept constant. The relationship between base concrete compressive strength, f_c', is shown in Figure 1.40.

The peak shear stress and the shear stress at 0.15 in. displacement increased with increasing f_c' in a non-linear fashion that resembles a root function. Knowing this, the measured shear stress can be normalized by $\sqrt{f_c'}$ to eliminate the effect of base strength on the desired results and allow for comparison amongst specimens with different base strengths (see Equation 1.2). Figure 1.41 demonstrates that comparing the measured shear stress and $\sqrt{f_c'}$ result in a linear relationship.

$$\tau_{normalized} = \frac{\tau_{measured}}{\sqrt{f_c'}} \tag{1.2}$$

Additionally, since two mix designs were used (see Appendix B), a series of test were done to determine if the mix design had an effect on the shear strength. Two sets of specimens, one composed of Mix A and one from Mix B, were tested with a target compressive strength of 4000 psi. The resulting shear strengths were close enough to conclude that the mix design has a negligible effect on the interfacial shear capacity at a given compressive strength.

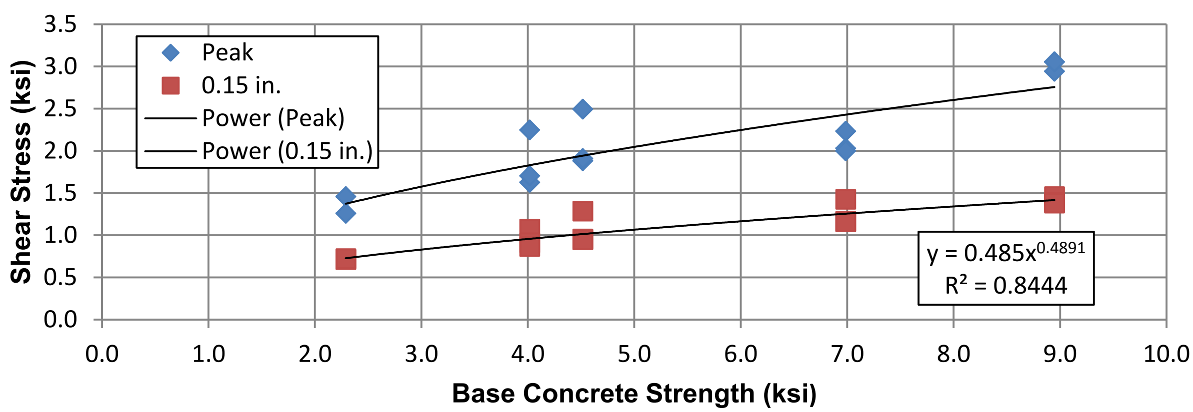

Figure 1.40 Relating the base concrete strength and shear stress.

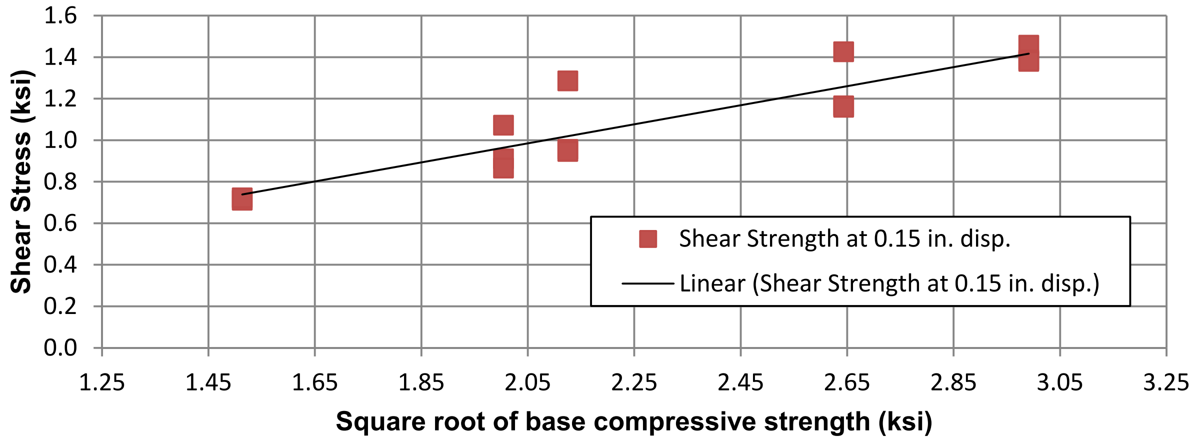

Figure 1.41 Relating the square root of base concrete strength and shear stress.

1.4.5 Effectiveness of Roughening Methods

The use of in-mold cement retarder resulted in a surface roughening composed mostly of exposed coarse aggregate. This occurs because the cement paste near the surface of the cylinder reacts with the retarder in such a way that inhibits the curing process. Once the core of the cylinder has set, the affected cement paste on the surface can be easily removed, leaving an exposed aggregate finish.

The two types of cement retarder used in this experiment differ by depth of penetration. The coarse retarder was the more aggressive of the two and resulted in an average depth of 0.08 in., while the fine retarder resulted in an average depth of 0.025 in. Table 1.10 compares the shear strengths of specimens that were treated with the different cement retarders. The shear strength achieved when using the coarse retarder was 20–33% greater than the shear strength of the specimens treated with the fine retarder. The coarse finish provided larger grooves in which the fresh footing concrete could fill, which proved to create a stronger interfacial bond.

The two mechanical methods used were meant to mimic the current method of roughening (triangular timber strips forming a saw-tooth pattern), which leaves corresponding ridges in the specimen. The timber strip method cannot be implemented on a curved surface, however; therefore, the novel mechanical methods had to work on a column with a circular cross section. Table 1.11 presents the shear strength of the specimens that were treated with the mechanical methods of roughening.

Even though the caulk and trowel method had the potential to produce deeper ridges, it performed worse than the plastic wire method. This could be due to the lack of repeatability of the caulk and trowel method. Creating a surface with uniformly sized ridges was much more difficult to achieve with the caulk and trowel method, leaving portions of the cylinder's surface with less roughening than others.

Table 1.10 Shear stress at 0.15 in. displacement from varying chemical retarder.

Chemical Roughening	Shear Stress (ksi) (small ring, 1.5-in. bond)	Shear Stress (ksi) (large ring, 1.5-in. bond)
Coarse Retarder (0.08 in. depth)	0.863	0.999
Fine Retarder (0.025 in depth)	0.717	0.750

Table 1.11 Shear stress at 0.15 in. displacement from different mechanical methods.

Mechanical Roughening	Shear Stress (ksi) (small ring, 1.5-in. bond)
Caulk and Trowel (0.0625 in. max depth, .095 in. spacing)	0.409
Plastic Wire (0.045 in. max depth, 0.095 in spacing)	0.690

Table 1.12 Normalized shear stress at 0.15-in. displacement.

Specimen Type	Normalized Shear Stress (√ksi) (small ring, 1.5-in. bond)
Smooth	0.044
Caulk and Trowel (0.0625 in. depth, .095 in. spacing)	0.247
Plastic Wire (0.045 in. depth, 0.095 in spacing)	0.417
Fine Retarder (0.025 in. depth)	0.474
Coarse Retarder (0.08 in. depth)	0.570
Monolithic	1.370

Additionally, it was decided that the results obtained from both of the mechanically roughened specimens may not be valid due to scaling imperfections. The ridges were too small to engage the 3/8 in. coarse aggregate; therefore, it is assumed that only cement paste and fine sand were incorporated in the failure plane. In an actual sized column, the ridges are large enough to incorporate coarse aggregate so shear strength of the connection should be reasonably different. However, for purposes of comparison, the results obtained from the mechanically roughened specimens are used for the remainder of the report.

To obtain an accurate comparison between roughened, smooth, and monolithic specimens, the shear stresses were normalized by dividing the measured value by $\sqrt{f_c'}$ [see Equation (1.2)]. The average normalized shear stresses for each specimen type can be seen in Table 1.12 and Figure 1.42.

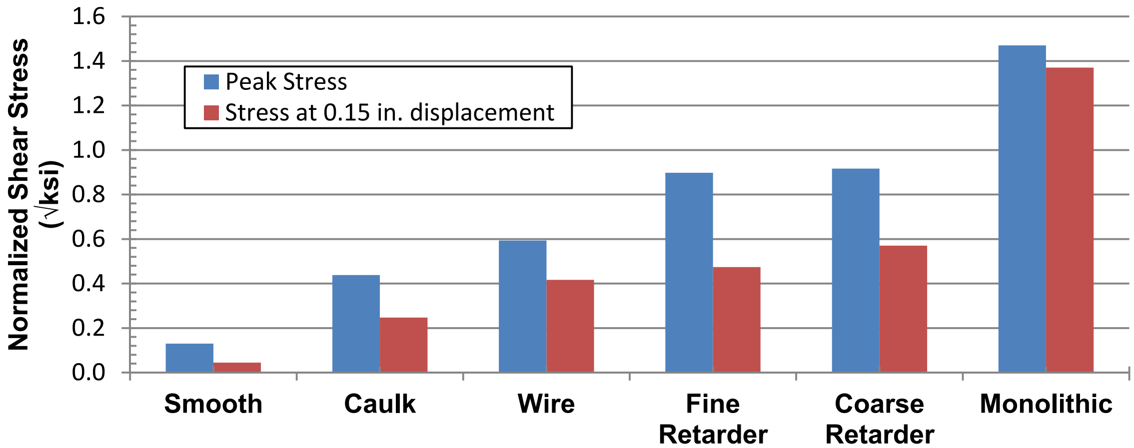

Figure 1.42 Normalized shear stress plot.

As expected, the smooth specimen failed at the lowest shear strength while the monolithic specimen failed at the highest shear strength. Also, chemical roughening performed better than mechanical roughening. The caulk and trowel method resulted in an average normalized shear stress at 0.15 in. that was 5.6 times greater than that of the smooth specimens, the plastic wire was 9.5 times greater, the fine retarder was 10.8 times greater, and the course retarder was 13 times greater than the smooth specimens. When comparing normalized peak stresses, there was even greater separation between the chemically and mechanically roughened specimens.

1.4.6 Comparison with AASHTO Shear Friction Provisions

Article 5.8.4 of the *AASHTO LRFD Bridge Design Specifications* [AASHTO 2012] prescribes the nominal shear resistance of an interface plane as follows:

$$V_n = cA_{cv} + \mu\left(A_{vf} f_y + P_c\right) \tag{1.3}$$

where V_n shall not be greater than the lesser of:

$$V_n \le K_1 f_c' A_{cv} \tag{1.4}$$

$$V_n \le K_2 A_{cv} \tag{1.5}$$

The cohesion factor, c, the friction factor, μ, the fraction of concrete strength available to resist interface shear, K_1, and the limiting interface shear resistance, K_2, are not specified for an intentionally roughened surface with an amplitude of less than 0.25 in. in article 5.8.4. However, Marsh et. al. [2013] recommend that the cohesion factor, c, be taken as zero to account for potential shrinkage cracking around the column and for the friction factor, μ, and the factors K_1 and K_2 to be taken as those for normal-weight concrete placed against a clean concrete surface specified in article 5.8.4. This makes $\mu = 0.6$, $K_1 = 0.2$, and $K_2 = 0.8$ ksi. Note that the base is cast after the column, so differential shrinkage would cause the base to tighten against the column, and not pull away from it. Thus using $c = 0.0$ is very conservative in this case.

The areas of concrete considered to be engaged in interface shear transfer, A_{cv} (in^2), and the area of steel reinforcement, A_{vf}, are known to be 18.85 in.^{2} and 0.232 in.^{2}, respectively. Additionally, the yield strength of the steel, f_y, is taken as 60 ksi, and the compressive force normal to the shear surface, P_c, is taken as zero which gives a more conservative value. The nominal shear resistance obtained from Equation (1.4) was converted to a shear stress by dividing by A_{cv} and then plotted against the measured shear stresses as seen in Figure 1.43.

Each roughening method produced a peak shear stress that exceeds the AASHTO capacity while all but the caulk and trowel method produced a shear stress at 0.15 in. displacement that exceeds it as well. Based on this design criterion, a lack of roughening (i.e., a smooth surface) is completely inadequate, but the peak strength for both retarders exceeds the AASHTO capacity by a factor of more than two.

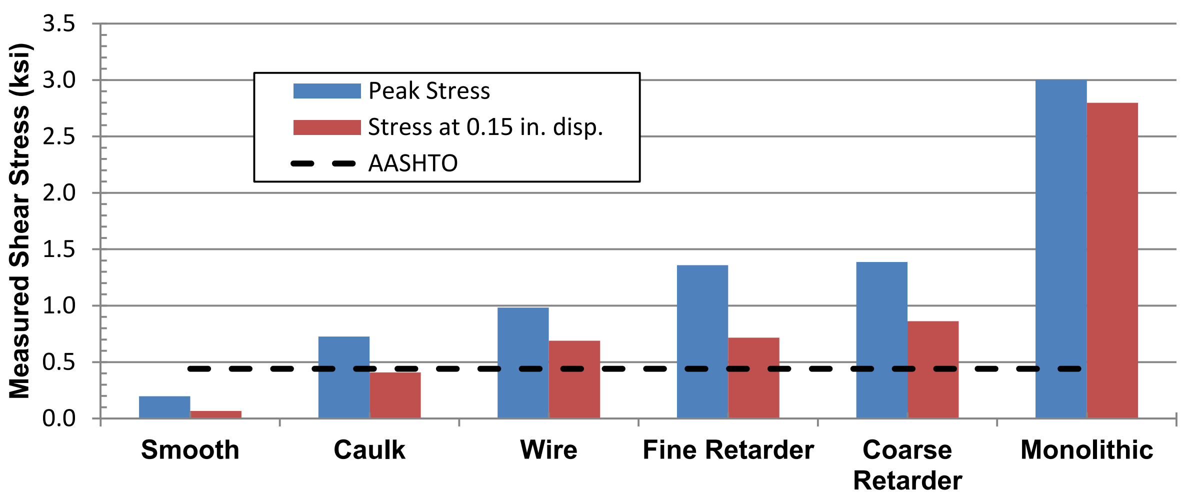

Figure 1.43 Comparing measured shear stress with AASHTO nominal capacity.

1.4.7 Shrinkage Analysis

Since the concrete in the column is cast before the concrete in the footing, it is expected that the footing will experience greater shrinkage than the column, thus producing radial and hoop stresses at the interface in both the column and the footing. An analysis was conducted in which the column, footing, and steel were treated as four concentric thick-walled cylinders (see Appendix C). Once the stress and deformations of a single, isolated cylinder under pressure and environmental loadings were obtained, post-shrinkage stresses between the four distinct cylinders were acquired by ensuring that the radial displacements were compatible and the radial stresses were in equilibrium at the interfaces.

This analysis showed (1) that the hoop steel reinforcement had almost no effect on the shrinkage effects. Shrinkage values of 200 and 500 $\mu\varepsilon$ were assumed for the precast cylinder and cast-in-place base respectively, and they led to a radial stress at the column-to-footing interface of 0.365 ksi. This suggests that shrinkage effects may significantly increase the interfacial shear capacity of the connection by imposing a non-trivial radial compressive stress on the column, which in turn creates friction capacity across the interface. The calculated peak hoop stress in the footing was 0.835 ksi, which exceeds the cracking strength of the footing concrete. In most of the specimens no shrinkage cracks were observed, so the assumed differential free shrinkage of 300 $\mu\varepsilon$ is probably too high. If the tensile strength of the base concrete were taken as $6\sqrt{f_c'}$, the differential shrinkage required to just cause cracking would be 113 $\mu\varepsilon$, and the radial stress would be 0.138 ksi. This stress is still enough to contribute to the interface shear capacity by friction. The radial stress, and thus the contribution to the shear capacity, depends on the relative diameters of the column and footing, so the additional shear capacity to be expected in a field application would have to be computed using the correct footing geometry.

1.5 SUMMARY AND CONCLUSIONS

1.5.1 Summary

The current method of achieving an intentionally roughened surface on a precast column developed for concrete bridges in seismic regions with a specified socket connection detail is relatively labor intensive; it requires numerous triangular timber strips to be manually cut and attached to a sheet of plywood before the formwork is assembled. Also, the practicality of this method is limited because it can only create roughening on a flat surface. This report describes the implementation and performance of novel roughening methods designed to both improve the constructability and practicality of the socket connection and create a roughened surface that provides adequate interfacial shear resistance under axial loading.

A final test specimen configuration (see Figure 1.4) was decided after conducting pilot tests in which the effects of hoop steel reinforcement, bond interface length, and support placement on the interfacial shear stress between the roughened precast column and cast-in-place footing were explored. Additional testing was done to determine the effect of the concrete strength of the footing on the shear strength. This permitted the most direct relationship between roughening and shear strength.

The methods of roughening used in this experiment were categorized as a chemical or a mechanical method of roughening. The chemical method utilized in-mold cement retarder. Two types of retarder were used, resulting in either a "fine" or a "coarse" finish. The two mechanical methods used were referred to as the "caulk and trowel" method, and "plastic wire" method. At least two specimens with the final test configuration were tested for a given roughening method. In addition, three non-roughened, smooth surfaced specimens and two monolithically cast specimens were tested to serve as a basis of comparison.

1.5.2 Conclusions

The following conclusions were drawn:

1. In-form cement retarder was the easiest to apply and consistently created a uniform roughness.
2. The plastic wire method created a uniform roughness but wrapping the wire was time consuming.
3. The caulk and trowel method was less time consuming than the plastic wire method, but it was difficult to create a uniform roughness.
4. The chemically roughened specimens performed better than the mechanically roughened specimens.
5. The shear strength data gathered from the mechanically roughened specimens may not be valid due to scaling imperfections and needs verification before use.
6. Each method of roughening resulted in a peak shear strength that exceeds the shear resistance based on current AASHTO shear provisions. For all but the caulk and trowel method, the shear stress at 0.15 in. displacement exceeded the AASHTO capacity as well.
7. In-form cement retarders are a viable means of roughening for the socket connection, but results should be confirmed by larger scale tests before field implementation.

1.5.3 Recommendations for Future Research

The chemically roughened specimens provided adequate shear resistance under purely axial loading, but further testing needs to be done on a larger scale to determine the effectiveness of the connection under axial and cyclic lateral loading. Also, the *AASHTO Guide Specifications for LRFD Seismic Bridge Design* does not provide specifications on achieving an intentionally roughened surface, so additional research should be done to obtain values for the cohesion factor, c, and the friction factor, μ, for specific methods of roughening. In addition, concrete shrinkage may have significant effects on the shear capacity of the connection based on thick-walled cylinder analysis, so further research is needed to confirm this conclusion based on experimental data. Lastly, further investigation should be done to compare the effectiveness of different types of aggregate. The differing surface characteristics of crushed aggregate versus river-rounded aggregate could potentially have a significant effect on the shear strength.

1.6 ACKNOWLEDGMENTS

This research was supported by the Pacific Earthquake Engineering Research Center (PEER) and the National Science Foundation (NSF) and would not have been possible without the help from graduate students, faculty, and staff at the University of Washington. We would like to thank our graduate student mentors Bryan Kennedy and Jeffrey Schaefer, as well as our faculty mentors Professors John Stanton and Marc Eberhard for their guidance and support throughout this project. Thank you to Travis Thonstad and Vince Chaijaroen for assisting with instrumentation, and Spencer Livermore and Yiming Liu for assisting with materials testing. Lastly, we want to thank Heidi Tremayne for organizing this internship program and giving us this amazing opportunity to explore our interest in earthquake engineering research.

1.7 REFERENCES

AASHTO (2012). *AASHTO Guide Specifications for LRFD Seismic Bridge Design*, American Association of State Highway and Transportation Officials, 6th ed., Washington D.C.

Culmo M.P. (2009). Connection details for prefabricated bridge elements and systems, *Publication FHWA-IF-09-010*, Federal Highway Administration, Washington D.C.

Haraldsson O.S., Janes T., Eberhard M.O., Stanton J.F. (2013). Seismic resistance of socket connection between footing and precast column, *J. Bridge Eng.,* 18(9): 910–919.

Hieber D., Wacker J., Eberhard M.O., Stanton J.F. (2005). Precast concrete pier systems for rapid construction of bridges in seismic regions, *Washington State Department of Transportation Report No. WA-RD-511.1*, Washington State Department of Transportation, Washington.

Khaleghi B. (2010). Washington State Department of Transportation plan for accelerated bridge construction, *Transportation Research Record*, (2200): 3–11.

Khaleghi B., Schultz E., Seguirant S., Marsh M.L., Haraldsson O.S, Eberhard M.O., Stanton J.F. (2012). Accelerated bridge construction in Washington State: From research to practice, *PCI Journal*, Precast/Prestressed Concrete Institute, pp. 34–49.

Marsh M.L. Wernli M., Garrett B.E., Stanton J.F., Eberhard M.O., Weinert M.D. (2011). System performance of accelerated bridge construction (ABC) connections in moderate-to-high seismic regions, National Cooperative Highway Research Program, *Synthesis of Highway Practice Report 698*, Washington, D.C.

Marsh M.L., Stringer S.J., Stanton J.F., Eberhard M.O., Haraldsson O.S., Tran H.V., Khaleghi B., Schultz E., Seguirant S. (2013). Precast bent system for high seismic regions, Final report, Appendix A: Design provisions, *Publication No. FHWA-HIF-13-037-A*, Federal Highway Administration, Washington, D.C.

Timoshenko S. (1941). *Strength of Materials, Part II, Advanced Theory and Problems*, 2nd ed., D. Van Nostrand Company, New York.

1.8 APPENDIX A: SHEAR STRESS VERSUS DISPLACEMENT PLOTS

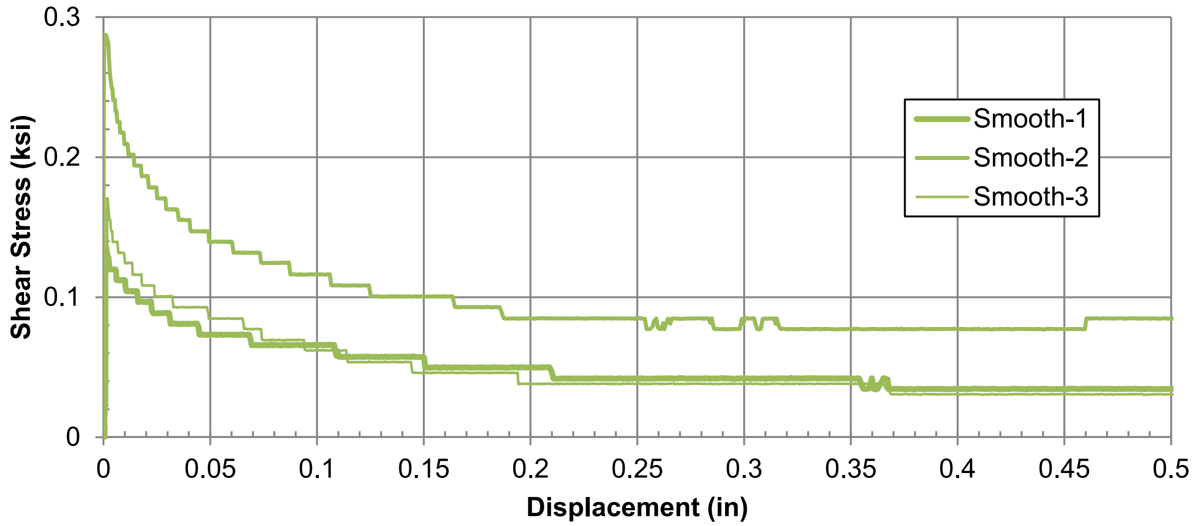

Figure A.1 **Shear stress versus displacement chart for nominally identical smooth specimens.**

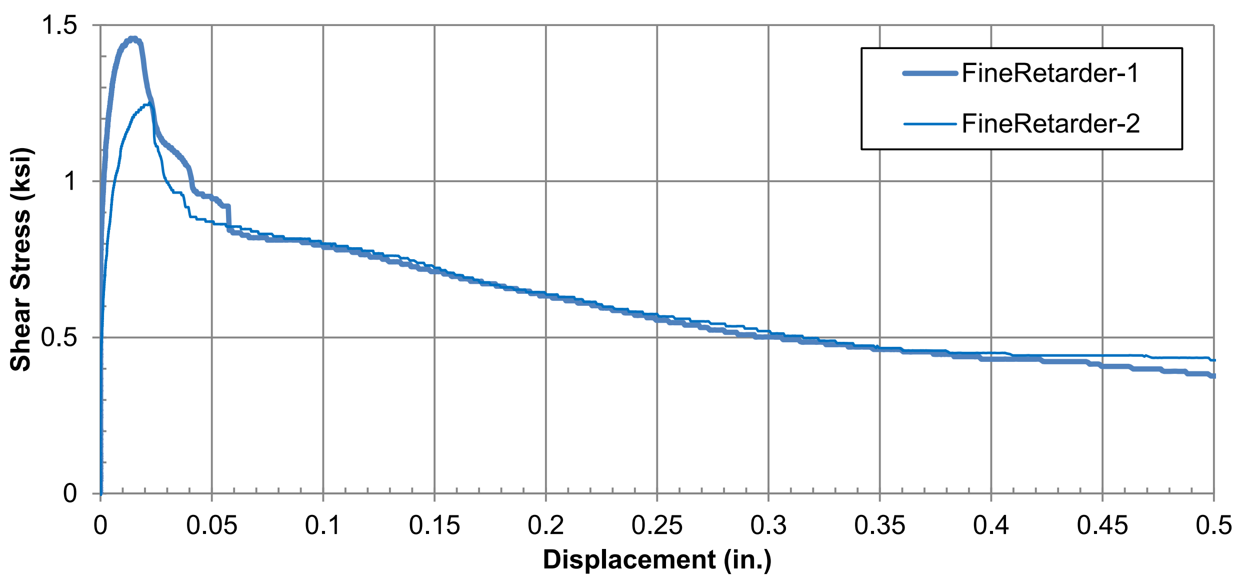

Figure A.2 **Shear stress versus displacement chart for nominally identical fine retarder specimens.**

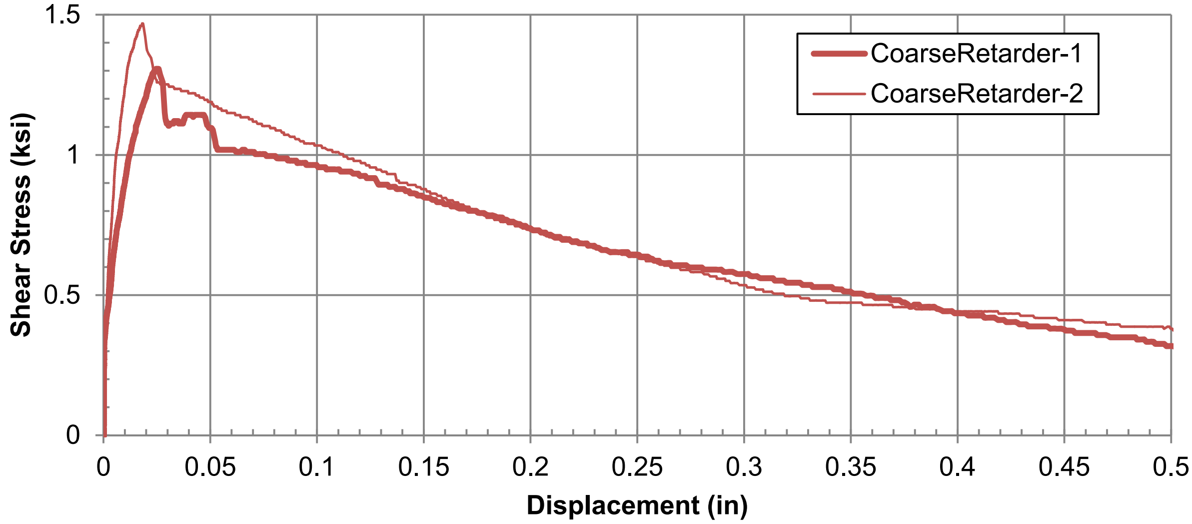

Figure A.3 Shear stress versus displacement chart for nominally identical coarse retarder specimens.

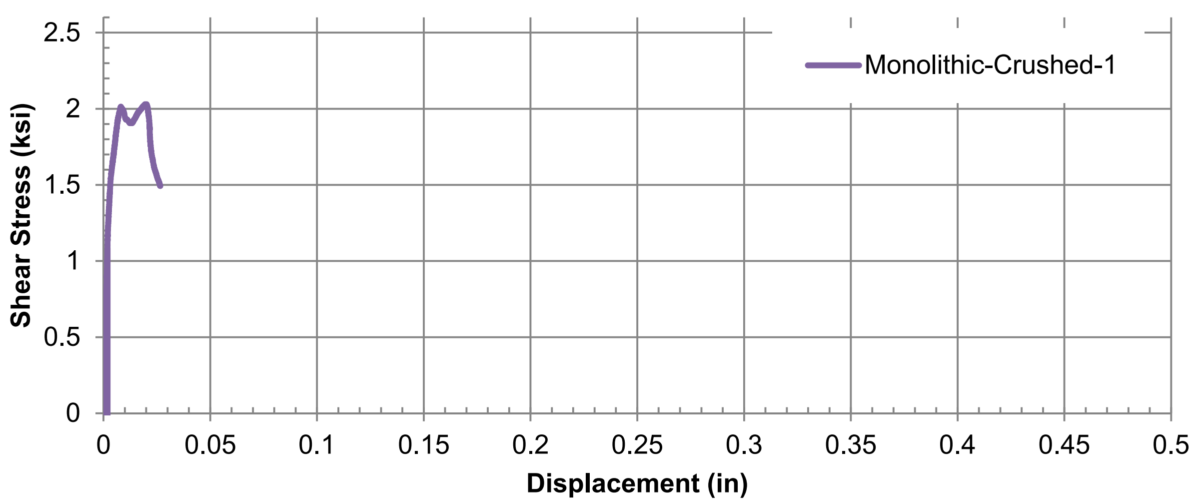

Figure A.4 Shear stress versus displacement chart for non-constrained monolithic specimen, in which the cylinder portion failed in compression.

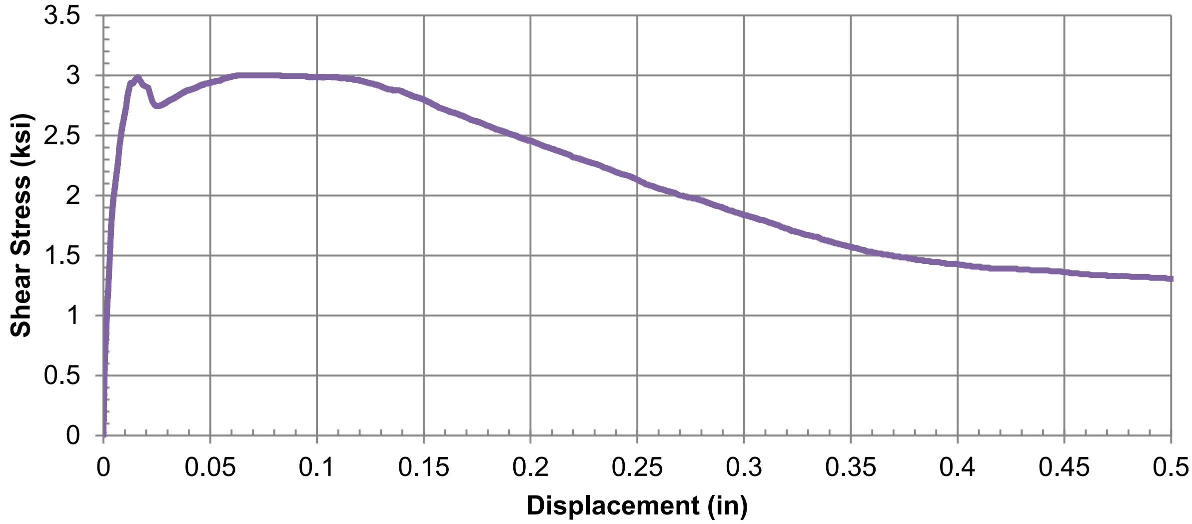

Figure A.5 **Shear stress versus displacement chart for confined monolithic specimen.**

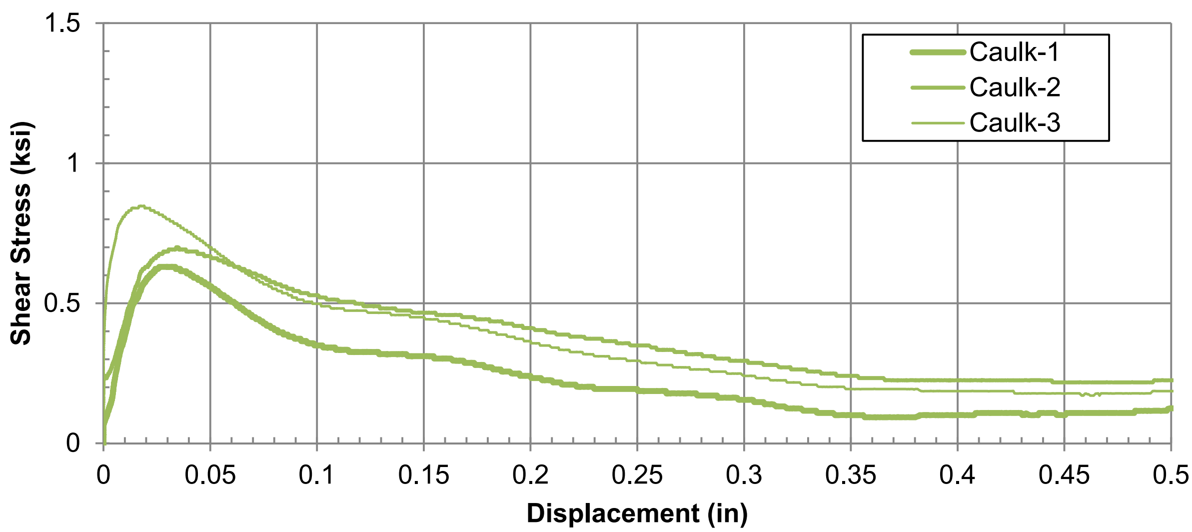

Figure A.6 **Shear stress versus displacement chart for caulk-comb mechanical roughening.**

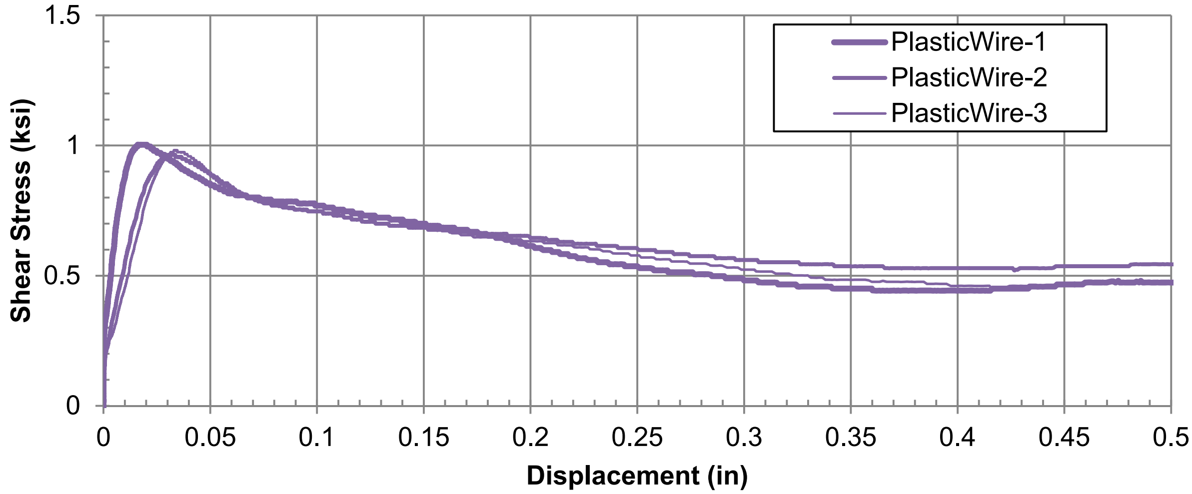

Figure A.7 **Shear stress versus displacement chart for plastic wire mechanical roughening.**

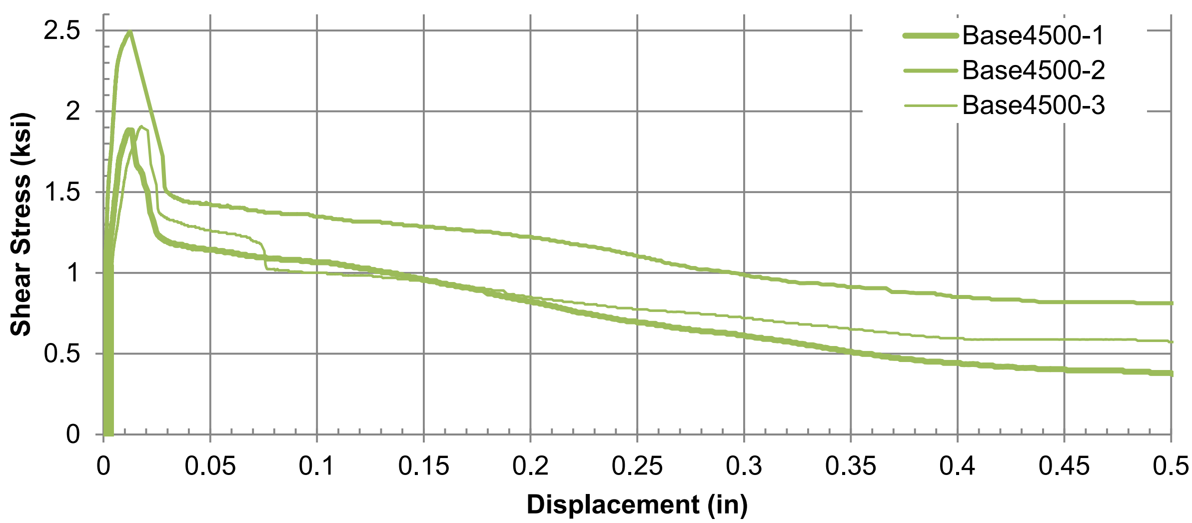

Figure A.8 **Shear stress versus displacement chart for fine retarder chemical roughening with base compressive strength of 4500 psi.**

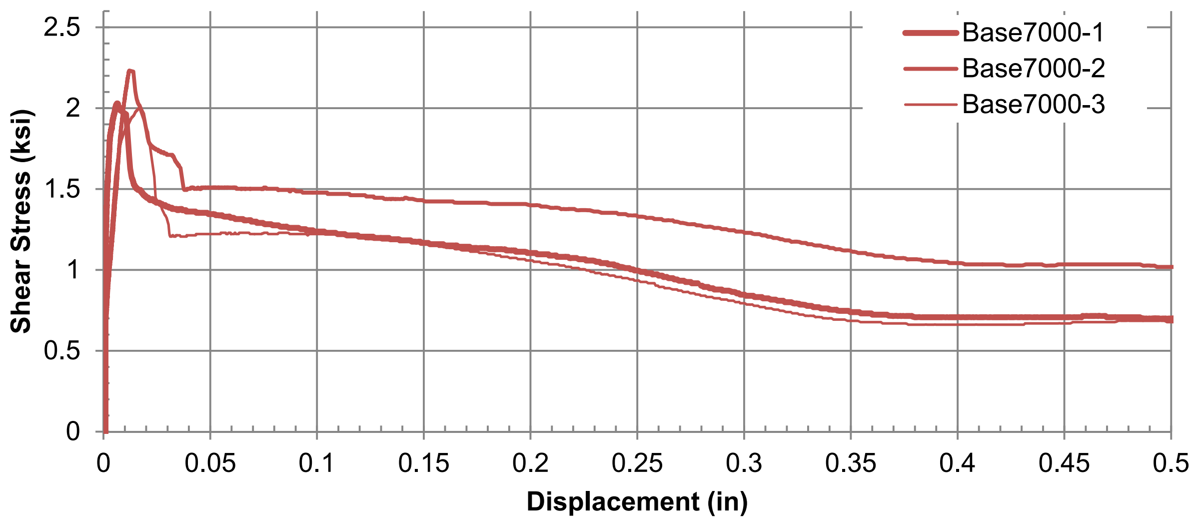

Figure A.9 **Shear stress versus displacement chart for fine retarder chemical roughening with base compressive strength of 7000 psi.**

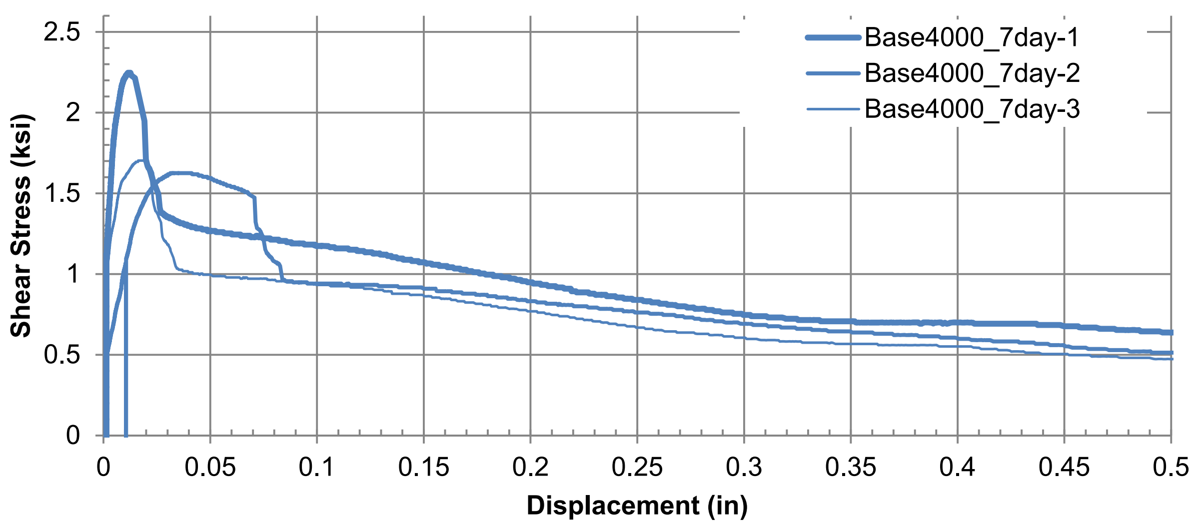

Figure A.10 **Shear stress versus displacement chart for fine retarder chemical roughening with base compressive strength of 4000 psi.**

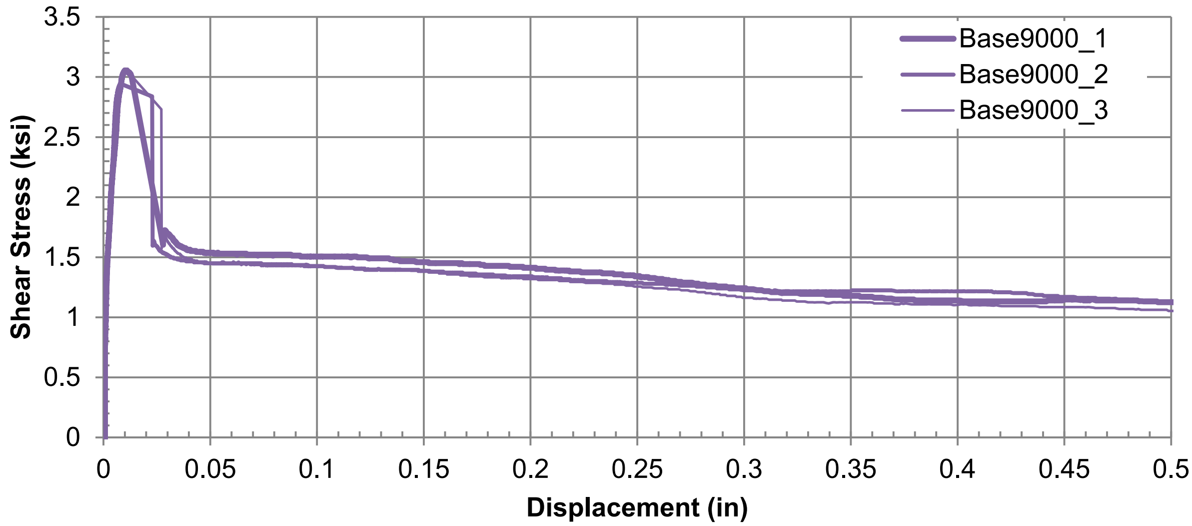

Figure A.11 Shear stress versus displacement chart for fine retarder chemical roughening with base compressive strength of 9000 psi.

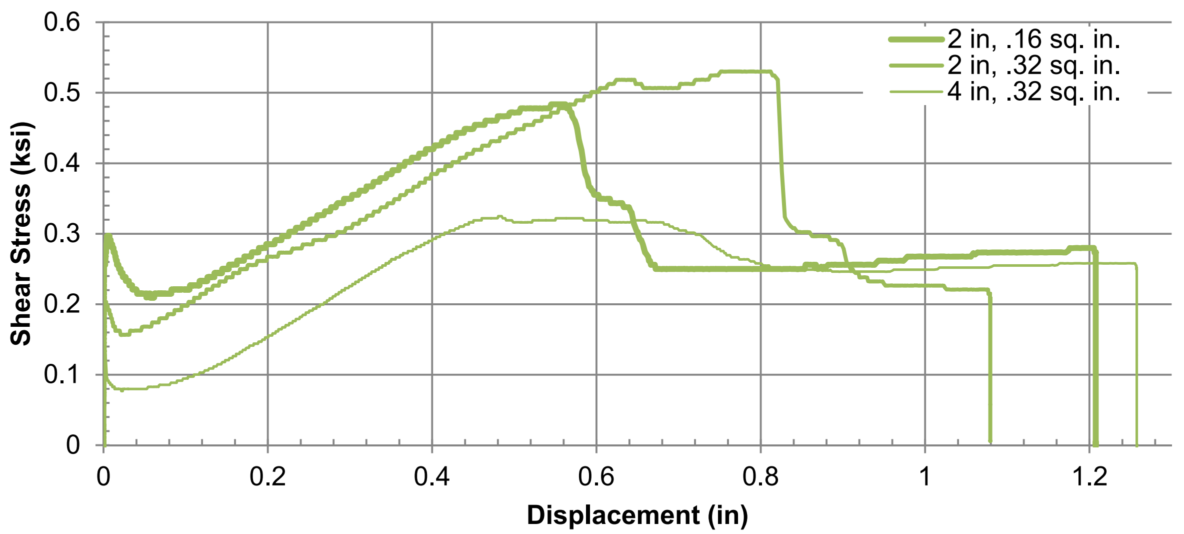

Figure A.12 Shear stress versus displacement chart for smooth cylinders without top steel ring or timber ring, varying bond length, and steel area.

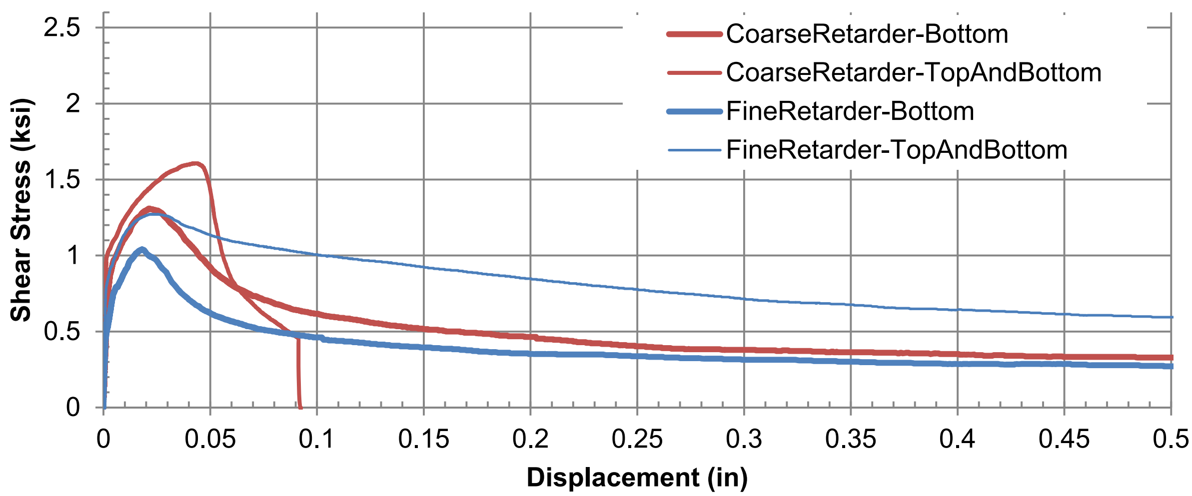

Figure A.13 **Shear stress versus displacement chart for coarse and fine chemical roughening, varying steel configuration.**

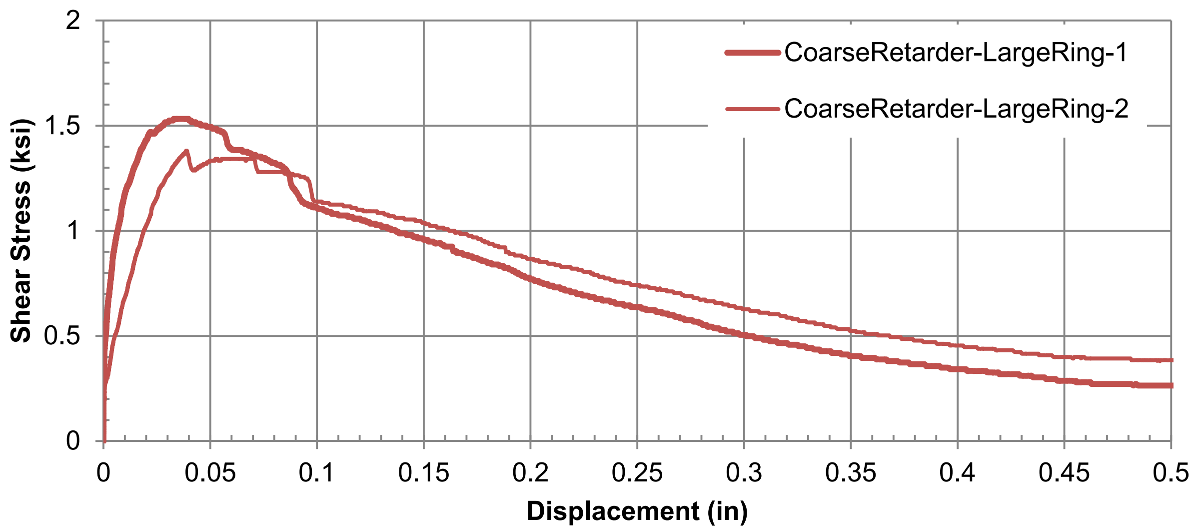

Figure A.14 **Shear stress versus displacement chart for coarse chemical roughening using large timber ring.**

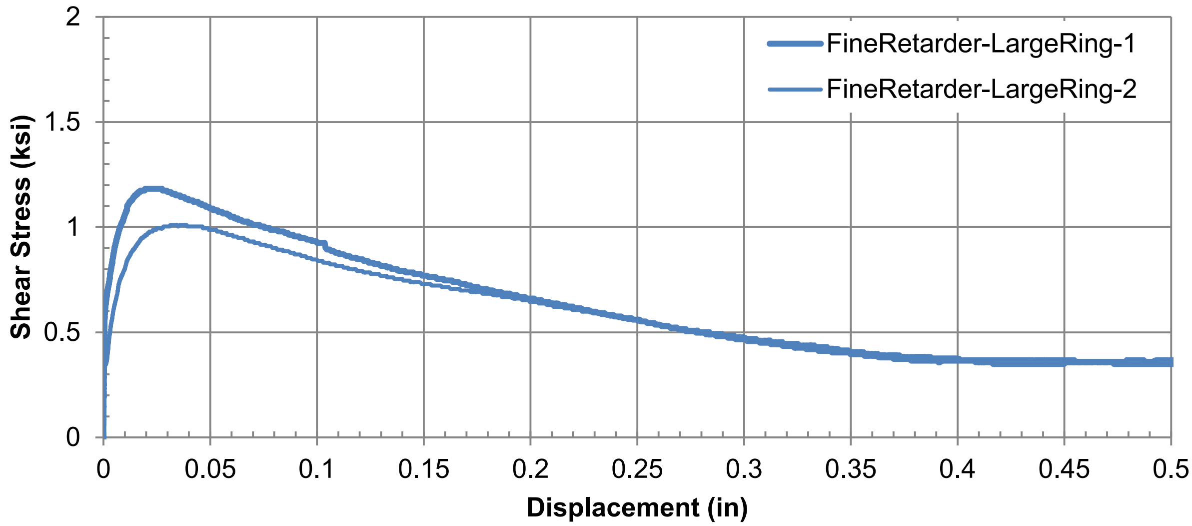

Figure A.15 **Shear stress versus. displacement chart for fine chemical roughening using large timber ring.**

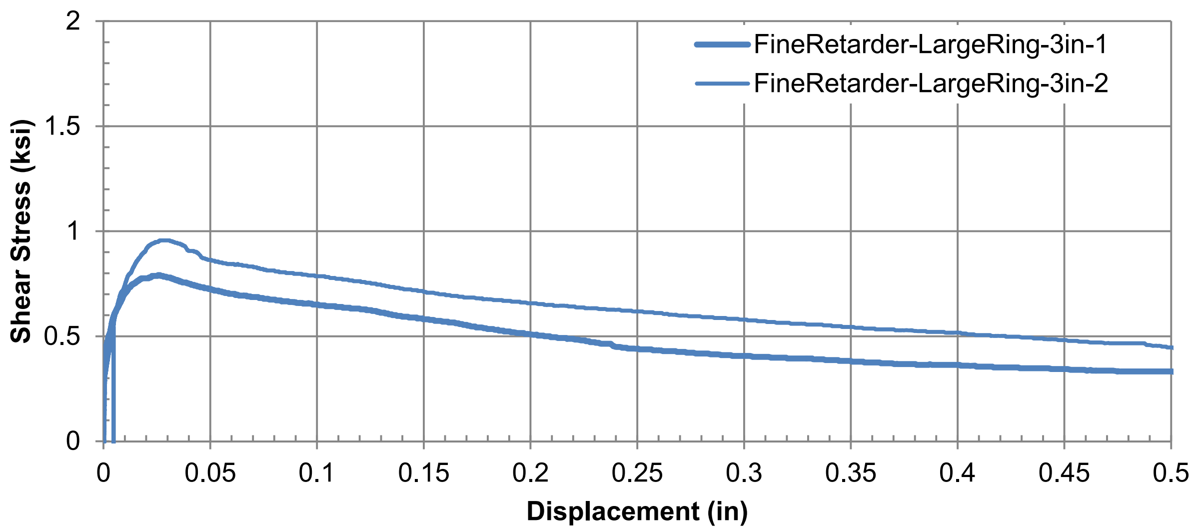

Figure A.16 **Shear stress versus displacement chart for fine chemical roughening, 3 in. bond length, and large timber ring.**

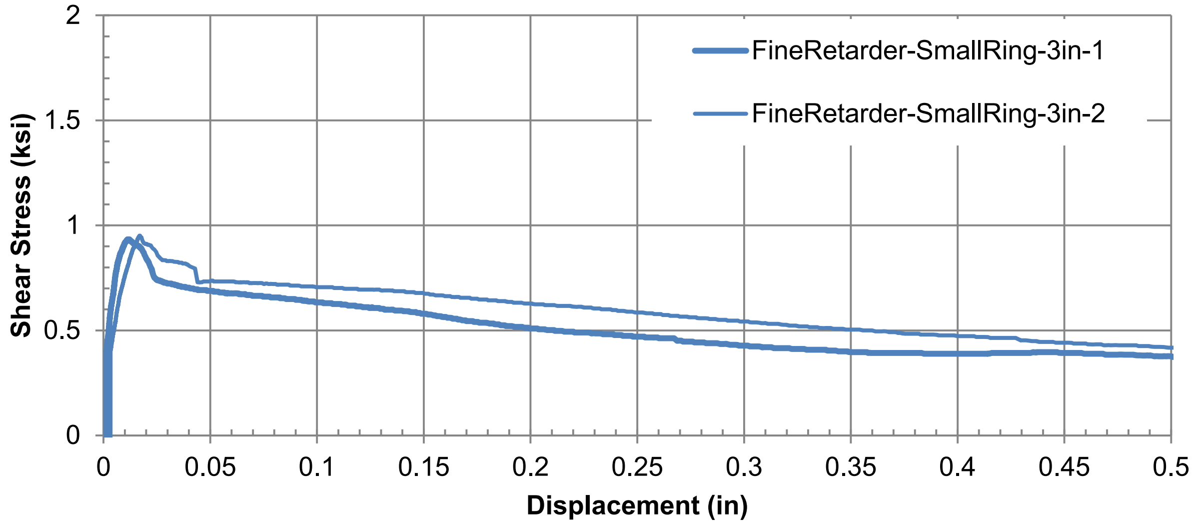

Figure A.16 **Shear stress versus displacement chart for fine chemical roughening, 3 in. bond length, and large timber ring.**

1.9 APPENDIX B: MIX DESIGN

Two different concrete mixes were utilized during testing. See Tables B.1 and B.2 for the mix design ratios. One mix had a water to cement ratio of 0.61, and achieved compressive strength of approximately 2500 psi after three days. This mix is referred to as "Mix A." A second mix had a water to cement ratio of 0.32, achieved a compressive strength of approximately 4000 psi in one day, and utilized a high range water reducer to increase workability. This mix is referred to as "Mix B."

Table B.1 **Mix design for Mix A, per cubic yard.**

Material	Specific Gravity	mL	Weight (lbs)	Volume (ft^3)
Coarse Aggregate	2.7	N/A	1880	11.158
Fine Aggregate	2.66	N/A	1520	9.157
Cement (Type I-II)	3.15	N/A	423	2.152
Water	1	N/A	258	4.134
Total			4081	27.00

Table B.2 Mix design for Mix B, per cubic yard.

Material	Specific Gravity	mL	Weight	Volume
Coarse Aggregate	2.7	N/A	1812	10.830
Fine Aggregate	2.65	N/A	1209	7.311
Cement (Type I-II)	3.15	N/A	735	3.739
Water	1	N/A	235	3.766
HRWR (Rheobuild 3000 FC)	1.2	1501.61	N/A	N/A
Total			3991	27.00

Additionally, Table B.3 shows which mix was utilized for each element of each testing type. Cylinders for the "Smooth 1" test set were not made with either of the mixes provided, but rather were extra smooth cylinders from previous unrelated tests.

Table B.3 Mix usage matrix.

Test Set	Cylinder Mix	Base Mix
Smooth 1	Unrelated smooth cylinders	B
Steel Configuration	A	A
Coarse Retarder	A	A
Fine Retarder	A	A
Caulk and Trowel	A	A
Plastic Wire	A	A
Monolithic	A	A
Base Strength (4000 psi)	B	A
Base Strength (4500 psi)	B	B
Base Strength (7000 psi)	B	B
Base Strength (4000 psi)	B	B
Smooth 2	A	A

1.10 APPENDIX C: ANALYSIS OF CONCENTRIC THICK-WALLED CYLINDERS

1.10.1 Introduction

The purpose of the analysis is to determine the stresses and deformations caused by shrinkage of the base relative to the cylinder. The cylinder, base and steel are treated as four concentric thick-walled cylinders. The stress and deformations of a single, isolated cylinder under pressure loading and environmental (thermal or shrinkage strains) are first obtained, then four such "elements" are linked by ensuring that the radial displacements are compatible and the radial stresses are in equilibrium at the interface. The procedure constitutes a finite element analysis with exact shape functions. It should be expected that a conventional finite element analysis, which uses approximate shape functions, should converge to the same solution if each "cylinder" were subdivided into sufficiently thin sub-layers.

1.10.2 Element Equations

The equations linking stress and deformation in a single cylinder, or element, are obtained here. Consider a cylinder with internal and external radii of *a* and *b*, with plane stress axial boundary conditions.

Strain-displacement relations require

$$\varepsilon_r = \frac{du}{dr} \tag{C.1}$$

$$\varepsilon_\theta = \frac{u}{r} \tag{C.2}$$

Constitutive laws (for plane stress) require

$$E\varepsilon_r = \sigma_r - \nu\sigma_\theta \tag{C.3}$$

$$E\varepsilon_\theta = \sigma_\theta\sigma_r - \nu\sigma_r \tag{C.4}$$

and equilibrium requires

$$r\frac{d\sigma_r}{dr} + \left(\sigma_r - \sigma_\theta\right) = 0 \tag{C.5}$$

where subscripts r and θ indicate the radial and hoop directions, and u is the radial displacement at radius r. Because the system is axi-symmetric, the problem is one-dimensional and the equations are all ordinary rather than partial, differential equations.

The strain-displacement and constitutive equations can be combined to give the stresses σ_r and σ_θ in terms of the radial displacement u:

$$\begin{Bmatrix} \sigma_r \\ \sigma_\theta \end{Bmatrix} = \frac{E}{1-\nu^2} \begin{bmatrix} 1 & \nu \\ \nu & 1 \end{bmatrix} \begin{Bmatrix} u' \\ u/r \end{Bmatrix} \tag{C.6}$$

These values for the stresses can now be substituted back into the equilibrium equation to give a single differential equation in *u*:

$$r^2 u'' + r u' - u = 0 \tag{C.7}$$

The solution is of the form $u = Ar + B/r$, where A and B are constants of integration that are found from the boundary conditions. If the radial stresses at the inner and outer surfaces of the cylinder (at $r = a$ and $r = b$) are taken to be σ_{ra} and σ_{rb}, the constants A and B can be found in terms of stresses within the wall of the cylinder can be found in terms of σ_{ra} and σ_{rb} as:

$$\begin{Bmatrix} A \\ B \end{Bmatrix} = \frac{1}{E\left(\dfrac{1}{a^2} - \dfrac{1}{b^2}\right)} \begin{bmatrix} -\dfrac{(1-\nu)}{b^2} & +\dfrac{(1-\nu)}{a^2} \\ -(1+\nu) & (1+\nu) \end{bmatrix} \begin{Bmatrix} \sigma_{ra} \\ \sigma_{rb} \end{Bmatrix} \tag{C.8}$$

and the stresses at any radius, r, can then be expressed as:

$$\begin{Bmatrix} \sigma_r(r) \\ \sigma_\theta(r) \end{Bmatrix} = \frac{1}{\left(\dfrac{1}{a^2} - \dfrac{1}{b^2}\right)} \begin{bmatrix} \left(\dfrac{1}{r^2} - \dfrac{1}{b^2}\right) & -\left(\dfrac{1}{r^2} - \dfrac{1}{a^2}\right) \\ -\left(\dfrac{1}{r^2} + \dfrac{1}{b^2}\right) & +\left(\dfrac{1}{r^2} + \dfrac{1}{b^2}\right) \end{bmatrix} \begin{Bmatrix} \sigma_{ra} \\ \sigma_{rb} \end{Bmatrix} \tag{C.9}$$

The sign convention used above is the conventional mechanics one, in which tension is positive. These equations for stress reduce to those given in texts such as Timoshenko [1941] for special cases such as internal pressure (σ_{ra}) only or external pressure (σ_{rb}) only.

1.10.3 System Equations

To analyze a system consisting of a series of concentric cylinders, the "element" equations for a single cylinder must be expressed in the form of an element stiffness matrix, which in this case relates radial stress (rather than the more usual force) to radial displacement at the boundaries $r = [a,b]$. This can be done by expressing the displacement $u(r)$ at a and b in terms of the stresses σ_{ra} and σ_{rb} to give the flexibility relation

$$\begin{Bmatrix} u(a) \\ u(b) \end{Bmatrix} = [F] \begin{Bmatrix} \sigma_{ra} \\ \sigma_{rb} \end{Bmatrix} \tag{C.10}$$

where

$$[F]=\frac{1}{E\left(\frac{1}{a^2}-\frac{1}{b^2}\right)}\begin{bmatrix} -a\left(\frac{1-\nu}{b^2}+\frac{1+\nu}{a^2}\right) & \frac{2}{a} \\ -\frac{2}{b} & +b\left(\frac{1-\nu}{a^2}+\frac{1+\nu}{b^2}\right) \end{bmatrix} \tag{C.11}$$

The flexibility matrix, F, can be inverted (numerically) to give the element stiffness matrix. Before doing so, it is convenient to switch from a mechanics-based sign convention (tension is positive) to a nodal sign convention in which radially outwards is positive. F then becomes

$$[F]=\frac{1}{E\left(\frac{1}{a^2}-\frac{1}{b^2}\right)}\begin{bmatrix} +a\left(\frac{1-\nu}{b^2}+\frac{1+\nu}{a^2}\right) & \frac{2}{a} \\ +\frac{2}{b} & +b\left(\frac{1-\nu}{a^2}+\frac{1+\nu}{b^2}\right) \end{bmatrix} \tag{C.12}$$

The resulting element stiffnesses can then be combined into a global stiffness matrix, from which the radial displacements at the nodes (interfaces between cylinders in this case) can be found from the loads (radial pressures at the interfaces).

1.10.4 Loading from Environmental Strains (Thermal and shrinkage)

Environmental strains, caused by thermal or shrinkage effects, may, if restrained from occurring freely, induce stresses in the cylinders. For example, the outer (base) cylinder used in the tests may shrink relative to the inner (solid) cylinder which was cast first. That relative shrinkage is partially restrained by the inner one, thereby inducing hoop tension and radial compression in the outer one. The hoop tension stress is, of course, the result of interest here.

The effects of the environmental strains can be expressed as loads as follows. Let u_t = total radial displacement; u_e = radial displacement caused by free environmental strain; and u_m = radial displacement due to stress ("mechanical strain"). Then

$$u_t = u_e + u_m \tag{C.13}$$

and

$$\underline{u_m} = \underline{\underline{F}}\,\underline{\sigma_r} \tag{C.14}$$

Inverting gives

$$\underline{\sigma_r} = \underline{\underline{F}}^{-1}\underline{u_m} = \underline{\underline{k}}\underline{(u_t - u_e)} \tag{C.15}$$

or

$$\sigma_r + k\left(u_e\right) = k\left(u_t\right) \tag{C.16}$$

Thus the environmental strain effects can be expressed as a load of $k\left(u_e\right)$ and added to the pressure loads, if any. Here, k is the element stiffness matrix and $\left(u_e\right)$ is the radial displacement caused by environmental strain, given for an axi-symmetric cylinder by $r\varepsilon_{\text{shr}}$, where ε_{shr} is the free shrinkage strain. The stiffness matrix and load vectors can be assembled using the direct stiffness matrix, and can be solved to give the total nodal radial displacements, $\left(u_t\right)$. These are then substituted back into the element equations, from which the internal radial and hoop stresses can be found from the mechanical component, $u_m = u_t - u_e$, of the radial displacement.

2. Composite Action of Concrete-Filled Tubes

Donovan Holder

ABSTRACT

Concrete filled tube (CFT) columns are an attractive alternative to conventional reinforced concrete and steel columns in bridge construction. Although CFTs are economical to construct and have desirable properties for seismic design, one main limitation is uncertainty in the composite interaction between the steel tube and the concrete fill in sections with large diameter to thickness (D/t) steel tube ratios. Due to this limitation, an experimental study was conducted to evaluate the composite behavior between the steel tube and concrete fill in CFTs. Primary variables included the concrete mix: one with and one without a low shrinkage admixture, and the tube type: straight seam or spiral welded.

Results demonstrate that the bond strength of CFTs constructed using spiral welded steel tubes were significantly stronger than sections constructed with straight seam tubes. Furthermore, the addition of low shrinkage admixture did not influence the observed bond strength in specimens with spiral welded tubes, while a large increase in bond strength was observed for straight seam tubes when this admixture was included.

2.1 INTRODUCTION

Concrete-filled tube (CFT) columns are structural elements that optimize the mechanical contributions of both steel and concrete in bridge construction. As the name implies, CFTs are structural members that consist of a steel tube filled with a concrete. The steel tube eliminates the need for form work, and reinforces the concrete fill to resist tension, shear, and bending, thereby eliminating the need for conventional longitudinal and transverse reinforcing. In turn, the concrete restrains tube buckling, supports compressive stress demands, and offers large stiffness [Raynor et al.2013]. Due to the fact that the resulting composite element has desirable properties for seismic design, can be constructed rapidly, and is cost efficient, CFTs are an attractive alternative to conventional structural steel and reinforced concrete construction in bridge construction.

To fully realize the structural benefits of both the steel tube and concrete feel in a CFT section, stress transfer between the steel and the concrete is required. This stress transfer is achieved by the bond between the two materials. In practice, the stress transfer of the section is attained by shear connectors on the inside of the tubes or the natural bond between steel and the concrete [Roeder et al. 1999].

2.2 BACKGROUND

2.2.1 Bond Strength Mechanisms

The bond strength for CFT sections is the shear transfer at the interface of the steel tube and the concrete fill. There are two general mechanisms to achieve this strength including natural and mechanical bonds. Natural bond includes the frictional resistance and chemical adhesion or chemical bond, between the two materials. Mechanical bond is caused by supplemental devices of significant irregularities in the steel to permit bearing of the steel on the concrete [Roeder et al. 2009]. Natural bond is the preferred method of stress transfer between the two materials in CFT sections because it allows CFT sections to be constructed more easily. Currently, it is recommended that low shrinkage concrete be used in CFT composite sections to ensure adequate natural bond strength develops.

2.2.2 Interface Conditions

The bond between the steel tube and the concrete fill depends on the radial displacement of the steel tube due to the pressure of the wet concrete core, and rugosity of the interior surface of the tube [Roeder et al. 1999]. Research by Roeder et. al [1999] identified three possible states that could exist at the interface:

State A:

$$\Delta_1 + \Delta_2 > 0 \tag{2.1}$$

State B:

$$\Delta_1 + \Delta_2 < -\Delta_3 \tag{2.2}$$

State C:

$$0 \geq \Delta_1 + \Delta_2 \geq -\Delta_3 \tag{2.3}$$

where Δ_1 = displacement due to radial enlargement of the steel tube due to the wet concrete, Δ_2 = displacement due to shrinkage of the concrete fill, and Δ_3 = the amplitude of the rugosity on the interior of the steel tube.

In State A, the concrete fill still applies pressure to the steel tube even after shrinkage is complete. In this state the bond strength is first due to the chemical bond between the two materials. Once the capacity of the chemical bond is exceeded, the bond strength depends on the mechanical bond at the interface. In State B, a separation between the steel tube and the concrete fill exists after concrete shrinkage. State C is an intermediate condition where chemical bond between the two materials exists, but the mechanical bond at the interface is the controlling factor in the bond strength of the section.

2.2.3 Past Bond Stress Studies

Past experimental studies of bond strength have defined bond stress capacity as the average interface stress associated with the initial rigid body slip of the concrete core relative to the steel tube [Roeder et al. 1999]. The equation used to calculate this average bond stress is:

$$f = P / \pi d L \tag{2.4}$$

where f = average bond stress, P = load at which slip occurred, d = diameter at steel/concrete interface, and L = length of material interface.

In general, previous experiments on bond stress capacity of CFTs used push-out test specimens Shakir-Khalil [1993]. In these types of tests, CFT specimens are constructed at varying sizes with varying concrete core mixtures, and axial loaded in compression with the force only applied only to the concrete core. A gap is placed at the bottom of each specimen to allow push through of the concrete fill. Several experiments on CFT bond strength have been performed in the past, but the majority of these tests have been performed on specimens with a d/t ratio for the steel tube substantially smaller than those used in the U.S. Specifically, prior bond stress experiments were generally conducted on specimens with d/t ratios of less than 60, while in the U.S. the d/t ratio is commonly about 100 [Roeder et al. 1999]. These past research initiatives were performed with CFT specimens of low d/t ratios because these d/t ratios are prevalently used in construction of structures and infrastructure in many countries outside the U.S. The use of low d/t ratios in CFT sections means that the load applied to the section is mainly taken by the steel tube and not the concrete core. Higher d/t ratios are used in the U.S. to utilize the strength of the concrete core more in the overall load carry capacity of the composite section.

Research on composite action in CFTs performed by Roeder et al. [1999] tested specimens with a d/t ratios closest to the ratio used in engineering practice within the U.S. These tests were undertaken to study the bond strength of CFT sections with varying concrete core diameters, steel tube thicknesses, and concrete core mixtures. A summary of these tests can be is shown in Table 2.1. The roman numeral in the specimen identification symbolized a specific type of concrete mixture used in the specimen. Series I used a concrete mixture with a moderate shrinkage potential, while Series II used a concrete mixture with little shrinkage. These tests by Roeder et al. primarily showed that shrinkage on concrete core can be detrimental to the bond stress capacity of CFT sections, and that bond stress capacity of CFT sections depends upon the characteristics of the concrete, the d/t ratio of the steel tube, and the rugosity of the steel tube interior.

Table 2.1 Summary of test specimens and results [Roeder et al. 1999].

Specimen identification (1)	Inside diameter of tube (mm) (2)	Length of tube (mm) (3)	Wall thickness of tube (mm) (4)	Concrete strength $f'c$ (MPa) (5)	Age of concrete at testing (days) (6)	Test method (7)	Ultimate load capacity (KN) (8)	Maximum average bond stress (MPa) (9)	Maximum local bond stress (MPa) (10)
I-1	247.6	758	13.46	29.3	38	Concentric	6.2	0.010	NA
I-2	247.6	758	13.46	29.3	56	Eccentric	15.6	0.026	0.69
I-3	341.4	1,064	7.11	27.9	37	Concentric	36.0	0.031	1.62
I-4	341.4	1,064	7.11	27.9	47	Concentric	42.7	0.037	0.40
I-5	341.4	1,775	7.11	37.3	45	Concentric	247.9	0.094	1.83
I-6	341.4	1,775	7.11	28.6	48	Concentric	82.8	0.043	0.42
I-7	598.4	1,927	5.59	29.3	46	Concentric	192.2	0.052	0.31
I-8	598.4	1,927	5.59	28.6	57	Eccentric	236.7	0.068	1.79
II-1	247.6	810	13.46	47.2	23	Concentric	486.4	0.773	3.01
II-2	247.6	810	13.46	46.6	28	Concentric	494.8	0.786	6.20
II-3	247.6	810	13.46	46.6	24	Concentric	488.2	0.775	5.68
II-4	247.6	1,495	13.46	43.9	30	Concentric with cyclic load	371.6	0.319	3.70
II-5	341.4	1,064	7.11	47.3	28	Concentric	315.5	0.282	2.25
II-6	341.4	1,064	7.11	47.3	24	Concentric	404.1	0.355	1.31
II-7	341.4	1,775	7.11	43.9	29	Concentric	332.0	0.175	3.94
II-8	341.4	1,775	7.11	43.9	29	Concentric	355.6	0.187	2.15
II-9	598.4	1,927	5.59	44.9	25	Concentric	523.3	0.145	1.62
II-10	598.4	1,927	5.59	47.2	25	Concentric	635.9	0.176	1.45
II-11	598.4	1,927	5.59	46.2	31	Concentric with dented tube	332.4	0.093	1.69
II-12	598.4	1,927	5.59	46.2	30	Concentric with dented tube	332.9	0.093	2.80

2.3 EXPERIMENTAL PROGRAM

2.3.1 Objectives

The primary objective of this research is to determine if a concrete mix containing no low shrinkage admixtures can achieve adequate bond strength to develop the necessary stress transfer between to the steel tube and the concrete core in CFT columns. The tests were further designed to study the contribution of the interior weld of spiral welded steel tubes to the overall bond strength of the composite section.

2.3.2 Specimen Design and Test Set-Up

Push-out tests were used to evaluate the influence of a concrete fill containing no low shrinkage admixtures, as well as the contribution of the interior spiral weld to the overall bond strength of the section. A total of four specimens were selected to properly reach the objectives of the experiment. Two specimens were constructed using spiral welded steel tubes, while the other two specimens used straight seam tubes. One spiral welded steel tube and one straight seam steel tube was filled with a low shrinkage concrete mix, and the other two were filled with a high strength concrete mix that contained no low shrinkage admixtures. An overview of the specimen geometry is shown in Figure 2.1.

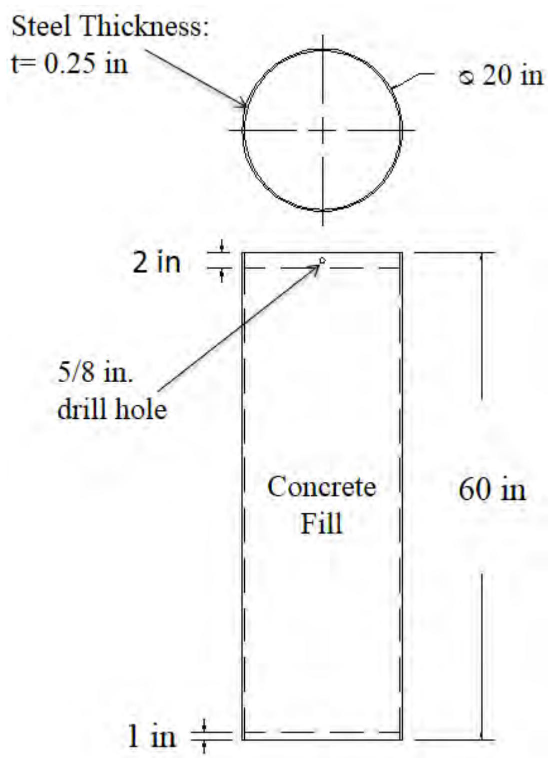

Figure 2.1 Specimen design.

The welds on the spiral welded steel tube had 42-in. spacing and protruded 1/8-in. from the exterior and interior of the tube. A height of 60-in. was selected to ensure that at least two spiral welds passed through the specimen. A 1-in. gap was placed at the bottom of each specimen to allow for push through of concrete fill. The push through gap at the bottom of the specimen was made small to limit the possibility of the steel tube buckling during the push out test. A 2-in. gap was placed at the top of each specimen to allow two 5/8-in. holes to be drilled perpendicular to each other and at least 7/8 in. away from the top of the specimen. These holes were placed into the design to increase portability of the specimens from construction to testing locations.

Axial load was applied to each specimen by the Baldwin Test Machine located in the structural testing lab at the University of Washington. The set-up for each test is shown in Figure 2.2. The Baldwin applied axial load to the specimens through a roller bearing connection to eliminate horizontal loading effects due to imperfections in the specimen base or loading surface. The roller bearing was placed only on the concrete fill of the specimens being tested. The Baldwin applied a load via displacement control at 0.0005-in./sec. to each specimen until the concrete core began to touch the rigid plate underneath the specimen.

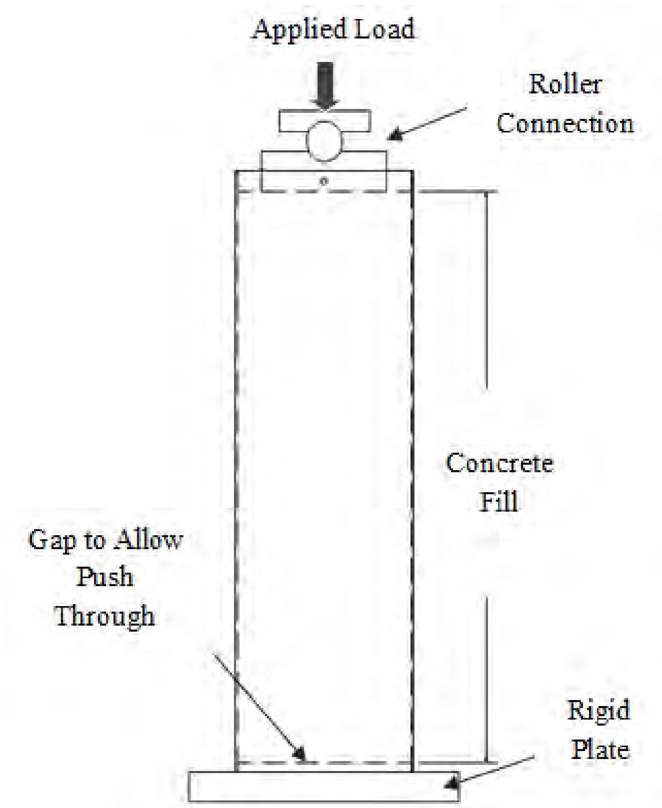

Figure 2.2 Push out test set-up.

2.3.3 Test Matrix

The test matrix consisted of four specimens, summarized in Table 2.2. The specimens have been identified using a combination of letters and Roman Numerals. Specimens labeled SS and SW were constructed using straight seam and spiral welded tubes respectively, while specimens containing roman numerals I and II were constructed with concrete containing low shrinkage admixture and no low shrinkage admixture, respectively.

Table 2.2 Test Matrix of Specimens

Specimen Identification	Type of Steel Tube	Type of Concrete
SS-I	Straight Seam	Low Shrinkage
SS-II	Straight Seam	High Strength, No low Shrinkage Admixture
SW-I	Spiral Welded	Low Shrinkage
SW-II	Spiral Welded	High Strength, No low Shrinkage Admixture

2.3.4 Instrumentation

The primary instruments used to collect data during testing were strain gauges, vibrating wire gauges, and linear potentiometers. A total of ten strain gauges were used on each specimen and positioned at the locations, as shown in Figure 2.3. All strain gauges were placed in the longitudinal direction of the steel tube. The gauges were placed closer together at the top and the bottom of the specimens because these were the areas of highest interest. The position of gauges were selected to ensure that the spacing of the top set of gauges were the same as the spacing of the bottom set of gauges away from the surface of the concrete fill.

The configuration of the vibrating wire gauges is shown in Figure 2.4. This configuration was replicated on both sides of the specimen. The mounting blocks for all vibrating wire gauges were tack welded in place prior to the pouring of the concrete fill. This was done to ensure that the weld heat did not influence the properties of the concrete fill.

Displacement of the concrete fill during testing was monitored by the use of three linear potentiometers. These instruments were attached to the top of the specimen by means of a magnet stand, and placed on the edge of the roller connection as shown in Figures 2.5.

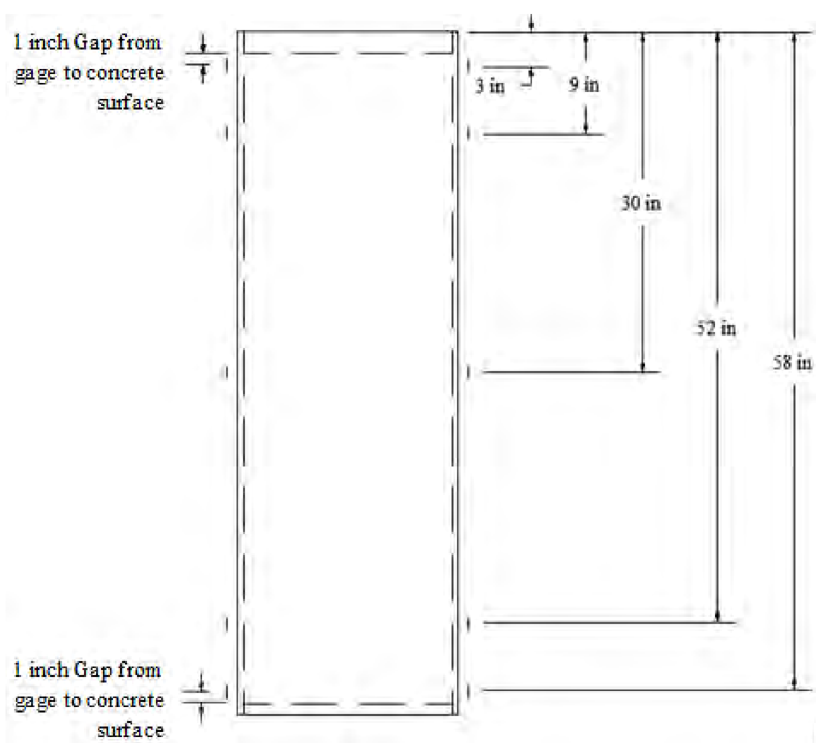

Figure 2.3 Locations of strain gauges.

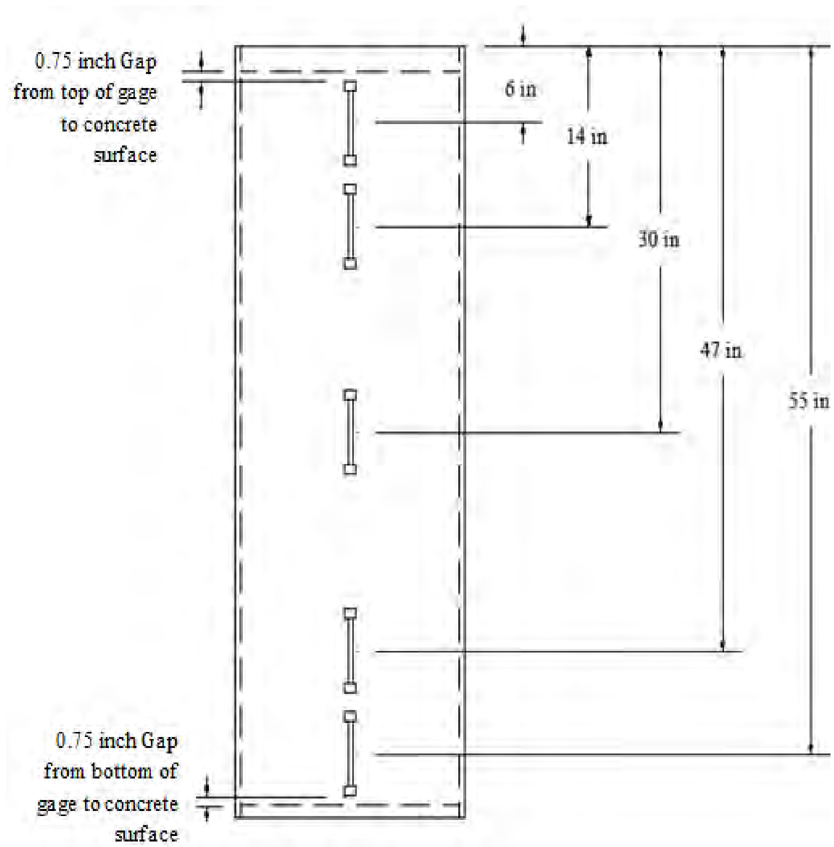

Figure 2.4 Locations of vibrating wire gauges.

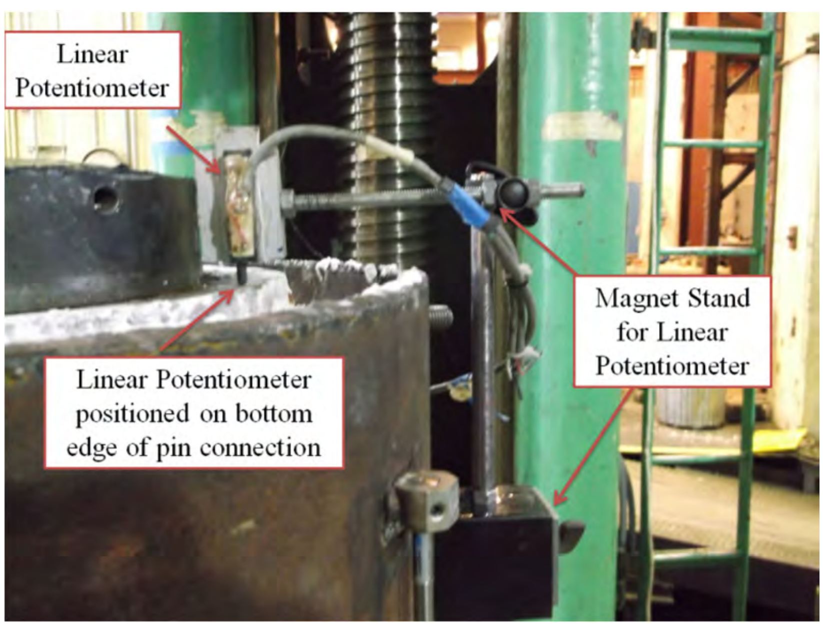

Figure 2.5 Example of linear potentiometer attached to specimen.

2.3.5 Specimen Properties

The compression strength of the concrete was taken on the day of testing by means of a standard cylinder test. Two cylinders were tested for each type of concrete mixture used in the specimens. The strength of the concrete and age of concrete on the day of testing are summarized in Table 2.3.

Table 2.3 Strength of concrete fill at testing.

Specimen Identification	Type of Concrete Mixture in Specimen	Concrete Strength *f'c* (ksi)	Age of Concrete at Testing (days)
SS-I	Low Shrinkage	7.95	7
SW-I			
SS-II	High Strength, No Low Shrinkage Admixture	7.53	15
SW-II			

2.4 TESTING

All specimens were loaded in compression by the Baldwin Testing Machine in the University of Washington Structural Engineering Lab. The roller bearing connection and rigid support plate were hydro-stoned into place in order to level both items and keep them fixed during testing. A representative specimen setup during testing can be seen in Figure 2.6.

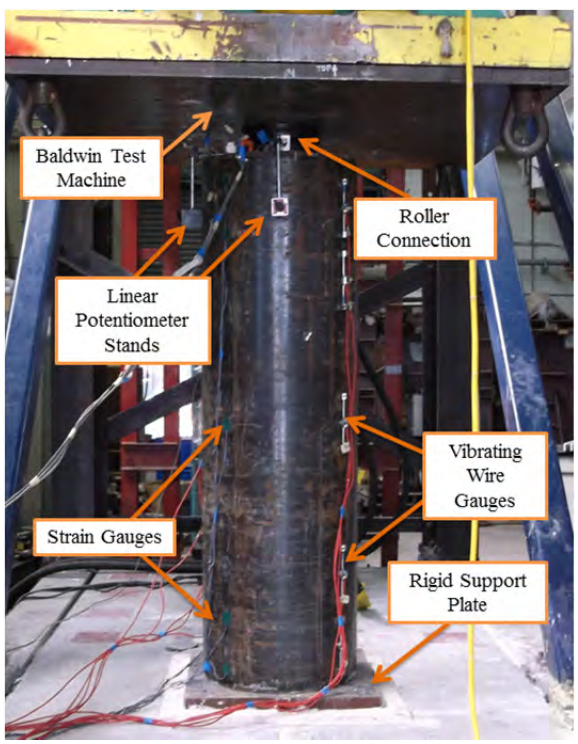

Figure 2.6 Test set-up of Specimen SS-I.

2.5 EXPERIMENTAL RESULTS

Specimens were considered to have failed when the concrete core touched the rigid plate underneath the specimen. SS-I and SS-II reached a max load carrying capacity of 176.3 kips and 19.3 kips, respectively. SW-I and SW-II reached a max load carrying capacity of 424 kips and 339.4 kips, respectively. Using the data collected from the Baldwin test machine and the linear potentiometers, the load versus displacement behavior of each specimen has been plotted in Figure 2.7.

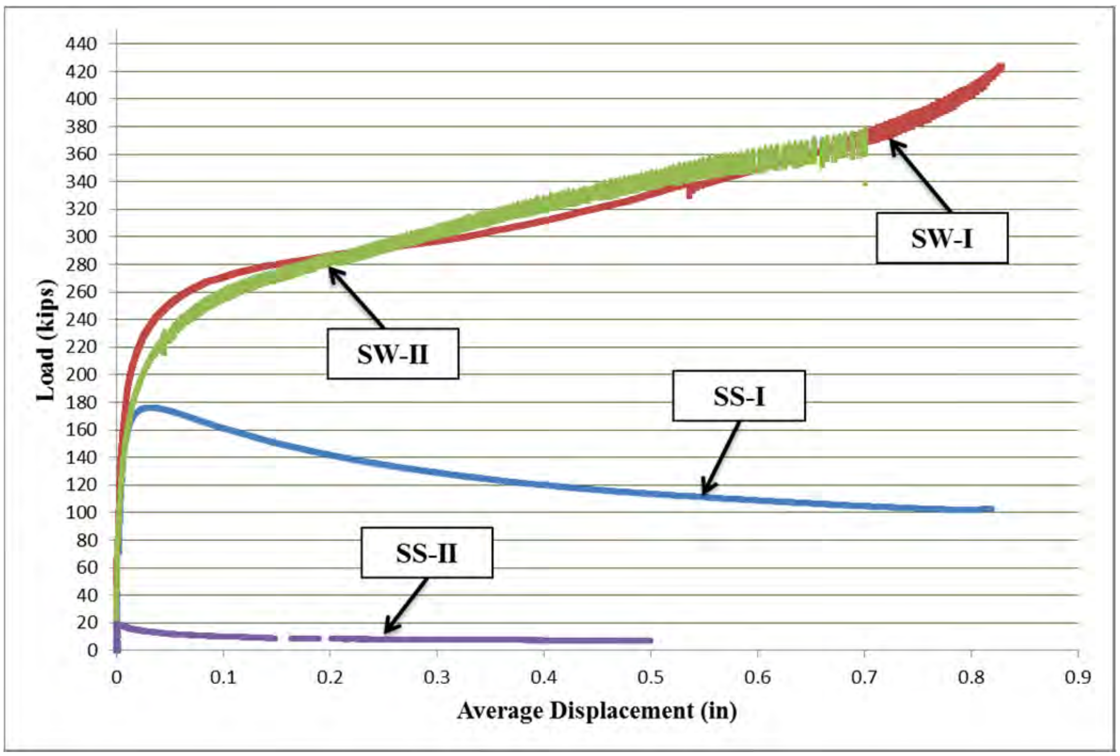

Figure 2.7 Load versus displacement of all four specimens tested.

From Figure 2.7, it can be seen that SS-II had the lowest load carrying capacity, while SW-I had the largest load capacity. SW-I and SW-II had very similar load versus displacement curves even though both specimens contained different concrete mixtures. Specimens constructed with a spiral welded steel tube increased their load carrying capacity throughout the entire test, while specimens constructed with a straight seam steel tube reached a peak load capacity, then decreased as the loading regiment progressed. Furthermore, post-test observations of each specimen constructed with a spiral welded steel tube showed significant concrete spalling in the top surface of the concrete core at the location where the concrete core interlocked with the interior spiral weld. Damage was not observed in specimens with the straight seam tubes.

Data collected from the strain gauges on each specimen was used to calculate bond stress using Equation (2.5):

$$\sigma' = \frac{\left(r_E^2 - r_I^2\right)E\varepsilon}{dL} \tag{2.5}$$

where σ' = bond stress, r_E = exterior radius of steel tube, and r_I = interior radius of steel tube, E= Young's modulus, ε = strain, d = interior diameter of the steel tube, and L = length from top of concrete fill to location of strain gauge. Derivation for this equation can be found in the Appendix.

The bond stress was plotted versus the depth from the top of the concrete core by taking strain data from three key locations during the loading regiment of each specimen. These locations for the straight seam specimens were in the region of bond stress development, at maximum load carrying capacity, and at the final loading point before specimens were considered failed. For the spiral welded specimens, these three points were in the initial region of bond stress development, at a point during the linear increase in load carrying capacity, and at maximum loading. These bond stress graphs along with the locations during the loading process where the strain data was used to calculate bond stress can be seen in Figures 2.8 through 2.11.

The strain data from each group of strain gauges, see Figure 2.8b, was used to calculate bond stress and graphed together on each bond stress versus depth graph. The blue line on the bond stress versus depth graphs represent group A strain gauges while the red line represents group B strain gauges. Each point on the graphs in Figures 2.8 through 2.11 corresponds to the location of a strain gauge on the specimen.

As shown in Figure 2.8, throughout testing of specimen SS-I the top of the specimen was in tension while the bottom was in compression. An shown in Figure 2.10, Specimen SS-II displayed very little bond stress throughout testing, but bond stress in the top section of the concrete core remained in tension throughout the loading process. The bond stress at the chosen locations for both spiral welded specimens varied over the loading process of the specimens.

During testing of the specimens containing low shrinkage concrete, it was observed that the fastest the vibrating wire gauges could take strain readings was once every 30 sec. This is due to the method in which the instruments collect strain readings. The data collection time of the vibrating wire gauges is significantly longer than the data collection time of the strain gauges used on each specimen; therefore, the data collected from the vibrating wire gauges has not been included in this report.

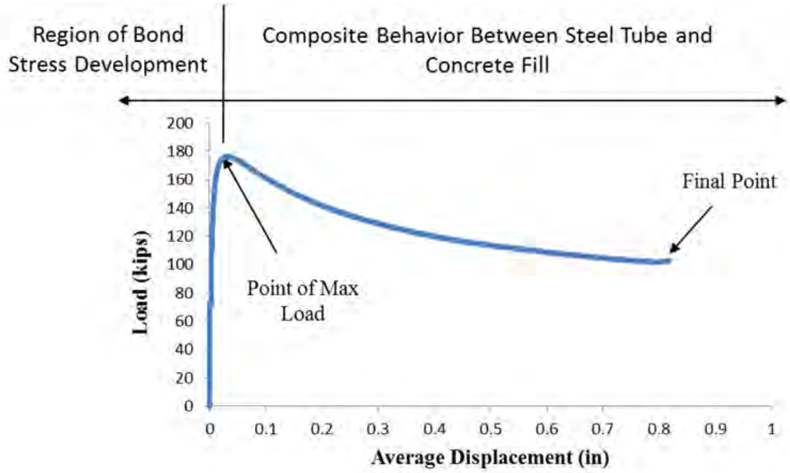

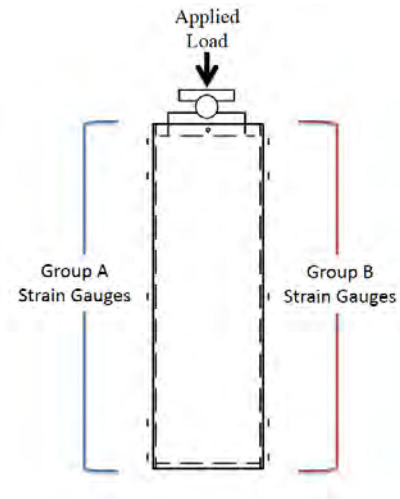

(a)

(b)

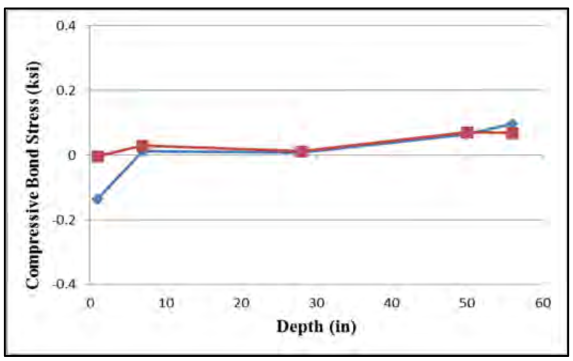

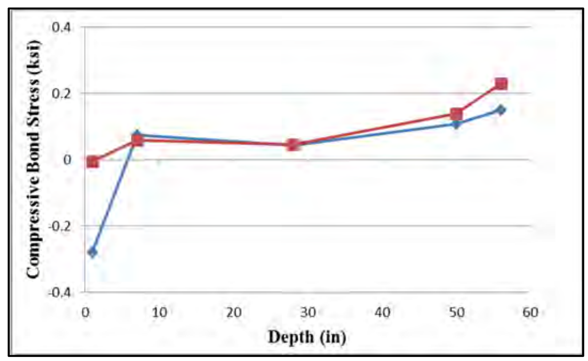

(c)

(d)

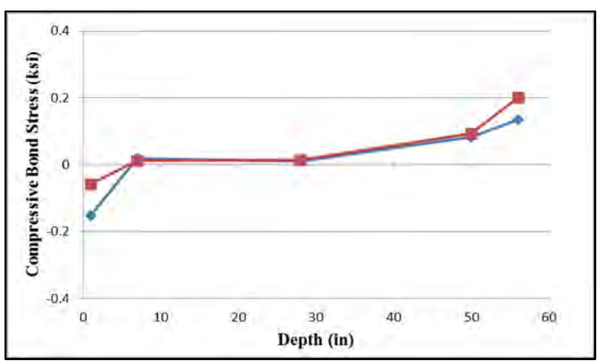

(e)

Figure 2.8 **Bond stress of Specimen SS-I; (a) load versus displacement curve for Specimen SS-I; (b) Location of strain gauge groups and direction of loading; (c) stress versus depth of concrete core in region of bond stress development on load versus displacement curve; (d) stress versus depth of concrete core at point of maximum load on load versus displacement curve; and (e) stress versus depth of concrete core at final point on load versus displacement curve.**

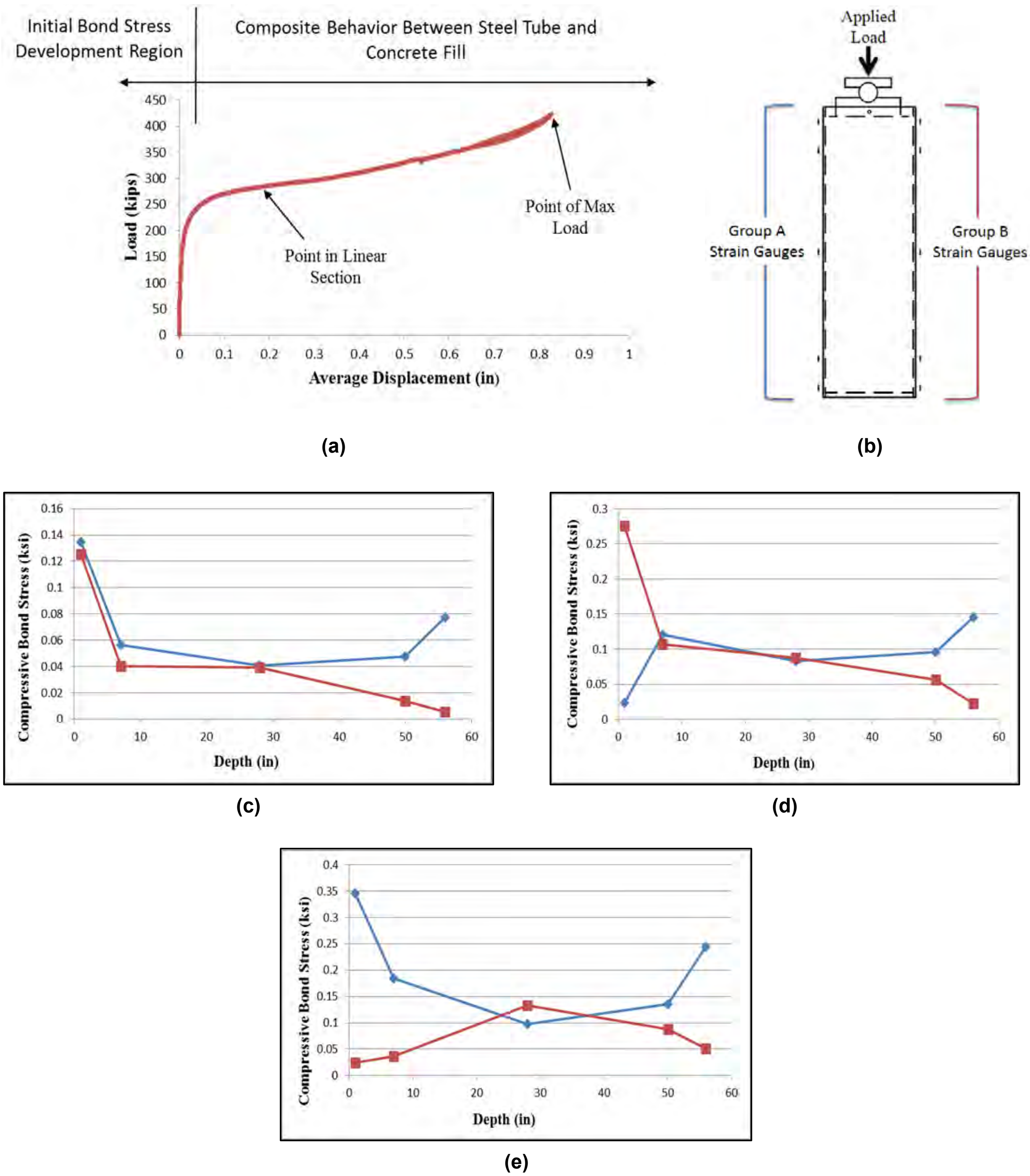

Figure 2.9 **Bond stress of Specimen SW-I; (a) load versus displacement curve for Specimen SW-I; (b) Location of strain gauge groups and direction of loading; (c) stress versus depth of concrete core in initial bond stress development region on load versus displacement curve; (d) stress versus depth of concrete core at point in linear section versus displacement curve; and (e) stress versus depth of concrete core at point on load versus displacement curve.**

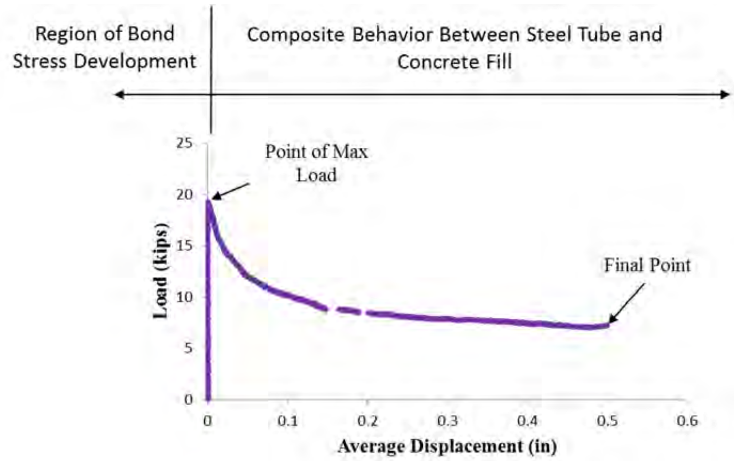

(a)

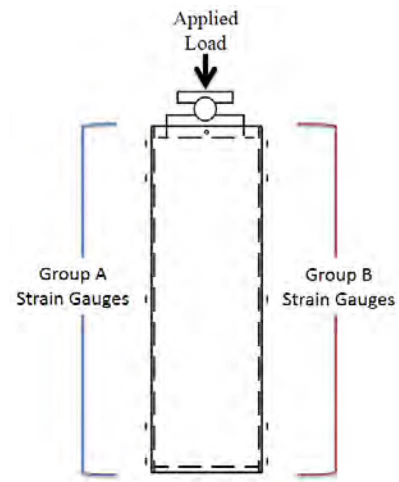

(b)

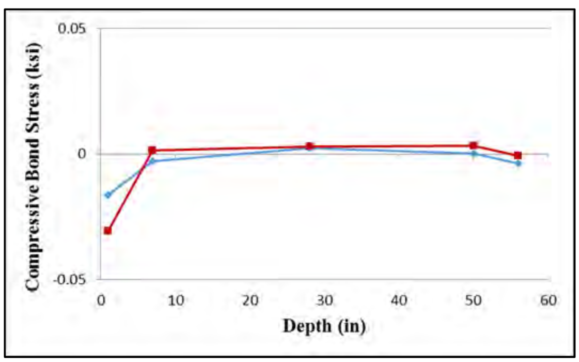

(c)

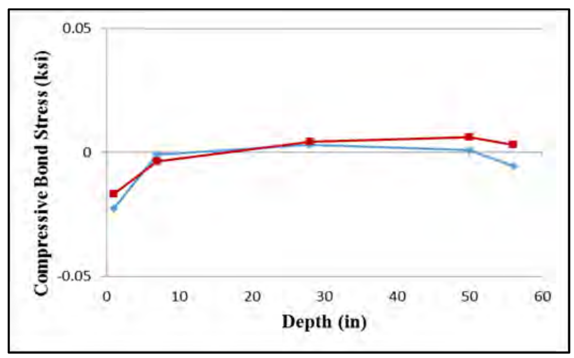

(d)

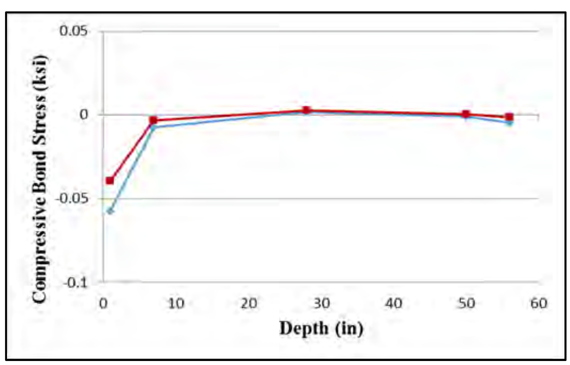

(e)

Figure 2.10 **Bond stress of Specimen SS-II; (a) load versus displacement curve for Specimen SS-II; (b) location of strain gauge groups and direction of loading; (c) stress versus depth of concrete core in region of bond stress development on load versus displacement curve; (d) stress versus depth of concrete core at point of maximum load versus displacement curve; and (e) stress versus depth of concrete core at final point on load versus displacement curve.**

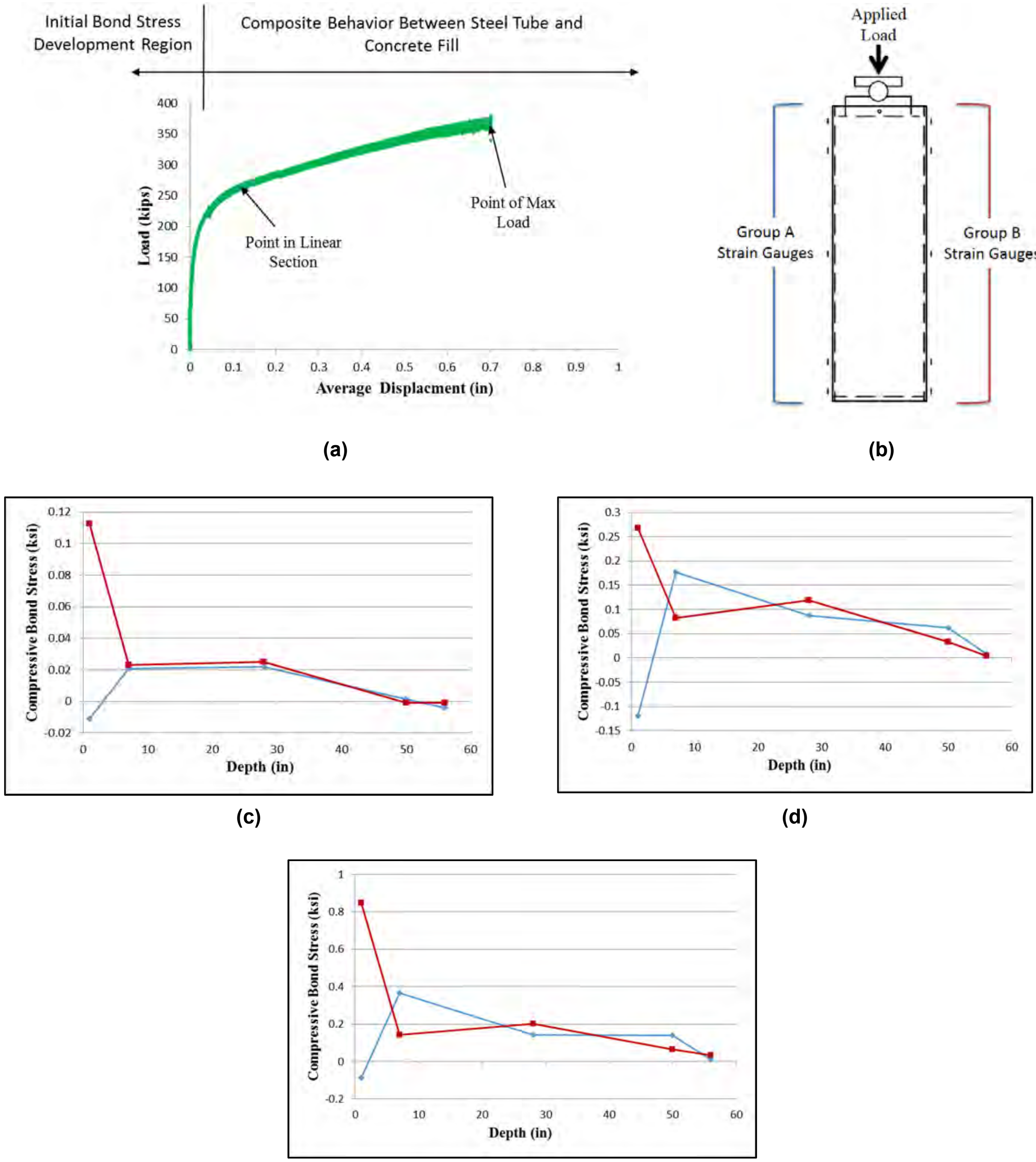

Figure 2.11 Bond stress of Specimen SW-II; (a) load versus displacement curve for Specimen SW-II; (b) location of strain gauge groups and direction of loading; (c) stress versus depth of concrete core in initial bond stress development region on load versus displacement curve; (d) stress versus depth of concrete core at point in linear section on load displacement curve; and (e) stress versus depth of concrete core at point of maximum load on load versus displacement curve.

2.6 ANALYSIS OF RESULTS

Analysis of Figure 2.7 shows that the specimens constructed with spiral welded steel tubes had a significantly higher load carry capacity than specimens constructed with straight seam steel tubes. This is because the interior weld of the spiral welded tubes contributes significant mechanical bond strength to the overall bond strength of the composite section. In order for the concrete core to pass the spiral weld, the concrete above the weld at the steel-concrete interface must crush. The constant crushing of the concrete core at the steel-concrete interface is also the reason why the load carrying capacity of the SW-I and SW-II continuously increased throughout testing.

Both specimens constructed using spiral welded steel tube had similar load carrying capacities even though the mixture of the concrete cores was different. This suggests that the mechanical bond strength achieved due to the interior weld contributes enough to the overall bond strength of the composite section to overcome the difference in natural bond strength due to varying amounts of shrinkage between the two types of concrete core mixtures.

The load carrying capacity of specimen SS-II was roughly 10.9% of the load carrying capacity of specimen SS-I. This shows that even though the difference in strength of the concrete core was only 5.5%, the lack of a low shrinkage admixture in the concrete fill has a significant effect on the bond strength of the composite section when straight seam tubes are used.

Analysis of Figures 2.9 and 2.11 shows that the bond stress of both specimens constructed with spiral welded tubes varied over the span of testing. In most cases, the bond stress calculated from group B strain gauge data did not match the bond stress calculated from group A strain gauge data. These variations are most likely due to the location of the strain gauges in relation to the location of the spiral welds as well as slight eccentricities in the axial load.

2.7 CONCLUSIONS

This study used push through tests to evaluate the influence of several parameters on the development of composite action between the steel tube and concrete fill in CFTs. Specifically, the influence of spiral welded and straight seam tubes as well as concrete with low shrinkage admixtures were evaluated. The following conclusions were drawn from the results of the experimental investigation:

- CFT sections constructed with spiral welded steel tubes have higher bond strength than CFT sections constructed with straight seam steel tubes.
- CFT sections constructed with spiral welded steel tubes and a concrete core with no low shrinkage admixture achieves similar bond strength as CFT sections constructed with spiral welded steel tubes and a concrete core containing a low shrinkage admixture.

2.8 ACKNOWLEDGMENTS

Special thanks to Mrs. Heidi Tremayne for accepting me into the PEER program, and Professors Dawn Lehman and Charles Roeder for providing me the opportunity to join their research team. I would also like to take this opportunity to thank Max Stephens for his demonstration and oversight throughout the project.

2.9 REFERENCES

Radhika K.S, Baskar K. (2012) Bond stress characteristics on circular concrete filled steel tubular columns using mineral admixture Metakoline, *J. Civil Struct. Eng*., 3(1): 1–8.

Raynor D., Lehman D.E., Stanton J.F. (2002). Bond-slip response of reinforcing bars grouted in ducts, *ACI Struct. J.,* 99: 568–576.

Roeder C., Cameron B., Brown C. (1999). Composite action in concrete filled tubes, *J. Struct. Eng*., 125(5): 477–484.

Roeder C., Lehman D.E., Thody R. (2009). Composite action in CFT components and connections, AISC, *Eng. J.,* 47(4): 229–242.

Shakir-Khalil, H. (1993). Pushout strength of concrete-filled steel hollow sections, *The Structural Engineer,* 71(13): 230–243.

2.10 APPENDIX: DERIVATION OF BOND STRESS EQUATION

The relation for stress and strain states that:

$$\sigma = E\varepsilon \tag{A.1}$$

where σ = stress, E = Young's modulus, and ε = strain. From mechanics of materials it is also known that:

$$\sigma = F/A \tag{A.2}$$

where F = applied force and A= cross-sectional area. This equation can be rewritten as:

$$F = A\sigma \tag{A.3}$$

The force acting on the bond between the concrete fill and steel tube of a cylindrical CFT section can be defined as:

$$F = A\sigma = \pi\left(r_E^2 - r_I^2\right)\sigma \tag{A.4}$$

where F= force acting on bond, r_E = exterior radius of steel tube, and r_I = interior radius of steel tube.

Using the definition of stress from mechanics of materials in Equation (A.2), Bond stress can be written as:

$$\sigma' = F / \pi d L \tag{A.5}$$

where σ' = bond stress at a given location, d = interior diameter of the steel tube, and L = length from top of concrete fill to location of strain gauge. The combination of Equation (A.3), (A.4), and (A.5) can be written as:

$$\sigma' = \frac{F}{\pi d L} = \frac{\pi\left(r_E^2 - r_I^2\right)\sigma}{\pi d L} = \frac{\left(r_E^2 - r_I^2\right)E\varepsilon}{dL} \tag{A.6}$$

Substituting E, r_E, r_I, and d variables for the elastic modulus of steel, and the dimensions of the specimens tested respectively, the below equation is obtained:

$$\sigma' = \frac{\left(r_E^2 - r_I^2\right)E\varepsilon}{dL} = \frac{\left(10^2 - 9.75^2\right)(29000)\varepsilon}{19.5L} = \frac{(4.9375)(29000)\varepsilon}{19.5L} \tag{A.7}$$

3. Evaluation of the Optotrak System for Concentrically Braced Steel Frames

Kelli Slaven

ABSTRACT

A series of concentrically braced frames were tested at the University of Washington and the National Center for Research in Earthquake Engineering (NCREE) to study the system behavior under cyclic seismic loading. Northern Digital Inc.'s Optotrak system was used to track the position of points on these frames. The data from this system was compared to the data from other instruments to determine if the Optotrak system is accurate and reliable for this type of project.

3.1 INTRODUCTION

This project studied the behavior of concentrically braced steel frames under cyclic seismic loading. The frames had different connection designs and brace sizes with the same columns and beams. The first two frames tested at the University of Washington used a connection design based on a survey of pre-1988 steel frame buildings. The connection was designed to have deficiencies commonly found in these older buildings. The third frame was a bolted design tested for AISC as a potential design for seismic zones on the east coast. This connection met current design codes. Two story frames were tested at the National Center for Research in Earthquake Engineering (NCREE) in Taiwan, and also had a combination of older connection designs and connections that meet current design codes.

The design of frames built before the implementation of the 1988 Uniform Building Code (UBC) used prescribed seismic forces for the brace and connection designs. Ductile detailing was not required, and overstrength was not considered. These frames are unlikely to have ductile responses to seismic loads due to connection failures and are defined as non-seismically designed concentrically braced frames, or NCBFs [Hsiao et al. 2012]. There has not been much research on pre-1988 NCBFs; therefore, their behavior is not yet fully understood. Many of these frames are still in use, and the designs of several steel frame buildings built before 1988 were studied prior to designing the connections for the NCBF specimens tested at the University of Washington.

The Optotrak system was used to record the positions of points on these frames throughout the tests. If the coordinate system is defined correctly, no adjustments need to be made to the Optotrak data. Corrections need to be made for many of the instruments currently being used, such as correcting for the angle of the string on string pots. The data from the Optotrak system was compared to other instruments to determine if the system is accurate and reliable for use on steel braced frames. If the Optotrak system is reliable, it could provide much more accurate data and replace many other instruments. The Optotrak system is non-invasive and does not require screw tapping or other forms of fastening to the frame, except taping the LED markers down. This would reduce the time and cost of instrumentation.

3.2 BACKGROUND

3.2.1 Concentrically Braced Frames

Concentrically braced frames are commonly used because they are economical and are designed to ensure serviceability during small frequent earthquakes. During large infrequent earthquakes, energy is dissipated through yielding and deformation in the brace [Roeder et al. 2012].

Concentrically braced frames act as a vertical truss system to resist lateral seismic forces. They develop ductility through inelastic action in the brace, and the beams and columns should remain elastic. When a lateral load is applied to a concentrically braced frame, half of the braces will be in tension while the other half are in compression. The braces are highly ductile when yielding in tension, but lose strength rapidly after buckling in compression. Because the braces have a much higher capacity in tension, it is ideal to have half of them in tension at all times. Figure 3.1 shows the behavior of a concentrically braced frame under a lateral load.

Load reversal causes braces to cycle between tension and compression. Under increasing cyclic loading, a brace will go through tension and compression cycles until it fails, or there is a failure in some other component of the system. If the applied lateral load places the brace in compression, it will begin to bow out of plane, as shown in Figure 3.2. The brace will bow a larger amount out of plane as the load increases in each compression cycle until it eventually buckles.

If the brace is then loaded in tension, it will straighten out and eventually begin to yield. The brace will now have some permanent elongation as well as out of plane deformation from buckling, as shown in Figure 3.3. The brace will continue to cycle between compression and tension as the applied load reverses directions and increases in magnitude until a failure occurs in the system.

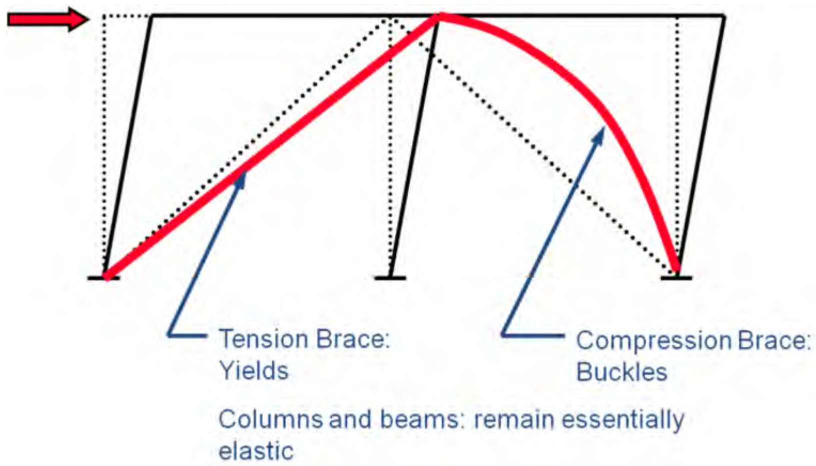

Figure 3.1 **Concentrically braced frame behavior [Berman 2012].**

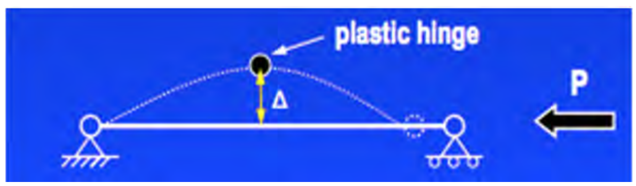

Figure 3.2 **Brace behavior in compression [Berman 2012].**

Figure 3.3 **Brace behavior in tension [Berman 2012].**

3.2.2 Test Set-Up

The specimens tested at the University of Washington were 12 ft×12 ft single story single bay frames. Figure 3.4 shows the test set-up. The specimen is attached to the strong wall through a channel assembly that simulates a composite slab that is common in steel frame buildings. Out-of-plane restraints are attached to both columns and the beam that is not attached to the channel assembly. A threaded rod is attached to the strong floor and holds the restraints resting on top of the frame to keep the components from deforming out of plane. The actuator is attached to the specimen through a load beam that distributes the load to the frame. Threaded rods attached to the channel assembly are tensioned before each test to apply an axial load to the columns. During the test, the actuator applies cyclic loads of increasing displacement to the frame.

The first two tests at the University of Washington were NCBFs with the connection design shown in Figure 3.5. The first frame used an HSS 7×7×1/4 in. brace (not deemed seismically compact); the second test used an HSS 5×5×3/8 in. brace (considered seismically compact). The necessity of a seismically compact brace was discovered after the first test. The connection used a shared shear tab, thin gusset plate, and short splice length, and did not include cover plates for the brace. The connection also did not include clearance between the end of the brace and the beam and column for a fold line to form. This connection was designed to have deficiencies found to be common in a survey of pre-1988 steel frame structures. Current designs typically include a clearance of twice the thickness of the gusset plate to allow the plate to fold as the brace bows out of plane, creating a fold line on the plate. Many of the welds used a non-ductile weld metal similar to the weld metal that was commonly used in pre-1988 steel frame structures, but is no longer allowed.

The third test at the University of Washington was the first specimen in a series of AISC tests exploring current connection possibilities for special concentrically braced frames (SCBFs). The connection design includes bolted beam to column and gusset plate to column shear tabs, as shown in Figure 3.6. The specimen was designed using the Uniform Force Method and current AISC Seismic Provisions. The connection has a two plate thickness clearance on the gusset plate to facilitate the formation of a fold line. Net section reinforcing plates were included on the brace, and a ductile weld metal was used for all welds. This bolted connection is being evaluated for use in seismic zones on the east coast, where it is more economical to use bolts rather than welded connections.

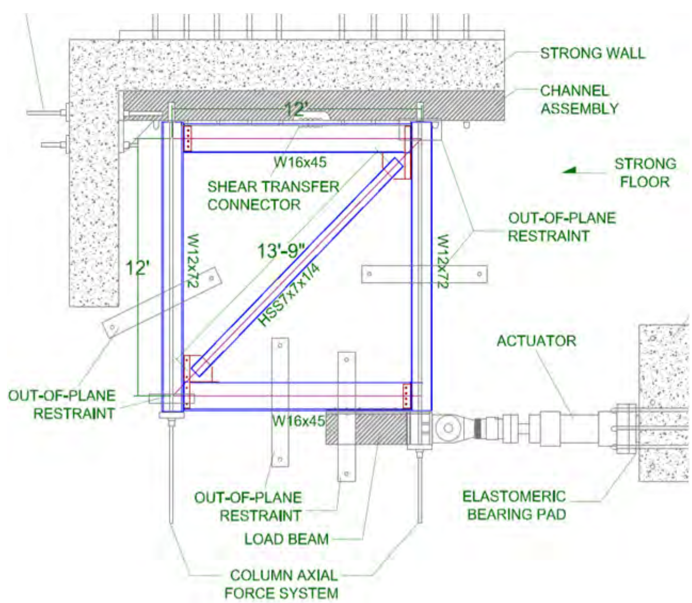

Figure 3.4 University of Washington test set-up; plan view.

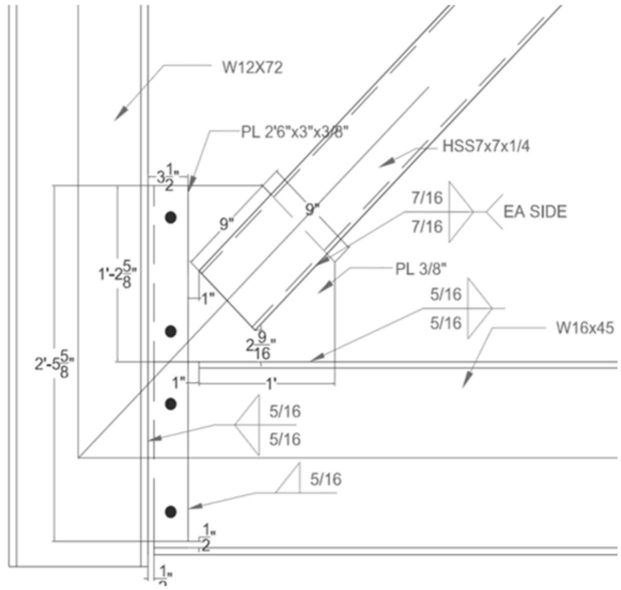

Figure 3.5 Specimen NCBF1 connection design.

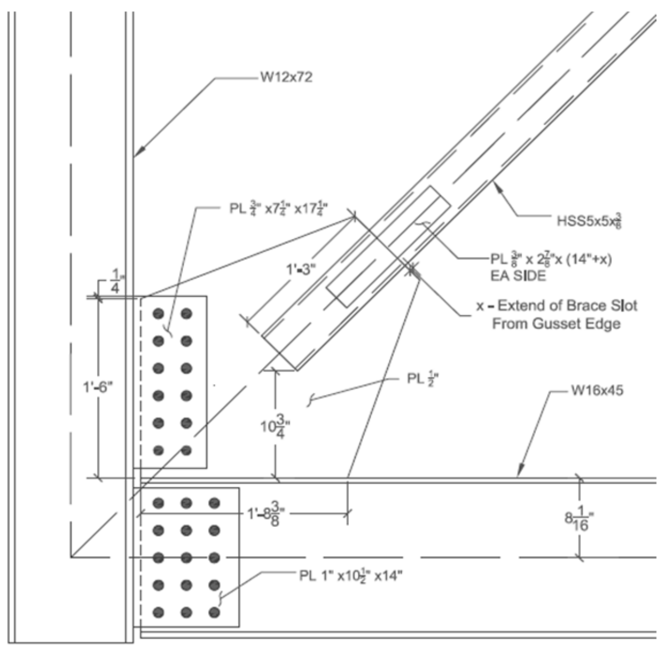

Figure 3.6. Specimen AISC SCBF1 connection design.

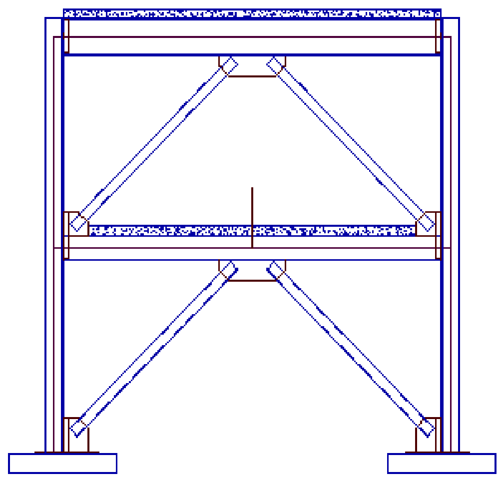

Figure 3.7 Specimen NCBV-INV-1.

The two story specimens built and tested at NCREE in Taiwan had braces configured in an inverted-V shape, as seen in Figure 3.7. The lower story has connections designed with deficiencies similar to the NCBF specimens tested at the University of Washington. The beam on the bottom story is designed to be too weak for the unbalanced forced in the braces, which was found to be common in the survey of pre-1988 structures. There is a concrete slab on the beam of each story. The lower story does not have shear studs connecting the slab to the beam; therefore, any composite action between the two must result from the welds between the steel deck and the beam flange. The lower story connection does not have gusset plate clearances that meet current standards and uses non-ductile weld metal. The upper story has more ductile connections.

3.3 OPTOTRAK SYSTEM

The Optotrak system uses LED markers and a position sensor camera to obtain the three-dimensional coordinates of points. The markers are connected to the frame and the position sensor is set-up so that it can detect the markers. The coordinates of the markers are recorded throughout the test and can be used to calculate many different values. According to Optotrak documentation, if the position sensor is set-up 2 m from the LED markers, the system has an accuracy of 0.1 mm for movement in the plane perpendicular to the camera and an accuracy of 0.15 mm for movement out of that plane [Northern Digital Inc. 2009]**.** This system is much more accurate than other instruments used on the specimens.

3.3.1 Placement of Position Sensors and LED Markers

The position sensors detect markers within a certain volume, as shown in Figure 3.8. This volume expands moving away from the sensor, and ranges about 7 m from the position sensor. Two sensors were used in the University of Washington test set-up to provide greater accuracy. When multiple cameras are used, there must be a large enough overlapping volume so that the sensors can be calibrated. The suggested overlap volume is roughly 3 m^2 [Northern Digital Inc. 2009]. To ensure this overlapping volume and create the largest detection volume, the two position sensors were mounted to the strong wall above the specimen, as seen in Figure 3.9. The sensors were mounted at angles that would allow as much of the frame to be detected as possible while maintaining a large enough overlapping volume. Although this set-up did not allow all of the frame to be detected, it did detect the connection opposite of the strong wall and over half of the brace.

The LED markers were concentrated at the connection opposite of the strong wall and ran out along the gusset plate, brace, beam, and column. Markers were attached to the flanges of the beam and column, as well as the web of the beam. The markers attached along the brace aligned with string pots screwed into the bottom of the brace so the data from these instruments could be compared. Markers on the gusset plate and beam web were attached in a grid pattern, about 3 in. apart. Figure 3.10 shows the markers on the lower story connection of the first two-story test at NCREE. The markers along the flanges and brace were placed about one foot apart along the flanges and several feet apart along the brace. This arrangement allowed for data to be collected over the entire area where yielding and hinging were expected at the connection.

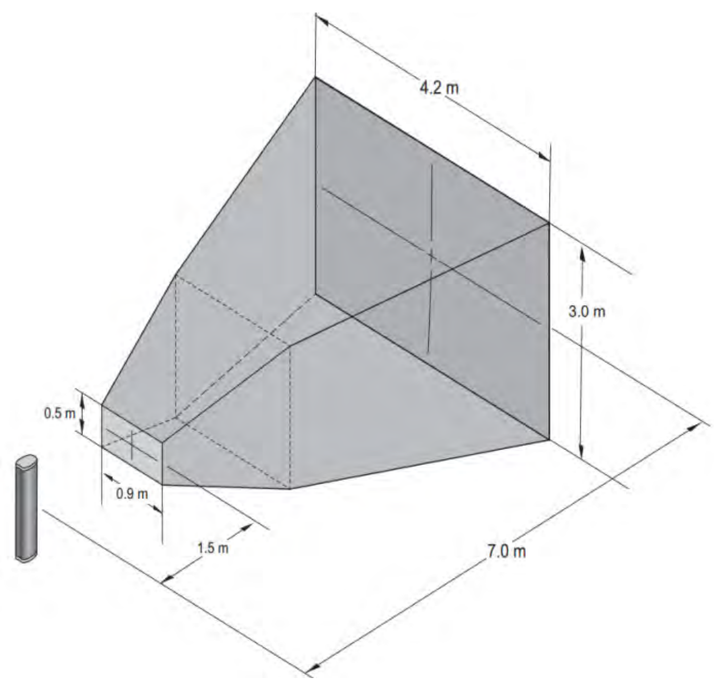

Figure 3.8 Range of position sensor [Northern Digital Inc. 2009].

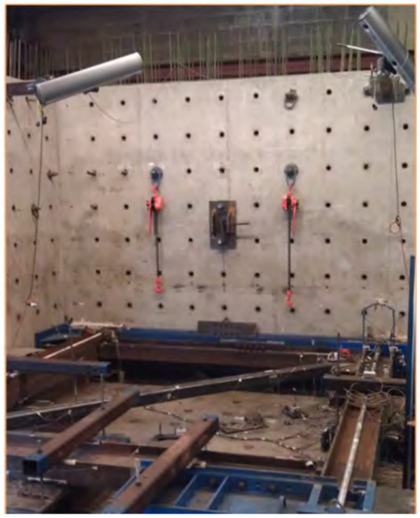

Figure 3.9. Position sensor placement.

Figure 3.10 LED markers in grid pattern on two-story frame at NCREE.

3.3.2 Matlab

The Optotrak system records the three-dimensional coordinates of each LED marker throughout the test. The collection frequency can be adjusted, and two frames per second was chosen for the tests at the University of Washington. This data is then processed with Matlab; however, before using the coordinates, the problems with the raw data must be resolved.

As observers move around the specimen throughout the test, different markers are blocked from the position sensor and no data is recorded for the frames in which a marker is blocked. For these frames, a zero is placed in each coordinate. This error must be remedied before the data can be processed. Matlab can be used to replace zeros with the value in the frame before or after. Since data is recorded every half of a second, this replacement should not cause much error unless a marker is blocked for a significant amount of time.

A second issue with the data is the frame of reference. If no coordinate system is specified when initially setting up the Optotrak system, the default coordinate system will be used. The default coordinate system is aligned with the Optotrak position sensor, as seen in

Figure 3.11. No coordinate system was specified for the first NCBF tests, so the data had to be adjusted to the desired coordinate system. One marker was first chosen as the origin, and the coordinates of each marker were translated to make the coordinates of this marker zero in the first frame. A marker on one of the desired axes was then used to determine the angle to rotate about each axis. The coordinate system was adjusted using a rotation matrix calculated from the angle between each axis of the desired coordinate system and the default coordinate system.

Once the data has been adjusted, many deformation values such as stress and strain can be found and physical behaviors can be quantified. Since the position of each marker is recorded at each time, strain between any two markers can be found throughout the test by finding the distance between the markers. The position of any group of markers can be plotted to show the behavior of the frame as a system, or to show the behavior of certain components. Figure 3.12 shows the rotation of the gusset plate in specimen NCBF 2 based on the two LED markers indicated. The plot shows that the gusset plate moves upward and rotates as the brace bows out of plane, which was expected. This behavior would be difficult to plot using data from other instruments, but it is easy to plot positions and behaviors when the coordinates of many points are known.

Another interesting measure calculated from the Optotrak data is the angle between the beam and column. This value was found using LED markers on the flanges of the beam and column. Figure 3.13 shows the change in this angle in radians plotted against percent lateral drift. The first plot uses markers closest to the corner, the middle plot uses markers around the end of the gusset plate, and the third plot uses markers farthest from the corner. The plots show a cyclic behavior. As the specimen is loaded with the brace in tension, this angle decreases and is less than 90°. When the specimen is loaded with the brace in compression, the angle increases to greater than 90°. This behavior was expected and physically makes sense for the cyclic loading that was applied to the frame.

Many other plots and values can be obtained from the data recorded by the Optotrak system, some of which cannot be obtained using other instruments. The data can be used to show the behavior of many different components, or the frame as a whole if enough LED markers are used.

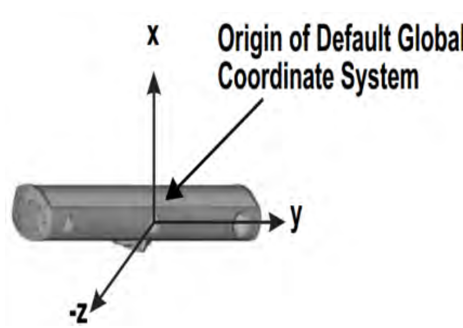

Figure 3.11 Optotrak default coordinate system [Northern Digital Inc. 2009].

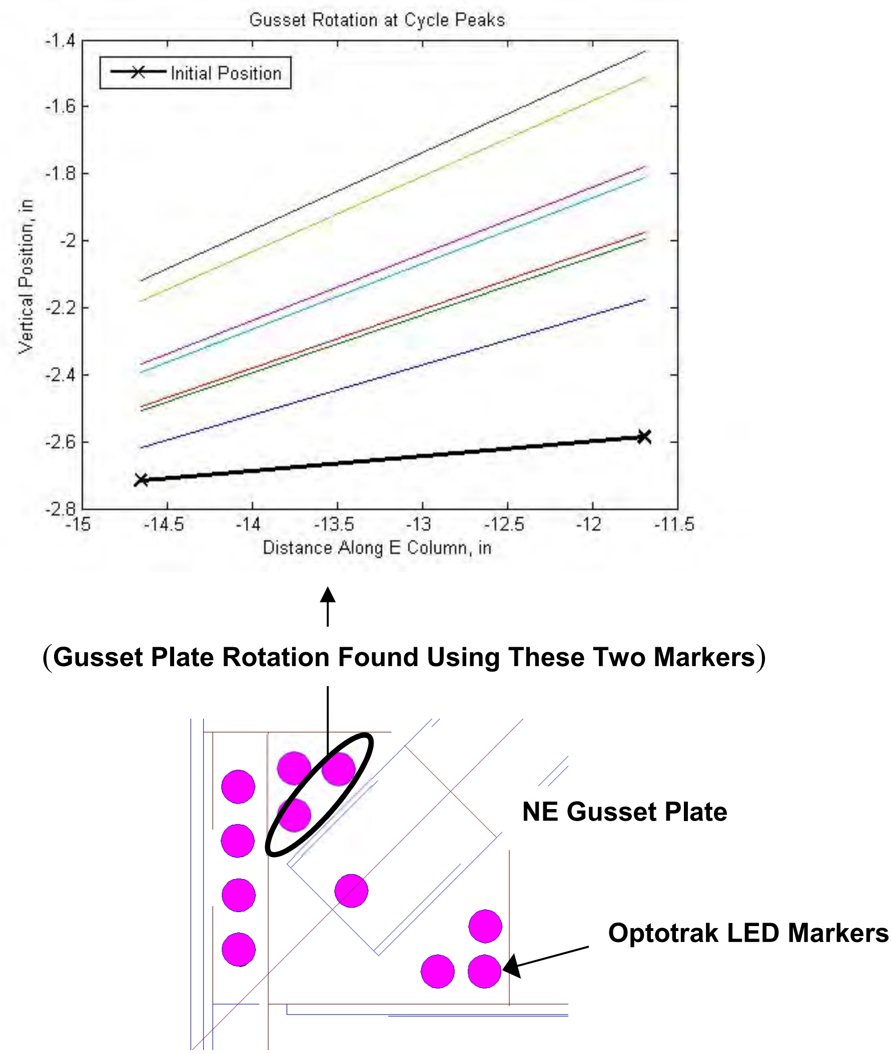

Figure 3.12 Specimen NCBF 2 gusset plate rotation.

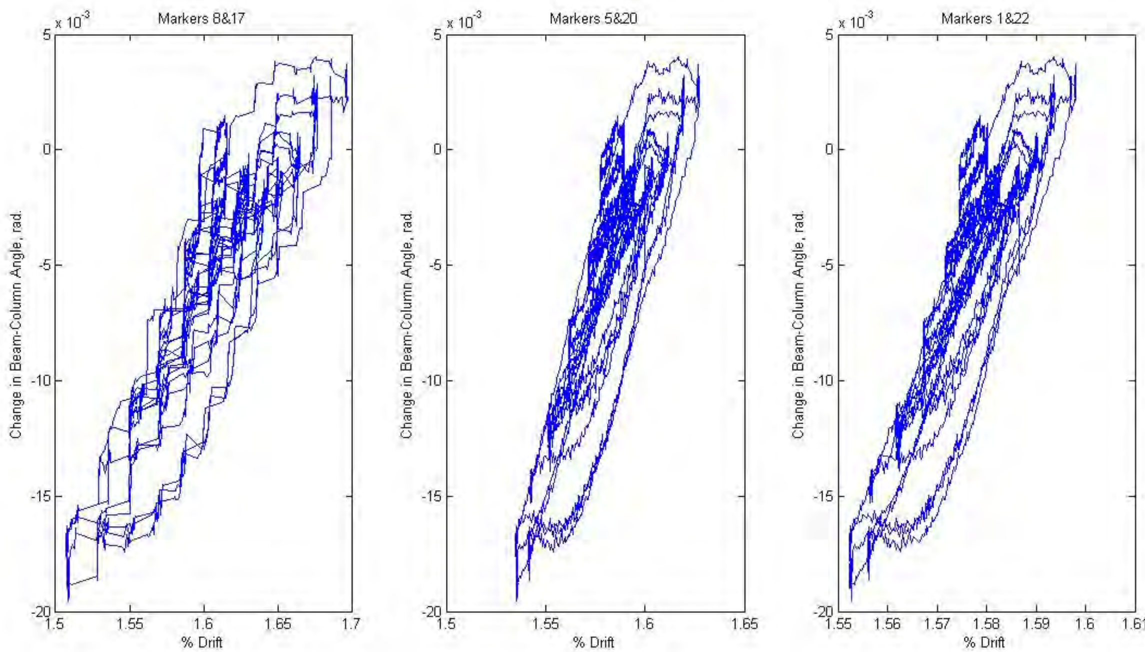

Figure 3.13 NCBF1 change in beam-column angle versus lateral drift.

3.3.3 Accuracy

The Optotrak system gave data with very little scatter that matched closely with the data from other instruments as well as observations of the tests. The scatter in the Optotrak data was very small. The plots in Figure 3.14 show the raw Optotrak data for a marker on the brace of specimen NCBF 2. This plot shows the position in millimeters in the first 1000 frames of the test in each of the default coordinate system directions. For this marker, the X-coordinate data had the most variance. In particular, the points around frame 140 seem to vary greatly. However, the difference between the top and bottom point in this region is only 0.055 mm. This is a very small variance, especially considering the size of the frame. The scatter in the other two directions is even smaller than this, as seen in the middle and right plots.

The plot on the left of Figure 3.15 uses the Optotrak data to show the deflected shape of the brace at the peaks of the last several cycles in the test of specimen NCBF 2. The plot on the right shows the brace mid-span deflection values measured by a string pot and recorded at different drift levels during the test. It can be seen that the Optotrak data follows the same pattern as the recorded brace deflection data, with very similar values for the mid-span deflection. The values should not be exactly equal because the observed values have not been corrected for geometry. Unfortunately, the data from the string pots was not recorded properly, so the exact values could not be used for comparison. Though the values didn't match exactly, the brace behavior depicted and the values from the two sources were very similar, suggesting that the data recorded by the Optotrak system is accurate.

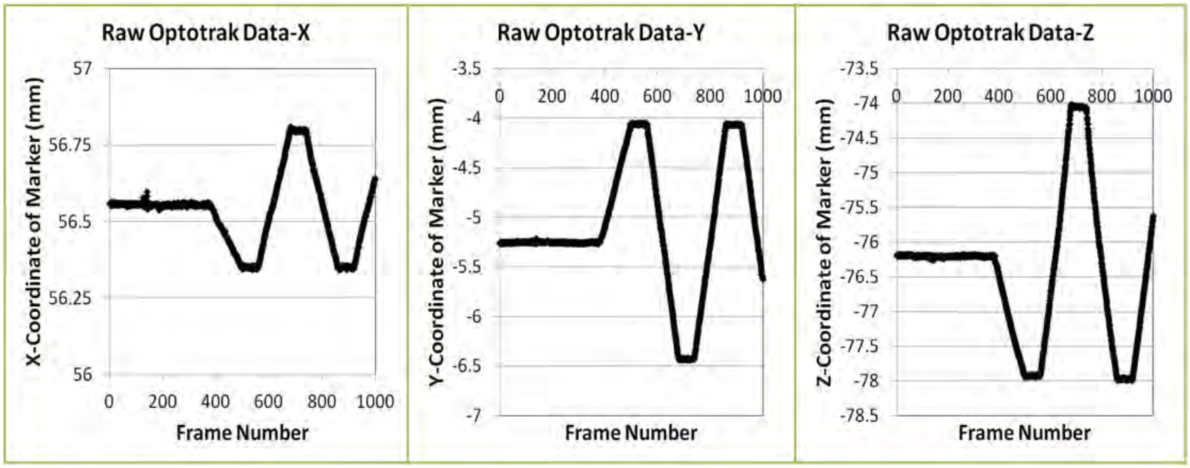

Figure 3.14. Raw Optotrak data.

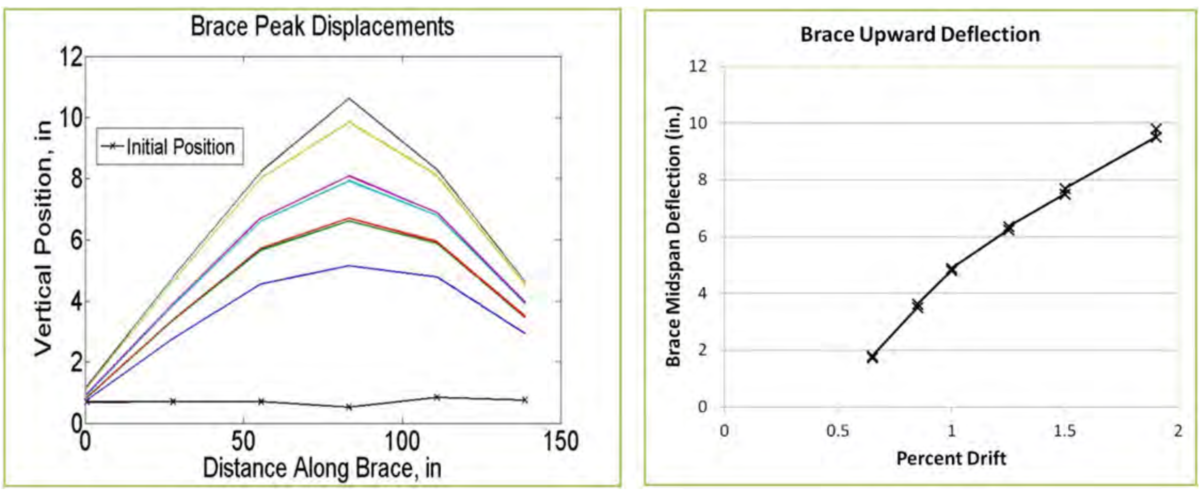

Figure 3.15 Specimen NCBF2 brace deflection.

3.4 CONCLUSIONS

Overall, the data from the Optotrak system was accurate and the system was reliable. The values and patterns matched closely with the values and patterns seen in data from other instruments on the specimens. The plots obtained from the Optotrak data showed behaviors that matched the observed system behavior. The system was reliable once it was set-up correctly, though it did take several trials to learn to calibrate and position the system correctly.

There were several problems encountered with the system while learning to use it, but once those problems were solved the system was fairly easy to use. One problem encountered was the positioning of the sensors so that the markers would be visible. The sensors must be mounted far from the frame in order to capture the entire specimen, but they must have a large enough overlapping volume to calibrate the system. This problem was solved by mounting the position sensors at the top of the strong wall, but the system still cannot detect the entire frame. It was also discovered during testing that the position sensors cannot detect the LED markers if there is sunlight on the frame. Data was not being recorded during a test, but when the blinds in the lab were closed, the system began to record again.

The greatest issue encountered in using the Optotrak system was the coordinate system alignment. Since the system records positions very accurately, the correction of a misaligned system can be the largest source of error. The system allows users to define a coordinate system by selecting an origin, a point on one axis, and a point on the *x*-*y* plane. However, this also leaves room for large error. Any error in the selection of points along an axis or plane will result in an error for the entire coordinate system. Since there is limited space in the area, the origin and point on an axis are relatively close together. This means that a small error in the direction of an axis will be amplified at points farther out on the axis.

Using a rotation matrix to transform the default coordinate system worked fairly well; however, there did seem to be some error in the data. The initial positions of the markers were not always aligned as they should have been when plotted after the coordinates were transformed. This error was not large, and the overall system behavior depicted by the data was not affected. This error is large compared to the variance in the raw data, and could be eliminated if the desired coordinate system is set-up correctly.

Ultimately, the Optotrak system is a reliable and accurate tool if used correctly. More work will need to be done at the University of Washington to set-up a coordinate system for use in future tests and to ensure that the data is collected in the desired coordinate system. Once this is set-up, there should be very little error in the data. This improvement would eliminate the error introduced by transforming the coordinates, and the raw data recorded by the system seems to have very little error.

3.5 ACKNOWLEDGMENTS

Special thanks to PEER and the National Science Foundation for funding and support; Heidi Tremayne for coordinating the program; Molly Johnson, Dan Sloat, and Andy Sen for their mentorship; and Professors Jeffrey Berman, Charles Roeder, and Dawn Lehman for their guidance throughout this project.

3.6 REFERENCES

Berman J.W. (2012). Design of Seismic-Resistant Steel Building Structures: Concentrically Braced Frames. Lecture Notes, University of Washington, Seattle, WA.

Hsiao P, Lehman, D.E., Berman J.W., Roeder C.W., Powell J. (2012). Seismic vulnerability of older braced frames, ASCE, *J. Performance Constructed Facilities*, doi: http://dx.doi.org/10.1061/(ASCE)CF.1943-5509.0000394.

Northern Digital Inc. (2009). Optotrak Certus User Guide, Northern Digital Inc., Canada.

Roeder C, Lehman D.E., Clark K., Powell J., Yoo J.-H., Tsai K.-C., Lin C.-H., Wei C.-Y. (2011). Influence of gusset plate connections and braces on the seismic performance of X-braced frames, *Earthq. Eng. Struct. Dyn.,* 40(4): 355–374.

4. Evaluating a Welded CFT-to-Cap-Beam Connection Detail

Vivian Steyert

ABSTRACT

Concrete filled tubes (CFTs) offer an efficient and economical alternative to conventional reinforced concrete and steel construction including rapid construction and reduced material and labor costs. However, their implementation has been limited partly due to un-reliable connections. The California Department of Transportation (Caltrans) has proposed a column-to-cap-beam connection for CFT columns in which reinforcing bars are welded into the CFT and developed into the cap. In this research, parameters affecting the welded connection detail within the Caltrans proposed connection were evaluated. Specific parameters of interest included the weld strength and the influence of de-bonding the reinforcing bars within the tube. Pullout tests were conducted on 24 reinforcing bars in sizes ranging from No. 7 to No. 11 to evaluate the proposed connection detail. The failure mode of all reinforcing bars was characterized by bar yielding and fracture and tube yielding was not observed in the weld region. Furthermore, de-bonding the bars from the concrete fill minimized concrete damage during pullout.

4.1 INTRODUCTION

Concrete-filled tubes are good candidates for use as bridge columns in seismically active areas; however their implementation is currently limited due to un-reliable connection details. The California Department of Transportation has proposed a CFT column-to-cap beam connection in which reinforcing bars are welded to the inside of the tube some feet below the joint, and extend into the cap beam.

This research aims to evaluate the performance of the proposed connection detail by performing a pullout test on the bars. Test specimens were constructed to resemble the tops of these proposed columns, with reinforcing bars welded in place. The bars were then pulled in axial tension until failure. The preferred failure mode, from a capacity design standpoint, is yielding of the bars, with no damage to the weld region.

4.2 BACKGROUND

There are several benefits to using CFTs, but they lack standard connection details. A brief literature review reveals a variety of connection designs. Not all of the connections included in the review are for CFTs – some are for steel or reinforced concrete. The proposed Caltrans connection differs from all of the connections found in the literature review.

4.2.1 Concrete-Filled Tubes

Concrete-filled tubes are composite sections which consist of steel tubes filled with concrete. As columns or piles, CFTs provide several benefits over conventional reinforced concrete. With the steel at the outside, its moment of inertia is larger, so it provides more flexural resistance. The concrete inside the tube delays buckling relative to a hollow tube, and provides more axial capacity. With the concrete confined inside the tube, the strength and strain capacity of the concrete are increased as well [Kingsley 2005]. In addition, CFTs provide several construction advantages. The steel tube acts as formwork and replaces reinforcing steel for the concrete, reducing the labor required. The steel tube can also support some loads before the concrete has been cast, so that construction may proceed [Kingsley 2005].

4.2.2 Previous Connection Research

Steunenberg et al. [1998] investigated a connection between steel pipes and concrete cap beams in which the pipe is welded to a steel plated embedded in the cap beam. The plate is anchored in the cap beam by reinforcing bars. They found that, as desired, the failure mode of this system under cyclic testing was plastic hinging in the pipe. However, they found signs of bond slip between the reinforcing bar and the embedded plate, and cited overstrength of the pile as a cause for concern, arguing that manufacturers are underreporting strengths for steel, which can lead to problems when attempting capacity design.

Lubiewski et al. [2006] worked on retrofitting cast in place steel shell columns (which are similar to CFT columns) for improved seismic performance. By testing a typical Alaskan connection design and three retrofitted improved designs, they found that cutting some of the longitudinal reinforcement reduced the moment capacity of the column so that there was a ductile seismic response, removing the steel shell near the bent cap reduced damage to the bent cap, and increasing bent cap dimensions allowed several other improvements to reinforce the joint and the bent cap, which initially would fail before the column. The enlarging of the bent cap was useful for decreasing reinforcement congestion, as the reinforcement schemes were quite complex.

Harn et al. [2010] summarize many pile-to-deck connections for steel pipe or pre-stressed concrete piles. They summarize existing test data and characterize each connection detail as an either full or partial moment connection. Full moment connections are capable of developing the plastic moment capacity of the pile while partial moment connections are designed to a lower strength. For steel pipe piles, they find that embedding the pile provides a full moment connection as did another connection which used an embedded plate. The latter is the subject of the paper by Steunenberg et al. [1998], which is discussed above. Other steel pipe connections discussed in this paper are dowels embedded in a concrete plug. These connections are characterized as partial moment connections, but display large ductility. Partially embedding the steel shell in the bent cap resulted in overstrength moments at the connection, so stopping the steel short of embedment is recommended. Reinforcing bars welded to the walls of the tube, with no concrete inside, were also mentioned, but not recommended for lack of test results, and due to concern about brittle fracture because of the weld. Several prestressed concrete pile connections were also addressed.

Stringer [2010] investigated pile to wharf deck connections with precast, prestressed concrete piles. An embedded dowel connection using T-headed bars was used, and details such as interface bearing pads, de-bonding the dowel, and isolating the pile with soft foam around the embedded length were examined.

Fulmer et al. [2013] investigated moment resisting connections between hollow steel pipe piles and steel cap beams. Simply welding the steel pile to the cap beams led to brittle cracking at the welded region, which is not the preferred failure mode. Several improvements were attempted. Adding gusset plates resulted in cracking in the tube near the base of the gusset plate, rather than the preferred failure mode of local buckling. Adding a "capital assembly" to the top of the tube, basically welding another tube around the pile with a thick section at the top and a thinner section lower down, did result in local pile buckling at the thinner part of the capital, moving the damage away from the welded joint as desired. However, the ductility was less than desired. Adding studs to the top of the pile, a steel tube around those, and grout to fill that space also successfully relocated the damage, with local buckling occurring below the welded region.

Kappes et al. [2013] verified Montana Department of Transportation (MDT) guidelines for CFT to concrete cap connections. The connection tested involved U-shaped reinforcement around the embedded part of the CFT, as well as other reinforcement. The test focused on the pile cap rather than on the CFT.

4.2.3 CALTRANS Proposed Connection Detail

The proposed CFT-to-cap-beam connection uses reinforcing bars welded to the inside of the steel tube, with the weld located well below the joint as shown in Figure 4.1. The welded bars extend into a grouted region in the cap beam, the rest of which can be precast. The proposed connection detail differs significantly from those previously studied, as evidenced by the above literature review. In particular, welding the bars to the inside of the tube, 24 bar diameters below the top of the CFT, is unusual.

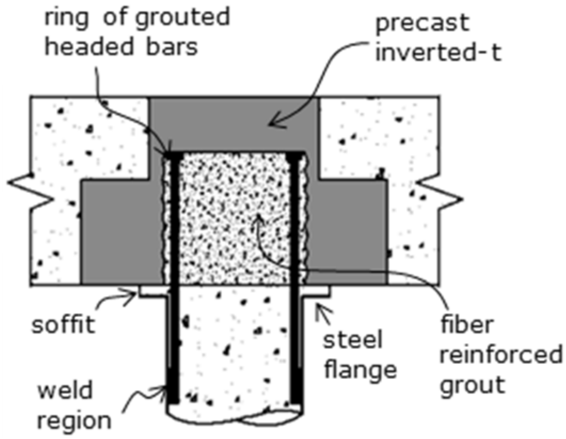

Figure 4.1 **The CFT-to-cap-beam connection proposed by Caltrans.**

4.3 METHODS

Four specimens were constructed and tested. Specimens A and B used No. 7 reinforcing bars, Specimen C used No. 9, and Specimen D used No. 11. Each specimen had several bars, with parameters varying from bar to bar. Welds were designed for a particular ratio of weld strength to bar strength, as explained below. The specimens were tested uniaxially using a 200-kip hydraulic ram.

4.3.1 Weld Design and Test Matrix

The focus of this test was how the weld would perform relative to the reinforcing bar. The weld strength was therefore an important consideration. The strength of a weld is given in Equation (4.1), and the strength of reinforcing bar is given in Equation (4.2)

$$\phi R_{n,w} = (\phi 0.6 F_{\text{exx}})(t_e L_w) \tag{4.1}$$

$$P_n = A_{\text{bar}} F_{y,\text{bar}} \tag{4.2}$$

where ϕ is the strength reduction factor for welds of 0.75, $R_{n,w}$ is the weld strength, F_{exx} is the electrode strength, t_e is the effective throat thickness of the weld, and L_w is the length of the weld; and where P_n is the bar tensile strength, A_{bar} is the cross-sectional area of the bar, and $F_{y,\text{bar}}$ is the yield stress of the bar material.

The standard weld type for reinforcing bars is a flare bevel groove weld, shown in Figure 4.2. Effective throat thickness for flare bevel groove welds is defined as t_e = 0.2 d_b [AWS 2010]. One other important note for these welds is that one weld occurs on each side of the bar, so L_w used in Equation (4.1) is twice the actual weld length on a side, as shown on one of the bar welds in Figure 4.2.

(a) (b)

Figure 4.2 Flare bevel groove weld: (a) shows a diagram of the weld, showing the effective throat thickness; and (b) shows one of the No. 7 bars welded to the inside of the tube.

Given a desired strength ratio $(\phi R_n/P_n)$ for a particular size of reinforcing bar, the necessary weld length per side $L_w/2$ can be calculated. However, there is another strength to consider besides that of the weld itself. The weld region can also fail if the base metal onto which the bar is welded fails. In this case, that means shear failure of the steel tube. Both yielding and fracture must be considered to find the appropriate reduced strength for the base metal, as shown in Equation (4.3). With that, the weld's base metal strength can be computed, as given in Equation (4.4).

$$\phi F_{bm} = \text{Minimum}\left[\left(0.6\phi_y F_y\right),\left(0.6\phi_u F_u\right)\right] \tag{4.3}$$

$$\phi R_{n,bm} = \phi F_{bm} t_{bm} L_w \tag{4.4}$$

where ϕF_{bm} is the reduced strength of the base metal, ϕ_y is the yield strength reduction factor of 1.0, F_y is the yield strength of the base metal, ϕ_u is the ultimate strength reduction factor of 0.75, and F_u is the ultimate strength of the base metal; and where $\phi R_{n,bm}$ is the reduced strength of the weld's base metal, and t_{bm} is the thickness of the base metal. Again, a required weld length per side $L_w/2$ can be calculated from a desired strength ratio $(\phi R_n/P_n)$. The weld length per side chosen should be the maximum of the two values given by considering the weld and the base metal.

The strength ratio was one of the specimen parameters varied in the test matrix. Other primary variables included bar size, embedment depth, and whether the bars were de-bonded from the concrete. De-bonded bars were tested to evaluate the strength contribution of the concrete-to-reinforcing-bar bond. The test matrix is shown in Table 4.1. To identify the specimens, each tube was given a letter, and each bar in the tube was given a number.

Table 4.1 Test parameters for each specimen.

Specimen and Bar	Bar No.	De-bonded	Strength ratio $\phi R_n/P_n$ specified	Embedment Depth (in bar diameters)
A1	7	No	0.8	24 d_b
A2	7	No	1.0	24 d_b
A3	7	No	1.1	24 d_b
A4	7	No	1.2	24 d_b
A5	7	Yes	0.8	24 d_b
A6	7	Yes	1.0	24 d_b
A7	7	Yes	1.1	24 d_b
A8	7	Yes	1.2	24 d_b
B1	7	No	0.8	24 d_b
B2	7	No	1.0	24 d_b
B3	7	No	1.1	24 d_b
B4	7	No	1.2	24 d_b
B5	7	Yes	0.8	24 d_b
B6	7	Yes	1.0	24 d_b
B7	7	Yes	1.1	24 d_b
B8	7	Yes	1.2	24 d_b
C1	9	No	1.0	18 d_b
C2	9	Yes	1.0	18 d_b
C3	9	No	1.0	24 d_b
C4	9	Yes	1.0	24 d_b
D1	11	No	1.0	18 d_b
D2	11	Yes	1.0	18 d_b
D3	11	No	1.0	24 d_b
D4	11	Yes	1.0	24 d_b

4.3.2 Specimen Construction

The test specimens were steel tubes with reinforcing bar welded to the sides, and with concrete fill, as shown in Figure 4.3. Specimens A and B were constructed by a previous researcher. Except where noted, construction procedures were similar to those used to construct specimens C and D. The following steps were taken to construct specimens C and D. A spiral welded steel tube with 20 in. outer diameter and ¼ in. thickness was torch-cut to the appropriate length. Two small holes were drilled near the top of each tube, so that the overhead crane could be used to move the specimens. Grinders were used on the inside of the tube at the top edge, so that the reinforcing bar would sit flush against the tube. Weld lengths and embedment depths were indicated on the reinforcing bar with duct tape, and the reinforcing bar was clamped in place.

A professional welder welded the reinforcing bar into place, welding from the back of the tube. The welder used a flux core arc welding method with E70 electrodes. These were flare bevel groove welds as shown in Figure 4.2 above. Specified and measured weld lengths are given in Table 4.2. The welder was unable to weld the exact length specified while reaching far into the tube. Especially for specimens A and B, the actual welds were mostly longer than specified, leading to weld overstrength.

Small wooden pallets were topped with plywood, and the specimens were strapped down onto the plywood. Hydrostone was used to seal the steel-tube-to-plywood connection, applied from outside the tube. The bars specified as "de-bonded" in specimens C and D in the test matrix were fitted with PVC as shown in Figure 4.4 on the right. The fit was tight, so slits were cut in the PVC where needed to allow the PVC into the proper position. Slits, where used, were between the reinforcing bar and the steel tube. The ends of the PVC tubes were sealed onto the reinforcing bar with caulk. For the de-bonded bars in specimens A and B, the de-bonding process was different. The bars were simply wrapped with duct tape over the embedded length, as shown in Figure 4.4 on the left. In both cases, bonded and de-bonded bars alternated around the tube, so that concrete damage due to one bonded bar would have less impact on the next bonded bar. The de-bonded bars were tested first in each tube, again to minimize the influence of concrete damage on subsequent tests. Hydrostone was poured into the base of the cylinders to further seal the bottoms and prevent concrete leaking. Concrete was cast inside the steel tubes. The concrete had a low-shrinkage admixture. Specimens C and D are shown in Figure 4.5.

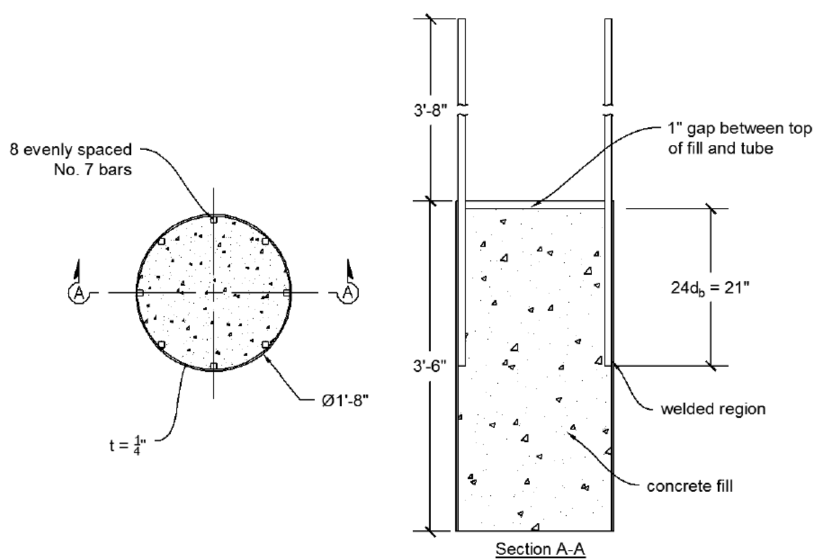

Figure 4.3 Schematic of specimen A or B, a steel tube filled with concrete, and with bars embedded in the concrete and welded to the tube. Specimens C and D were similar, but with larger bars and varying embedment depths as detailed in Table 4.1 above. Specimens C and D also differ from this figure because they only have four evenly spaced bars, rather than eight.

Table 4.2 **Specified and measured weld lengths. Measured weld lengths are calculated as an average of the length of the weld on both sides of the bar, and measured from the outside and the inside of the tube. The rightmost column is the strength ratio as calculated by substituting in the measured weld length.**

Specimen and Bar	Bar No.	Strength Ratio $\phi R_n/P_n$ Specified	Weld Length Specified (in.)	Weld Length Measured (in.)	Strength Ratio $\phi R_n/P_n$ from Measured Length
A1	7	0.8	2.98	3.94	1.06
A2	7	1.0	3.72	4.72	1.27
A3	7	1.1	4.09	4.00	1.08
A4	7	1.2	4.47	5.22	1.40
A5	7	0.8	2.98	3.69	0.99
A6	7	1.0	3.72	4.623	1.24
A7	7	1.1	4.09	5.06	1.36
A8	7	1.2	4.47	4.88	1.31
B1	7	0.8	2.98	3.69	0.99
B2	7	1.0	3.72	4.38	1.18
B3	7	1.1	4.09	4.44	1.19
B4	7	1.2	4.47	4.88	1.31
B5	7	0.8	2.98	3.44	0.92
B6	7	1.0	3.72	4.31	1.16
B7	7	1.1	4.09	4.56	1.23
B8	7	1.2	4.47	4.81	1.29
C1	9	1.0	4.80	4.72	0.98
C2	9	1.0	4.80	4.80	1.00
C3	9	1.0	4.80	4.69	0.98
C4	9	1.0	4.80	4.58	0.95
D1	11	1.0	7.07	7.31	1.03
D2	11	1.0	7.07	7.13	1.01
D3	11	1.0	7.07	7.08	1.00
D4	11	1.0	7.07	7.48	1.06

Figure 4.4 **De-bonded and bonded bars alternating inside steel tubes: (a) shows No. 7 bars de-bonded with duct tape, and (b) shows No. 9 bars de-bonded with PVC tubes.**

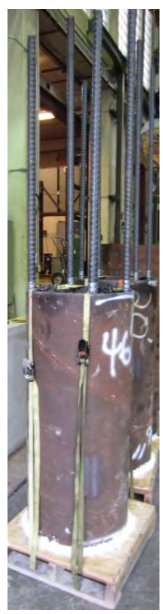

Figure 4.5 **Specimens C and D before concrete casting.**

4.3.3 Instrumentation

Instrumentation for these tests consisted of string potentiometers and a load cell. Strain gages were also used for three of the bars. The load cell was calibrated using a small Baldwin compressive testing machine and an indicator for the load that machine was applying. In Figure 4.6, the load cell is shown stacked with the other equipment around the bar.

Two string potentiometers were used to measure global bar displacement. The strings ran from below the exposed bars up to above the chuck, where a rod was affixed perpendicular to the bar under test. The strings were vertical at the start of each test, and remained essentially vertical throughout. Although the goal was to load the bars in uniaxial tension only, some bending was observed, so two string potentiometers were necessary to calculate the actual height change, as shown in Figure 4.7. Strain gages were placed on the weld regions of three of the bars in Specimen A. Strain gage placement is shown in Figure 4.8.

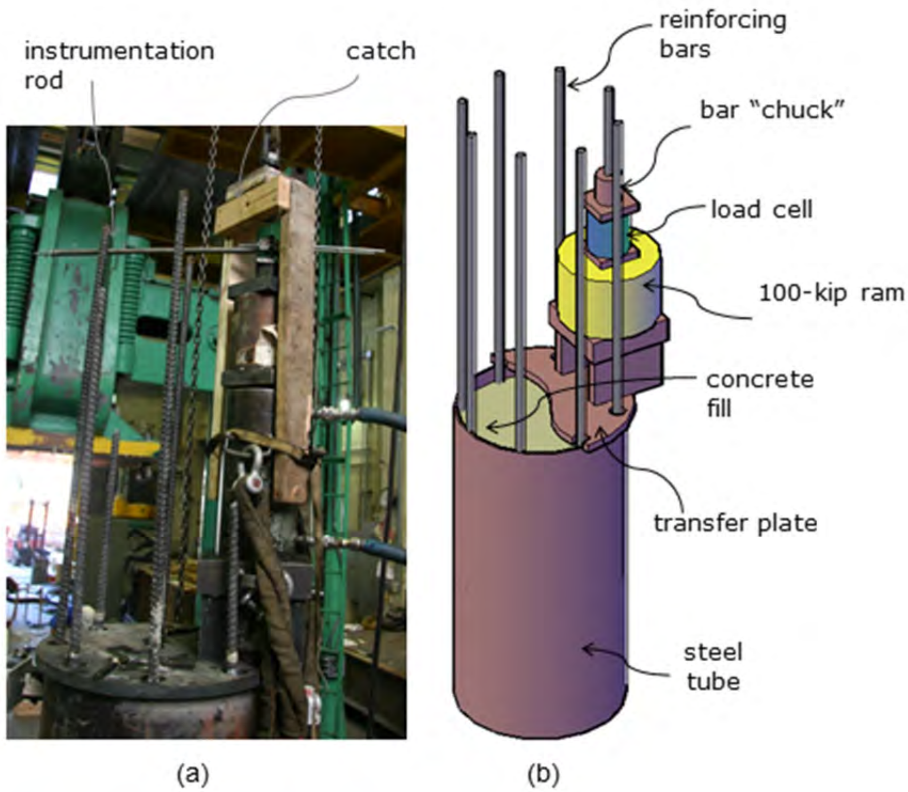

Figure 4.6 **Experimental test setup photo and schematic. String potentiometers, instrumentation rod, and catch removed from schematic for clarity.**

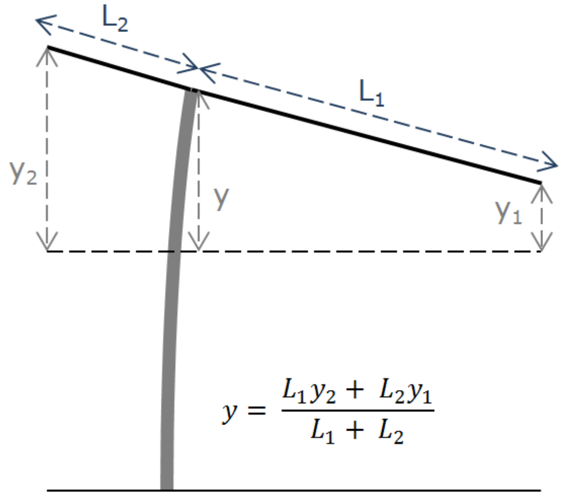

Figure 4.7 **Diagram of string potentiometer setup. The reinforcing bar, although bent, had a height change of y. To measure this height change, two string potentiometers measure the height changes y_1 and y_2. These are attached at perpendicular distances L_1 and L_2 from the bar. The distances are necessary so that the potentiometer can attach to the side of the CFT.**

Figure 4.8 **Close up of strain gage layout. The gages are placed above, beside, on, and below the weld.**

4.3.4 Test Set-Up and Procedure

The test setup is shown in Figure 4.6 above. A ram pushed up (through some plate washers) on a bar "chuck" which gripped the reinforcing bar. The ram reacted against a stand, which was placed on a reaction plate resting on top of the steel tube. For Specimens C and D, the reaction plate was welded to the tube. A load cell was also included in the stack surrounding the bar, to measure the force being applied.

The instrumentation rod was placed above the bar "chuck." A safety "catch" was suspended above the bar from a crane. Both of these are shown in Figure 4.6 (a). When the reinforcing bar eventually fractured, the "catch" prevented the top part from shooting up. A piece of PVC was also included in the test setup. It was fit into the uppermost plate washer, using duct tape to make the fit tight, and extended down to the reaction plate before the bar started elongating. The purpose of this tube was to keep the broken off part of the bar aligned on top of the other part after fracture, so that the top part would not fall to the ground. This idea worked as long as the bar fractured somewhere along the length the PVC covered.

Once the test was set-up for a particular bar, the test procedure was simple. A hydraulic pump was used to push up the ram, and the force and displacement data were monitored using LabVIEW. For most tests, the string potentiometers were removed as soon as the force began decreasing after strain hardening. This decrease indicated that fracture was imminent, and it was important not to damage the string potentiometers. For specimen C and the last bar tested of specimen D, testing was halted at this same point. It was unnecessary to break the bars, and the possibility for damaging equipment was too high.

4.4 RESULTS

In each case, the reinforcing bar fractured, or at least yielded, underwent strain hardening, and was about to fracture when the test was stopped.

4.4.1 Quantitative Results

Force versus displacement curves were plotted for each bar. Force was given by the load cell, and displacement of the bar was calculated from the string potentiometer data as shown in Figure 4.7 above. Some representative force-displacement curves are shown in Figure 4.9. The curves match well with the expected curve for a bar yielding. From these plots, the yield and ultimate strengths could be determined. Averages for each bar size are given in Table 4.3. The strain gage data were mostly noise, and did not provide insight beyond what could be determined from observation. There was no failure in the weld region.

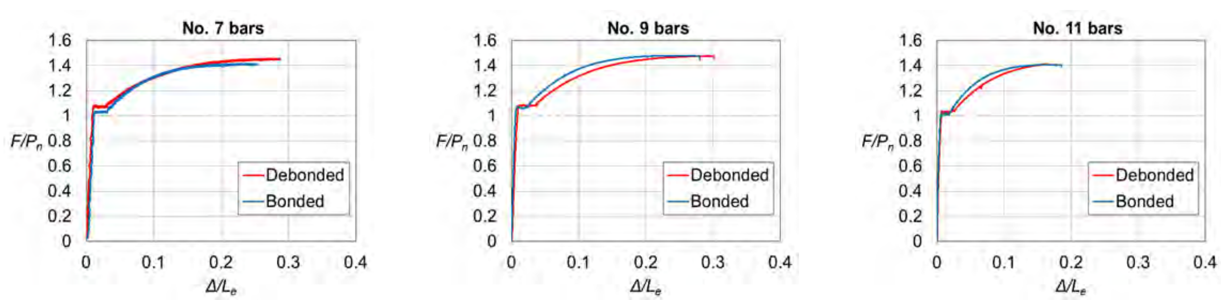

Figure 4.9 Representative force-displacement curves for each bar size. Force is normalized by the theoretical bar yield strength P_n. Displacement is normalized by the embedded length L_e.

Table 4.3 Average yield and ultimate strengths of bars of each size. Theoretical yield strength is also included.

Bar No.	Theoretical Yield Strength P_n (kips)	Yield Strength (kips)	Ultimate Strength (kips)
7	40.8	42 ± 1	60 ± 1
9	68.0	72 ± 1	99 ± 2
11	106.1	108 ± 1	150 ± 2

4.4.2 Observations

The failure mode of the reinforcing bars was visible. A typical reinforcing bar failure is shown in Figure 4.10. In Figure 4.11, a typical weld region is shown after testing. The weld region was whitewashed so that damage would be more visible, but still no damage was observed. More damage to the concrete was observed after bonded bar pullout than after de-bonded bar pullout, as shown in Figure 4.12.

Figure 4.10 Typical failed No. 7 reinforcing bar.

Figure 4.11 Typical weld region after testing. The whitewash shows no damage.

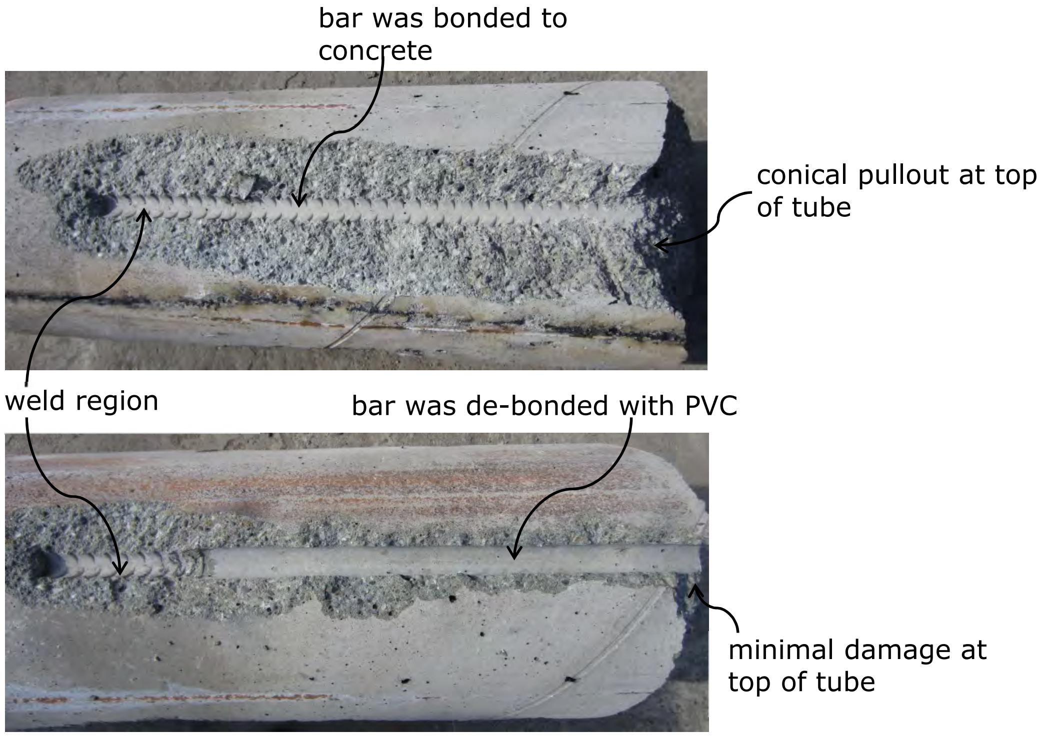

Figure 4.12 Concrete damage from No. 11 reinforcing bar pullout. Photographs were taken after the steel tube was torch-cut off to expose the concrete.

4.5 CONCLUSIONS

The failure mode of the connection was reinforcing bar fracture in all cases. Thus, that aspect of the design works as desired. Further testing will be required before the entire column-to-cap-beam connection can be used in practice. De-bonding the reinforcing bar from the concrete decreases concrete damage. It also increases ductility by increasing the effective length over which the bar is straining.

4.6 ACKNOWLEDGMENTS

Thanks to PEER and NSF for supporting my research this summer, and Caltrans; Professors Dawn Lehman and Charles Roeder for their guidance; Max Stephens for his excellent mentorship and advice; Heidi Tremayne for coordinating the PEER internship program; and Donovan Holder, Lisa Berg, and Vince Chaijaroen for their assistance in the lab.

4.7 REFERENCES

AWS (2010). *Structural Welding Code – Sheet Steel*, American Welding Society, D1.3, Miami, FL.

Fulmer S.J., Kowalsky M.J., Nau J.M. (2013). Seismic performance of steel pipe pile to cap beam moment resisting connections, University of Alaska Transportation Center, *DOT FHWA-AK-RD-13-02*, Fairbanks, AK.

Harn R., Mays T.W., Johnson G.S. (2010). Proposed seismic detailing criteria for piers and wharves, ASCE, *Ports 2010,* Reston, VA, pp. 460–469.

Kappes L., Berry M., Stephens J. (2013). *Performance of Steel Pipe Pile-to-Concrete Cap Connections Subject to Seismic or High Transverse Loading: Phase III Confirmation of Connection Performance*, Montana State University, Bozeman, MO.

Kingsley A.M (2005). *Experimental and Analytical Investigation of Embedded Column Base Connections for Concrete Filled High Strength Steel Tubes*, M.S. thesis, Department of Civil and Environmental Engineering University of Washington, Seattle, WA.

Lubiewski M.C., Silva P.F., Chen G. (2006). Seismic retrofit of CISS pile bent cap connections, Alaska Department of Transportation, Statewide Research Office, Juneau, AK.

Steunenberg M., Sexsmith R.G., Stiemer S.F. (1998). Seismic behavior of steel pile to precast concrete cap beam connections. *J. Bridge Eng.,* 3(4): 177–185.

Stringer S.J. (2010). *Seismic Performance of Improved Damage Resistant Pile to Wharf Deck Connections*, M.S. thesis, Department of Civil and Environmental Engineering University of Washington, Seattle, WA.

5. Effect of Fines and Plasticity on Evaluating Sample Disturbance

Shelly Dean

ABSTRACT

The occurrence of earthquake induced liquefaction and cyclic softening in low plasticity silts and clays indicates the importance of evaluating the seismic behavior of existing intermediate soil foundations. Obtaining high-quality *in situ* samples provides the best prediction of the seismic behavior of these intermediate soils. Currently, sample disturbance criteria are only available for pure clays. This study aims to develop practical sample disturbance criteria for intermediate soils in order to accurately estimate seismic behavior. Strain controlled consolidation tests are performed on samples of silica silt or Nevada sand with varying amounts of kaolin clay and different levels of induced sample disturbance. The $\Delta e/e_0$ index and sample quality designation (SQD) criteria are then used to evaluate these mixtures. As an additional measure of sample disturbance, the swell index (C_s), recompression index (C_r), and compression index (C_c) are evaluated. These results show the $\Delta e/e_0$ index and SQD criteria are not solely dependent on sample disturbance but decrease as a function of fines and plasticity. The C_s/C_r ratio appears to be less dependent on the amount of fines and level of plasticity, and seems to be a viable alternative for classifying sample disturbance for intermediate soils.

5.1 INTRODUCTION

Ground failure due to earthquake loading has occurred over a broad range of low plasticity clays and silts, indicating the need for direct data that identifies the properties and strengths of intermediate soils [Boulanger and Idriss 2006]. Intermediate soils have grain size distributions between pure sands and pure clays, and are often referred to as sands with fines. Understanding the seismic behavior of intermediate soils is an important research effort that requires laboratory testing. Laboratory testing on undisturbed soil samples provides the best prediction of the behavior of natural soil foundations under loading [Rutledge 1944]. Experts recommend obtaining samples and performing laboratory tests for low plasticity soils for determination of their seismic response [Bray and Sancio 2006; Idriss and Boulanger 2008]. To evaluate the seismic behavior of structures founded on or constructed by intermediate soils, practical, scientific characterization of sample disturbance criteria needs to be developed.

Sample disturbance alters the structure of the soil from its *in situ* conditions. Disturbance can be caused by stress relief, mechanical disturbance, extrusion, transportation, storage environment, and sample preparation [Lunne and Long 2005]. Although soil sampling disturbance can be minimized by employing the best equipment and techniques, some disturbance is inevitable due to the removal of surrounding and covering soil pressures [Rutledge 1944]. Sample disturbance effects on high plasticity clays have been given much attention due to their low strength and high compressibility [Lunne et al. 2006]. Research studies on Lierstranda clay [Lunne et al. 2006] and Bothkennar clay [Lunne et al. 1997] indicate that the change in void ratio relative to the initial void ratio, $\Delta e/e_{0,}$ is the best parameter to quantify sample disturbance for highly plastic clays.

This study performs strain controlled consolidation tests on samples of silica silt or Nevada sand with varying amounts of kaolin clay. Each mixture experiences different levels of induced sample disturbance. The $\Delta e/e_0$ index and sample quality designation (SQD) criteria are applied to these mixtures to determine the amount of fines and level of plasticity that these criteria are valid. As a possible measure of sample disturbance, the swell index (C_s), recompression index (C_r), and compression index (C_c) are evaluated. The objective of this study is to establish a relationship between fines, plasticity, and level of sample disturbance for intermediate soils.

5.2 BACKGROUND

5.2.1 Intermediate Soils

Intermediate soils are heterogeneous mixtures that have grain size distributions between pure sands and pure clays. These mixtures can include low plasticity silts and clays and are often referred to as sands with fines. These soils include course grained sands, fine grained silts, and clays. Due to varying particle sizes and structure (Figure 5.1), intermediate soils exhibit a wider range of engineering behavior, which can make characterization difficult. The engineering behavior of soils is characterized by its ability to be molded (plasticity) and ability to stick together (cohesiveness). Sands exhibit nonplastic and cohesionless behavior, while clays typically exhibit plastic and cohesive behavior. Although silts are fine grained, they can exhibit plastic or nonplastic behavior. The presence of water can have a significant effect on fine-grained soils, particularly clays, affecting their engineering behavior. The engineering behavior of course-grained soils (e.g., sands) is greatly affected by the particle shape and size of the coarse grained material [Holtz et al. 2011].

Intermediate soil deposits are often encountered in engineering practice. Geological surface processes such as weathering and surface water can result in varied soil types and the formation of intermediate soils [Holtz et al. 2011]. Man-made intermediate soil foundations can be created when soil deposits are altered at construction sites. Most levees consist of intermediate soils due to the alluvial deposition environment of rivers.

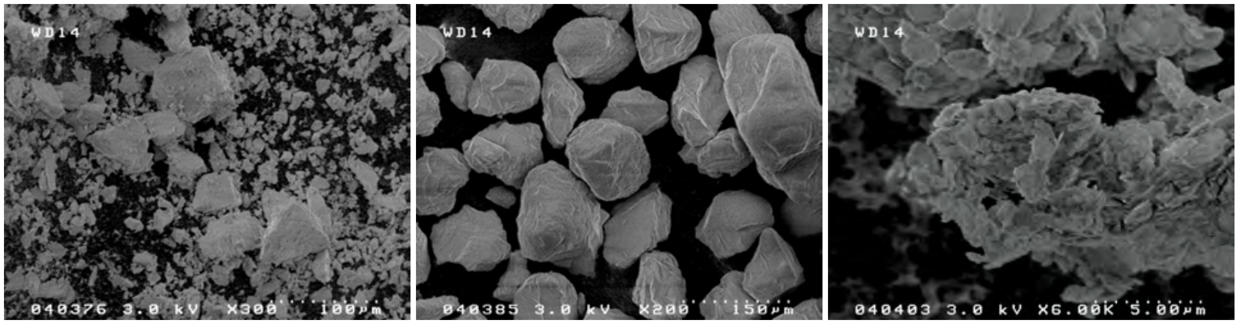

Figure 5.1 **The scanning electron micrographs (SEM) of silica silt, Nevada sand, and kaolin clay (left to right) show how these soil types vary in particle size and structure.**

The occurrence of earthquake induced liquefaction and cyclic softening in low plasticity silts and clays indicates the importance of evaluating the seismic behavior of existing intermediate soil foundations [Boulanger and Idriss 2006]. The loss of soil strength due to seismic loading is known as liquefaction in cohesionless sand-like soils and cyclic softening in cohesive clay-like soils [Boulanger and Idriss 2006]. Studies performed by Boulanger and Idriss [2006] show the dependence of fine grained soils to levels of plasticity, indicating clay-like, sand-like, or intermediate behavior under monotonic and cyclic undrained loading (see Figure 5.2). These results show that cyclic softening occurs over a wide range of low-plasticity clays and liquefaction occurs in low-plasticity silts, with intermediate behavior in between. Boulanger and Idriss [2006] recommended obtaining samples for laboratory testing in order to estimate strengths in low-plasticity silts and clays. Before performing these laboratory tests, the effects of sample disturbance in these low plasticity soils must be evaluated.

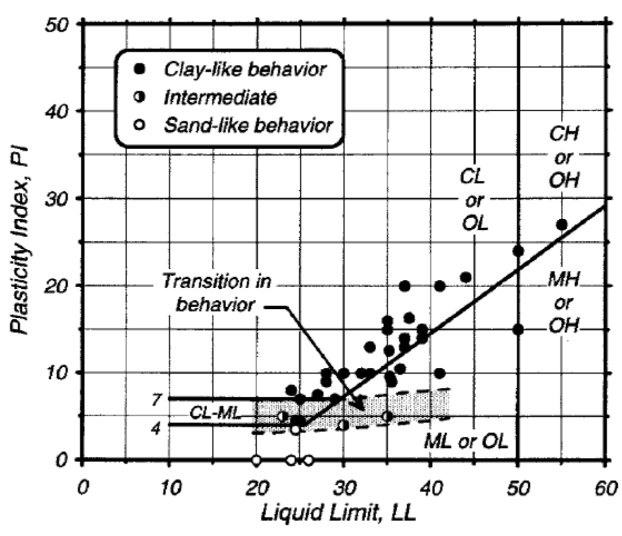

Figure 5.2 **Casagrande chart of soils prone to sand-like liquefaction, clay-like cyclic softening, or intermediate behavior [Boulanger and Idriss 2006].**

5.2.2 One-Dimensional Consolidation Testing

Determining the effects of sample disturbance is limited to tests that measure physical soil properties [Rutledge 1944]. Consolidation tests, which compress saturated soils while measuring load and volume changes, are often used to predict soil settlement and quantify sample disturbance [Rutledge 1944]. One-dimensional consolidation testing implies that the soil samples are loaded vertically over a larger area than height [Holtz et al. 2011]. There are two types of consolidation tests: incremental consolidation load (ICL) and constant rate of strain (CRS) consolidation. The ICL tests load the soil samples in increments and are best used to determine the coefficient of consolidation (c_v); and CRS consolidation tests apply loads by controlling strain and are better at measuring a soil's stress history.

Consolidation curves are used to evaluate sample disturbance and the structural properties of soils. These curves are presented in semi-log form as strain or void ratio versus the logarithm of the vertical effective stress (σ'_v). A soil sample's preconsolidation stress (σ'_p) is the maximum vertical overburden stress experienced by the soil sample and can be estimated from stress history or consolidation plots using Casagrande's method. The initial slope of the void ratio versus effective stress curve is labeled the swell index (C_s), the slope of the unload-reload loop is the recompression index (C_r), and the slope that follows the recompression index is the virgin compression index (C_c) (Figure 5.3).

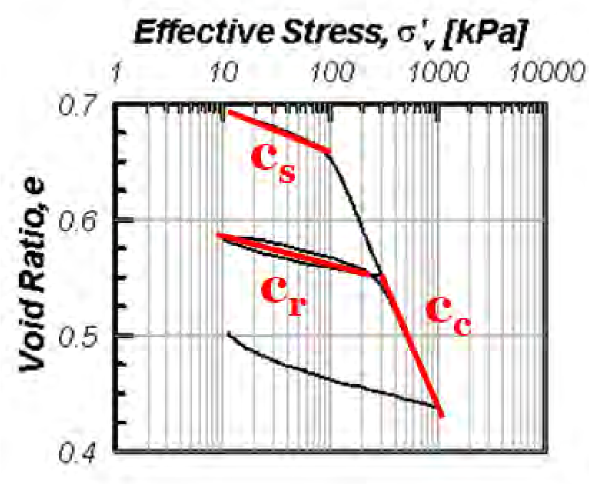

Figure 5.3 Consolidation test curve with labeled swell index (C_s), recompression index (C_r), and compression index (C_c).

5.2.3 Evaluating Sample Disturbance

5.2.3.1 Volumetric Strain and SQD

Sample disturbance for clay samples has been quantified by the change in volumetric strain up to the soil's *in situ* vertical effective stress (ε'_{v0}) [Andresen and Kolstad 1979]. The specimen quality designation (SQD) criteria developed by Andresen and Kolstad [1979] correlate lower volumetric strain rates with lower levels of disturbance (Table 5.1). High-quality samples are determined to have SQD values of B or better [Terzaghi et al. 1996]. Clay samples that do not meet this standard should not be used to evaluate *in situ* soil strengths. The SQD criteria are intended for cohesive soils with OCR values less than 3–5 [Terzaghi et al. 1996]. In one research study, consolidation tests performed on high-quality undisturbed block samples produced slightly lower changes in volumetric strain than the high-quality undisturbed piston samples for soft clays [Holtz et al. 1986]. Because block samples have been used as the standard in high-quality sampling, the change in strain observed at the *in situ* vertical effective stress was determined to be a good indicator of sample quality [Holtz et al. 1986].

Table 5.1 Specimen quality designations based on volumetric strain [Andresen and Kolstad 1979].

Volumetric Strain (%)	Specimen Quality Designation (SQD)
<1	A
1-2	B
2-4	C
4-8	D
>8	E

5.2.3.2 Δe/e0 Index

All soils are composed of solids, fluids, and gases. Void ratio is the term used to describe this composition, defined as the volume of fluids and gases (voids) over the solids volume. Typical void ratios for clays and sands are 0.3–1.5 and 0.4–1.0, respectively [Holtz et al. 2011]. Based on consolidation, triaxial, and direct simple shear tests performed on marine clays, the change in void ratio over the initial void ratio ($\Delta e/e_0$) was observed be systematically dependent on sample disturbance [Lunne et al. 1997; 2006]. The change in void ratio (Δe) is the difference between the initial void ratio and the void ratio at the soils *in situ* vertical effective stress (σ'_{v0}). Tests performed on Norwegian clays at depths of 0–25 m and with PI values between 6 and 53 and water contents between 20–67% produce low $\Delta e/e_0$ values for high-quality block samples and higher $\Delta e/e_0$ values for ordinary piston tube samplers [Lunne et al. 1997, 2006]. These sample disturbance criteria are currently used an accepted standard for distinguishing between good and poor clay samples [Lunne et al. 2006]. The $\Delta e/e_0$ index has also been recommended over the volumetric strain sample disturbance criteria discussed previously [DeGroot et al. 2005]; see Table 2.5.

Table 5.2 Sample disturbance criteria based on $\Delta e/e_0$ [Lunne et al. 1997].

OCR	Sample Quality Category			
	Very good to excellent	Good to fair	Poor	Very poor
1-2	<0.04	0.04-0.07	0.07-0.14	>0.14
2-4	<0.03	0.03-0.05	0.05-0.10	>0.10

5.2.3.3 Consolidation Curve Indices

The magnitude of the swell index depends on the soil composition and history of the soil sample [Holtz et al. 2011]. Sample disturbance increases the swell index and makes the pre-consolidation stress point harder to identify [Santagata et al. 2002]. However, silts and other low plasticity soils rarely exhibit a defined pre-consolidation stress because these soils can adjust to the new maximum stress and allow a continuous breakdown of soil structure [Holtz et al. 2011]. Because low-plasticity soils are less compressible, they have smaller swell indices [Holtz et al. 2011].

The recompression and compression indices are determined by loading the sample past the pre-consolidation stress. Because these consolidation parameters are dependent on loads greater than its stress history, they are independent of sample disturbance and are dependent on soil properties [Holtz et al. 2011]. Higher-plasticity soils exhibit greater compressibility and therefore have greater recompression and compression indices.

5.3 METHODS

5.3.1 Soil Characterization

Consolidation tests were performed on non-cohesive silica silt (SS) or Nevada sand (NS) with varying amounts of cohesive kaolin clay (KC). The mixtures tested were 100%, 80%, 60%, 40%, 20%, and 0% of dry weight silica silt or Nevada sand mixed with kaolin clay. To eliminate fines the Nevada sand was passed through a No. 200 sieve in accordance with *ASTM D6913* [2009]. The soil gradation curves of kaolin clay, silica silt, and Nevada sand (Figure 5.4) were determined from sieve and hydrometer analysis.

The liquid limit (LL), plastic limit (PL), and plasticity index (PI) of each soil mixture were measured according to *ASTM D4318*. The plasticity index indicates the range of water contents that the soil mixture behaves plastically. Typically, clays have high PI values, silts have low PI values, and coarse-grained soils exhibit non-plastic behavior. The silica silt used in this study is non-plastic. All mixtures were prepared at initial water contents of 1.5 times the mixture's liquid limit and were left saturated for at least 24 hr. prior to consolidation. Test mixtures were chosen to sweep across a range of plasticity and fines content. Figure 5.6 shows that increasing the percentage of kaolin clay increased the soil's plasticity. Using the gradation curves (Figure 5.4) the fines content was determined for each sample mixture (Table 5.3).

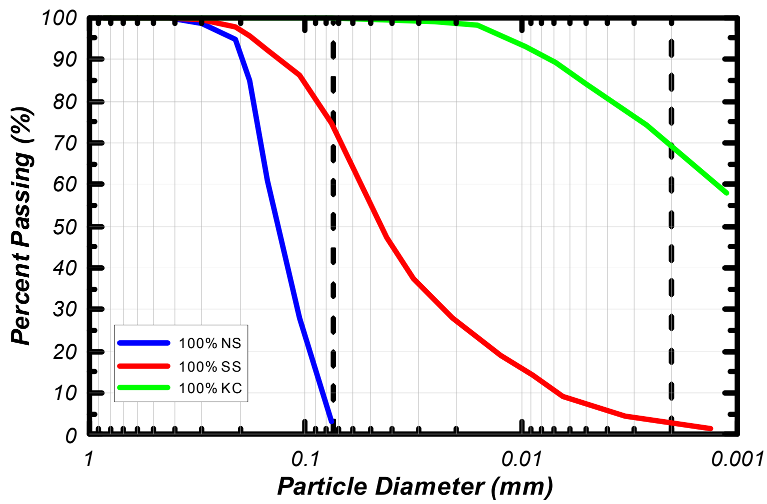

Figure 5.4 Grain size distribution curves for 100% kaolin clay, silica silt, and Nevada sand.

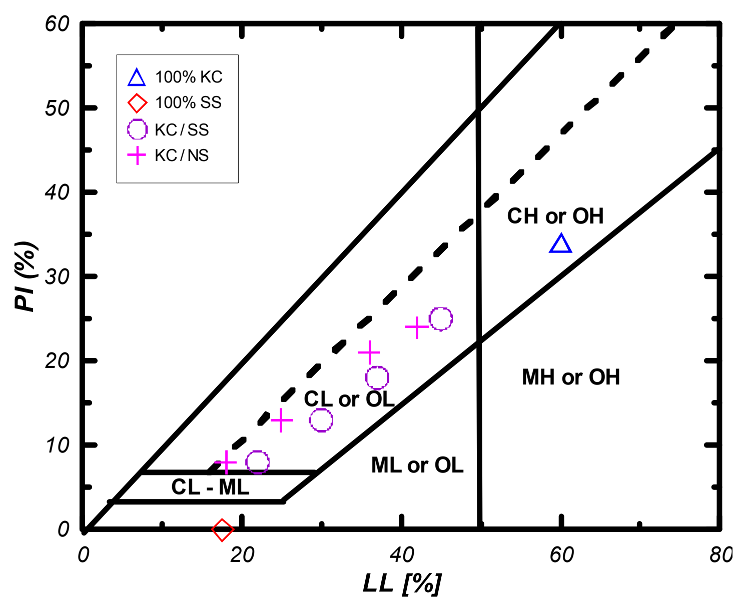

Figure 5.5 Casagrande chart of tested mixtures.

Table 5.3 Fines content of tested mixtures.

KC (%)	SS (%)	NS (%)	Fines Content (%)
100	0	0	100.0
80	20	0	95.0
60	40	0	89.9
40	60	0	84.9
20	80	0	79.8
0	100	0	74.8
0	0	100	3.3
20	0	80	22.6
40	0	60	42.0
60	0	40	61.3
80	0	20	80.7

5.3.2 Strain Rate Selection

A soil's resistance to compression is less at lower rates of compression because the soil material responds to deformation as individual particles instead of as a whole unit [Gorman 1981]. Slower strain rates more closely duplicate field conditions and create stress-strain curves that are less susceptible to error [Gorman 1981]. At faster strain rates, the pre-consolidation stress can be passed over, producing inaccurate consolidation curves. However, slower strain rates require longer consolidation tests, which can minimize the amount of tests able to be performed.

According to *ASTM D4186* [1998], CRS consolidation tests must be performed at strain rates that cause the ratio of excess pore pressure over the applied vertical stress to be between 3–30%; however, achieving a ratio of 20% is considered good practice. Controlling this ratio is important to determine the effective stress of the soil during loading. One study used CRS consolidation tests of kaolin clay samples to establish a relationship between strain rate, the ratio of pore pressure over vertical stress, and coefficient of consolidation [Gorman 1981]. The strain rate selection equation is shown in Equation (5.1):

$$r = \frac{c_v * \ln\left(1 - \frac{u_b}{\sigma_u}\right)}{0.22} \tag{5.1}$$

where r is the strain rate (%/min), c_v is the coefficient of consolidation (in.^{2}/min), u_b is the excess pore water pressure, and σ_u is the applied vertical stress. The Casagrande log time method was used to estimate the coefficient of consolidation from increment controlled load (ICL) consolidation tests and the corresponding target strain rates using Equation (5.1) are shown in Table 5.4.

Table 5.4 Selected strain rates based on soil mixture.

KC (%)	SS (%)	NS (%)	Strain Rate (%/hr)
100	0	0	0.6-1
80	20	0	0.6-1
60	40	0	1
40	60	0	2
20	80	0	7
0	100	0	8
0	0	100	8
20	0	80	7
40	0	60	2
60	0	40	1
80	0	20	0.65

5.3.3 Controlled Rate of Strain (CRS) Consolidation

5.3.3.1 Apparatus

Consolidation tests were performed by a GEOTAC Sigma-1 automated consolidation system (Figure 5.5a) Soil samples with less than 80% kaolin clay were loaded in a floating ring consolidometer (Figure 5.5b). This creates two-dimensional drainage since porous stones are located at the top and bottom faces of the soil specimen. The remaining soil mixtures were loaded in a fixed-ring consolidometer (Figure 5.5c) with one-dimensional drainage occurring at the top of the sample and pore pressures measured at the bottom of the sample. Pore pressure is measured in the samples with 80% kaolin clay or greater because their high compressibility creates excess pore pressure stresses that cannot be neglected and is necessary to convert from total to effective stress. In both consolidometers, filter paper is placed on the top and bottom of the soil sample. Porous stones allow the passage of water and air, but restrict the passage of solids. These consolidation procedures were performed in accordance to *ASTM D4186* [1998].

(a)

(b)

(c)

Figure 5.6 (a) Soil sample loaded in the GEOTAC Sigma-1 automated consolidation system; (b) floating ring consolidometer; and (c) fixed ring consolidometer.

5.3.3.2 Testing Procedure

For each soil mixture, three different preparation methods were performed to mimic different levels of sampling and sampling disturbance. Undisturbed samples were preloaded to 100 kPa in the consolidometer. After reaching this preload, the undisturbed samples were unloaded for a minimum of 1 hr. prior to running the consolidation test to allow the soil to rebound and the pore pressure to equilibrate. In addition to undisturbed tests, two types of disturbed samples were preloaded to 100 kPa in a 71-mm- (2.8-in.-) diameter steel tube (loaded in four sub-increments of 26, 51, 77, and 100 kPa). The 100 kPa load was allowed to consolidate overnight before the soil samples were extruded and trimmed to the 63.5-mm- (2.5-in.-) diameter consolidometer rings. Trimmings from this process were used to determine the initial water content of the disturbed samples. Each preloaded tube allowed for two consolidation tests; one of the samples was immediately loaded in consolidometer and labeled as “disturbed,” while the other disturbed sample, or “highly disturbed,” was frozen in a freezer overnight and thawed at room temperature for 4 hr. the next day before being loaded in the consolidometer. Before performing the CRS consolidation test, all initial soil heights were measured and recorded.

The soil samples loaded in the consolidation apparatus had an initial seating load of 10 kPa. Once the initial seating load was established, the sample would be consolidated at the given strain rate (Table 5.3). Each sample was loaded to 300 kPa, unloaded to 10 kPa, and reloaded to a final load of 1000 kPa. Upon reaching 1000 kPa, the samples were unloaded and the test was completed. Each sample was weighed and placed in an oven to determine the final moist mass, dry mass and water content.

The effective stresses for the samples with less than 80% kaolin clay were assumed to be equal to the total stress because no excess pore pressure was assumed to be generated due to selected strain rates in Table 5.4. For samples with 80% kaolin clay or greater (where pore pressure generation could not be neglected), the effective stress was calculated as:

$$\sigma'_{v0} = \sigma - \frac{2}{3} u_b \tag{5.2}$$

where σ'_{v0} is the effective stress, σ is the applied total stress, and u_b is the measured excess pore water pressure at the bottom of the sample. The calculations for the initial void ratio and change in void ratio for each test are shown below:

$$e_0 = \frac{V_{\text{initial}} * SG}{m_{\text{dry}}} - 1 \tag{5.3}$$

$$\Delta e = \varepsilon * (1 + e_0) \tag{5.4}$$

where e_0 is the initial void ratio, V_{initial} is the initial soil volume, SG is the specific gravity of soil (assumed to be 2.65), m_{dry} is the dry mass of soil, Δe is the change in void ratio, and ε is the measured strain.

The swell index was defined as the slope of the linear regression line of the void ratio versus effective stress points from the initial seating load (10 kPa) to its vertical effective stress. The slope of the unload-reload loop, ranging from 10 kPa to 300 kPa defined the recompression index (C_r) The virgin compression index (C_c) slope ranged from 300 kPa to 1000 kPa.

5.4 RESULTS AND DISCUSSION

5.4.1 Effect of Fines and Plasticity

Increasing the fines content and plasticity of the undisturbed soil samples increases strain, C_s, C_r, and C_c (Figure 5.7). Note that the 80% kaolin clay with silica silt mixture behaves almost identically to the 100% kaolin sample (Figure 5.7b) due to the silica silt floating in the kaolin clay matrix [Holtz et al. 2011]. The 100% kaolin clay has similar consolidation behavior as the 80% and 60% kaolin clay with Nevada sand samples (Figure 5.7a). The fines particles are also able to float within a larger granular matrix, observed between the 20% kaolin clay with Nevada sand and the 100% Nevada sand sample. Samples with higher fines content and plasticity tend to exhibit a larger initial void ratio and change in void ratio during consolidation. The area inside the unload/reload loop of the consolidation curve also increases with plasticity. Similar trends are observed in the disturbed and highly disturbed samples. This suggests that the effects of sample disturbance are not only dependent on the amount of disturbance, but also depend on the level of plasticity.

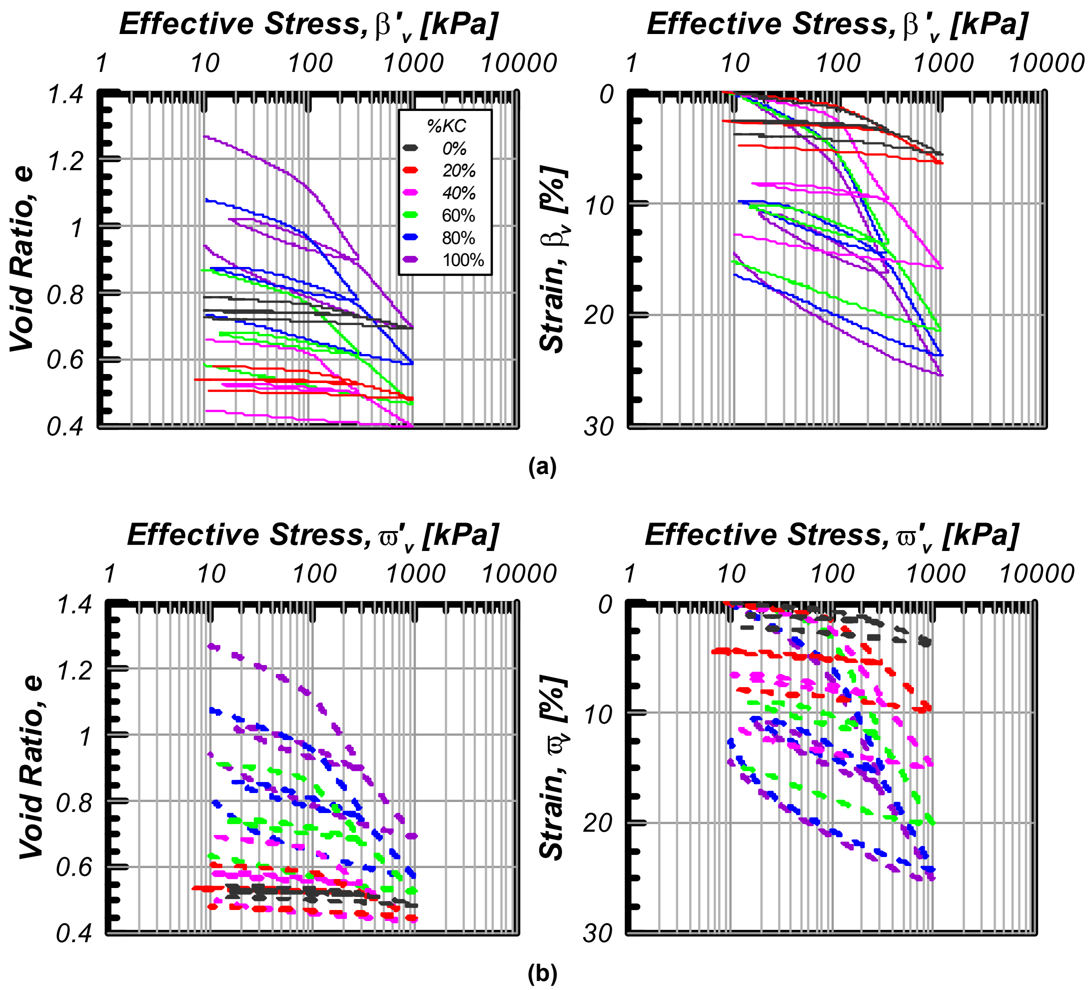

Figure 5.7 **The undisturbed consolidation curves demonstrate that increasing the amount of fines and level of plasticity increases strain, C_s, C_r, and C_c: (a) kaolin clay with Nevada sand (solid lines); and (b) kaolin clay with silica silt (dashed lines).**

5.4.2 Effect of Sample Disturbance on Consolidation Test Results

Sample disturbance is shown to affect the swell index, but has little effect on the recompression and compression indices (Figure 5.8). As disturbance increases, the swell index tends to increase, suggesting this parameter is a possible indicator of sample disturbance. The level of strain the soil undergoes during recompression to 100 kPa increases with increasing levels of disturbance (Figure 5.8). Increasing the kaolin content causes the consolidation behavior to curve before reaching its pre-consolidation stress, creating a less defined pre-consolidation point. Therefore, the $\Delta e/e_0$ ratio and ε'_{v0} values are larger for higher kaolin contents at 100 kPa due to transitional behavior between the swell and virgin compression slopes.

The $\Delta e/e_0$ index, ε'_{v0}, C_s, C_r, and C_c parameters were evaluated for each consolidation test. When consolidation tests are performed on excavated soil samples the *in situ* vertical effective stress is known, but since the samples tested in this study are artificially prepared and consolidated to 100 kPa in the laboratory, they are normally consolidated (e.g., $\sigma'_{v0} = \sigma'_p = 100\,\text{kPA}$, therefore OCR = 1). In order to understand the effects of $\Delta e/e_0$ and ε'_{v0} on over-consolidated samples, an apparent over-consolidation term (OCR*) is used to evaluate $\Delta e/e_0$ and ε'_{v0} at different vertical effective stresses. The sample disturbance parameters are evaluated at OCR* values of 1, 1.5, 2, 3, and 4 to determine how the measured *in situ* vertical stress affects levels of disturbance. Note that unlike excavated soil samples, the load applied to the samples in this study was not allowed to creep under secondary compression (significant for clays).

The change in ε'_{v0} increases with increasing levels of disturbance, amount of fines, and level of plasticity (Figure 5.9). At lower OCR* values, the change in volumetric strain is smaller since less strain is required to mobilize smaller strengths. Figure 5.9 shows how undisturbed samples with high fines content and plasticity have SQD ratings of C or better for an OCR* of 2. These samples only have SQD ratings of B or better when evaluated with an OCR* 4.

Applying the $\Delta e/e_0$ index to intermediate soils shows that the $\Delta e/e_0$ ratio is not only dependent on the level of sample disturbance, but also on the fines content and plasticity (Figure 5.10). Decreasing the fines content and plasticity produces a decrease in the $\Delta e/e_0$ index. As observed previously with the SQD plots, higher plasticity undisturbed samples did not provide an accurate classification of disturbance for all intermediate soil mixtures.

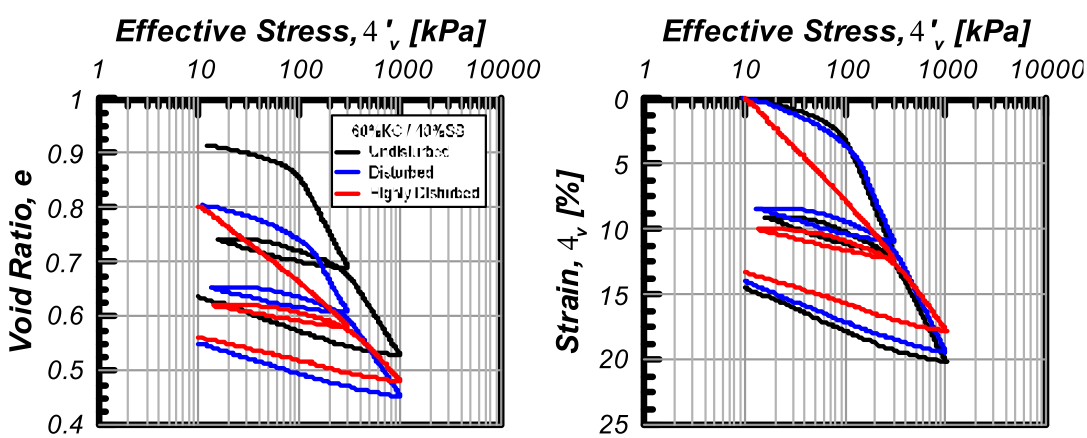

Figure 5.8 The swell index is most affected by sample disturbance.

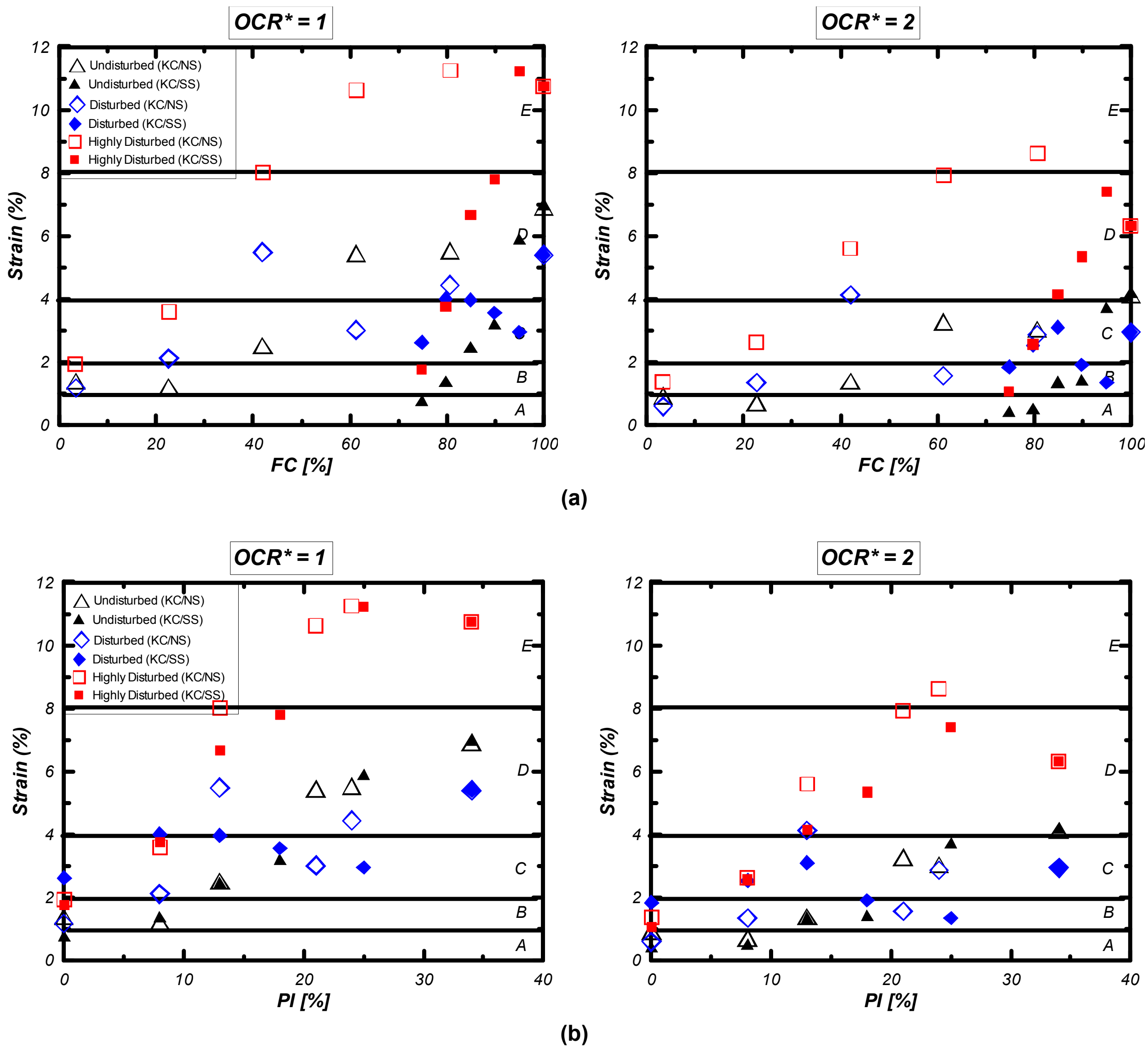

Figure 5.9 **The sample quality designations based on volumetric strain are evaluated at different OCR* levels: (a) versus fines content; and (b) versus plasticity index. Plasticity better describes the observed trends rather than fines content.**

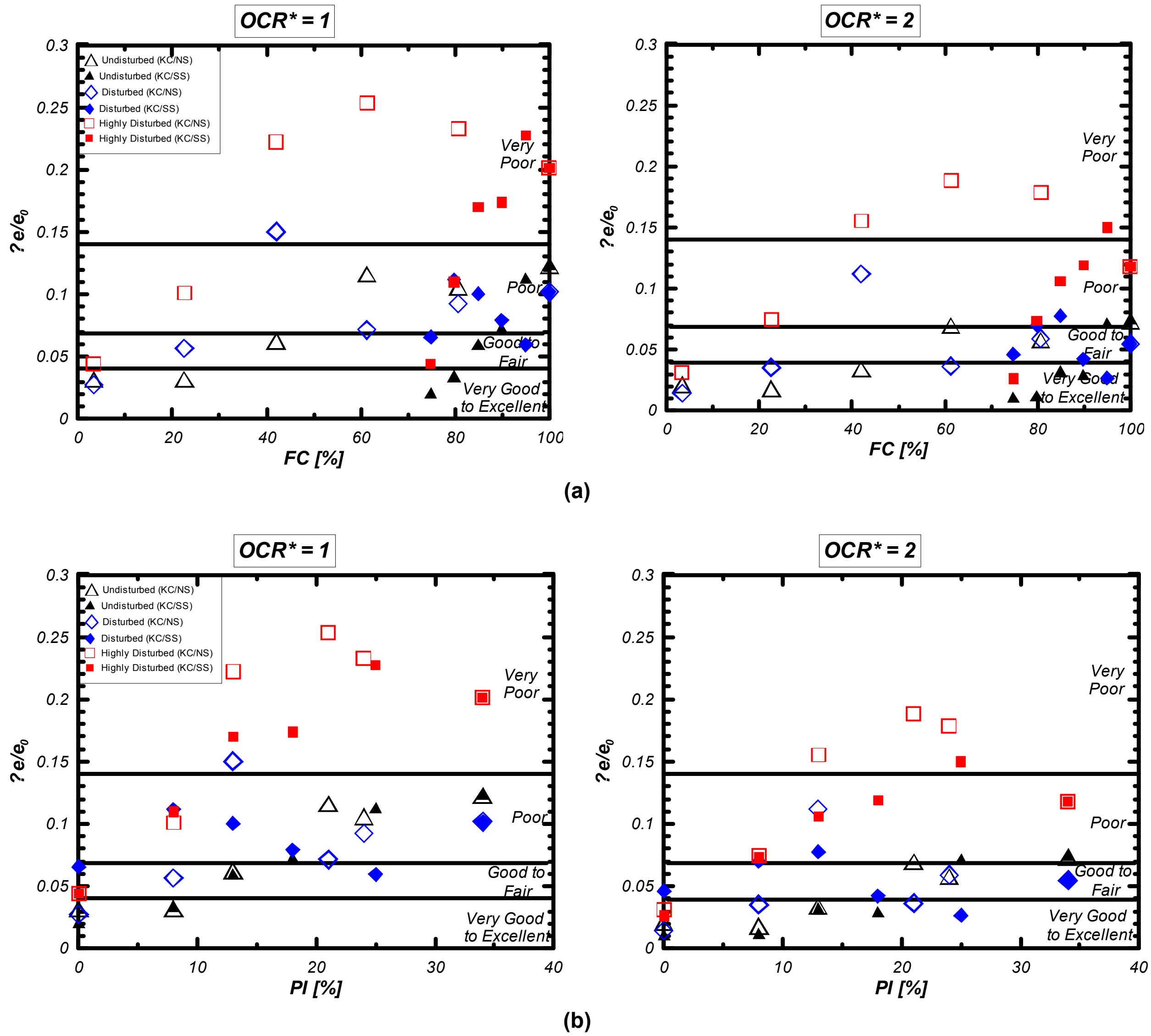

Figure 5.10 **The sample disturbance criteria based on $\Delta e/e_0$ index are evaluated at different OCR* values: (a) versus fines content; and (b) versus plasticity index. Plasticity better describes the observed trends rather than fines content.**

The C_s/C_r ratio is explored as an alternative measure of sample disturbance since C_s is affected by sample disturbance while C_r is largely unaffected. The C_s/C_r ratio is dependent on level of sample disturbance and seems to be less dependent on amount of fines and level of plasticity than $\Delta e/e_0$ and ε'_{v0}, (Figure 5.11). The undisturbed samples have an average C_s/C_r value of 1.5 and exhibit little variation. The disturbed samples have an average C_s/C_r value of 1.5 with little variation at PI values greater than 15%. At PI values between 8–15%, the C_s/C_r ratio for the disturbed samples appears to increase with increasing plasticity. The C_s/C_r ratio of the highly disturbed samples tends to increase with decreasing level of plasticity. The relatively high C_s/C_r ratios for the two types of disturbed samples at lower PI values (FC = 22, 41) may have been caused by the trimming process. The lower plasticity samples exhibited less cohesion and trimming could have induced more disturbances. As observed in the $\Delta e/e_0$ and ε'_{v0} plots, plasticity appears to better describe the observed trends than fines content.

From the plots of $\Delta e/e_0$, ε'_{v0}, and C_s/C_r, sample disturbance was evaluated for varying fines content and plasticity indices. The sample disturbance criteria tend to be more dependent on plasticity rather than fines content. These trends show that $\Delta e/e_0$ decreases as a function of decreasing plasticity and level of disturbance (Figure 5.12). The C_s/C_r is not dependent on plasticity index for undisturbed samples. However, by increasing disturbance, C_s/C_r becomes more dependent on plasticity index and increases with decreasing plasticity.

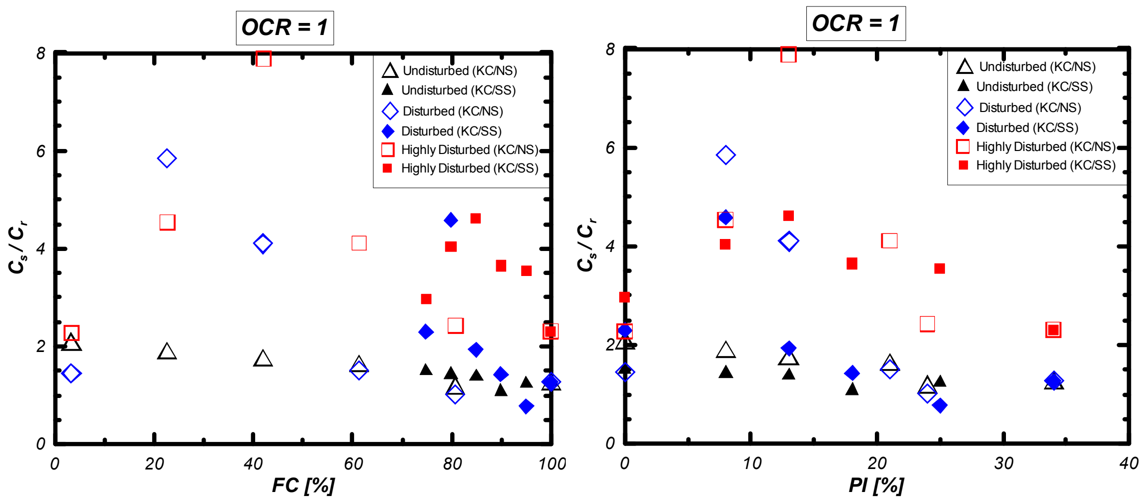

Figure 5.11 **The relationship between C_s/C_r ratio, fines content, and plasticity index is compared for normally consolidated soils.**

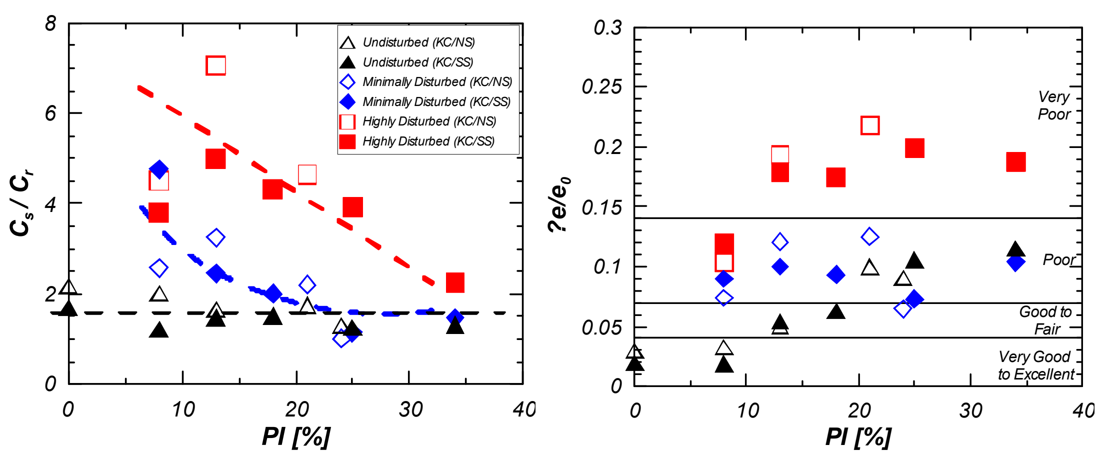

Figure 5.12 **Summary trends of the relationship between C_s/C_r ratio and $\Delta e/e_0$ versus plasticity index for normally consolidated soils.**

5.5 CONCLUSIONS

The preliminary results from this research show that a relationship between the fines content, plasticity, and sample disturbance exists for intermediate soils. The intermediate soil samples tested exhibit low plasticity behavior which can be prone to earthquake induced liquefaction or cyclic softening. Experts recommend obtaining samples and lab tests for low plasticity soils to determine their seismic response. Developing sample disturbance criteria to quantify the effects of sample disturbance for these mixtures is needed for evaluating their in-situ seismic response.

Sample disturbance was observed to increase ε'_{v0}, $\Delta e/e_0$, and C_s, but had no observable effect on C_r, and C_c. Increasing the fines content and plasticity of the soils tested resulted in an increase in $\Delta e/e_0$, ε'_{v0}, C_s, C_r, and C_c. Therefore, the $\Delta e/e_0$ index and SQD criteria are not only dependent on disturbance but also fines content and plasticity. The sample disturbance criteria tend to be more dependent on plasticity rather than fines content. To avoid inaccurate SQDs, samples with PI values less than 15% should not be evaluated. For the higher plasticity undisturbed samples, the SQDs did not provide an accurate classification of disturbance. This is likely because the samples were not allowed to creep under secondary consolidation for a long enough time (e.g., natural clays sit under significant secondary compression for thousands of years). To avoid inaccurate sample quality designations based on the $\Delta e/e_0$ index, samples with PI values less than 15% should not be evaluated. The non-plastic behavior of the 100% silica silt and 100% Nevada sand produced the same sample disturbance classifications for all levels of induced disturbance. This confirms that sample disturbance criteria based on ε'_{v0} and $\Delta e/e_0$ should never be used to classify soils with no plasticity.

Use of the C_s/C_r ratio was proposed for development of sample disturbance criteria independent of the amount of fines and level of plasticity. From the samples tested, the C_s/C_r ratio appears to be less dependent on plasticity and more dependent on level of sample disturbance than $\Delta e/e_0$ and ε'_{v0} sample disturbance criteria. The undisturbed samples have an average C_s/C_r value of 1.5 and exhibit little variation. The disturbed samples have an average C_s/C_r value of 1.5 with little variation at PI values greater than 15%. At PI values between 8−15%, the C_s/C_r ratio for the disturbed and highly disturbed samples appears to increase with decreasing plasticity. The increase in C_s/C_r ratio for the two types of disturbed samples at lower PI values could have been caused by disturbances induced by the difficulty in trimming non-cohesive samples. Although the C_s/C_r ratio seems to be a viable alternative for classifying sample disturbance for intermediate soils, additional research is needed to fully develop sample disturbance criteria that can be applied to intermediate soils. It is hoped that this research will provide a framework for future studies needed to fully quantify the effects of sample disturbance for intermediate soils.

5.6 ACKNOWLEDGMENTS

This research is based upon the support of PEER and funding from the National Science Foundation. I would like to acknowledge graduate mentor Chris Krage and Professor Jason

DeJong for their invaluable guidance throughout this study. Much appreciation also goes out to Heidi Tremayne for her role in establishing the support for this study.

5.7 REFERENCES

Andresen A. Kolstad P. (1979). The NGI 54 mm samplers for undisturbed sampling of clays and representative sampling of coarser materials, *Proceedings, International Symposium on Soil Sampling*, Singapore, pp. 1–9.

ASTM (1998). Standard test method for one-dimensional consolidation properties of soils using controlled strain loading, *ASTM D4186, Annual Book of ASTM Standards*, West Conshohocken, PA.

ASTM (2000). Standard test methods for liquid limit, plastic limit, and plasticity index of soils, *ASTM D4318, Annual Book of ASTM Standards*, West Conshohocken, PA.

ASTM (2009). Standard test methods for particle-size distribution (gradation) of soils using sieve analysis, *ASTM D6913, Annual Book of ASTM Standards*, West Conshohocken, PA.

Boulanger R.W., Idriss I.M. (2006). Liquefaction susceptibility criteria for silts and clays, *J. Geotech. Eng*., 132(11): 1413−1426.

Bray J., Sancio R. (2006). Assessment of the liquefaction susceptibility of fine-grained soils, *J. Geotech. Geoenviron. Eng*., 132(9): 1165–1177.

DeGroot D., Poirier S.E., Landon M.M. (2005). Sample disturbance–soft clays, *Studia Geotechnica et Mechanica*, 24(3–4): 91−105.

Gorman C.T. (1981). Strain-rate selection in the constant-rate-of-strain consolidation test, *Research Report 556*, Division of Research, Kentucky Department of Transportation, Frankfort, KY.

Holtz R.D., Jamiolkowski M.B., Lancellotta R. (1986). Lessons from oedometer tests on high quality samples, *J. Geotech. Eng.*, 112(8): 768–776.

Holtz R.D., Kovacs W.D., Sheahan T. (2011). *An Introduction to Geotechnical Engineering*, Pearson Education Inc., Upper Saddle River, NJ.

Idriss I.M., Boulanger R.W. (2008). *Soil Liquefaction during Earthquakes*, Earthquake Engineering Research Institute, Oakland, CA.

Lunne T., Berre T., Strandvik S. (1997). Sample disturbance effects in soft low plastic Norwegian clay, *Proceedings, Recent Developments in Soil and Pavement Mechanics,* Rio de Janeiro, Brazil, pp. 81−102.

Lunne T., Berre T., Anderson K., Strandvik S., Sjursen M. (2006). Effects of sample disturbance and consolidation procedures on measured shear strength of soft marine Norwegian clays, *J. Geotech. Eng*. 43: 726–750.

Lunne T., Long M. (2005). Review of long seabed samplers and criteria for new sampler design, *J. Marine Geology*, 226(1-2): 145−165.

Rutledge P.C. (1944). Relation of undisturbed sampling to laboratory testing, ASCE, *Transactions*, 1155−1183.

Santagata M.C., Germaine J.T. (2002). Sampling disturbance effects in normally consolidated clays, *J. Geotech. Eng*., 128: 997–1006.

Terzaghi K., Peck R.B., Mesri G. (1996). *Soil Mechanics in Engineering Practice*, John Wiley & Sons, New York.

6. One-Dimensional Compressibility of Intermediate Non-Plastic Soil Mixtures

Sean E. Salazar

ABSTRACT

The results of high stress, one-dimensional compression testing on intermediate soils are presented. Nevada sand and silica silt mixtures were subjected to very high vertical stresses (140 MPa) in one-dimensional (1D), monotonic compression. Each soil mixture was tested in a nominally loose condition. A specially designed mold with an integrated sensor array was fabricated to contain the soil during pre-consolidation and loading. The 1D compression curve was plotted for each mixture in the double-logarithmic void ratio (e), and vertical effective stress (σ'_v) space, and apparent slopes of the Limiting Compression Curve (LCC) were identified. Initial and post-test grain size distribution curves were plotted. Significant crushing of the soil grains was observed during 1D loading. The influence of factors including initial density, mineralogy, particle shape, particle size, and grain size distribution on compression behavior of intermediate soil mixtures is discussed. Specimen preparation techniques and testing protocol are presented herein.

6.1 INTRODUCTION

Loose sand matrices tend to contract under cyclic, partially drained loading induced by earthquake shaking. If the soil is saturated and drainage is limited, stress may be transferred from the soil matrix to the pore water, causing the soil to lose strength and "liquefy." The concomitant effects are the loss of strength and stiffness of the soil and the seepage of water to the surface [Idriss and Boulanger 2008]. Liquefaction may lead to settlement and bearing capacity failures of structures embedded in the soil, cause failure in earth structures, including earth dams and levees, trigger landslides, and cause flotation of buried pipes and tanks [Cox et al. 2009]. The evaluation of liquefaction potential in seismic zones is of great interest to geotechnical and earthquake engineers. To determine susceptibility to liquefaction, a site may be characterized by means of *in situ* and laboratory testing.

There is a fundamental lack of understanding of the behavior of intermediate soils (silty sands, sandy silts, clayey sands, sandy clays, and low-plasticity silts); though the importance of intermediate soils is pervasive in earthquake engineering, particularly in liquefaction susceptibility assessments. There is a plethora of strength data for clean sands and pure clays, and the strengths of intermediate soils are usually interpolated. However, these interpolations are not based on any solid theory or data that relate to the fundamental behavior of intermediate soils. For liquefaction analyses, fines content corrections have been formed empirically. Boulanger and DeJong [2012] have proposed a research program that contains laboratory testing including: one-dimensional (1D) compression, Direct Simple Shear (DSS), and triaxial testing, numerical simulations using FLAC to implement the MIT-S1 constitutive model [Pestana and Whittle 1999], and using an Arbitrary Langragian-Eulerian (ALE) remeshing technique and small centrifuge modeling, to determine reliable intermediate soil strength data and characterization under cyclic seismic loading. Strength data measured in the laboratory will be used to calibrate the FLAC model to determine the relationship between cone penetration resistance (q_c) in cone penetration testing (CPT), and properties including monotonic strengths and cyclic resistance ratios (CRR). The model will be validated using centrifuge testing.

The correlation that will be obtained in this project aims to determine a triggering curve that describes the liquefaction potential of intermediate soils. It has been shown that plotting a curve with q_c as a monotonic strength indicator on the abscissa against CRR (the ratio between shear stress, τ_{cyc}, and the initial effective confining stress, σ'_{vc} required to cause liquefaction) on the ordinate, may predict a triggering curve that describes the potential for soils to liquefy as a function of earthquake induced stresses. This concept is represented in Figure 6.1. These plots are based only on case histories where liquefaction either occurred (solid points) or did not occur (hollow points); the triggering curve represents the boundary between these two conditions. The liquefaction correlations are determined using a combination of empirical data, lab testing, numerical modeling and physical modeling. Historically, such relationships have been developed only for clean sands and sedimentary clays. As a result, the goal of this project is to better characterize the liquefaction potential of intermediate soils.

The testing program of this project includes one-dimensional compression testing that comprises three stages: testing on mixtures of clean Nevada sand with non-plastic fines, non-plastic silica flour with Kaolin clay, and clean Nevada sand and Yolo loam. The first stage of laboratory testing presented herein investigates the influence of the proportion of non-plastic fines content on the compressibility of granular soils. In this context, non-plastic fines are defined as non-cohesive silt particles. The testing program loosely follows previous testing conducted at the Soil Interactions Laboratory at the University of California, Davis, by Erickson [2013]; however, attempts were made to reduce uncertainty due to equipment limitations by improving testing equipment and establishing a revised testing protocol that will be the standard for future 1D compression testing.

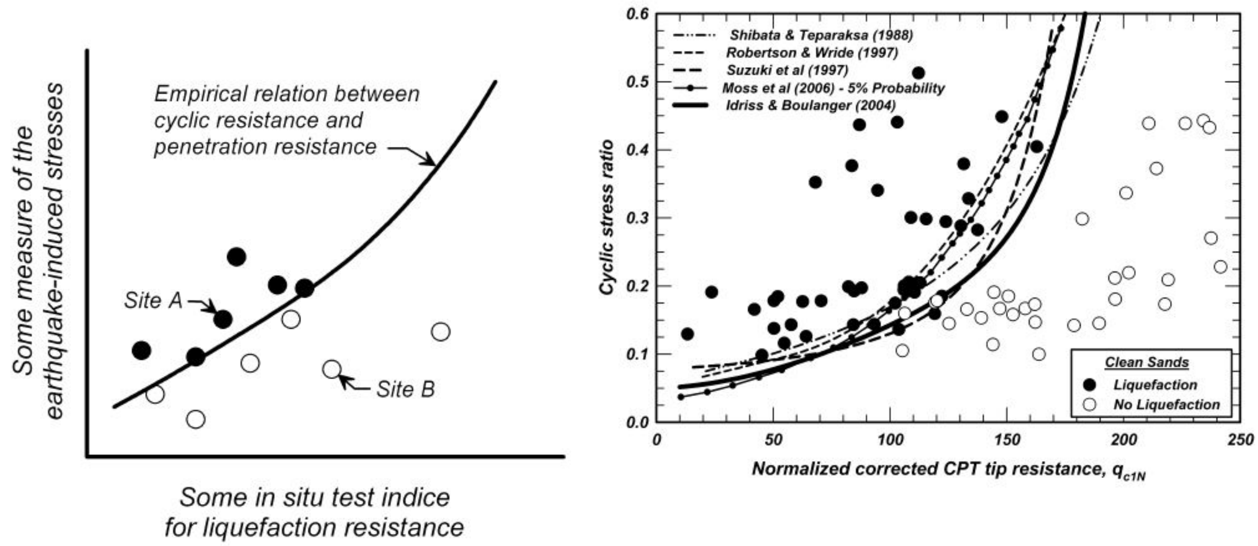

(a) (b)

Figure 6.1 **Liquefaction triggering curves: (a) conceptual curve, (b) curves relating the CRR to q_{c1N} for clean sands with M = 7.5 and σ_{vc} = 1 atm. (from Idriss and Boulanger [2008]).**

6.2 BACKGROUND

Previous work on the influence of factors including initial density, mineralogy, particle shape, particle size, and grain size distribution on compression behavior of soils is discussed.

6.2.1 Limiting Compression Curve (LCC)

Monotonic soil strength tests have been conducted for decades. Roberts and de Souza [1958] investigated the 1D compressibility of sands up to stresses of 10,000 psi (69 MPa) and observed significant deformation in specimens after the onset of crushing and fracturing of particles. It was observed that the initial void ratio (e_o) had a significant effect on the "breakdown stress," defined as the point at which the sand started to crush significantly. Vesić and Clough [1968] investigated the compressibility of uniformly graded sand in standard triaxial compression. The specimens were loaded up to 1000 kg/cm^2 (98 MPa), and it was observed that the granular material behaved in a dilative manner at low confining pressures, eventually reaching a state of high relative compressibility at high stresses, where linear deformation was observed, regardless of e_o. The initial dilative behavior of the specimens was explained as a rearrangement of particles (rolling and sliding). The observed behavior at high stresses was in good agreement with the work of Roberts and de Souza [1958]. Given a set of soil specimens prepared at varying initial densities when subjected to high compressive stresses, the void ratio-effective stress behavior of the specimens has been shown to converge [Pestana and Whittle 1995]. In double logarithmic void ratio-effective stress space, the LCC is characterized as the linear portion of the compression curve during which the primary means of volumetric strain development is particle crushing. A conceptual depiction of the LCC is presented in Figure 6.2. Hagerty et al. [1993]

showed that the steeper and more linear the portion of the curve after the soil has yielded, the more the material is being crushed. It was also observed that as the angularity of particles increased, the break-point stress decreased and became more difficult to define. Very significant crushing of particles was observed at stress levels above 138 MPa.

Lade et al. [1998] investigated the effects of non-plastic fines on the minimum and maximum void ratios of sand. An illustration of the relationship between fines content and void ratio is depicted in Figure 6.3. There is an optimum grain-size ratio that will produce the maximum density in soil mixtures, but once this ratio is surpassed, the density of the soil may decrease. Nakata et al. [2001a] investigated the relationship between single particle crushing and collective crushing in 1D, monotonic compression tests. The maximum compression index (C_c) characterized by major grain splitting was shown to be independent of initial void ratio. The compression index increased during the early stages of compression as the initial void ratio increased. Higher initial void ratio resulted in lower yield strengths. It was shown that single particle strength increased as particle size decreased and that collective crushing was dependent on particle angularity. The compression behavior was marked by the breakage of particle asperities during particle rearrangement before grain splitting occurred. The load was theorized to increasingly distribute and transfer throughout the soil matrix with increasing angularity of particles.

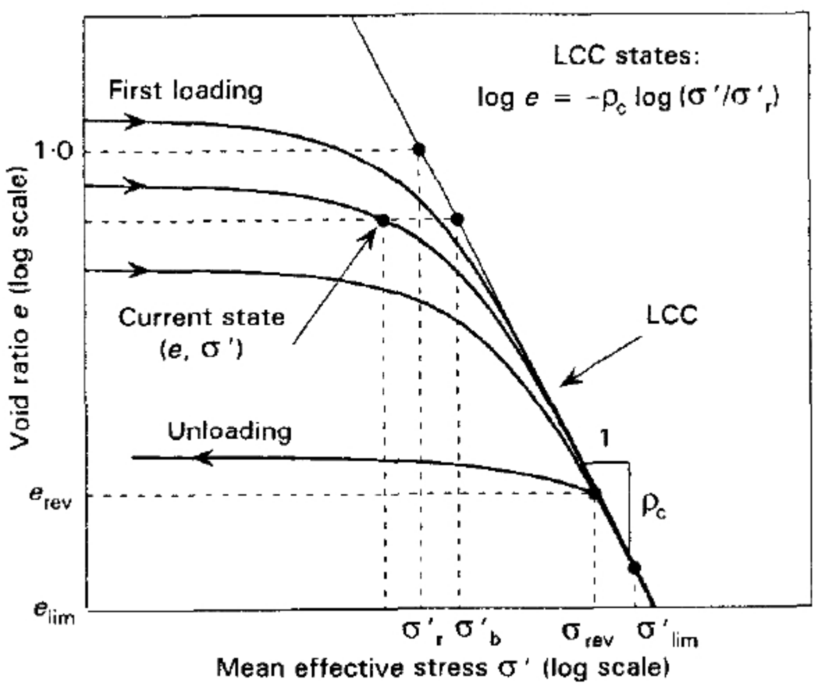

Figure 6.2 Conceptual representation of first loading and unloading of freshly deposited cohesionless soils (from Pestana and Whittle [1995]).

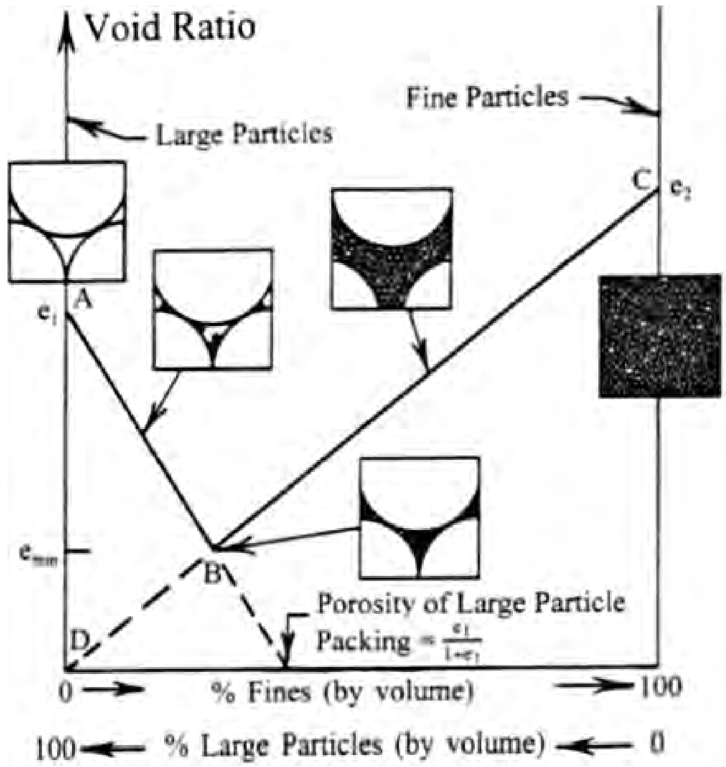

Figure 6.3 **Theoretical representation of the effect of fine particle content on void ratio of granular material (from Lade et al. [1998]).**

Nakata et al. [2001b] conducted 1D, monotonic compression tests on silica sand. The LCC behavior indicated that the stress corresponding to the maximum curvature of the compression curve was greater for well-graded material than for uniformly graded material. The rate of increase in particle damage slowed down considerably in well-graded materials; therefore, as the coefficient of uniformity increased, so the curvature of the compression curve decreased. Nakata et al. [2001a] observed that 90% of particles sustained some kind of damage and 50% had undergone major splitting. Particle size analyses showed that the soils had a tendency to approach a stable gradation after full development of crushing.

Erickson [2013] performed thirteen 1D, monotonic compression tests on loose and dense state soil mixtures of Nevada sand and silica silt. Compliance was observed in testing equipment during compression, which may have affected the results. Additionally, the compression curves were only plotted up to 100 MPa in log void ratio (e), log effective vertical stress (σ'_v) space. The literature suggests that the lack of data above 100 MPa does not allow for full development of the slope in the critical region of the compression curve corresponding to the LCC.

6.3 TESTING MATERIALS AND APPARATUS

The testing materials and the testing apparatus used in this study for 1D compression testing are described herein.

6.3.1 Soil Characteristics

Two types of soil were tested. Clean Nevada sand (N) and ground silica (S), SIL-CO-SIL® 250, manufactured by U.S. Silica. Erickson [2013] tested the same two soils and reported a specific gravity, G_s, of 2.66 for the Nevada sand, according to an evaluation by Cooper Testing Laboratory (August 2010). According to manufacturer specifications, the silica silt has a specific gravity of 2.65. To ensure as little fines content as possible, the batch of Nevada sand was sieved mechanically to remove particles passing the #200 sieve (<0.075 mm diameter) following the general guidelines of American Society of Testing and Materials (ASTM) *ASTM D6913* [2006], Standard Test Method for *Particle-Size Distribution (Gradation) of Soils Using Sieve Analysis.* The grain size distribution of the Nevada sand batch was determined as per *ASTM D422* [2007], Standard Test Method for *Particle-Size Analysis of Soils.* A plot of the grain size distribution is presented in Figure 6.4. From the grain size distribution curves, it can be seen that the Nevada sand is more uniformly graded with a D_{50} = 0.11 mm, whereas the silica silt is more well-graded with a D_{50} = 0.045 mm. The significant difference in median grain size allows for the smaller silt particles to fill the voids between the granular sand particles when mixed. Each soil mixture will have a unique grain size distribution, and is thus expected to vary in density when prepared using the same method. Scanning electron microscope images of both types of soil are presented in Figure 6.4. From these images, the high angularity of the silt particles relative to the sand grains is apparent. Both types of soil possess essentially the same silicon dioxide mineralogy.

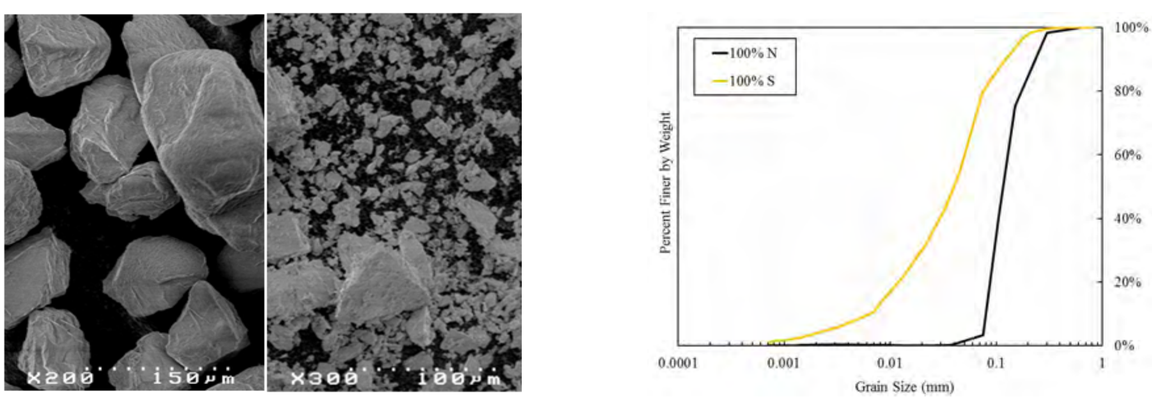

(a) (b) (c)

Figure 6.4 SEM images: (a) Nevada sand, (b) silica silt, and (c) Initial grain-size distribution of Nevada sand batch and silica silt.

6.3.2 Compression Mold

A cylindrical, high-grade 4140 stainless steel alloy mold was fabricated for compression testing of soil mixtures. Designed to withstand very high stresses, the inner vessel of the mold was 63.6 mm (2.50 in.) in diameter, 31.7 mm (1.25 in.) deep, with 12.6-mm- (0.50-in.-) thick walls. A top cap was designed to fit into the vessel of the mold and slide down into the vessel during compression. Two glands were milled into the top cap to allow for the placement of two lubricated o-rings to help keep the cap level during pre-consolidation of the soil. An aluminum collar clamps around the upper circumference of the top cap to provide a rigid platform for attachment of two position transducers. In addition, two holes on opposing sides of the mold have been tapped to allow for thumb screws to attach directly to the mold. Small holes in the heads of these bolts provide an anchor for the shafts of the two position transducers to screw into. There are porous stone inserts in the bottom of the vessel and in the top cap to allow for drainage during consolidation of wet soil mixtures. However, testing presented in this paper was conducted primarily on dry soil mixtures. Images of the mold are presented in Figure 6.5.


Figure 6.5 Stainless steel compression mold vessel and top cap.

6.3.3 Load Frames

A frame with a pneumatic piston and a GEOTAC 500-lb.-capacity load cell was designed and fabricated for the pre-consolidation stage of testing. The purpose of the pre-consolidation stage is to obtain an accurate initial void ratio (e_0) for a specimen before compression testing. The frame is designed to load the specimen to 100 kPa, which serves as a reference stress. This reference stress simulates the *in situ* effective stress condition at 10 ft below the surface during CPT and is an input for calibration of cavity expansion modeling. In addition, the reference stress allows for a more consistent measurement of specimen height since the specimens may be disturbed between transportation of the mold from preparation to compression stages of testing. A uniaxial MTS load frame (50/100 kip/model 311.21) with a capacity of 100 kips was used to load the specimens to approximately 428 kN (96 kips), corresponding to a maximum of 135 MPa on the specimens. The full capacity of the machine was reached in order to maximize the range of testing data. Images of the testing apparatus are found in Figure 6.6.

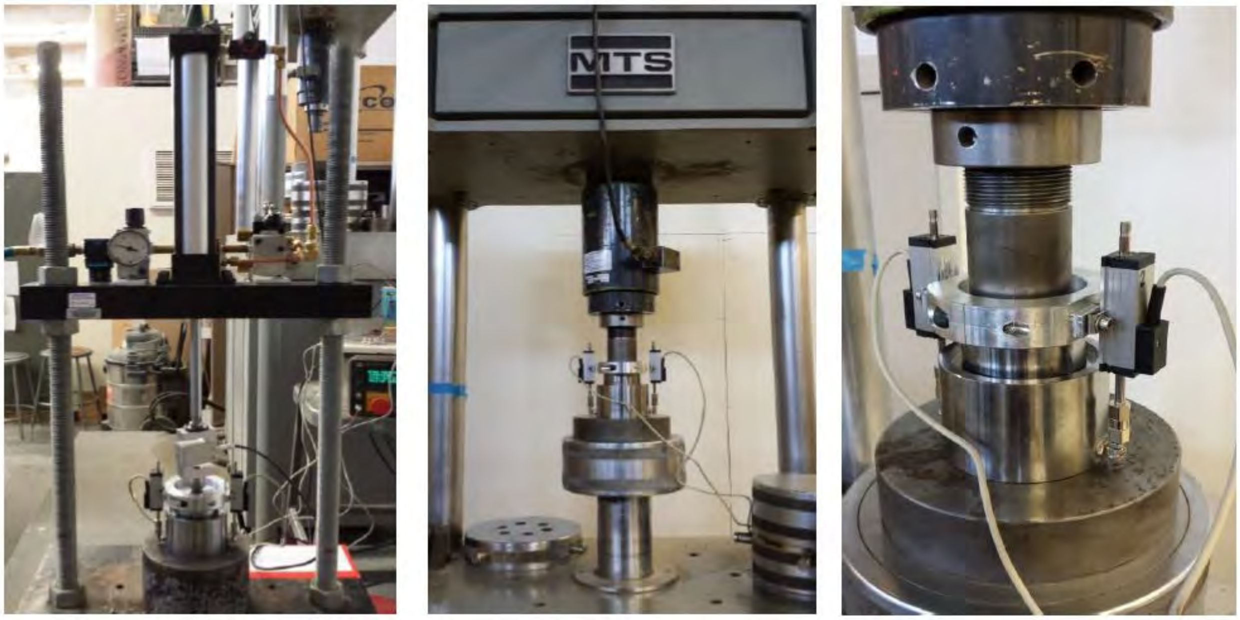

(a) **(b)** **(c)**

Figure 6.6 Testing apparatus: (a) pre-consolidation load frame; (b) MTS compression machine; and (c) mold during compression of specimens.

6.3.4 Data Acquisition

Voltage output signals from the GEOTAC load cell, during pre-consolidation, and from the MTS load cell, during compression, were interpreted with a National Instruments USB-6009 Interface and recorded with ResDAQ software. Output signals from both Novotechnik T-series potentiometric position transducers (LPTS) were interpreted by the same USB interface, so that data from all devices was captured simultaneously and could be distinguished with assigned channels in the software.

6.4 TESTING PROCEDURE

Below is an outline of the testing procedures from specimen preparation through post-compression grain-size analyses:

6.4.1 Initial Grain Size Distribution

Six soil mixtures were prepared in the following proportions: 100% N, 90% N/10% S, 80% N/20% S, 65% N/35% S, 50% N/50% S, and 100% S. The initial grain size distributions for each soil mixture were obtained following the guidelines of *ASTM D422* [2007], Standard Test Method for *Particle-Size Analysis of Soils*; see Figure 6.7. A plot of the grain size distribution curves is shown in Figure 6.8.

Figure 6.7 **Particle size analyses performed using hydrometer and sieve analyses tests.**

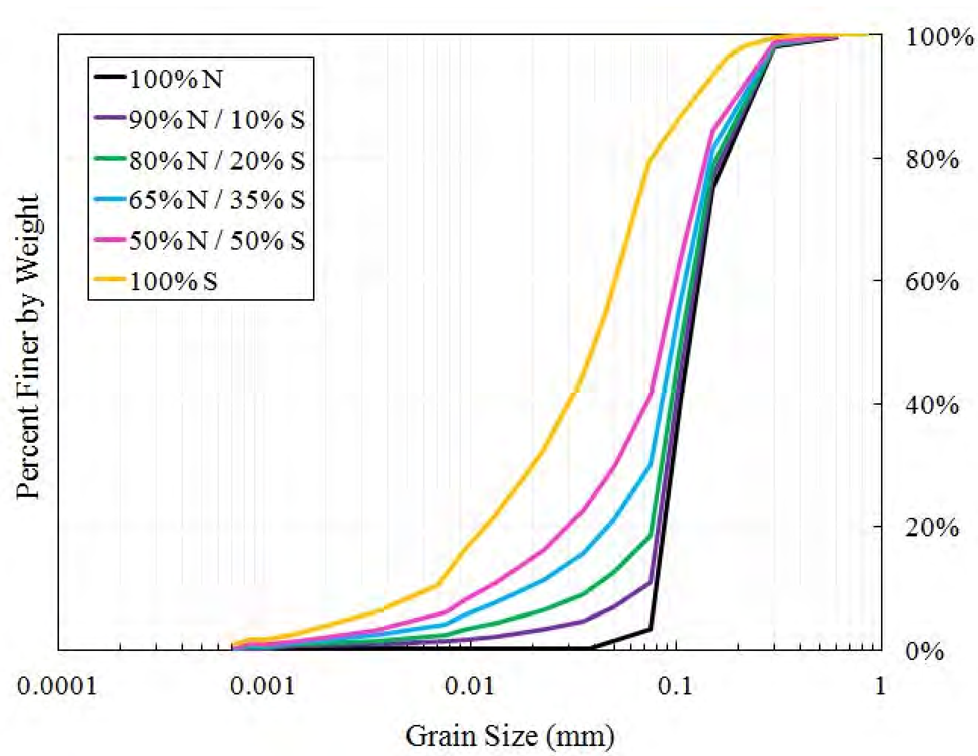

Figure 6.8 **Initial grain size distribution curves for each soil mixture.**

6.4.2 Specimen Preparation

Loose state specimens were prepared according to ASTM Standard D4254 (2000), Standard Test Method for *Minimum Index Density and Unit Weight of Soils and Calculation of Relative Density*. The remaining soil in the upper half of the mold vessel was trimmed with use of a vacuum. The specimens were prepared with much caution because sample disturbance was a concern between each stage of preparation. Any disturbance could influence the initial void ratios of the specimens. In order to calculate the initial void ratio of a specimen, a consistent specimen mass was ensured in each test. Soil mixtures were prepared proportionally by mass percent of overall specimen mass and mixed with a spatula until homogeneity was evident. Controlling the mass of each soil specimen proved to be a more accurate and repeatable alternative to controlling the height of the specimen. Christoph's parametric study [2005] determined that the ideal specimen height to be approximately 20 mm (0.79 in.) as this would maximize sample size and the accuracy of height measurements. Taking this into account and the dimensions of the compression mold, a height-to-diameter (H/D) ratio of approximately 0.3 was achieved in all tests. Another benefit of this ratio lies in minimizing frictional effects of the specimen on the inside walls of the mold during compression. To provide some perspective on the loose, dry specimens, some compression tests were also run on initially dense 100% silica silt and 100% Nevada sand specimens. In order to achieve dense specimens, the 100% silt specimens were prepared in a slurry and poured into the mold. Although dense sand specimens were prepared following the same procedures as the loose specimen preparation, the dense specimens were "densified" with a series of hammer taps under overburden pressure applied to the mold top cap. Both methods of preparing dense specimens produced significantly smaller initial void ratios.

6.4.3 Compression Loading

The specimens were pre-consolidated to 100 kPa (1 atmosphere) prior to compression loading. This allowed for a higher resolution due to limitations in the MTS compression machine. The specimens were then transferred from the pre-consolidation load frame to the MTS compression machine. The integration of linear potentiometers on the mold ensured that changes in specimen height were recorded during the entire process of loading, including the transfer of specimens from the pre-consolidation load frame to the compression machine. The specimens were then loaded at a displacement rate of 0.025 in./min. for the dry specimens and at a rate of 0.007 in./min. for the wet samples to allow for the drained testing condition during consolidation.

6.5 RESULTS

6.5.1 Limiting Compression Curves

Compression curves for six different soil mixtures prepared in a loose state are presented in Figure 6.9. A comparison of compression curves for loosely and densely prepared specimens of 100% Nevada sand and 100% silica silt are presented in Figure 6.10.

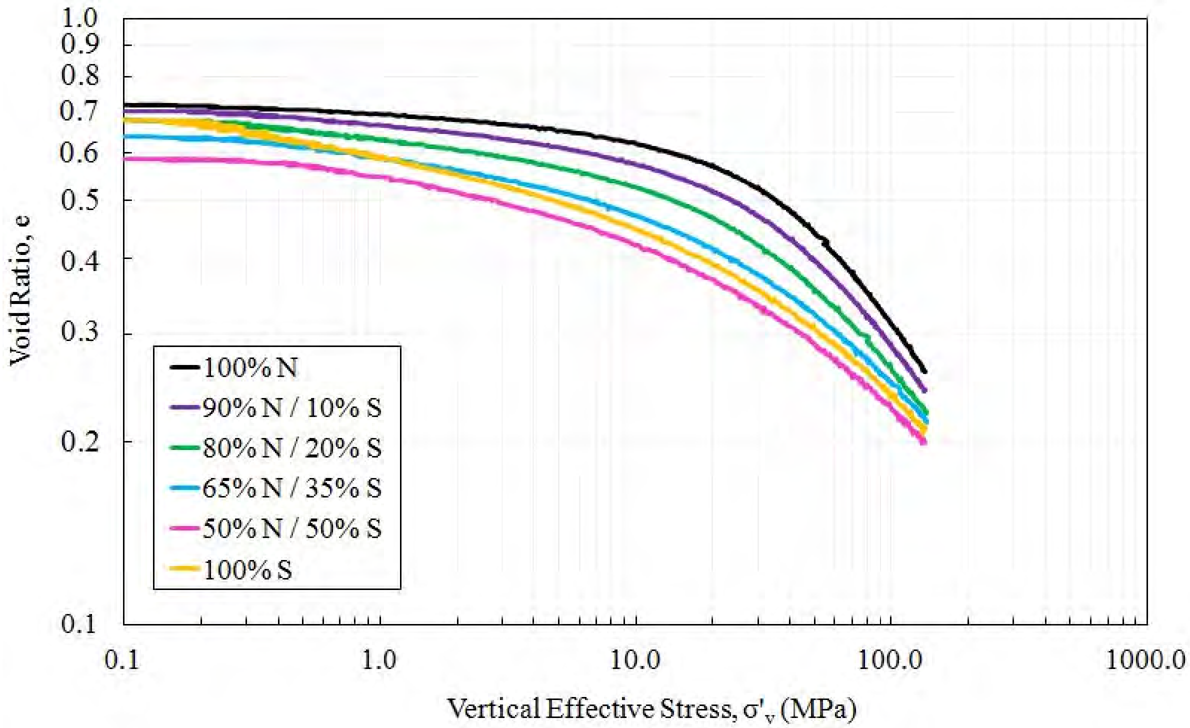

Figure 6.9 **Compression curves for each soil mixture prepared at similar densities.**

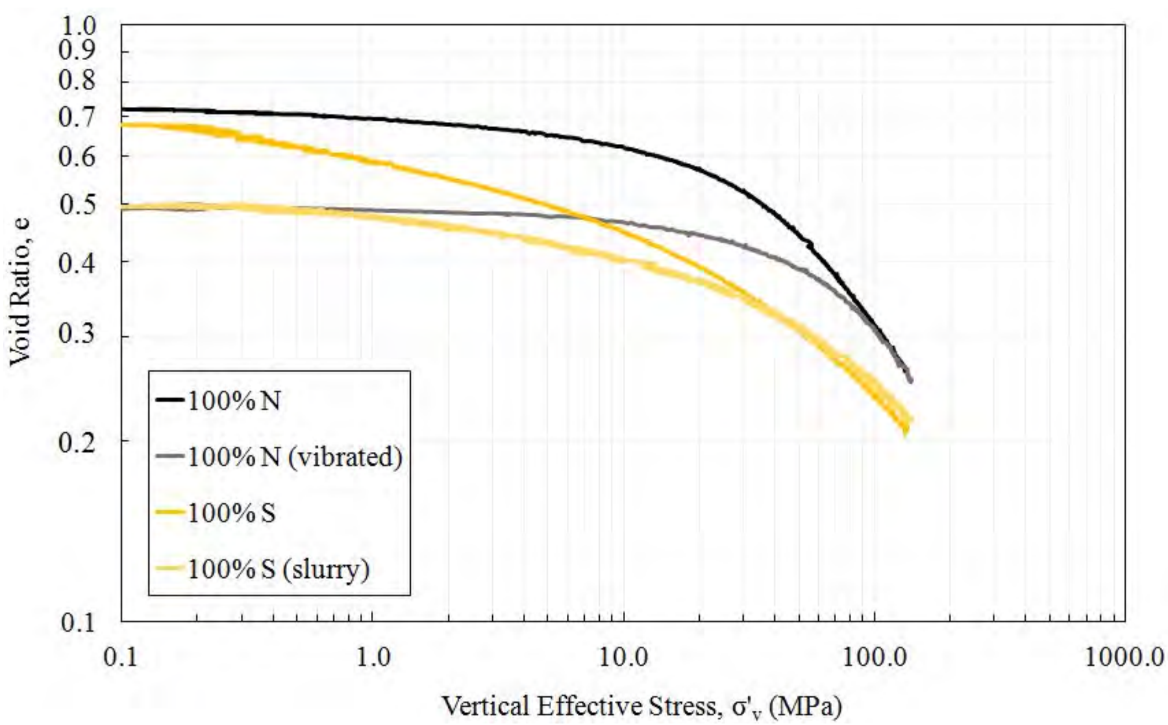

Figure 6.10 **Compression curves for loose and dense 100% Nevada sand (N) and 100% silica silt (S) specimens.**

6.5.2 Influence of Fines Content

From the increased smoothness of the compression curves as they approach LCC behavior in Figure 6.9, it appears that as the proportion of silica fines increases, the yield point becomes less defined. One hundred percent silica silt specimens exhibited high compressibility in the early loading stages during plastic rearrangement of particles. Due to the angularity of the silt particles, it is hypothesized that bridging caused large stable voids in the specimens during loose, dry preparation.

Particle rearrangement (rolling and sliding) is a likely cause of dilation in those specimens that showed a gentler slope in the earlier stages of loading. It is hypothesized that the rearrangement of larger, rounded Nevada sand granules resulted in a dilatory effect, causing flatter slopes in the early stages of loading. As discussed in Section 6.2.1, the more abrupt break-point stresses in those mixtures with increasing Nevada sand content may be explained by the onset of full particle breakage. These findings agree with Hagerty et al. [1993] that as the angularity of particles increases, the break-point stress becomes more difficult to define. This may be seen in the compression curves of those soil mixtures with increasing silica silt content. Additionally, the slopes of these curves increase in the early stages of loading with increasing silica silt content. This is due to the interlocking nature of the angular silica silt particles, providing less opportunity for rearrangement of particles before the breakage of asperities and particle breakage. Curvature and slope of the compression curves were not evaluated mathematically or evaluated according to the Pestana and Whittle [1995] LCC framework as this was beyond the scope of this research project.

It was observed that during loose, dry preparation of specimens, the mixtures had a natural tendency toward smaller initial void ratios as the proportion of silica silt to Nevada sand increased (up to 50%). This supports the findings presented by Lade et al. [1998]. In the early loading stage, the specimens showed increasing compressibility with increasing fines content, despite typically lower initial void ratios. This phenomenon may be explained by metastable contacts in the sand skeleton during dry specimen preparation. These contacts are highly unstable until force is applied to the specimen, causing the silt particles to get lodged between the larger sand particles [Monkul 2010]. The specimen preparation methods likely produced substantially different overall soil fabrics. The slurry preparation method eliminated the stable voids observed in the loose, dry preparation method of the silt specimens.

The difference in preparation methods is well represented by comparing the slopes of the compressions curves in the low stress region for 100% N and 100% S specimens in Figure 6.10. The compression curve for the dense 100% S (slurry) specimen exhibits an almost horizontal slope in the early stages of loading. Similarly, the compression curve for the dense 100% N (vibrated) specimen exhibits a flat slope. Both loose and dense specimen compression curves approach unique LCCs for 100% N and 100% S, respectively.

6.5.3 Crushing Behavior

The grain size distribution of each of the soil mixtures was determined prior to testing and after testing was complete. These distributions are compared in Figure 6.11. The distributions all show that the percent of fines increased during testing, proving that crushing occurred; however, some doubt may be cast on the accuracy of the grain size analyses performed. The grain size evolution curves are indicative of procedural error during the hydrometer portion of the analyses. It is believed that not all of the fines were washed through a No. 200 sieve after conducting hydrometer analyses on specimens after compression testing. This does not meet all requirements of *ASTM Standard D422* [2007], *Standard Test Method* for *Particle-Size Analysis of Soils.* Single particle breakage was not investigated in this testing program.

Additionally, as visually observed during testing, some of the silicon oil used to lubricate the o-rings was pushed into the soil specimen around the inside walls of the compression mold. This caused some of the fine-grained material to clump together forming larger particles. After loading to high stresses, it was observed that the slurry-prepared specimens had cemented in place, which proved difficult to remove from the compression mold. Not obtaining the full specimen from the compression mold after testing may have reduced the overall amount of fine material in post-test grain size analyses.

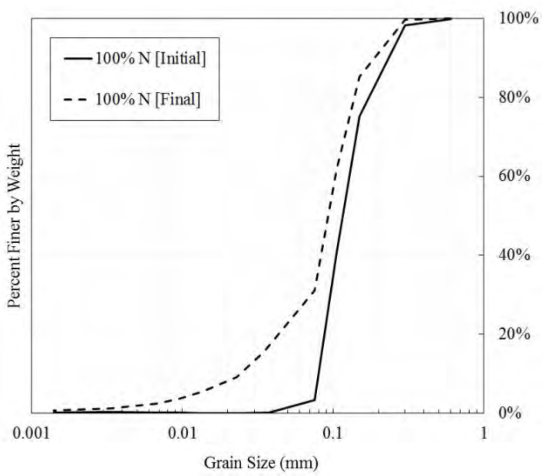

(a)

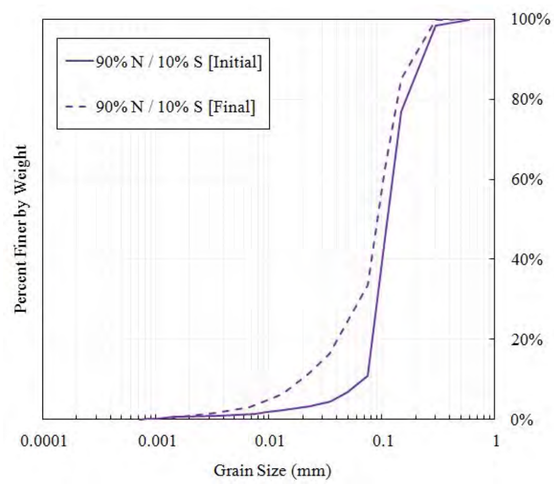

(b)

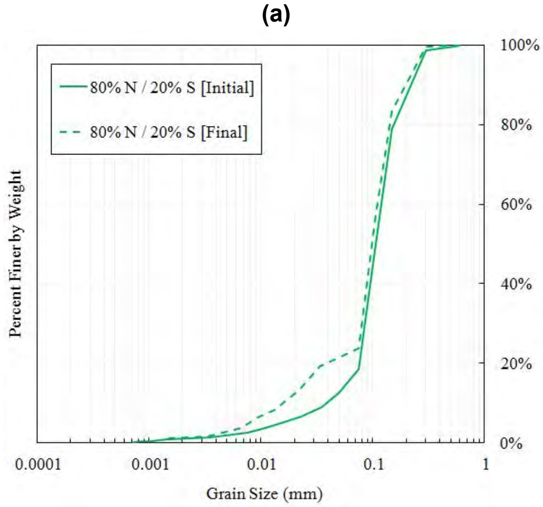

(c)

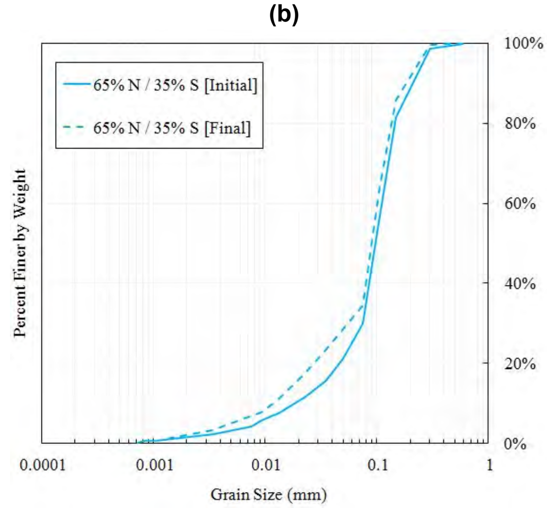

(d)

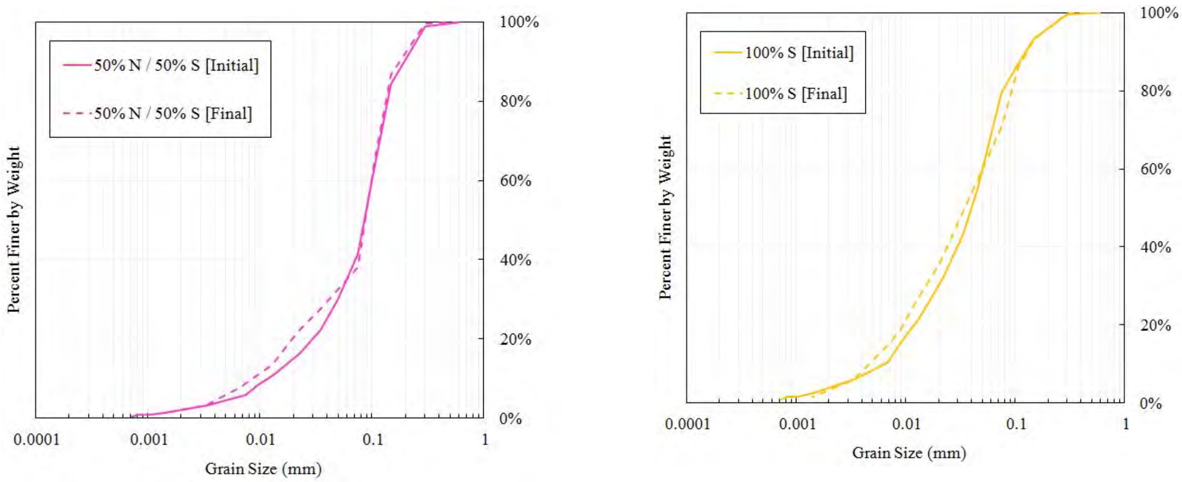

(e) (f)

Figure 6.11 Grain size evolution curves for soil mixtures before and after testing: (a) 100% N; (b) 90% N/10% S; (c) 80% N/20% S; (d) 65% N/35% S; (e) 50% N/50% S; and (f) 100% S.

6.6 CONCLUSIONS

A one-dimensional, monotonic compression testing program has been presented. Six intermediate soil mixtures with varying amounts of non-plastic fines were prepared and loaded to 140 MPa. Soil mixtures consisted of rounded granular Nevada sand and angular silica silt. Both types of soil are quartzitic in composition and non-plastic. It was found that the slopes of the apparent linear portions of the compression curves showed good correlation upon visual inspection, suggesting that any remaining structure in each of the specimens had little or no influence on specimen behavior at high stresses. It is unclear whether a unique LCC slope was achieved for the tests performed. It may be argued that the compression curves were not fully developed and that the high-stress, linear portions of the compression curves in fact approached different slopes, depending on soil mixture. Results indicate that the following occur under 1D loading as presented: (i) all intermediate soil mixtures approach LCC behavior, regardless of mix proportions and initial void ratio; however, testing to higher stresses would be necessary to confirm this; (ii) the onset of crushing was observed in all tests and verified by grain size analyses; and (iii) sample preparation methods were shown to influence initial specimen density significantly.

Due to the high amount of variance in the initial void ratios of specimens during the loose preparation method presented, it is suggested that an alternative, more controlled method be used to produce more consistent initial void ratios. This would allow for more direct comparison of compression curves among different soil mixtures. Additional tests on densely prepared specimens would add more perspective on the LCC behavior of loosely prepared specimens. Slurry preparation of 100% silica silt specimens has been shown to be reliable; however, it is believed that preparing a sand specimen in a slurry would prove problematic in terms of homogeneity and workability. Vibration has been shown to be a more effective method for preparing dense, dry sand specimens.

6.7 ACKNOWLEDGMENTS

The author would like to express gratitude to the National Science Foundation Research for Undergraduates program, the Pacific Earthquake Engineering Research Center, the University of California, Davis Soil Interactions Laboratory, Professors Ross Boulanger and Jason DeJong, Ana Maria Parra and Adam Price, and Heidi Tremayne, Outreach Director of the Pacific Earthquake Engineering Research Center at the University of California, Berkeley.

6.8 REFERENCES

ASTM (2010). *Annual Book of Standards*, American Society for Testing and Materials, Vol. 4.08, Soil and Rock (I): D420–D5779.West Conshohocken, PA.

Boulanger R.W., DeJong J.T. (2013). CPT-based characterization of intermediate soils, *National Science Foundation Award No.1300518*, 15 pgs.

Christoph G.G. (2005). Influence of Particle Properties and Initial Specimen State on One-Dimensional Compression and Hydraulic Conductivity. M.S. Thesis, University of Massachusetts, Amherst, MA, 286 pgs.

Cox B.R., Stokoe II, K.H., Rathje E.M. (2009). An in-situ test method for evaluating the coupled pore pressure generation and nonlinear shear modulus behavior of liquefiable soils, ASTM*, J. Geotech. Testing J.,* 32(1): 11–21.

Erickson R.P.C. (2013). The influence of non-plastic fines on intermediate soil compressibility: a laboratory study, M.S. Thesis, Dept. of Civil and Environmental Engineering, University of California, Davis, CA, 47 pgs.

Hagerty M.M., Hite D.R., Ullrich C.R., Hagerty D.J. (1993). One-dimensional high pressure compression of granular media.=, *J. Geotech. Eng.,* 119(1): 1–18.

Idriss I.M., Boulanger R.W. (2008). *Soil Liquefaction during Earthquakes*, Earthquake Engineering Research Institute, Oakland, CA, 261 pgs.

Lade P.V., Yamamuro, J.A. (1997). Effects of non-plastic fines on static liquefaction of sands, *Canadian Geotech. Testing J*., 34(6): 918–928.

Lade P.V., Liggio C.D. Jr., Yamamuro J.A. (1998). Effects of non-plastic fines on minimum and maximum void ratios of sand, *Canadian Geotech. Testing J*., 21(4): 336–347.

Monkul M.M. (2010). *Influence of Silt Size and Content on Static Liquefaction Potential of Sand*, Ph.D. Thesis, Oregon State University, Corvallis, OR, 141 pgs.

Pestana J.M., Whittle A.J. (1995). Compression model for cohesionless soils, *Géotechnique*, 45(4): 611–631.

Pestana J.M., Whittle A.J. (1999). Formulation of a unified constitutive model for clays and sands, *Int. J. Numer. Anal. Meth. Geomech.,* 23: 1215–1243.

Nakata Y., Hyodo M., Hyde A.F.L., Kato Y., Murata H. (2001a). Microscopic particle crushing of sand subjected to high pressure one-dimensional compression, *Soils and Foundations*, 41(1): 69–82.

Nakata Y., Kato Y., Hyodo M., Hyde A.F.L., Murata H. (2001b). One-dimensional compression behavior of uniformly graded sand related to single particle crushing strength, *Soils and Foundations*, 41(2): 39–51.

Roberts J.E., de Souza J.M. (1958). The compressibility of sands, ASTM, *Proceedings*, 58: 1269–1277.

Vesić A.S., Clough G.W. (1968). Behaviour of granual materials under high stresses, ASCE, *J. Soil Mech. Foundations Div*., SM3: 313–326.

7. Biostimulation of Native Ureolytic Bacteria for Biocementation of Sands

Salvador Tena

ABSTRACT

Microbially Induced Calcite Precipitation (MICP) is a bio-mediated cementation process that can alter the engineering properties of granular soils through the precipitation of calcite at soil particle contacts. To date, many of the previous research efforts have relied on the introduction of highly specialized non-native microbes such as *Sporosarcina pasteurii* (*S. pasteurii)* to soils in order to complete this reaction (bio-augmentation). Recent studies have demonstrated the potential of native ureolytic bacteria to complete this process in what is referred to as a bio-stimulation approach. If native microbes can be used to complete the cementation process, benefits such as reduced treatment costs, increased spatial uniformity, and reductions in environmental impacts may be realized. This study was completed to assess how properties such as permeability, shear wave velocity, and calcite content change for a specific bio-stimulation application over twenty days. Six identical soil columns (5.1 cm in diameter and 10.2 cm high) were treated with solutions containing urea, ammonium chloride, yeast extract and sodium acetate for the first ten days, and the identical solutions with the addition of calcium chloride for the subsequent ten days. Methods used to evaluate and monitor columns included pH, shear wave velocity, permeability, and calcite content measurements. Following the twenty-day treatment period, shear wave velocities in soil columns were shown to increase by nearly 900%, and calcite contents were measured as high as 3.30% by mass. These results are promising and suggest that native microbes may be used to complete bio-cementation with results that are comparable to improvement achieved using the bio-augmentation approach.

7.1 INTRODUCTION

Microbially Induced Calcite Precipitation (MICP) is a bio-mediated soil improvement method that can alter soil engineering properties through the precipitation of calcite at soil particle contacts [DeJong et al. 2010]. Previous experimental studies have shown that MICP improvement can result in reduced soil compressibility, increased shear strength and shear stiffness, and only modest reductions in permeability [DeJong et al. 2010]. Possible applications for MICP include: liquefaction prevention, general ground improvement, groundwater contaminant immobilization, permeability reduction, concrete remediation, and surficial erosion prevention [DeJong et al. 2010]. The MICP reaction is referred to as being "bio-mediated" because it is made possible by ureolytic bacterial species (bacterial species containing the urease enzyme), which complete urea hydrolysis and produce an alkaline environment in the soil pore fluid. When in the presence of sufficient calcium (from added calcium chloride) and carbonate (from cell respiration), the alkaline pore fluid will promote calcite precipitation by making the aqueous solution become supersaturated with respect to calcite. The full MICP reaction network is complex and referred to as being biogeochemical in nature because it involves many reactions, each of which involves aspects of biology, geology, and chemistry. In order to understand how MICP occurs in soils, it is best to start by explaining the role of microorganisms in this process.

The MICP process is made possible through the use of ureolytic bacteria, which contain active urease enzymes that can hydrolyze urea and can control several key chemical reactions that allow for calcite precipitation. These ureolytic bacteria can be either cultured and injected into soils (bio-augmentation) or stimulated *in situ* (bio-stimulation). The reaction starts with the hydrolysis of urea by ureolytic bacteria. This results in the production of two moles of ammonia (NH_3) and one mole carbon dioxide [$CO_{2\ (aq)}$] per mole of urea. Once in the aqueous solution, ammonia (NH_3) will react with H_2O and undergo speciation resulting in a net production of hydroxide (OH^-) and ammonium (NH_4^+) ions. The increased concentration of hydroxide ions in solution will increase the solution pH and create an alkaline environment that will allow for precipitation to occur more readily [Stocks-Fischer et al. 1999; Wang et al. 2010]. When sufficient concentrations of calcium (Ca^{2+}) ions are made available through the addition of the calcium chloride ($CaCl_2$) in the treatment solutions, the high concentrations of carbonate in the solution resulting from the speciation of CO_2 (aq) in a high pH solution in combination with the calcium can supersaturate the solution with respect to calcite. The supersaturation of the aqueous solution with respect to calcite will result in the precipitation of calcite on nucleation surfaces on or near bacteria and at soil particle contacts [DeJong et al. 2010]. The process is best illustrated in Figure 7.1 below, which demonstrates the biogeochemical reactions that are taking place in the system. It is important to realize that the system is much more complex than this as other elements may participate in these reactions in natural soils; many of these reactions, namely urea hydrolysis and calcite precipitation, are kinetically controlled processes.

The MICP biogeochemical reaction has been most commonly studied in experiments using the bio-augmentation approach, which relies on the cultivation of non-native ureolytic bacteria in a laboratory and injection of these cultures into the soils during treatment. Numerous studies have further explored many specific aspects of bio-augmented MICP, including the effects of chemical concentrations, e.g., Mortensen et al. [2011], Al Qabany and Soga [2012], Al Qabany et al. [2013] and others, and the specific rates of ureolytic processes of *S. pasteurii*, e.g., Bang et al. [1999], Whiffin et al. [2007], and others. While applications of bio-augmented MICP have been shown to be successful at a variety of different scales, bio-augmentation may not be the optimal approach for field scale applications for several reasons. First, culturing bacteria for application at the field scale would likely be cost-prohibitive due to the high concentrations of bacteria needed. Second, non-native bacterial species may be invasive and result in unknown consequences with respect to native microbial ecology. Lastly, the bio-augmentation approach relies on the transport of bacteria uniformly through soils by injection, which may be difficult to achieve at the field scale. Due to these challenges, the bio-augmentation approach may not be the optimal approach for field-scale application if native microbes can be used.

Recently, researchers have explored the bio-stimulation approach for MICP treatment. Bio-stimulation stimulates native *in situ* ureolytic bacteria to complete bio-cementation without the need for the injection of non-native and potentially invasive microbes [Ivanov and Chu 2008]. In addition to environmental benefits, it is believed that because native bacteria may be more resilient than laboratory-cultured strains and are already existing in their native environment, with the added bonus that bio-stimulation techniques may allow for more uniform distributions of bacteria in the soil [Burbank et al. 2011]. Greater spatial uniformity in bacterial populations may correspond to more uniform distributions of calcite precipitation and as a result uniformity in geotechnical improvement. Recent studies have demonstrated the capabilities of bio-stimulation techniques to precipitate calcite for ground improvements [Burbank et al. 2011; 2013]. These studies are promising and suggest that bio-cementation can be achieved without the need for injection of non-native bacteria into the ground.

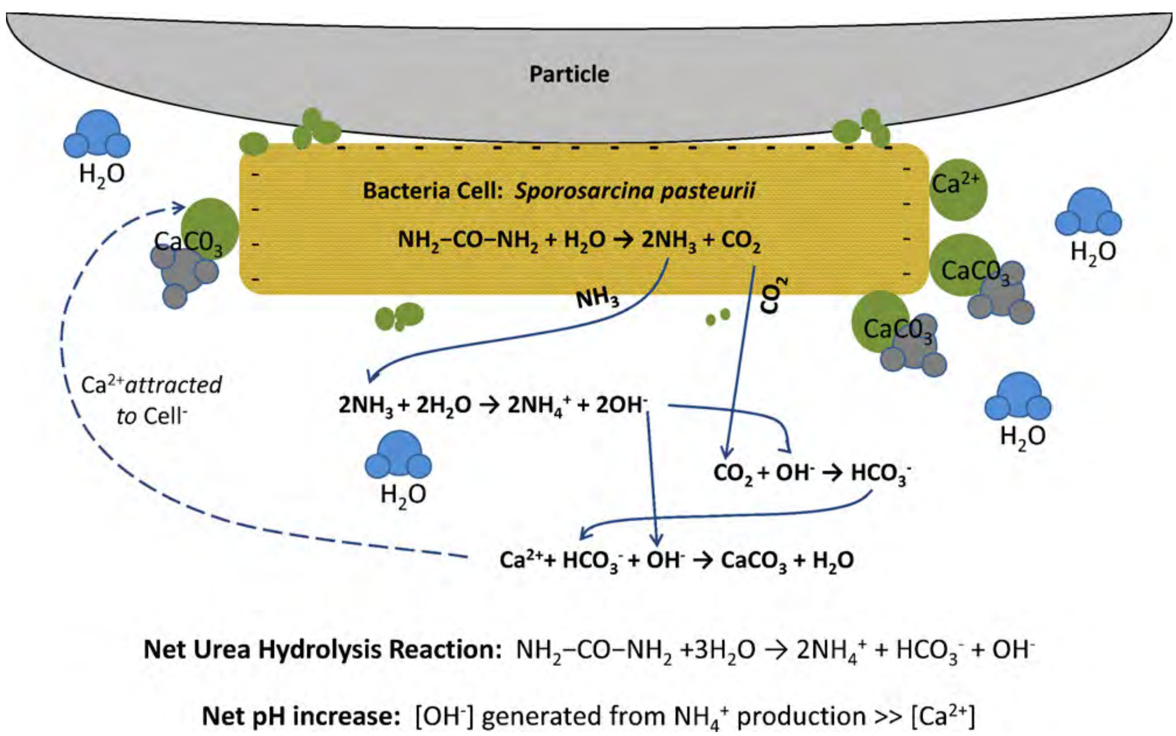

Figure 7.1 Diagram of MICP processes and bio-geochemical reactions [DeJong et al. 2010].

In this study six identical soil columns were treated with identical solutions for a duration of twenty days in order to monitor how geotechnical properties changed with successive treatments. A seventh column received only deionize water at similar volumes and was used as a control. During the first ten days of treatment, treated soil columns received urea, sodium acetate, ammonium chloride, and yeast extract to stimulate growth of bacterial populations. For the final ten days of treatment, soil columns received solutions with the same constituents as the first ten days but contained the addition of calcium chloride to precipitate calcite. The six treated columns were used to assess variability in treatment results and allow for the destructive sampling of columns to achieve calcite content and permeability at different periods.

7.2 MATERIALS AND METHODS

7.2.1 Sand Material

In this study concrete sand, a poorly-graded sand (SP) from a commercial quarry located off-channel of Cache Creek in Woodland, California, was used for all bio-stimulation tests. Higher populations of soil microorganisms are expected at locations where water tables fluctuate; therefore, the alluvial environment from which this soil was extracted made it an ideal candidate for bio-stimulation. A sieve analysis was completed on this sand to obtain coefficient of uniformity (C_u), coefficient of curvature (C_c), D_{10}, D_{30}, and D_{60}; see Table 7.1. Concrete sand was selected for this study following previous tests using bio-stimulation techniques, which were completed with success at the University of California, Davis.

Table 7.1 Concrete sand source, deposition, and sizes.

Source	Deposition	C_u	C_c	D_{10} (mm)	D_{30} (mm)	D_{60} (mm)
Woodland, California	Alluvial	10.1	0.6	0.18	0.45	1.81

7.2.2 Specimen Preparation

Soil column specimens were prepared in 10.2 cm high×5.1 cm hollow acrylic cylinders. Soil columns were prepared targeting an initial relative density of approximately 60%. Soil specimens were prepared in three lifts, using a moist tamping procedure. In order to achieve a uniform relative density across the specimen, tamping was increased with each lift. The first lift received 10 tamps, the second lift received 15 tamps, and the last lift received 25 tamps. Following specimen preparation, soils were saturated using deionized water and a confinement stress of 100 kPa was applied to soil columns uniformly from a load applied at the top of the column.

7.2.3 Treatment

Treatment solutions were formulated following previous work to achieve substantial soil improvement following ten days of successive applications of cementation solutions. Table 7.2 presents the composition of the stimulation treatment solution applied during the first 10 days, and the cementation treatment solution applied the last 10 days. All solutions were prepared using deionized water. Treatment volumes of 300 mL were applied to each soil column daily. This daily treatment volume was estimated to be approximately 1.5 pore volumes. Treatment solutions were applied using a gravity feed percolation system that utilized an upward flow gradient to ensure soils remained saturated during treatment.

Previous studies completed at the University of California, Davis (UCD) showed that rapid calcite precipitation could occur following the initial application of cementation solutions on Day 10 if solutions were not buffered correctly. Calcite that precipitates rapidly is generally more disordered in structure than calcite that precipitates more slowly. Therefore, rapidly precipitated calcite does not contribute significantly to the geotechnical improvement of soils; instead, it exists as weak crystallization of calcite. Several studies were conducted to determine the optimal approach for buffering solutions and transitioning soil columns from the stimulation to cementation phase while minimizing immediate rapid calcite precipitation. It was concluded that directly before application of cementation solutions, soil columns should be treated with the same stimulation solution to flush out the high pH conditions existing in soil columns. This technique was used in this study to transition soil columns from the stimulation to cementation phase.

Table 7.2 Treatment solutions for each phase of MICP.

Constituent	Solution Type	
	Stimulation	Cementation
Urea (mol/L)	0.25	0.25
Ammonium Chloride (mol/L)	0.00625	0.00625
Sodium Acetate (mol/L)	0.085	0.085
Yeast Extract (g/L)	0.1	0.1
Calcium Chloride (mol/L)	-	0.125

7.2.4 Shear Wave Velocity Measurements

Soil columns were instrumented with bender element piezoelectric transducers to monitor changes in shear wave velocity over time. Bender elements were positioned at mid-height of soil columns (5.1 cm) and were fitted to the sides of the column through drilled holes and silicon pucks, which isolated the bender elements. Bender element measurements were taken daily before treatment to monitor changes in shear wave velocity over time. The shear wave velocity is related to the small strain shear modulus (G_{max}), the confinement stress, density, and mineralogy of the soil [DeJong et al. 2010]. Previous experiments have demonstrated that shear wave velocity will increase as soil grain contacts become cemented during treatment [DeJong et al.

2010]. The increase in connectivity between sand grains allows for the shear wave to travel a more direct path between bender elements, resulting in a reduced wave propagation lag time.

Bender elements used in this test were fabricated following the recommendations in Montoya et al. [2011]. Bender elements can produce shear waves by contracting a transmitting bender element using an applied excitation voltage. The shear wave signal is then received by a receiving bender element, which deflects and produces a voltage in response that can be measured by a DAQ system. Before testing, the time lag and distance between bender elements were obtained to determine shear wave velocity of the soil columns more accurately. During the experiment, the shear wave was filtered to remove background noise by using both high- and low-pass frequency Butterworth filters. The filters were set at a high pass of 1 kHz with input gain of 50, and a low pass of 20 kHz.

7.2.5 pH Measurements

During this study the pHs of influent and effluent solutions were monitored to ensure consistency in solutions and monitor biologic changes. Due to the production of hydroxyl ions as a result of urea hydrolysis, pH can be used to indicate biological activity of ureolytic microorganisms. When the aqueous solution is unbuffered (no calcium), the pH of solutions is anticipated to be between 9.3 and 9.5 during active urea hydrolysis. Following the addition of calcium to solutions (buffered solutions), however, pH values are anticipated to be near 9.0 during active urea hydrolysis. All pH measurements were completed using an Acumet standard electrode that was calibrated daily before taking measurements.

7.2.6 Permeability Measurements

Following the disassembly of a soil column specimen, the permeability (k) of the specimen was measured. Permeability measurements were completed using a constant head parameter in accordance with *ASTM D2434-68* for granular soils. As shown in Equation (7.1), permeability can be calculated from the fluid volume in a given time (Q), the soil column length (l), the cross-section area of the column (A), the time it takes between readings (t), and the constant head difference across the column (h). For each soil column specimen, three replicates of permeability measurements were completed to achieve an average permeability coefficient. Following bio-cementation, the permeability was expected to decrease due to the precipitated calcite, which can oppose flow when it fills the void space [DeJong et al. 2010]. Therefore, it was anticipated that the permeability of the soil column specimens would decrease in time as more calcite precipitated.

$$k = Ql / Ath \tag{7.1}$$

7.2.7 Calcite

Calcite percent by mass was measured in accordance with *ASTM D4373* using a calcite pressure chamber and transducer. A previously established relationship between calcite mass and carbon dioxide pressure (generated after reacting with hydrochloric acid) was used to determine calcite mass from achieved pressures.

7.2.8 Column Disassembly Schedule

The schedule for soil column disassembly is presented in Table 7.3. Soil columns were disassembled in order to obtain the permeability and calcite content of the soil with time. The schedule disassembled one column every two days with the exception of columns 4, 5, and 6, which were spaced one day apart. Sampling intervals were reduced as the twenty-day mark was approached in order to ensure successive treatments were still improving properties near the end of the treatment schedule. If similar properties could be obtained after 18 or 19 days rather than 20, then future treatments could end earlier and reduce material costs.

Table 7.3 Cell disassemble schedule for MICP.

Soil Column Disassembled Schedule	
Column	**Day**
1	12
2	14
3	16
4	18
5	19
6	20
7 (control)	20

7.3 RESULTS

7.3.1 Shear Wave Velocity

As shown in Figure 7.2, shear wave velocity measurements showed similar trends in time for all treated soil columns. While it was not certain if shear wave velocity measurements would change during the stimulation phase due to high pH values, from the data it can be seen that no shear wave velocity increases occurred during the first ten days of treatment, thus no calcite precipitation occurred during the first ten days of treatment. This result was expected because no calcium chloride was added to solutions during the first ten days. Solutions were therefore under-saturated with respect to calcite for the first ten days. Shear wave velocities for treated columns were shown to increase following only one treatment of calcium-enriched cementation solutions (Day 11).

Increases in shear wave velocity were anticipated for soil columns as cementation treatment progressed. This can be explained physically by particles being cemented and able to propagate shear waves more rapidly. Increases in shear wave velocity are also indicative of increases in small strain shear stiffness (G_{max}). Figure 7.3 plots the normalize shear wave velocity values versus time for each column in order to reduce the effect of initial shear wave velocity; note that trends are approximately linear. In addition, following ten days of cementation, shear wave velocities were shown to increase by nearly 900% percent relative to the Day 10 initial non-treated shear wave velocity. As expected, as the number of cementation treatments increased, shear wave velocities also increased due to accumulation of calcite precipitation within the soil column. The relationship between final shear wave measurements and number of treatments (or days) appears almost linear in behavior between the initiation of cementation on Day 10 and Day 18; however, the rate of increase was not exactly equal among all the columns. This could be due to variations in soil density and/or microbial activity.

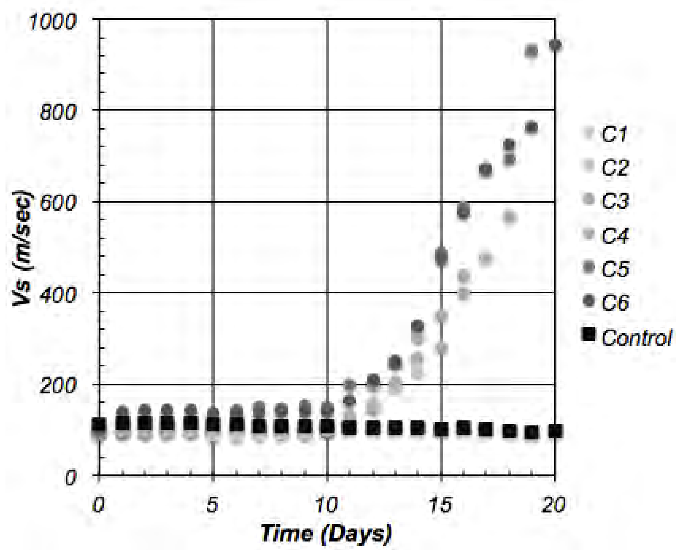

Figure 7.2 Shear wave velocity measurements (m/sec) versus time.

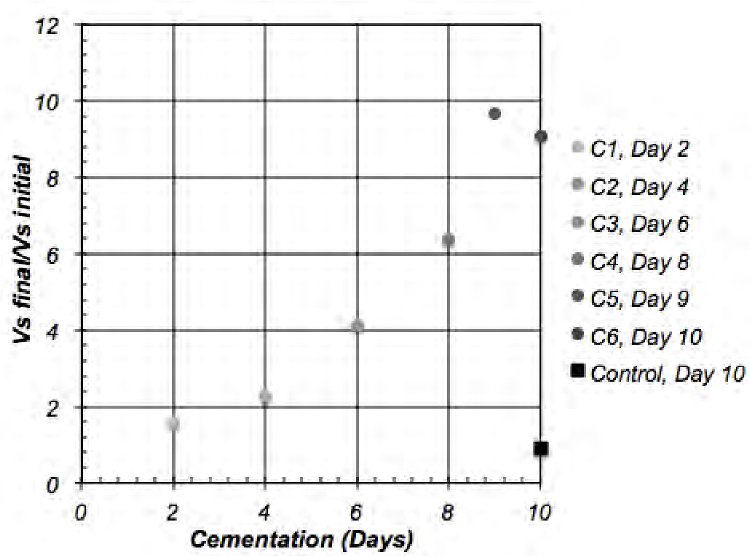

Figure 7.3 Normalized shear wave velocity measurements versus cementation time.

7.3.2 pH Measurements

As shown in Figure 7.4, effluent pH measurements indicated that columns reached a pH of approximately 9.5 by Day 4 of the stimulation phase and dropped to 9 during the cementation phase. The introduction of urea during stimulation caused an increase in pH that stabilized at 9.5 during the first 10 days. The initial increase in pH is an indication of active bacteria as they are consuming urea by the biochemical reaction of urea hydrolysis. For bacteria to perform urea hydrolysis, they first need to produce ureolytic enzymes to break the urea. In the process of breaking the urea, byproducts NH_3 and CO_3 (aq) are produced. The presence of NH_3 in the soil introduces OH^- ions that cause an increase pH. During the process of treatment the pH drops in the last 10 days due to the calcium behaving as a buffer. The calcium ions cause a reduction in the activity of OH^- ions that results in a pH of 9 in the last 10 days.

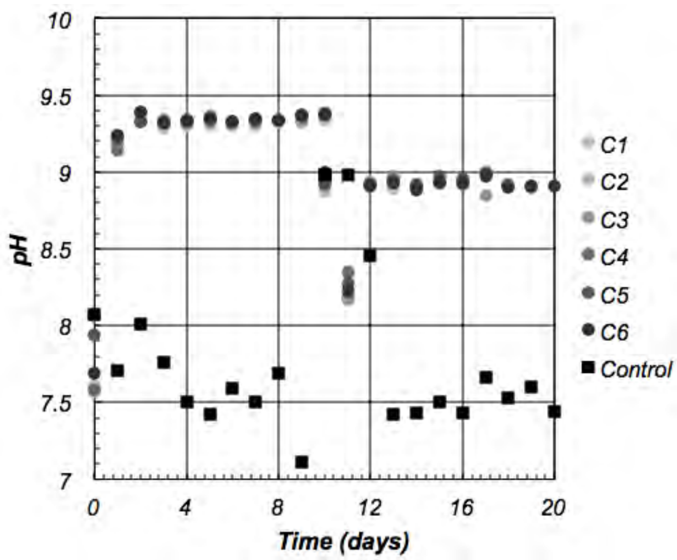

Figure 7.4 Effluent pH versus time.

7.3.3 Permeability

Permeability was expected to decrease with the number of treatments due to reduced porosity. As shown in Figure 7.5, the permeability decreased with time. The permeability coefficient decreased 87% compared to the untreated column, which had an initial value of 1.90E-04 m/sec. Calcite precipitation caused the reduction of permeability as calcite filled the voids of the soil. Based on the results from Figure 7.5, permeability decreased primarily on the first 6 days of cementation treatment and plateaued near Day 19.

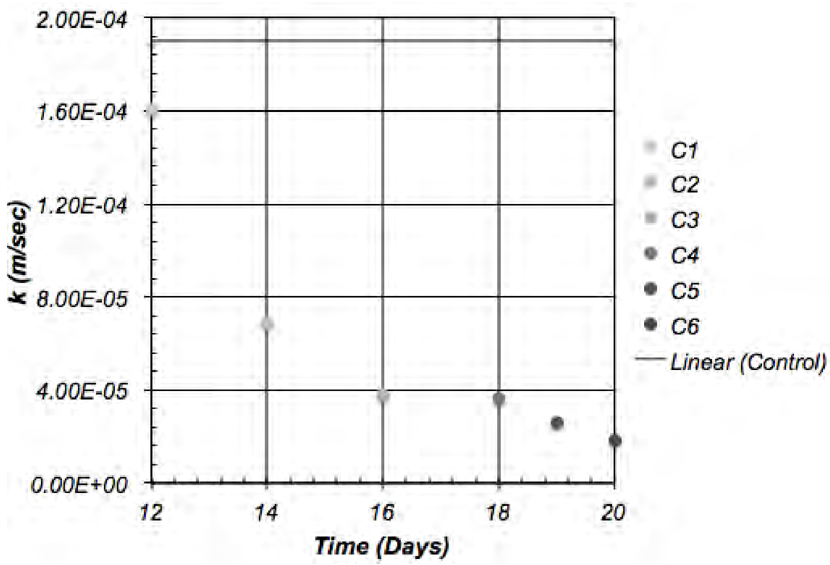

Figure 7.5 Permeability (*k*) versus time.

7.3.4 Calcite

Calcite measurements with depth are shown in Figure 7.6 for the treated columns. The maximum increase of calcite during treatment was 3.3% by mass. Calcite measurements were observed to have a higher percentage at the base of the soil columns. The reason for a higher concentration of calcite was due to the injection source being at the column base. It was observed that soil columns 5 and 6 had a greater percentage of calcite content at the base relative to the top of the column. The explanation of soil columns 5 and 6 showing a greater difference in calcite content with depth was due to consumption of calcite ions for a longer time period. Calcite crystals form as the flow of treatment moves from the base of the column to the top of the soil column. Calcite crystallization results in a decrease of calcite ions in the solution, which results in lower calcite concentration at the top of the column as the ions are been consumed at the base. The result of calcite crystallization at the base results in a disproportion of calcite distribution with depth in the soil column, as illustrated in Figure 7.6.

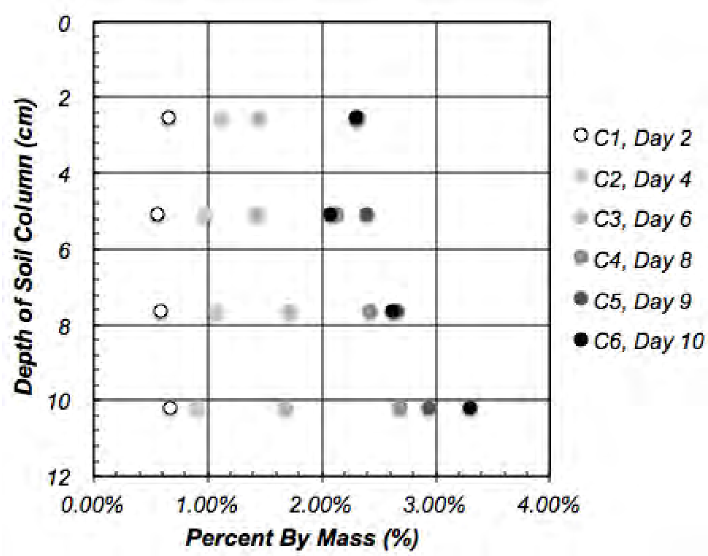

Figure 7.6 Calcite by mass (%) versus depth (cm).

7.4 DISCUSSION

7.4.1 Property Relationships

7.4.1.1 Shear Wave Velocity versus Calcite Content

It was believed that calcite content and shear wave velocity were correlated. To illustrate this relationship, Figure 7.7 plots mean value of calcite versus final shear wave velocity of each soil column. Initially there appears to be a linear behavior between the two properties; but a discontinuity is evident at the last two points where columns 5 and 6 deviated from the linear relationship. The shear wave velocities were approximately 900 m/sec for the two columns, which discontinues the linear behavior between the two properties, which may be due to differences in soil composition and bacterial activity with respect to the other samples.

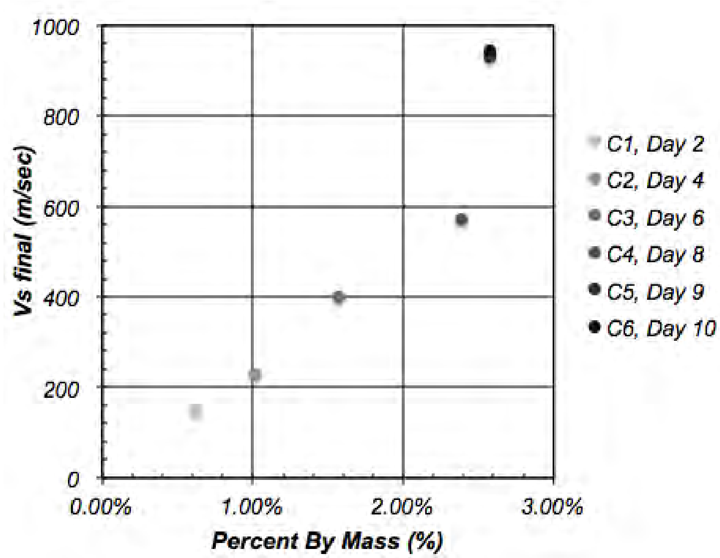

Figure 7.7 Final shear wave velocity (m/sec) versus average calcite by mass (%).

7.4.1.2 Permeability versus Shear Wave Velocity

As shown in Figure 7.8, permeability reduction is correlated with increases in shear wave velocity. It is believed that the calcite precipitation caused an increase in the strength of the soil by cementing soil particles together however it also reduced porosity and therefore decreased permeability. It was observed that permeabilty reductions were nearly constant once a shear wave veleocity of about 400 m/sec was achieved.

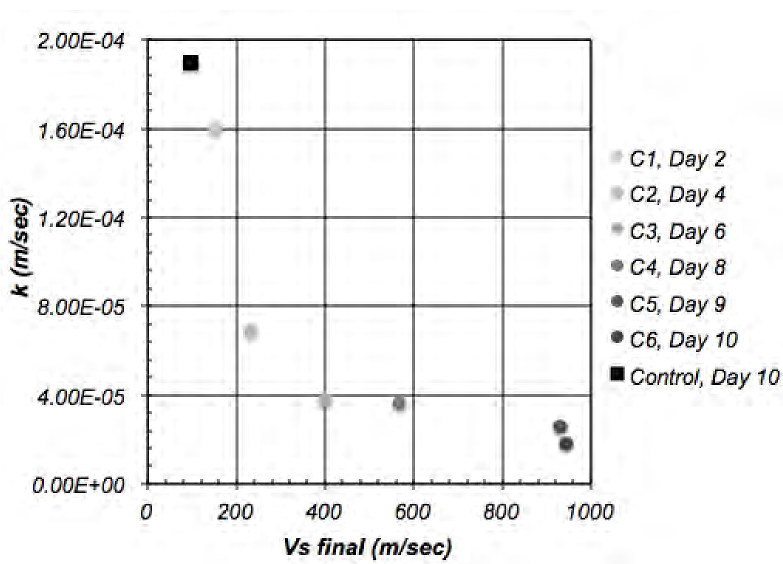

Figure 7.8 Permeability (k) versus final shear wave velocity (m/sec).

7.4.1.3 Permeability versus Calcite Content

Permeability was shown to decrease by approximately one order magnitude following ten-day cementation treatment; see Figure 7.9. The dropped in permeability was due to void space having been filled by the formation of calcite crystals initiated during the cementation, resulting in a less permeable soil. Figure 7.9 plots permeability versus calcite by percentage of mass, which depicts an inverse relationship between the two properties. The permeability reached a minimum at a calcite content of 1.5% by mass, with little further change with increased calcite. Columns 5 and 6 show a discontinuity with the rest of soil columns—see Figure 7.9—and the reason for this discrepancy is not clear.

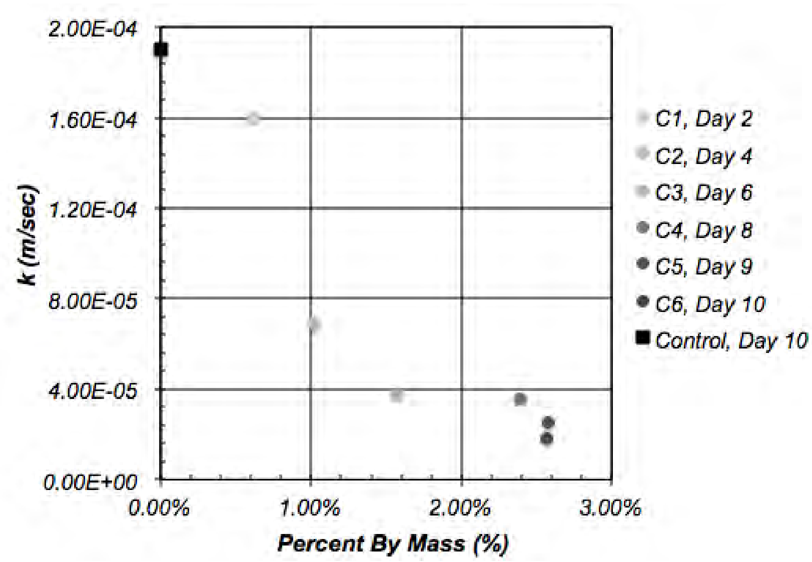

Figure 7.9 Permeability (*k*) versus calcite by mass (%)

7.5 CONCLUSIONS

The purpose of this research was to obtain and evaluate the geotechnical properties of a specific soil treated for a specific MICP treatment using native microbes. Property relationships were obtained with time using six soil columns treated using the bio-stimulation approach to MICP. The properties that were analyzed in this research project were permeability, calcite content, and shear wave velocity. It was observed that permeability decreased by a maximum of 87% following treatment. Calcite contents were measured as high as 3.5% by mass. The final shear wave velocities increased and reached a maximum of 900 m/sec at the end of the treatment period. In addition, permeability was inversely related to changes in shear wave velocity. A direct linear relationship between the calcite content and shear velocity was shown to exist for most cases.

7.6 ACKNOWLEDGMENTS

I would like to thank to my mentor Professor Jason DeJong, Collin Anderson, and my graduate mentor Michael Gomez for their guidance and support during this summer research internship. I would also like to thank the Pacific Earthquake Engineering Center (PEER) for giving me this opportunity and the National Science Foundation for their funding. Lastly, I would like to give thanks to Heidi Tremayne for organizing the PEER summer internship program.

7.7 REFERENCES

Al Qabany A., Soga K. (2013). Effect of chemical treatment used in MICP on engineering properties of cemented soils, *Geotechnique*, 63(4): 331–339.

Al Qabany A., Soga K., Santamarina C. (2012). Factors affecting efficiency of microbially induced calcite precipitation, *J. Geotech. Geoenviro. Eng.,* 138(8): 992–1001.

ASTM (2006). *Standard Test Method for Permeability of Granular Soils (Constant Head), D2434-68,* American Society for Testing and Materials, West Conshohocken, PA.

ASTM (2007). *Standard Test Method for Rapid Determination of Carbonate Content of Soils*, *D4373,* American Society for Testing and Materials, West Conshohocken, PA.

Bang S.S., Galinat J.K., Stocks-Fisher S. (1999). Microbiological precipitation of $CaCO_3$, *Soil Biology and Biochem*., 31: 1563–1571.

Burbank M., Weaver T., Green T., Williams B., Crawford, R. (2011). Precipitation of calcite by indigenous microorganisms to strengthen liquefiable soils, *Geomicrobiol. J.*, 28(4): 301–312.

Burbank M., Weaver T., Lewis R., Williams T., Williams B., Crawford, R. (2013). Geotechnical tests of sands following bio-induced calcite precipitation catalyzed by indigenous bacteria, *J. Geotech. Geoenviron. Eng.*, 139: 928–936.

DeJong J.T., Mortensen B.M., Martinez B.C., Nelson D.C. (2010). Bio-mediated soil improvement, *Ecological Eng.,* 36: 197–210.

Ivanov V., Chu J. (2008). Applications of microorganisms to geotechnical engineering for bioclogging and biocementation of soil in situ, *Reviews in Environmental Sci. & Biotech.*, 7(2): 139–153.

Montoya B.M., Gerhard R., DeJong J.T., Wilson D., Weil M., Martinez B., Pederson L. (2011). Fabrication, operation, and health monitoring of bender elements for aggressive environments, ASTM, *Geotech. Testing J.,* 35(5): 15 pgs.

Mortensen B.M., Haber M.J., DeJong J.T., Caslake L.F., Nelson D.C. (2011). Effects of environmental factors on microbial induced calcium carbonate precipitation, *J. Appl. Microbiol.*, 111(2): 338–349.

Stocks-Fisher S., Galinat J.K., Bang S.S. (1999). Microbiological precipitation of CaCO3, *Soil Biol. Biochem.*, 31(11): 1563–1571.

Wang J.-L., Chun X.-Q., Rui X.-W. (2010). Study on soil solidification based on microbiological precipitation of $CaCO_3$, *Sci. China Tech. Sci*., 53: 2372–2377.

Whiffin V.S., van Paassen L.A., Harkes M.P. (2007). Microbial carbonate precipitation as a soil improvement technique, *Geomicrobiol. J.,* 24: 417–423.

8. Risk Analysis of Levee Failure: Optimization of Levee Height and Crown Width

Elizabeth R. Jachens

ABSTRACT

Most traditional risk analysis studies of levee systems only consider levee failure due to overtopping. Despite evidence that most levees fail before overtopping, few studies have included structural or intermediate failures with risk analysis–the ones that have only covered these failure modes conceptually. This paper presents a risk based analysis and optimization of levee height and crown width for a symmetrical two-levee river channel section that includes overtopping and intermediate failure modes. Levees along a small river, the Cosumnes, and a large river, the Sacramento River (both in California), are analyzed and the optimal results are compared.

8.1 INTRODUCTION

Levees partially protect areas of land from flood damage by restricting water from entering the protected area. Even the best levees cannot guarantee protection; they can only decrease the likelihood of flooding. Levees can fail by overtopping or intermediate structural failure. The Federal Emergency Management Agency (FEMA) requires levees to be designed to provide protection from at least a 1% annual-chance flood [FEMA 2013]. As a taller levee will have a smaller chance of failure by overtopping and a wider levee will have a lower probability of intermediate failure [Tung 1981b; Wood 1977; USACE 2011; Sturm 2012], height and width are two significant factors in levee design.

For existing levee systems, periodic levee field inspections help describe and analyze flood probability. Both the California Department of Water Resources (DWR) and the U.S. Army Corps of Engineers (USACE) conduct tests and analyses of project levees using field and laboratory data, stability and seepage analysis, and provide suggestions to improve insufficient levees [USACE 2013]. They consider the present state and future performance of the levee under changing regulations for levee failures relating to seepage, stability, erosion, settlement and seismic vulnerabilities [DWR 2013]. For agencies desiring to decrease the risk of levee failure, similar analysis techniques are required for design and construction of an accredited levee [USACE 2000].

Considered here are two types of levee failure modes: overtopping and intermediate failure. Overtopping failure is only a function of flood water stage. The two decision variables are levee height and levee crown width. Levee height will be a determining factor for both overtopping and intermediate failures, while levee crown width will only affect the likelihood of the intermediate failure. By minimizing the annual expected cost, which is the sum of the annualized construction cost and expected annual damage (EAD), a risk-based optimization model for levee design or evaluation of existing levees is developed. This optimization method will be performed on two distinctly different levee systems; one with a low mean annual peak flow surrounded by agricultural land and one with a high mean annual peak flow surrounded by urban development.

8.2 BACKGROUND

As defined by Bogardi and Zoltan [1968], levee failure can be classified into four modes The first and possibly most widely studied failure mode is overtopping, which occurs when flood water stage exceeds the maximum height of the levee. The second mode is structural failure as a result of slope instability. The third failure mode includes structural failures from soil failures usually from piping and internal erosion. The last mode of failure is a net reduction in levee strength caused by wind wave action that scours levee walls. The three structural modes of failure occur when the water stage is between the toe and crest of a levee. These failures, referred to as intermediate failures, are a function of the water stage at intermediate elevations along the levee sides (among other things). Other intermediate failure modes include: through-seepage, under-seepage, burrowing animals, vegetation, and seismic vulnerabilities such as liquefaction. For this study, the structural failure modes can be modeled using a single intermediate failure mode [Sturm 2012; Wolff 1997]. The combined intermediate failure probability assumes independence between individual failure modes [Sturm 2012]. In cases where two modes may be dependent (i.e., through-seepage and slope instability), the assumption of independence may be too conservative and can produce an upper bound estimate of the failure probability [Wolff 1997].

The probability of intermediate failure for different water elevations can be graphically summarized in a levee fragility curve. A fragility curve is a conditional probability of failure based on a loading condition; however, it does not account for the probability of the loading condition [Sayers et al. 2002]. To calculate the final probability of failure, fragility curves need to be combined with hydraulic loading probabilities. Some fragility curves acknowledge the presence of multiple failure modes but primarily take into account overtopping. It is assumed that this analysis method is valid for new levees, which have sufficient strength to withstand intermediate failures but are still susceptible to overtopping [Hall et al. 2003; Merz 2006].

The USACE first developed a relationship of intermediate failure and river stage using probable non-failure points and probable failure points, where the highest elevation likely not to fail (85%) is the probable non-failure point, and lowest elevation likely to fail (85%) is the probable failure point. In between these two points, the probability of failure was assumed to be linear [Wolf 1997; USACE 1999; USACE 2000]. This assumption of a linear relationship can be unreasonable when more levee characteristics are known. The combined effects of overtopping, seepage, erosion, wave impacts, and other structural failure methods have been analyzed to disprove the linear relationship [Wolff 1997; Sturm 2012; Ketchum et al. 2011].

A simplified version of combined modes of failure is used for the fragility curve in this analysis. Vorogushyn et al. [2009] presents fragility curves in sensitivity analysis for various breach mechanisms to avoid dependency on expert judgments. The author concluded this sensitivity analysis by commenting that the curves are sensitive to permeability because the range of values can vary several orders of magnitude and affect seepage, piping, erosion, and other failure mechanisms. Permeability of soils used for levee construction and foundation play an important role in levee failure modes, including through seepage and under seepage; the path of least resistance for water moving from waterside to landside seepage depends on the relative permeability of the levee construction material and the foundation material [Meehan 2012].

With increasing risk and damage from levee failure, there is a need for more accurate levee modeling and failure analysis. One challenge to improving levee design is representing the hydrologic and hydraulic uncertainties in the design method. Previous studies [Tung 1981a; Tung 1981b; USACE 1996] have evaluated the uncertainties in the risk models for overtopping cases only. A more recent study by Wood [1997] discusses levee reliability using both overtopping and structural failures. Wood comments that professional and field experience suggests that most levees will fail due to intermediate failure before overtopping. He concludes that a risk analysis that ignores intermediate or structural failure will overestimate the levee protection and the expected flooding return period, and significantly underestimate the annual expected damages. For these reasons, a risk model should incorporate both intermediate and overtopping failures for new and existing levees.

8.3 METHODS

For this study, methods includes developing a hydraulic and economic risk model, describing the performance of a levee system, and optimizing levee design parameters (height and width) to minimize total expected annual costs, including expected annual damage and annualized construction cost.

8.3.1 Model Description and Set-Up

An idealized river cross section developed by Tung (1981b) was used for this study (Figure 8.1). The modified levee dimensions for the Cosumnes River example are summarized in Table 8.1. Other parameters not listed in Table 8.1 are based on the design standards developed by DWR and the federal government, Bulletin 192-82 and PL 84-99, respectively. Each set of standards includes minimum crown widths, side slopes, freeboard height, and overtopping frequency. Summarized in Table 8.2 are the PL 84-99 standards [DWR 2011]. This set of standards was selected, and all minimum requirements were met for the levee design parameters. In the event of a flood, any levees not meeting or exceeding the PL 84-99 minimum standards are ineligible to apply for federal aid in response to flood damage.

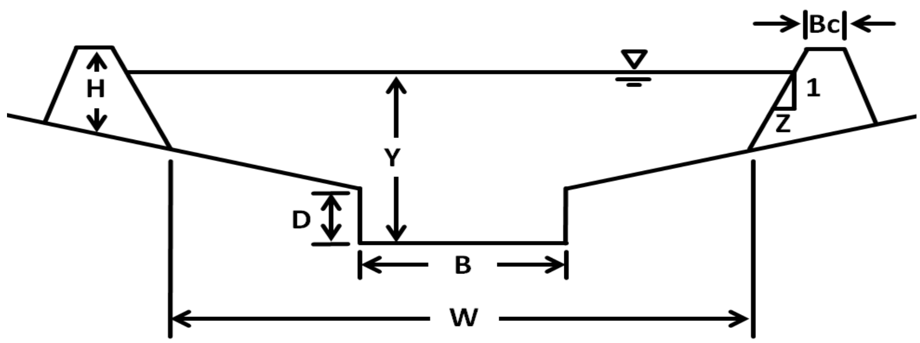

Figure 8.1 Idealized cross-section of a symmetrical two levees river channel system.

Table 8.1 Dimensions of the idealized river channel system for Cosumnes River.

Description	Reach 1
B: Channel Width (ft.)	200
D: Channel Depth (ft.)	3
Nc: roughness factor of the channel section	0.05
τ: the slope of the symmetrical floodplain section (ft/ft)	0.01
S: longitudinal slope of the stage (ft/ft)	0.0005
L: length of the stage (ft)	2640
UC: unit cost of land purchase ($/ft^2)	0.066

Table 8.2 Minimum levee standards to qualify for flood damage federal aid.

Standards Source	Crown Width (ft)	Land-Side Slope	Water-Side Slope	Design Flood (years^{-1})
PL 84-99	16	3:1 – 5:1	2:1	1:100

8.3.2 Levee Fragility Curves

Levee fragility curves graphically illustrate the relationship of levee failure probability for intermediate modes and the height of the free surface of the water (stage). Wolff [1997] suggests five possible conditional probabilities of failure functions. This conditional probability function can be restated as: “The probability of failure, given the flood water elevation, is a function of the flood water elevation and other random variables.” Figure 8.2 illustrates three possible levee performance curves similar to the conceptual performance curves in DWR’s Attachment 8E [2012b] and Wolff’s research [1997]. The levee fragility curves represent three levee conditions: good, fair, or poor. Failure probability for a levee in good condition is a convex curve, remaining low when the stage is low and increasing dramatically when the stage approaches the levee height. In contrast, the levee in poor condition has a concave failure probability curve, with a high failure probability even at relatively low stages. Levees in fair condition tend to be in good condition at low stage heights, but come to resemble poor quality levees at higher stages. In Figure 8.2, the toe of the levee is at a stage of 3.5 ft, the levee is 5 ft tall, and the crest of the levee is 8.5 ft. A water stage below the toe of the levee will not induce levee failure, so the probability is 0. When the stage reaches the levee crest, at 8.5 ft, the failure probability from overtopping is 1.0. The exact probability distribution between these two points is somewhat uncertain given the conceptually shaped curves are based on professional opinions [Perlea and Ketchum 2011]. During initial and continuing eligibility inspections for existing levees, USACE evaluates the condition of the levee segment as acceptable, minimally acceptable, and unacceptable [USACE 2013]. Using this method in evaluating existing levees, the overall levee rating assigned by the USACE can be comparable to a good, fair, or poor quality levee, respectively.

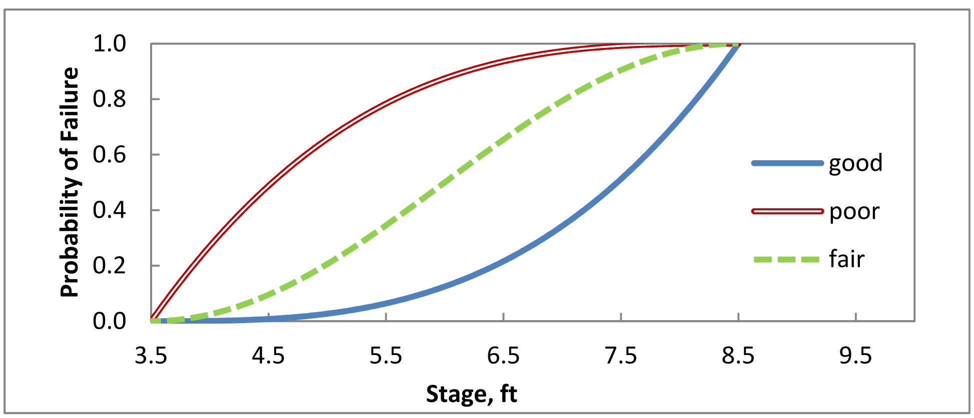

Figure 8.2 Levee fragility curves for levees in good, fair, and poor condition.

Traditional levee performance curves consider stage as the independent variable and failure probability as the dependent variable. For many risk analysis applications to levee failure, this model is too simplistic for intermediate failure modes. Wolff [1997] and Sturm [2012] model multiple individual failure modes and create a combined failure probability assuming the modes are independent. They summarize that under-seepage and through-seepage modes are the most dominant intermediate failure modes, and may trigger other failure modes, such as erosion and slope stability. If a levee is designed and constructed with soil of a lower permeability than the foundation, the seepage that occurs should be focused underneath the levee in the foundation instead of through the mass of the levee [Meehan and Benjasupattananan 2012].

In an effort to define a second decision variable that can account for the change in failure probabilities due to seepage, numerous seepage variables were considered. Seepage depends on levee geometry such as levee height, crown width, and side slopes, and properties such as soil conductivity and compaction [Kashef 1965; USACE 2000]. Here, levee crown width is chosen as the second decision variable because of its influence on intermediate failure performance curves and the wide range of acceptable values [USACE 2006].

Crown width can be used to calculate seepage through an earthen dam using geotechnical relationships given in Schaffernak's solution [Das 2010]. Independent variables in this method include water height, levee height, crown width, landside angle, and waterside angle, as shown in Figure 8.3. There are three main assumptions for this model. The first assumption is that the base of the levee is impervious, disregarding underseepage as a failure mode. This assumption implies seepage as a primary cause of intermediate failure, and the flood plain and river channel are modeled as having no risk of failure. Second, the waterside slope angle of the dam is less than 30°, otherwise the Casagrande correction factor needs to be applied (The 2:1 horizontal to vertical ratio selected does not require the Casagrande correction factor). The third assumption is that the hydraulic gradient is constant: it is equal to the slope of the free surface as water flows through the dam according to the Dupuit assumption [Das 2010].

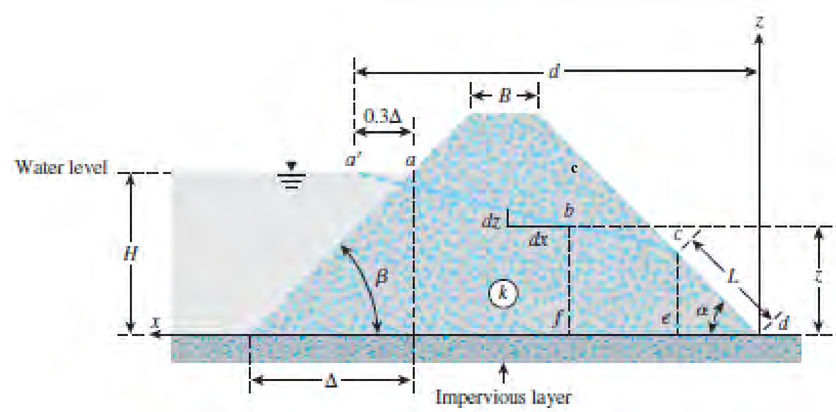

Figure 8.3 Seepage through an earthern dam [Das 2010].

Schaffermak's solution uses L, the slope elevation of the discharging water, and the soil hydraulic conductivity to calculate the rate of seepage per unit length of the dam. Because the hydraulic conductivity is unknown, it is assumed to be constant for the given sample space for all possible levee heights and crown widths. Given this assumption, relative rates of seepage can be compared using the ratio of the slope elevations of discharge for two crown widths; therefore the rate of seepage can be calculated as given in Equation (8.1).

$$q = k * L * \tan\alpha * \sin\alpha \tag{8.1}$$

where q is the rate of seepage per unit length of the levee, k is the soil conductivity, α is the angle of the landside slope, and L is the sloped elevation of the discharging water defined in Equation (8.2).

$$L = \frac{d^2}{\cos a} - \sqrt{\frac{d^2}{\cos a} - \frac{H^2}{\sin a}} \tag{8.2}$$

where H is the water level, and d is the horizontal distance between the landside toe of the levee and the effective seepage entrance as defined in Equation (8.3).

$$d = 0.3 * \frac{H}{\tan \beta} + \frac{h - H}{\tan \beta} + B_c + \frac{h}{\tan \alpha} \tag{8.3}$$

where β is the angle of the waterside slope, h is the levee height, and B_c is the crown width.

The slope elevation of the discharge water can be described as a vertical elevation using geometry and expressed as a percentage of the total levee height. The relative rates of seepage can be viewed as changes in the levee's efficiency to resist failure, specifically seepage failure. The increase in the levee efficiency, given a varying crown width, is described by the relative decrease of the seepage elevation when comparing between two crown widths. The standard crown width for comparison is chosen to be the minimum standard of 16 ft. The levee efficiencies for all other selected crown widths are normalized using the vertical seepage heights relative to that of this standard crown width. For example, the increase in efficiency for the maximum crown width of 56 ft calculated using this method is 63%. Assumptions are then made that a change in seepage elevation corresponds to a relative change in efficiency; therefore, the efficiency change can be used to predict the change of the probability of failures accordingly. The new levee fragility curves depending on both crown width and levee height have similar shapes as the levee fragility curves depending only on levee height. The resulting fragility curve is responsive to crown width so that the probability of failure decreases for increasing crown widths given a stage height.

8.3.3 Risk Analysis Calculations

Risk is the probability of failure multiplied by the consequences of failure, while reliability is one minus the probability of failure [Hashimoto et al. 1982]. The theory of reliability analysis is not new to levee failure [Tung 1981a; Tung 1981b; USACE 2006; Wood 1997]. Risk management and reliability methods have been used to evaluate flood consequences since the twentieth century, using a capacity-demand model where failure occurs when the capacity of the levee system is less than the demand [NRC 2013; USACE 2006]. Reliability analysis uses individual components of a system to estimate its overall reliability. For levee reliability analysis, uncertainties in channel flow (hydrologic) and channel capacity (hydraulic) are used to calculate the total levee system reliability. The reliability analysis is then used in decision making by optimizing objective variables or function [Bras 1979]. However, only a few studies include intermediate failure in the reliability analysis. This model ignores hydraulic uncertainty, i.e. no uncertainty in the levee's capacity to resist flood flows exists. Ignoring hydraulic uncertainty can compromise the accuracy of the expected damages, and should be avoided when adequate knowledge about the probability distribution function of the levee capacity is available [Tung 1981b].

In this study, however, we assumed an idealized cross section where no levee dimension uncertainty exists. Considering hydrologic uncertainties only, the annual expected damages of the system for intermediate and overtopping failures combined can be calculated, as shown in Equation (8.4). The first term represents intermediate failure when the given flow is below channel capacity flow, while the second term represents the overtopping case when the given flow is above the channel capacity flow.

$$EAD = \int_0^{Q_c} D(Q) * f_q(Q) * f_L(Q)\, dQ + \int_{Q_c}^{\infty} D(Q) * f_q(Q)\, dQ \tag{8.4}$$

where $D(Q)$ is the damage cost as a function of flow, Q_C is the flow capacity of the levee system, $f_q(Q)$ is the probability distribution function of a given flow, and $f_L(Q)$ is the probability distribution function of the intermediate levee failure for the given flow. The probability distribution of flow was modeled using unconfined river flow frequency distribution from the HEC-DSSVue database, a program obtained from the Hydrologic Engineering Center at USACE. If the damage cost per failure occurrence is assumed constant and independent of flow, Equation (8.4) can be simplified to Equation (8.5).

$$EAD = D * \int_0^{Q_c} f_q(Q) * f_L(Q)\, dQ + D * \left[1 - F_Q(Q_C)\right] \tag{8.5}$$

where *D* is the damage cost per levee failure in U.S. collars, and $F_Q(Q_C)$ is the cumulative distribution function of a given flow.

Because the failure probability is expressed as a function of flood water stage in feet and the flow probability is a function of flow in ft^3/sec, Equations (9.4) and (9.5) can't be integrated with the conflicting units [Wolff 1997]. Manning's equation can be used to calculate flow for a given stage elevation, and, more importantly, stage given a flow rate. The probability of intermediate failure is a function of flood stage and Manning's equation is nonlinear, but it is still assumes that the behavior of flood water elevation and flow is linear for linear geometries. For the case of overtopping, the maximum capacity, Q_C levee system for Reach 1 can be calculated using Manning's equation for the maximum stage before overtopping.

The levee system is optimized to minimize the total expected annual cost, which is the sum of the annualized construction cost and expected annual damage cost, Equation (8.6).

$$\text{Min } TC = EAD + ACC \tag{8.6}$$

where *TC* is the total expected annual cost, *EAD* is the expected annual damages from Equation (8.5), and *ACC* is the annualized construction cost calculated in Equation (8.7).

$$ACC = (s * V * c) * \left[\frac{i * (1+i)^n}{(1+i)^n - 1} \right] + LC \tag{8.7}$$

where s is a cost multiplier assumed to be 1.3 to cover engineering and construction administrative costs, V is the total volume of the levee along the entire length of the reach in yd^3, i is the interest rate assumed to be 5%, n is the number of useful years the levee will be repaid over, c is the soil compaction cost of \$10 per yd^3 [Suddeth et al. 2010], and LC is the land cost primarily for purchasing land to build the levee, calculated in Equation (8.8).

$$LC = UC * A * i \tag{8.8}$$

where UC is the unit cost of the land in dollars per square foot, A is the area of land the base of the levee occupies in square feet, and i is the discount rate. Land cost is an additional cost added to represent the different site locations of a levee based on the cost of purchasing an acre of agricultural or urban land.

The physical constraints for this optimization model include upper and lower limits for crown width and levee height as well as non-negative constraints for all variables.

8.4 RESULTS AND DISCUSSION

A levee system located in an agricultural area with a low peak annual flow (the Cosumnes River) and a levee system with a high peak annual flow (the Sacramento River) will be analyzed and the optimal levee heights and crown widths are compared.

8.4.1 Small Levee System

For analysis in this section, the river flow frequency data is from the Cosumnes River, a river with a median annual peak flow of 930 ft^3/sec, a mean annual peak flow of 1300 ft^3/sec, the cost of the land adjacent to the river valued at \$3000 per acre, and a total damage amount of \$8 million if the surrounding area were flooded. This levee is assumed to be in fair condition and uses the levee fragility curve for intermediate failure probabilities. Using these site specific values, the annualized construction cost, expected annual damage cost, and total expected annual cost are compared for a minimum levee crown width of 16 ft (Bc = 16 ft) and a maximum of 56 ft (Bc = 56 ft) in Figure 8.4. For shorter levees, total costs are governed by the expected annual damage costs. For the taller levees, construction cost has a larger impact on total costs. For tall and wide levees, the expected annual damage cost becomes very small as the chance of overtopping and intermediate failure decreases rapidly and total cost becomes dominated by construction cost. The transition of the total cost line between the expected annual damage cost and the annualized construction cost creates a concave curve, at which the minimum cost corresponds to an optimum levee height and crown width combination.

The optimum height and width combination can also be compared using a total cost contour plot, shown in Figure 8.5. This contour plot identifies the trend that the optimum levee height decreases with increasing crown width for a comparable total cost. As the crown width increases, the intermediate failure probability decreases, thereby decreasing the first term of the expected annual damage equation. As the levee height increases, the water capacity of the levee system increases and therefore decreases the probability of overtopping failure.

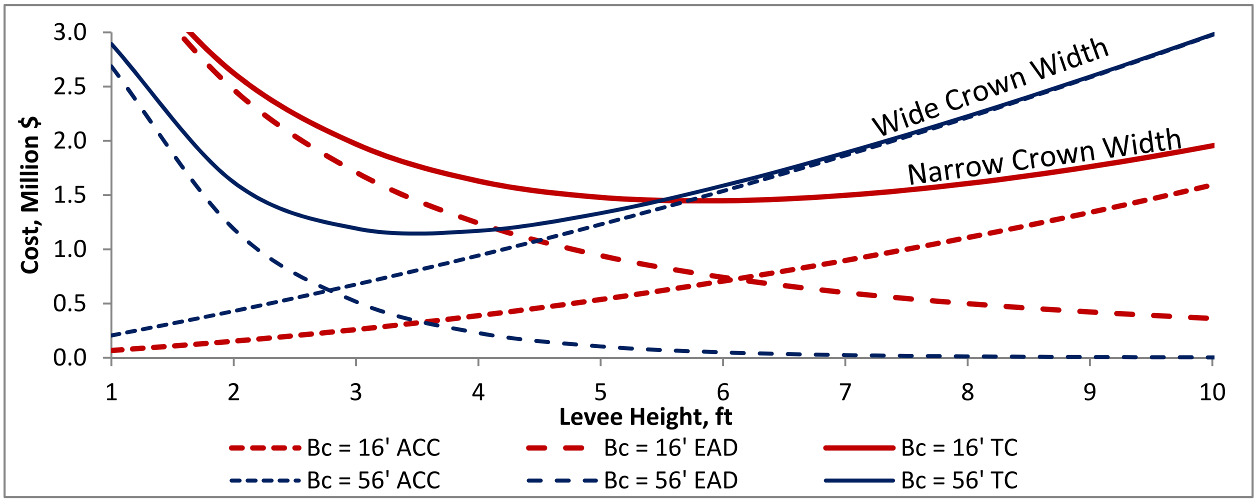

Figure 8.4 **Annualized construction costs, expected annual damage costs, and total expected annual costs for minimum and maximum levee crown widths.**

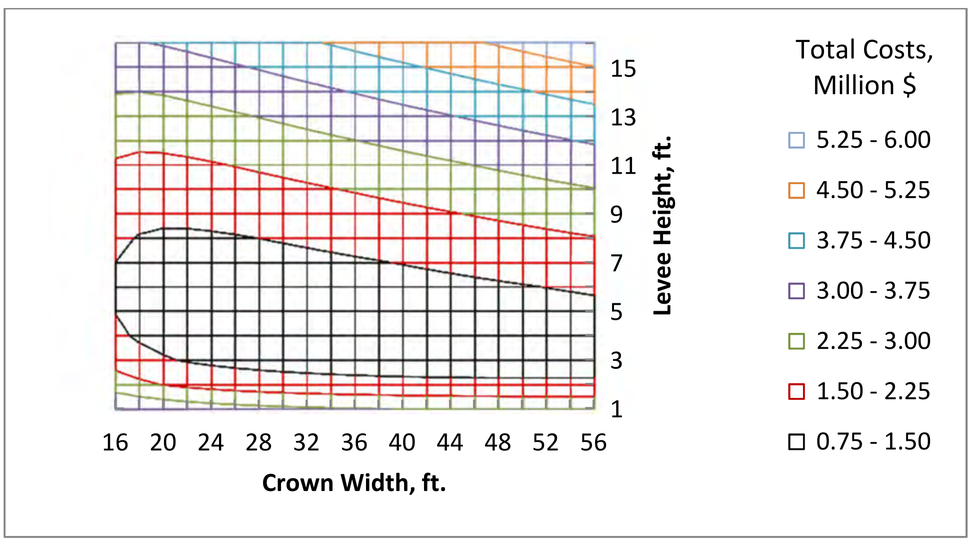

Figure 8.5 **Contour plot of total costs for various levee geometries.**

Because the total annual expected cost of the levee is a function of levee height and crown width, there are local minimums for each levee height and crown width increment. Figure 8.6 compares combinations of levee height and crown widths in increments of 10 ft to show the resulting local minimum of total cost for each combination. For a range of levee heights, the crown width with the lowest net cost should be selected. A levee height less than 2.8 ft should have a crown width of 56 ft, a levee height between 2.3 and 3.1 ft should optimally have a crown width of 46 ft, a crown width of 3.1–4.6 ft should have a crown width of 36 ft, the crown width should be 26 ft wide when the levee height is 4.5–9.8 ft, and finally for a levee that is taller than 9.8 ft, a crown width of 16 ft is sufficient. The global minimum from Figure 8.6 occurs at a levee height, H*, of 4.1 ft and a crown with of 36 ft.

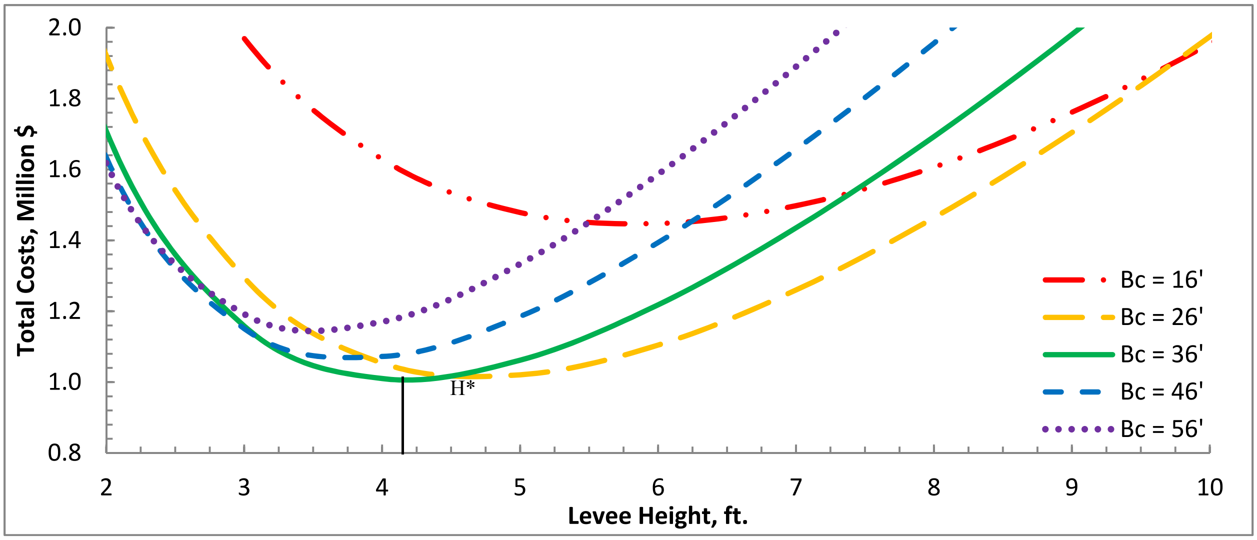

Figure 8.6 Results of total expected annual costs for various levee geometries for the Cosumnes River.

To summarize the results from Figure 8.6, taller levees require a narrower crown width when compared to lower levees. This can be largely attributed to the levee geometry of the side slopes of 1V:2H (water side) and 1V:4H (landside). The annualized construction cost, which is a function of levee volume, is more sensitive to levee height than crown width according to the Lagrange multiplier; when a levee height increases by one foot, the base width of the levee will increase by 6 ft (1*2 +1*4 = 6), which increases the horizontal distance of the seepage path and therefore decreases seepage related failures. Figure 8.7 compares the optimal crown width and levee height combinations with levee height as a function of crown width.

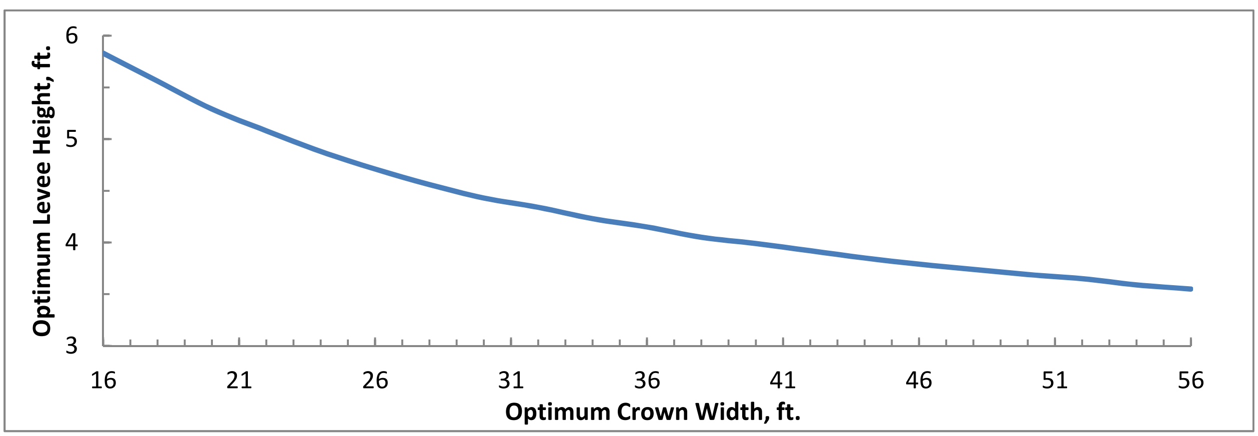

Figure 8.7 Optimum crown width and optimum levee height combinations.

According to FEMA, a levee crown height must provide overtopping protection for at least a 1:100 year flood. In addition, the channel holds a flow capacity for a reoccurrence interval of approximately two years. To meet these standards, the levee height must be a minimum of 4.0 ft high to accommodate a flow of 4365 ft^3/sec, which has a 1% annual occurrence probability. In this analysis, it is assumed that levee heights can be built in increments of 1/10 of a foot, while crown widths can only be constructed in whole foot increments. The optimal crown width for a 4.0-ft-tall levee would be 33 ft. Using a computer solver, the absolute minimum cost is found to occur at a levee height of 4.4 ft and a crown width of 31 ft, while the return period for flood that would cause overtopping is once every 144 years. When land-use cost is not considered, the optimum height is 4.5 ft and the crown width is 30 ft. Because land-use cost depends on the base area of the levee and the base width increases by 6 ft for every foot of additional height but only increases 1 ft per foot of additional crown width, the optimal combination will be a slightly shorter but wider levee as the unit land cost increases.

In cases where the optimum crown width is too large given the constraints of the land use, steeper landside slopes or a smaller crown width can be analyzed. In many urban areas where the price of land is very high, levees may be replaced with flood walls as they occupy less area even though they are significantly more expensive to build. According to the Urban Levee Planning Guide from FloodSafe California, the current base flood of 100 years of protection has been proposed to be increased to 200 years for urban levees in California by 2025 [DWR 2012a]. To provide protection from a 200-year flood, the levee would need have a maximum capacity of 5150 ft^3/sec and be a minimum height of 4.7 ft to comply. For a 4.7-ft levee, the optimal levee width would be 29 ft. The area surrounding the Cosumnes River levees is primarily agricultural land and does not need to meet the increased protection standards. In contrast, the next section looks at the Natomas levee section of the Sacramento River, where because of the high annual peak flow of the area at risk is highly urbanized, the increased protection is justified.

Construction and flood damage costs are highly variable for different site locations. Table 8.3 compares the effects of changing damage cost and unit construction cost on optimum levee height and width; the same ratio of the damage cost to the construction cost produces the same optimum combination of levee height and crown width, with different minimum total costs. When the ratio of damage cost divided by unit construction cost increases, i.e., the damage cost has increased proportionally more than the unit construction cost, the optimum levee height and crown width both increase to provide additional protection to the increased value of the land-side area. The larger D/CC ratio has a higher return period compared to the smaller ratio as a result of the increased flood risk and damage. The small differences in values have insignificant effects on the total cost as the levee heights are constructed in 1/10 ft and crown width in whole integers.

The analysis above assumes the levee is in fair condition. However, different levee conditions have different intermediate failure probabilities for a given stage. Figure 8.8 compares the cost curves for the three different levee conditions. The crown widths used for each set of data is the optimum crown width: optimum crown width is 17 ft, 31 ft, and 38 ft for a levee in good, fair, and poor condition, respectively. For a levee in better condition, the optimum crown widths are smaller than that of a levee in worse condition. For all levee conditions and their respective optimum crown widths, the optimum levee height remains fairly constant between 4.4 and 4.5 ft.

Table 8.3 **Effects on optimal results from damage costs and unit construction costs.**

Damage Costs (millions of $)	Unit Construction Costs ($)	D/CC	Optimum Height (ft)	Optimum Crown Width (ft)
10	16.67	0.6	3.83	29.1
6	10	0.6	3.83	29.1
10	12.50	0.8	4.15	30.1
8	10	0.8	4.15	30.1
10	10	1.0	4.39	31.2
10	8.33	1.2	4.59	31.7
12	10	1.2	4.59	31.7
10	7.14	1.4	4.75	32.2
14	10	1.4	4.74	32.2

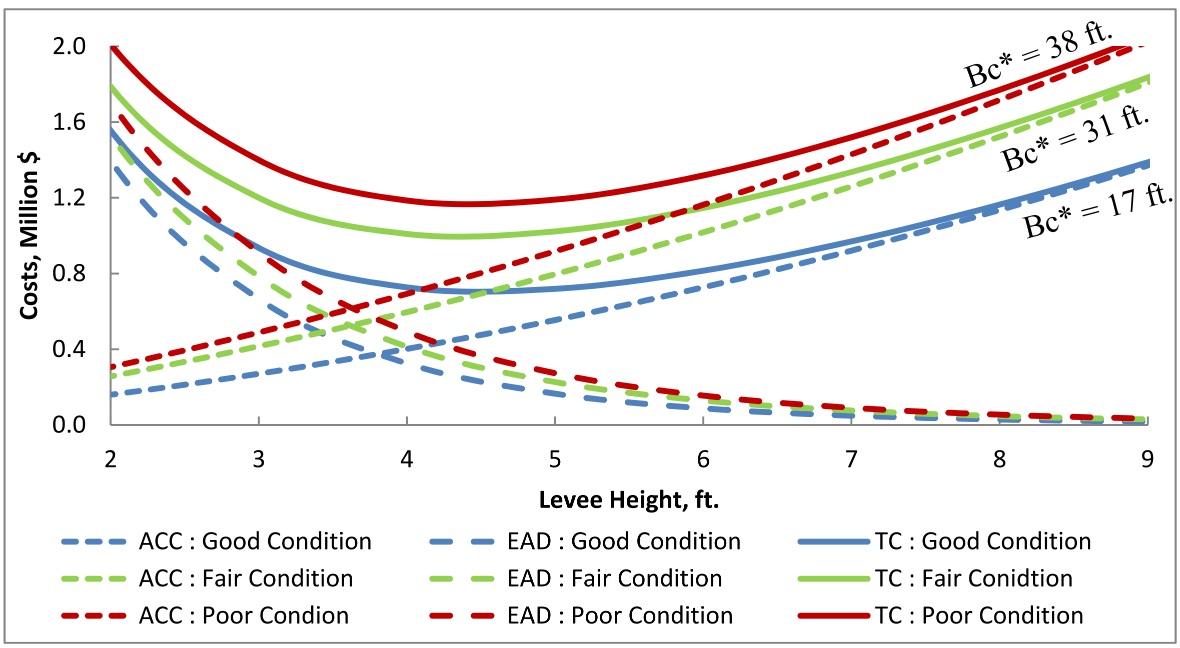

Figure 8.8 **Comparison of good, fair, and poor levee conditions for optimal crown widths.**

8.4.2 Large Levee System

For analysis in this section, the river flow frequency data is from the Natomas Levee on the Sacramento River that ends at the confluence of the Sacramento River and American River. The river has an estimated mean annual peak flow of roughly 60,000 ft^3/sec, lognormal distribution with a coefficient of variation of 1.0, the cost of the land adjacent to the river valued at $30,000 per acre, and a damage amount of $8.2 billion is the surrounding urban area was flooded. The channel depth, channel width, and levee length have been measured using Google Earth to be 10 ft, 1000 ft, and 18 miles respectively (Figure 8.9). There is no floodplain present in this case, and no data is available for the channel roughness or the longitudinal slope of the stage. Values are assumed to be consistent with values N_c and S, respectively, in Table 8.1. This levee is assumed to be in fair condition and uses the levee fragility curve for intermediate failure probability.

For all reaches, the levee geometry is required to meet USACE 20-ft-minimum crown width. Most levees in the American River North levee have crown widths ranging for 30–60 ft with 2–4 lane roads on the crest, have a waterside slope of 3H:1V and a landside slope of 2H:1V at the steepest. A complete set of dimensions of the improved levees is not explicitly listed for many of the reaches along the Sacramento River. The geometry of the Natomas Cross Channel levee is mentioned to be approximately 15 ft tall, with a crown width of 25 ft and a base width of 75 ft [USACE 2009].

Figure 8.10 compares combinations of levee height and crown widths (increments of 20 ft) to show the resulting local minimum for net costs for each combination. A levee height less than 20 ft should have a crown width of 90 ft, a levee height between 20 and 25.5 ft should optimally have a crown width of 70 ft, the crown width should be 50 ft wide when the levee height is 25.5–35 ft, and finally for a levee that is taller than 35 ft, a crown width of 30 ft is sufficient. The global minimum from Figure 8.10 occurs at H*, with a levee height of 23.5 ft and a crown with of 70 ft. Using a computer solver, the absolute minimum net cost occurs at a levee height of 24.3 ft and a crown width of 61 ft, and a return period of 150 years. With an additional required freeboard of 2–3 ft, the return period will increase to a 200-year flood that meets the new urban levee criteria.

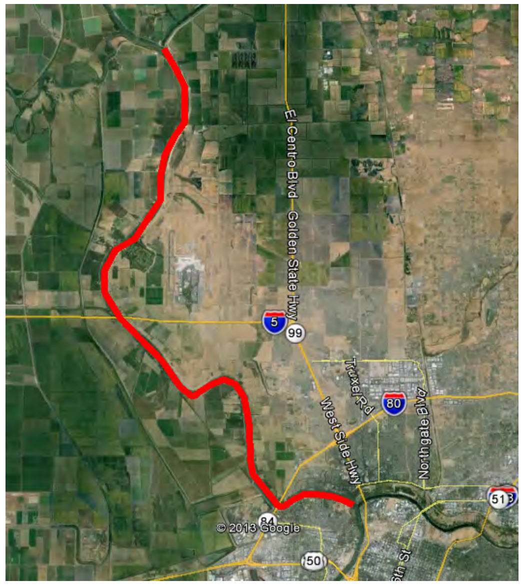

Figure 8.9 **Eighteen miles of levee on the Sacramento River protecting the Natomas Basin to the east.**

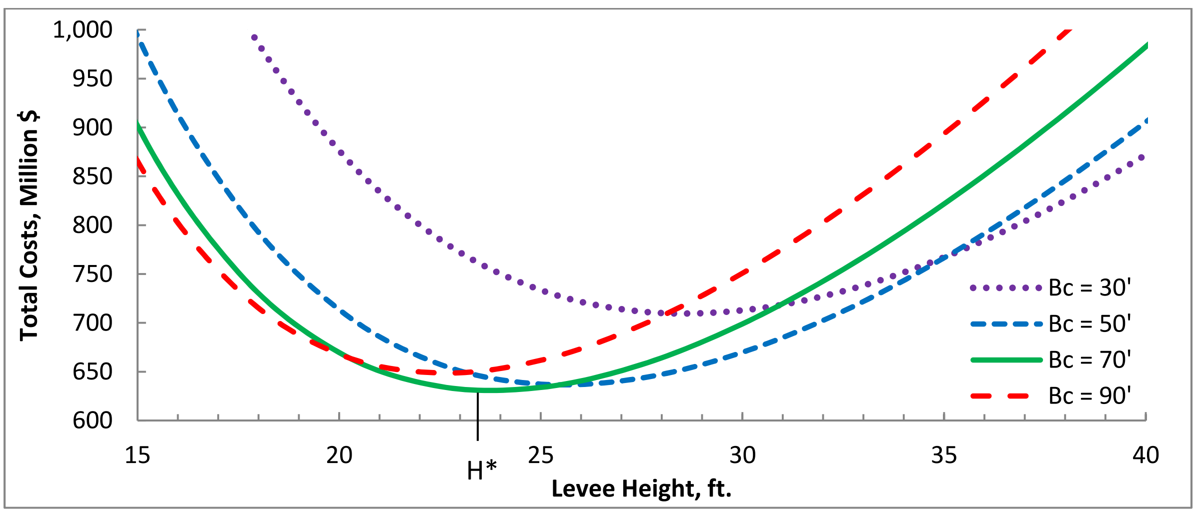

Figure 8.10 **Results of total expected annual costs for various levee geometries for the Natomas Levee on Sacramento River.**

The current Natomas levee basin is under improvement by the Natomas Levee Improvement Plan to increase flood protection and ensure all levees meet codes and standards set by FEMA and the State of California. Together, The Sacramento Area Flood Control Agency (SACFA) and USACE have the task of updating all levees to achieve a 100 year flood protection while determining the costs of upgrading the levees to 200-year protection [SAFCA 2013]. Considering most of the levees were built in the early 1900s to protect agricultural area and currently has a 99% probability of failure in the next 30 years, the levees are extremely vulnerable to flooding risk [USACE 2013b]. Analysis of through seepage, under seepage, stability, and erosion was performed to classify areas into risk categories to identify priority reach locations for future improvements. The proposed levee design for new levees includes a slurry wall to mitigate seepage and an increase of channel capacity to decrease the stage at a given flow to hydrostatic pressures on the levee.

8.5 CONCLUSIONS

This paper presents a quantitative risk analysis for a symmetrical levee system including intermediate and overtopping failure modes to decide optimal levee height and crown width. The levee risk analysis modeling is performed for both a small and large levee system. Levee height dictates overflow probability while crown width and levee height together determine intermediate failure probabilities.

Increasing the levee height is the most effective way to reduce overtopping failure while increasing crown width is effective at decreasing intermediate failures. As the probability of intermediate failure can be much larger than the probability of overtopping failure, intermediate failure should be included in all analyses. Increasing crown width will result in the decreased optimal levee height and similar total costs.

Different levee conditions have different intermediate failure probabilities for a given stage. For a levee in good condition, the optimum crown width can be significantly smaller compared to the optimum crown width of a levee in poor condition. For all levee conditions and their respective optimum crown widths, the optimum levee height remains fairly constant.

In some situations where levees are adjacent to dense urban development, increasing crown width to mitigate seepage is not practical. The wide crown widths and tall levee heights needed to ensure a 200-year flood protection for high damage areas calls for an extremely large levee footprint. In situations where the land area required for levee construction is not available or cost effective to purchase, structural additions demanding a smaller land footprint such as slurry walls will reduce seepage and seepage related failures.

The model analyzed in this paper used a symmetrical cross section. For practical applications, the two levees should not be identical. It is economically beneficial to know which side should fail first. If one levee were to fail, the water would flood that side, decreasing the flood stage in the levee channel, thereby decreasing the pressure on the other bank's levee so that *its* probability of failure decreases; additional protection is provided to the side that has more damage vulnerabilities. Future work on this optimization should extend the model to an unsymmetrical levee system.

8.6 ACKNOWLEDGMENTS

This research was supported by the National Science Foundation and the Pacific Earthquake Engineering Research Center at the University of California, Berkeley. I would like to thank my UC Davis graduate student mentors, Rui Hui and Nate Burley, for their guidance throughout my

project. Additional thanks to my faculty advisor, Professor Jay Lund, and the PEER Outreach Director, Heidi Tremayne, for all of their time and support.

8.7 REFERENCES

Bogardi I., Zoltan M. (1968). Determination of degree of protection offered by flood levees and the economic improvement thereof, Report to the Department for Flood Control and River Training, National Water Authority, Budapest, Hungary.

Bras R.L. (1979). Hydraulic and hydrologic uncertainty: Two aspects of reliability, *Proceedings, National Convention*, ASCE, Atlanta, Georgia.

Das B.M. (2010). *Principles of Geotechnical Engineering*, 7th ed., Cengage Learning, Stamford, CT, pp. 198–225.

DWR (2011). *Guidelines: Procedures and Criteria*, Department of Water Recourses, Delta Levees Maintenance Subventions Program, Sacramento, CA.

DWR (2012a). *Urban Levee Design Criteria*, Department of Water Resources, Sacramento, CA.

DWR (2012b). *Levee Performance Curves, Attachment 8E*, Department of Water Recourses, Central Valley Flood Management Planning Program, Sacramento, CA.

DWR (2013). Levee Repair, *Department of Water Resources, Levee Evaluation Program,* http://www.water.ca.gov/levees/evaluation/.

FEMA (2013) *Levees: Information for Cooperating Technical Partners and Engineers*, Federal Emergency Management Agency, http://www.fema.gov/levees-information-cooperating-technical-partners-and-engineers#1

Hall J.W., Dawson R.J., Sayers P.B., Rosu C., Chatterton J.B., Keakin R. (2003). A methodology for national-scale flood risk assessment, *Proceedings, ICI—Water and Martine Engineering*, 156(3): 235–247.

Hashimoto T., Stedinger J.R., Loucks D.P. (1982). Reliability, resiliency, and vulnerability criteria for water resource system performance evaluation, *Water Resources Res*., 18(1), 14–20

Kashef A.-A. (1965). Seepage through earthen dams, *J. Geophys. Res*., 70(24).

Ketchum E., Perlea M., Kynett M., Deus A. (2011). Geotechnical risk and reliability evaluation of the levees Protecting the City of Sacramento, California, *Proceedings, Geo-Frontiers 2011*, pp. 3018–3028.

Meehan C.L., Benjasupattananan S. (2012). An analytical approach for levee underseepage analysis, *J. Hydrology*, 470-471: 201–211. doi:10.1016/j.jhydrol.2012.08.050.

Merz B. (2006). Absch¨atzung von Hochwasserrisiken. Methoden, Grenzen und Mglichkeiten, Habilitationsschrift, E. Schweizerbart'sche Verlagsbuchhandlung (N¨agele und Obermiller), Stuttgart, Germany.

NRC (2013). *Levees and the National Flood Insurance Program: Improving Policies and Practices*, National Research Council, Washington, D.C., National Academic Press, pp. 39–73.

Perlea M., Ketchum E. (2011). Impact of non-analytical factors in geotechnical risk assessment of levees, *Proceedings, Geo-Risk*, ASCE, pp. 1073–1081.

SACFA (2013). *Natomas Levee Improvement Program*, Sacramento Area Flood Control Agency http://www.safca.org/programs_natomas.html.

Sayers R.B., Hall J.W., Rosu C., Chatterton J.B., Deakin R. (2002). Risk assessment of flood and coastal defenses for strategic planning - A high level methodology, *Proceedings DEFRA Conference of Coastal and River Engineers*, Keel University, United Kingdom.

Sturm A. (2012). Multi-mode probability of levee failure curves, *PEER Report 2012.07*, Pacific Earthquake Engineering Research Center, University of California, Berkeley, CA.

Suddeth R.J; Mount J., Lund J.R. (2010). Levee decisions and sustainability for the Sacramento-San Joaquin Delta, *San Francisco Estuary and Watershed Sci.*, 8(2).

Tung Y.-K., Mays L.W. (1981a). Risk models for flood levee design, *Water Resources Res.,* 17(4): 833–841.

Tung Y.-K., Mays L.W. (1981b). Optimal risk-based design of flood levee systems, *Water Resources Res*., 17(4): 843–852.

USACE (1996). *Engineering and Design: Risk-Based Analysis for Flood Damage Reduction Studies,* EM 110-2-1619, http://www.corpsnedmanuals.us/FloodDamageReduction/FDRIncludes/FDR_EM111021619.pdf.

USACE (1999), Risk Based Analysis in Geotechnical Engineering for Support of Planning Studies, ETL 1110-2-556, U.S. Army Corp of Engineers.

USACE (2000). *Engineering and Design - Design and Construction of Levees,* EM 1110-2-1913, U.S. Army Corp of Engineers.

USACE (2006). Reliability Analysis and Risk Assessment for Seepage and Slope Stability Failure Modes for Embankment Dams, Report TL 1110-2-561, U.S. Army Corp of Engineers.

USACE (2009). Final Environmental Impact Statement on the Natomas Levee Improvement Program: Phase 3 Landside Improvement Project, U.S. Army Corp of Engineers.

USACE (2011). Cranford Levee Reliability Project for Flood Risk Management, Cranford, NJ.

USACE (2013a). Missions: Civil Works: Levee Safety Program: Levee Inspection. Retrieved from http://www.usace.army.mil/Missions/CivilWorks/LeveeSafetyProgram/LeveeInspections.aspx

USACE (2013b). Natomas Flood Risk, U.S. Army Corp of Engineers, Sacramento District, http://www.youtube.com/watch?v=GRYdVyUVkSs.

Vorogushyn S., Merz B., Apel H. (2009). Development of dike fragility curves for piping and micro-instability breach mechanisms, *Natural Hazards Earth System Sci.,*, 9(4): 1383−1401.

Wolff T.F. (1997). Geotechnical reliability of levees, *Proceedings, Hydrology and Hydraulics Workshop on Risk-Based Analysis for Flood Damage Reduction Studies*, Paper 6, U.S. Army Corps of Engineers, Hydrologic Engineering Center.

Wood E. (1977). An analysis of flood levee reliability, *Water Resources Res*., 13(3): 665–671.

9. Seismic Performance Assessment of Pre-1988 Steel Concentrically Braced Frames

Mara Minner

ABSTRACT

Steel concentrically braced frames designed prior to 1988, herein termed non-seismic-detailed concentrically braced frames (NCBF), are a potentially vulnerable yet vastly understudied structural system. At present, the seismic performance of NCBFs is largely uncertain due to a lack of testing; many more studies have been devoted to understanding the performance of modern special concentrically braced frames (SCBF). Performance-based measures are necessary for owners of existing NCBFs to make informed decisions about possible retrofit strategies, potentially increasing safety and reducing the losses associated with their damage and disruption following an earthquake. This report contains a performance-based analysis of a prototype NCBF building, assessing the expected repair costs, repair time, casualties, and probability of unsafe placarding following various intensities of earthquake shaking. The results of the analysis were compared to those of an SCBF system. It was determined that the SCBF system is generally expected to outperform the NCBF system in terms of repair cost, repair time, and probability of unsafe placarding. An experimental study is currently underway that will seek to validate the analytical model and reveal the hierarchy of failure modes that may occur in an NCBF.

9.1 INTRODUCTION

Many existing buildings throughout the U.S. have lateral load-resisting systems utilizing steel concentrically brace frames designed using codes prior to the 1988 Uniform Building Code [UBC 1988]. Although code changes have made them noncompliant with modern requirements in regions of high seismicity, these older frames, referred to herein as non-seismic-detailed concentrically braced frames (NCBF), continue to be designed for use in regions of low seismicity, and many are still in service in existing buildings in highly seismic regions. Due to differences in detailing, the ductility of NCBFs is considerably lower than that of modern special concentrically braced frames (SCBF). As a result, the seismic safety of older NCBF buildings is likely lower than that of current AISC-compliant SCBF buildings, and older NCBF buildings may be vulnerable to collapse in response to seismic activity. While the notion that NCBFs may be seismically at-risk is recognized by the earthquake engineering community and is accordingly reflected in current design codes, the seismic vulnerability of NCBFs has not previously been studied extensively, and presently very little is known about their seismic performance [Hsiao et al. 2012].

This project sought to model and analyze a three-story NCBF office building in order to predict its seismic performance. Structural analysis data was obtained by modeling the building using the Open System for Earthquake Engineering Simulation (OpenSees) [McKenna et al. 2000]. Performance was evaluated using a recently-developed computer program known as the Performance Assessment Calculation Tool (PACT) [ATC 2012a]. Seismic performance was measured probabilistically in terms of repair cost, casualties, repair time, and unsafe placarding. A parametric study on PACT was also performed in order to gain an understanding of its robustness. Following the dynamic analyses of the NCBF building, analyses were performed on a similar SCBF office building, and the results were compared to those of the NCBF building. Additionally, a companion experimental study is planned in which full-scale two-story NCBF specimens will be constructed for quasi-static testing with the actuators in the nees@berkeley laboratory. This experimental study will be used to validate the analytical model as well as observe the failure hierarchy in the NCBF buildings. The results of the experimental study will not be discussed herein, as that testing will be performed at a later date.

9.2 LITERATURE REVIEW

9.2.1 Differences between the 1985 UBC and Modern Seismic Provisions

Codes prior to the 1988 UBC [1988] offered limited guidance on the seismic design of steel concentrically braced frames. Many revisions and additions appear in today's ASCE 7-10 [ASCE 2010] and AISC Seismic Provisions for concentrically braced frames [AISC 2010]. This section highlights some main differences between the design requirements of NCBFs and SCBFs.

A major change in the codes occurred in the ductility factor used for determining the design base shear. The *K* factor from the 1985 UBC was initially replaced by an R_w factor in the 1988 UBC, and the relation is shown in Equation (9.1).

$$R_w = \frac{8}{K} \tag{9.1}$$

An *R* factor, which is approximately equivalent to the R_w factor, is currently the basis for defining the relative ductility of a structure in today's ASCE 7-10. The base shear is defined as follows in Equations (9.2) and (9.3) according to older and newer codes:

$$V = ZIKCSW \qquad \left(1985\text{ UBC}\right) \tag{9.2}$$

$$V = C_s W, \text{ where } C_s = \frac{S_{DS}}{\left(\frac{R}{I_e}\right)} \qquad (\text{ASCE } 7-10) \tag{9.3}$$

where Z is a seismic zone factor depending on the location of the structure, I and I_e are importance factors, C is a numerical coefficient depending on the soil conditions of the site and the period of the structure, S_{DS} is the design spectral response accelerations parameter in the short period range, and K and R are ductility factors.

In an SCBF system, an R factor of 6 corresponds to a K factor of 1.33, which exceeds the NCBF's R_w factor of 8.0 or K factor of 1.0. Thus, NCBF systems were designed for a lower base shear than SCBF systems. While both factors serve similar purposes in the codes, the R factor is defined for more systems than was the K factor and adds clarity to the effect the ductility factor has on the base shear.

The story drift limit has been greatly altered since the 1985 UBC. The story drift limit of an SCBF by ASCE 7-10's standards is 2.5% of the story height. This value is much higher than that of an NCBF defined by the 1985 UBC, which allowed 0.5% story drift.

The slenderness ratio, l/r, of braces was another variable of interest in the 1985 UBC. Multiple tests performed in the 1980s demonstrated that increasing the l/r ratio causes a dramatic reduction in the energy dissipation capacity of compression struts after buckling [Black et al. 1980; Astaneh-Asl et al. 1982]. The lack of energy dissipation limits the strut's ability to deform inelastically, which results in limited overall system ductility. The 1985 UBC recognized this limited ductility by using a larger design base shear and by requiring members to be designed for a factor of 1.25 above the base shear [Malley 1989]. The current AISC seismic provisions have more stringent slenderness and compactness requirements for the braces, which results in reduced post-buckling degradation with higher resistance to low-cycle fatigue [Hsaio et al. [2012].

The width-to-thickness ratio, b/t, of braces in CBFs should be sufficient to delay local buckling and provide energy dissipation during seismic activity. In comparison to the 1985 UBC, the 2010 AISC Seismic Provisions provides much more stringent width-to-thickness ratios for different elements. The 1982 UBC allowed the use of Appendix C to reduce allowable stress for braces that did not meet width-thickness requirements. Rectangular tube bracing sizes in NCBFs were allowed to be much larger than the maximum HSS10×10×5/8 allowed by the b/t requirements of the current AISC code [Simpson, *personal communication*, 2013].

Modern seismic provisions place additional requirements on the bracing configurations of SCBFs that were not specified in the 1985 UBC. The 2010 AISC Seismic Provisions specifically address chevron braced frames, requiring that beams be continuous between columns and stating that K bracing is not allowed in SCBFs. Additionally, one problem that plagued NCBF chevron configurations was the concept of the weak beam. In each chevron brace, the forces are initially balanced because one brace is in tension while the other is in compression. However, this balance is upset when the brace in compression buckles before the brace in tension yields, at which point the strength of the buckled brace is approximately 30% of its original capacity. The imbalance in forces is then taken by the beam, which was not considered in the design of the NCBF system; only the pre-buckling state of the braces was considered in older codes. The 2010 AISC Seismic Provisions require that "post-buckling brace strength shall be taken as a maximum of 0.3 times the expected brace strength in compression," which generally results in a larger beam to account for the unbalanced load [Simpson, *personal communication*, 2013].

The design of the brace connections in SCBF and NCBF systems differs greatly; SCBF connections are capacity-designed, meaning the design demand is based on the capacity of the brace. NCBF connections, however, are designed not based on the brace capacity, but rather on the demands from the prescriptive seismic lateral forces. In addition, SCBF brace connections are typically designed such that the brace end is further away from the working point, shown in Figure 9.1, whereas NCBF braces extend much further along the gusset plate closer to the working point, as seen in Figure 9.2. Consequently, a yield line is able to develop in the SCBF connection when the brace buckles out of plane, allowing for more ductility in the connection with a lower chance of brittle failure. However, because the NCBF brace connection is much more rigid, less ductility is allowed in the NCBF system, and brittle failure of the connection is more likely.

Because NCBFs do not have any special detailing requirements, the respective strengths of the connection and braces relative to each other are uncertain. Some connections will outlast the brace, whereas other connections will be weaker than the brace. Thus, in the NCBF system, there is no clear hierarchy of failure, and the system may be more vulnerable to connection failure, frame member damage, and soft-story collapse than the SCBF system [Hsiao et al. 2012].

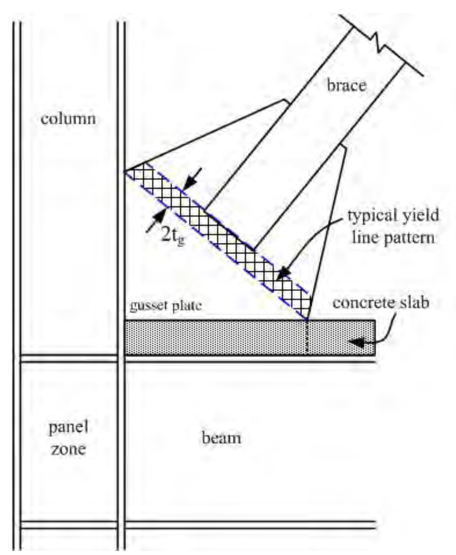

Figure 9.1 SCBF connection [Lai 2012].

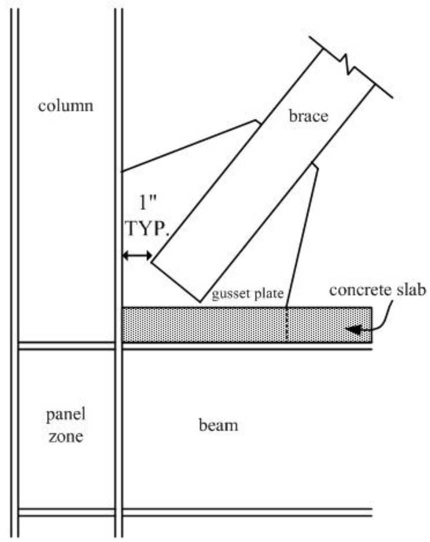

Figure 9.2 NCBF connection [Lai 2013].

9.2.2 Performance-Based Design

Performance-based earthquake engineering (PBEE) can be used to assess expected building performance over a structure's operational life or in response to scenario events [Mahin et al. 2012]. This methodology seeks to "improve seismic risk decision-making through assessment and design methods that have a strong scientific basis and that express options in terms that enable stakeholders to make informed decisions" [Moehle and Deierlein 2004]. Common metrics of performance include direct costs of construction and repair, impacts associated with loss of use, and potential for injuries and casualties. Due to inherent uncertainties in the characteristics of future earthquakes and in the seismic response of structures, performance is usually described in probabilistic terms [Mahin et al. 2012].

A few performance-based seismic assessment methodologies exist. One such methodology was developed by the Pacific Earthquake Engineering Research (PEER) Center and is shown schematically in Figure 9.3.

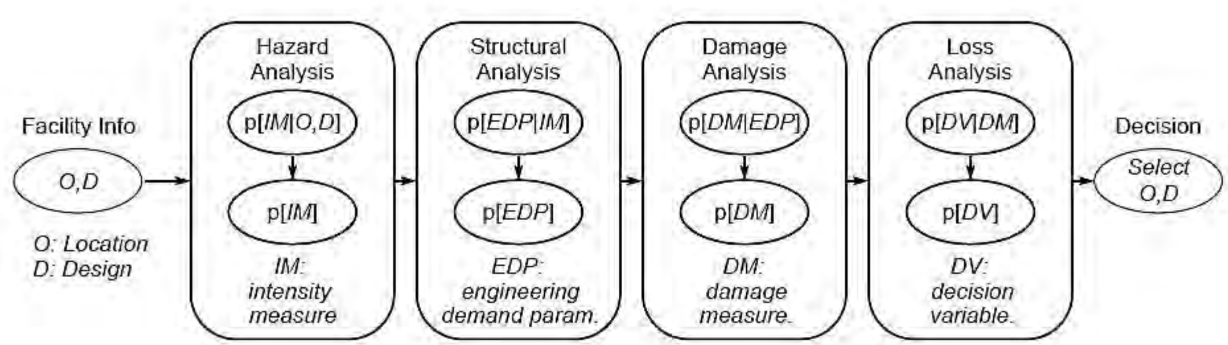

Figure 9.3 Schematic of PEER PBEE methodology [Moehle and Deierlein 2004].

PEER's probabilistic assessment procedure involves four main analysis steps: hazard analysis, structural/nonstructural analysis, damage analysis, and loss analysis. Each of these steps is mathematically characterized in a probabilistic sense by one of four generalized variables: Intensity Measure (IM), Engineering Demand Parameter (EDP), Damage Measure (DM) and Decision Variable (DV). The PEER methodology shown in Figure 9.1 can also be expressed as a triple integral that is based on the Total Probability Theorem, as displayed in Equation (9.4) [Moehle and Deierlein 2004].

$$v(DV) = \iiint G\langle DV/DM \rangle \mid dG\langle DM/EDP \rangle \mid dG\langle EDP/IM \rangle \mid d\lambda(IM) \qquad (9.4)$$

The following steps describe the assessment procedure:

1. Seismic Hazard Analysis: One or more ground motion Intensity Measures are evaluated. These are typically described as mean annual probabilities of exceedance, *p*[IM], and are specific to the location (O) and design characteristics of the building (D).
2. Structural/Nonstructural Analysis: Structural analysis is performed in order to calculate EDPs that characterize the building response, such as story drift ratios, floor velocities, and floor accelerations. The conditional probability of EDP given IM, p[EDP|IM], is integrated with the *p*[IM] to calculate the mean annual EDP probability of exceedance, *p*[EDP].
3. Damage Analysis: The EDPs are related to Damage Measures (DMs), which include descriptions of damage to the structural components, nonstructural components, and contents of the building. The DMs enable the quantification of necessary repairs and functional or life safety implications of the damage. The mean annual DM probability of exceedance, *p* [DM], is calculated by integrating the conditional probability of DM given EDP, *p* [DM|EDP], with *p* [EDP].
4. Loss Analysis: Decision Variables that are meaningful to the stakeholders are evaluated. DVs are generally related to direct costs of repairs or replacement, downtime, and casualties. In a similar manner as performed for the previous variables, the conditional probability of DV given DM, *p* [DV|DM], is integrated with *p* [DM] to compute the mean annual DM probability of exceedance, *p* [DM] [Moehle and Deierlein 2004].

9.2.3 NCBF Behavior during Past Earthquakes

Past earthquakes have provided some insight on how NCBFs may behave under seismic loading. A few examples of NCBF behavior during past earthquakes are briefly noted.

Some notable earthquakes of the past have caused massive amounts of damage to CBFs. A magnitude 9.0 earthquake occurred in Tohoku, Japan, on 11 March 2011 and was the largest earthquake recorded to have hit Japan. Figure 9.4 displays the complete fracture of a gusset plate in an NCBF following this earthquake. Local buckling is shown in Figure 9.5 in an HSS brace following the 17 January 1994 magnitude 6.9 Northridge, California, earthquake. Figure 9.6 displays global buckling of braces after the 16 January 1995 earthquake in Hoygoken-Nanbu, Japan. The damage exhibited after these major earthquakes highlights the need for more comprehensive studies on older frames in order to gain a better understanding of their expected behavior and how best to retrofit them to enhance their performance.

Figure 9.4 Complete fracture of a gusset plate during 2011 Tohoku earthquake [Lignos 2011].

Figure 9.5 Local buckling of a square HSS brace during 1994 Northridge earthquake [NISEE, 1994].

Figure 9.6 Global buckling of steel braces during 1995 Hyogoken-Nanbu, earthquake [AIJ 1995].

9.3 METHODOLOGY

9.3.1 Prototype Building

The prototype building design selected for this study is a three-story office building intended for construction in Los Angeles, California, (Latitude: 34.50 N, Longitude: 118.2 W) on stiff soil of site class D. The prototype was based off of a SCBF building designed by Troy Morgan and

Forell/Elsesser Engineers for a project under the Network for Earthquake Engineering Simulation (NEES) entitled “Tools for Isolation and Protective Systems” [Morgan 2008].

The building consists of three stories, each 15 ft in height, and has a rectangular footprint that is 180 ft×120 ft, with 30-ft bays. The building contains four identical NCBFs, one on each side of the building’s perimeter, with members arrayed in an inverted V (chevron) bracing configuration. Figure 9.7 shows details of the floor plan of the first and second story, including the locations of the braced frames (BF). A penthouse lies between lines C and D, and lines 2 and 4 on the roof. The NCBFs were designed by Barb Simpson [*Personal communication* 2013)] according to the 1985 UBC, and the dimensions and member sizes are displayed in an elevation view in Figure 9.8. In the NCBF model, the chevron braces were designed such that the first and second stories featured braces of the same size, HSS10×10×5/8. Additionally, there is a column splice in the third story, where the column is reduced in size. This braced frame was intended to be representative of a real pre-1988 NCBF and featured design practices that may be different from today’s standards. For comparison, Figure 9.9 displays a SCBF featured in the original design of this prototype building by Morgan [2008]. The SCBF design will be discussed later in this report in a comparison of the building performance of the NCBF and SCBF.

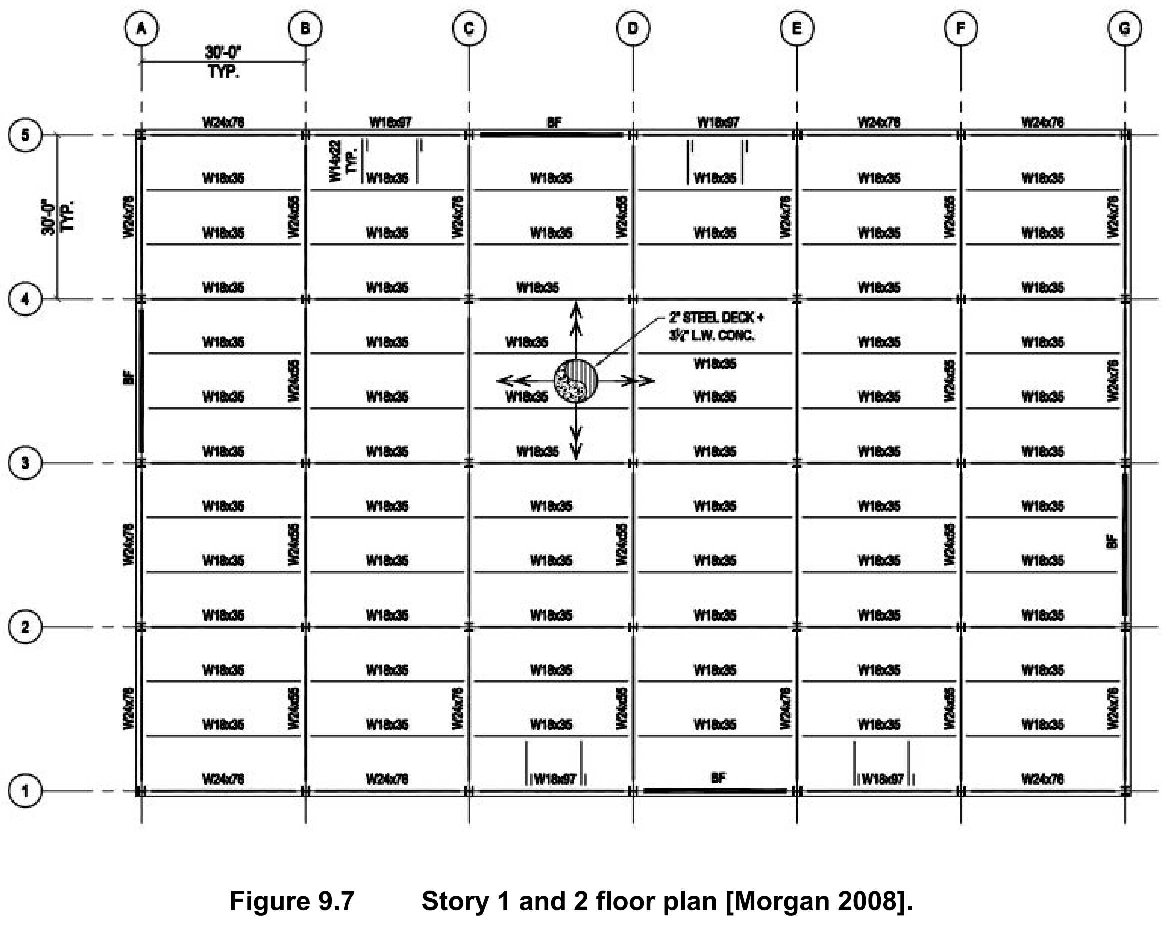

Figure 9.7 Story 1 and 2 floor plan [Morgan 2008].

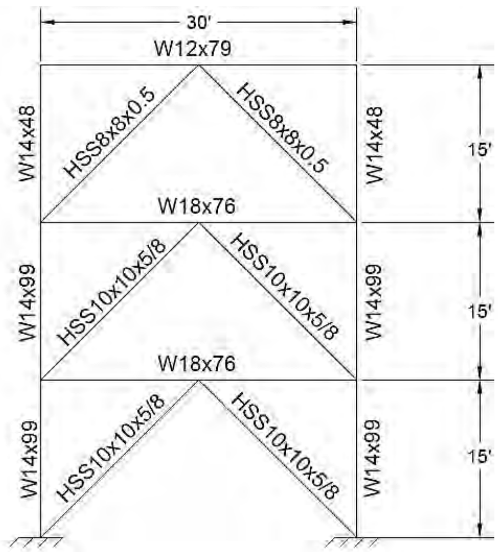

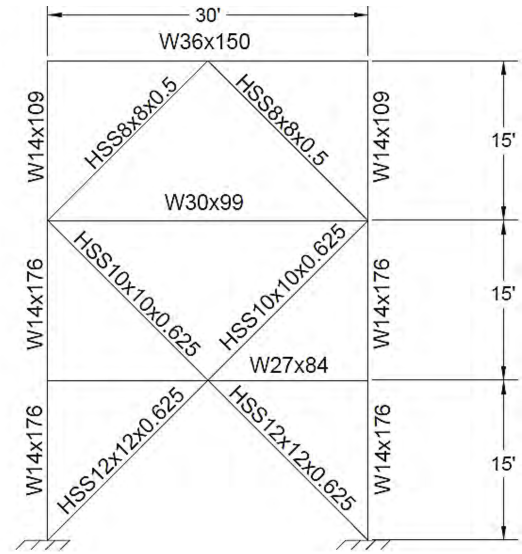

Figure 9.8 NCBF elevation.

Figure 9.9 SCBF elevation.

9.3.2 OpenSees Model

Using the computer program OpenSees, nonlinear dynamic response history analyses were performed on the two-dimensional model using a script that was created by Vesna Terzic and modified for this project by Barb Simpson. To simplify the analysis, several modeling assumptions were employed in the OpenSees model. Half of the lateral floor mass was assigned at each floor of the two-dimensional frame, equally distributed among three nodes of that floor. Vertical mass equal to the (tributary weight)/g was assigned to the same nodes. Floor slabs in the system were assumed to be axially inextensible. A damping ratio was generally taken to be 5%. Two leaning columns were used to represent the rest of the building and model P-Δ effects [Gupta and Krawinkler 1999]. Each node of the leaning columns contained one quarter of the total floor gravity load minus half of the gravity load carried by the selected braced frame. The penthouse, although not directly included in the OpenSees model for lack of information, was incorporated in the floor weights and their contribution to the equivalent lateral forces and fundamental periods in the N-S and E-W directions [Simpson, *personal communication*, 2013].

Ground motions from real earthquakes were selected to run in the OpenSees model. Although the prototype building was designed for Los Angeles, California, similar soil structure and near-fault characteristics can be found at the Oakland, California, site of the I-880 viaduct from the intersection of Center and Third Streets to Market and Fifth Streets (37.803N×122.287W). As such, 40 ground motions selected and scaled to match the uniform hazard spectrum and associated causal events for the Oakland site [Baker et al. 2011] were chosen for this project to be used in the OpenSees response history analyses of the prototype building.

Response history analyses were performed using the 40 ground motions. For each of the ground motions, this project considered three hazard levels that were based on the probability of exceedance in 50 years: 2%/50 years, 10%/50 years, and 50%/50 years. Additionally, two earthquake directions, fault normal and fault parallel, were analyzed in the OpenSees model; thus, the frames were subjected to two horizontal and no vertical components of ground motion. Performing the analysis for all combinations of these three variables resulted in 240 separate response history analyses, each of which recorded the story drift ratios, floor velocities, floor accelerations, and residual drifts for each story of the building.

9.3.3 PACT Model

To assess building performance, PACT was utilized [ATC 2012a]. PACT is a computational tool developed by the Applied Technology Council (ATC) that measures performance in terms of:

- repair and replacement costs
- the probability of incurring casualties
- repair time
- the probability that unsafe placards will be posted on the building×

The technical basis for PACT lies in the framework for the PBEE methodology developed by PEER. While the PBEE methodology applies the Total Probability Theorem and a triple integral to predict building performance, PACT uses a modified Monte Carlo approach to implement the integration based on inferred statistical distributions [ATC 2012a].

The first step in building the PACT model involved inputting basic building information, including the building size and the cost of total building replacement as well as core and shell replacement. To obtain ballpark estimates of these costs, the estimator tool RS Means Online was utilized. The Square Foot Estimator gave a rough estimate of the total replacement cost to be $14,548,500 based on the type of building and basic building parameters. This online estimator indicated that total replacement of the building, with labor included, would cost approximately $218 per square foot. It was assumed that the core and shell replacement cost was $5,819,400, which is 40% of the total replacement cost. This assumption was verified by using RS Means cost data to estimate the cost of the structural and typical nonstructural components of a three-story office building, which resulted in a similar value.

The model was specified to be of commercial office occupancy. As such, PACT automatically generated the expected distribution of people in the building as well as the variability of the distribution throughout the day. This information would later be used to generate the estimated number of casualties in the building based on the population model.

The quantities of all vulnerable structural and nonstructural components of the building were entered into PACT. The structural components of the prototype building were counted according to the design of the braced frame and the building plans designed by Troy Morgan [2008]. Since the nonstructural components were unknown, they were estimated using the Normative Quantity Estimation Tool provided by ATC [2012a] a for a typical office building of this size. A few modifications to the normative quantities were made based on judgment. All building components are specified as either directional or non-directional in PACT, depending on whether or not the direction of shaking affects the level of damage to the component. The quantities of the directional components were proportioned in each direction based on the ratio of the sides of the building's perimeter; thus, the direction associated with the longer building side (180 ft) contained more directional components than the shorter side (120 ft). In order to simplify the model, it was assumed that the roof and the penthouse were combined on the fourth floor because the penthouse was not modeled as a separate story in the OpenSees model. Thus, the nonstructural components that would likely be in the penthouse were entered into the PACT model on the fourth floor.

In order to define the collapse fragility function in PACT, MATLAB [The MathWorks Inc. 2009] was used to assess whether or not collapse was predicted to have occurred for each ground motion at the three hazard levels. In this project, building collapse was assumed to have occurred if the frame experienced story drift greater than 7.5%, assuming that the shear connections at the beam-column interface could not withstand such large story drifts. This story drift limit was adopted as an intermediate between the 5% limit used by Hsiao et al. [2012] and the 10% limit assumed by Chen [2010] in their respective dissertations. Additionally, given that collapse occurred, the mutually exclusive probability of all possible modes of collapse was entered into the PACT model. Seven different collapse modes were defined as follows:

Mode 1: Soft story in 1st story

Mode 2: Soft story in 2nd story

Mode 3: Soft story in 3rd story

Mode 4: Complete building collapse

Mode 5: Concentrated damage in 1st and 2nd story

Mode 6: Concentrated damage in 2nd and 3rd story

Mode 7: Concentrated damage in 1st and 3rd story

In all cases that caused collapse of the NCBF building, the collapse occurred due to a soft story in the first story. The Conditional Probability of Collapse Curve Fit Tool provided by ATC was used to find the median spectral acceleration and dispersion for structural collapse to further define the collapse fragility. Figure 9.10 shows the curve that was fit to data consisting of six spectral acceleration points, one for each combination of the three hazard levels and two earthquake directions. Although the number of data points was limited, the median spectral acceleration for collapse was estimated to be 2.46*g* with a dispersion of 0.21.

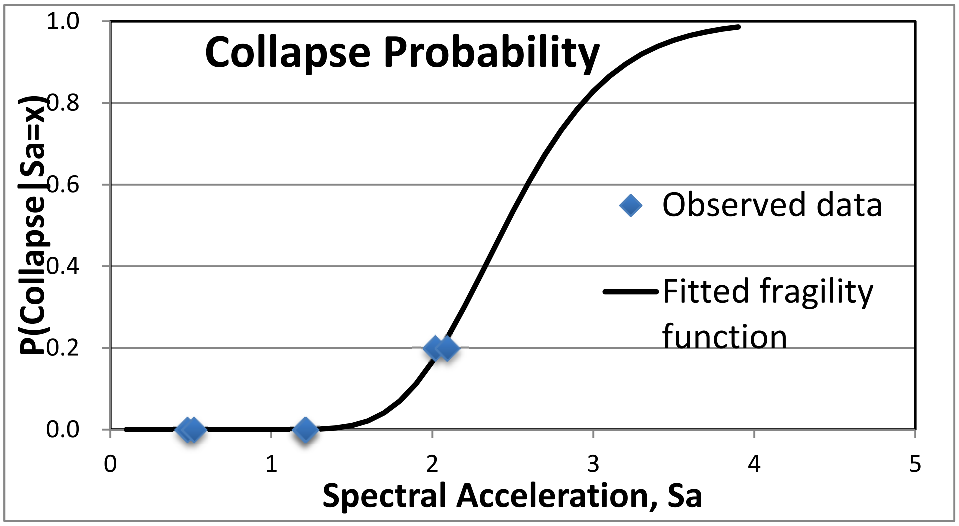

Figure 9.10 Collapse probability curve.

Each component in the building is sensitive to certain EDPs: story drift ratio, floor acceleration, or floor velocity. For each component, PACT uses the maximum of one of the aforementioned parameters—the one deemed most influential to the component's damageability—to determine the expected extent of damage to the component in response to ground motions. MATLAB was utilized for post-processing of the OpenSees data in order to obtain the structural analysis data that could be used as input for the PACT model. Maximum values of each of the parameters recorded in OpenSees at each story of the frame were extracted for all 240 cases. Because they would skew the median and dispersion of the non-collapse cases, data from cases in which structural collapse was predicted to have occurred were not included in the structural analysis results section of PACT. The collapse cases were treated separately by requiring the user to define the previously discussed collapse fragility function.

Residual drift data from OpenSees was also entered into the PACT model. Residual drift plays in an important role in determining the economic reparability and post-earthquake safety of a building [ATC 2012a]. As shown in Figure 9.11, PACT utilized a fragility function that is based on the user-entered median irreparable residual story drift ratio and its dispersion, which were taken to be 0.0125 and 0.3, respectively. The fragility function expresses the probability that the building will be repaired given a residual story drift ratio of 1.25%.

Three types of performance assessments may be performed in PACT: intensity-based, scenario-based, and time-based. In this project, the performance assessments were intensity-based, and the three hazard levels represented different earthquake intensities based on their acceleration response spectra. The PACT models were run with 700 realizations, 40% more than the minimum 500 recommended to obtain accurate results [ATC 2012b]. The PACT analysis was performed for the NCBF prototype building and repeated for an SCBF system, using the same prototype building but with an SCBF lateral load-resisting system. Screenshots of the NCBF model can be found in the Appendix.

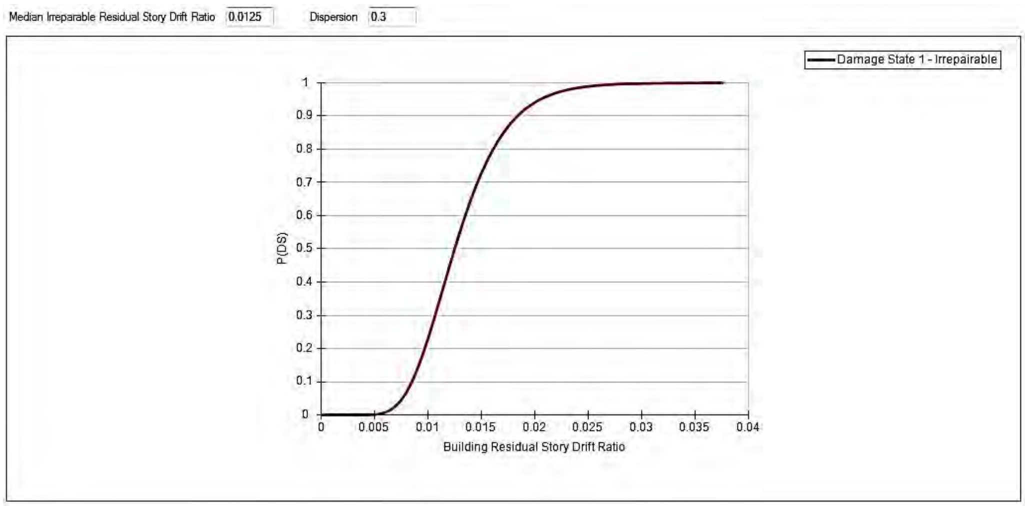

Figure 9.11 PACT residual drift fragility function.

9.4 RESULTS

The OpenSees structural analysis data indicating building response is briefly discussed first for the NCBF and SCBF buildings, as this data is directly used by PACT to evaluate building performance. General trends in the building response data are noted prior to being entered into PACT. Subsequently, the building performance results obtained from PACT are presented and compared for the NCBF and SCBF systems.

9.4.1 Comparison of Building Response (OpenSees)

The peak values of the EDPs of story drift, floor velocity, and floor acceleration are often correlated with building performance and are required inputs for PACT analysis. As such, a brief presentation of the OpenSees structural analysis data follows. The OpenSees model responses in terms of the aforementioned EDPs are displayed in Figures 9.12, 9.13, 9.14, and 9.15. The results for the NCBF model are displayed on the left side, while those of the SCBF model are shown on the right. The responses for both categories of frames can be compared side-by-side and may be viewed as preliminary indicators of overall building performance.

In Figures 9.12–9.15, each hazard level was plotted separately for the NCBF and SCBF models. Responses are shown for all 40 ground motions tested in both the fault-normal and fault-parallel earthquake directions in each plot, for a total of 80 lines on each graph. Ground motions that resulted in probable building collapse—previously defined by this project as experiencing story drift greater than 7.5%—are plotted as dotted lines to reflect the fact that they were not included in the PACT structural analysis data. Non-collapse cases are graphed as solid lines and were included in the PACT input. Note that ground motions for which collapse occurred in only one earthquake direction were also plotted as dotted lines and removed from the PACT input data for the other earthquake direction as well, as required by PACT. The median for each plot is shown in blue for the NCBF or red for the SCBF and reflects only the solid black lines—the non-collapse cases that were included in the PACT structural analysis input. The median values are shown in a table below each graph.

Figure 9.12 contains the peak story drift data obtained from OpenSees. PACT uses this input to assess the amount of damage experienced by the structural components and certain nonstructural components of the building, including the braced frame, shear tab connections, and wall partitions. The NCBF results display highest story drift levels on the first floor, indicating that a soft story likely formed on the first floor; this effect becomes more exaggerated as the intensity of the hazard level increases. Because the NCBF features braces of the same size in the first and second stories, a soft story was expected to form because the demand/capacity ratio is highest in the first story. In the SCBF building, however, the story drift is more uniform over the height of the building. Thus, the tendency to form a soft story is lower in the SCBF model compared to the NCBF. Examining the results for the different hazard levels, both the NCBF and SCBF model display the overall trend that as the earthquake probability of occurrence in 50 years decreases, the story drift percentage increases.

Figure 9.13 displays peak velocity data, which is used in PACT to assess damage to unanchored nonstructural components, such as bookcases and filing cabinets. The velocities are relatively stable from floor to floor, as shown by the nearly vertical lines in the plots. Like the general drift trend, velocity tends to increase as the probability of earthquake occurrence in 50 years decreases. After collapse data were removed from the NCBF results as shown by the dotted lines, the NCBF system and SCBF system appeared to experience relatively similar velocities.

Figure 9.14 displays the peak acceleration data, which PACT uses to measure the damageability of nonstructural components that are anchored in the building, including piping, elevators, and suspended ceilings. More variability in the data is exhibited at the 2%/50-year hazard level for both systems, indicating more nonlinear behavior in the buildings. This occurs because initial accelerations are higher at this hazard level due to the intensity of the ground motions, causing more damage to structural components of the building, which results in lower stiffness and a higher building period. The largest accelerations in the SCBF tended to be greater than the largest accelerations experienced by the NCBF because the building period of the SCBF is lower than that of the NCBF.

Figure 9.15 displays the residual drift data obtained from OpenSees, which PACT uses to measure the building's global reparability. The graphs demonstrate that residual drift was concentrated in the first floor of the NCBF; whereas in the SCBF it was more evenly distributed over all stories. The median values indicate that the NCBF generally experienced more residual drift than did the SCBF on the first and third floors.

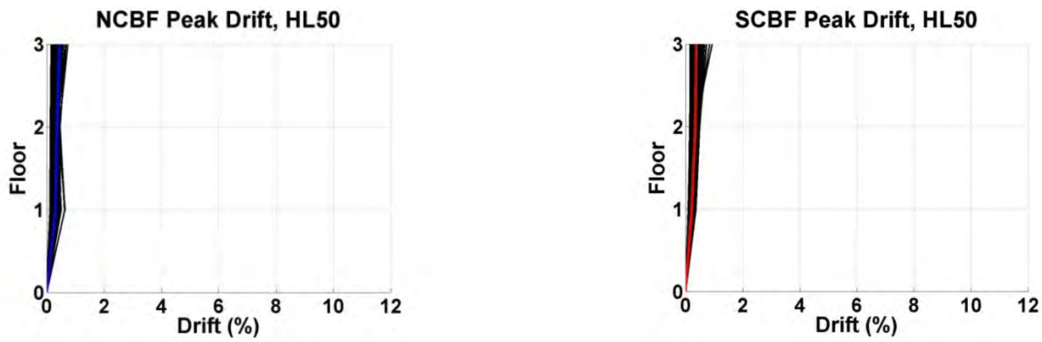

Median Drift (%)	NCBF	SCBF
Floor 1	0.316	0.219
Floor 2	0.357	0.344
Floor 3	0.448	0.376

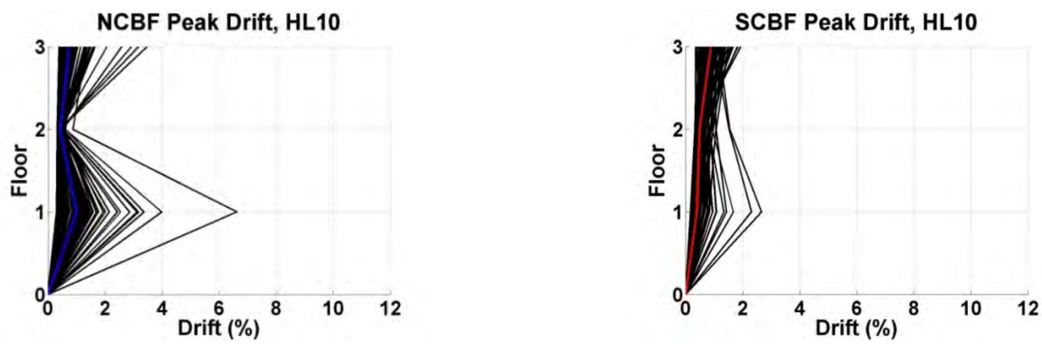

Median Drift (%)	NCBF	SCBF
Floor 1	1.013	0.398
Floor 2	0.438	0.496
Floor 3	0.749	0.886

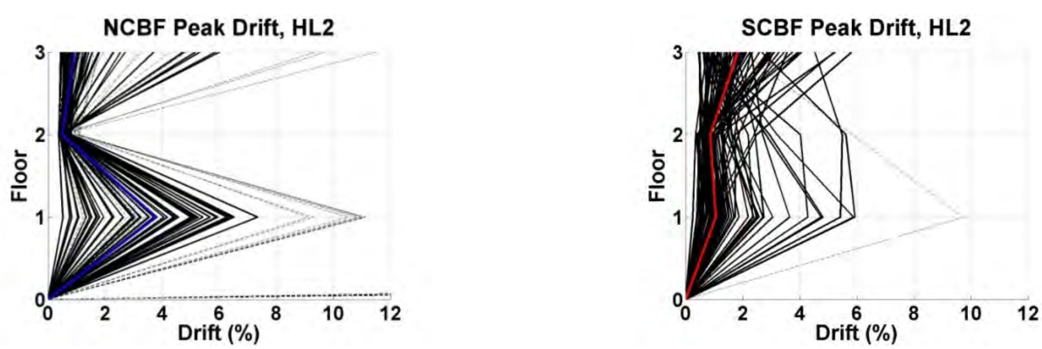

Median Drift (%)	NCBF	SCBF
Floor 1	3.824	1.062
Floor 2	0.503	0.879
Floor 3	0.938	1.829

Figure 9.12 Peak story drifts with median values shown in color.

Median Vel. (in./s)	NCBF	SCBF
Ground	103.06	103.06
Floor 1	101.88	102.61
Floor 2	98.12	99.82
Floor 3	100.95	100.91

Median Vel. (in./s)	NCBF	SCBF
Ground	229.19	229.19
Floor 1	222.44	222.64
Floor 2	220.31	219.42
Floor 3	220.78	219.26

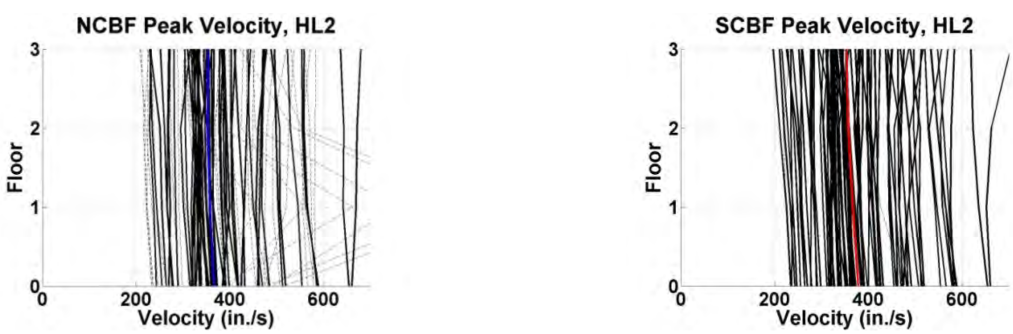

Median Vel. (in./s)	NCBF	SCBF
Ground	366.59	378.67
Floor 1	357.66	366.99
Floor 2	353.00	357.26
Floor 3	353.91	353.86

Figure 9.13 Peak velocities with median values shown in color

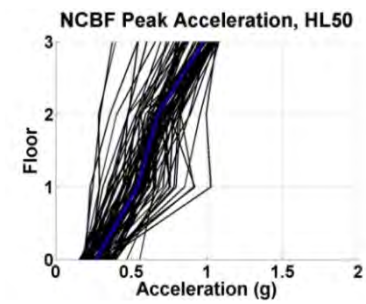

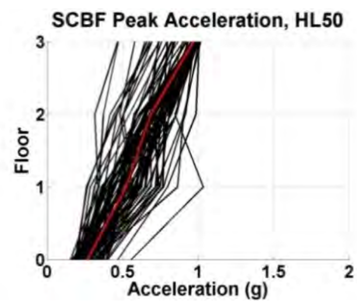

Median Acc. (g)	NCBF	SCBF
Ground	0.267	0.267
Floor 1	0.542	0.524
Floor 2	0.675	0.688
Floor 3	0.981	0.970

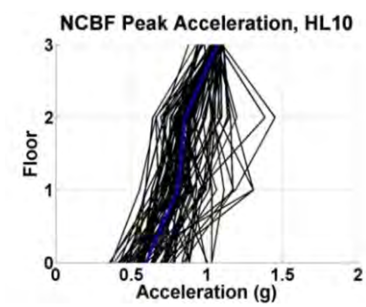

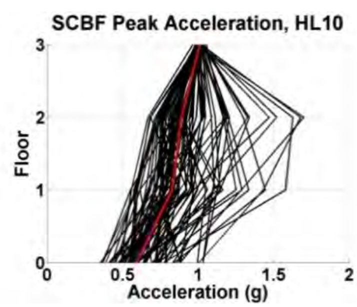

Median Acc. (g)	NCBF	SCBF
Ground	0.594	0.594
Floor 1	0.809	0.829
Floor 2	0.856	0.891
Floor 3	1.067	1.011

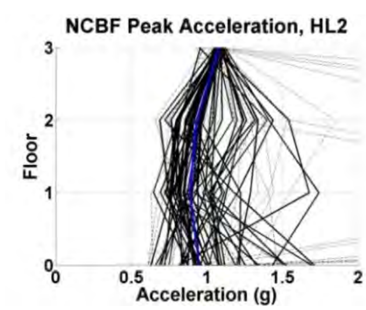

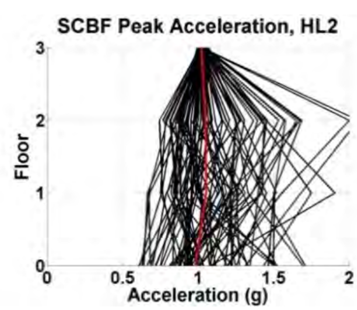

Median Acc. (g)	NCBF	SCBF
Ground	0.950	0.981
Floor 1	0.890	1.055
Floor 2	0.933	1.050
Floor 3	1.081	1.022

Figure 9.14 Peak accelerations with median values shown in color.

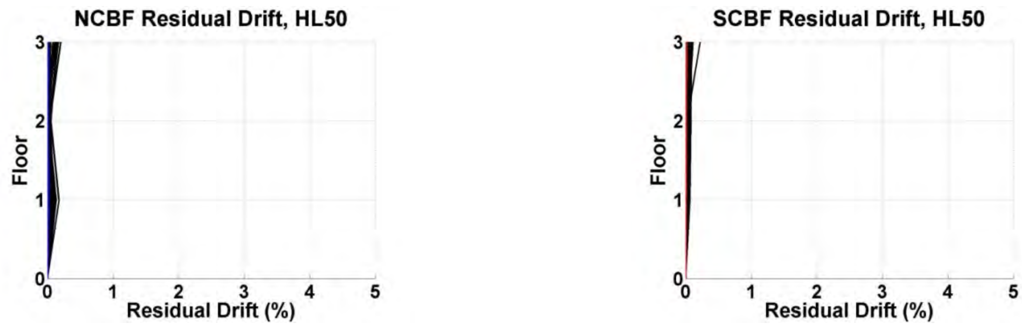

Median Resid. Drift (%)	NCBF	SCBF
Floor 1	0.013	0.005
Floor 2	0.005	0.005
Floor 3	0.009	0.009

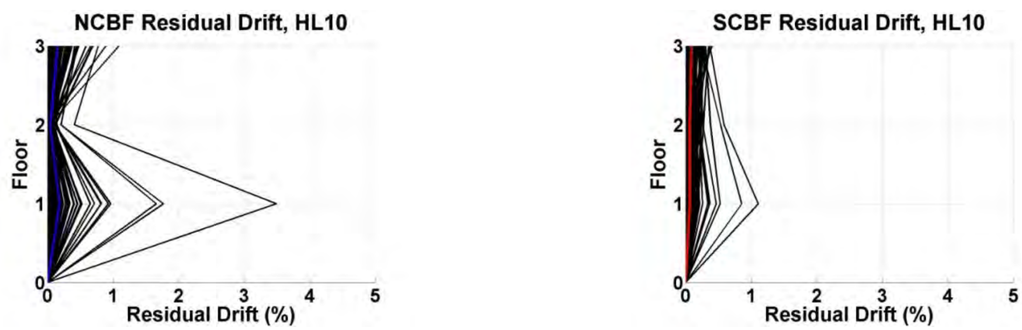

Median Resid. Drift (%)	NCBF	SCBF
Floor 1	0.186	0.063
Floor 2	0.043	0.064
Floor 3	0.158	0.093

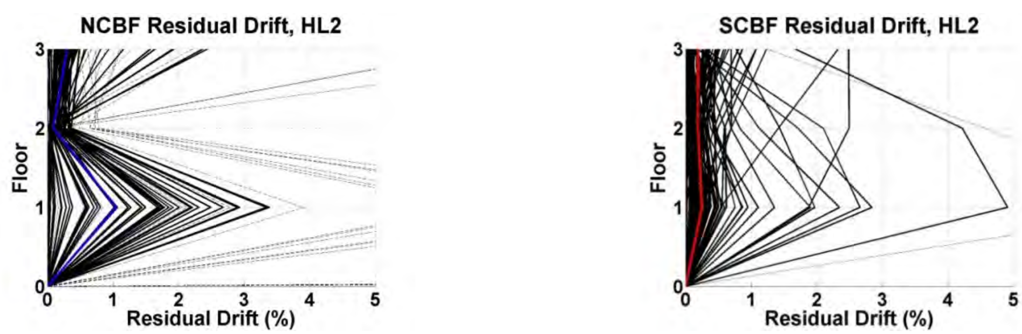

Median Resid. Drift (%)	NCBF	SCBF
Floor 1	1.050	0.252
Floor 2	0.091	0.189
Floor 3	0.304	0.191

Figure 9.15 Residual drifts with median values shown in color.

9.4.2 Comparison of Building Performance (PACT)

Using the OpenSees structural analysis results and a number of other user-defined inputs, PACT was utilized to measure building performance. First a parametric study was performed in order to examine the effect of changing certain variables in PACT. Following this analysis, the PACT results of the NCBF and SCBF model buildings were compared, and their differences were evaluated. Note that PACT is able to provide results in terms of graphs depicting the structural and nonstructural component contributions to each EDP. However, because this study is more concerned with probabilistic results and not with the contributions from various building components, the median value (50^{th} percentile) and one standard deviation above the median (84^{th} percentile) for each EDP were of the greatest concern. These two values were extracted from the graphs and reported in the following sections.

9.4.2.1 Parametric Study

Because PACT is a relatively new program, a parametric study was performed in order to examine its robustness. This was done by running many different PACT models, each containing one change from a proposed baseline model. The differences in results were evaluated to determine which changes become amplified in the PACT results. The results of the parametric study are displayed in Tables 9.1 through 9.7. Table 9.1 is the baseline model, and the subsequent tables reflect the changes as noted in their titles. Only numbers that differ from those of the baseline model are displayed in Tables 9.2 through 9.7; a blank space indicates that the value is the same as that shown in Table 9.1 of the baseline model.

Table 9.1 displays the baseline PACT model, which uses 700 realizations. This model contains the original NCBF design discussed in the methodology. It assumes 7.5% story drift signifies collapse, and consequently the structural analysis data for ground motions causing greater than 7.5% drift were removed from the model. The residual drift input used in this model was obtained from the structural analysis results from OpenSees.

One parameter of concern was the design of the NCBF frame in the OpenSees model. In the original OpenSees model, the chevron braces were designed such that the first and second stories featured braces of the same size. Additionally, there is a column splice in the third story, where the column is reduced in size. The original braced frame was purposely designed poorly by today's standards in order to be representative of a real pre-1988 NCBF. In three of the parametric study cases, the design of the NCBF was altered to determine the effect the NCBF design may have on the PACT results. Table 9.2 displays results for a model designed with different brace sizes at every story. Table 9.3 contains the results of a design in which the column size is constant at every story. The design used to obtain the results in Table 9.4 is a combination of the previous two designs and features different brace sizes at every story along with constant column size. Comparing the PACT results of the original design (Table 9.1) with those of the three new designs (Tables 9.2, 9.3, and 9.4) reveals slight differences in repair cost and repair time, and almost no difference in casualties and unsafe placarding. The only major difference occurs in Table 9.3, in which the repair cost and repair time for the 10%/50 years hazard level at the 84^{th} percentile are surprisingly at their maximums and are thus significantly higher than those of the original design.

Table 9.1 Baseline NCBF PACT model (700 realizations).

HL	Repair Cost		Casualties				Repair Time				Unsafe Placarding
%/50 yr	1000 U.S. $		Deaths		Injuries		Parallel Time (days)		Serial Time (days)		Total Probability
	50%	84%	50%	84%	50%	84%	50%	84%	50%	84%	
50	1124	1692	0	9	1	35	78	118	168	258	0.82
10	1971	3280	0	10	0	40	125	258	291	475	0.99
2	14535	14549	0	13	0	42	543	548	544	548	1

Table 9.2 New OpenSees NCBF design with different brace sizes at every story.

HL	Repair Cost		Casualties				Repair Time				Unsafe Placarding
%/50 yr	1000 U.S. $		Deaths		Injuries		Parallel Time (days)		Serial Time (days)		Total Probability
	50%	84%	50%	84%	50%	84%	50%	84%	50%	84%	
50	1088	1671		10	0	34	76	113	162	255	0.84
10	1829	2855				41	116	176	273	419	
2	14529					43					

Table 9.3 New OpenSees NCBF design with constant column size.

HL	Repair Cost		Casualties				Repair Time				Unsafe Placarding
%/50 yr	1000 U.S. $		Deaths		Injuries		Parallel Time (days)		Serial Time (days)		Total Probability
	50%	84%	50%	84%	50%	84%	50%	84%	50%	84%	
50	1098	1665				34	77	116	164	252	0.81
10	2096	14535					136	543	308	544	
2	14548					40	545		545		

Table 9.4 New OpenSees NCBF design with different brace sizes at every story and constant column size.

HL	Repair Cost		Casualties				Repair Time				Unsafe Placarding
%/50 yr	1000 U.S. $		Deaths		Injuries		Parallel Time (days)		Serial Time (days)		Total Probability
	50%	84%	50%	84%	50%	84%	50%	84%	50%	84%	
50	1113	1672			0		76	116	165	255	0.83
10	1809	2650				41	112	160	267	394	
2	14527					44					

An additional parameter under consideration was the source of the residual drift data used in the PACT model. In the original model, the residual drifts were obtained through the OpenSees structural analysis results. However, ATC provides formulas for calculating residual drift based on the median story drift ratio calculated by analysis and the median story drift ratio calculated at yield. These formulas are displayed in Equation (9.5) [ATC 2012a].

$$
\begin{aligned}
&\Delta_r && \text{for } \Delta \le \Delta_y \\
&\Delta_r = 0.3\left(\Delta - \Delta_y\right) && \text{for } \Delta_y < \Delta < 4\Delta_y \\
&\Delta_r = \left(\Delta - 3\Delta_y\right) && \text{for } \Delta \ge 4\Delta_y
\end{aligned}
\tag{9.5}
$$

A PACT model was generated using the residual drift values as calculated by Equation (9.5); the results are displayed in Table 9.5. All of the casualties and unsafe placarding results are very close to those of the baseline model. At the 50%/50 year hazard level, the repair cost and repair time results in Table 9.5 are also very similar to those of the baseline model. They are reasonably similar at the 10%/50 year level, but differ significantly at the 2%/50 year level. For the higher intensity ground motions, the residual drift formulas appear to be less conservative than the structural analysis data.

The number of realizations used in PACT was found to impact the PACT results more significantly than expected. Table 9.6 displays the results for 699 realizations, rather than the 700 realizations used in the original model. A comparison of Tables 9.1 and 9.6 reveals that changing one realization can result in significantly different results in repair cost, casualties, and repair time. For example, the model with 699 realizations resulted in five fewer injuries for the 2%/50 year hazard level at the 84th percentile than did the model with 700 realizations. These differences were attributed to the probabilistic nature of PACT and may indicate limitations in the precision of the model.

One final parameter explored in the parametric study was the PACT user-required input of the maximum workers per square foot that would be allowed to make repairs in the building. The original model utilized the default PACT value of 0.001 workers per square foot. Table 9.7 shows the results when this number was changed to 0.0005, the minimum value in the range provided by ATC [2012b]. The results indicate that the repair times for the 50%/50 years and 10%/50 years hazard levels are greatly increased when this change is made, but the repair time for the 2%/50 years hazard level stays roughly the same because it is at its maximum in both cases. The number inputted for the maximum workers per square foot was directly correlated with and had a large effect on the repair time results. The default PACT value of 0.001 was assumed to be sufficient for the final PACT models in this project.

Table 9.5 PACT results (using residual drift from formulas rather than from structural analysis data).

HL	Repair Cost		Casualties				Repair Time				Unsafe Placarding
%/50 yr	1000 U.S. $		Deaths		Injuries		Parallel Time (days)		Serial Time (days)		Total Probability
	50%	84%	50%	84%	50%	84%	50%	84%	50%	84%	
50	1108	1681				34	79	113	165	256	
10	1800	2680				39	118	177	266	396	0.98
2	4323					41	364	546	542	547	

Table 9.6 PACT results (number of realizations = 699).

HL	Repair Cost		Casualties				Repair Time				Unsafe Placarding
%/50 yr	1000 U.S. $		Deaths		Injuries		Parallel Time (days)		Serial Time (days)		Total Probability
	50%	84%	50%	84%	50%	84%	50%	84%	50%	84%	
50	1108	1655		8		31	79	116	165	253	
10	1922	3408				41		287	284	495	
2	14534			14		37					

Table 9.7 PACT results (decreasing maximum workers per square foot from 0.001 to 0.0005).

HL	Repair Cost		Casualties				Repair Time				Unsafe Placarding
%/50 yr	1000 U.S. $		Deaths		Injuries		Parallel Time (days)		Serial Time (days)		Total Probability
	50%	84%	50%	84%	50%	84%	50%	84%	50%	84%	
50							156	236	336	516	
10							249	517	541	547	
2							544		545		

9.4.2.2 NCBF and SCBF Comparison

The parametric study helped to determine and verify which baseline parameters should be used in the PACT models. Following this analysis, the expected building performance results for an NCBF model and an SCBF model were compared.

The median expected repair costs for the NCBF and SCBF buildings at each of the three hazard levels are displayed in Figure 9.16(a), while the 84th percentile (one standard deviation above the median) repair costs are displayed in Figure 9.16(b). In general, the SCBF building is expected to have lower repair costs than the NCBF building. Of particular interest is the 2%/50 year hazard level. The median values are vastly different: the NCBF building repair costs are nearly at the limit of the total replacement cost, while the SCBF repair costs are much lower. These median values likely indicate that the NCBF building has either collapsed or experienced too much damage to effectively be repaired and would require replacement, while the SCBF building is repairable. At the 84th percentile, however, both the NCBF and SCBF would be expected to require total replacement, and there is no difference in their repair costs.

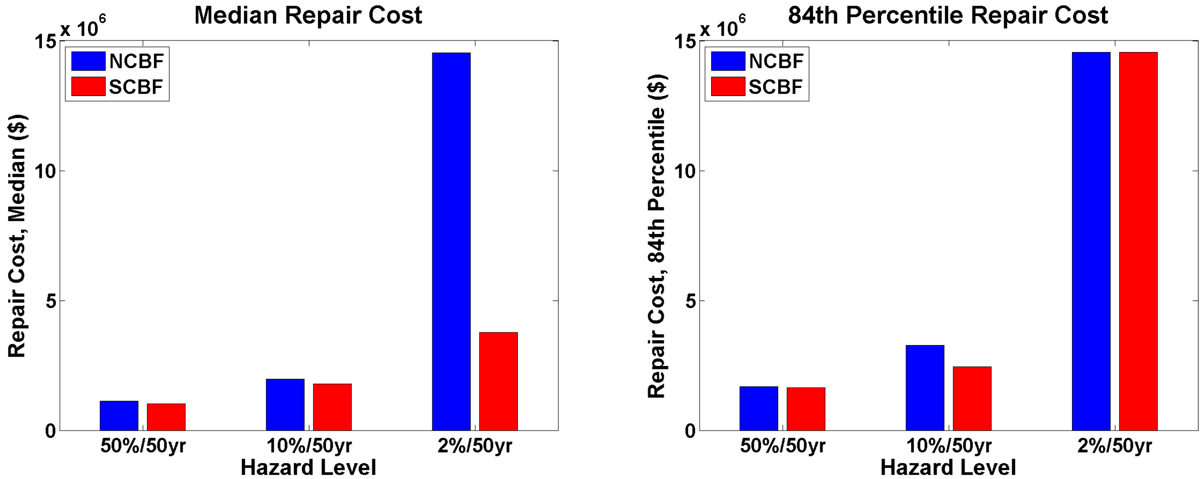

(a) (b)

Figure 9.16 Comparison of repair costs: (a) Median values and (b) 84th percentile.

PACT reports repair time using two different metrics: parallel time and serial time. Parallel time assumes repairs can take place at all levels of the building simultaneously. Serial time assumes repairs on a given floor cannot begin until repairs on all lower floors are complete, and thus the building is repaired from the ground up. Results for parallel time can be interpreted as a lower limit, and those for serial time can be taken as an upper limit, as the actual repair time of the building is likely somewhere in between. Figure 9.17 displays the median and 84th percentile expected repair times for both parallel and serial time. A similar trend as exhibited by the repair cost results occurs in the repair time results. The SCBF building would generally be expected to require less time for repair than the NCBF building. The exception to this trend is when the repair time for both the NCBF and SCBF are at or near the maximum total replacement time, in which case both values are equal, as seen for the 2%/50 year hazard level in Figure 9.17 (b), (c), and (d).

PACT reports casualties in terms of the number of injuries and deaths, and these results are displayed in Figures 9.18(a) and 9.18(b), respectively. In the NCBF building at the 50%/50 year and 10%/50 year hazard levels, typically casualties are caused by loose building components, such as independent pendant lighting, hitting occupants. At the 2%/50 year level, however, the majority of casualties are consequences of structural collapse of the NCBF building. In the SCBF building, only one ground motion out of the 40 resulted in expected collapse; thus, most casualties were caused by swinging objects at all hazard levels in the SCBF building. Figure 9.18 displays results for the 84th percentile alone because the median results were approximately zero for all hazard levels. There is not a clear trend indicating which system—the NCBF or SCBF— tends to cause more casualties. At the 50%/50-year hazard level, the SCBF produces fewer casualties in terms of both injuries and deaths, but this observation is reversed at the 10%/50-year level. Mixed results occur at the 2%/50-year hazard level, with SCBF causing more injuries and the NCBF causing more deaths. As mentioned in the discussion of the OpenSees building response results, the SCBF building tended to experience higher floor accelerations, which would cause more damage to nonstructural components such as the pendant lighting. This may explain why more injuries were expected to occur in the SCBF building at the 10%/50-year and 2%/50-year hazard levels. The NCBF likely resulted in more deaths for the highest intensity earthquakes at the 2%/50-year level due to collapse, as the SCBF was much less likely to collapse.

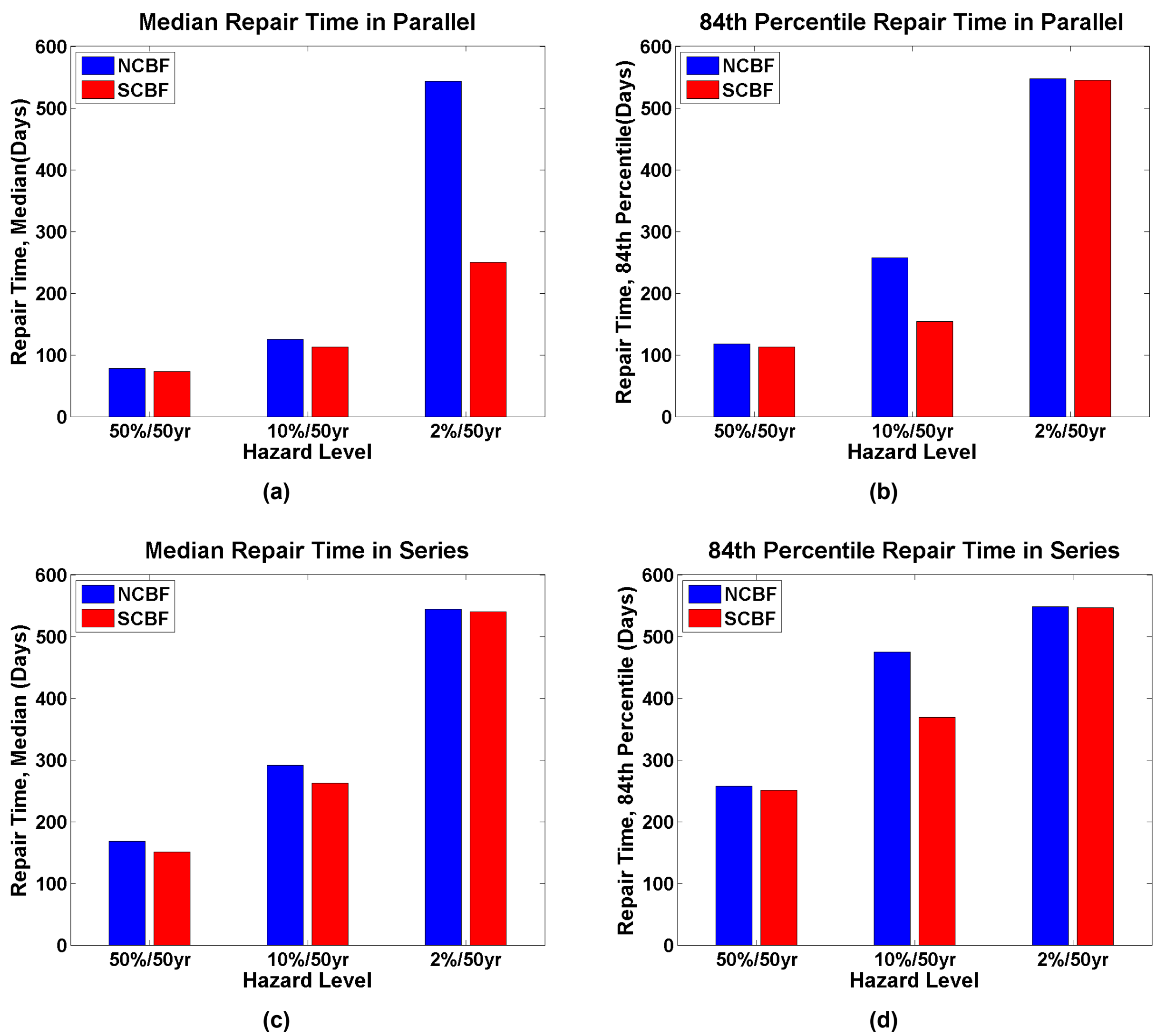

Figure 9.17 **Comparison of repair times: (a) median in parallel time; (b) 84th percentile in parallel time; (c) median in serial time; and (d) 84th percentile in serial time.**

The total probability that an unsafe placard would be posted on the building was evaluated for each hazard level in PACT, and the results are displayed in Figure 9.19. The NCBF system had a higher probability of unsafe placarding at all three hazard levels. The difference in results for the NCBF and SCBF systems is more pronounced at the 50%/50 years and 10%/50 years hazard levels.

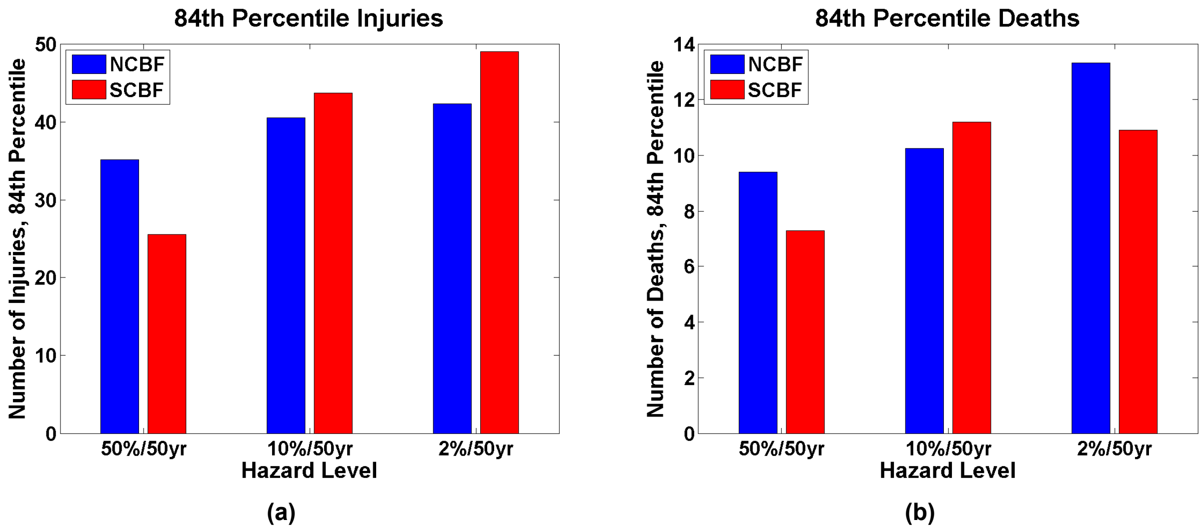

Figure 9.18 Comparison of casualties: (a) 84th percentile deaths and (b) 84th percentile injuries.

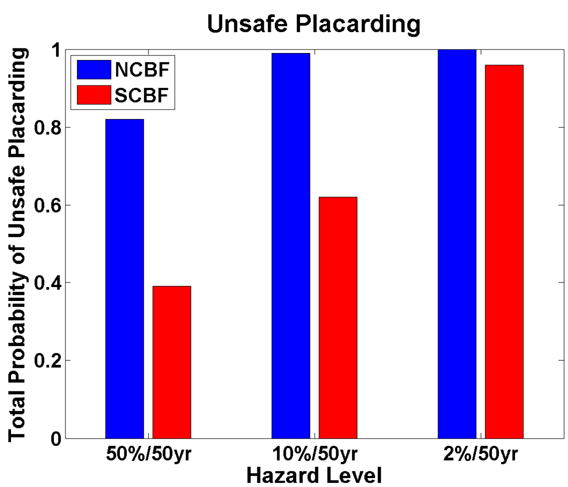

Figure 9.19 Comparison of the total probability of unsafe placarding.

9.5 COMPANION EXPERIMENTAL STUDY ON NCBF

In addition to the analytical modeling and assessment, an experimental study is currently underway in which a nearly full-scale two-story NCBF specimen will be tested using the actuators in the nees@berkeley laboratory. The experimental study will be used to validate the analytical model and to observe the failure hierarchy that would be expected to occur in the NCBF systems. The test configuration is displayed in Figure 9.20.

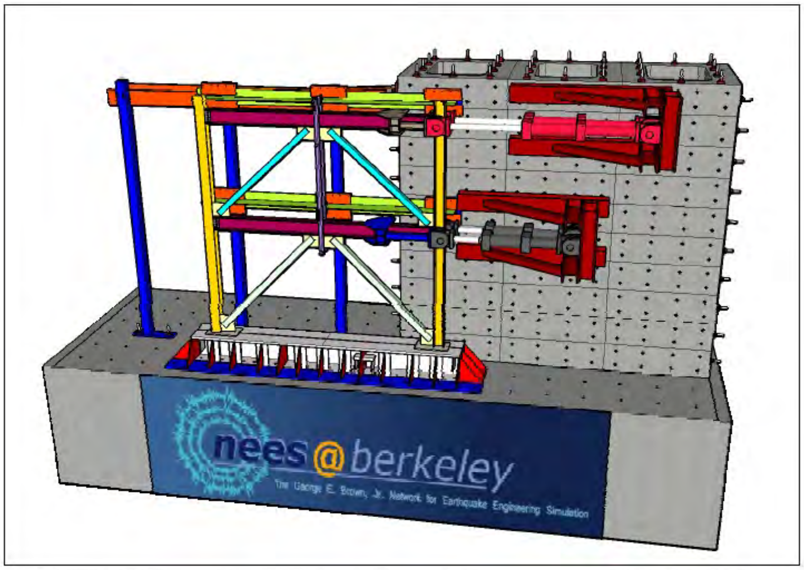

Figure 9.20 Test configuration at nees@berkeley Laboratory [Lai 2013].

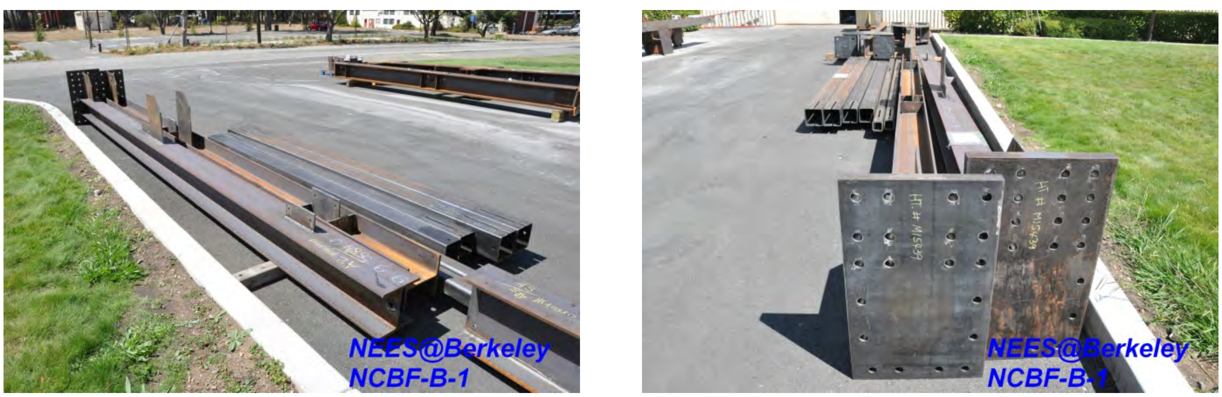

(a) **(b)**

Figure 9.21 NCBF specimen at nees@berkeley Laboratory [Lai 2013].

At this time, the materials have been transported from the shop to the nees@berkeley laboratory, where strain gauges are currently being installed on the specimen. Figure 9.21 displays the test specimen before lab erection. Shop drawings for the test specimen can be found in the Appendix.

9.6 CONCLUSIONS AND FUTURE WORK

From the analytical methods discussed herein, general trends in the PACT results indicate that an SCBF building would generally be expected to outperform an NCBF building in terms of:

- Repair cost
- Repair time
- The probability of unsafe placarding.

It is difficult to infer concrete conclusions about which system outperforms the other in terms of casualties. This may be because the casualty calculations in PACT are based on empirical data and on only six data points in the collapse fragility curve. The number of casualties in a building is dependent on the time of day, week, and year that the earthquake occurs, and so the results may be expected to vary widely. No conclusions comparing NCBF casualties to SCBF casualties shall be drawn because of the significant number of variables that contribute to the outcome, as evidenced by the mixed results obtained from the PACT model.

To continue this research effort, more PACT analyses should be performed investigating other details of the NCBF system. PACT can also be used to assess the performance of other systems, such as the ordinary concentrically braced frame (OCBF). Additionally, upon completion of the experimental study, retrofit strategies should be explored based on the failure modes that are observed.

9.7 ACKNOWLEDGMENTS

This research was organized by the Pacific Earthquake Engineering Research (PEER) Center as part of the 2013 Internship Program with financial support provided by the National Science Foundation (NSF). The author would like to thank Professor Stephen Mahin for his invaluable direction and overall geniality during the program. Additionally, the author is deeply grateful for mentors Jiun-Wei Lai and Barb Simpson for their guidance, encouragement, patience, and willingness to answer an interminable number of questions throughout the research process. Much appreciation is likewise directed towards Heidi Tremayne, the coordinator of the PEER Internship Program, for her never-ending effort and commitment to making this program a success.

9.8 REFERENCES

AIJ (1995). *Reconnaissance Report on Damage to Steel Building Structures Observed from the 1995 Hyogoken-Nanbu Earthquake*, Architectural Institute of Japan.

AISC (2010). *Seismic Provisions for Structural Steel Buildings ANSI/AISC 341-10*. American Institute of Steel Construction, Chicago, IL.

ASCE (2010). Minimum Design Loads for Buildings and Other Structures, ASCE 7-10, American Society of Civil Engineers, Reston, VA.

Astaneh-Asl A., Goel S.C., Hanson R.D. (1982). Cyclic behavior of double angle bracing members with end gusset plates, *Report No. UMEE 82R7*, University of Michigan, Ann Arbor, MI.

ATC (2012a). *Seismic Performance Assessment of Buildings Volume 1 – Methodology*, Applied Technology Council, Redwood City, CA [electronic version: https://www.atcouncil.org/files/FEMAP-58-1_Volume%201_Methodology.pdf].

ATC (2012b). *Seismic Performance Assessment of Buildings Volume 2 – Implementation Guide*, Applied Technology Council, Redwood City, CA [electronic version: https://www.atcouncil.org/files/FEMAP-58-2_Volume%202_Implementation.pdf].

Baker J.W., Lin T., Shahi S.K., Jayaram N. (2011). New ground motion selection procedures and selected motions for the PEER Transportation Research Program, *Report PEER 2011/03*, Pacific Earthquake Engineering Research Center, University of California, Berkeley, CA.

Black R.G., Wenger W.A., Popov E.P. (1980). Inelastic buckling of steel struts under cyclic load reversal, *EERC Report 80-40*, Earthquake Engineering Research Center, University of California, Berkeley, CA.

Chen C.-H. (2010). *Performance-Based Seismic Demand Assessment of Concentrically Braced Steel Frame Buildings,* Ph.D. Dissertation, Dept. of Civil and Environmental Engineering, University of California, Berkeley, CA.

G.K. Welding, Inc. (2013). Shop Drawings, Richmond, CA.

Gupta A., Krawinkler, H. (1999). Seismic demands for performance evaluation of steel moment resisting frame structures, *Report No. 132*, Stanford University, Stanford, CA.

Hsiao P., Lehman D.E., Berman J.W., Roeder C.W., Powel J. (2012). Seismic vulnerability of older braced frames, ASCE, *J. Performance of Constructed Facilities,* doi: 10. 1061(ASCE)CF.1943-5509.0000394).

Lai J.W. (2012). *Experimental and Analytical Studies on the Seismic Behavior of Conventional and Hybrid Braced Frames*, Ph.D. Dissertation, Dept. of Civil and Environmental Engineering, University of California, Berkeley, CA.

Lai, J.W. (2013). Personal Communication, Berkeley, CA.

Lignos D. (2011). Tohoku Japan Earthquake & Tsunami Clearinghouse, *EERI*, retrieved August 15, 2013 from http://www.eqclearinghouse.org/2011-03-11-sendai/2011/08/03/eeri-steel-structures-reconnaissance-group/pgarage-gussetfracture/.

Mahin S.A., Terzic V., Nagy C. (2012). Using performance-based earthquake evaluation methods to assess the relative benefits of different structural systems, *Proceedings, 9th International Conference on Urban Earthquake Engineering/4th Asia Conference on Earthquake Engineering,* Tokyo Institute of Technology, Tokyo, Japan.

Malley J.O. (1989). The 1988 UBC: Revisions and additions to the requirements for braced steel frames, Degenkolb Associates, San Francisco, CA.

MathWorks, Inc., The. (2009). MATLAB Version 7.9.0, Natick, Massachusetts.

McKenna F., Fenves G.L., Scott M.H., Jeremic B. (2000). Open System for Earthquake Engineering Simulation (OpenSees), Pacific Earthquake Engineering Research Center, University of California, Berkeley, CA.

Moehle J.P., Deierlein G.G. (2004). A framework methodology for performance-based earthquake engineering, *Proceedings, 13th World Conference of Earthquake Engineering,* Vancouver, B.C., Canada, Paper No. 679.

Morgan T. (2008). Summary of design basis for 3-Story NEES-TIPS model buildings, Forell/Elsesser Engineers, San Francisco, CA.

NISEE (1994). Tube fractured due to local buckling, date accessed August 2013, http://nisee.berkeley.edu/jpg/5074_1631_0641/IMG0027.jpg.

Simpson B. (2013) Personal Communication, Berkeley, CA.

ICBO (1985). *Uniform Building Code*, International Conference of Building Officials, Whittier, CA.

ICBO (1988). *Uniform Building Code,* International Conference of Building Officials, Whittier, CA.

9.9 APPENDIX

9.9.1 PACT Screenshots:

Project Info | Building Info | Population | Component Fragilities | Performance Groups | Collapse Fragility | Structural Analysis Results | Residual Drift | Hazard Curve

Number of Stories: 3

Total Replacement Cost ($): 14,548,500
Replacement Time (days): 550.00
Total Loss Threshold (As Ratio of Total Replacement Cost): 0.4
Core and Shell Replacement Cost ($): 5,819,400
Max Workers per sq. ft.: 0.001

Most Typical Defaults
Floor Area (sq. ft.): 21,600.00
Story Height (ft.): 15

Floor Num	Floor Name	Story Height (ft.):	Area (sq. ft.):	Height Factor	Hazmat Factor	Occupancy Factor
1	Ground	15.00	21,600.00	1	1	1
2	Floor 2	15.00	21,600.00	1	1	1
3	Floor 3	15.00	21,600.00	1	1	1
4	Floor 4 (roof)	[redacted]	21,600.00	1	1	1

Project Info | Building Info | Population | Component Fragilities | Performance Groups | Collapse Fragility | Structural Analysis Results | Residual Drift | Hazard Curve

Direction
◉ Direction 1 ○ Direction 2 ○ Non-Directional

Update Table

Floor 1 of 4 (Ground)

No.	Component Type	Performance Group Quantities	Quantity Dispersion	Fragility Correlated	Population Model	Demand Parameters
B1031.001	Bolted shear tab gravity connections	56.00	0.00	☐	Commercial Office	Story Drift Ratio
B1031.011a	Steel Column Base Plates, Column W < 150 plf	4.00	0.00	☐	Commercial Office	Story Drift Ratio
B1033.071b	Braced frame, design for factored loads, no additional seismic detailing, Chevron Brace, 41 PLF < w < 99 PLF	2.00	0.00	☐	Commercial Office	Story Drift Ratio
B2022.001	Curtain Walls - Generic Midrise Stick-Built Curtain wall, Config: Monolithic, Lamination: Unknown, Glass Type: Unknown, Details: Aspect ratio = 6:5, Other details Unkn...	86.00	0.60	☐	Commercial Office	Story Drift Ratio
C1011.001a	Wall Partition, Type: Gypsum with metal studs, Full Height, Fixed Below, Fixed Above	9.00	0.20	☐	Commercial Office	Story Drift Ratio
C2011.001a	Prefabricated steel stair with steel treads and landings with seismic joints that accommodate drift	1.00	0.20	☐	Commercial Office	Story Drift Ratio
C3011.001a	Wall Partition, Type: Gypsum + Wallpaper, Full Height, Fixed Below, Fixed Above	1.00	0.70	☐	Commercial Office	Story Drift Ratio

Project Info | Building Info | Population | Component Fragilities | Performance Groups | Collapse Fragility | Structural Analysis Results | Residual Drift | Hazard Curve

Direction
○ Direction 1 ○ Direction 2 ◉ Non-Directional

Update Table

Floor 1 of 4 (Ground)

No.	Component Type	Performance Group Quantities	Quantity Dispersion	Fragility Correlated	Population Model	Demand Parameters
C3027.001	Raised Access Floor, non seismically rated.	162.00	0.20	☐	Commercial Office	Acceleration
C3032.001a	Suspended Ceiling, SDC A,B, Area (A): A < 250, Vert support only	77.76	0.00	☐	Commercial Office	Acceleration
C3033.002	Recessed lighting in suspended ceiling - with independent support wires	324.00	0.00	☐	Commercial Office	Acceleration
C3034.001	Independent Pendant Lighting - non seismic	324.00	0.30	☐	Commercial Office	Acceleration
D1014.011	Traction Elevator – Applies to most California Installations 1976 or later, most western states installations 1982 or later and most other U.S installations 1998 or later.	2.00	0.70	☐	Commercial Office	Acceleration
D2021.011a	Cold Water Piping (dia > 2.5 inches), SDC A or B, PIPING FRAGILITY	0.32	0.20	☐	Commercial Office	Acceleration
D2022.011a	Hot Water Piping - Small Diameter Threaded Steel - (2.5 inches in diameter or less), SDC A or B, PIPING FRAGILITY	1.81	0.70	☑	Commercial Office	Acceleration
D2022.021a	Hot Water Piping - Large Diameter Welded Steel - (greater than 2.5 inches in diameter), SDC A or B, PIPING FRAGILITY	0.65	0.20	☑	Commercial Office	Acceleration
D2031.011b	Sanitary Waste Piping - Cast Iron w/flexible couplings, SDC A,B, BRACING FRAGILITY	1.23	0.60	☑	Commercial Office	Acceleration
D3041.011a	HVAC Galvanized Sheet Metal Ducting less than 6 sq. ft in cross sectional area, SDC A or B	1.62	0.20	☐	Commercial Office	Acceleration
D3041.012a	HVAC Galvanized Sheet Metal Ducting - 6 sq. ft cross sectional area or greater, SDC A or B	0.43	0.20	☐	Commercial Office	Acceleration
D3041.031a	HVAC Drops / Diffusers in suspended ceilings - No independent safety wires, SDC A or B	19.44	0.50	☐	Commercial Office	Acceleration
D3041.041a	Variable Air Volume (VAV) box with in-line coil, SDC A or B	10.80	0.20	☐	Commercial Office	Acceleration
D4011.021a	Fire Sprinkler Water Piping - Horizontal Mains and Branches - Old Style Vitaulic - Thin Wall Steel - No bracing, SDC A or B, PIPING FRAGILITY	4.32	0.10	☐	Commercial Office	Acceleration
D4011.031a	Fire Sprinkler Drop Standard Threaded Steel - Dropping into unbraced lay-in tile SOFT ceiling - 6 ft. long drop maximum, SDC A or B	1.94	0.20	☐	Commercial Office	Acceleration
D5012.021a	Low Voltage Switchgear - Capacity: 100 to <350 Amp - Unanchored equipment that is not vibration isolated - Equipment fragility only	1.00	0.40	☐	Commercial Office	Acceleration
E2022.001	Modular office work stations.	151.20	0.20	☐	Commercial Office	Acceleration
E2022.102a	Bookcase, 2 shelves, unanchored laterally	43.20	0.60	☐	Commercial Office	Peak Floor Velocity
E2022.112a	Vertical Filing Cabinet, 2 drawer, unanchored laterally	17.28	0.60	☐	Commercial Office	Peak Floor Velocity

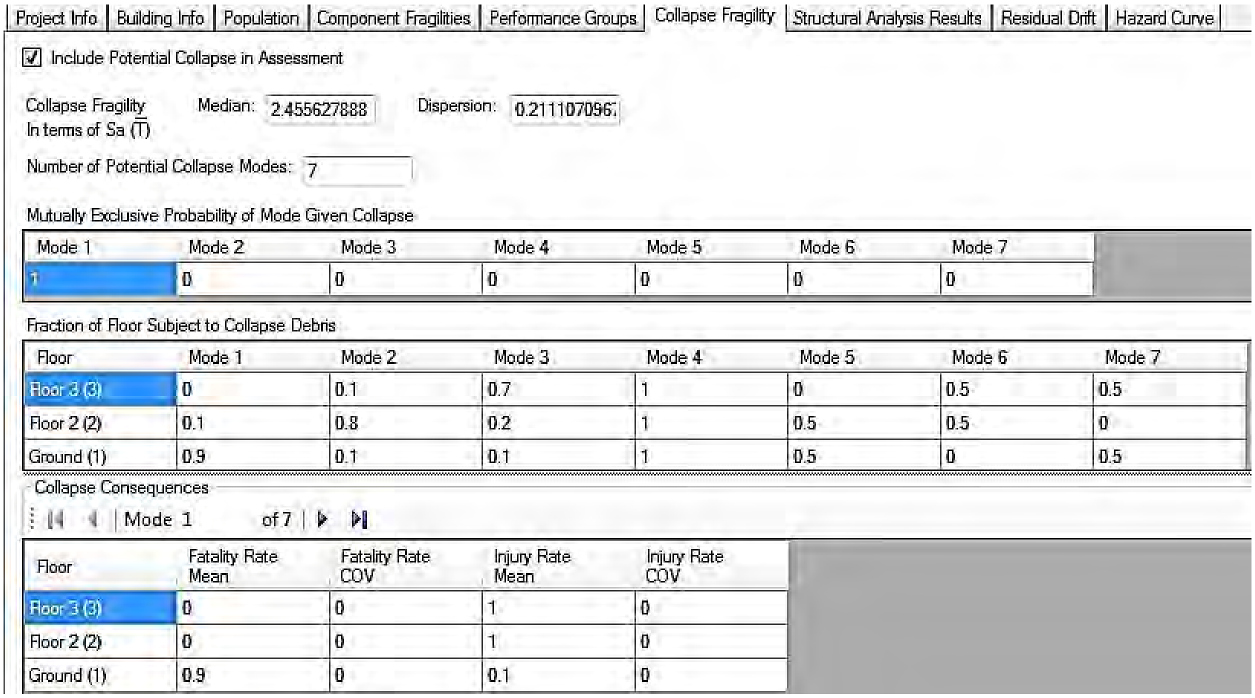

Mode 1	Mode 2	Mode 3	Mode 4	Mode 5	Mode 6	Mode 7
1	0	0	0	0	0	0

Floor	Mode 1	Mode 2	Mode 3	Mode 4	Mode 5	Mode 6	Mode 7
Floor 3 (3)	0	0.1	0.7	1	0	0.5	0.5
Floor 2 (2)	0.1	0.8	0.2	1	0.5	0.5	0
Ground (1)	0.9	0.1	0.1	1	0.5	0	0.5

Floor	Fatality Rate Mean	Fatality Rate COV	Injury Rate Mean	Injury Rate COV
Floor 3 (3)	0	0	1	0
Floor 2 (2)	0	0	1	0
Ground (1)	0.9	0	0.1	0

9.9.2 NCBF Experimental Study Shop Drawings [G.K. Welding, Inc. 2013].

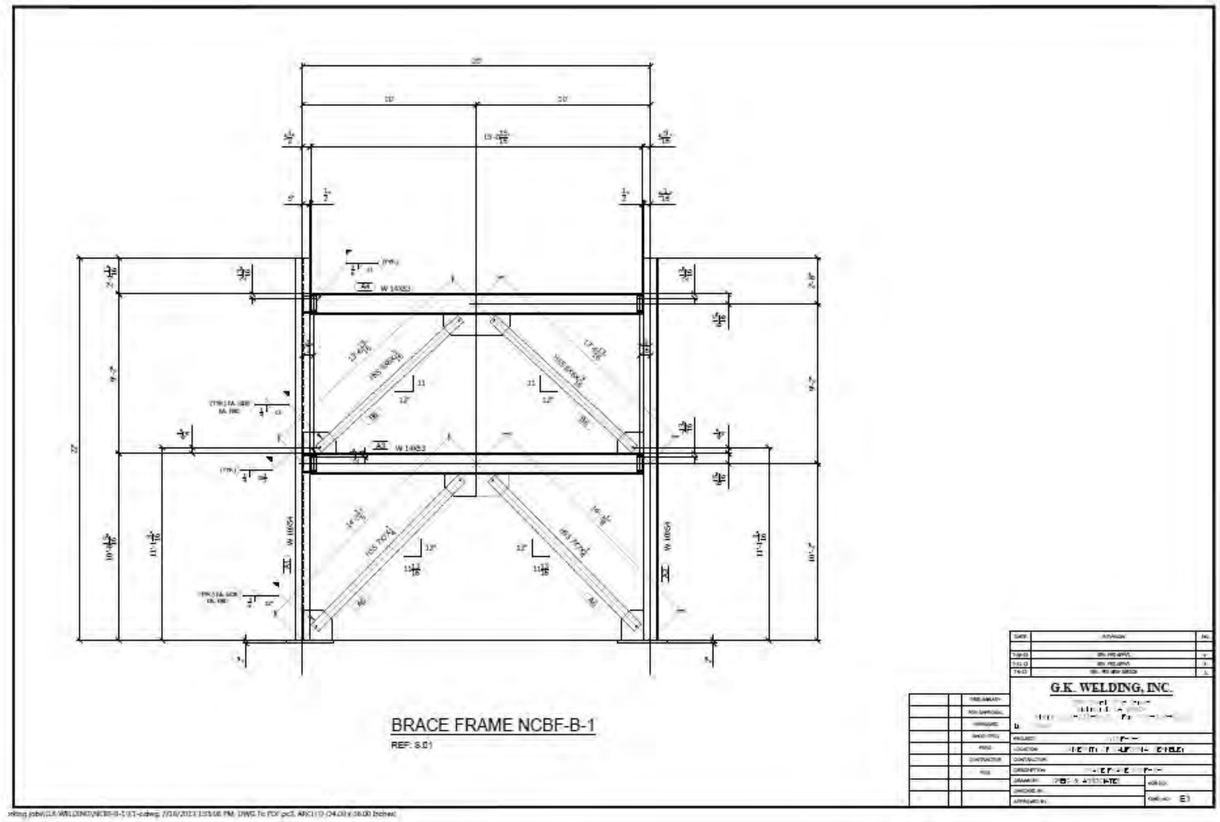

10. Economic Loss Assessment for an Existing Tall Building

Melissa C. Quinonez

ABSTRACT

This project investigates the seismic performance of a tall building constructed between the 1960s and 1980s. Seismic safety concerns exist because these buildings were generally designed for demands less than current design codes. However, a retrofit measure that addresses safety but neglects financial losses due to downtime for structural or nonstructural repairs does not fully mitigate the hazard faced by an owner. The primary motivation of this project is to preemptively reduce post-earthquake disruption and repairs. Projects such as the Tall Building Initiative-2 (TBI-2) have been developed to address this issue. The overall goal of the TBI-2 is to develop performance based seismic design guidelines to retrofit existing steel tall moment resisting frame (MRF) buildings. As a part of TBI-2, the Pacific Earthquake Engineering Research (PEER) Center is currently working on a project that investigates the economic advantages gained by retrofitting existing steel MRF buildings greater than 20 stories. This investigation uses the performance-based earthquake engineering (PBEE) methodology to conduct the assessment. The PBEE methodology consists of four stages: hazard analysis, structural analysis, damage analysis, and loss analysis. This report focuses on the loss analysis of a 40-story steel MRF building completed in the early 1970s located in downtown San Francisco. This investigation concludes that the considered building performed poorly at the service level hazard in terms of repair cost. Similarly, the performance of the considered building under earthquake shaking levels consistent with the design level and above was poor considering significant damage and repair costs that dictate replacement.

10.1 INTRODUCTION

The 1994 Northridge earthquake resulted in the discovery of the non-ductile failure of beam to column connections in moment-resisting frame (MRF) buildings that were considered to be capable of resisting earthquake-induced structural damage. It was also thought that if this system were to suffer damage, it would be limited to ductile yielding of members and connections. However, some MRF buildings that experienced ground shaking less severe than the design level had connection failures [Anderson et al. 1995; Foutch 2000].

The failures caused by the Northridge earthquake could be explained by reviewing the different Uniform Building Codes (UBC) used to construct most of the steel MRF buildings. As seen in Table 10.1, prior to 1970, the UBC had no seismic requirements for steel MRF buildings. Between 1970 and 1988 a few seismic requirements were adopted. These included minimum story drift ratios, strong-column-weak beams, and the strength of column panel zones [Lee and Foutch 2002]. Overall, before 1988, there were few to no seismic requirements for steel MRF buildings.

Many of the tall buildings built before 1988 still exist and are being occupied all around the world. Depending where they are in the world, these tall buildings may pose a hazard to the cities since they were designed for demands less than current design codes. For example, as seen in Figure 10.1, in San Francisco, California, a high seismic zone, there are approximately 122 buildings that have 20 or more stories. Of those 122 buildings, 49 were built between 1960 and 1979, as seen in Figure 10.2 [SkyscraperPage.com]. These buildings were constructed during the time period when there were few to no seismic requirements for steel MRF tall buildings, raising questions as to the buildings' seismic performance when the next earthquake occurs.

The Tall Building Initiative (TBI) developed guidelines for the performance-based seismic design of new tall buildings [Tall Buildings Initiative 2010]. TBI-2's goal is to continue TBI's objective by creating retrofit guidelines for tall steel MRF buildings by implementing the performance-based earthquake engineering (PBEE) methodology. The scope of TBI-2 is to generate the seismic performance of tall buildings built between the 1960s and 1980s and analyze the economic advantages gained by retrofitting those building. The focus of this research paper relates to the performance of a 40-story steel MRF building built in the early 1970s, located in downtown San Francisco, California.

Table 10.1 Summary of key building specifications from the UBC 1958-1988 [Foutch 2000].

UBC Version	Base Shear	Story Drift Limit	SMRF Requirements
1958	F=CW	None	None
1961, 1964, 1967	V=ZKCW K=0.67 (SMRF)	EOR decide	None
1970, 1973	V=ZKCW K=0.67 (SMRF)	EOR decide	Connections should be able to develop full plasticcapacity
1976, 1979, 1982, 1985	V=ZIKCSW K=0.67 (SMRF)	0.005	Local buckling → satisfy plastic design
1988, 1994	V=ZICW/Rw Rw=12 (SMRF)	Min. (0.04/Rw, 0.004| T>0.7s)	Panel zone strength and thickness; strong column weak beam

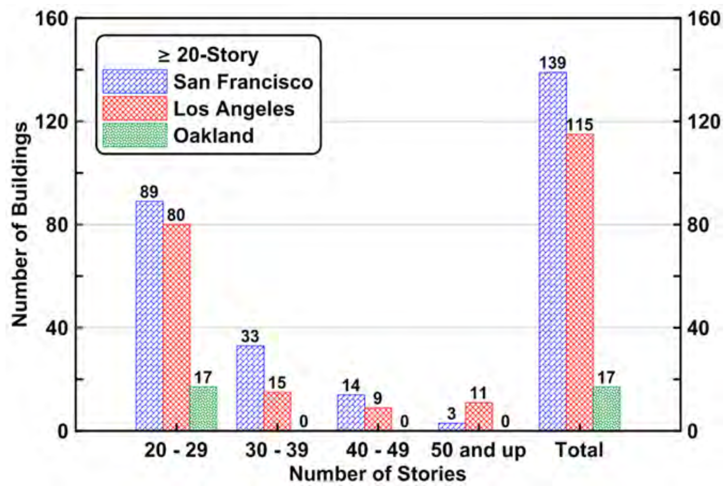

Figure 10.1 Buildings between 20 and 40 stories (courtesy of Jiun-Wei Lai).

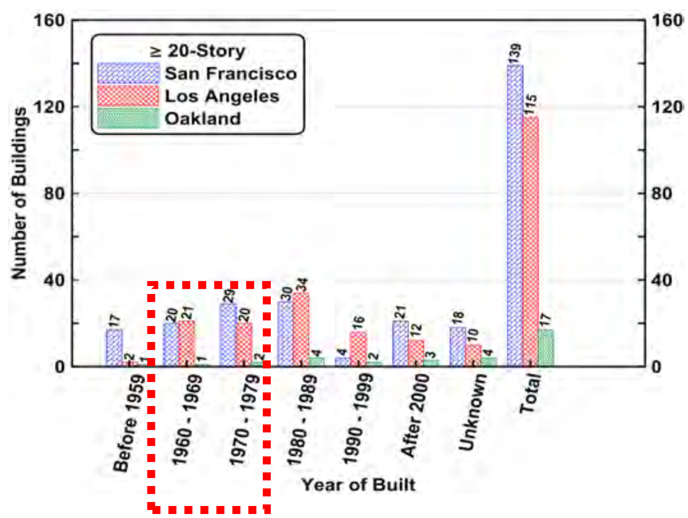

Figure 10.2 Vintage of 20-story buildings or higher in California (courtesy of Jiun-Wei Lai).

The objectives of this assessment include:)1) analyzing the response of the prototype building using nonlinear time history analysis; (2) summarizing the structural response data as an input into the Performance Assessment Calculation Tool (PACT) [ATC 2012a]; (3) running an economic loss estimate; and (4) implementing the PBEE methodology for the considered building to inform owners and insurers on the economic loss associated with this vintage of tall buildings. This report focuses on the loss analysis of the PBEE methodology depicted in Figure 10.3. The structural analysis can be found in Rodriguez [2013] contained herein.

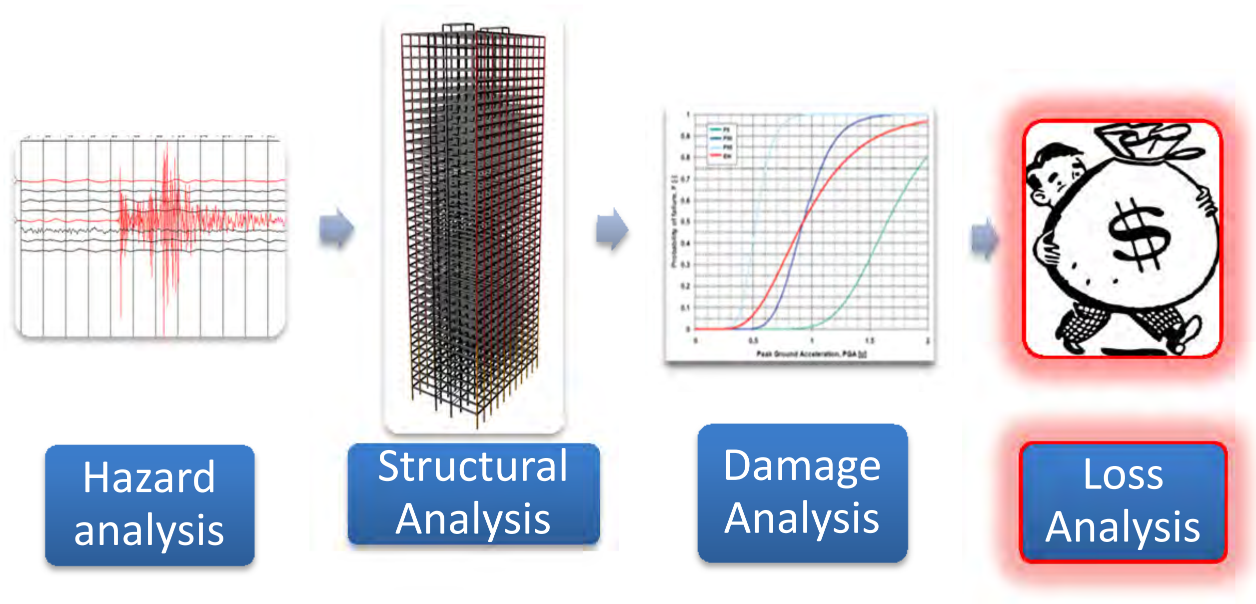

Figure 10.3 Four stages of the PBEE methodology.

10.2 HAZARDS

This assessment analyzed two hazard levels and a separate case study. These included the service level, design level and a Loma Prieta case study. The service level represents a frequent earthquake with a return period of 43 years and a 50% probability of exceedance in 50 years; the design level is the current design hazard level with a return period of 475 years or a 10% probability of exceedance in 50 years. At each hazard level, 20 ground motions were selected, each with three components: fault normal, fault parallel, and the vertical component. The maximum considered earthquake (MCE) level, with a return period of 2475 years and a 2% probability of exceedance in 50 years, was also analyzed; however, non-convergence of analyses showed that this hazard level produced demands not compatible with sustainable member deformations and results not discussed here. The Loma Prieta case study was adopted to verify the reliability of the loss estimation software, but there was no actual repair cost data available to complete the verification. For this case study, three ground motions were selected from the 1989 Loma Prieta earthquake.

10.2.1 Selection and Scaling of Ground Motions

10.2.1.1 Hazard Levels

Professor Jack W. Baker of Stanford University selected the ground motions from the PEER NGA library for each of the hazard levels. According to Baker (personal correspondence), the following considerations were used when selecting the ground motions:

- No more than five ground motions were taken from any single earthquake

- The magnitudes of the selected ground motions are greater than or equal to 6.5
- The closest distance of the selected ground motions range from 0 to 50 km
- Ground motions were selected if the geometric mean of their two horizontal response spectra approximately matched the associated target spectrum between 0.05 and 7 sec.

The square root sum of the horizontal components is taken to generate the geometric mean. The target and median for each hazard level is seen in Figure 10.4. At each hazard level, the median of the 20 ground motions was determined and compared to the target spectrum, which was obtained from a generic site in downtown San Francisco using the computer program Open Seismic Hazard Analysis [OpenSHA]. As seen from Figure 10.4, the median of each hazard level match the target over the building period between 4 and 7 sec. Ground motion selections for each hazard level, which include the name of the ground motion, station, magnitude, distance, V_{s30}, and scale factor, can be found in the following report contained herein [Rodriguez 2013].

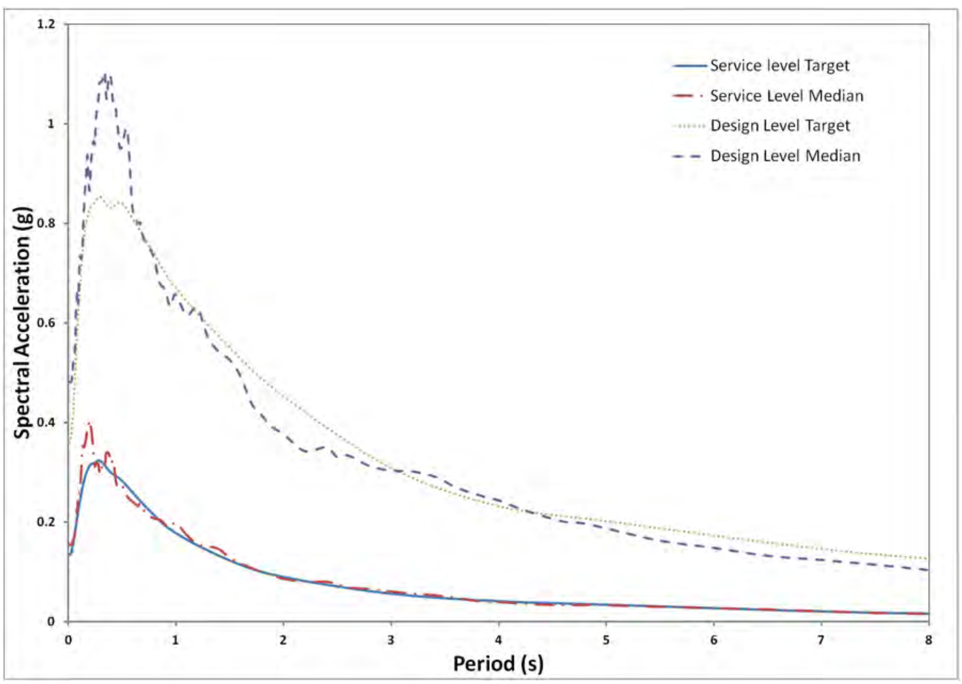

Figure 10.4 5% damped response spectra (geometric mean) of hazard levels.

10.2.1.2 Loma Prieta Case Study

In order to gauge the accuracy of the PACT model at estimating damage and downtime, the Loma Prieta case study was adopted. For this case study, three ground motions were selected by Dr. Matt Schoettler of PEER from the PEER strong-motion database. The three ground motions were all recorded in San Francisco relatively close to each other as seen in Figure 10.5.

The ground motions for the Loma Prieta case study were not associated with one of the investigated hazard levels. The response spectrum for each ground motion are shown in Figure 10.6. It is very clear that the ground motions cannot be considered a service-level earthquake, but it is unclear by what amount the ground motions are deviating from the service level at a building period between 4 and 7 sec. Therefore, the spectral displacement was plotted for each ground motion against the target displacement spectrum; see Figure 10.7. Note that the displacement demand is about one-third of the anticipated displacement in a service-level earthquake for the building period range between 4 and 7 sec. Therefore, a hazard level that matched the demand at the period range of interest was generated using OpenSHA. A return period of 16 years was obtained for the Loma Prieta case study, as seen by a dashed line in Figure 10.7.

As shown in Figure 10.8, when the target spectrums for each hazard level and the case study are plotted, the generated hazard level for the Loma Prieta case study is significantly lower than the service level. This figure will be very useful later on when comparing the results.

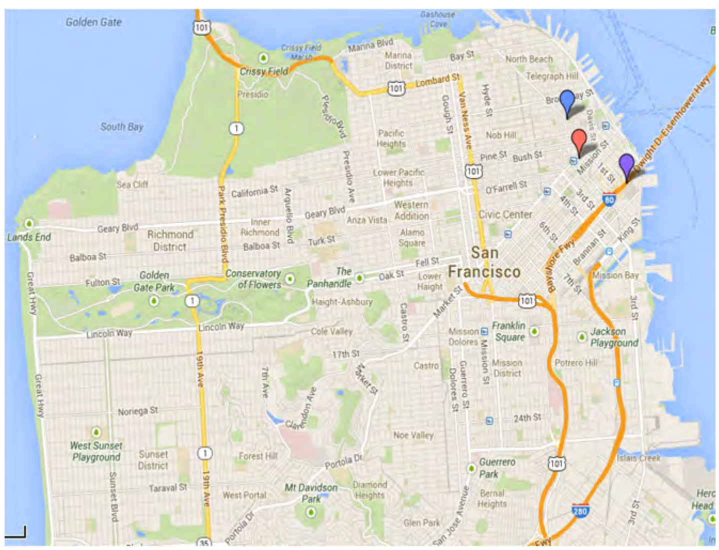

Figure 10.5 **Location of Loma Prieta recordings (courtesy of M. Schoettler).**

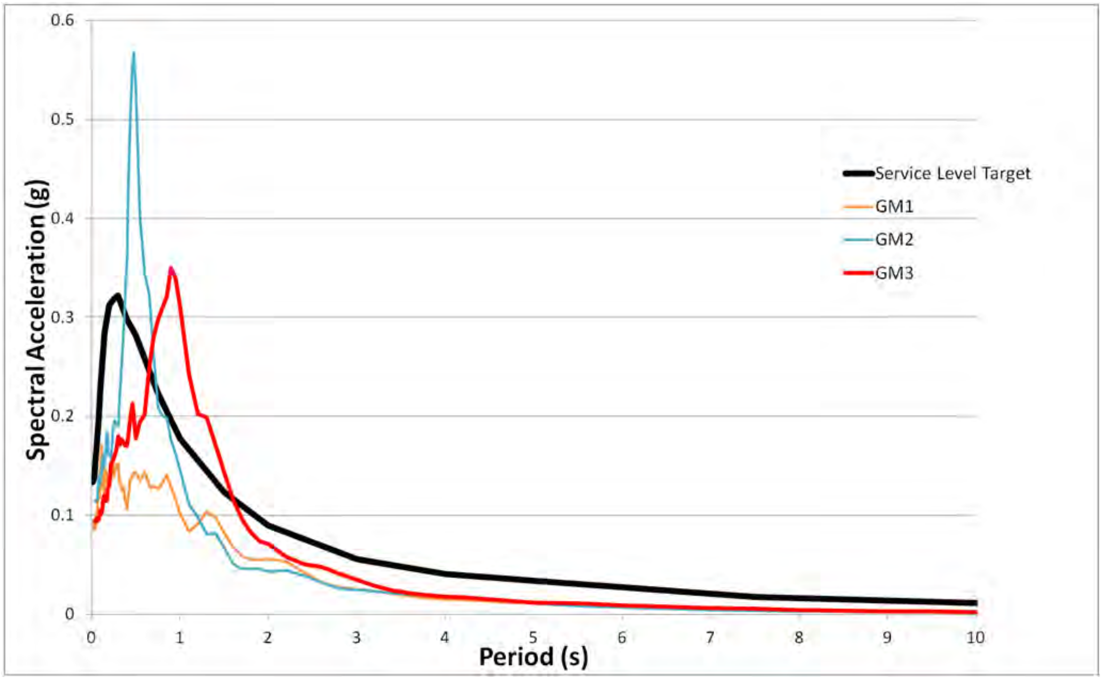

Figure 10.6 Ground motion for Loma Prieta case study compared to service-level target spectrum.

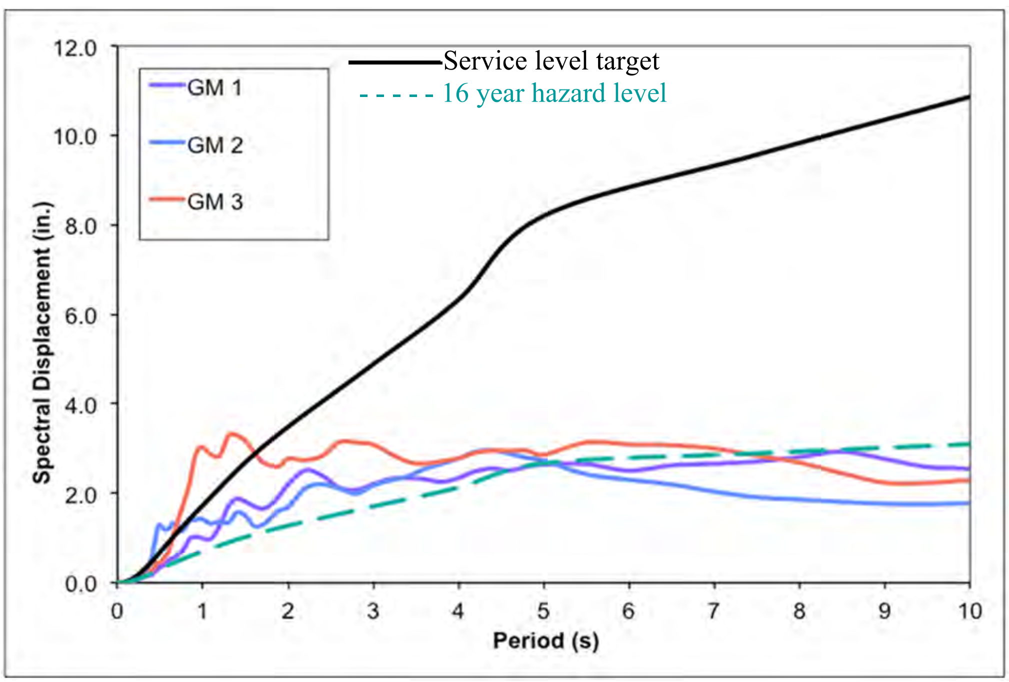

Figure 10.7 Ground motion spectral displacement compared to service-level target spectrum.

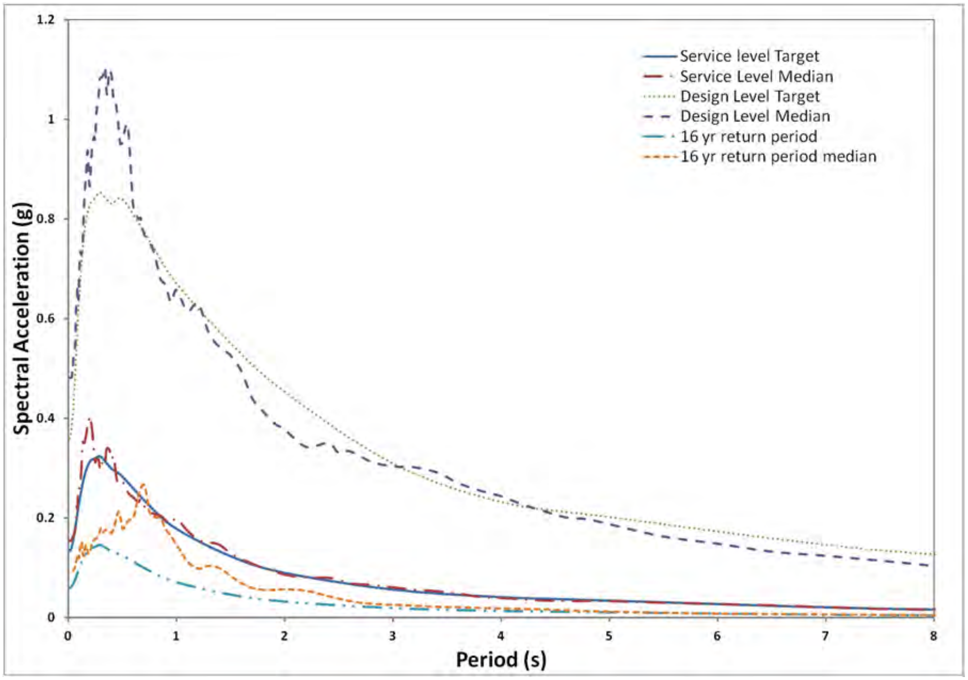

Figure 10.8 Hazard levels and Loma Prieta case study target spectrums.

10.3 BUILDING AND STRUCTURAL MODEL

10.3.1 Building Considered

Located in downtown San Francisco, the 40-story, steel MRF building used in this assessment was completed in the early 1970s. The basic building plan is regular with dimensions of 128 ft-4 in.×198 ft-4 in. with varying bay spacing in each direction as seen in Figure 10.9. The story height throughout is the same except at the first floor where the story height is 23 ft-3 in. as seen in Figure 10.10. There is also a penthouse on top of the roof that consists of two systems, 80 ft apart, between girder lines H and D, and column lines 4 and 5, and 9 and 10, as seen in Figure 10.10. Referenced from the datum, the total building height is 496 ft-11 in.

The typical slab thickness is approximately 6 ft-1/4 in. The girder dimensions range from W16×26 to W36×260, and the typical column material is ASTM A36 except for some columns located between the first and sixth floor, which consist of ASTM A572 Grade 42 steel. For details on the cross sections and connection details of this building, reference the report located herein [Rodriguez 2013].

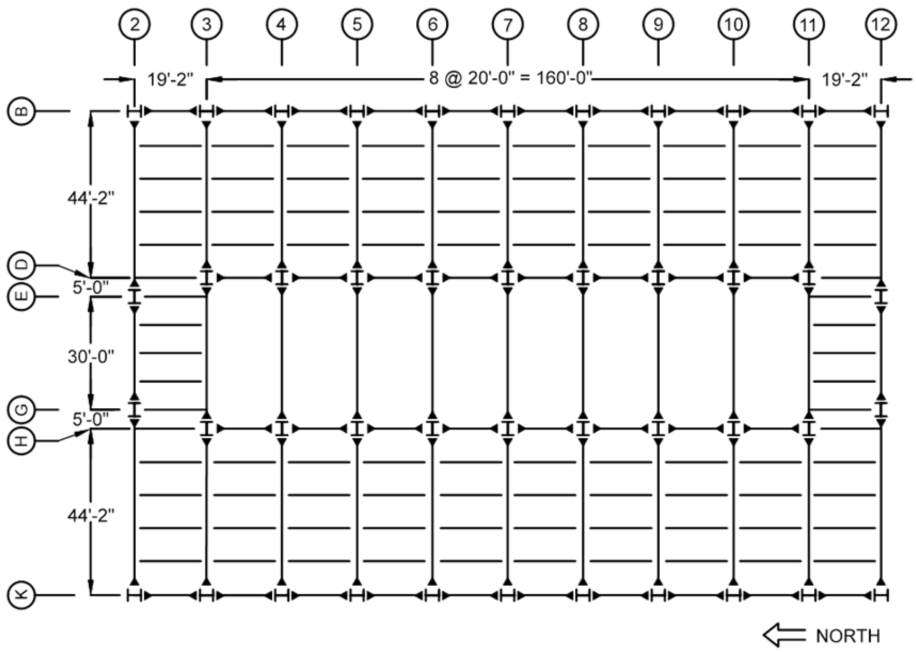

Figure 10.9 Typical floor plan.

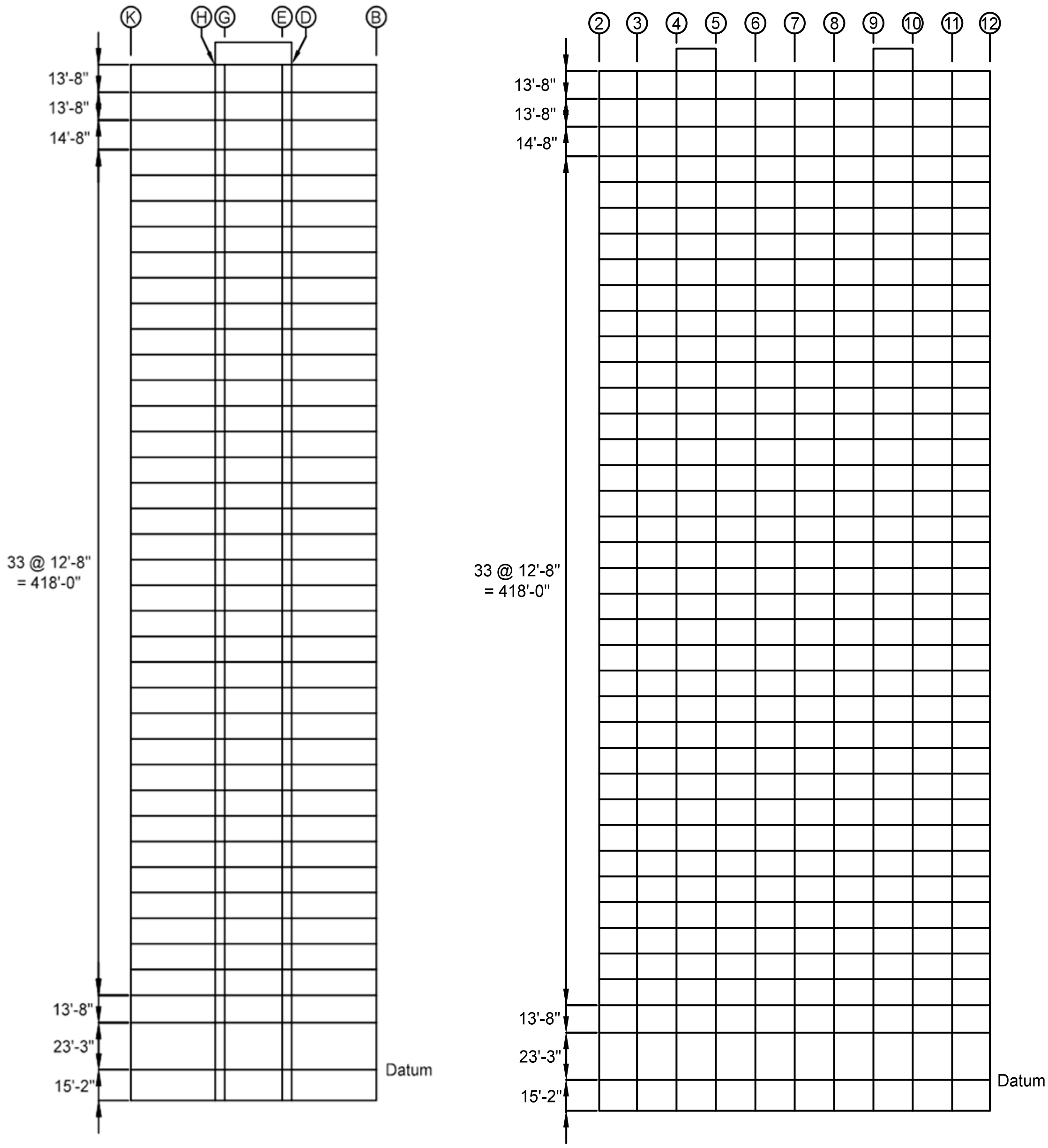

Figure 10.10 Elevation views of the north-south (left) and east-west (right) directions.

10.3.2 Structural Analysis

Once all the necessary information was extracted from the building structural plans, OpenSees [McKenna et al. 2000] was used to model a fully ductile representation of the building as seen in Figure 10.11. In order to simplify the model, foundations, walls, ramps, and non-structural components were disregarded. Nonlinear time history analysis were conducted on the OpenSees building model using all of the ground motions selected for each hazard level and case study in order to obtain the dynamic structural response of the building. Once the time history analysis was finished, envelopes of the response of the structure for the acceleration, story drift, and velocity were obtained in the fault-normal and fault-parallel directions. From these envelopes, story drift ratio and residual drift ratio envelopes were also calculated. Tables 10.2 through 10.4 contain a summary of the peak demands in each direction for each hazard level and the case study.

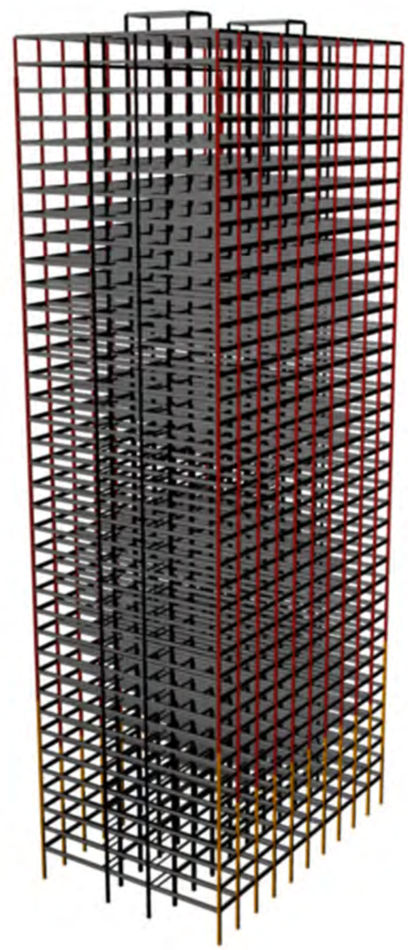

Figure 10.11 OpenSees building model.

Table 10.2 Service-level peak demands.

	Fault Normal	**Fault Parallel**
Story Drift Ratio (rad)	0.004	0.006
Velocity (ips)	29.3	33.1
Acceleration (g)	0.34	0.40
Residual Drift Ratio (rad)	0.000022	

Table 10.3 Design-level peak demands.

	Fault Normal	Fault Parallel
Story Drift Ratio (rad)	0.044	0.029
Velocity (ips)	98.2	81.7
Acceleration (*g*)	0.98	1.19
Residual Drift Ratio (rad)	0.017	

Table 10.4 Loma Prieta case study peak demands.

	Fault Normal	Fault Parallel
Story Drift Ratio (rad)	0.003	0.003
Velocity (ips)	15.5	12.4
Acceleration (*g*)	0.30	0.30
Residual Drift Ratio (rad)	0.000019	

10.4 PERFORMANCE ASSESSMENT

As stated before, this investigation used the Performance Assessment Calculation Tool (PACT), which aims to implement the PBEE methodology to obtain decision variables from engineering demand parameters (EDPs), in order to perform an economic loss estimate. PACT's basic input information for the building considered included type of structural systems used, building occupancy, number of stories, plan dimensions, and the quantities of the various structural and non-structural building components that are grouped together into performance groups by their similar damage patterns. PACT also needs demand parameters to characterize structural and non-structural damage in the considered building for the various intensity measures used to characterize ground motions [Mahin et al. 2012]. For this assessment, these EDPs include story drift ratio, floor velocity, floor acceleration, and residual drift ratio that were generated in the fault-normal and fault-parallel directions for each ground motion used. These EDPs are then input to a set of fragility functions that model the probability of various levels of damage to individual building components. These damages are then used to evaluate the performance of the considered building, which is measured in terms of incurring certain consequences or decision variables that include repair cost, repair time, and unsafe placarding.

In order to generate the decision variable, PACT obtains the median and standard deviation values from the EDP values for the 20 ground motions for each of the two hazard levels. The same process was used for the three ground motions in the Loma Prieta case study. These were expanded into a set of 500 realizations by PACT, which is used as the basis of the Monte Carlo estimation of the decision variables.

10.4.1 Model Description

The PACT model studied herein used a nonlinear, intensity-based assessment where two decision variables—repair cost and downtime—were determined for the system at each hazard level and case study. A summary of the basic input information for the model is summarized in Table 10.5. Only the peak EDP values for all ground motions in each hazard level were extracted from the structural analysis as input into the PACT model.

To simplify the analysis for the purpose of this comparison, some assumptions were made when creating the PACT model for the considered building. The basement and penthouse were not included in the model, and the floor velocity for the first floor was assumed to be the same as the second floor. The non-structural quantities in the building were generated using the Normative Quantity Excel Worksheet [ATC 2012b] and were assumed to be consistent throughout all the floors except for the first floor. Results were dependent on these assumed quantities, and since an estimation of the true building contents was not attempted, the results depend on PACT normative quantity estimates. The replacement time was assumed to be five years or 1825 days. The replacement cost was estimated using the Tall Building Initiative findings for initial structural and content [Moehle et al. 2011].

10.4.1.1 Total Replacement Cost Parametric Study

Since an accurate estimation for the total replacement and core and shell replacement cost was not available, a parametric study to evaluate how changing the previous values would impact the results of the analysis. Different replacement costs were inputted into the PACT model as seen in Table 10.6.

The different cases were run through PACT, and the results had a similar pattern. Similar repair costs were required for the service-level earthquake for all the cases. For all the cases at the design-level hazard, the repair cost was set as the total replacement cost as PACT has a threshold for the repair cost. When the ratio of the repair cost and the total replacement cost reach a certain percentage, PACT automatically sets the repair cost of the building as the replacement cost: this is known as the total loss threshold. When this is reached, the repair costs are so high compared to the replacement cost that it is more beneficial for the owner to replace the building than repair it. PACT uses a default of 40% as the total loss threshold [ATC 2012a].

In this study, determining how changing the total loss threshold impacted the repair cost became a problem because it was not known how the repair cost varied between different thresholds. There were not enough hazard levels to assess how the replacement cost affected repair decisions since the threshold was reached at the design-level earthquake for all cases; determining the replacement costs could not be captured with only the two hazard levels.

Since the repair cost reached the total loss threshold at the design-level earthquake for all cases, the replacement cost was inconsequential. Case 2 (Table 10.6) replacement values were chosen for the PACT analysis since the repair cost at the service level and the Loma Prieta case study level did not reach the total loss threshold. Consequently, the influence of replacement cost was not obtained, but the design level hazard is likely to cause replacement.

Table 10.5 Basic PACT input data.

Total Replacement Cost	$352,650,000
Core and Shell Replacement Cost	$284,400,000
Replacement Time	1825 days
Realizations	500

Table 10.6 Total replacement and core and shell replacement cost [Moehle et al. 2011].

	Total Replacement	Core and Shell
Case 1	$296,100,000	$237,600,000
Case 2	$352,650,000	$284,400,000
Case 3	$409,200,000	$331,200,000

10.5 RESULTS

The model was implemented in PACT with 500 realizations, and the repair costs, downtime, and probability of unsafe placarding for the considered building were generated for both hazard levels and the Loma Prieta case study. Since PACT gives results as the probability of incurring the decision variable previously stated, the following results were taken at the median (50^{th} percentile).

10.5.1 Hazard Levels

Table 10.7 summarizes the PACT analysis results for both hazard levels. For the service level, the considered building had a repair cost of about $5.3 million and a downtime between 7 and 147 days at the 50^{th} percentile. As seen in Table 10.7, PACT uses two different repair strategies to calculate downtime: serial and parallel. The parallel repair strategy assumes repair work occurs on all floors simultaneously, while the serial repair strategy assumes repair work occurs sequentially between floors (meaning that the second floor cannot be repaired until the first floor is completely repaired). Although both of these repair strategies are unrealistic to represent the actual schedule used to repair a building, the two extremes represent reasonable bounds to the probable repair time. The probability of the building incurring unsafe placarding was less than 5% for the service-level earthquake. Most of the cost is generated by repairing the building's wall partitions, independent pendant lighting, and traction elevator, contributing $2.4 million, $0.7 million, and $1.3 million respectively, as seen in Figure 10.12. Non-structural components are expected to contribute the majority of the damage at the service-level earthquake. Although the repair cost contribution for each component varies depending on the quantity input, results are significantly dependent on the non-structural Normative Quantities mentioned previously, it serves as a basis for future comparison.

As predicted by the parametric study discussed previously, at the deign level, the building's repair cost reached the total loss threshold ratio and was approximately the same as the total replacement cost. The downtime for the design level was also very close to the total replacement time of five years, which makes sense because according to the PACT results, the whole building would be replaced instead of repaired. As shown in Figure 10.13, most of the repair cost—~$350 million—was generated by residual drift. Because quantifying the damage to the building at the design-level earthquake could not be determined since it was unclear what other components contributed to the repair cost other than residual drift, a probability assessment of the building incurring unsafe placarding was needed to clarify the contribution. As seen in Figure 10.14, the total probability of the building incurring unsafe placarding from the design-level earthquake is about 99% with welded column splices, Pre-Northridge welded unreinforced flange bolted web (WUF-B) beam-column joints, and prefabricated steel stairs as the main contributors other than residual drift.

Table 10.7 PACT results for hazard levels.

	Repair Cost	Downtime	
		Parallel	Serial
Service Level	$5,260,000	7 days	147 days
Design Level	$352,287,749	1822 days	1822 days

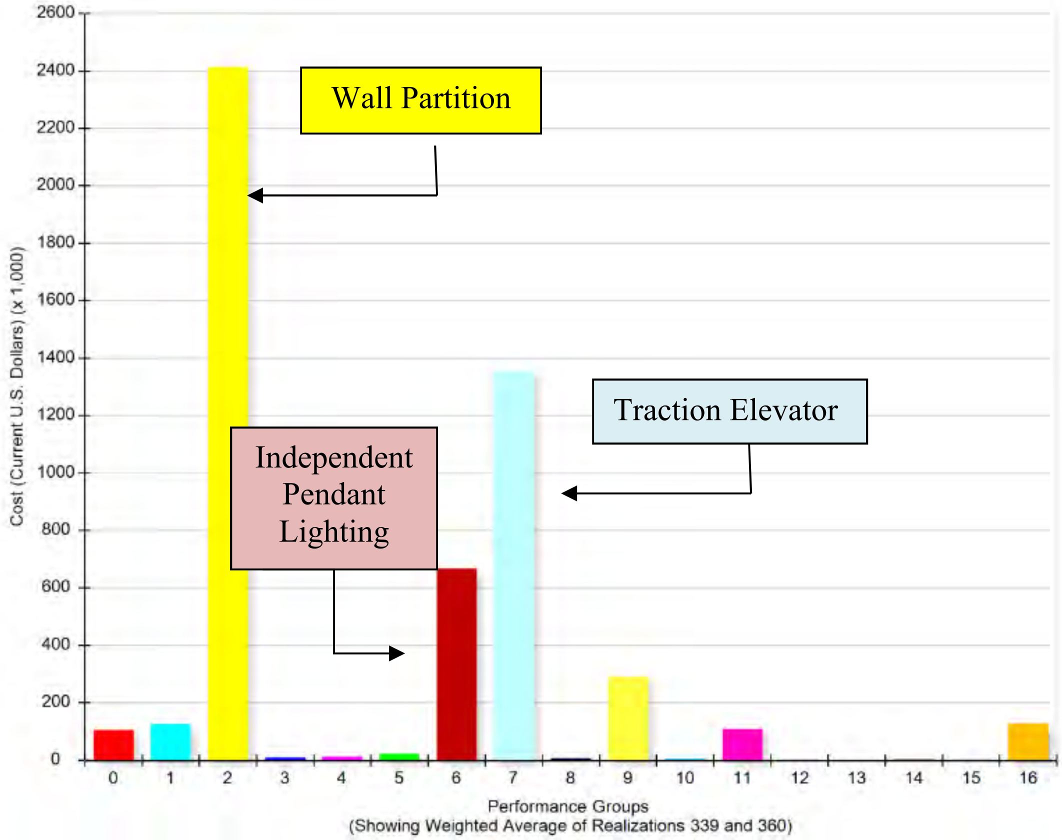

Figure 10.12 Repair cost contributions at the service-level earthquake.

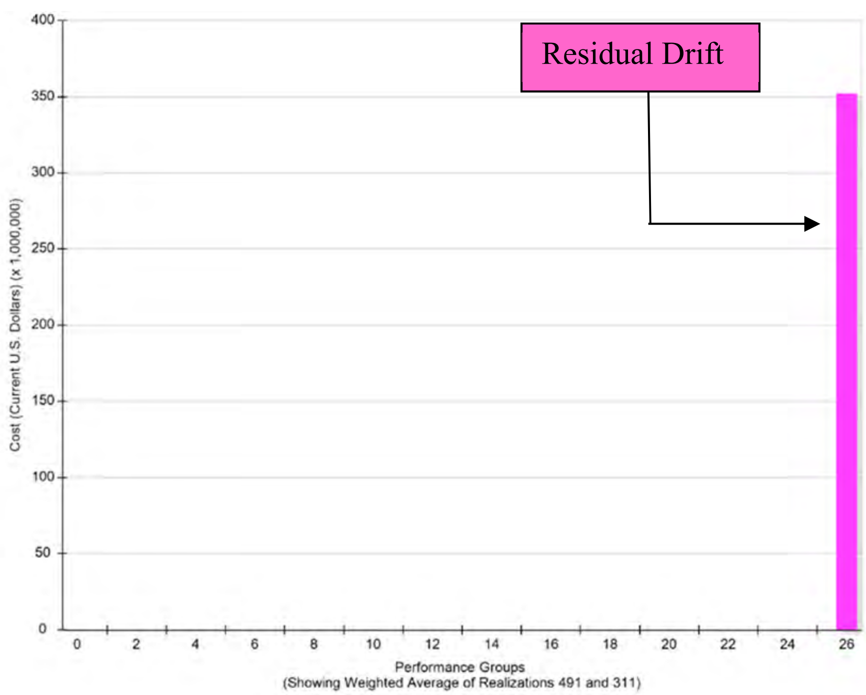

Figure 10.13 Repair cost contributions at the design-level earthquake.

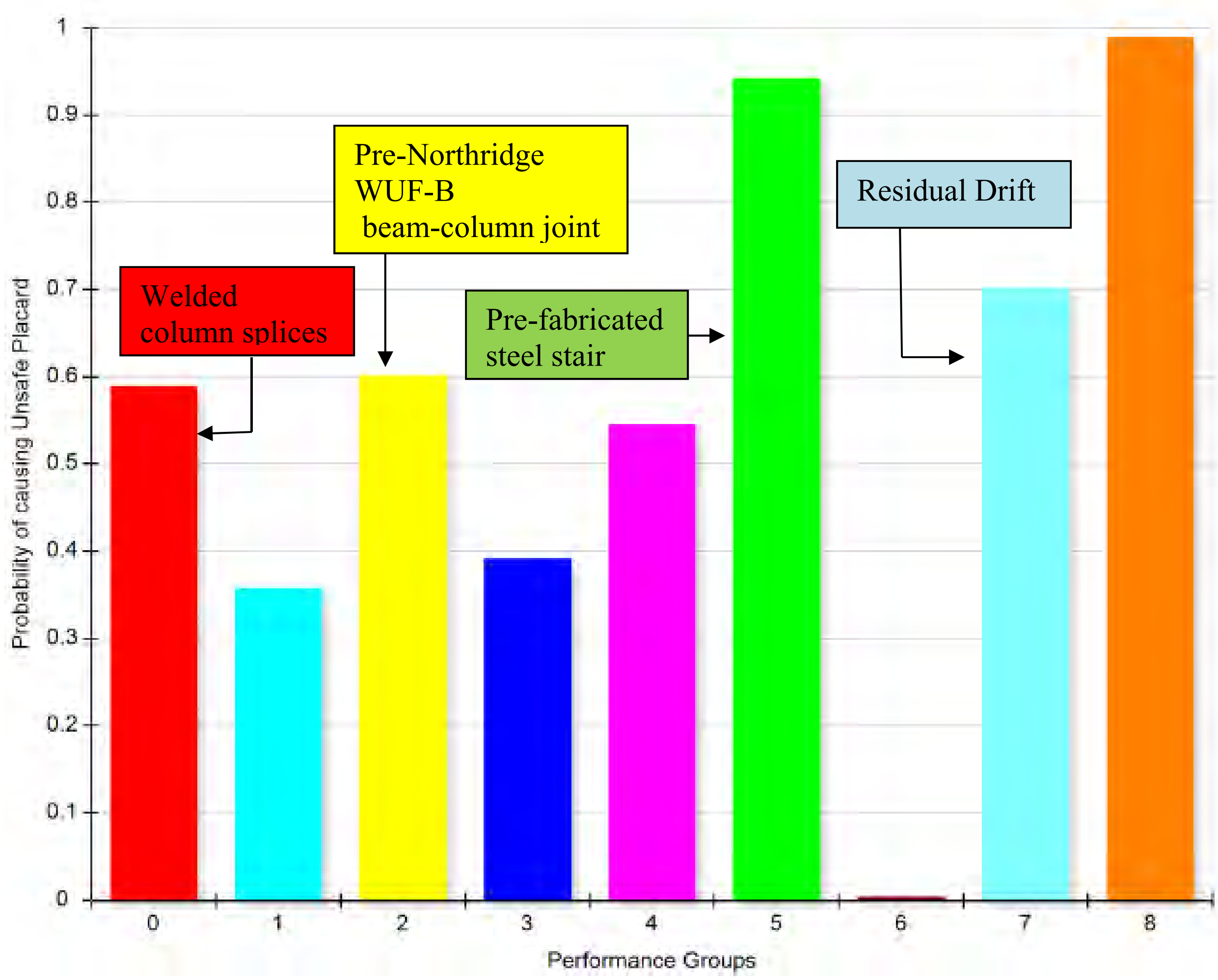

Figure 10.14 **Contributions of each performance group to unsafe placarding at the design-level earthquake.**

10.5.2 Loma Prieta Case Study

Table 10.8 contains a summary of the PACT analysis results for the Loma Prieta case study. The repair cost was about \$1.5 million, with a downtime between 2 and 42 days at the 50th percentile (see Table 10.8).The probability of incurring unsafe placarding was zero. Most of the repair cost was generated by damage to wall partitions, pre-Northridge WUF-B beam-column joints, and prefabricated steel stairs, generating \$1.45 million, \$0.04 million, and \$0.02 million, respectively, in repair costs as seen in Figure 10.15.

Table 10.8 **PACT results for Loma Prieta case study.**

	Repair Cost	Downtime	
		Parallel	Serial
Loma Prieta	$1481,578	2 days	42 days

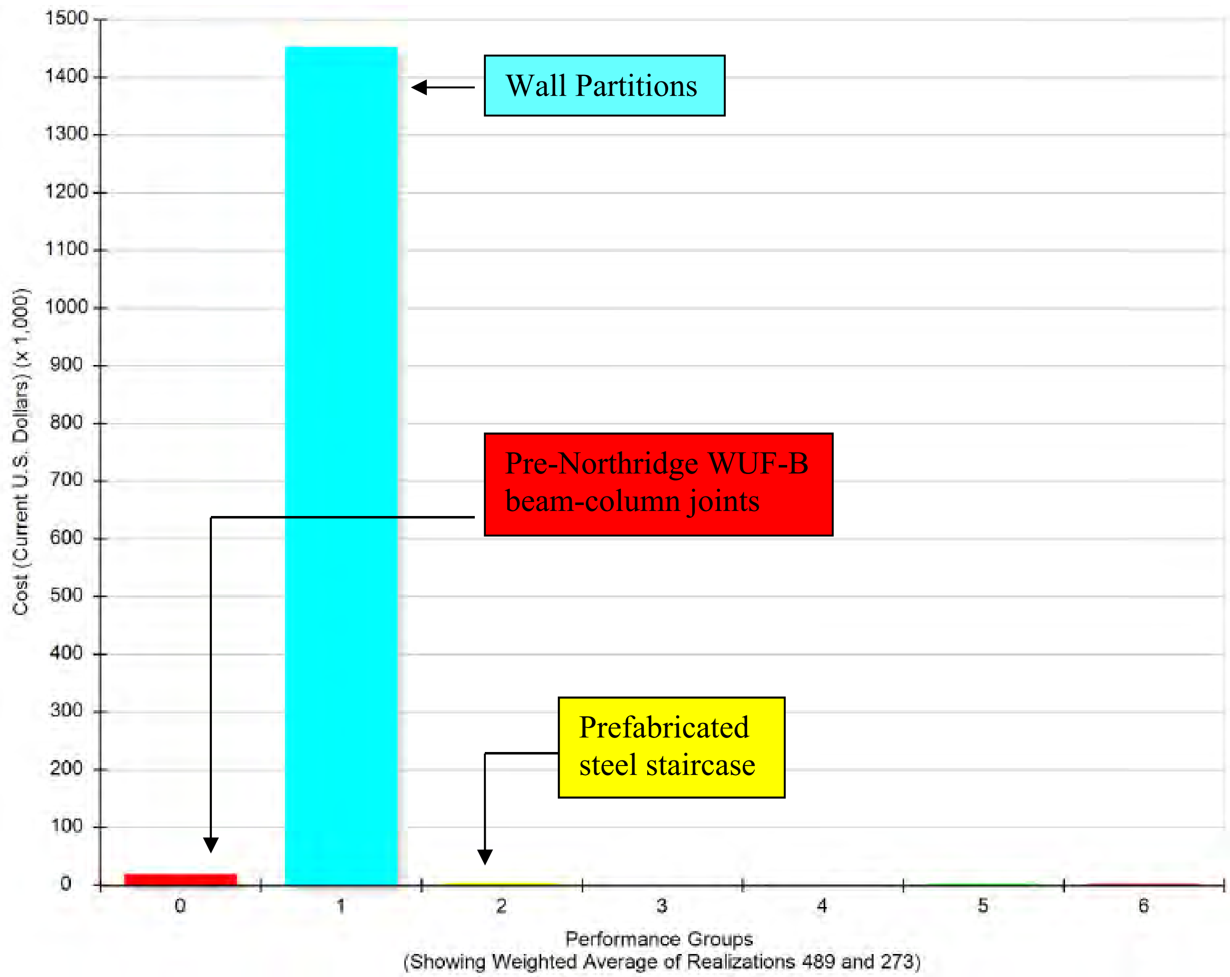

Figure 10.15 Repair cost contribution for the Loma Prieta case study.

10.6 IMPLICATIONS OF RESULTS

As seen in Figure 10.16, the repair cost for the Loma Prieta case study was significantly smaller than the repair cost at the service-level hazard, which was expected considering the Loma Prieta hazard level has an inferred return period of 16 years, while the service-level earthquake had a return period of 43 years (see Figure 10.8). The $1.5 million in damages seems high considering the low level of shaking of the Loma Prieta earthquake. However, accuracy of these costs could not be confirmed with real repair costs. Even though most of the damage came from the wall partitions and pre-fabricated steel stairs, some of the repair cost was also due to the failure of the pre-Northridge WUF-B beam-column joints, suggesting there could be damage to structural components or that the fragility functions need refinement. At the service-level hazard, the building performed poorly. Even though most of the damage came from non-structural components and the total repair cost was lower than the total loss threshold, spending $5.2 million every 43 years in repairs is inefficient. The considered building did not fare well at the design-level hazard. It incurred severe damage, including large residual drifts that damaged pre-

Northridge WUF-B beam-column joints, which resulted in a 99% probability of incurring unsafe placarding and the replacement of the building.

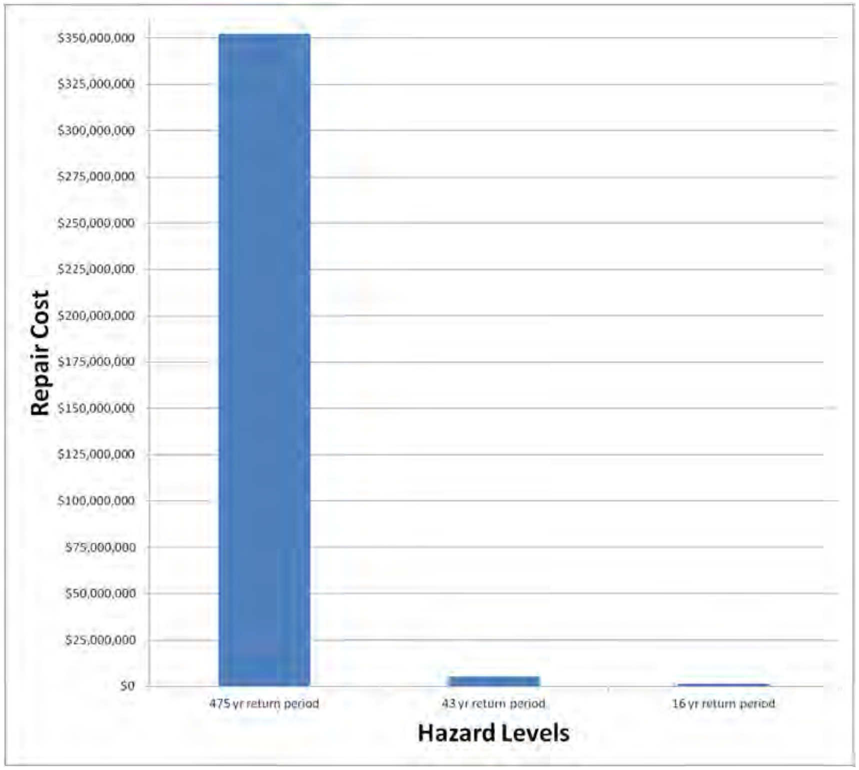

Figure 10.16 Comparison of repair costs.

10.7 CONCLUSIONS

Analysis of the results predicted that the 40-story steel MRF building performed poorly in the Loma Prieta case study and at the service-level hazard. As stated before, the Loma Prieta case study was adopted to gauge how well PACT estimates damages and downtime. The considered building had $1.5 million in repair costs and an estimated downtime between 2 and 42 days. Without being able to compare the results to actual data from the 1989 Loma Prieta earthquake, this repair cost was $1.63 per square foot. At the service-level earthquake, the building had a repair cost of about $5.2 million, with a downtime between 7 and 147 days with most of the damage resulting from non-structural components. At the design-level hazard, the considered building experienced large residual drifts and many structural components were damaged. Damaged components included welded column splices, pre-Northridge WUF-B beam-column joints, and prefabricated steel stairs, culminating in a high repair cost of about $352 million with a downtime of 5 years, which was the default replacement value. Therefore, the tall steel MRF building studied in this paper under earthquake shaking levels consistent with the design-level earthquake and above is expected to generate high repair costs near the total loss threshold and will likely need to be replaced. In order to reduce post-earthquake repair costs and downtime, structural retrofits should be considered. Similarly, at the service-level earthquake, vulnerable non-structural components contribute heavily to the overall repair costs; modifications to these components could also reduce costs.

PACT results stated previously were affected by the replacement cost parametric study mentioned before because even though a replacement cost was chosen from the parametric study, it was still very difficult to estimate a true replacement cost due to the many unknown variables and the inability to determine how repair costs varied between different total loss thresholds. The variables include the structural system, design basis (code-based or performance-based), number of stories, anticipated rents, insurance, and economic outlook for the region. Similar repair costs at the service-level hazard were reached for all the cases studied, and at the design-level hazard, the total loss threshold was always reached regardless of the replacement cost. This meant that at the design-level hazard, the damage was so extensive that the building would likely need to be replaced. However, at a level of shaking between the service and design level, the replacement cost remains relevant as a higher replacement cost gives a larger allowable repair cost for the same total loss threshold. So there is a level of shaking, not investigated, that would trigger replacement with a less expensive building, but not the more expensive building. Therefore, there were not enough hazard levels to assess the importance of the replacement cost in affecting repair decisions since the threshold was always reached at the design level. Therefore, verification of PACT through additional case studies is recommended.

PACT results also heavily relied on the non-structural quantities assumed in the Normative Quantities used, and since an estimation of the true building contents was not attempted, the results relied on PACT to include realistic estimates. These quantities produced results that were reasonable, but since these values are generic, the quantities must still be reviewed and changed to match the considered building's occupancy at every floor before input into the PACT model. There was no attempt to change the Normative Quantities and assess the impact on the results. Therefore, further case studies should be done to understand these effects.

Without any data to compare, the PACT software gave realistic repair costs and fared well. Problems encountered with the PACT software included input of the non-structural and structural components, memory usage, and limited realizations. To input the different quantities of the building, all of the components must be chosen first from different performance groups and then the quantity of each component in each direction is inputted into every floor. This method is very inefficient when the considered building has 40 stories. A recommendation would be to develop a means to allow for the uploading of data containing all the building's components and quantities instead of having to input every component one by one. During the PACT analyses, a memory drain in the software severely limited its capabilities. Consequently, this limited the number of realizations possible to 500. The more realizations that are used, the more accurate the results that PACT generates. Even though 500 is the typical number of realizations, more realizations could not be completed to assess the adequacy of this number for this building.

This assessment represents the initial stages to a more extensive body of work that is being undertaken by the Tall Building Initiative-2. The ultimate goal of this research is to develop performance based seismic design guidelines to retrofit existing tall steel moment frame buildings. Future work includes:

- Comparing the Loma Prieta case study results with typical repair cost, downtime, and damage types for tall buildings and assess building response
- PACT economic loss analysis for non-ductile connections and upgraded structural systems

10.8 ACKNOWLEDGMENTS

I would like to thank my mentors, Dr. Matt Schoettler and Dr. Jiun-Wei Lai, for all of their time, guidance, and patience throughout this project. Thank you to Lorena Rodriguez, my co-worker, who encouraged me every step of the way. I would also like to thank my faculty advisor, Professor Stephen Mahin, for his guidance and support. Special thanks goes to PEER Outreach Director, Heidi Tremayne, for organizing the internship and giving me the opportunity to be part of this amazing experience. Finally, I would like to thank my fellow interns for their support and guidance throughout this project. This project was supported by the National Science Foundation and the Pacific Earthquake Engineering Research Center at the University of California, Berkeley.

10.9 REFERENCES

ATC (2012a). *Seismic Performance Assessment of Buildings Volume 1 – Methodology*, Applied Technology Council, Redwood City, CA.

ATC (2012b). *Seismic Performance Assessment of Buildings Volume 3 – Supporting Electronic Materials and Background Documentation*, Applied Technology Council, Redwood City, CA.

Anderson J.C. et al. (1995). Technical report: Case studies of steel moment frame building performance in the Northridge earthquake of January 17, 1994. *Report No. SAC-95-07*, SAC Joint Venture, Sacramento, CA.

Foutch D.A. (2000). *State of the Art Report on Performance Prediction and Evaluation of Steel Moment-Frame Buildings, FEMA-355F*, Federal Emergency Management Agency, Washington, D.C.

Lee K., Foutch D.A. (2002). Seismic performance evaluation of pre-Northridge steel frame buildings with brittle connections, *J. Struct. Eng.* 128: 546–555.

Mahin S.A., Terzic V., Nagy C. (2012). Using performance-based earthquake evaluation methods to assess the relative benefits of different structural systems, *Proceedings, 9th International Conference on Urban Earthquake Engineering/ 4th Asia Conference on Earthquake Engineering*, Tokyo Institute of Technology, Tokyo, Japan.

McKenna F., Fenves G.L., Scott M.H., Jeremic B. (2000). *Open System for Earthquake Engineering Simulation (OpenSees),* Pacific Earthquake Engineering Research Center, University of California, Berkeley, CA.

Moehle J., Bozorgnia Y., Jayaram N., Jones P., Rahnama M., Shome N., Zareian F. (2011). Case studies of the seismic performance of tall buildings designed by alternative means, *PEER Report 2011/05*, Pacific Earthquake Engineering Research Center, University of California, Berkeley, CA.

OpenSHA. *A Developing Community-Modeling Environment for Seismic Hazard Analysis,* viewed Aug. 9, 2013, http://www.opensha.org/.

SkyscraperPage.com.(n.d.). Retrieved September 18, 2013, from http://skyscraperpage.com/database/state/14.

Tall Buildings Initiative (2010). Guidelines for performance-based seismic design of tall buildings, *PEER Report 2010/05*, Pacific Earthquake Engineering Research Center, University of California, Berkeley, CA.

11. Seismic Performance of an Existing Tall Steel Building

Lorena Rodriguez

ABSTRACT

As a result of the 1994 Northridge earthquake, the performance of steel moment resisting frame (MRF) buildings designed under past design codes became a concern. A primary concern is that drift limits were not imposed on many buildings constructed between the 1960s and 1970s, which greatly impacts their seismic performance. Furthermore, testing and analyses made on steel MRF buildings have shown that beam-to-column connections did not perform as expected; they failed in a brittle manner. Consequently, pre-Northridge MRF buildings may not have acceptable performance during future earthquakes. Organizations, like the SAC Joint Venture, have investigated this issue for the purpose of minimizing post-earthquake damage and repairs. Likewise the Tall Building Initiative 2 (TBI-2) was formed to develop performance-based seismic design guidelines for existing tall buildings. As part of TBI-2, the Pacific Earthquake Engineering Research (PEER) Center is currently working on a project that investigates the economic advantage gained by retrofitting MRF buildings constructed between the 1960s and 1980s. The approach used in this assessment consists of a performance-based earthquake engineering (PBEE) methodology. PBEE is composed of four stages: hazard analysis, structural analysis, damage analysis, and loss analysis. For the purpose of this project, this report focuses on the structural analysis phase. To this end, the seismic performance of a 40-story building located in downtown San Francisco was examined. Results show that there are large concentrations of drift demands at the design level, and the response of the building under earthquake shaking levels consistent with the MCE is not sustainable. Ongoing research and further testing is required to establish performance-based seismic evaluation guidelines and a retrofit framework.

11.1 INTRODUCTION

The seismic performance of buildings constructed between the 1960s and 1980s was analyzed in this investigation because they were designed for demands lower than what the current design code requires. Structures more than 20 stories tall were assessed because of limited investigations performed on high-rise buildings. Structures built in this era have large story drift demands since drift limits were not imposed. Furthermore, they have connections that are potentially brittle. In the 1994 Northridge earthquake many beam-to-column connections experienced brittle fracture [Mahin 1997]. Thus, questions have been raised about the performance of buildings completed under historic design codes. The scope of this project is to investigate the economic advantage gained by retrofitting steel moment resisting frame (MRF) buildings in the 20- to 40-story range by using a performance-based earthquake engineering (PBEE) methodology. By upgrading these structures with dampers, braces, or seismic isolation, post-earthquake damage and repairs may be significantly reduced. This report presents the structural response of the as-built building located in downtown San Francisco as the baseline for comparison with future analyses of a model with upgrades to the structural system.

The objectives are to analyze the response of the as-built building using nonlinear time history analysis, and to summarize the response quantities for input into the Performance Assessment Calculation Tool (PACT) [ATC 2012] for economic loss estimates. The loss analysis can be found in another report included within [Quinonez 2013].

11.2 BACKGROUND

Why should the seismic performance of older buildings be analyzed and why should they be retrofitted? To answer these questions and assess the significance of this project, this section will present some background information on historic building codes, the Northridge earthquake, and existing tall buildings.

11.2.1 Historic Building Codes

Over the years the Uniform Building Code (UBC) has been updated in order to improve the performance of structures and thus promote public safety. Due to outdated standards in historic building codes, the performance of buildings constructed prior to 1976 should be assessed. Major changes in the codes are highlighted in the tables in the following pages. As seen in Table 11.1, there were no seismic requirements on steel MRF until 1970. Local buckling and connection strength requirements were first incorporated into the UBC in 1970. Some requirements that were overlooked between 1958 and 1973 include the strength of column panel zones and strong-column-weak beams. These requirements were first introduced in 1988 [Lee and Foutch 2002].

One of the most important parameters in the UBC for controlling structural damage is the drift limit for seismic loads. As seen in Table 11.1 there were no drift limitations prior to 1976. During this period drift control was set by the design engineer. Drift limitations largely control member sizes. If disregarded, beams will perhaps be less strong and stiff, this impacting the structural response. Furthermore, as noted in Table 11.2, the design base shear has increased over the years. Drift limitations and the design base shear are important factors in design because they strongly affect the expected drift demand [Foutch 2000].

Table 11.1 Summary of key specifications from the UBC, years 1958 to 1964 [Foutch 2000].

Seismic Requirements	1958 UBC	1961 UBC	1964 UBC
Allowable stress	All allowable stresses can be increased 1/3 when considering earthquake forces.	All allowable stresses can be increased 1/3 when considering earthquake forces.	All allowable stresses can be increased 1/3 when considering earthquake forces.
Live load reduction	allowed	allowed	allowed
Seismic zone (LA)	Zone No. 3	Zone No. 3	Zone No. 3
Base shear	F=CW C=Horizontal force factor	V=ZKCW $C=0.05/T^{1/3}$ - K=0.67 for MRF	V=ZKCW $C=0.05/T^{1/3}$ - K=0.67 for MRF
Period (T)		$T=0.05hn/D^{1/2}$ T=0.1N for MRF	$T=0.05hn/D^{1/2}$ T=0.1N for MRF
Distribution of Lateral Forces		V=Ft+ΣFi Ft=0.1*V	V=Ft+ΣFi $Ft=0.004V(hn/D)^2$
Story drift limit		Drift shall be considered in accordance with accepted engineering practice	Drift shall be considered in accordance with accepted engineering practice
ADS STEEL PART			
Bending	20,000psi, when (Ld/bt)<600	20,000psi, when (Ld/bt)<600	$Fb=0.66Fy, (13330/Fy^{1/2}$ psi)
Axial + bending	$17{,}000-0.485(L/r)^2$ when L/r<120	$17{,}000-0.485(L/r)^2$ when L/r<120	$\frac{f_a}{F_a}+\frac{C_m f_b}{(1-f_a/_{F'_e})F_b}\leq 1.0$
Steel MRF requirements	- no seismic regulation	- no seismic regulation	- no seismic regulation

Table 11.2 Summary of key specifications from the UBC, years 1967 to 1976 [Foutch 2000].

Seismic Requirements	1967 UBC	1970 UBC	1973 UBC	1976 UBC
Allowable stress	All allowable stresses can be increased 1/3 when considering earthquake forces.	All allowable stresses can be increased 1/3 when considering earthquake forces.	All allowable stresses can be increased 1/3 when considering earthquake forces.	All allowable stresses can be increased 1/3 when considering earthquake forces.
Live load reduction	allowed	allowed	allowed	allowed
Seismic zone (LA)	Zone No. 3	Zone No. 3	Zone No. 3	Zone No. 4
Base shear	V=ZKCW $C=0.05/T^{1/3}$ - K=0.67 for MRF	V=ZKCW $C=0.05/T^{1/3}$ - K=0.67 for MRF	V=ZKCW $C=0.05/T^{1/3}$ - K=0.67 for MRF	V=ZIKCSW $C=1/(15*T^{1/2})$ - K=0.67 for SMRF -S=coefficient for site-structure resonance
Period (T)	$T=0.05hn/D^{1/2}$ T=0.1N for MRF	$T=0.05hn/D^{1/2}$ T=0.1N for MRF	$T=0.05hn/D^{1/2}$ T=0.1N for MRF	$T = 2\pi\sqrt{(\Sigma\omega_i\delta_i^{\ 2}) \div (g\Sigma f_i\delta_i)}$ $T=0.05hn/D^{1/2}$ T=0.1N for MRF
Distribution of Lateral Forces	V=Ft+ΣFi $Ft=0.004V(hn/D)^2$	V=Ft+ΣFi $Ft=0.004V(hn/D)^2$	V=Ft+ΣFi $Ft=0.004V(hn/D)^2$	V=Ft+ΣFi Ft=0.07V
Story drift limit	Drift shall be considered in accordance with accepted engineering practice	Drift shall be considered in accordance with accepted engineering practice	Drift shall be considered in accordance with accepted engineering practice	Story drift ≤0.005 Drift = displacement*(1/K)
ADS STEEL PART				
Bending	$Fb=0.66Fy$, ($13330/Fy^{1/2}$ psi)	$Fb=0.66Fy$, ($52.2/Fy^{1/2}$)	$Fb=0.66Fy$, ($52.2/Fy^{1/2}$)	$Fb=0.66Fy$, ($65/Fy^{1/2}$)
Axial + bending	$\frac{f_a}{F_a} + \frac{C_m f_b}{(1 - {f_a}/{F'_e})F_b} \leq 1.0$	$\frac{f_a}{F_a} + \frac{C_m f_b}{(1 - {f_a}/{F'_e})F_b} \leq 1.0$	$\frac{f_a}{F_a} + \frac{C_m f_b}{(1 - {f_a}/{F'_e})F_b} \leq 1.0$	$\frac{f_a}{F_a} + \frac{C_m f_b}{(1 - {f_a}/{F'_e})F_b} \leq 1.0$
Steel MRF requirements	- no seismic regulation	-connections are able to develop full plastic capacity -local buckling => satisfy plastic design	-connections are able to develop full plastic capacity -local buckling => satisfy plastic design	-connections are able to develop full plastic capacity -local buckling => satisfy plastic design

11.2.2 Northridge Earthquake

Welded steel MRF were incorporated into design in the 1960s because they were considered to be one of the most ductile systems. This was partly due to the belief that steel MRF buildings were capable of resisting earthquake induced structural damage through their ductile response, and if any damage were to occur it would be limited to ductile yielding of members and connections [Foutch 2000]. However, the Northridge earthquake of 17 January 1994 proved that ductile systems require well-detailed connections to enable ductile response.

In response to the 1994 Northridge earthquake, MRF buildings did not collapse and it was believe that the buildings only experienced limited structural damage. Damage was not visible at first sight, but with removal of nonstructural components it became evident that beam-to-column connections failed in a non-ductile manner [Anderson et al. 1995]. Some buildings that experienced ground shaking less severe than the design level were also observed to have brittle failure connections [Foutch 2000].

Column fracture occurred in many buildings at the beam-column joint. Observations made on these connections indicated that fracture typically initiated at the complete joint penetration (CJP) weld and then progressed through the column flange material behind the CJP weld as illustrate in Figure 11.1 [Foutch 2000]. Fracture also occurred at the panel zone (Figure 11.2). Research and testing of moment frame connections has revealed that weak column-strong beam configurations, soft story behavior, partial joint column splice weld fracture, and ineffective welding inspection were present in pre-Northridge designs, according to Forell/Elsesser Engineers (http://www.forell.com/pre-northridge/).

Figure 11.1 Beam-to-column joint fracture [Foutch 2000].

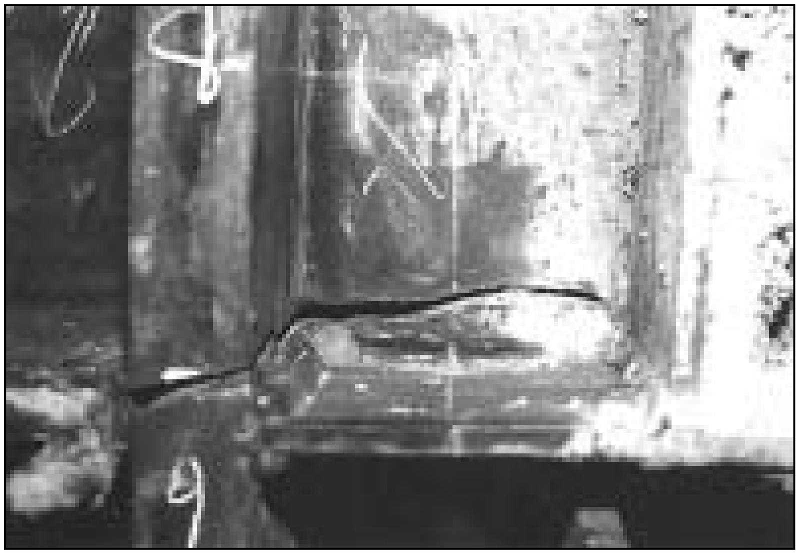

Figure 11.2 **Column fracture at the panel zone [Foutch 2000].**

11.2.3 Existing Tall Buildings

Existing tall buildings are a concern because design guidelines in the U.S. are intended for low to mid-rise structures [EPICentre 2012], with only limited guidelines that address the complex dynamic behavior of existing tall buildings. The SAC steel project assessed the performance of buildings up to 20 stories tall. However, not many detailed analyses have been performed on buildings that are over 20 stories that investigate their performance due to large distant or moderate near-source earthquakes [Krishnan et al. 2006]. A recent study performed by Almufti et al. [2002] examines the seismic collapse risk of a prototype 40-story existing building in San Francisco using a modern performance-based assessment. Within their findings, it was concluded that the performance of tall steel moment frame buildings constructed in the 1970s are expected to undergo very large deformations at the MCE level [Almufti et al. 2002].

Alternatives to the guidelines in current codes have been recommended. Many of these have been published including the *Guidelines for Seismic Design of Tall Buildings*, created by the Pacific Earthquake Engineering Research Center (PEER), and the *Next Generation Performance Based Seismic Design Guidelines*, created by the U.S. Federal Emergency Management Agency [EPICentre 2012]. However, there are no specific requirements for existing tall buildings. To improve the reliability of these high-rise structures, guidelines should be adopted and the retrofit of existing buildings considered.

11.3 METHODOLOGY

To address the issues highlighted in the background section of this report, the Tall Building Initiative 2 (TBI-2) was formed with the objective to develop performance-based seismic design guidelines for existing tall buildings. The PBEE methodology developed by PEER was used to investigate the economic advantage of retrofitting existing steel MRF buildings. A PBEE analysis works in four stages, as illustrated in Figure 11.3. In the first stage the seismic hazard at the facility site is evaluated. Ground-motion time histories are produced with an appropriate intensity measure for the various hazard levels. Nonlinear time-history analyses are performed in the structural analysis phase to calculate the response of the facility to a ground motion of a given intensity measure in terms of the following parameters: drift, acceleration, and ground failure. In the damage analysis stage these parameters are used with component fragility functions to determine the measures of damage. With the given damage, repair costs, operability, downtime, and potential casualties are determined in the loss analysis phase [Porter 2003].

As highlighted in Figure 11.3, this report will focus on the structural analysis stage. In this phase, the seismic performance of a 40-story building is evaluated using non-linear time history analysis and the Open System for Earthquake Engineering Simulation (OpenSees) software [McKenna et al. 2000]. The procedure used in this assessment consisted of selecting a prototype building that met the targeted number of stories, obtaining structural properties, generating the simplified numerical model, analyzing the structural model, and compiling generated results.

Structural details and dimensions were retrieved from the building's plans. Structural details extracted from the plans included beam, girder, and column sizes; material properties; connection details; and general notes. This information was obtained from the San Francisco Department of Building Inspection (DBI). Unfortunately, the original plans were not accessible, so they were viewed on microfiche through a reader similar to the one illustrated in Figure 11.4.

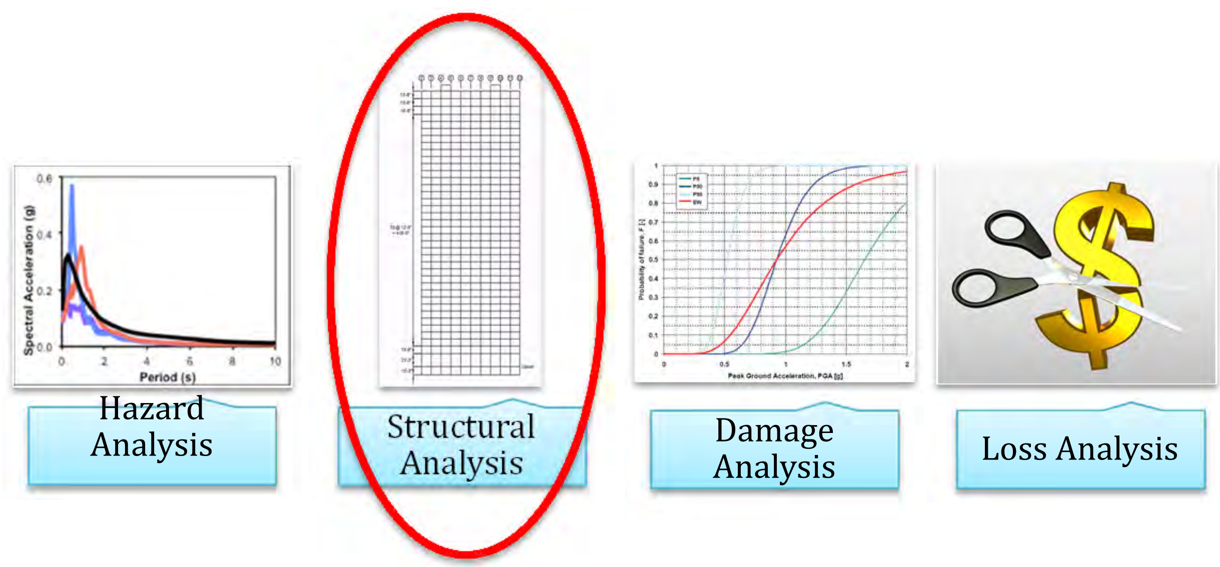

Figure 11.3 Four stages in the performance-based earthquake engineering (PBEE) methodology.

Figure 11.4 Microfiche reader [Altobello 2010].

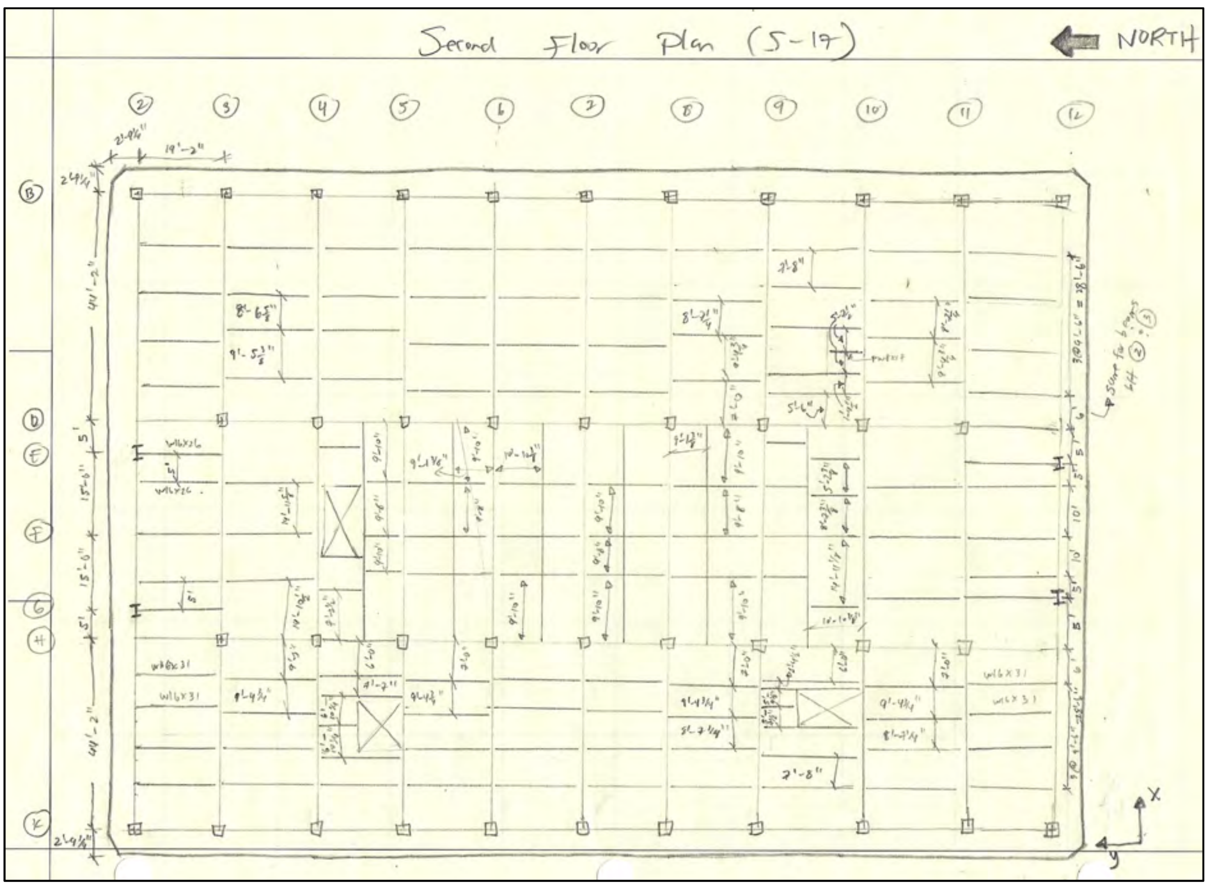

Figure 11.5 Sketch of the 2nd floor plan.

This process was long and tedious since the DBI does not permit flash photography or tracing of the plans. Thus, beam, girder, and column sizes were organized in an Excel spreadsheet while dimensions, floor plans, and connection details were neatly sketched. An example of a sketch made at the DBI is illustrated in Figure 11.5. It took a week to obtain all of the necessary information to then create the model of the building.

Once all of the required information was obtained from the structural plans, the excel spreadsheet that included the element sizes was organized in a specific format for ease of access. This information, as well as the geometry of the building, was imported to script files created by Dr. Matt Schoettler (project mentor and postdoctoral researcher at PEER). The scripts generated were used as input for OpenSees to perform gravity and non-linear time history analysis. After completion of the simulations, peak accelerations, velocities, story drifts, and residual displacements were analyzed and summarized for input into PACT.

11.4 STRUCTURAL SYSTEM

11.4.1 Building Description

The 40-story steel MRF building analyzed in this investigation is located in downtown San Francisco. This model is based on typical details found in the prototype building. This building consists of 3×10 bays and is rectangular in plan, as seen in Figure 11.6. The building is198 ft-4 in. long, 128 ft-4 in. wide, and 496 ft-11 in. tall. A penthouse is located on the roof, between lines H and D in the north-south direction and between line 5 and 9 in the east-west direction (Figure 11.7). All story heights are relatively the same throughout the building with the exception of the first floor, where first floor is 23 ft-3 in. high.

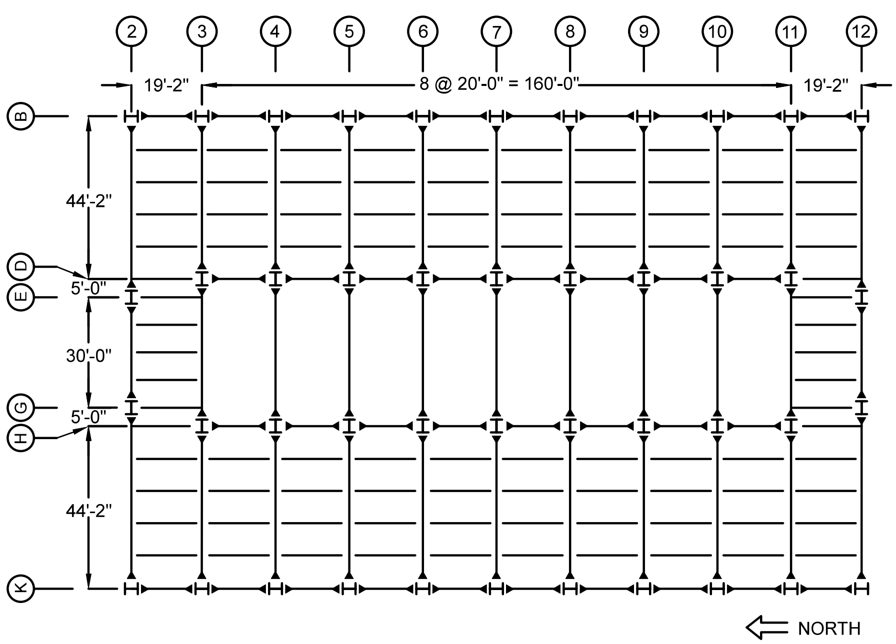

Figure 11.6 Typical floor plan of the 40-story building.

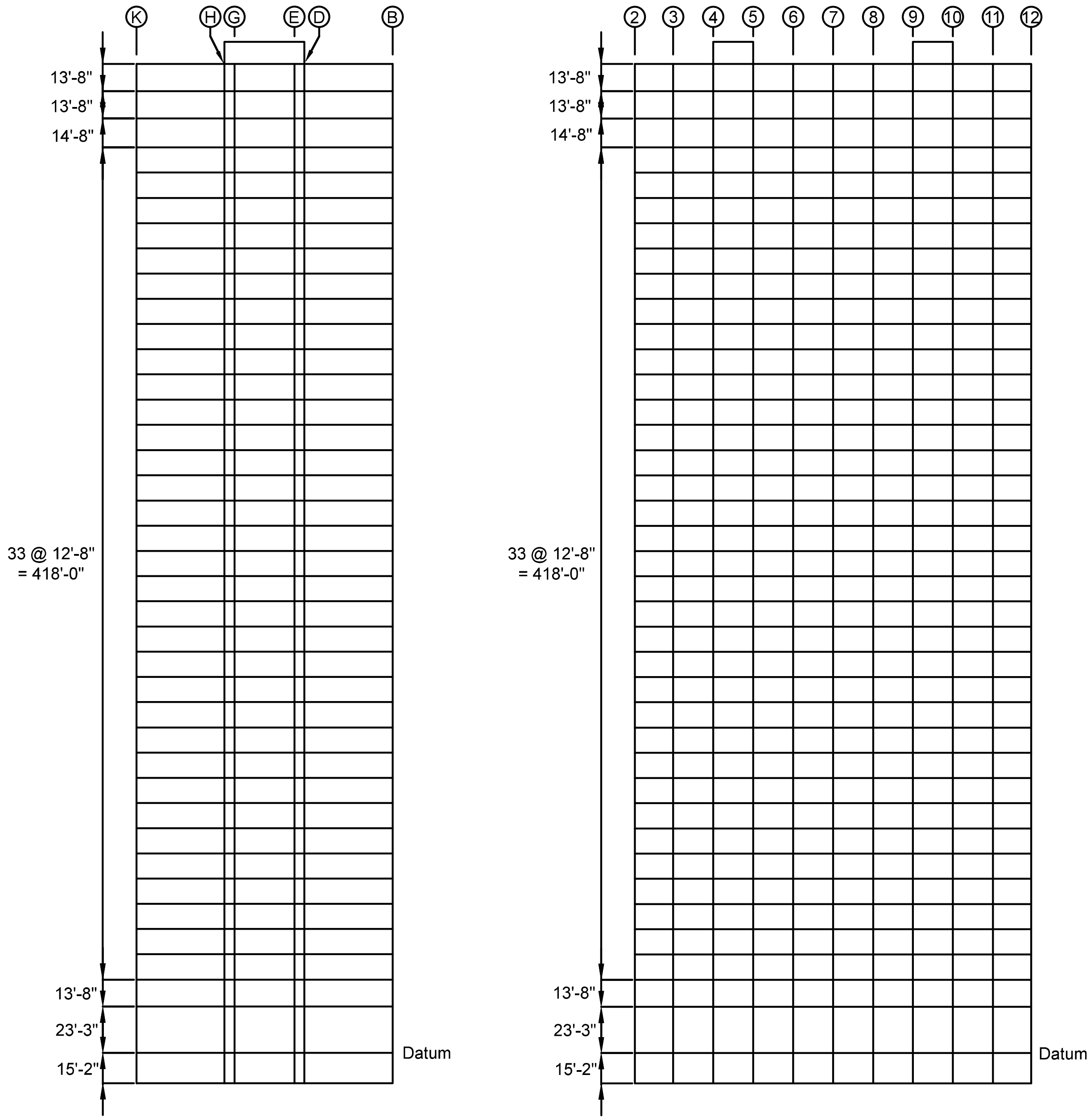

Figure 11.7 Elevation views of the north-south (left) and east-west (right) directions.

The typical floor plan is illustrated in Figure 11.6. All of the floors have the same configuration except for the 38th floor**.** The core area details of the floor (between lines H and D and between lines 3 and 11) are not included in the typical floor plan, but can be retrieved from the structural plans if desired. An example of the details contained in the core area is illustrated in the sketch of the 2nd floor (Figure 11.5).

The slab thickness is approximately 6 ft-1/4 in. throughout the floors, except on the 37th floor here the slab thickness is 3 ft-1/4 in. Girder sizes range from a maximum of W36×260 at the first floor to a minimum of W16×26 at the roof. The columns are typically made from ASTM A36 steel, except for all the columns below the sixth floor, which are made from ASTM A572 Grade 42 steel.

11.4.2 Cross Sections

The cross section of the columns varied along the building. Columns were 496 ft-11 in. tall. Two different cross section types are illustrated in Figure 11.8: (1) built-up box columns are located between the first and third floors; and (2) H-columns and wide flange columns span the rest of the building. The orientation of the H-columns can be seen in the typical floor plan of the structure (Figure 11.6). Some of the floors used special beams where the depth of these beams is larger than that of the wide flange beams. The cross section of these special beams is illustrated in Figure 11.8 (3).

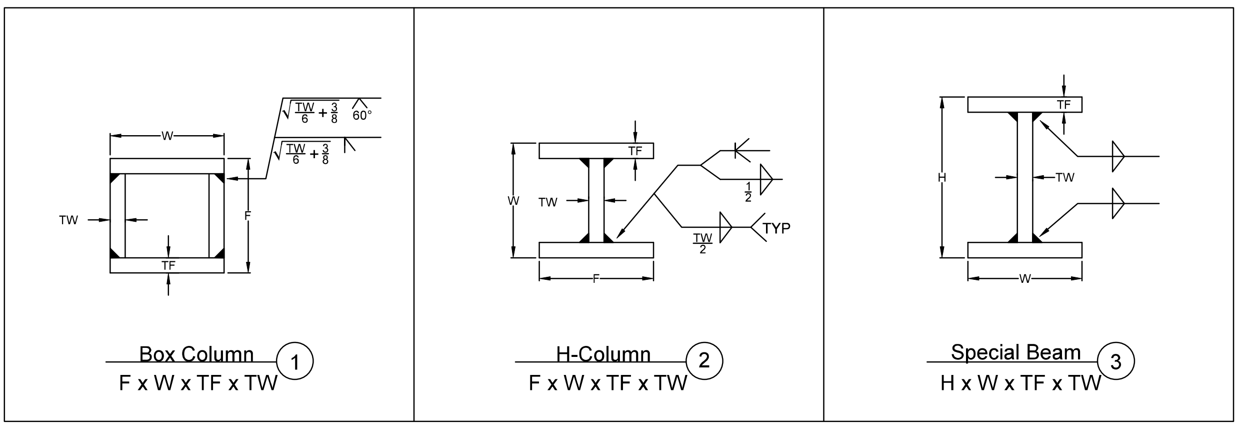

Figure 11.8 Typical details of different cross-sections types: (1) box column, (2) H-column, and (3) special beam.

11.4.3 Connection Details

The term riser was used to designate the spliced column sections. The building consisted of 16 risers, which are assembled by splice connections. Columns splices were typically located 5 ft above the finished floor and typically span every three floors. Typical details of the splice connections are shown in Figure 11.9. From the connection details it is seen that shear tabs were welded and used for erection.

Girders and columns are joined by moment connections, as illustrated in Figures 11.10 and 11.11. Typical moment connection details for H and WF columns are shown in Figure 11.10. Typical moment connection details for box columns are shown in Figure 11.11. Note that in both of these connection details continuity plates serve as internal diaphragms and shear tabs for erection.

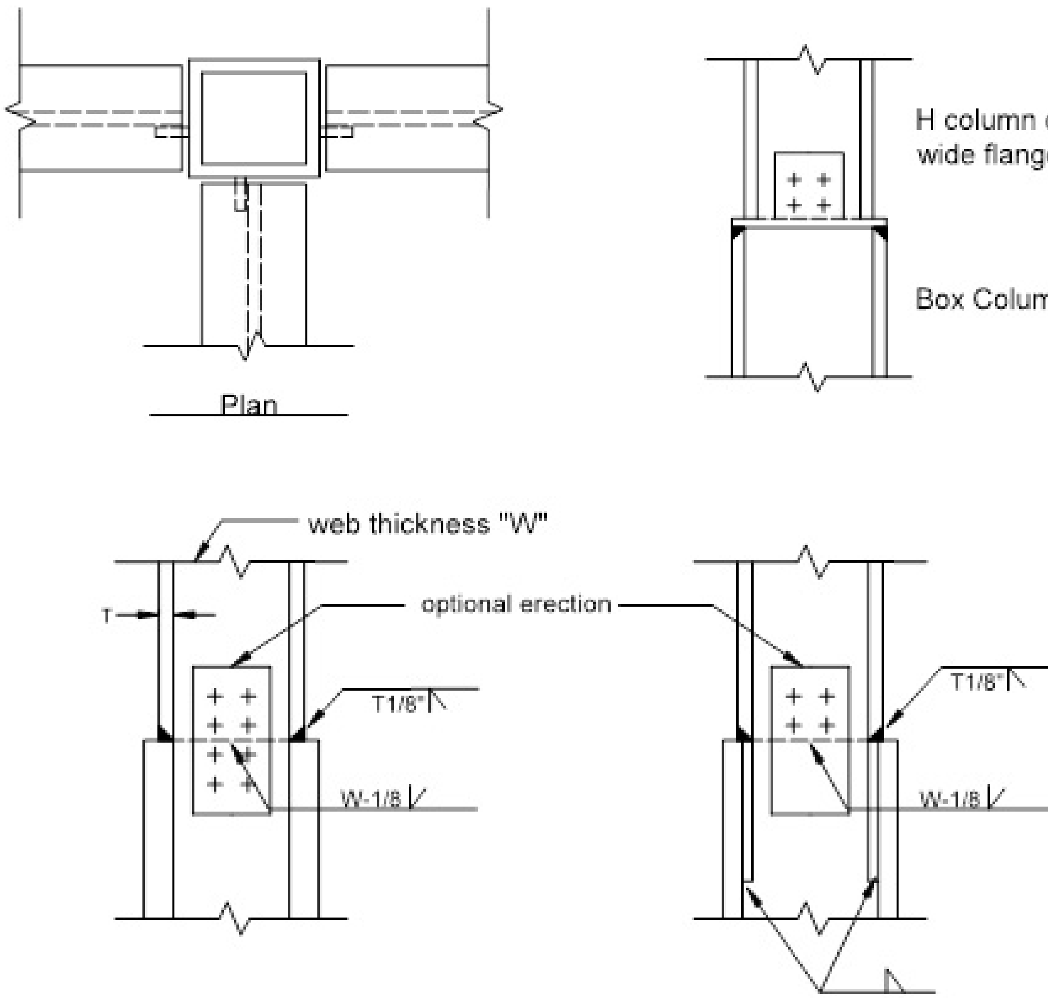

Figure 11.9　　Typical splice connection details.

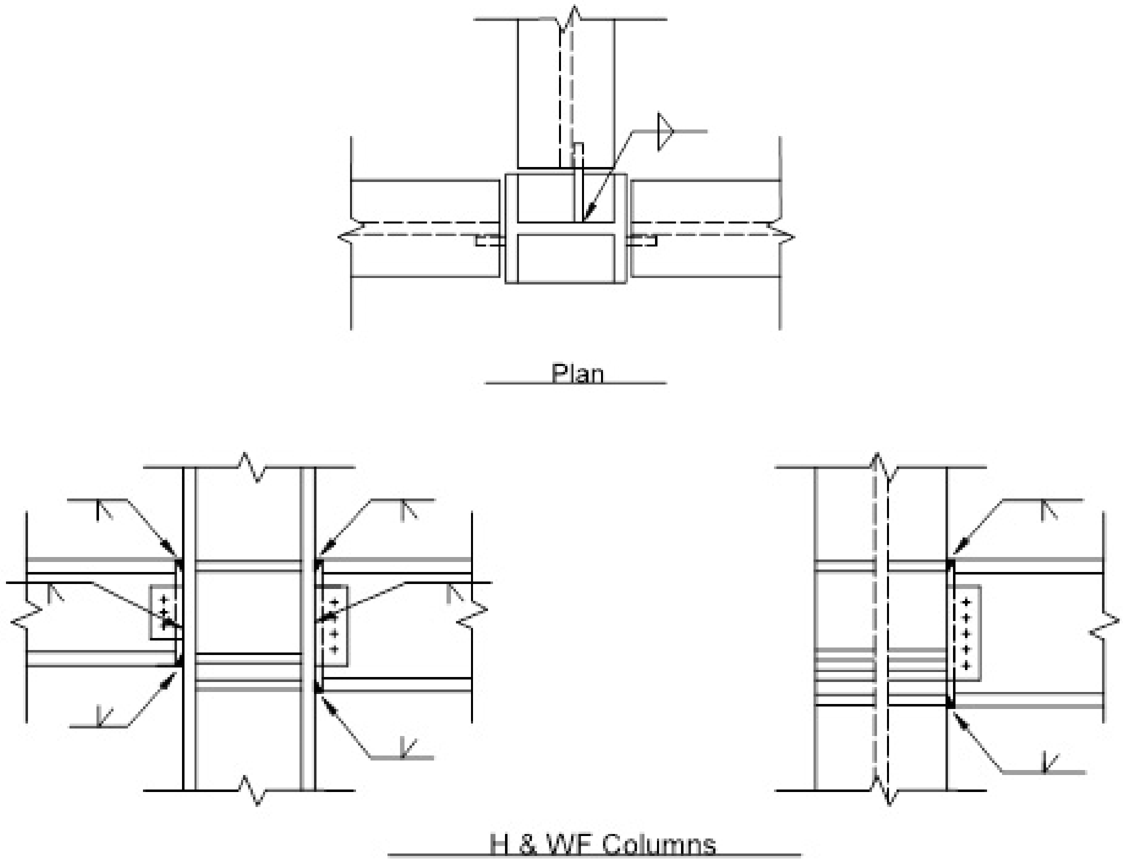

Figure 11.10 Typical girder to column connection details for H and wide flange (WF) columns.

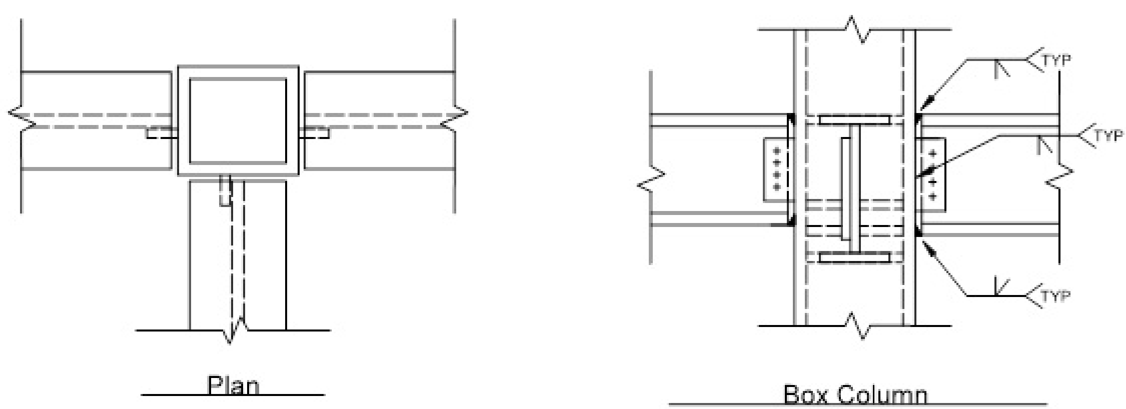

Figure 11.11 Typical girder to column connection details for a box column.

11.5 MODEL DESCRIPTION

Once all of the structural information was extracted from the building's plans, the script files were imported into OpenSees to generate the model of the building. For simplicity the foundation, walls, ramps, and nonstructural components were disregarded. Other simplifications and assumptions used in the nonlinear time history analysis are discussed in the following section.

11.5.1 Assumptions

Many assumptions were made when creating the ductile model of the 40-story steel MRF building, illustrated in Figure 11.12. Simplifications were made to facilitate the analysis and calculation time. To simplify the model, the basement was not included. As shown in Figure 11.13, a fixed-base building that begins at the ground level was analyzed.

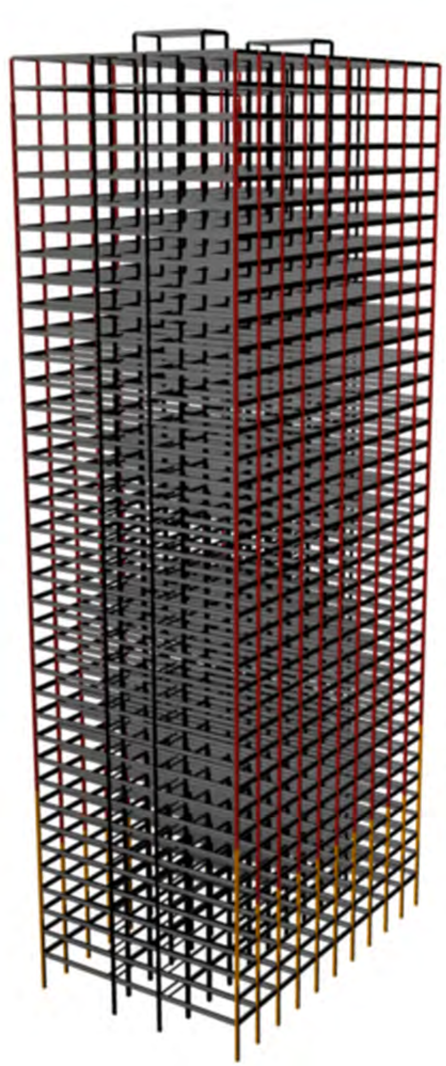

Figure 11.12 Fully ductile model of the 40-story building

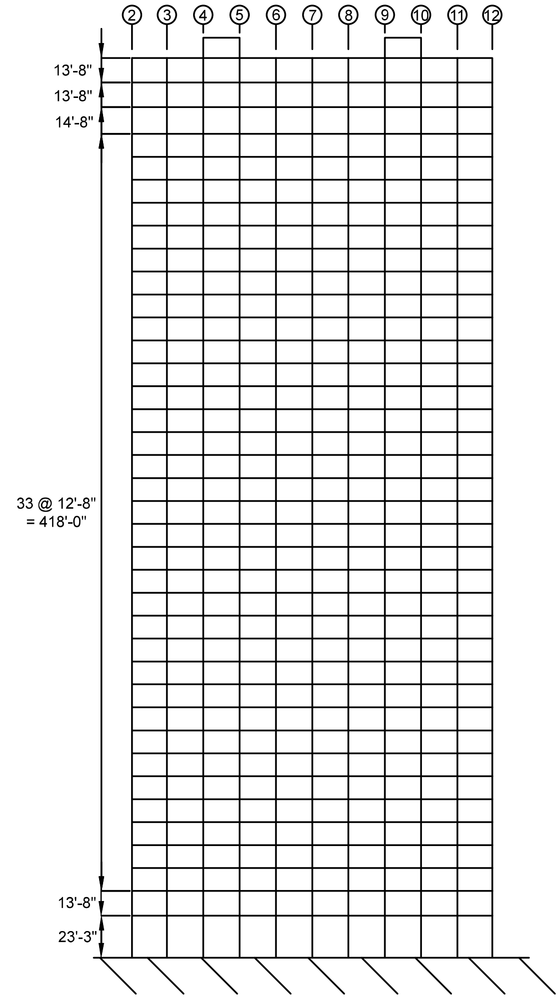

Figure 11.13 Fixed base building, beginning at the ground level

.

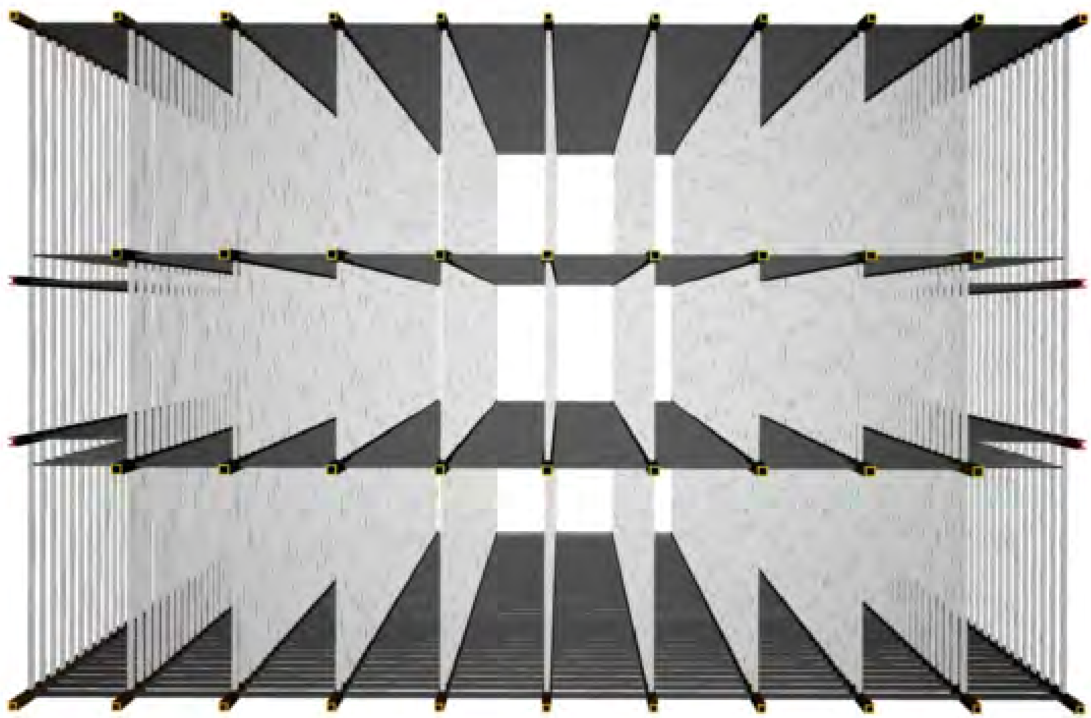

Figure 11.14 Typical model of the floor system.

Intermediate beams were omitted from the model (Figure 11.14) as they were not intended to be part of the lateral force system. They were part of the gravity system and were connected to girders with bolted connections. Including these beams increases the number of assigned nodes, which increases the calculation time. Nodes were modeled with six-degrees-of-freedom.

For simplicity, the roof penthouse was symmetrically modeled. To further simplify the model, all connections were assumed to be fully ductile moment connections. Moreover, no soil-structure interaction was considered. Force-based beam column elements were assigned. They permit the spread of plasticity along the components, which allows yielding to occur at any location along each element [McKenna et al. 2000].

11.5.2 Mass Distribution and Diaphragm

A typical floor weight of 125 psf was used for gravity load, and a seismic mass was lumped at the column nodes instead of being distributed along the beams and floors. The mass and stiffness distribution defines fundamental modes of the structure. The first mode of response is 7 sec in the fault-normal direction and the second mode of response is 6 sec in the fault-parallel direction. The building was modeled with a rigid diaphragm. Thus, the nodes have a rigid body translation, which condenses the total number of lateral-degrees-of -freedom.

11.6 HAZARD LEVELS

In this analysis three sets of hazard levels were analyzed. These included a service-level, design-level, and maximum considered earthquake (MCE) level. The service-level earthquake represents a very frequent earthquake with a return period of 43 years or a 50% probability of exceedance in 30 years; the design-level earthquake represents a less frequent earthquake with a return period of 475 years or a 10% probability of exceedance in 50 years; and the MCE level represents a very rare earthquake with a return period of 2475 years or a 2% probability of exceedance in 50 years. At every hazard level twenty ground motions were selected, each containing three components: a vertical component and two horizontal components, designated as fault normal and fault parallel oriented in the east-west and north-south directions, respectively. These components were scaled to match the 5% damped response spectrum. To establish a concrete analysis, three additional ground motions were selected from the 1989 Loma Prieta earthquake.

11.6.1 Ground Motion Selection and Scaling for Three Hazard Levels

For this assessment, Professor Jack W. Baker of Stanford University selected the ground motions from the PEER NGA database for each of the three hazard levels. No more than five ground motions were taken from a single earthquake. The magnitudes of the ground motions are greater than or equal to 6.5; all three components for each ground motion were scaled by the same scale factor. Detailed descriptions for each of the selected records are provided in Tables 11.3, 11.4, and 11.5 located in the Appendix.

According to Baker (personal communication), ground motions were selected if the geometric mean of their two horizontal response spectra matched the target spectrum approximately between 0.5 and 7 sec. The geometric mean response spectra for each of the three hazard levels are shown in Figures 11.15, 11.16, and 11.17. At each return period, the median of the twenty ground motions (in red) was determined, plotted, and compared to the target (in black). The target was obtained from a generic site in downtown San Francisco using the computer program Open Seismic Hazard Analysis (OpenSHA). Note that the median of the selected ground motions match the target over the period range of interest.

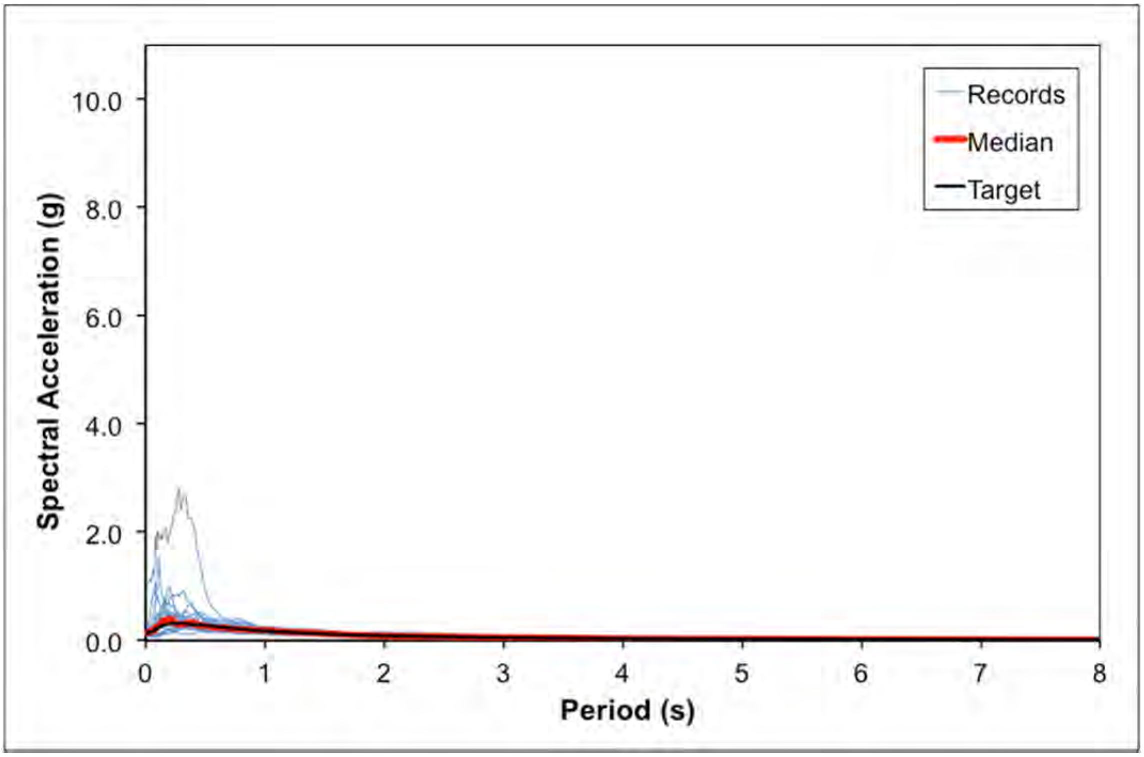

Figure 11.15 5% damped response spectra (geometric mean) of the 43-year return period.

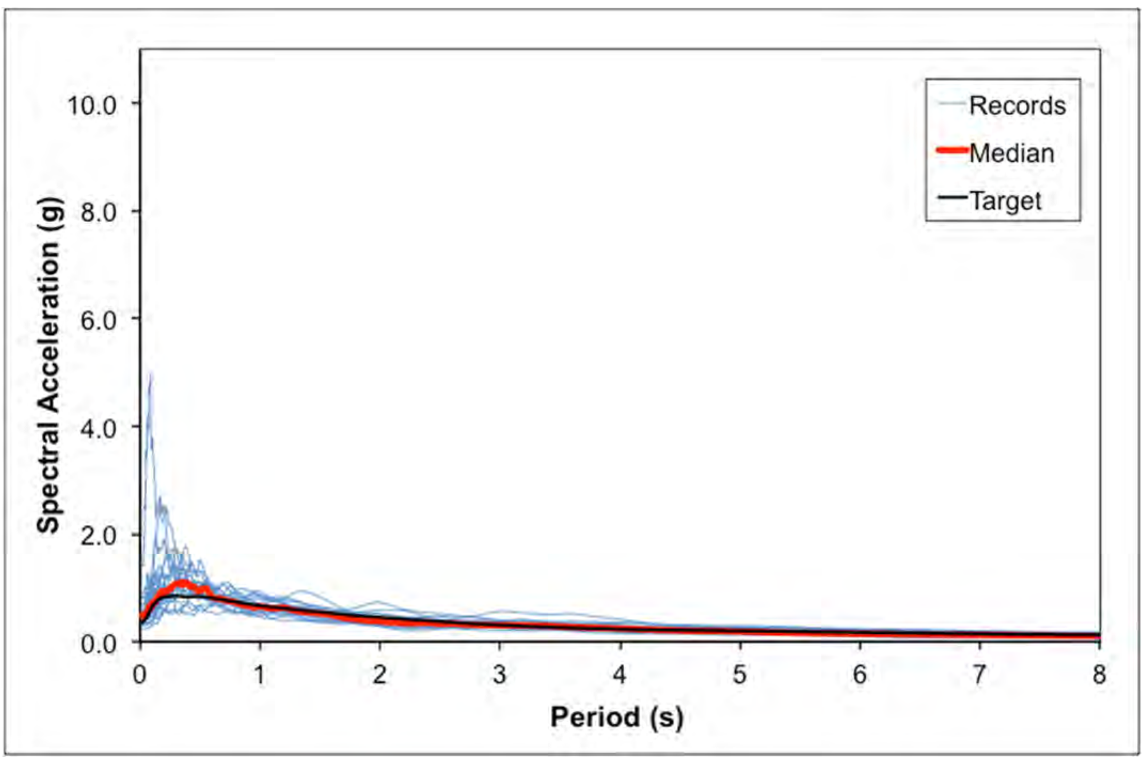

Figure 11.16 5% damped response spectra (geometric mean) of the 475-year return period.

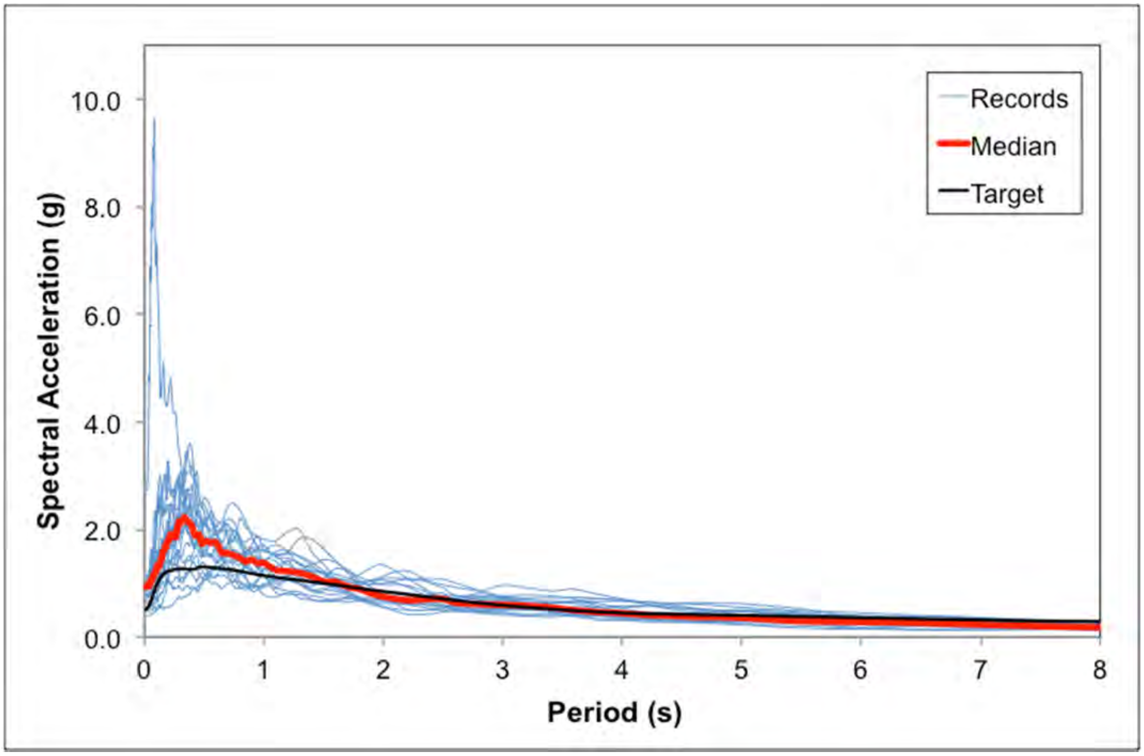

Figure 11.17 **5% damped response spectra (geometric mean) of the 2475-year return period.**

11.6.2 Ground Motion Selection and Scaling for Loma Prieta

To further assess the performance of the 40-story MRF structure and to a limited extent verify the numerical model, three 1989 Loma Prieta earthquake recordings were selected. The three ground motions are located in San Francisco as shown in Figure 11.18. The response spectra of the time histories for the Loma Prieta recordings are provided in Figure 11.19. Unlike the selection and scaling described in the previous section, the Loma Prieta ground motions were not selected for a particular hazard level but for their close proximity to the generic downtown site. These were not scaled but represent the level of shaking likely encountered by high rises during the 1989 event.

As shown Figure 11.19 , the high-frequency content of the three recordings between 0 and 1 sec is scattered well above and below the 43-year return period hazard. However, looking at the spectral displacements (Figure 11.20) the demands are well below a 43-year return period event between 4–7 sec, the period range of interest for this building. To find the hazard that matches the demand at the period of interest, OpenSHA was used to find a hazard compatible with the average of the three recordings. A return period of 16 years was obtained (green dashed line in Figure 11.20).

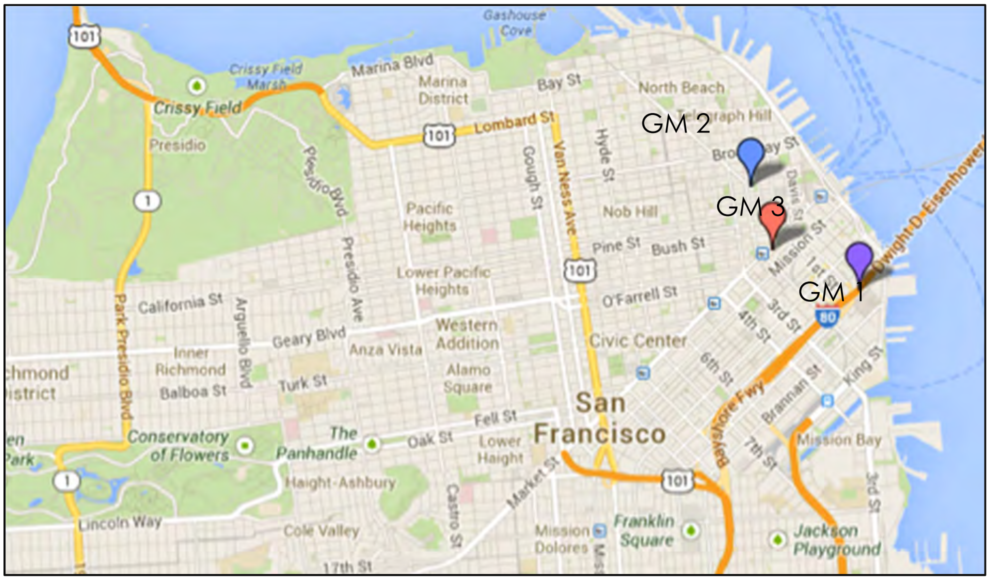

Figure 11.18 **Location of Loma Prieta recordings (courtesy of Matt Schoettler).**

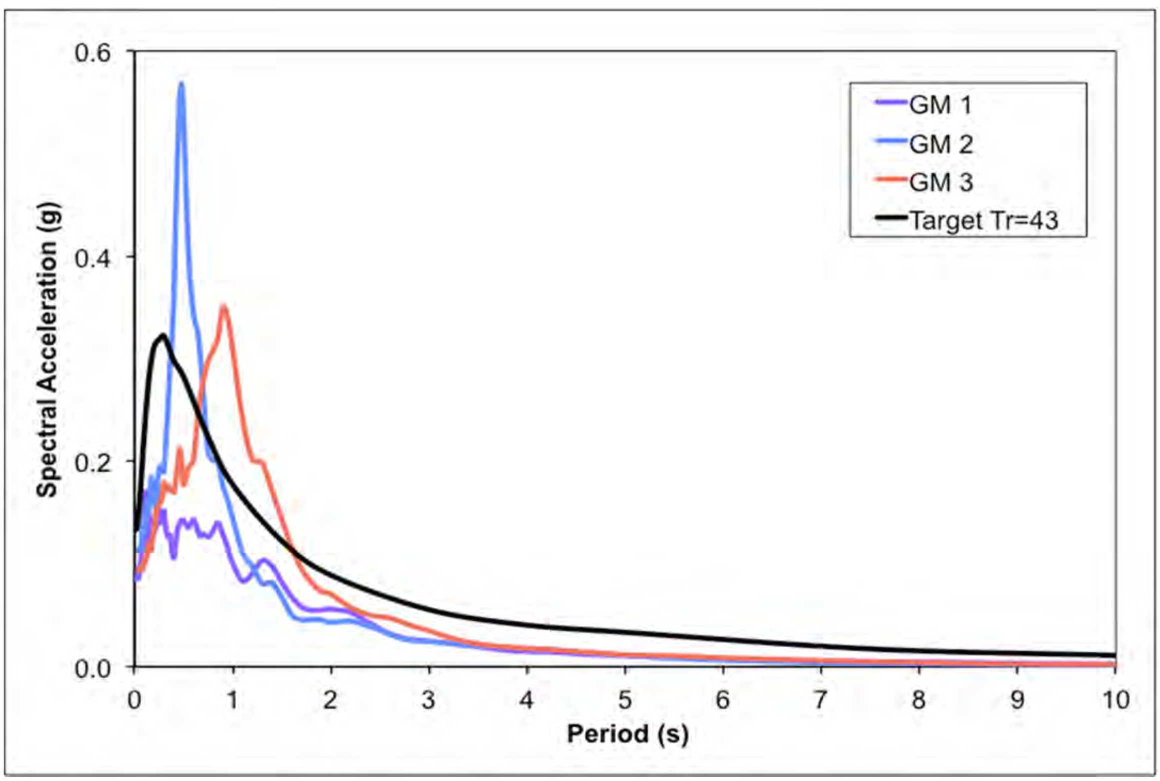

Figure 11.19 **Response spectra for Loma Prieta recordings compared to the 43-yr return period.**

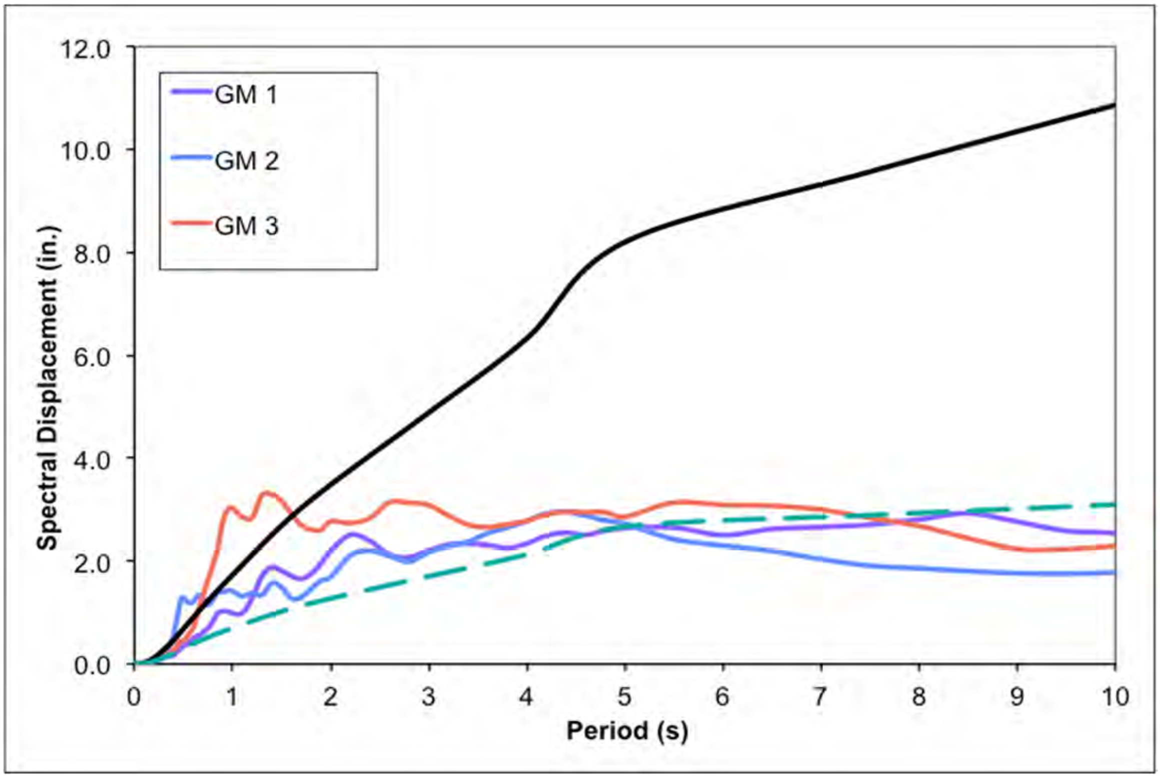

Figure 11.20 Displacement spectra for Loma Prieta recordings

11.7 RESULTS

Three dimensional non-linear time history analyses were conducted on the 40-story building using all sixty ground motions. The earthquakes were analyzed using OpenSees. The simulations took several days for their full duration plus a portion of free vibration where damping was increased to capture the residual displacement more quickly. To further speed the process, an overclocked computer assembled by PEER researcher Andreas Schellenberg was used. It took about three and a half days for each hazard level to complete. Two of the twenty ground motions did not converge (earthquakes 9 and 14) at the service- and design-level earthquakes. At the MCE-level earthquake, there was only convergence for three ground motions (earthquakes 1, 2, and 4). To further assess the model, Loma Prieta recordings were run in OpenSees and a pushover analysis was performed by Dr. Jiun-Wei Lai, project mentor and postdoctoral researcher at PEER.

11.7.1 OpenSees Results for the Hazard Levels

The OpenSees analysis determined that the 40-story structure has a period of 7 sec for the first mode. However, as a rule of thumb, for every 10 stories the period should be about 1 sec. According to the design documentation of the 40-story structure, the design period of the first mode of the building is approximately 6 sec, justifying the 7 sec obtained in OpenSees as the assumed mass distribution was likely not the same.

The response envelopes of the structure for acceleration, story drift, and velocity in the fault-normal and fault-parallel directions at the service- and design-level earthquakes are shown in the Figures 11.21 to 11.32. The MCE level was not accounted for in this assessment since most of the ground motions at this level did not converge. Convergence refers to whether the incremental displacement in an analysis step is less than a prescribed value; in these cases they were not satisfied because of extremely large and unsustainable lateral deformations. The acceleration envelopes are shown in Figures 11.21 to 11.24. Note that the design-level earthquake produces the strongest accelerations in both directions, with the maximum occurring at the top of the structure. The median peak acceleration is 0.99*g* and 1.20*g* for both the fault-normal and fault-parallel directions at the design-level earthquake, and 0.35*g* and 0.41*g* in both directions at the service-level earthquake, respectively.

The story-drift envelopes over the height of the model are shown in Figures 11.25 to 11.28, where the design-level earthquake produced the maximum story drift in both directions, and reflects a tendency towards soft-story behavior in the bottom half of the structure. In the fault-normal direction (Figure 11.26) the median peak drift is concentrated around the 14th and 15th floors, and is about 4.0%. In the fault-parallel direction (Figure 11.28), the median peak drift is concentrated around the 18th and 19th floors and is about 2.2%. At the service-level earthquake, the median peak drift is 0.58% in the fault-normal direction (Figure 11.25) and 0.54% in the fault-parallel direction (Figure 11.27).

The velocity envelopes are shown in Figures 11.29 to 11.32. Maximum velocities were observed to occur at the design-level earthquake in both directions. The median peak velocities at the 475-year return period were 98.2 in./sec and 81.7 in./sec for the fault-normal and fault-parallel directions, respectively (see Figures 11.30 and 11.32). The median peak velocities at the 43-year return period were 29.9 in./sec in the fault-normal and 31.5 in./sec in the fault-parallel direction (see Figures 11.29 and 11.31).

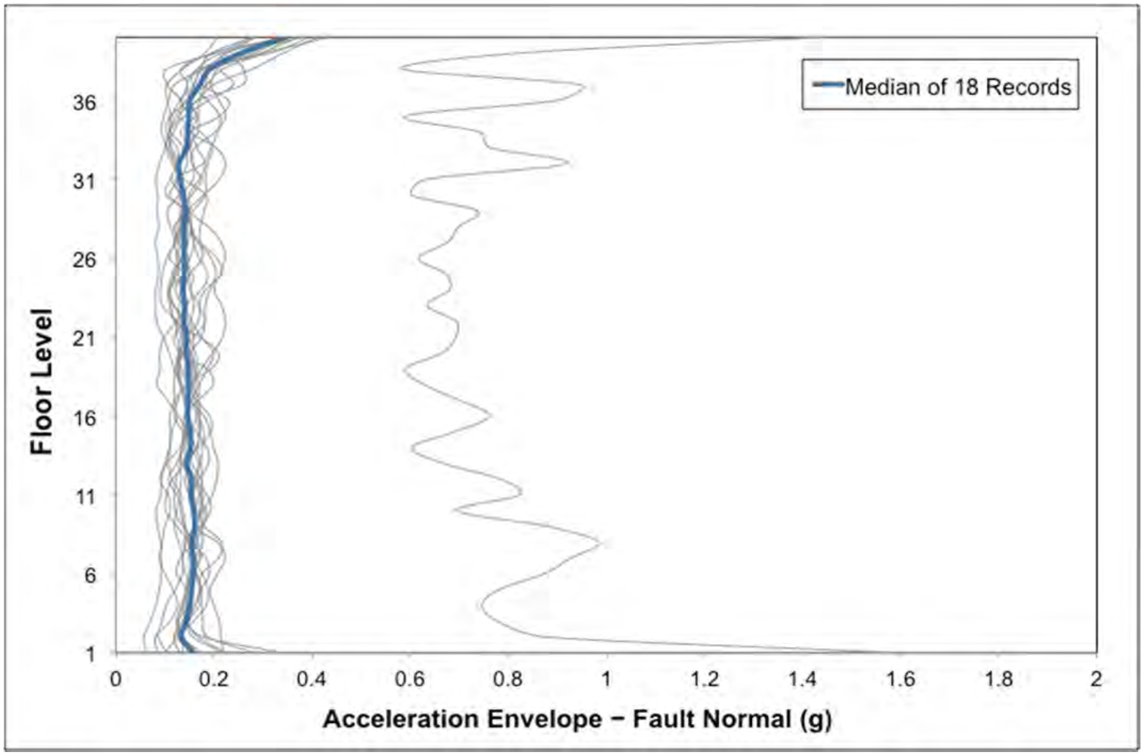

Figure 11.21 Acceleration envelope for the fault-normal component at the service-level earthquake at a return period of T_r = 43 years.

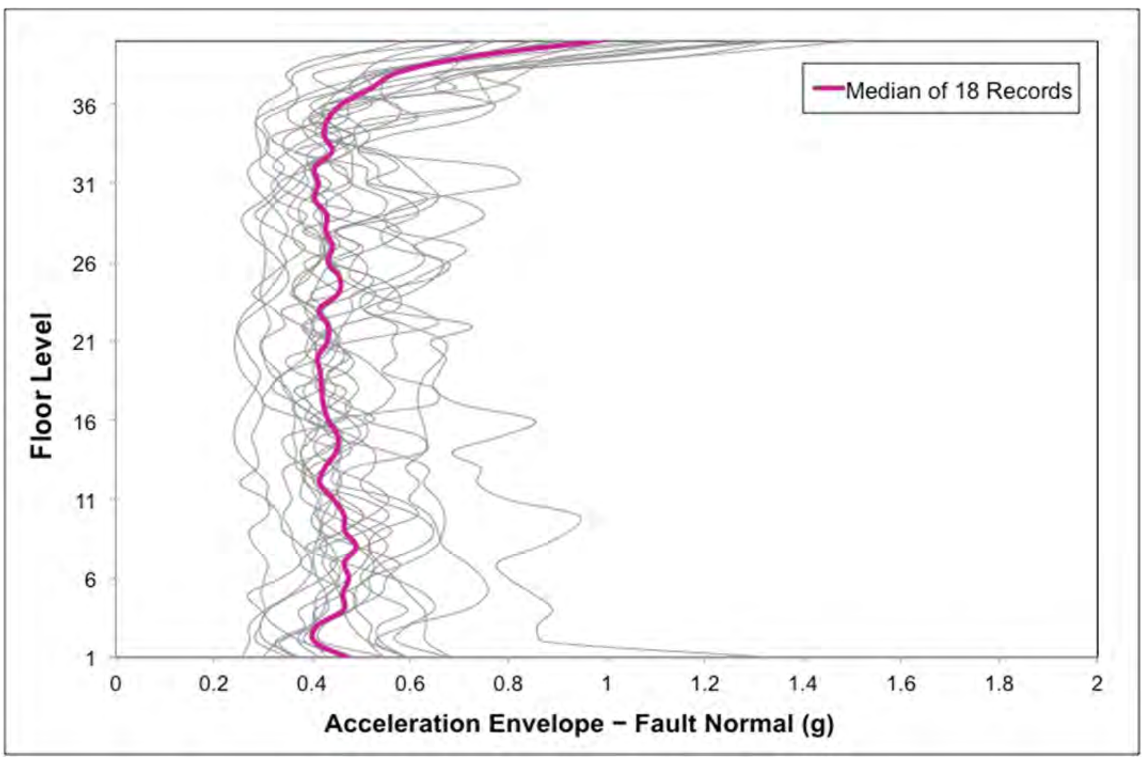

Figure 11.22 Acceleration envelope for the fault-normal component at the design-level earthquake at a return period of T_r = 475 years.

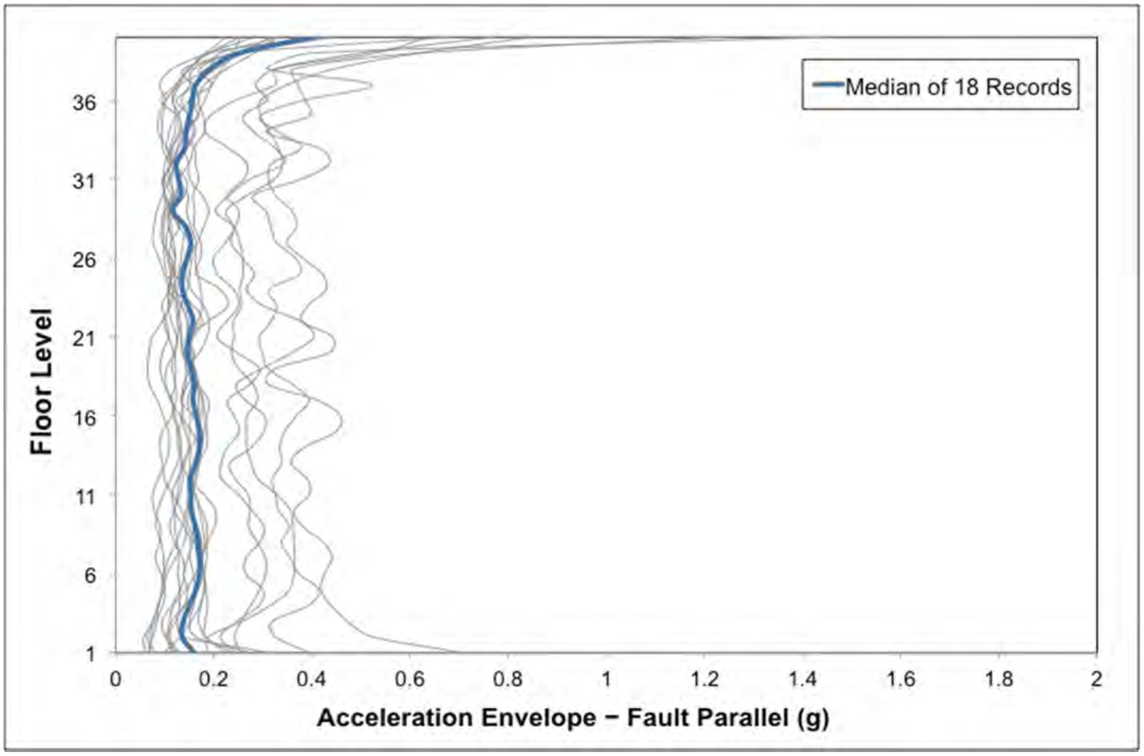

Figure 11.23 Acceleration envelope for the fault-parallel component at the service-level earthquake at a return period of T_r = 43 years.

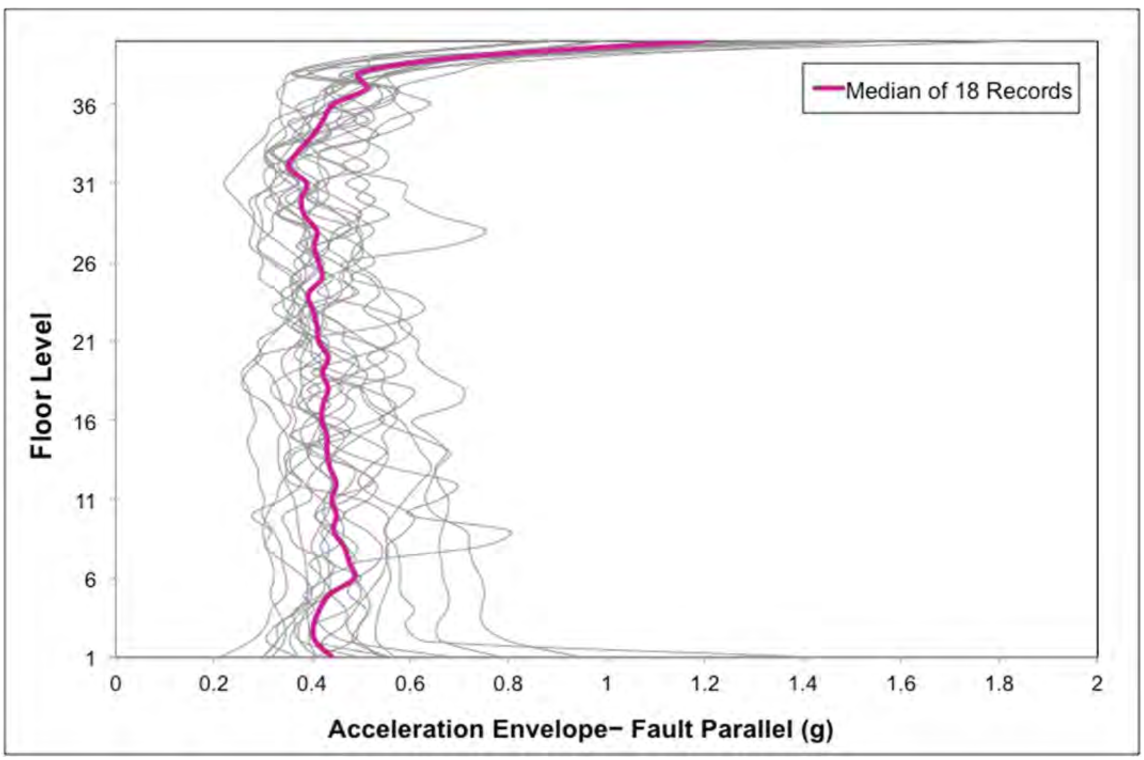

Figure 11.24 Acceleration envelope for the fault-parallel component at the design-level earthquake at a return period of T_r = 475 years.

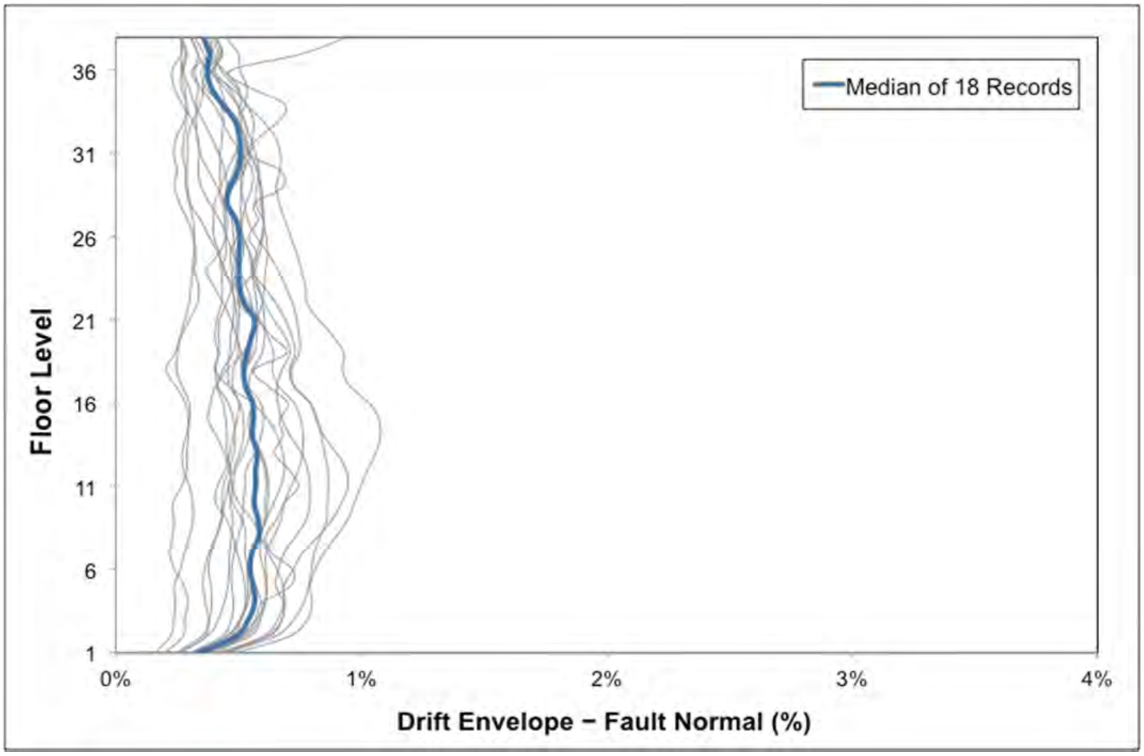

Figure 11.25 Drift envelope for the fault-normal component at the service-level earthquake at a return period of T_r = 43 years.

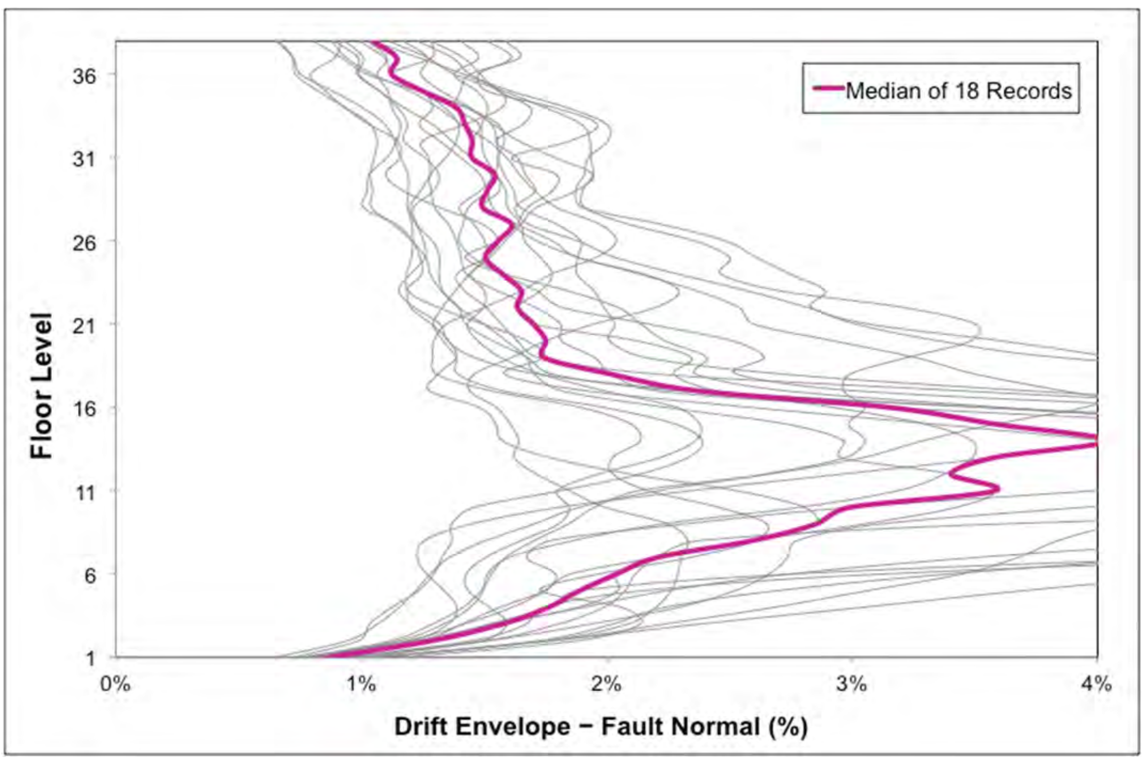

Figure 11.26 Drift envelope for the fault-normal component at the design-level earthquake at a return period of T_r = 475 years.

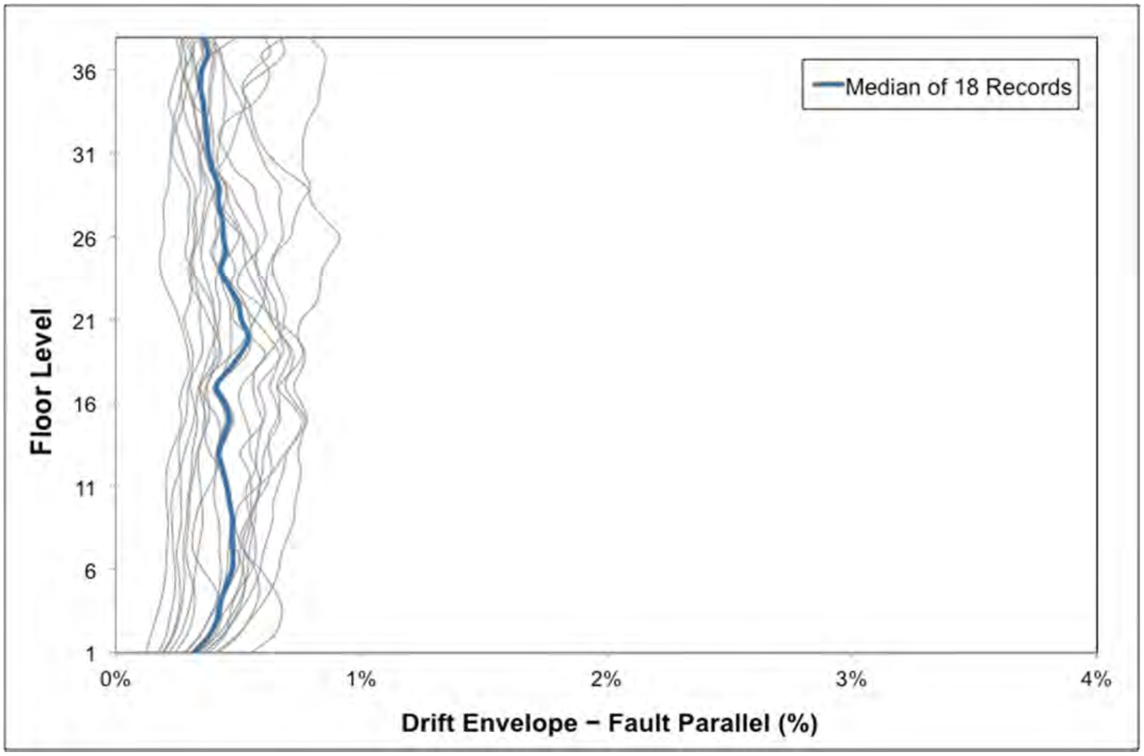

Figure 11.27 Drift envelope for the fault-parallel component at the service-level earthquake at a return period of T_r = 43 years.years.

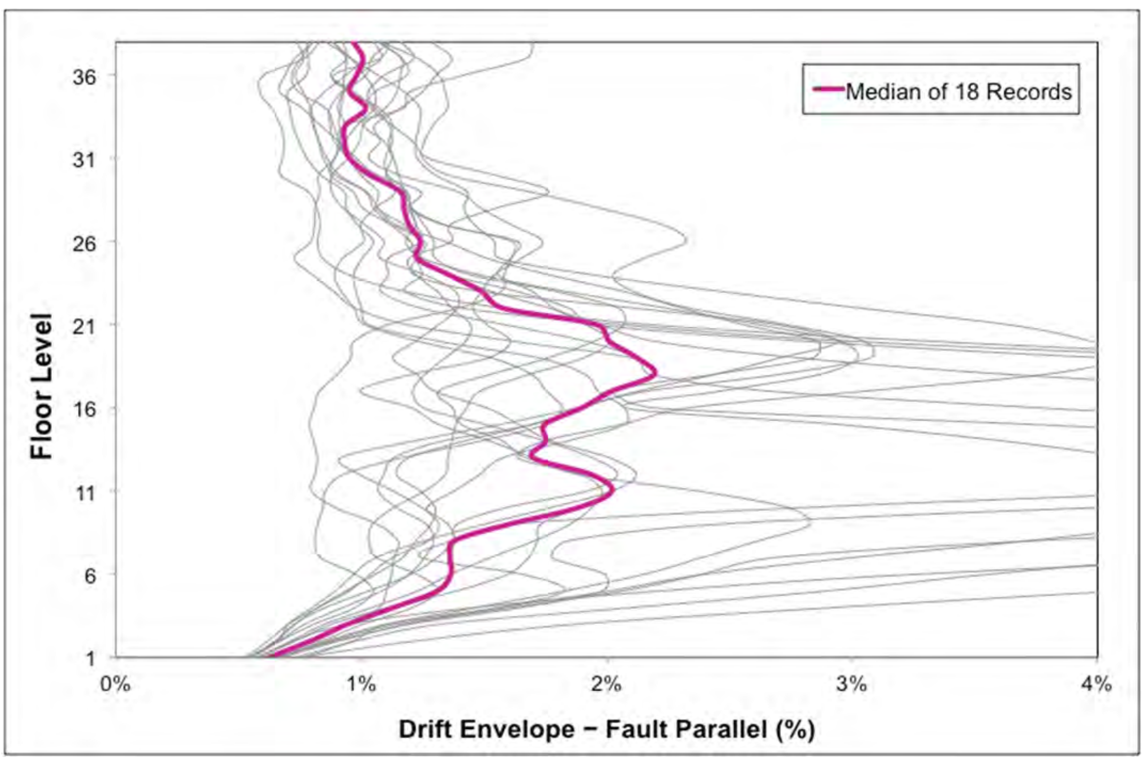

Figure 11.28 Drift envelope for the fault-parallel component at the design-level earthquake at a return period of T_r = 475 years.

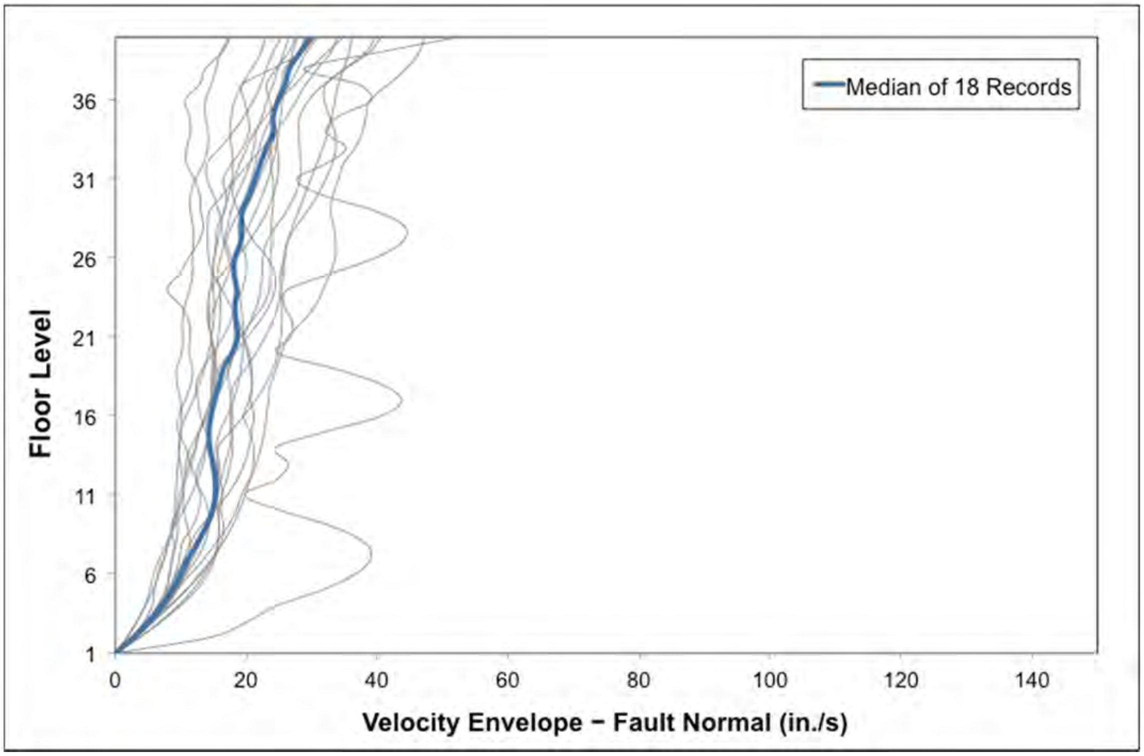

Figure 11.29 Velocity envelope for the fault-normal component at the service-level earthquake at a return period of T_r = 43 years.years.

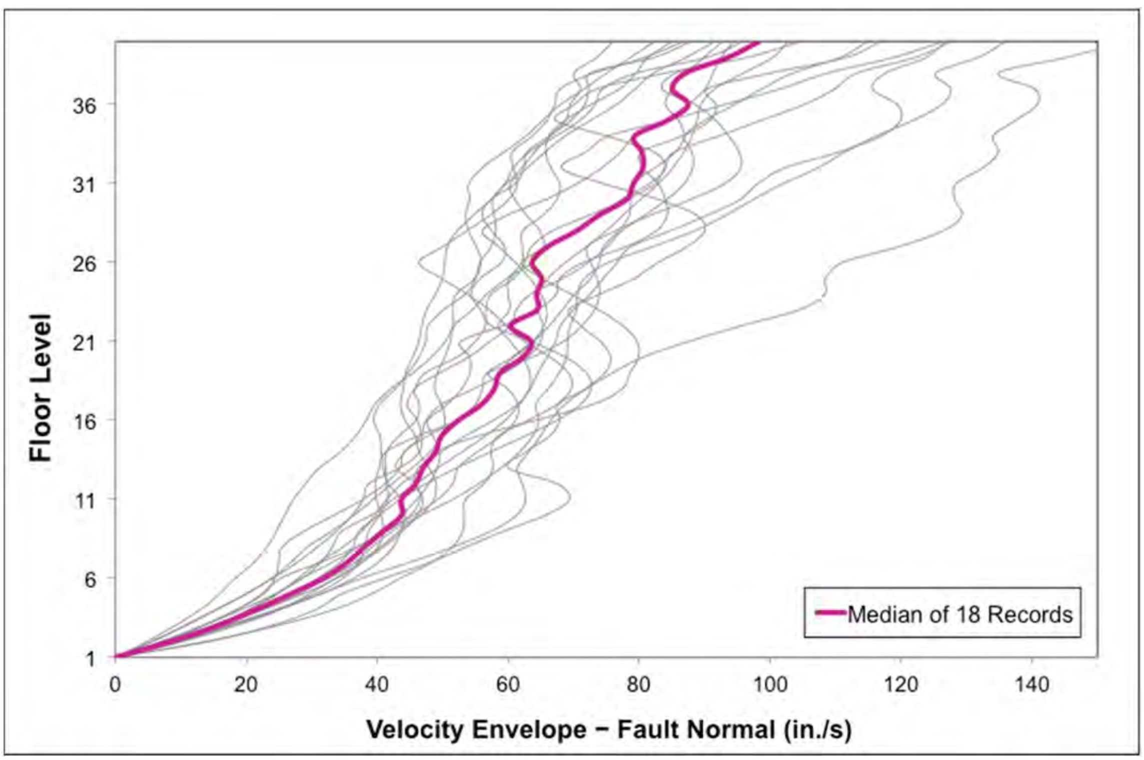

Figure 11.30 Velocity envelope for the fault-normal component at the design-level earthquake at a return period of T_r = 475 years.

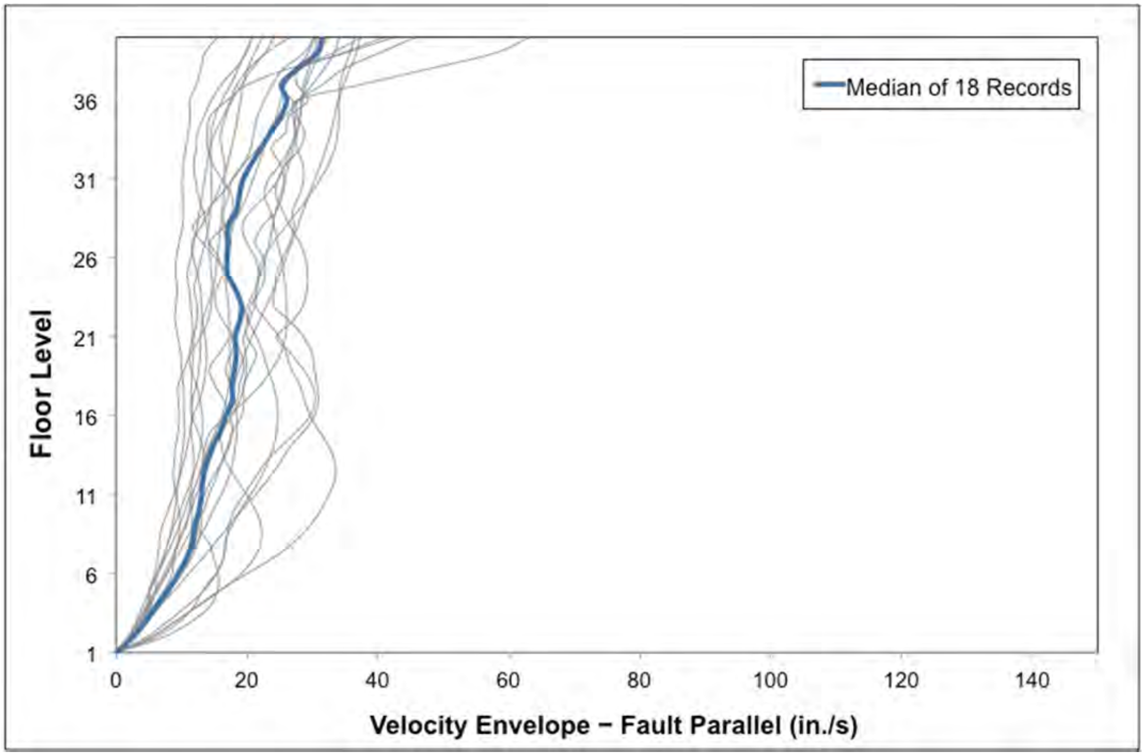

Figure 11.31 **Velocity envelope for the fault-parallel component at the service-level earthquake at a return period of T_r = 43 years.**

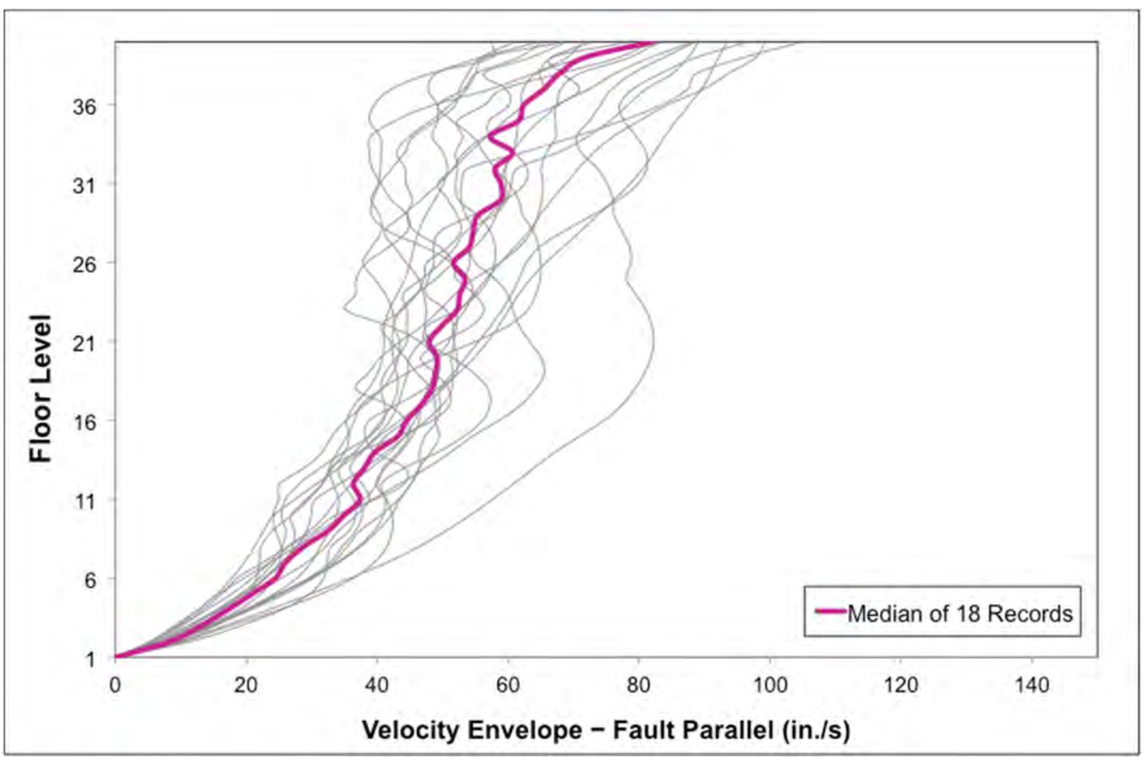

Figure 11.32 **Velocity envelope for the fault-parallel component at the design-level earthquake at a return period of T_r = 475 years.**

Peak residual drifts were summarized for input into PACT to conduct an economic loss assessment, discussed in Quinonez [2013]. PACT only accepts a single residual drift value for each hazard level. Thus, the maximum residual drift was obtained from each ground motion, and the median of these maxima was taken. Peak residual drifts for each of the hazard levels were: 2.25×10^{-5} rad. for the service level and 1.78×10^{-2} rad. for the design level.

11.7.2 OpenSees Results for Loma Prieta

Envelopes of the response of the structure for the acceleration, story drift, and velocity in the fault-normal and fault-parallel directions for the Loma Prieta recordings are illustrated in Figures 11.33 to 11.38. The envelopes of acceleration are shown in Figures 11.33 and 11.34. The maximum acceleration was observed to occur at the top of the structure and is relatively the same for the fault-normal and fault-parallel directions, 0.30*g* and 0.31*g*, respectively.

The envelopes of story drift are shown in Figures 1.35 and 1.36. The median peak story drift is 0.36% for the fault-normal direction and 0.31% for the fault-parallel direction. The envelope for the velocity in the fault-normal and fault-parallel directions are shown in Figures 11.37 and 11.38, respectively. Here, the maximum velocity occurred at the top of the structure, at 15.5 in./sec and 12.4 in./sec for the fault-normal and fault-parallel directions, respectively.

The peak residual drift at a value of 2.00×10^{-5} rad was obtained for the Loma Prieta recordings to use as input into PACT.

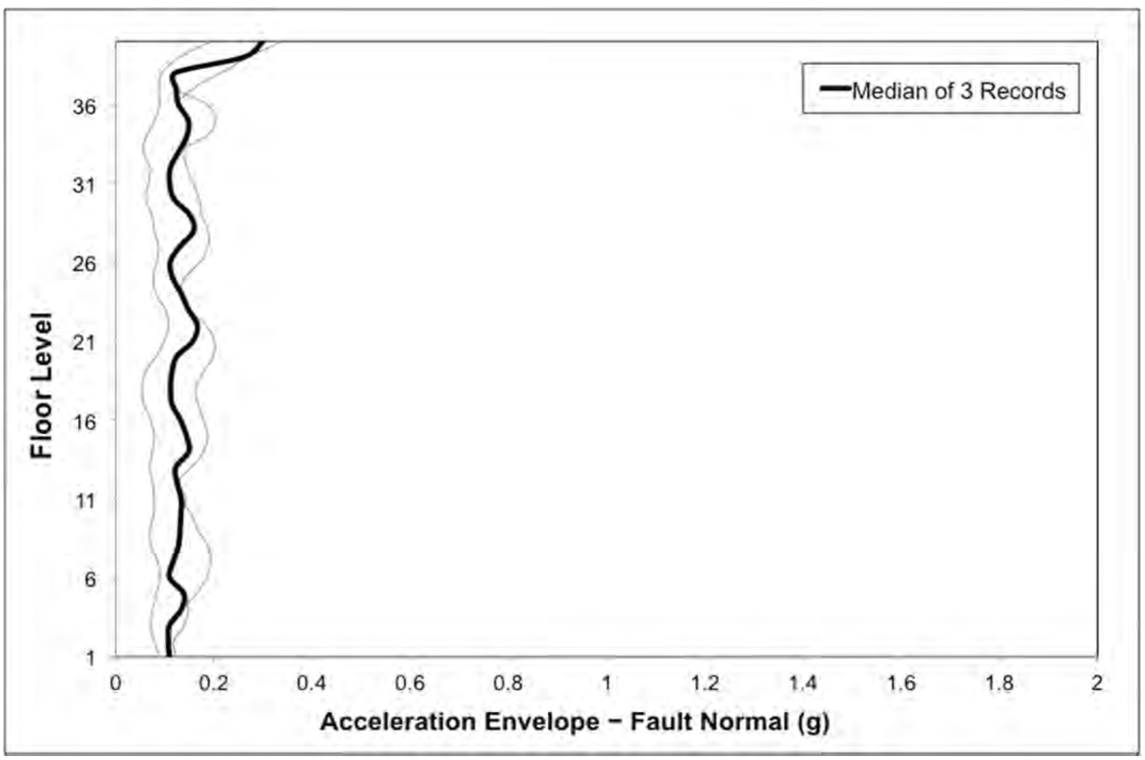

Figure 11.33 Acceleration envelope for the fault-normal component of the Loma Prieta recordings.

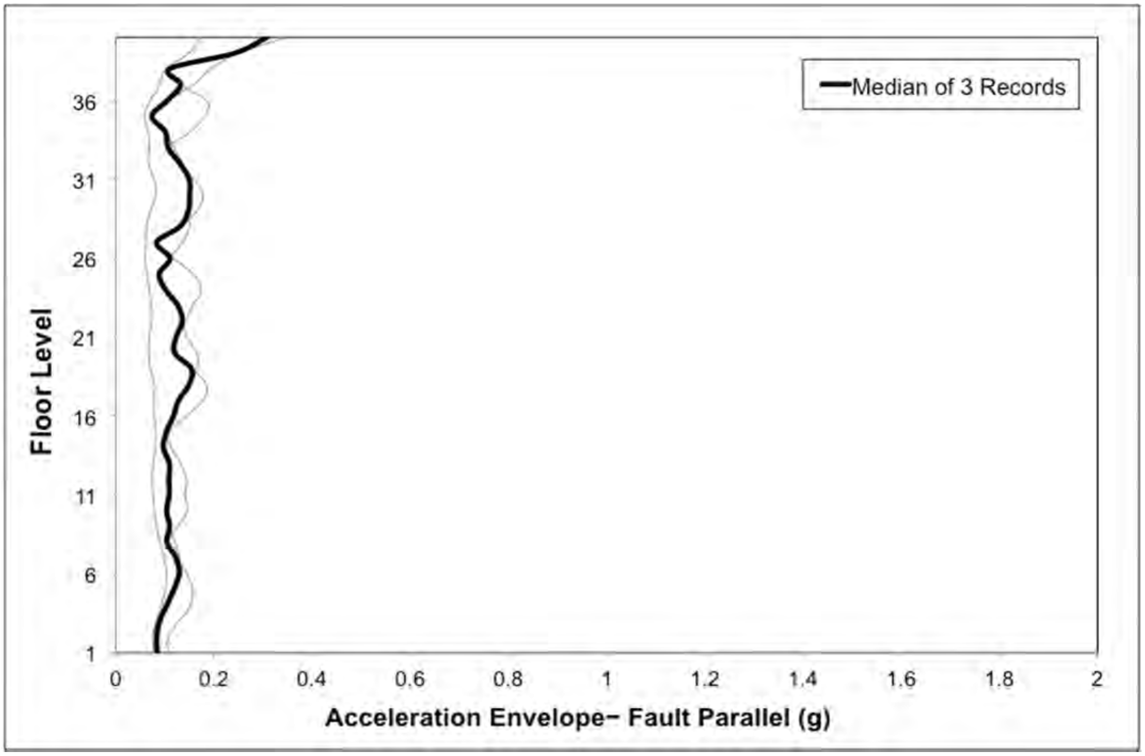

Figure 11.34 **Acceleration envelope for the fault-parallel component of the Loma Prieta recordings.**

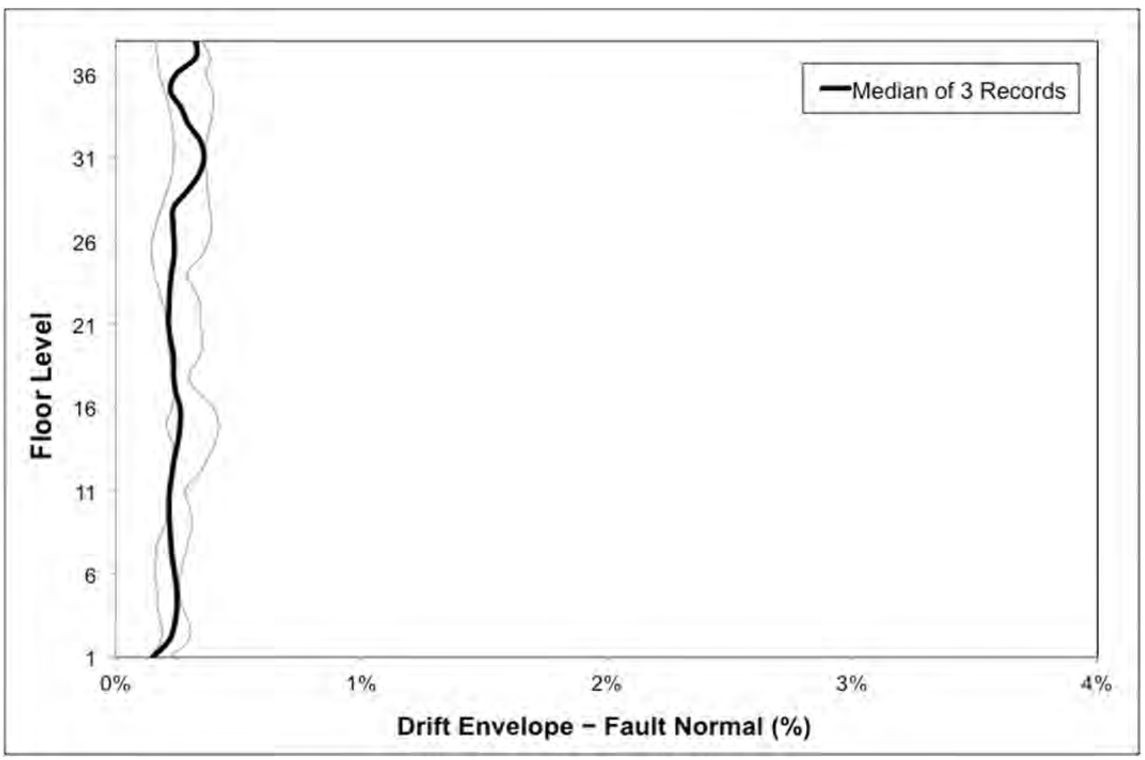

Figure 11.35 **Drift envelope for the fault-normal component of the Loma Prieta recordings.**

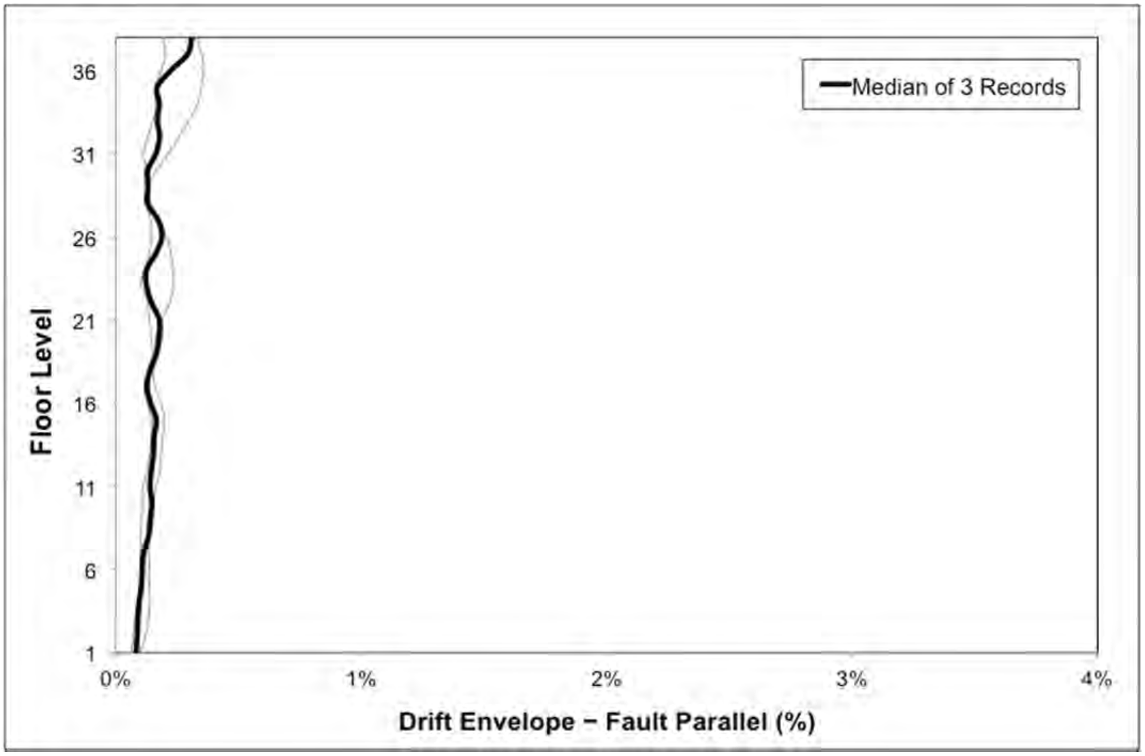

Figure 11.36 **Drift envelope for the fault-parallel component of the Loma Prieta recordings.**

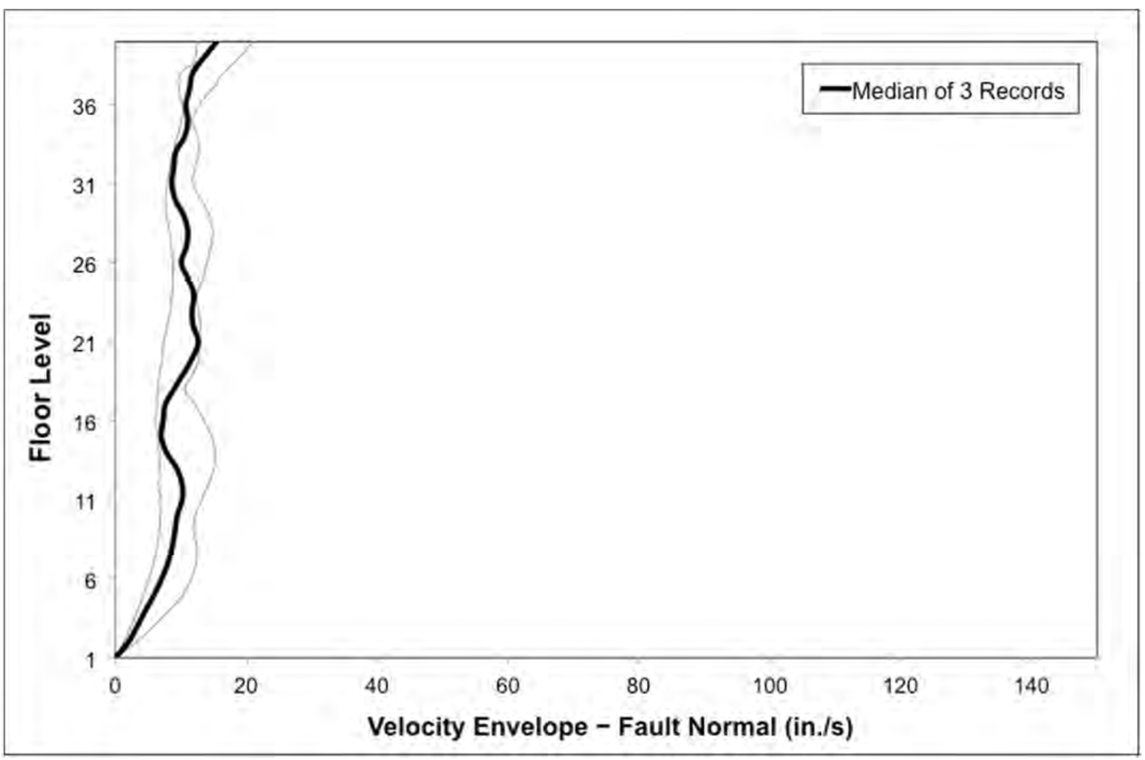

Figure 11.37 **Velocity envelope for the fault-normal component of the Loma Prieta recordings.**

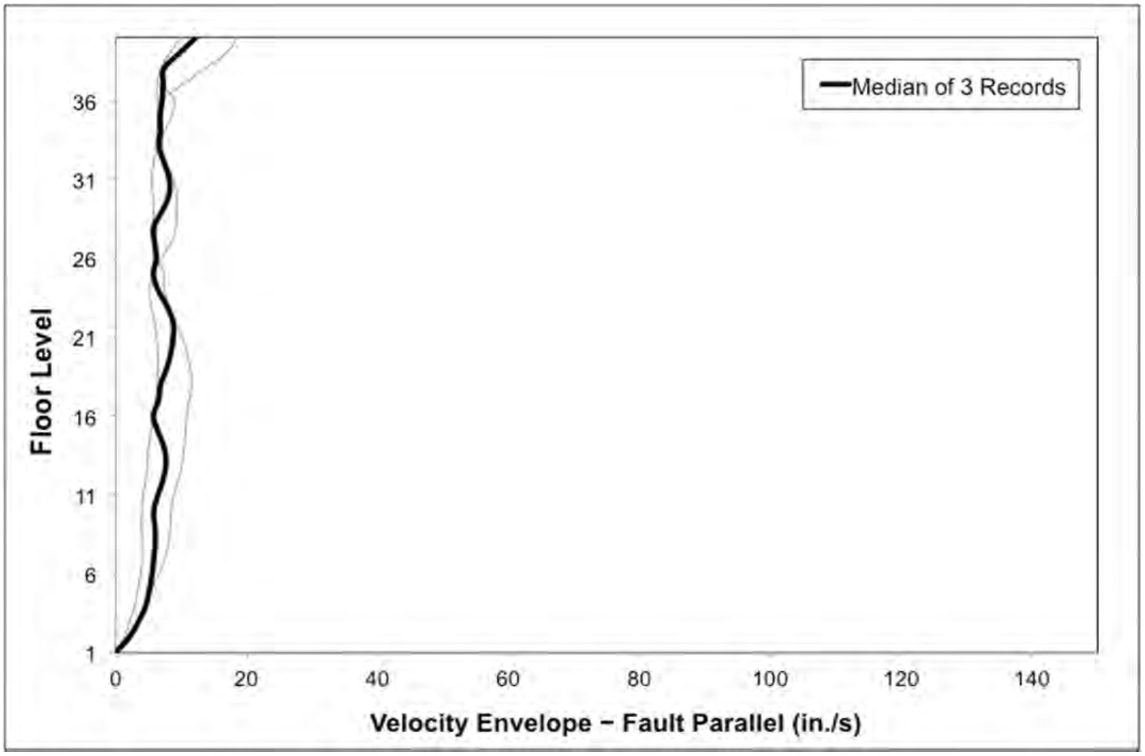

Figure 11.38 Velocity envelope for the fault-parallel component of the Loma Prieta recordings.

11.7.3 Pushover Analysis

To estimate the lateral resistance of the 40-story structure, Dr. Jiun-Wei Lai performed a pushover analysis. Modes 1 and 2 were used as load patterns for the fault-normal and fault-parallel directions, respectively. As seen in Figure 11.39, the roof displacement is uniform up until the yield point. Note the peak base shear capacity is approximately 8800 kips in the fault-normal direction (Figure 11.39a) and 7500 kips in the fault-parallel direction (Figure 11.39b). P-delta effects caused negative stiffness in the building once a roof displacement of about 63 in. or a 1.1% roof drift ratio was reached in the fault-normal direction and about 45 in. or a 0.75% roof drift ratio in the fault-parallel direction. Negative post-yield stiffness is undesirable. In this case the structure was unable to sustain the force, which may lead to collapse.

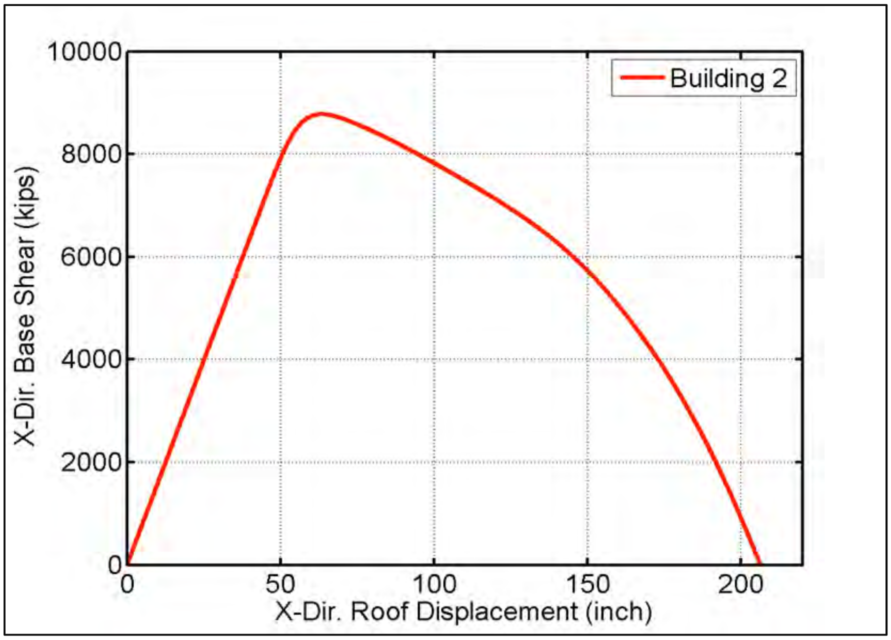

(a)

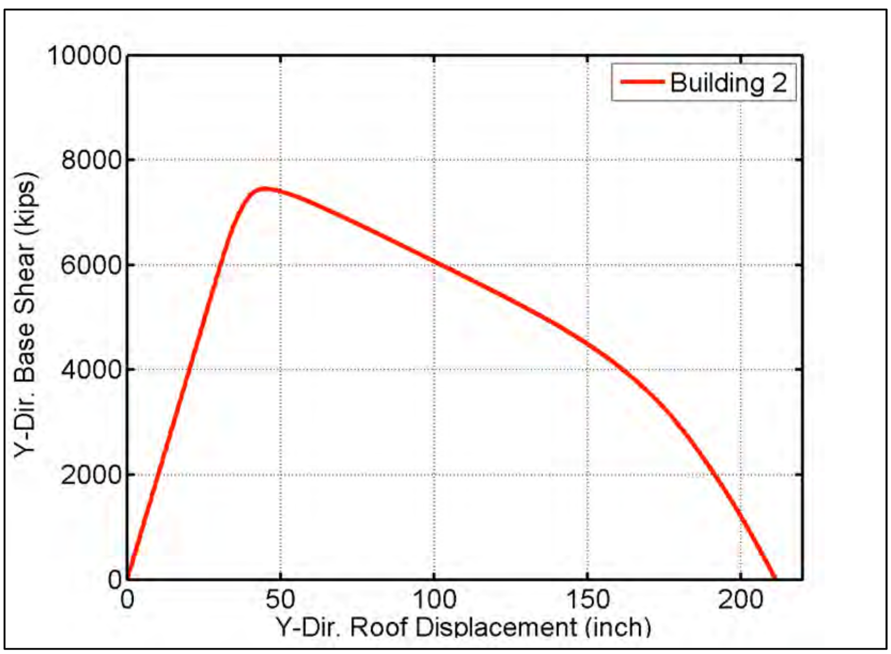

(b)

Figure 11.39 Pushover analysis results in the (a) fault-normal and (b) fault-parallel directions.

11.8 IMPLICATIONS OF RESULTS

As shown in Figure 11.40, at the service-level earthquake and Loma Prieta cases, the 40-story structure fared well; the maximum story drift demands were below the current threshold of 2%. However, at the design-level earthquake, there were large concentrations of interstory drift demands. As previously mentioned, median peak drifts of about 4.0% and 2.2% were observed at the design-level earthquake—see Figure 11.40—exceeding the 2% requirement specified in current code provisions.

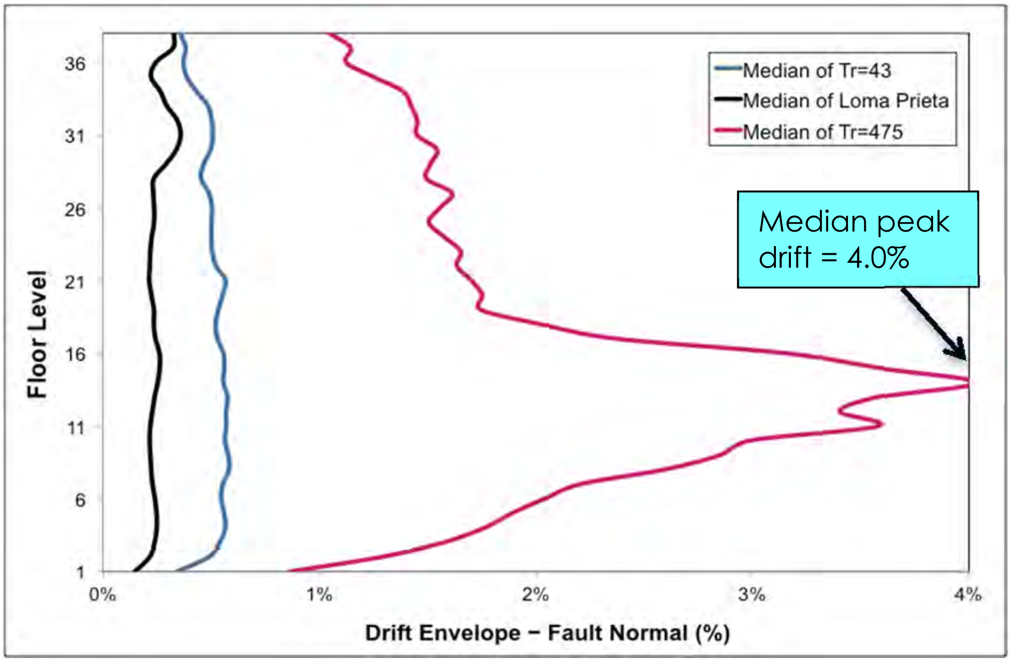

(a)

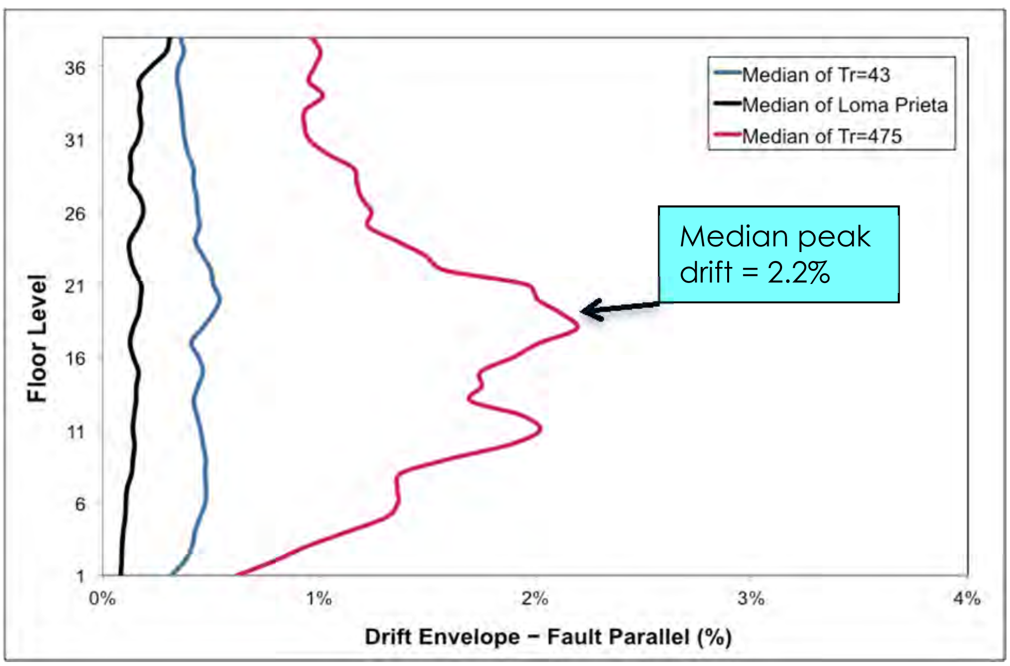

(b)

Figure 11.40 Drift envelope summary for the Loma Prieta and the 43- and 475-year return periods in the (a) fault-normal and (b) fault-parallel directions.

11.9 CONCLUSIONS

With close examination of the results, it can be concluded that the performance of existing tall buildings is unacceptable. The 40-story structure analyzed herein experienced soft-story behavior at the bottom half of the building and failed at the MCE level. Thus, tall steel MRF buildings under earthquake shaking levels consistent with the MCE are expected to face severe damage due to large story drifts. To avoid structural collapse under extreme events, a retrofit should be considered. Possible retrofits include the addition of stiffness or damping to these structures. At the design-level earthquake, displacement demands are large and likely unsustainable considering possible brittle connection behavior. Connection strengthening or capacity limiting retrofits may be necessary if the connections are deemed to be non-ductile. The results presented considered fully ductile connections, and the consequence of non-ductile connections remains to be addressed.

This investigation presents the initial phase to a more extensive body of work that is currently being undertaken at PEER. The ultimate goal is to establish performance-based seismic evaluation guidelines for existing tall buildings and to establish a retrofit framework for these structures. Further research is required to meet these objectives. Future work includes incorporating non-ductile elements in the analysis and an assessment of possible upgraded structural systems.

11.10 ACKNOWLEDGMENTS

This research project would have not been possible without the funding provided by the National Science Foundation. The success of this project was achieved through the help from mentors Dr. Matt Schoettler and Dr. Jiun-Wei Lai. I thank them for their time and invaluable guidance and direction. I give special thanks to Professor Stephen Mahin and Heidi Tremayne for the opportunity of being part of PEER and assigning me this research project. Thanks to my coworker Melissa Quinonez for her support and brightening my day at the office. Thanks to the Department of Building Inspection in San Francisco for permitting my coworker and I to use their facility to extract the required information from the structural plans. I would also like to thank the staff at the Richmond Field Station for their hospitality and welcoming environment. I would like to end by giving thanks to my family for always being there for me and supporting me in my endeavors and achievements; special thanks to my sister, Vanessa Rodriguez, and mother, Maria De Jesus Rodriguez Figueroa. This has been a great learning experience.

11.11 REFERENCES

Almufti I., Molina Hutt C. Willford M., Deierlein G. (2012). Seismic assessment of typical 1970s tall steel moment frame buildings in downtown San Francisco, *Proceedings, 15th World Conference on Earthquake Engineering,* Lisbon, Portugal.

Altobello S. (2010). viewed Aug. 14, 2013, http://peelslowlynsee.wordpress.com/category/gripes/.

Anderson J.C. et al. (1995). Technical report: Case studies of steel moment frame building performance in the Northridge earthquake of January 17, 1994. *Report No. SAC-95-07*, SAC Joint Venture, Sacramento, CA.

ATC (2012). *Seismic Performance Assessment of Buildings Volume 1 – Methodology.* Applied Technology Council, Redwood City, CA.

EPICentre (2012). *Seismic Assessment of Existing Tall Buildings via Non-Linear Response History Analysis*, University College London, [http://www.epicentreonline.com/researchproject/view/idprojects/46}

Forell/Elsesser Engineers. *"Pre-Northridge" Moment-Resisting Frame Buildings,* viewed Aug. 14, 2013, http://www.forell.com/pre-northridge/.

Foutch D.A. (2000). *State of the Art Report on Performance Prediction and Evaluation of Steel Moment-Frame Buildings, FEMA-355F*, Federal Emergency Management Agency, Washington, D.C.

Krishnan S., Ji C., Komatitsch D., Tromp J. (2006). Case studies of damage to tall steel moment-frame buildings in Southern California during large San Andreas earthquakes, *Bull. Seismol. Soc. Am.,* 96(4A): 1523–1537.

Lee K., Foutch D.A. (2002). Seismic performance evaluation of pre-Northridge steel frame buildings with brittle connections, *J. Struct. Eng.* 128: 546–555.

Mahin S.A. (1997). *Lessons from Steel Buildings Damaged by the Northridge Earthquake,* National Information Service for Earthquake Engineering, University of California Berkeley, [http://nisee.berkeley.edu/northridge/mahin.html].

McKenna F., Fenves G.L., Scott M.H., Jeremic B. (2000). *Open System for Earthquake Engineering Simulation (OpenSees),* Pacific Earthquake Engineering Research Center, University of California, Berkeley, CA.

OpenSHA. *A Developing Community-Modeling Environment for Seismic Hazard Analysis,* viewed Aug. 9, 2013, http://www.opensha.org/.

Porter K.A. (2003). *An Overview of PEER's Performance-Based Earthquake Engineering Methodology,* Department of Civil Engineering, California Institute of Technology, Pasadena, CA.

11.12 APPENDIX

11.12.1 Recorded Data Tables for the Hazard Levels

Table 11.3 Recorded data for the 43-year return period.

Ground Motion	NGA No.	Earthquake	Station	Magnitude	Distance (km)	V_s30 (m/sec)	Scale Factor
1	6		El Centro Array #9	7.0	6.1	213	0.7
2	15	Kern County	Taft Lincoln School	7.4	38.9	385	1.1
3	88	San Fernando	Santa Felita Dam (Outlet)	6.6	24.9	376	1.9
4	93	San Fernando	Whittier Narrows Dam	6.6	39.5	299	2.0
5	175	Imperial Valley-06	El Centro Array #12	6.5	17.9	197	0.9
6	187	Imperial Valley-06	Parachute Test Site	6.5	12.7	349	1.2
7	286	Irpinia, Italy-01	Bisaccia	6.9	21.3	1000	1.1
8	721	Superstition Hills-02	El Centro Imp. Co. Cent	6.5	18.2	192	0.5
9	728	Superstition Hills-02	Westmorland Fire Sta	6.5	13.0	194	0.6
10	754	Loma Prieta	Coyote Lake Dam (Downst)	6.9	20.8	295	1.4
11	812	Loma Prieta	Woodside	6.9	34.1	454	1.4
12	838	Landers	Barstow	7.3	34.9	371	0.9
13	879	Landers	Lucerne	7.3	2.2	685	0.4
14	1144	Gulf of Aqaba	Eilat	7.2	44.1	355	1.8
15	1194	Chi-Chi, Taiwan	CHY025	7.6	19.1	278	0.4
16	1289	Chi-Chi, Taiwan	HWA041	7.6	47.8	273	1.3
17	1605	Duzce, Turkey	Duzce	7.1	6.6	276	0.2
18	1615	Duzce, Turkey	Lamont 1062	7.1	9.2	338	1.6
19	1617	Duzce, Turkey	Lamont 375	7.1	3.9	425	1.6
20	2111	Denali, Alaska	R109 (temp)	7.9	43.0	964	2.0

Table 11.4 Recorded data for the 475-year return period.

Ground Motion	NGA No.	Earthquake	Station	Magnitude	Distance (km)	V_s30 (m/sec)	Scale Factor
1	179	Imperial Valley-06	El Centro Array #4	6.5	7.1	209	1.7
2	180	Imperial Valley-06	El Centro Array #5	6.5	4.0	206	1.3
3	185	Imperial Valley-06	Holtville Post Office	6.5	7.7	203	2.1
4	187	Imperial Valley-06	Parachute Test Site	6.5	12.7	349	5.0
5	286	Irpinia, Italy-01	Bisaccia	6.9	21.3	1000	4.9
6	838	Landers	Barstow	7.3	34.9	371	4.3
7	879	Landers	Lucerne	7.3	2.2	685	1.9
8	900	Landers	Yermo Fire Station	7.3	23.6	354	2.5
9	1148	Kocaeli, Turkey	Arcelik	7.5	13.5	523	4.9
10	1158	Kocaeli, Turkey	Duzce	7.5	15.4	276	1.5
11	1161	Kocaeli, Turkey	Gebze	7.5	10.9	792	2.9
12	1176	Kocaeli, Turkey	Yarimca	7.5	4.8	297	1.3
13	1494	Chi-Chi, Taiwan	TCU054	7.6	5.3	461	2.2
14	1500	Chi-Chi, Taiwan	TCU061	7.6	17.2	273	2.1
15	1515	Chi-Chi, Taiwan	TCU082	7.6	5.2	473	1.9
16	1528	Chi-Chi, Taiwan	TCU101	7.6	2.1	273	2.0
17	1546	Chi-Chi, Taiwan	TCU122	7.6	9.4	475	2.1
18	1611	Duzce, Turkey	Lamont 1058	7.1	0.2	425	5.0
19	1628	St Elias, Alaska	Icy Bay	7.5	26.5	275	3.4
20	2114	Denali, Alaska	TAPS Pump Station #10	7.9	2.7	329	1.1

Table 11.5 Recorded data for the 2475-year return period.

Ground Motion	NGA No.	Earthquake	Station	Magnitude	Distance (km)	V_s30 (m/sec)	Scale Factor
1	175	Imperial Valley-06	El Centro Array #12	6.5	17.9	197	8.5
2	286	Irpinia, Italy-01	Bisaccia	6.9	21.3	1000	9.0
3	728	Superstition Hills-02	Westmorland Fire Sta	6.5	13.0	194	5.1
4	729	Superstition Hills-02	Wildlife Liquef. Array	6.5	23.9	207	4.4
5	838	Landers	Barstow	7.3	34.9	371	8.5
6	879	Landers	Lucerne	7.3	2.2	685	3.6
7	900	Landers	Yermo Fire Station	7.3	23.6	354	4.9
8	1158	Kocaeli, Turkey	Duzce	7.5	15.4	276	3.1
9	1161	Kocaeli, Turkey	Gebze	7.5	10.9	792	5.7
10	1176	Kocaeli, Turkey	Yarimca	7.5	4.8	297	2.5
11	1494	Chi-Chi, Taiwan	TCU054	7.6	5.3	461	4.0
12	1504	Chi-Chi, Taiwan	TCU067	7.6	0.6	434	2.5
13	1510	Chi-Chi, Taiwan	TCU075	7.6	0.9	573	3.4
14	1527	Chi-Chi, Taiwan	TCU100	7.6	11.4	474	4.7
15	1529	Chi-Chi, Taiwan	TCU102	7.6	1.5	714	2.1
16	1605	Duzce, Turkey	Duzce	7.1	6.6	276	2.2
17	1611	Duzce, Turkey	Lamont 1058	7.1	0.2	425	9.0
18	1628	St Elias, Alaska	Icy Bay	7.5	26.5	275	5.8
19	1762	Hector Mine	Amboy	7.1	43.1	271	5.8
20	2114	Denali, Alaska	TAPS Pump Station #10	7.9	2.7	329	2.1

12. Performance of Concrete Shear Wall Boundary Elements under Pure Compression

Jorge Archbold Monterrosa

ABSTRACT

Reinforced concrete shear walls are one of the most widely used vertical elements to resist seismic forces around the world. Following the M_w 8, 2010 Chilean earthquake, a reconnaissance visit was conducted by several investigators to have a better understanding of seismic performance of concrete structures. Such visit exposed some deficiencies of the Chile's building code related to the performance of reinforced concrete boundary elements of shear walls. This is of great interest since Chile adopted that code in 1996 based on ACI 318-95. This visit along with previous research conducted in 2010 and 2012 have shown that current U.S. standards for concrete boundary elements are not achieving the necessary ductile behavior for shear wall boundary elements under seismic loads. The objective of this research is to understand the effect of the vertical spacing between transversal reinforcement, the spacing of tied longitudinal reinforcement, and the cross-tie orientation in the ductile behavior of boundary elements under pure compression.

12.1 INTRODUCTION

Shear walls are structural elements that are commonly used to resists lateral wind or earthquake forces parallel to the plane of the wall along with the gravity loads from upper stories. These types of walls are commonly designed with longitudinal reinforcement concentrated in special regions located at each edge to increase their flexural strength; these special regions are known as boundary elements (see Figures 12.1. and 12.2). Searching to optimize the design of these elements, engineers have pushed design limits in recent years, resulting in wall with high structural demands and thinner profiles These walls are believed to vulnerable to an unconventional failure mechanism that is not driven by prior yielding in tension, as was expected, but instead is the result of the instability of boundary elements. The behavior of these walls has not been fully understood yet, and deeper study is necessary to generate new models to analyze and predict the performance of these walls and to achieve adequate ductile behavior.

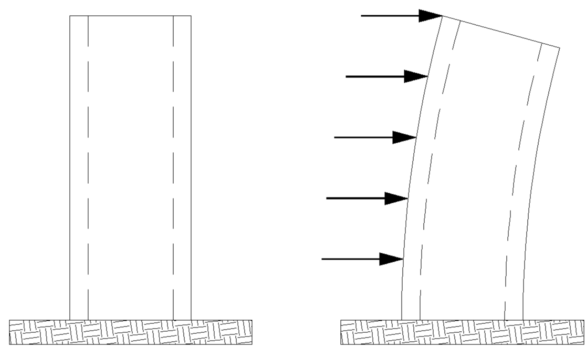

Figure 12.1 Shear walls under seismic force.

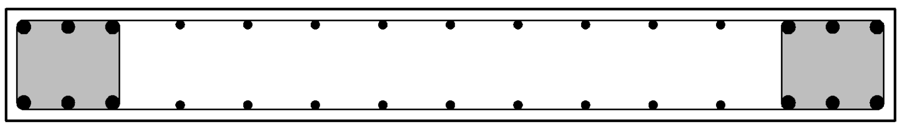

Figure 12.2 Boundary element within dimension of wall.

This project studied four different specimens of boundary elements of reinforced concrete walls. Each specimen was designed to comply with the ACI-318 [ACI 2011]. All specimens were similar to each other and to those tested previously [Acevedo et al. 2010; Cook et al. 2012]. The variables of interest in this case study were the vertical spacing between transversal reinforcement, the spacing of tied longitudinal reinforcement, and the cross-tie orientation. All specimens were assembled, cast, instrumented, and tested at the University of California, Berkeley (UCB), laboratory facilities. Each wall was compared to a numerical nonlinear model created using OpenSees software [McKenna et al. 2000].

This report discusses the test results of the specimens Wall 6 and Wall 7. Results of the performance of Wall 4 and Wall 5 can be found in Chapter 13 of this report [Martinez 2013]. Preliminary results suggests that designing this type of boundary elements according to ACI-318 does not result in ductile structural elements for this special type of shear wall.

Section 12.2 presents the state-of-the-art, with emphasis on previous investigations conducted at UCB. Section 12.3 details laboratory and modeling procedures. Comparison of the nonlinear model created with the OpenSees software [McKenna et al. 2000] and experimental data obtained from the test is given in Section 12.4. Finally, the models are used to compare the expected ductile behavior of the elements with the actual behavior, and the conclusions and suggestions for future research are presented in Section 12.5.

12.2 BACKGROUND

This research project is an extension of the previous work conducted in 2012 by interns Dustin Cook and Andrew Lo, and directed by Professor Jack P. Moehle [Cook 2012; Lo 2012]. In that previous project, four full-scale shear walls with boundary elements were built. Due to construction issues, only three of them could be instrumented and tested successfully under pure compression, with the purpose of determining their structural response and analyzing their ductile behavior. These specimens were designed according to ACI-318-11 Section 21.9.6.4.c. The first two specimens (Wall 1 and Wall 2) were designed with overall dimensions of 8-in wide, 24 in. long, and 48 in. high. Wall 3 was designed with a different gross section of 12 in. wide, 36 in. long, and 72 in. high. All three specimens had concrete heads added to their top and bottom ends in order to ensure a fully distributed load pattern while testing; see Table 12.1. Identifying he configuration that provided the best confinement to the concrete within the core section was a key objective for both studies in 2012.

12.3 METHODS

12.3.1 Specimen Design and Layout

This report discusses the results found for two out of the four specimens (Wall 6 and Wall 7). All four specimens complied with ACI-318 [ACI 2011; Eq. 21-5]. These two walls were designed to test the importance of the variable h_x, which is the distance measured from center-to-center of cross ties or hoop legs in the long direction of the cross section. Wall 6 and Wall 7 were designed with the same gross dimensions of Wall 3 of the 2012 study, i.e., 12 in. wide, 36 in. long, and 72 in. high. Both walls had concrete heads added to guarantee that the compressive load was uniformly distributed along the region of interest. Wall 6 and Wall 7 were also designed with similar longitudinal reinforcement, but the spacing h_x was reduced from 10.3 in. to 7.7 in. (approximately a 25% reduction). A second variable of interest was the cross-tie configuration. These two specimens differed in the type of cross tie used in their construction, Wall 6 had 135° hooks, and Wall 7 had 135° hooks, as shown in Figure 12.3.

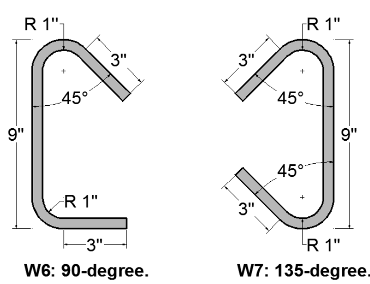

Figure 12.3 Cross-tie configuration used.

Table 12.1 Dimensions and reinforcement detailing of UC Berkeley 2012 walls.

	Wall	s (in.)	h_x (in.)	A_{shx} (in.^{2})	A_{shy} (in.^{2})	ACI-318 (Eq. 21-5) $0.09sl_c \dfrac{f'_c}{f'_{yt}}$ (in.^{2})	ACI-318 (Eq. 21-4) $0.3sl_c \dfrac{f'_c}{f'_{yt}}\left(\dfrac{A_g}{A_{ch}}-1\right)$ (in.^{2})	$\dfrac{h_x \cdot s}{A_{ch}}$
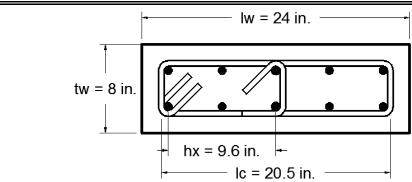	W1	2.66	9.6	0.39	0.59	0.31	0.85	0.28
	W2	1.69	9.6	0.39	0.59	0.20	0.55	0.18
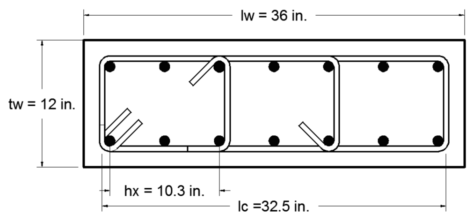	W3	3.96	10.3	0.39	0.79	0.61	0.93	0.15

where:

s	=	center-to-center spacing of transverse reinforcement
A_{shx}	=	total cross-sectional area of transverse reinforcement within spacing s, in the long direction of the section
A_{shy}	=	total cross-sectional area of transverse reinforcement within spacing s, in the short direction of the section
l_c	=	long direction of the section core
h_x	=	center-to-center horizontal spacing of crossties or hoop legs in the long direction of the section
A_{ch}	=	total core area
A_g	=	total gross area of concrete section
f'_c	=	compressive strength of unconfined concrete
f'_{yt}	=	yield strength of transverse reinforcement

Table 12.2 Dimensions and reinforcement detailing of UC Berkeley 2013 Walls 6 and 7.

	Wall	s (in.)	h_x (in.)	A_{shx} (in.^{2})	A_{shy} (in.^{2})	ACI-318 (Eq. 21-5) $0.09sl_c \frac{f'_c}{f'_{yt}}$ (in.^{2})	ACI-318 (Eq. 21-4) $0.3sl_c \frac{f'_c}{f'_{yt}}\left(\frac{A_g}{A_{ch}}-1\right)$ (in.^{2})	$\frac{h_x \cdot s}{A_{ch}}$
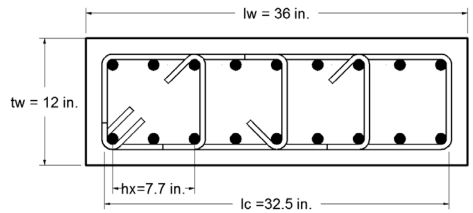	W6	3.96	7.7	0.39	0.98	0.73	1.11	0.11
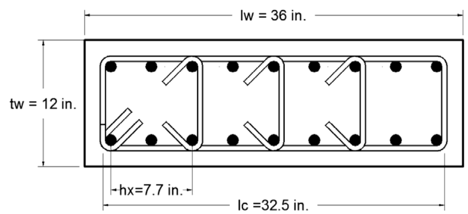	W7	3.96	7.7	0.39	0.98	0.73	1.11	0.11

where:

s = center-to-center spacing of transverse reinforcement

A_{shx} = total cross-sectional area of transverse reinforcement within spacing s, in the long direction of the section

A_{shy} = total cross-sectional area of transverse reinforcement within spacing s, in the short direction of the section

l_c = long direction of the section core

h_x = center-to-center horizontal spacing of crossties or hoop legs in the long direction of the section

A_{ch} = total core area

A_g = total gross area of concrete section

f'_c = compressive strength of unconfined concrete

f'_{yt} = yield strength of transverse reinforcement

To provide the longitudinal reinforcement in these walls, two curtains of nine #7 bars $\left(d_b = 7/8\,\text{in.}\right)$ were used. Nineteen #4 transverse hoops spaced at 3.96 in. (center-to-center) were used along with a set of three #4 cross ties per layer of transversal reinforcement equally distributed within the longitudinal rebars. A concrete cover of 1.5 in. was used to protect all rebar against corrosion and other attacks. Table 12.2 summaries the dimensions and detailing of Wall 6 and Wall 7. Figure 12.4 shows the reinforcement layout of Wall 6 and Wall 7.

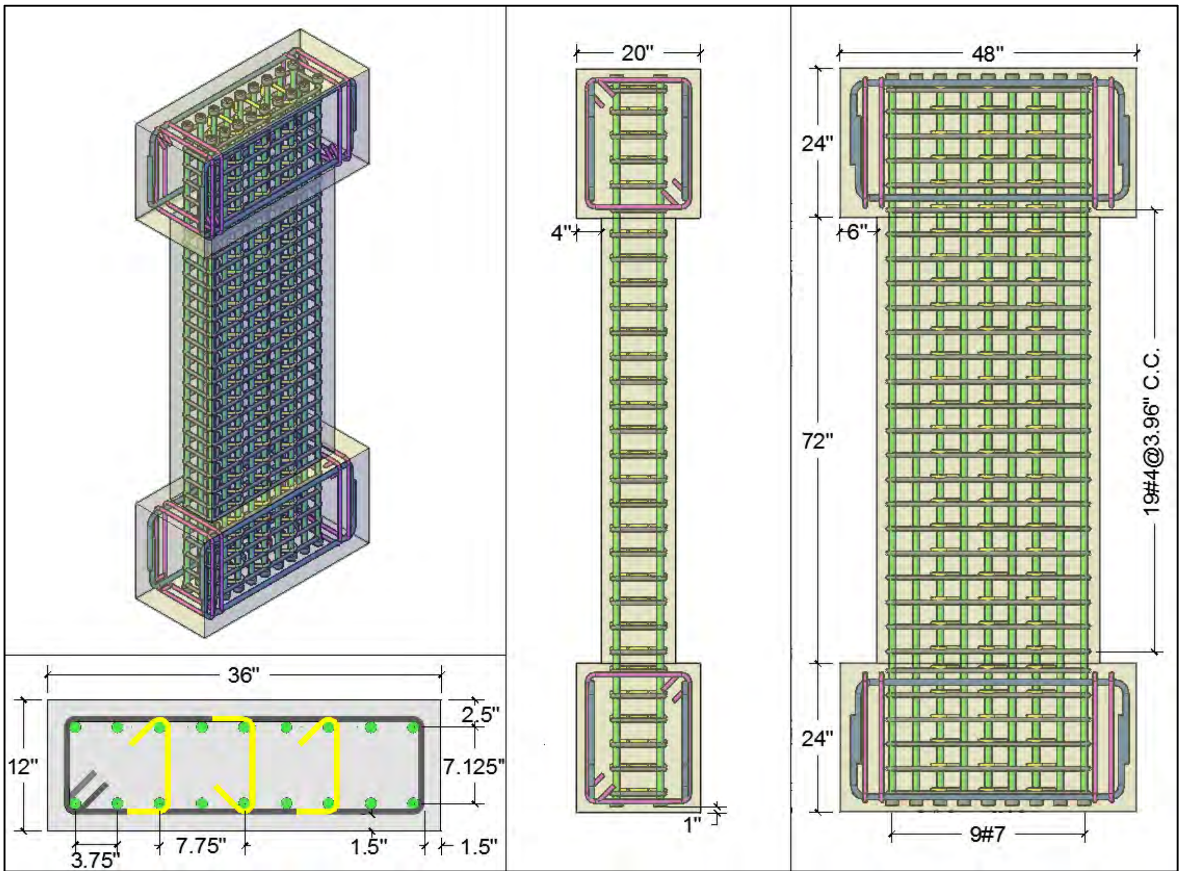

Figure 12.4 Reinforcement layout.

12.3.2 Material Properties

Four specimens were cast using a ready-mixed concrete with 3/4 in. maximum aggregate size and a specified slump of 5 in, and a specified compressive strength of 4500 psi at 28 days. Standard 6 in. diameter×12 in. high cylinders were cast using the same concrete. Both the walls and the cylinders were moist cured for four days and then air-cured for the rest of the period.

The compressive strength and the stress-strain curve of the unconfined concrete used were determined by testing a set of the above-mentioned cylinders. The average unconfined compressive strength at 28 days was 4.04 ksi. The range of strength during the period of testing varied from 3.96 ksi for the first specimen tested at 24 days to 4.35 ksi for the last specimen tested at 57 days. Refer to Figure 12.5 to see the evolution of the strength of the concrete versus time. Table 12.3 shows the average yielding strength in tension $\left(f_y\right)$, the average ultimate strength $\left(f_{su}\right)$, and the average strain corresponding to ultimate strength $\left(\varepsilon_{su}\right)$ for the different reinforcing steel used in the specimens construction.

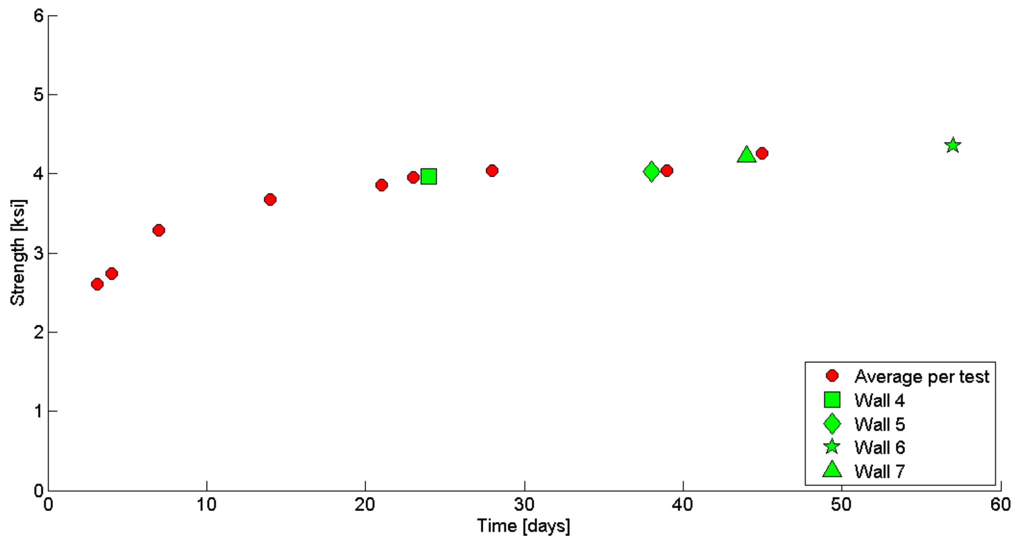

Figure 12.5 Strength versus time relationship of the unconfined concrete.

Table 12.3 Properties of reinforcing steel.

Bars No.	Average f_y (ksi)	Average f_{su} (ksi)	Average ε_{su}
4	66.1	96.6	0.173
7	67.9	87.9	0.17
8	69.6	92.2	0.16

12.3.3 Instrumentation and Test Set-Up

To determine whether or not the wall specimens behaved in a ductile manner, it was necessary to compute a load versus strain curve. The load was obtained from the data acquisition system connected to load cell of the 4-million-pound-capacity Universal Testing Machine (UTM), which was used to applied force to the specimens. Both the longitudinal strain and the transversal strains were of interest.

Four steel strain gauges were attached to each of the four corners of the longitudinal rebar of each specimen to obtain the longitudinal strain. Seven linear variable differential transformer (LVDT) displacement transducers were placed along each of the long side (front and back) of the wall, which had been divided into seven levels. In addition, four LVDT displacement transducers were installed on each wall (left and right), two of them at each side and located at each head (top and bottom). Five concrete strain gages were attached on the front sides along the length of the wall and evenly distributed along the depth of the specimen. Different instruments were used to assure that there was redundancy in the data acquisition. See Figure 12.6 for a layout of the instrumentation.

Strain in the transverse reinforcement was measured using six additional steel strain gages. Three strain gauges measured the transversal hoops, and the rest of them measured the three cross ties. As shown in Figure 12.6, a set of eight wire potentiometers were used to measure the out-of-plane displacement of the wall. Figure 12.7 shows the specimens throughout different stages of the construction process and their instrumentation, including reinforcement assembly, concrete casting, and concrete curing.

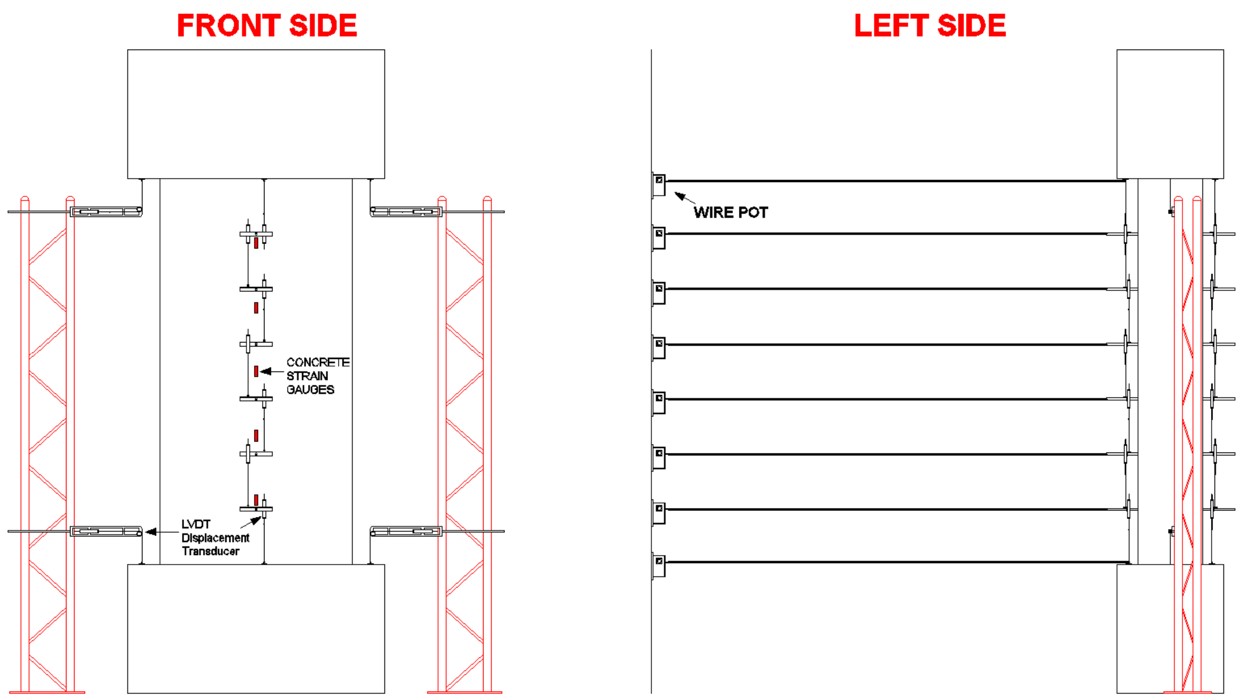

Figure 12.6 Layout of the instrumentation used during testing.

Figure 12.7 Different stages during the construction and set-up of the specimens.

12.3.4 Nonlinear Model

The response of both specimens were compared to a numerical nonlinear model created using the OpenSees software [McKenna et al. 2000]. The monotonic load that was applied during the test to the specimens was applied to the model using a pushover analysis approach. Element truss were used to model the specimens. The total height of the walls (72 in.) was divided into seven sections, using eight equally spaced nodes (10.28 in). Using the *Non-LinearAnalysisofFiberSections* approach, each section was divided into three different truss elements, representing the different materials with their corresponding stress versus strain curves obtained from theoretical models. The unconfined concrete was modeled using a zero tensile strength model using some of Mander et al.'s [1988] parameters as input. To model the confined concrete, a uniaxial concrete material with tensile strength and linear tension stiffening was used based on Mander et al. [1988]. Longitudinal rebars were modeled using a uniaxial Giuffre-Menegotto-Pinto steel material object with isotropic strain hardening [Filippou et al. 1983].

12.4 RESULTS

Figure 12.8 presents the behavior of all material within each level according to the nonlinear model. They are compared to the expected behavior of the wall based on the displacement of the top node. Figures 12.9 and 12.10 show the structural response of Wall 6 and Wall 7, respectively. Each figure compares the data obtained from the test and the numerical nonlinear model. The expected load-strain relationship from the model was compared to the test results. Wall 6 and Wall 7 reached a peak load of 2318 kips and 2343 kips, respectively. Figure 12.11 plots different load versus strain curves obtained from the tests results and compares them to the expected behavior. Figure 12.12 shows Wall 7 tested to failure after being tested under pure compression.

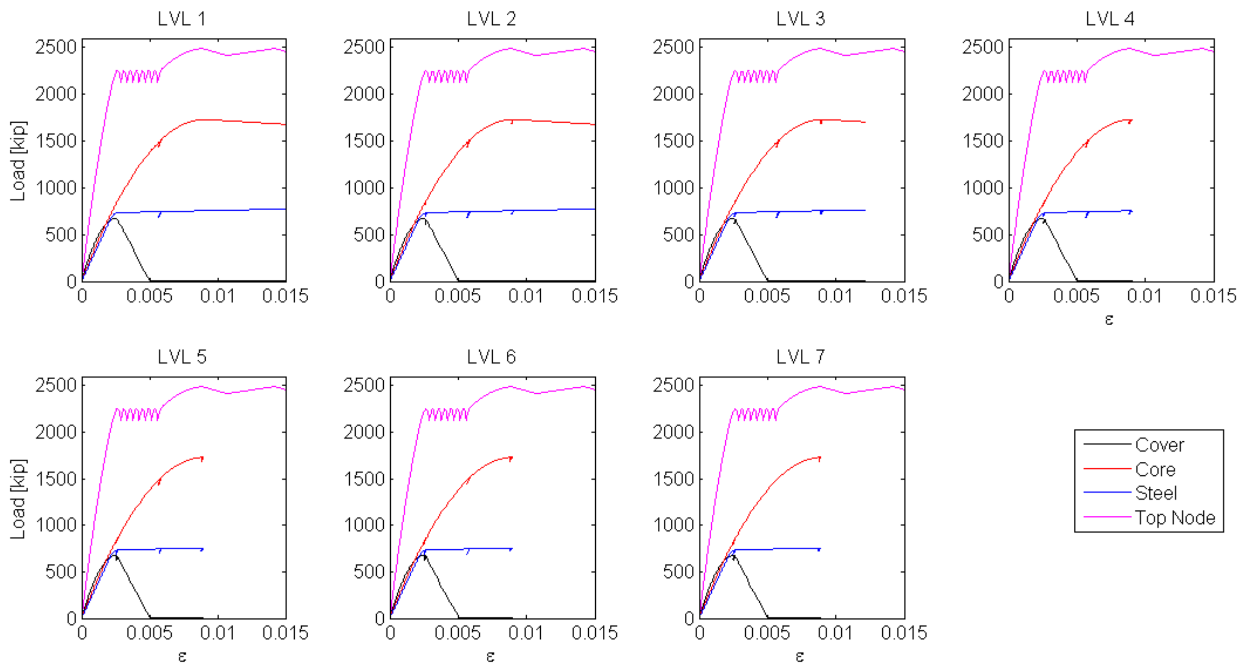

Figure 12.8 Wall 6: structural response under pure compression.

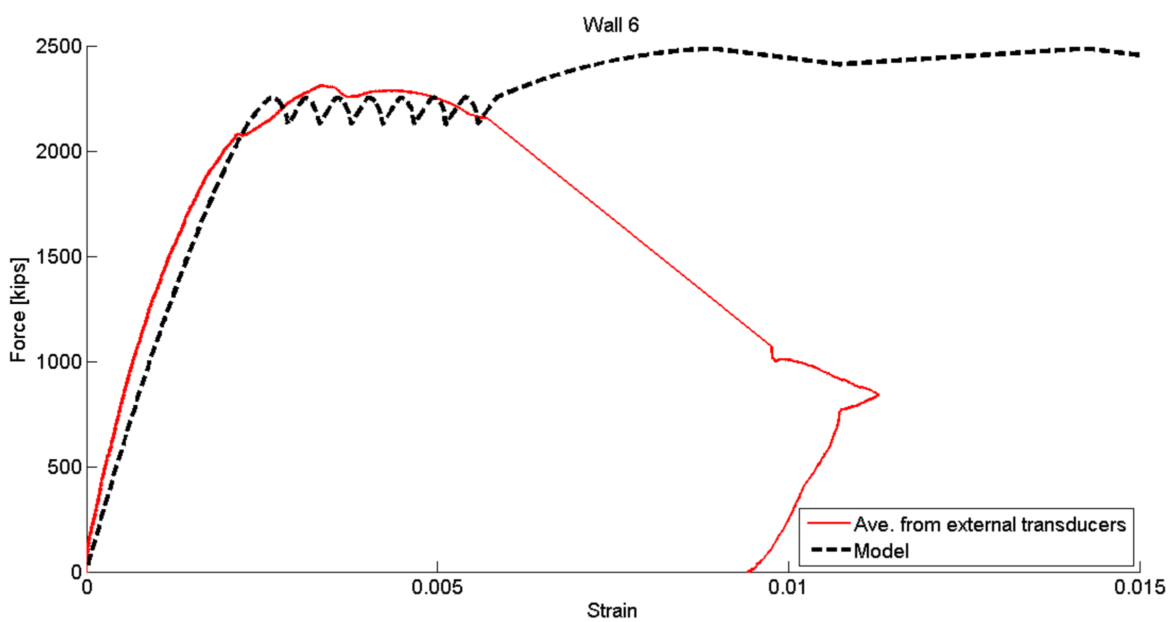

Figure 12.9 Wall 6: structural response under pure compression.

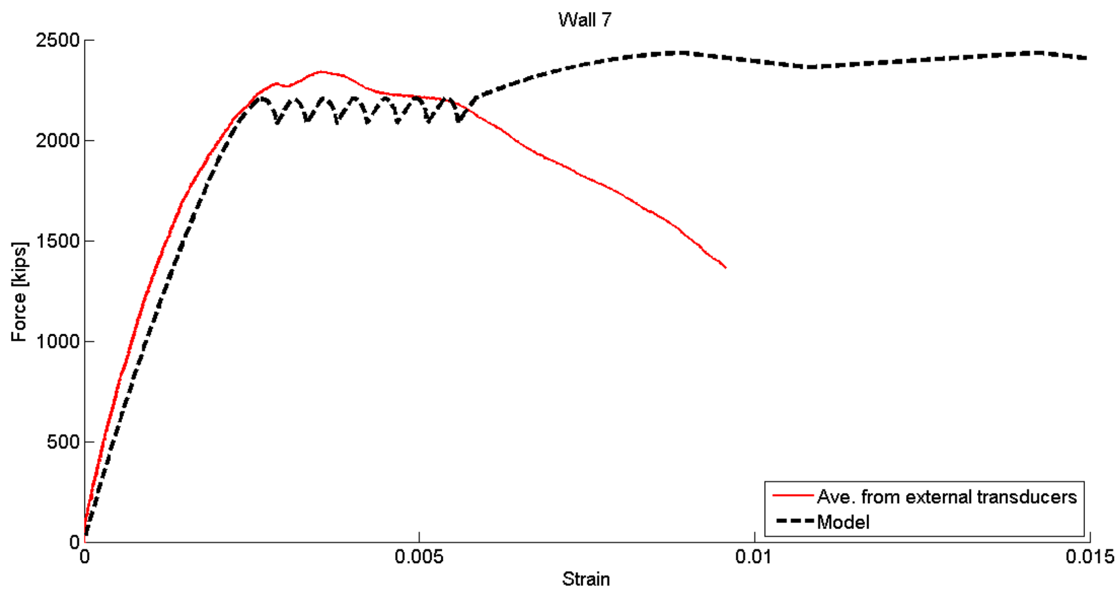

Figure 12.10 Wall 7: structural response under pure compression.

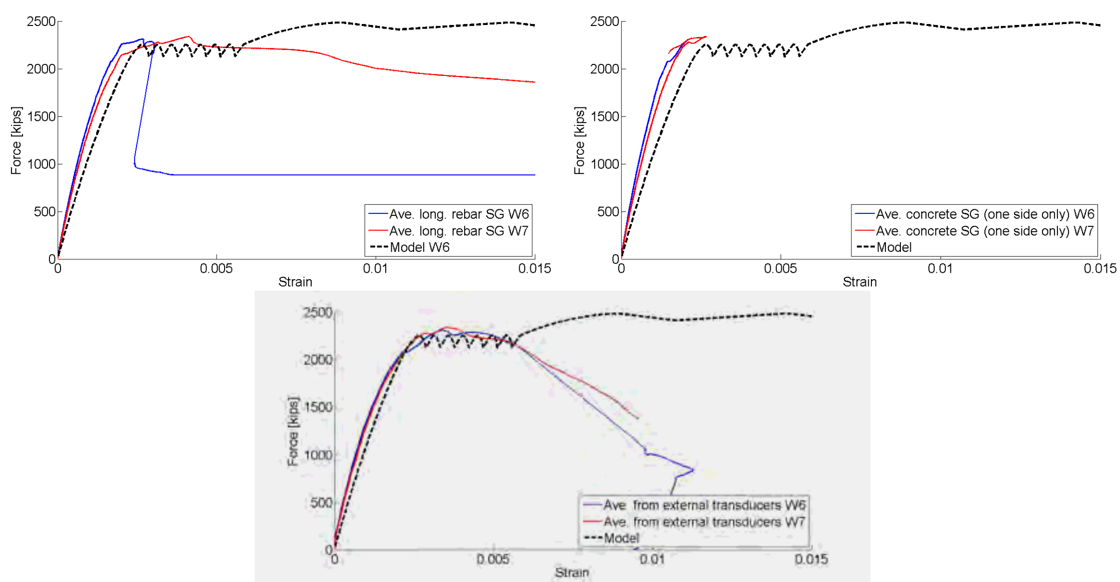

Figure 12.11 Wall 6 versus Wall 7: comparison of response.

Figure 12.12 Wall 7 after failure.

12.5 CONCLUSIONS

Both specimens behaved similarly before failure. Upon reaching peak load, each specimen behaved differently, but neither of them continued to gain strength, exhibiting non-ductile behavior. The results obtained in this study and previous research results corroborate the inadequacy in ACI 318-11 regarding special reinforced concrete boundary elements. All specimens studied experienced brittle failures and did not achieve the expected ductile behavior.

Cross-tie orientation (90 or 135° ties) within boundary elements does not appear to be a critical variable in achieving ductile performance; Wall 6 and Wall 7 only differed in configuration of their ties. The vertical spacing between the transversal reinforcement does not appear to be a factor either, since walls with spacing as small as 1.69 in. and 2.80 in. were tested in 2012. Not only did varying the vertical spacing not achieve ductile behavior, constructability became an issue.

Further research is needed in order to acquire a better understanding of the performance of these shear walls, with the objective of producing more accurate analytical models that reflect non-ductile behavior and new designs that can achieve ductile behavior. It is hoped that improved models and designs will lead to revision of the ACI code for concrete shear walls.

12.6 ACKNOWLEDGMENTS

This research project was supported and funded by The George E. Brown, Jr. Network for Earthquake Engineering Simulation (NEES), through the 2013 PEER internship program. I would like to thank everyone that was involved somehow in this research program, especially, Professor Jack P. Moehle, our faculty advisor, and Ph.D. student Carlos Arteta, our committed graduate mentor, for their support and guidance during the project. I also would like to thank my coworkers Daniela Martinez Lopez and Itria Licitra for their constant help, and for making this experience more enjoyable and to all the staff at both UC Berkeley lab facilities (Richmond Field Station and Davis Hall). And last, my gratitude to Heidi Tremayne for gathering us all together and making this internship program possible.

12.7 REFERENCES

ACI (2011). *Building Code Requirements for Structural Concrete and Commentary, ACI 318-11*, American Concrete Institute, Farmington Hills, MI.

Acevedo C.E. (2010). Seismic vulnerability of non-speical boundary element of shear wall under axial force reversals., Pacific Earthquake Engineering Research Center, University of California, Berkeley, CA.

Cook D. (2012). Ductility of reinforced concrete shear wall boundary elements in compression, *PEER Report 2012/07*, Pacific Earthquake Engineering Research Center, University of California, Berkeley, CA, pp. 5–16.

Filippou F.C., Popov E.P., Bertero V.V. (1983). Effects of bond deterioration on hysteretic behavior of reinforced concrete joints, *Report UCB/EERC-83-19*, Earthquake Engineering Research Center, University of California, Berkeley, CA.

Lo, A. (2012). Exploring behavior of thin shear wall boundary element in compression, *PEER Report No. 2012/07*, Pacific Earthquake Engineering Research Center, Universiyt of California, Berkeley, CA, pp. 19–54.

Mander J.B., Priestley M.J.N., Park R. (1998). Theoretical stress-strain model for confined concrete, *J. Struct. Eng*., 114(8): 1804–1825.

Martinez D. (2013). Exploring adequate layout for ductile behavior of reinforced concrete shear walls boundary element in compression, *PEER Report No. 2013/25*, Pacific Earthquake Engineering Research Center, Universiyt of California, Berkeley, CA.

McKenna F., Fenves G.L., Scott M.H., Jeremic B. (2000). Open System for Earthquake Engineering Simulation (OpenSees), Pacific Earthquake Engineering Research Center, University of California, Berkeley, CA.

13. Exploring Adequate Layout for Ductile Behavior of Reinforced Concrete Shear Walls Boundary Elements in Compression

Daniela Martinez Lopez

ABSTRACT

Four reinforced concrete shear walls specimens were assembled, instrumented, cast, and tested in pure compression during summer of 2013.The main purpose of the experiments was to evaluate current ACI-318 Building Code provision in order to develop an adequate reinforcement layout that is both constructible and provides the confinement necessary to achieve the ductile behavior desired during seismic events. Results from tests confirm that the layout design of using 135° cross ties anchored in the longitudinal bars do not provide the specimen with a better restraint or a ductile response.

13.1 INTRODUCTION

Reinforced concrete shear walls are structural systems that have been commonly used worldwide due to their high capacity in resisting seismic forces during an earthquake event. Seismic forces acting on the building are transferred to the shear walls as distributed horizontal forces. These forces are supported by internal shear stresses in the wall and require the development of a force coupling mechanism that resists the moment and axial load demand at the various levels along the height of the wall. To achieve large deformations in a ductile manner at levels of high demand, this tension-compression coupling mechanism requires special reinforcement detailing at the ends of the walls, known as boundary elements. Figure 13.1 shows a schematic localization of the boundary elements of a special structural wall.

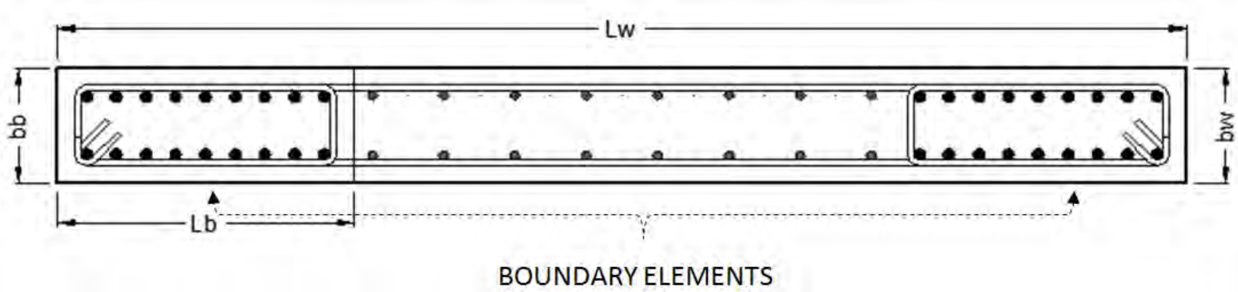

Figure 13.1 Plan view of boundary element in concrete reinforced shear walls.

This project studied four separate shear wall boundary elements in pure compression. Each design followed ACI 318-11 [ACI 2011] provisions. This research analyzed whether different reinforcement configurations used to confine the concrete core could achieve ductile performance of the walls. The different configurations tested differed in the number of ties per level, the spacing between transverse reinforcement, and the configuration of tie hooks. The four specimens were modeled and analyzed using the computer software OpenSees [McKenna et al. 2000] prior to being tested at the nees@berkeley Laboratory, U.C. Berkeley (UCB), Richmond Field Station, using a four-million-pound universal testing machine. Preliminary research has demonstrated that a more confined concrete core can provide the boundary elements with the ductile behavior desired under compression loads.

The 2013 specimens were part of a larger group of shear walls designed, constructed, and tested in 2012 as part of the 2012 PEER Summer Internship Program [Cook 2012; Lo 2012]. The performance and test results of Wall 3 from 2012 and Wall 5 from 2013 are discussed and compared in this report. Wall 4 from the 2013 wall tests was constructed and tested, but defects in the foundation during the construction process affected the test results. The data obtained was considered only partially valid. Wall 6 and Wall 7 from the 2013 wall tests are analyzed in Chapter 12 of this report by Archbold [2013].

13.2 BACKGROUND

In 2012, three reinforced concrete shear wall boundary elements—referred to herein as Wall 1, Wall 2, and Wall 3—were constructed, assembled, and cast at UCB in order to study their behavior under monotonic compression loads. Wall 1, Wall 2, and Wall 3 complied with Section 21.9.6.4.c of ACI-318 [ACI 2011]. Wall 2 also complied with ACI-318 Eq. 21-4, which, although required for reinforced concrete columns transverse reinforcement design, is not obligatory for special boundary elements in shear walls. Table 13.1 specifies the transverse reinforcement arrangement and geometry used in the designs of the tested Wall 1, Wall 2, and Wall 3.

Table 13.1 Proposed geometry and transverse reinforcement of 2012 UCB test of Wall 1, Wall 2 and Wall 3.

	Wall	s (in.)	h_x (in.)	A_{shx} (in.^{2})	A_{shy} (in.^{2})	ACI-318 (Eq. 21-5) $0.09 s l_c \frac{f'_c}{f'_{yt}}$ (in.^{2})	ACI-318 (Eq. 21-4) $0.3 s l_c \frac{f'_c}{f'_{yt}}\left(\frac{A_g}{A_{ch}}-1\right)$ (in.^{2})	$\frac{h_x \cdot s}{A_{ch}}$
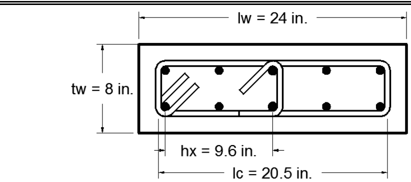	W1	2.66	9.6	0.39	0.59	0.31	0.85	0.28
	W2	1.69	9.6	0.39	0.59	0.20	0.55	0.18
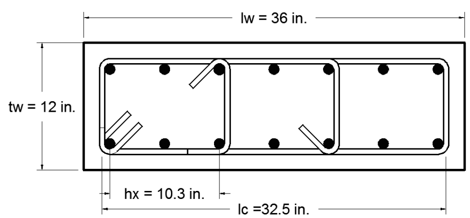	W3	3.96	10.3	0.39	0.79	0.61	0.93	0.15

where:

s = center-to-center spacing of transverse reinforcement

A_{shx} = total cross-sectional area of transverse reinforcement within spacing s, in the long direction of the section

A_{shy} = total cross-sectional area of transverse reinforcement within spacing s, in the short direction of the section

l_c = long direction of the section core

h_x = center-to-center horizontal spacing of crossties or hoop legs in the long direction of the section

A_{ch} = total core area

A_g = total gross area of concrete section

f'_c = compressive strength of unconfined concrete

f'_{yt} = yield strength of transverse reinforcement

Figure 13.2 shows the axial load and average strain relations for the 2012 specimens. As shown in the figure, these walls did not behave in a ductile manner, losing strength quickly. All walls experienced brittle failure, with buckling after the steel yielded and the concrete cover spalled off, demonstrating that the concrete core was not stronger than the overall wall section [Cook 2012]. These results were the impetus behind the current project, which investigates if reducing reinforcement spacing or adding 135° hooks to the ties engaging the longitudinal bars will produce a ductile response in the specimens.

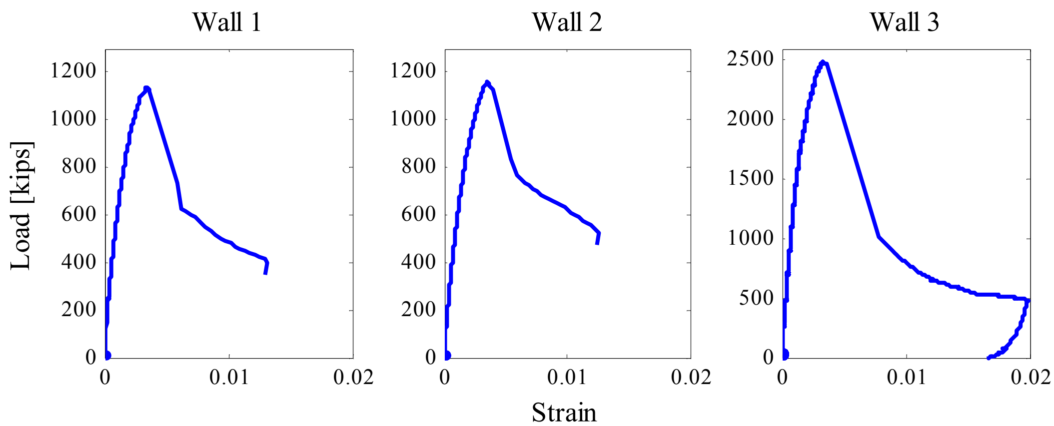

Figure 13.2 **Axial load and average compressive strain relations results from 2012 UCB wall tests.**

13.3 PROPOSED GEOMETRY AND REINFORCEMENT LAYOUT

The walls tested in 2013 have similar characteristics in terms of geometry, materials, and the amount of transverse reinforcement as those tested in 2012. Table 13.2 summarizes the geometry and reinforcement characteristics of the 2013 walls. Transverse reinforcement of the four specimens complies with Section 21.9.6.4.c of ACI-318.

Specimen Wall 4 also complied with ACI-318-Eq. 21-4, which is not mandatory, but because a construction defect caused failure of its base, the results obtained are not necessarily valid (see notes in Table 13.2). Wall 5 had the same design as the 2012 Wall 3; however, both ends of the ties were anchored into the core with 135° hooks in order to study the influence of this configuration on the performance of the confined concrete core.

Wall 6 and Wall 7 had similar areas of longitudinal reinforcement, but these two specimens were constructed with a 25% reduction in the distance between the tie bars. Wall 6 had ties with 90° hooks, and Wall 7 had ties with 135° hooks to test the influence of these configurations in the adequate restraint of longitudinal rebar.

Table 13.2 Proposed geometry and transverse reinforcement of 2013 UCB walls.

	Wall	s (in.)	h_x (in.)	A_{shx} (in.^{2})	A_{shy} (in.^{2})	ACI-318 (Eq. 21-5) $0.09sl_c\dfrac{f'_c}{f'_{yt}}$ (in.^{2})	ACI-318 (Eq. 21-4) $0.3sl_c\dfrac{f'_c}{f'_{yt}}\left(\dfrac{A_g}{A_{ch}}-1\right)$ (in.^{2})	$\dfrac{h_x \cdot s}{A_{ch}}$
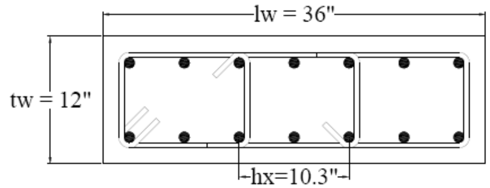	4	2.80	10.3	0.39	0.79	0.52	0.79*	0.10
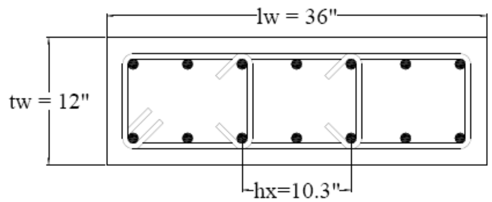	5	3.96	10.3	0.39	0.79	0.73	1.11	0.15
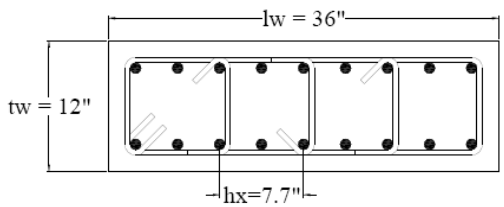	6	3.96	7.7	0.39	0.98	0.73	1.11	0.11
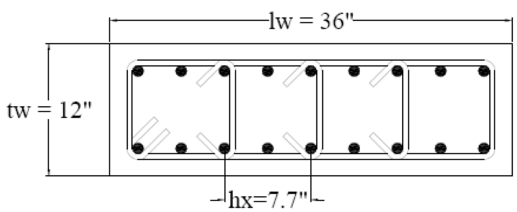	7	3.96	7.7	0.39	0.98	0.73	1.11	0.11

where:

s	=	center-to-center spacing of transverse reinforcement
A_{shx}	=	total cross-sectional area of transverse reinforcement within spacing s, in the long direction of the section
A_{shy}	=	total cross-sectional area of transverse reinforcement within spacing s, in the short direction of the section
l_c	=	long direction of the section core
h_x	=	center-to-center horizontal spacing of crossties or hoop legs in the long direction of the section
A_{ch}	=	total core area
A_g	=	total gross area of concrete section
f'_c	=	compressive strength of unconfined concrete
f'_{yt}	=	yield strength of transverse reinforcement

*Construction defect resulted in unreliable data, thus, no results were included from this specimen in this report.

Figure 13.3 shows the longitudinal and transverse reinforcement layout of Wall 5. The layout for Wall 6 and Wall 7 are detailed in Archbold [2013]. The 2013 Wall 3 has an identical configuration and reinforcement layout of Wall 5, only differing in the configuration of the cross ties; Wall 3 was constructed with 90° cross-tie detailing.

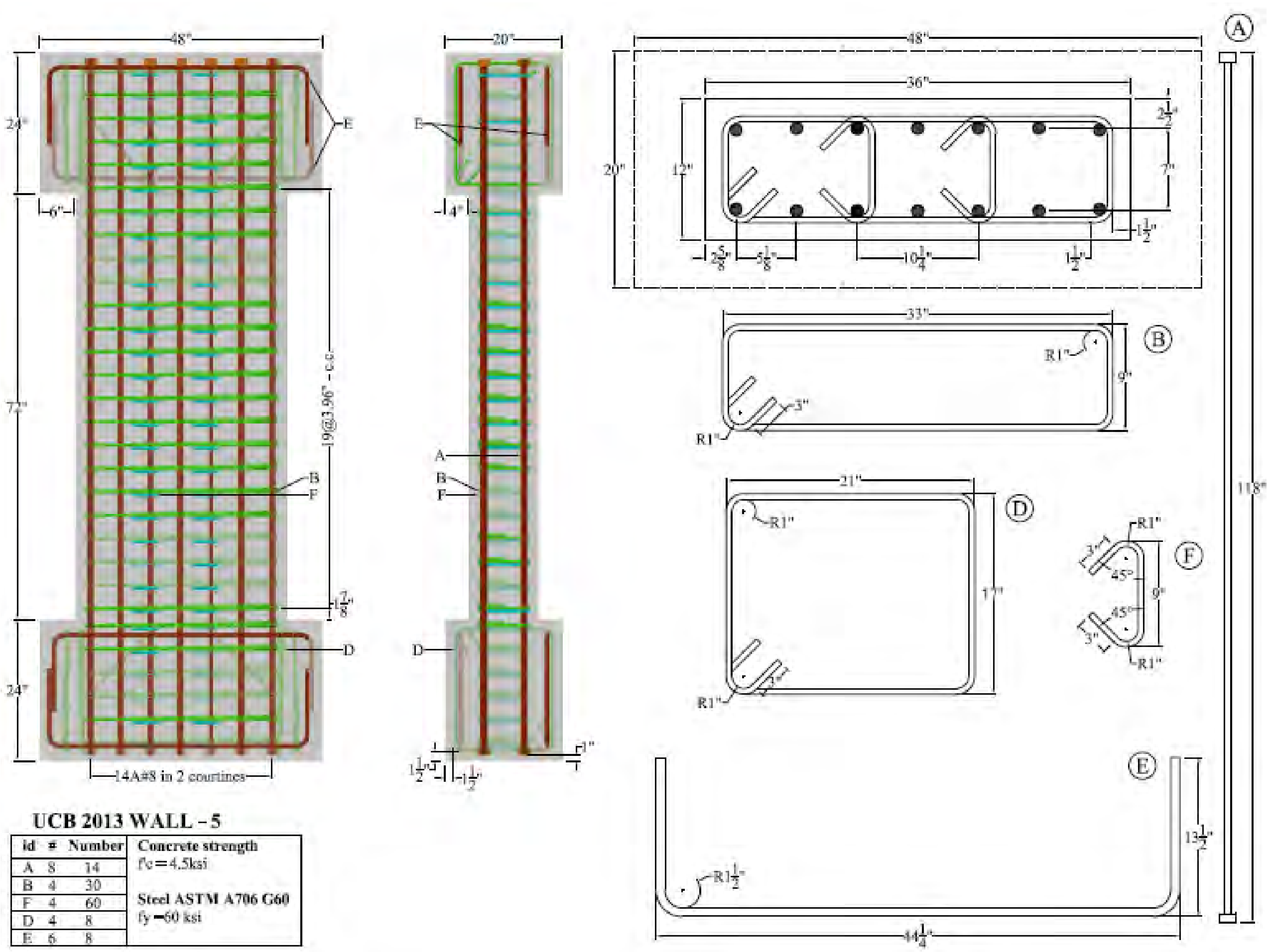

Figure 13.3 Reinforcement layout of Wall 5 [Arteta 2013].

13.4 EXPECTED MATERIAL CHARACTERISTICS AND MATHEMATICAL MODELING

13.4.1 Evaluation of Unconfined Concrete Compressive Strength

Twenty-four concrete cylinders were cast to evaluate concrete compressive strength gain with time according to Section 5.2.2.1 of ASTMC39/C39M–12 [ASTM 2011]; see Figure 13.4. Cylinders were tested in pairs 7, 14, 21, and 28 days after casting. One cylinder was tested after the first three days and another was tested at day 4. The remaining cylinders were tested in trios each day of specimen tests. Figure 13.5 summarizes the observed compressive strength behavior of the unconfined concrete over time.

Figure 13.4 **Concrete cylinders: (a) dimensions of cylinder mold per ASTM standards; (b) concrete cylinder set-up and instrumentation; and (c) concrete cylinder failure pattern.**

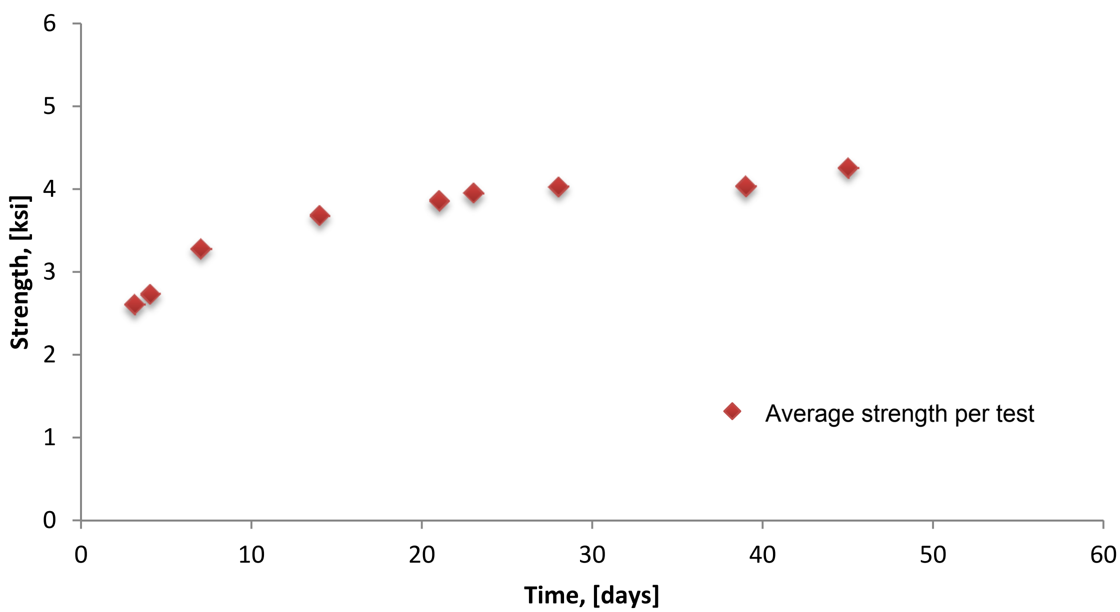

Figure 13.5 **Reported average strength of unconfined concrete with time.**

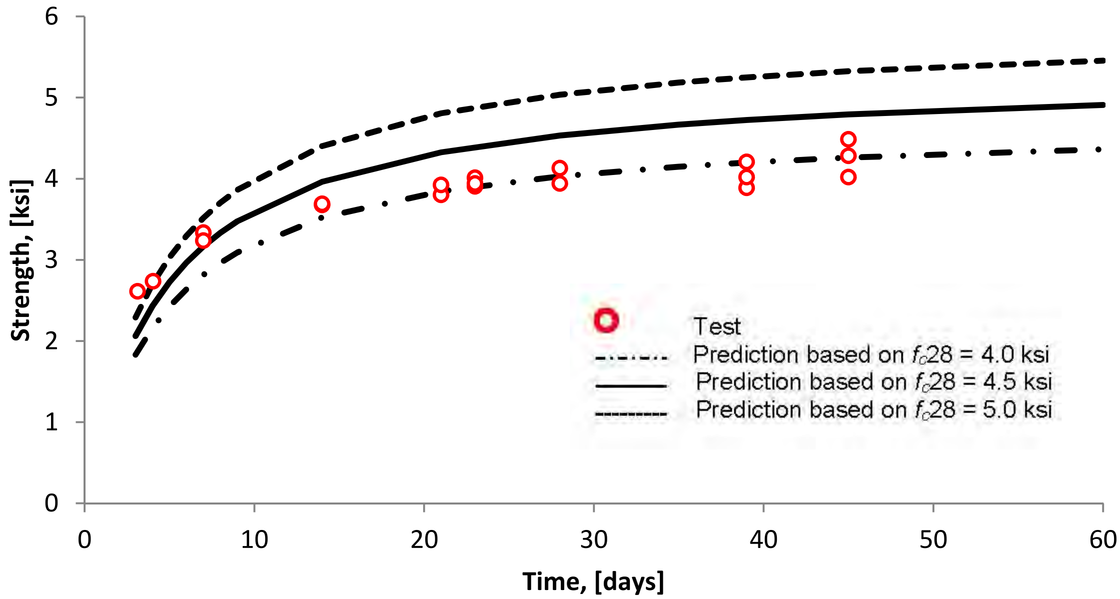

Figure 13.6 Comparison of concrete cylinder tests results and predictions based on Equation (13.1).

Equation (13.1) characterizes the evolution of compressive strength in concrete at 28 days as a function of time and the compressive strength [Monteiro 2006]:

$$f_{cm}(t) = f_{c28}\left(\frac{t}{4+0.85t}\right) \tag{13.1}$$

Figure 13.6 compares the observed average strength of the concrete cylinder tests and the estimations made according to Equation (13.1) based on compressive strengths at 28 days at 4.0 ksi, 4.5 ksi, and 5 ksi. The burlap placement was removed four days after the concrete was poured to slow down the hydration and prevent concrete from gaining more resistance than the one required for the designs. After this, the behavior of the concrete over time was very similar to the prediction made with a compressive strength of 4.0 ksi at 28 days.

13.4.2 Evaluation of Confined Concrete Compression Strength

For the proposed 2013 tests, the confined concrete compressive strength was calculated using the model by Mander et al. [1998]. This model uses a set of equations to calculate the stress-strain behavior of concrete confined with different types of transverse reinforcement, including circular, spiral, or rectangular hoops, and subjected to compressive load. Equations were based on the confinement effectiveness of concrete core after the cover has spalled off. Table 13.3 describes the confined concrete compressive strength of 2012 Wall 3 and 2013 Wall 5, Wall 6, and Wall 7, calculated using the results of the analytical model.

Table 13.3 Confined concrete compressive strength f'_{cc} of the 2012 UCB Wall 3 and 2013 Wall 5, Wall 6, and Wall 7 specimens.

Wall ID	f'_{cc} (ksi)
W3	5.36
W5	6.07
W6	6.52^{+}
W7	6.52^{+}

$^{+}$Wall 6 and Wall 7 only differ in the configuration of the cross ties. This variable was not taken into account in the Mander et al. model [1998].

13.4.3 Mathematical Modeling

Specimen Wall 5 was modeled using OpenSees software [McKenna et al. 2000], which accounts for geometric and material nonlinearities to calculate force-displacement relations. The specimen was modeled with a static nonlinear analysis (pushover). Three different case scenarios were studied to observe how the number of sections and nodes included in the model influence the global behavior of the mathematical model. The specimen was sub-divided in seven sections (8 nodes for the first case, five sections (6 nodes) for the second case, and three sections (4 nodes) for the third case. Each section was modeled along a single path in series, with three separate elements truss set in parallel representing the cross-section materials: the steel, the unconfined concrete localized in the cover of the specimen, and the confined concrete from the core; see Figure 13.7. The properties for each material modeled as an element truss are also inputs for the OpenSees model. Table 13.4 shows the properties inputs from Wall 3 and Wall 5 in particular.

Table 13.4 Wall 3 and Wall 5 properties inputs for OpenSees model.

	Unconfined Concrete Properties				Confined Concrete Properties				Steel Properties	
	f'_c	ε_c	f'_{cu}	ε_{cu}	f'_c	ε_c	f'_{cu}	ε_{cu}	F_y	E
WALL 3	3.7 ksi	0.0026	0.045 ksi	0.005	5.36 ksi	0.008	5.10 ksi	0.018	68.8 ksi	29000
WALL 5	4.5 ksi	0.0026	0.045 ksi	0.005	6.01 ksi	0.009	5.61 ksi	0.024	68.8 ksi	29000

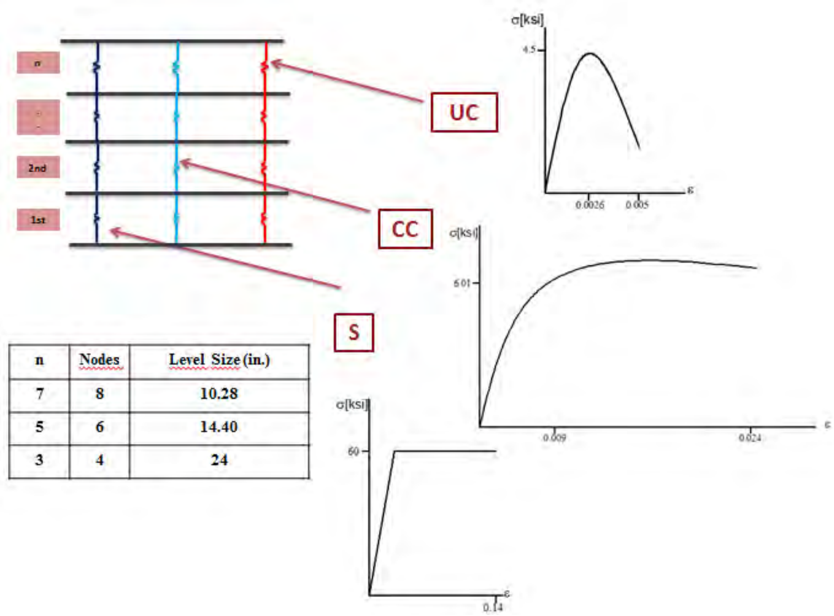

n	Nodes	Level Size (in.)
7	8	10.28
5	6	14.40
3	4	24

Figure 13.7 **OpenSees model schema using seven, five, and three sections. Elements truss S, CC, and UC refer to the steel, the confined concrete from core, and the unconfined concrete from cover, respectively.**

13.5 TEST SET-UP

The 2012 UCB Wall 3 and 2013 UCB Wall 5 were tested in nees@berkeley Laboratory at Richmond Field Station using the 4-million-pound-capacity Universal Testing Machine (UTM). Both specimens were grouted to the floor to ensure a distributed load across their face and instrumented in order to obtain the stress-strain curves and study their ductile behavior. The displacements were measured using strain gages and displacement transducers. Ten strain gages were attached to the longitudinal and transverse reinforcement of each specimen, and external displacement transducers were located at specific points on the walls to measure the relative and total displacement as the specimens deform; additional displacement transducers were located perpendicular to the specimen to obtain the out-of-plane deformation and buckling. Finally, several concrete strain gages were attached along one face of walls for an additional measurement of the wall's relative displacement.

Figure 13.8 shows the instrumentation used in 2013 UCB Wall 5. The specimen had seven displacement transducers in each face and two in each side of the wall in order to measure relative and total displacement, respectively. Figure 13.9 illustrates the set-up process of 2013 UCB Wall 5 before being tested.

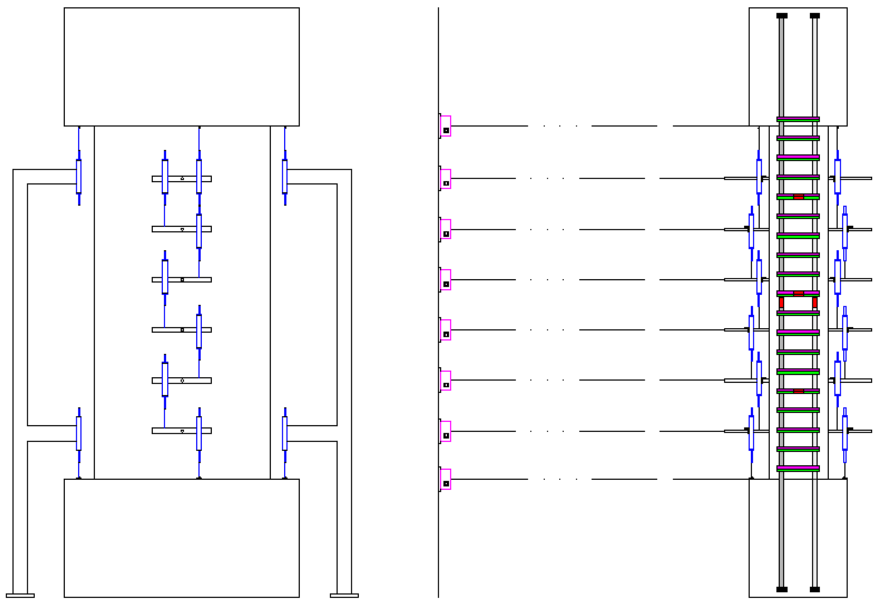

Figure 13.8 2013 UCB Wall 5 instrumentation plan and displacement transducers orientation.

Figure 13.9 **Different stages in the instrumentation and set-up process of the 2013 UCB Wall 5 test.**

13.6 RESULTS

The results obtained from the mathematical model show that the sizes of the sections studied had a significant effect on the overall behavior of the wall. The three models using eight, six, and four nodes predicted a clear brittle failure after yielding, and the wall modeled with the minimum of nodes (four nodes) tended to predict a higher post-peak strength compared to the six- and eight-node models.

Figure 13.10 compares the stress-strain behavior obtained the external transducers and the three mathematical models from OpenSees for walls. As predicted, Wall 5 exhibited a stiffness very similar to the models. It resisted a maximum load of 2300 kips but did not continue to gain strength after yielding, and was accompanied with a slow loss of load capacity, which is evidence of brittle failure as opposed to a ductile response.

As shown in Figure 13.11, the 2013 UCB Wall 5 exhibited very similar behavior compared to the 2012 UCB Wall 3 specimen. During the test, the Wall 5 longitudinal rebar also buckled, causing slow loss of confining force and producing brittle failure. Before reaching peak load carrying capacity, both specimens experienced similar stiffness. Wall 5 showed a steeper slope with reducing strength right after yielding, while Wall 3 showed more axial load capacity than Wall 5. Clearly, the use of cross ties with 135° hooks at both ends in some of the longitudinal rebar did not achieve ductile performance in the walls tested. See Figure 13.12 for illustrative images of the 2013 UCB Wall 5 test.

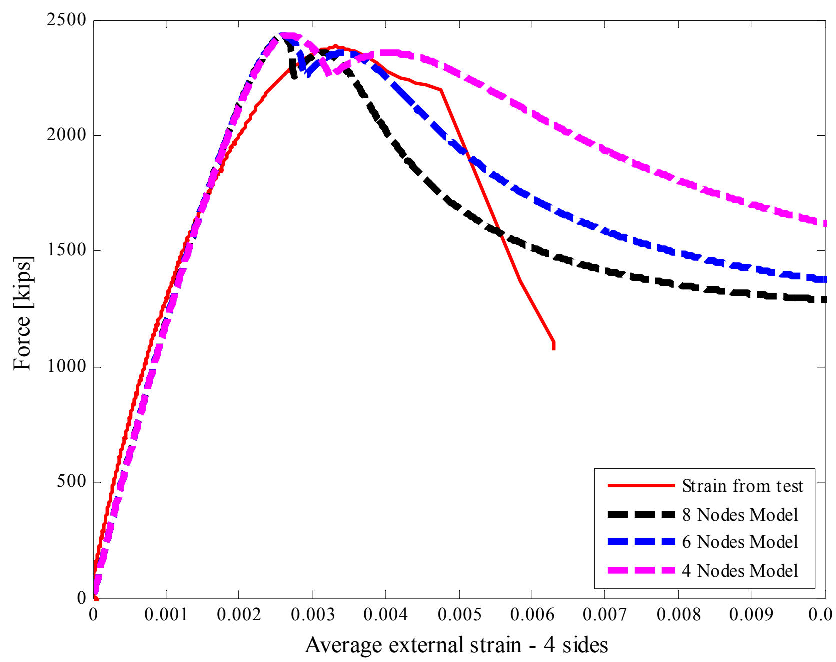

Figure 13.10 Wall 5: comparison of predicted and actual testing results.

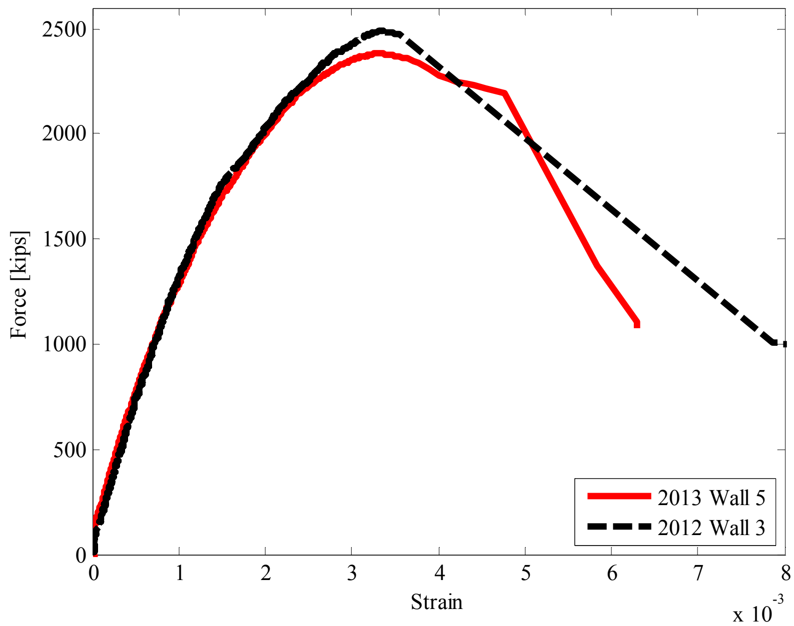

Figure 13.11 2012 Wall 3 and 2013 Wall 5: comparison of test results.

Figure 13.12 2013 Wall 5: tested to failure.

13.7 CONCLUSIONS

The results obtained from the tests showed that using cross ties anchored with 135°hooks at both ends on the transverse reinforcement did not provide more confinement to the concrete core. After the concrete cover spalled off and the steel yielded, the concrete core did not gain strength and experienced brittle failure. The walls tested did not achieve the ductile response intended by the provisions of ACI-318 code.

According to the results obtained from 2012 and 2013 tests, neither tighter spacing between longitudinal and transverse reinforcement nor the use of 135°hooks at both ends in some of the longitudinal rebar produced a ductile response in the tested specimens. Clearly, further investigation is required to determine the adequate layout that provides the confinement required and devise modifications to improve the current code standards. Finally, further testing should examine if better performance can be achieved if cross ties are included at each longitudinal bar of the boundary element.

13.8 ACKNOWLEDGMENTS

I would like to thank PEER for the opportunity to participate in this internship and being involved in this research project. I would also like to thank my research team: Professor Jack Moehle for his knowledge and guidance during the project and his wisdom in giving us the correct advice to solve the problems presented, graduate student Carlos Arteta for his trust, patience, and leadership through all the process, and Jorge Archbold and Itria Licitra for their help and support and for making this project more fun. Thanks to all the technicians in the from Davis Hall and RFS labs, for really making the impossible possible; without their effort we could not have been done this project. Finally, I would like to thank Heidi Tremayne for her support and enthusiasm in making this internship a success.

13.9 REFERENCES

ACI (2011). *Building Code Requirements for Structural Concrete and Commentary (ACI 318-11),* American Concrete Institute, Farmington Hills, MI.

Arteta C.A., Moehle J.P. (2013). UCB 2013 Wall Proposal, Dept. of Civil and Environmental Engineering, University of California, Berkeley, CA.

ASTM (2011). *Standard Test Method for Compressive Strength of Cylindrical Concrete Specimens, ASTM C39/C39M-12A*, American Society for Testing and Material, West Conshojocken, PA.

Cook D. (2012). Ductility of reinforced concrete shear wall boundary elements in compression, *PEER Report 2012/07*, Pacific Earthquake Engineering Research Center, University of California, Berkeley, CA, pp. 5-16.

Lo, A. (2012). Exploring behavior of thin shear wall boundary element in compression, *PEER Report No. 2012/07*, Pacific Earthquake Engineering Research Center, Universiyt of California, Berkeley, CA, pp. 19–54.

Mander J.B., Priestley M.J.N., Park R. Theoretical stress-strain model for confined concrete, *J. Struct. Eng*., 114(8): 1804–1825.

McKenna F., Fenves G.L., Scott M.H., Jeremic B. (2000). *Open System for Earthquake Engineering Simulation (OpenSees),* Pacific Earthquake Engineering Research Center, University of California, Berkeley, CA.

Monterrosa Archbold J. (2013). Performance of concrete shear wall boundary elements under pure compression. *PEER Report 2013/25*, Pacific Earthquake Engineering Research Center, University of California, Berkeley, CA.

Monteiro P.J.M. (2006). *Concrete, Microstructure, Properties and Materials*, McGraw-Hill: New York.

14. Seismic Safety of San Francisco's Private Schools

Julia Pavicic

ABSTRACT

Approximately one third of the children in San Francisco attend private schools. There currently are different laws governing seismic safety of private and public school buildings. To ensure the safety of all San Francisco children and the resiliency of the city following an earthquake, a private school working group is proposing that private schools should meet the seismic safety standards of public schools.

The Earthquake Safety Implementation Program (ESIP), created by the City and County of San Francisco, evaluated private school buildings to determine the probable earthquake safety of its structures. The ESIP formed the Private School Working Group to gather and evaluate research on private school buildings, and then to consider seismic hazard reduction recommendations based on the data analyzed by its private school structural engineering subcommittee. Prior to the formation of this working group, there was no public documentation on the structural safety of private schools in San Francisco. The Working Group's report, including its recommendations on earthquake safety, will be presented to the City Administrator and Mayor by the end of 2013. The likely major recommendation from the Working Group is to require an evaluation of private school facilities so that further review can be made of these issues. This report summarizes the progress of the ESIP Private School Working Group and compiles and compares data collected to date.

14.1 BACKGROUND

The 1933 magnitude 6.3 Long Beach earthquake rattled the people and the status quo of California. Thousands of buildings were severely damaged in the Long Beach/Los Angeles area, with the most the severe damage incurred by schools; see Figure 14.1. According to Meehan and Jephcott [1993], "Seventy schools were destroyed, 120 schools suffered major damage, and 300 schools received minor damage." Luckily the earthquake occurred after school hours, but this brought to light the need for state seismic standards for public schools. People became worried about student safety, as well as the economic recovery of the city. If schools cannot open quickly after an earthquake occurs, then parents of those children cannot go to work, severely disrupting a city's functionality and economic stability.

Figure 14.1 The front entrance of John Muir School in Long Beach, California, after the 1933 Long Beach earthquake.

14.1.1 Field Act of 1933

The California legislature passed the Field Act one month after the Long Beach amid demands for improved performance of public schools in an earthquake.

> *The series of earthquakes occurring in the southern portion of the State has caused great loss of life and damage to property. The public school buildings, constructed at public expense, were among the most seriously damaged buildings. Much of this loss and damage could have been avoided if the buildings and other structures had been properly constructed. The school buildings which will be erected, constructed, and reconstructed to replace the buildings damaged or destroyed by the earthquake, should be so constructed as to resist, in so far as is possible, future earthquakes. These buildings will be erected, constructed and reconstructed at once and accordingly it is necessary that this act go info immediate effect in order that the lives and property of the people will be protected. (California Legislature)*

The Field Act grants the Division of the State Architect the responsibility to approve or reject plans for the construction of new public school buildings as well as alterations to existing buildings. Private schools were not included in the Field Act. The Division of the State Architect also reviews the building after completion and grants the school a certificate of compliance. The Field Act increased public school safety standards and ensured state regulation, and was one of the first of many state provisions regulating the safety of public schools. It wasn't until 1986 that private school safety was addressed by the state legislature.

14.1.2 Private School Act of 1986

The Private School Act of 1986 requires local enforcement agencies to review the construction or alteration of a private school structure through the means of a qualified inspector. However, its language was intentionally vague regarding "enforcement agency" and "qualified inspector," and left to local interpretation. The Private School Act was put into the California State Educational Code rather than the California State Building Code. It is currently unclear to what degree San Francisco has ever enforced this code, as there are no records detailing its strict enforcement. The Private School Act only applies to new buildings and new school buildings, not retrofits to existing buildings.

Uncertainty in compliance with the Private School Act of 1986 presents a potential hazard for the City of San Francisco where earthquakes are strong and prevalent. The U.S. Geological Survey (USGS) concluded there is a 62% chance of at least one magnitude 6.7 earthquake hitting the greater San Francisco region over the next thirty years (2003–2032). According to California's Department of Education Private School Directory, there are 103 private schools in San Francisco City and County; to which about one third of San Francisco's children attend. There is a likelihood some private schools in San Francisco will not fare well in the next expected earthquake. This unsettling truth caused the city of San Francisco to include the need for recommended changes to private schools seismic safety requirements in its Community Action Plan for Seismic Safety (CAPSS) report.

14.1.3 The Community Action Plan for Seismic Safety

The Community Action Plan for Seismic Safety (CAPSS) project of the San Francisco Department of Building Inspection (DBI) was a ten-year, $1 million study created to provide DBI and other City agencies and policymakers with a plan of action policy road map to reduce earthquake risks in existing, privately-owned buildings and develop repair and rebuilding guidelines that will expedite recovery after an earthquake [ATC 2010].

It is feared that if these identified problems are not addressed, San Francisco may be slow to recover, leading to severe social and economic consequences. Should an earthquake occur, many people and businesses will relocate and not return, greatly changing the character of the City as was seen in New Orleans after Hurricane Katrina. This is a strong motivator to improve San Francisco's resilience to earthquake hazard.

14.1.4 Earthquake Safety Implementation Program

The CAPSS study led to the creation of San Francisco's Earthquake Safety Implementation Program (ESIP), which was established to carry out these recommendations over a span of thirty years. The work plan was broken up into different phases: recommended action, mandatory evaluation, and mandatory retrofit. This work plan displayed the discrepancies between private schools and public schools related to seismic safety. Two tasks within the work plan explicitly relate to private schools: (a) Task A.6.f. Review performance requirements for private schools K–12; and (2) Task B.3.a Mandatory evaluation and retrofit of Private K–12 schools to public-equivalent standards: see Figure 14.2.

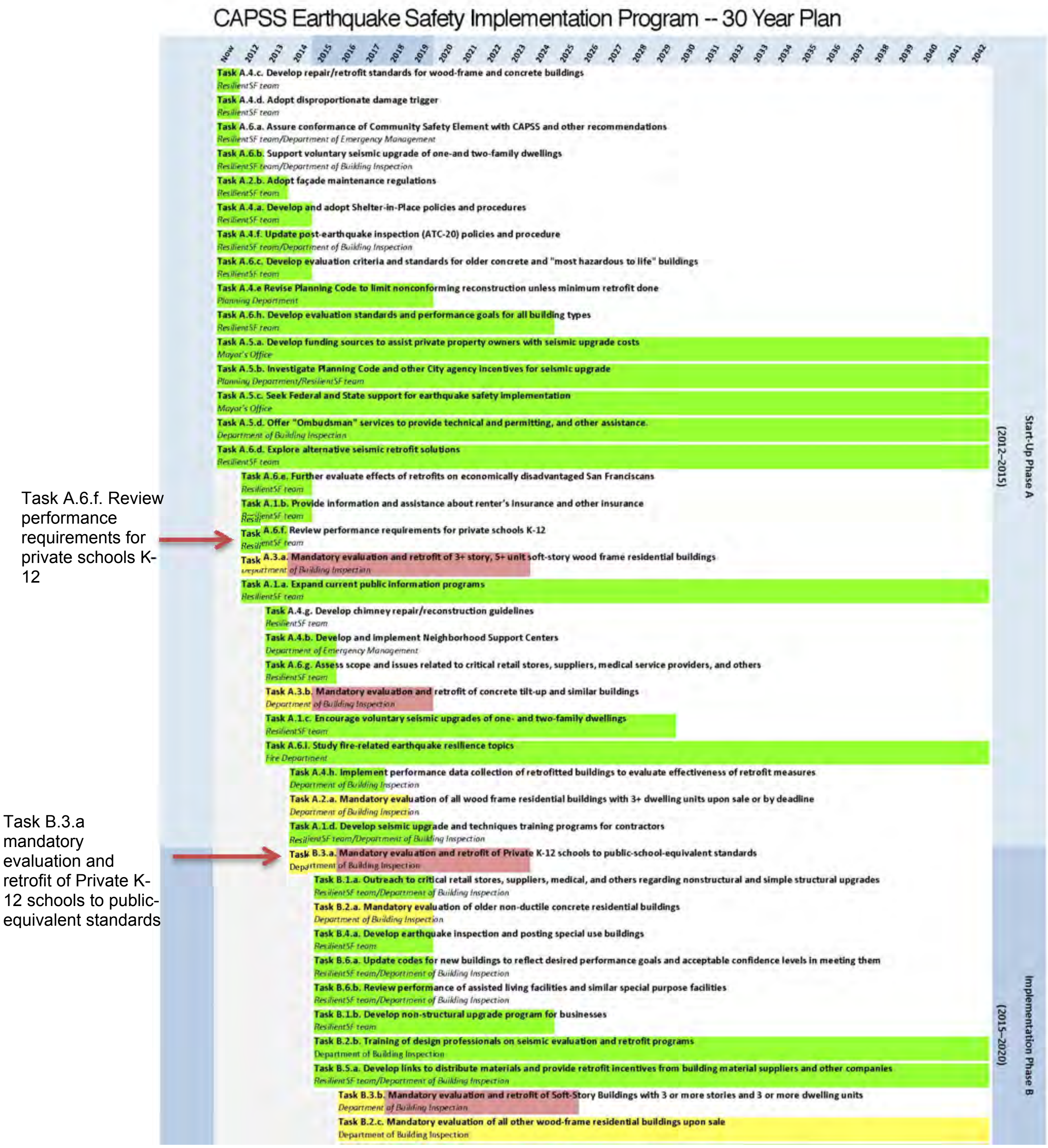

Figure 14.2 **The ESIP thirty-year plan to make San Francisco a more resilient city [City and County of San Francisco 2011].**

14.2 INTRODUCTION

The CAPSS report focused attention on the safety of private schools in the event of an earthquake, and their ability to recover after an earthquake. The San Francisco City Administrator's Office, under the direction of Patrick Otellini, Director of Earthquake Safety, created the Private Schools Earthquake Safety Working Group to address private school structural concerns and to dispel the public's expectations that all schools provide adequate and equal safety. Laura Dwelley-Samant is the chairperson of this group and head of the Private School Earthquake Safety Working Group Structural Subcommittee. She and David Bonowitz spearhead this work and help guide the group. The same research gathered on private schools is also currently being done on San Francisco charter schools. Although they are technically public schools, charter schools are given the freedom to adopt independent rules, and it is believed that many do not to meet Field Act safety standards. Charter schools are currently in a gray area, which is worrisome when related to earthquake safety.

14.3 PRIVATE SCHOOLS RISK

The results from the CAPSS report refocused attention to the safety of private schools in the event of an earthquake and their ability to recover. According to the California Department of Education, there are 103 private schools in San Francisco, with a total enrollment of approximately 23,000 children. This represents one-third of the total school age population in San Francisco; it is the highest in the state. The California Department of Education defines a private school as following:

> *A private business or nonprofit entity that offers or conducts full-time instruction with a full complement of subjects at the elementary, middle, or high school level. Private schools function outside the jurisdiction of the California Department of Education (CDE) and most state education regulations. Private schools do not participate in California's educational accountability system and are directly accountable to students and their parents or guardians, based on the terms of the private school enrollment contract." (California Department of Education.)*

14.3.1 Private School Working Group

The Private School Working Group is the San Francisco city-sponsored working group concerned with the safety of San Francisco private schools. It is a large group of stakeholders, including structural engineers, educators, school administrators, and concerned parents. The Working Group is made-up of volunteers and is open to the public. Its first task was to identify how to evaluate private school building earthquake risk from both a policy and technical viewpoint. After agreeing upon how to identify private schools' vulnerability, the group has met once a month to discuss research challenges, receive updates, and brainstorms solutions. The end goal of the Private School Working Group is to write a report to City policymakers and recommending how the City may best address private school earthquake safety.

Figure 14.3 Private School Working Group meeting at San Francisco's EPICENTER.

14.3.1.1 Private School Working Group Methodology

The next step in addressing private school safety was collecting and compiling background research on all private schools in San Francisco. Each member of the working group was assigned schools to research. Although information was found on each school, no individual school seismic evaluations were made. It was agreed the goal of this data collection was to create a broad database of the schools categorized by building type, building age, and building retrofit history. The results of these studies would provide data needed for the Private School Working Groups next steps, and their recommendations to the City Administrator and the Mayor.

14.3.2 Research

Comprehensive data was collected on each school. The Private School Working Group members created a master private school database on Google docs where all members were able to add and share information. To protect each school, the information collected by the working group will not be published or shown to the public. The database consists of the following information: school name, school researcher's initials, parcel block and lot, school ID, building name and description, occupancy (use), date constructed, date retrofitted, number of stories, area, enrollment, apparent gravity system, apparent lateral system, data sources, and other notes. Most of the general demographic information, such as address and enrollment, was found on individual school websites. The school ID is an abbreviated version of the private school's name (which was usually the initials of the school). Information was found in various locations but primarily in the City and County of San Francisco Planning Department's database.

The property database was the most useful research tool throughout this process. The date of the building's erection, number of stories, and square footage also came from the property database. The building information was not always complete, but it often provided substantial information. The property database usually contained a Sanborn map, which gives a top view of buildings. Sanborn maps were originally used to determine each building's fire insurance liability. These floor plans sometimes have the date the building was constructed, the number of stories in the building, and the gravity lateral system. Figure 14.4 is a typical Sanborn map. The property database also sometimes contained building permits. Permits show the structural and sometimes nonstructural components of a building that are being remodeled. Permits also show when a building has undergone a change of occupancy. Major changes of occupancy in a building (such as from a warehouse into a school) triggers retrofit; unfortunately, these records are not necessarily complete or up to date.

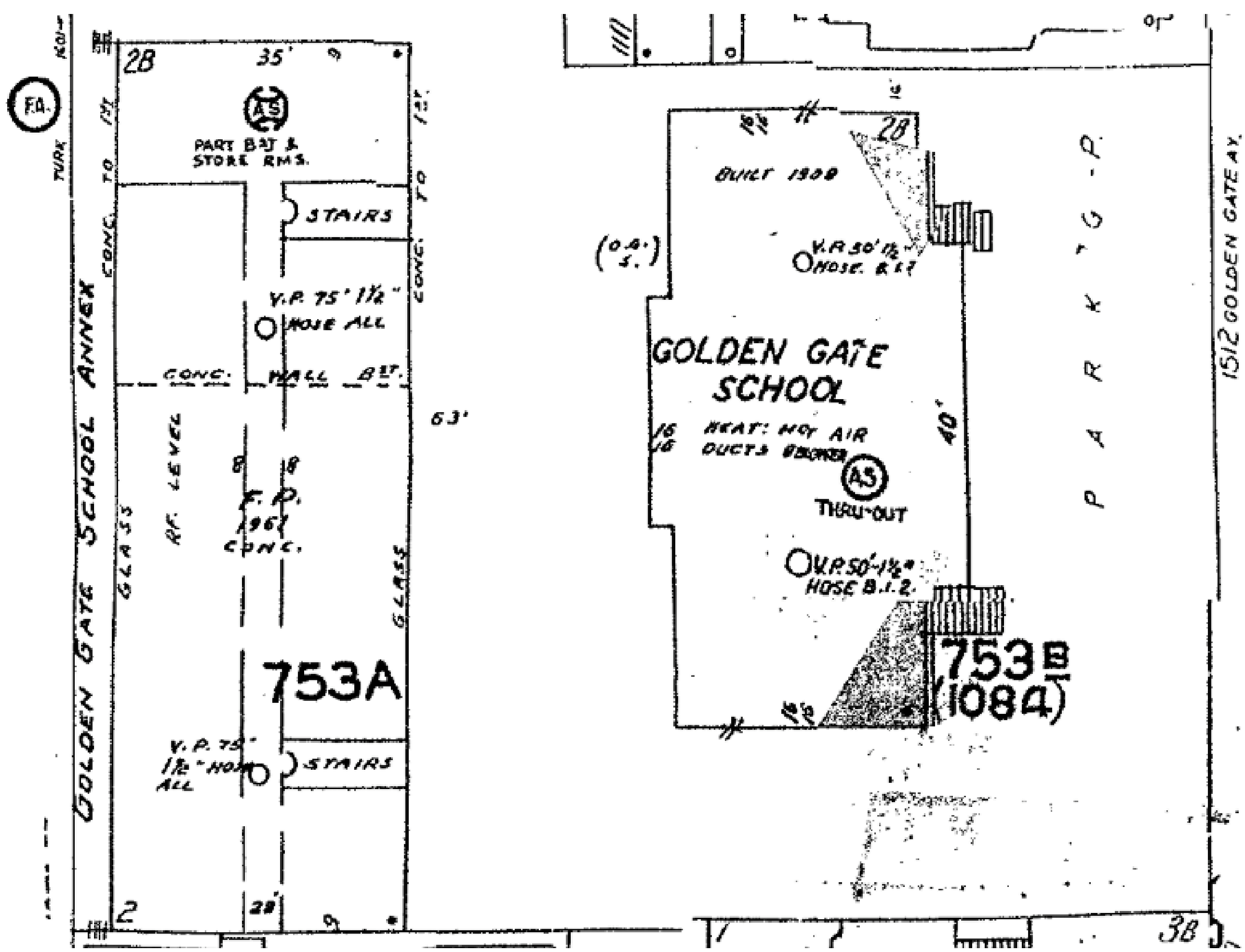

Figure 14.4 Sanborn Map used to extract detailed information about a school.

14.3.3 Private Schools Earthquake Working Group Structural Subcommittee

The Private Schools Earthquake Working Group Structural Subcommittee is a subgroup of the Private Schools Earthquake Working Group. It is made up of structural engineers and other technical experts who used the private school database to develop rough conclusions about the lateral system of each school building. These assumptions were made primarily using the buildings date of construction, gravity system, retrofit permits, and Google image pictures, combined with general knowledge of San Francisco's building history. No individual private school building plans were used to gather information. For the purpose of the Working Group only, very general information was needed to determine how to proceed. The private school subcommittee presented their results to the members of the Working Group and discussed how to make the data more understandable to the general public.

14.3.4 Meetings

The Private School Working Group meets roughly once a month to discuss progress with the database. The meetings begin with a sign-in sheet and introductions, followed by a recap of the last meeting. In these meetings individuals share problems, voiced complaints, and discussed strategies about how to move forward with private school safety. These meetings are open to the public and on average twenty-five people attend. At each meeting there are both new and familiar faces, each bringing a unique background and special interests to the working group. Usually school representatives, structural engineers, and concerned parents attend the meetings.

14.3.5 Private School Interviews

To date, one school has been interviewed about San Francisco seismic safety standards that pertain to their school. The purpose of each interview is to understand more about the earthquake concerns of individual schools, and discuss how the school will be affected by the City of San Francisco's actions. For privacy purposes, the school name and location cannot be disclosed. The main questions the interview targeted were as follows: What would be the costs or impacts to your school if your building(s) were unusable after an earthquake? What do you think will happen to your schools building during a big earthquake?

The school interviewed is currently under reconstruction, a portion of which incorporates seismic retrofits. This proactive approach to private school safety is highly appreciated, but makes it very challenging to extrapolate this school's feedback to other San Francisco schools. The school explained that the driver for remodeling came from a demand for more teaching space; seismic improvements were an additional element. It was stated that the school would probably not have undergone reconstruction only to improve earthquake safety. The school also acknowledged its privilege in being able to afford an expensive and extensive retrofit, and sympathized with schools that do not have this luxury. The school interviewed also mentioned that earthquake safety and preparedness is rarely, if ever, talked about among parents. The school explained that it does have earthquake drills and follows all other regular safety programs.

14.3.5.1 Interview Takeaways

The Private School Working Group was grateful for being allowed to interview. However the school in question school is not a representative sample of San Francisco private schools, as most have not performed any building retrofits. It would be in the best interest of the Private School Working Group to conduct interviews with schools with different structure types, financial situations, and size. School safety is a very sensitive issue that worries school administrators and faculty as well as parents.

14.4 CHARTER SCHOOLS

A charter school is a state-funded public school that is not required to follow educational codes specified by the state. Specific goals and operating procedures for the charter school are detailed in an agreement (or "charter") between the sponsoring board and charter organizers. There have been sixteen charter schools identified in San Francisco County. Some charter school buildings may be subject to the Field Act provisions. It is unclear which rules apply to charter schools when the Field Act does not. A research report was written that compiled all educational codes related to the creation and operation of charter schools. A charter school spreadsheet was also made, which contained the following information: school name, initials of who researched the school, parcel block and lot, school ID, building name and description, occupancy (use), date constructed, date retrofitted, number of stories, area, enrollment, gravity system, lateral system, data sources, and other notes. Beyond the gathering of this data, no further steps have been taken to address charter schools at this time.

14.5 PROJECT RESEARCH RESULTS

The charts and graphs below show the results from the findings of the Private School Working Group that compared private school buildings to public school buildings. Although incomplete, they do provide an overall picture of private school building concerns. Table 14.1 below shows the data gathered to date on each private school.

Private schools were categorized following the AB300 report used by public schools in California. AB300 is an earthquake safety inventory methodology that uses a triage filtration system to determine the likely safety of public school buildings. The AB300 report provides a list of public school buildings determined to be possibly unsafe by the Division of the State Architect. The AB300 methodology requires engineering review of building plans and other documentations, such as the year the building was erected and the building's lateral system, rather than conducting expensive on-site investigations. Buildings are divided into two categories based on building date: pre-1978 and post-1978. The year 1978 was chosen because buildings constructed after the 1976 California Building Code were required to incorporate higher seismic safety standards, and are expected to adequately well in the event of an earthquake. Buildings are also divided into two categories based on structural system: wood and non-wood. All wood frame buildings are expected to perform well in the event of an earthquake and were therefore removed from AB300 consideration. School retrofits were also included in this table, although they are not included in the AB300 report because they increase the seismic safety of buildings. This information is listed Table 14.2, which shows private schools that do not fit the AB300 criteria and are, therefore, suspected of being unsafe (pre-1978 non-wood frame construction).

The two most important columns in Table 14.2 are "Meets AB300 list" and "Level of Concern." It is evident after looking at this table that there are a great number of unknowns. The identifying of unknowns related to safety is essential to moving forward with private school safety. To be on the cautious side, many within the Private School Working Group believe unknown buildings should be classified as high levels of concern. Figure 14.5 and Table 14.3 below further simplify the data.

Table 14.1 Summary of data collected regarding private schools (courtesy of Private School Workshop Group).

Date Built	Lateral System	Retrofit	Number of Buildings	Total Square Footage*	Total Enrollment
Post-1978			46	1,124,155	3157
Pre-1978	Non-Wood	Not Retrofitted	47	1,168,925	6389
		Retrofitted	10	211,423	868
		Unknown	25	245,319	3079
		Potential Retrofit	14	262,418	1229
	Non-Wood Total		96	1,888,085	11565
	Unknown		30	475,538	3113
	Wood	Not Retrofitted	15	80,349	1057
		Retrofitted	5	4,602	772
		Unknown	3	6,000	14
		Potential Retrofit	8	28,186	132
	Wood Total		31	119,137	1975
Pre-1978 Total			157	2,482,760	16653
Unknown			42	89,000	2551
Grand Total			245	3,695,915	22361

*Square footage and enrollment figures are currently available for most but not all schools, making these numbers estimates.

Table 14.2 Private schools AB300 list (courtesy of Private School Workshop Group).

Date Built/Structural System	Number of Buildings	Meets AB300 list	Level of Concern
Post 1978	46	No	Low
Pre 1978 non wood frame - no retrofit	47	Yes	High
Pre 1978 non wood frame - yes retrofit	10	No	Low
Pre 1978 non wood frame - unknown retrofit	25	Unknown	Unknown
Pre 1978 non wood frame - maybe retrofit	14	Unknown	Unknown
Unknown date non wood frame	30	Unknown	Unknown
Pre 1978 wood frame -no retrofit	15	No	Medium
Pre 1978 wood frame -yes retrofit	5	No	Low
Pre 1978 wood frame - unknown retrofit	3	No	Medium
Pre 1978 wood frame - maybe retrofit	8	No	Medium
Unknown date or system	42	Unknown	Unknown
TOTAL	**245**		

Table 14.3 Private school buildings level of concern (courtesy of Private School Workshop Group).

Level of Concern	Number of Buildings	% of Buildings
Low Concern	61	25%
Medium Concern	26	11%
High Concern	47	19%
Unknown Concern	111	45%

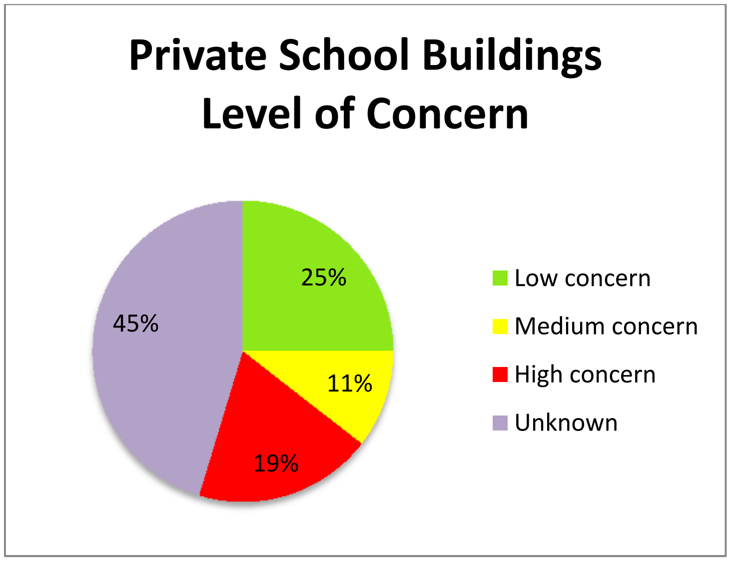

Figure 14.5 **The concern level of private school buildings from the information in Table 14.3 (courtesy of Private School Workshop Group).**

Table 14.4 **Private school buildings on AB300 (courtesy of Private School Workshop Group).**

Private Schools	Number of Buildings
Meets AB300 criteria	47
Unknown	111
Does not meet AB300	87
TOTAL	245

Again Table 14.3 and Figure 14.5 reaffirm the major conclusion that there are many unknowns when dealing with private schools. These unknowns validate the need for further evaluation of private schools. Ignorance of building weakness as related to school safety is unacceptable, and hopefully will be identified in the future. Currently 45% of private schools structural systems are unknown, and it is believed that once more unknowns are identified, then the 19% of private school buildings in AB300 suspect category will significantly increase. Table 14.4 shows private school buildings that are in accordance with AB300.

14.6 COMPARISON BETWEEN PRIVATE SCHOOLS AND PUBLIC SCHOOLS

The Private School Working Group's is primarily interested in knowing if public schools safer than private schools in the event of an earthquake? It is a general belief that public schools are safer because they are regulated by the state and have been retroactively required to be reinforced. Structural data from both types of schools were evaluated using the criteria established by AB300. David Bonowitz, a prominent structural engineering member of the Private School Working Group, compiled public school information in an Excel database and aligned it with the AB300. His hard work and dedication allowed direct comparisons between public schools and private schools shown in Tables 14.5 and 14.6 along with Figure 14.6 and 14.7.

Table 14.5 San Francisco public school buildings (courtesy of Private School Workshop Group).

Public Schools	Number of Buildings
On AB300 list	62
Not on AB300 list, permanent	223
Not on AB300 list, modular	178
TOTAL	**463**

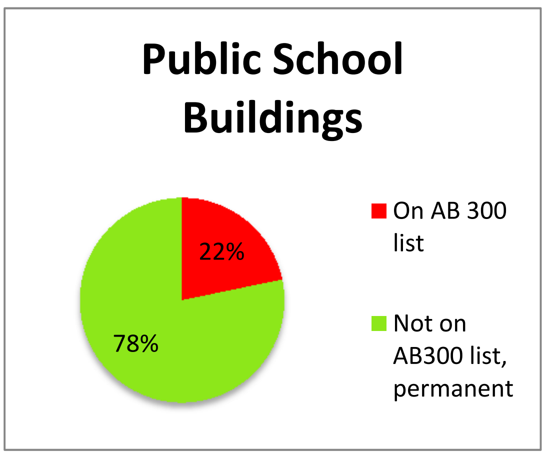

Figure 14.6 San Francisco public school buildings (courtesy of Private School Workshop Group).

Table 14.6 San Francisco private school buildings (courtesy of Private School Workshop Group).

Private Schools	Number of Buildings
Meets AB300 criteria	47
Unknown if it meets AB300 criteria	111
Does not meet AB300 criteria	87
TOTAL	**245**

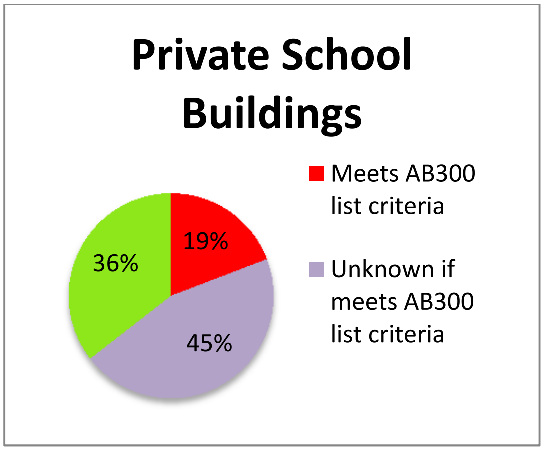

Figure 14.7 San Francisco private school buildings (courtesy of Private School Workshop Group).

As shown in Figures 14.6 and 14.7, 22% of public schools buildings are on the AB300 list, whereas only 19% of private school buildings meet AB300 criteria. However these tables and graphs are deceiving. The most prominent conclusion that should be drawn from these figures is the enormous amount of unknowns with private schools compared to public schools. It is strongly believed that the 19% of private school buildings meeting AB300 criteria will drastically increase as the 45% of unknowns associated with private schools decreases. Currently 64% (45% + 19%) of private school buildings are potentially unsafe, compared with 22% of public school buildings.

14.7 NEXT STEPS

The purpose of the Private School Working Group is to propose hazard reduction recommendations to be given to the City Administrator and Mayor by the end of 2013. Background research was done on schools to first ensure that private school seismic safety is a problem, and second to have the necessary information needed to determine those recommendations. The Private School Working Group's work is ongoing. It has created a public survey to gain better understanding of the public's perception of private school safety. Once the survey results have been compiled, they will be incorporated into the report along with all the other findings and recommendations.

14.7.1 Public Perception Survey

A public perception survey with an eight questions was electronically distributed to parents of children that reside in San Francisco. It aims at identifying parent's expectations of seismic safety of the school which their child attends. The survey also addresses the expected time to reoccupy a school after the "expected 6.3 earthquake." The Private School Working Group presumes most parents believe all schools to be equally safe. This survey will determine the accuracy of this assumption. It should be acknowledged that this survey was created and written without any expertise in surveying and no formulation of sample sizes and outreach range. The survey has yet to be finalized or distributed.

14.7.2 Policy Recommendation Statements

Currently a rough draft of the Private School Working Groups policy recommendations is in progress. These conceptual ideas will be solidified in the future. The Private School Working Group determined that all recommendations must address the following two topics: (1) private school safety; and (2) each school's contribution to San Francisco's resilience and recovery after an earthquake.

The most important preliminary recommendation from the Working Group is to establish a mandatory structural evaluation of private school buildings. This evaluation should distinguish buildings that pose life-safety risks, as well as the likely usability of the building after an earthquake. The size of this earthquake is still to be determined. Non-structural components of each building should also be examined. All of these school evaluations will be completed and given to the City of San Francisco by a specified date. The level of evaluation detail as well as the level of public disclosure on evaluation results is still to be determined.

14.8 CONCLUSIONS

The Private School Working Group is a San Francisco city-sponsored working group that is working diligently to ensure safety of all San Francisco's schools. After looking at the research and data collected, it is evident that schools in San Francisco are not monitored for seismic safety. There are many "unknowns" that need to be identified and require further analysis, reinforcing the need for action. The clarification of school unknowns related to safety is crucial to moving forward with private school safety. Recommendations for Mayor Edwin Lee are likely to incorporate a mandatory evaluation that distinguishes buildings that pose life safety risks. Until then, many members of the Private School Working Group believe buildings with unknown seismic risk should be classified as high levels of concern. The Private School Working Group understands the scope of the problem and are working to create safety solutions aligned with the political and practical reality of what can be done.

The goal of the Private School Working Group's recommendations is to make San Francisco a more resilient city after an earthquake. The Working Group believes there should be parity in safety between public and private schools. Preliminary survey results seem to support that same position from parents' point of view. People assume all schools are safe, and this is false. The fallacy is especially troubling in San Francisco where one-third of children attend private schools. Private schools are not regulated to the same extent as public schools, and there is little public knowledge about the condition of private school buildings. All children are entitled to equal protection in school, and parents of these children have the right to know the structural condition of the school buildings in which they place their child.

14.9 ACKNOWLEDGMENTS

This research was sponsored by the Pacific Earthquake Engineering Research (PEER) Center and funded by the National Science Foundation (NSF). I would like to thank my mentors Laurence Kornfield and Patrick Otellini with the City of San Francisco's Seismic Safety Department for their insight, expertise, and guidance, throughout the project. I would also like to thank Laura Dwelley-Samant and David Bonowitz. This project would have been impossible without their perseverance, and leadership in the Private School Working Group. Finally I would like to thank PEER's Outreach Director Heidi Tremayne for all her encouragement, assistance, and hard work making this program possible. The job of an engineer is to protect the safety and welfare of the public, and I'm grateful for the opportunity this internship gave me to apply my engineering skills to benefit the City of San Francisco.

14.10 REFERENCES

ATC (2010). *Here Today-Here Tomorrow: The Road to Earthquake Resilience in San Francisco. A Community Action Plan for Seismic Safety, ATC 52-2*. Applied Technology Council, retrieved from http://www.sfgsa.org/modules/showdocument.aspx?documentid=9757.

California Department of Education. Charter Schools FAQ 2, http://www.cde.ca.gov/sp/cs/re/qandasec2mar04.asp. California Department of Education. 7/27/12 Web.7/16/13

California Department of Education. Private Schools Frequently Asked Questions, http://www.cde.ca.gov/sp/ps/rq/psfaq.asp#a1. California Department of Education. 7/27/12 Web. 7/16/13.

California Legislature. The Field Act. Statutes of California, 50th Session, Session Lows of the California Legislature, Chapter 60, page 355.

City and County of San Francisco (2011). CAPSS Earthquake Safety Implementation Program, Workplan 2012-2042, draft, San Francisco, CA.

CSSC (2004). Seismic Safety in California's Schools, State of California Seismic Safety Commission, retrieved from http://www.sfgsa.org/modules/showdocument.aspx?documentid=10639.

Division of the State Architect. AB 300, http://www.dgs.ca.gov/dsa/AboutUs/ab300.aspx. Department of General Services. 2013. Web. 9/3/13.

Huber W.L. John Muir School, Photograph, Long Beach, http://earthquake.usgs.gov/earthquakes/states/events/1933_03_11_photos.php. USGS. Web. 8/16/13

Meehan J., Jephcott D. (1993). The review and analysis of the experience in mitigating earthquake damage in California public school buildings, *NSF Grant BCS-9117732*, National Science Foundation, Arlington, VA.

San Francisco Planning Department (2013) San Francisco Property Information Map, http://ec2-50-17-237-182.compute-1.amazonaws.com/PIM/. San Francisco Planning Department. Web. 7/10/13-8/30/13.

USGS. Summary of Main Results, Bay Area Earthquake Probabilities, U.S. Geological Survey, http://earthquake.usgs.gov/regional/nca/wg02/index.php. USGS. 7/23/12. Web. 8/5/13.

15. Improving San Francisco's Seismic Resiliency through Retrofits of Cripple Wall Homes

Jenny Taing

ABSTRACT

Most residents acknowledge that a major earthquake is expected to occur in the San Francisco Bay Area. After a study reported the catastrophic consequence of a major earthquake, the city has made great efforts to increase its seismic resiliency. One of the methods of doing so is through encouragement of voluntary seismic upgrades of single- and double-family homes. This project aims to contribute to that task by making an inventory of cripple wall homes (a type of structure that is known to perform especially poorly during earthquakes) and investigating various approaches of incentivizing voluntary retrofits. Additionally, this research will provide information on the housing stock of San Francisco to better understand what ways San Francisco is at seismic risk.

15.1 INTRODUCTION

The concept of resiliency is not a new one. Although there are slight variations in the way that different communities and organizations define resiliency, the goals are ultimately quite similar. In broad terms, a disaster-resilient nation is one whose communities are able to resume performing essential functions and recover quickly following a major disaster. This is generally accomplished by mitigation efforts and having a thorough disaster plan prior to a catastrophic event [NRC 2011].

The term, "shelter-in-place," is a term used frequently when describing resiliency in San Francisco. The concept of shelter-in-place is quite basic, but meaningful: shelter-in-place is achieved when a resident is able to continue to live in their home (generally after a disaster) even if repairs are necessary or in progress. There is a major difference between homes that meet the standard of "shelter-in-place" and homes that meet minimum building code requirements. A home that meets minimum building code requirements only meets life-safety standards. This means that the homes will not be a threat to human life during a catastrophic earthquake. However, minimum building code requirements do not make any guarantees with regards to the state of the building following a disaster. A building that meets only life safety standards may or may not be habitable post-disaster. It can range from being completely unscathed to needing repairs that displace its occupants to needing to be torn down. Shelter-in-place standards are a stricter standard that not only guarantee life safety, but also sheltering following a major disaster.

Several faults run through the San Francisco Bay Area. Of special interest are the Hayward Fault and the San Andreas Fault. The Hayward Fault runs through the East Bay, passing through major cities such as Oakland, Hayward, and Berkeley. The San Andreas Fault runs through the South Bay, penetrating San Francisco, and continuing into the North Bay. These faults are of particular interest because of their high probability of rupturing in the next 30 years. In a 2008 collaboration between the U.S. Geological Survey (USGS), Southern California Earthquake Center (SCEC), California Geological Survey (CGS), and California Earthquake Authority (CEA), scientists and engineers produced an earthquake forecast for California. It estimated that there was a 63% probability that one or more magnitude 6.7 earthquakes would occur in the Bay Area in the next 30 years. There is a 31% chance that a rupture would occur on the Hayward Fault [Brocher 2008] and a 21% that a rupture would occur on the San Andreas Fault [Field et al. 2008]. Five years have passed since the forecast and we have yet to see an event of that size on either faults; the probabilities are even higher today. These probabilities illustrate the need to make efforts towards a resilient region that is able to shelter-in-place.

15.1.1 Case Studies of Past Disasters

It is important to examine disasters in the past in order to evaluate past methods of response and develop an appropriate plan for when the next disaster strikes. Of particular interest are past San Francisco earthquakes and recent natural disasters such as Hurricane Katrina and the Kobe earthquake.

15.1.1.1 Past San Francisco Earthquakes

San Francisco has experienced a couple major earthquakes in the past. In 1906, an estimated 7.8 magnitude earthquake occurred along the San Andreas Fault, with an epicenter very near to San Francisco. The shaking was very intense and was claimed to have been felt as far north as Oregon and as far south as Los Angeles. The damage in San Francisco was substantial (see Figure 15.1). The earthquake left over 3000 dead, 225,000 homeless (for reference, San Francisco had a population of about 400,000 at the time), and 28,000 homes were destroyed. At the time, San Francisco was a financial, trading, and cultural center of the west. However, with over 80% of the city destroyed, many of those who were evacuated sought refuge across the bay in Berkeley and Oakland. Others fled south to Los Angeles, which became the largest urban area in the west in the 20th century. The homeless who stayed in San Francisco erected tents in Golden Gate Park, the Presidio, the Panhandle, and the beaches between Ingleside and North Beach. These makeshift neighborhoods were still in operation over two years later. Reconstruction was mostly complete in 1915, nearly a decade later.

Figure 15.1 Panorama of the destroyed Financial District in San Francisco (courtesy of S.F. Musuem).

Figure 15.2 Collapsed upper deck of the Cypress Street Viaduct [Wilshire 1989].

The 1989 magnitude 6.9 Loma Prieta earthquake occurred along the San Andreas Fault, with its epicenter in Santa Cruz County. It was far less catastrophic than the 1906 earthquake. There were under 10 deaths in San Francisco, which was not as heavily affected as other cities such as Santa Cruz or Oakland [SPUR 2012]. The two distinct characteristics that caused the major differences between the 1989 Loma Prieta and the 1906 earthquakes' impact on San Francisco was the that 1989 Loma Prieta earthquake was a whole magnitude smaller (equating to about 1/30th of the energy of the 1906 earthquake) and was much farther away from San Francisco than the 1906 earthquake (roughly 60 miles versus 2 miles). However, the 1989 Loma Prieta earthquake should receive special attention because of the impact it had on transportation in the Bay Area. The greatest damage on transport systems was the collapse of the Cypress Street Viaduct, a 1.6-mile-long two-tiered freeway on the Interstate 80 in Oakland (See Figure 15.2). Forty-one people were crushed to death.

Less catastrophic was the damage done to the San Francisco-Oakland Bay Bridge. However, there were serious lessons to be learned from the bridge's response to the earthquake. A small portion of the bridge collapsed (see Figure 15.3) due to the shearing off of some bolts and was shut down for a month due to repairs. The Loma Prieta earthquake illustrated the effect that even a smaller, farther away earthquake could have on transportation systems in the Bay Area and led to the mandated seismic retrofitting of all bridges in the Bay Area [SPUR 2010].

Figure 15.3 Collapsed section of the San Francisco-Oakland Bay Bridge [Meyer 1989].

15.1.1.2 Hurricane Katrina and the Kobe Earthquake

Hurricane Katrina in 2005 and the 1995 Kobe Earthquake are important cases to examine because they are recent disasters in first-world regions. Of particular interest are the ways in which each region responded to its respective disaster and the current state of the regions today.

In 2005 Hurricane Katrina formed in the Bahamas in and grew unusually rapidly. It ripped through Louisiana and continued northeast, finally losing strength in central Mississippi.

Causing $81 billion in damage, Hurricane Katrina was the costliest natural disaster in the U.S.. New Orleans, Louisiana, was critically damaged by Hurricane Katrina due to over 50 levee and flood wall failures. Over 800,000 people were displaced and 204,000 homes were destroyed. After the disaster, repopulation was very gradual. Five years later, several thousand people still live in temporary housing and the 2010 census showed that the population of New Orleans was only 80% its pre-disaster population. However, the percentage of returning locals is actually lower since a large portion of that percentage was due to a large in-migration.

The case of Kobe is frequently examined because of its similarity to San Francisco. Both Kobe and San Francisco are extremely dense metropolitan cities located next to faults that can potentially cause great damage. In 1995, a 6.8 magnitude earthquake struck Kobe, Japan. It caused $150 billion in damages and temporarily displaced almost 450,000 people. Nine months after the quake, the population was estimated to be 6.3% lower than the pre-disaster population, and it took the city five to ten years to reach and exceed the city's rebuilding goal. Today, almost two decades after the disaster, Kobe has regrown itself to be a robust city as the fifth largest city in Japan. However, it is important to note the time required for this regrowth to happen.

15.1.1.3 San Francisco at Risk

There are several lessons to learn from these case studies. The first and most obvious is that the two faults that surround San Francisco, the San Andreas and the Hayward Fault, both have the potential to cause large earthquakes that impact San Francisco as illustrated by the 1906 earthquake and the Loma Prieta earthquake, respectively. The second lesson is that cities are not permanent. In the case of Kobe, we see that the city eventually rebuilt itself, but in the case of New Orleans, the city has yet to return to its pre-disaster numbers.

It is not impossible that San Francisco may face struggles similar to those of New Orleans if a large and close enough earthquake strikes. What are the major characteristics that make San Francisco unique? First, with its diverse mixed-use neighborhoods and numerous theaters, museums, and art galleries, San Francisco is a major cultural center. Second, San Francisco is also a giant financial center, with approximately 350,000 workers who commute to just downtown San Francisco daily. Third, tourists flock to San Francisco daily, grossing $8.9 billion in 2012, making tourism the backbone of the city's economy [San Francisco Business Times 2013]. Due to its frequent portrayal in media, many of San Francisco's landmarks are easily distinguishable and a target of many travelers. With these features, it is no wonder that San Francisco flourishes as such a unique major city. However, an examination of these features makes one realize that none of them are uniquely tied to San Francisco's geography. In other words, these San Franciscan features can easily exist at any other place. An earthquake can destroy many of San Francisco's precious theaters, museums, and art galleries. Perhaps the owners of those said establishments might prefer not to be at such a risk to harm again and choose to relocate. An earthquake can place a significant halt on the commuters who work in San Francisco as well as the companies that are established in San Francisco. Many companies may choose to relocate as there isn't anything that physically ties a company to San Francisco. In our exponentially evolving and heavily technologically-based society, relocation may not be as difficult as it was several years ago. Lastly, many landmarks sought after by curious tourists may be destroyed in an earthquake. In addition to those consideration, a large enough catastrophe will surely halt tourist activity for a substantial amount of time. It seems that although the city of San Francisco is extremely robust and successful, it is also quite fragile. A large portion of its culture is shaped by people who do not even live in the city and can very easily choose to no longer be a contributor at any time.

What does this mean for a city like San Francisco? It is apparent that San Francisco is very much at risk of losing its identity in the event of a large and close enough earthquake [SPUR 2004]. The only way to safeguard against such a catastrophe is to focus on efforts to increase the resiliency of San Francisco so that when the expected disaster does strike, the city will be braced for the damage that will occur and prepared for the chaos that is likely to follow.

15.1.2 The Community Action Plan for Seismic Safety Project and the Earthquake Safety Implementation Program

Realizing the dangers that it faced, the Department of Building Inspection in San Francisco implemented the Community Action Plan for Seismic Safety (CAPSS) [ATC 2010b] Project to better understand and prepare for potential earthquakes that are expected to occur. This project was funded at $1 million for nine years and ended 31 December 2010. In addition to being a collaborative effort among engineers, CAPSS encouraged input from community leaders, earth and social scientists, economists, tenants, and homeowners to contribute to a mitigation plan that was most beneficial and effective for the city.

The CAPSS Project was based on estimating the impact of four scenario earthquakes of varying sizes and locations (see Figure 15.4). It is impossible to predict the location and the size of an earthquake, so it is necessary to inspect several probable cases. The four scenario earthquakes that the CAPSS project studied are as follows: a magnitude 6.9 earthquake on the Hayward fault in the East Bay and magnitudes 6.5, 7.2, and 7.9 earthquakes on the San Andreas fault. Out of the four, the Hayward fault rupture is statistically the most likely rupture to occur. The 7.2 magnitude earthquake on the San Andreas fault would produce the amount of shaking in San Francisco that new buildings are expected to resist without collapse. The 7.9 earthquake is an imitation of the 1906 earthquake and is the largest known earthquake to have occurred on the San Andreas fault. Although it is unlikely that any of these scenario earthquakes would actually occur exactly as theorized due to the highly variable nature of earthquakes, the consequences are expected to be similar enough that these estimates are valid.

The CAPSS study found that San Francisco could face serious consequences if it did not make any efforts towards earthquake damage mitigation. San Francisco will suffer most in terms of building damage and economic loss, leading to struggles with rebuilding. Housing will be especially hit hard, with an estimated 85,000 of the city's housing units to be uninhabitable due to damage after the scenario magnitude 7.2 earthquake. Of those, 11,000 would have to be demolished, and as demonstrated in past earthquakes, rebuilding is a long process. Building damage caused by the scenario earthquakes ranged from $17 to $54 billion. However, the cost of the earthquake would be much greater—lost wages, damages to building content, and a decrease in tourism are just a few of many indirect costs that any of these four scenario earthquakes is likely to incur.

The CAPSS study is monumental in that it provided quantitative examples of the consequences that San Francisco may face in the event of several scenario earthquakes that are similar to the ones that are forecasted to occur. The results do not paint a bright future for a post-earthquake San Francisco. The good news is that many of these losses can be significantly lessened with mitigation efforts.

The CAPSS study concluded with a list of 17 recommendations of actions that San Francisco should undertake in order to strengthen the resiliency of the city. As a result, the Earthquake Safety Implementation Program (ESIP) was established to carry out these recommendations over a span of thirty years (see Figure 15.5). The plan outlines a list of tasks to be completed, specifying the timeline and who is affiliated for its implementation. Currently, the program is two years in and on track. There are numerous projects that occur simultaneously because these are such long-term tasks. Each task involves various parties with differing interests, and, as a result, compromises are a challenge. Despite this, agreement and progress is possible, as showcased by the recently passed Mandatory Soft-Story Retrofit Ordinance, which requires the evaluation and retrofit of soft-story homes that meet a certain criteria. The ordinance was in progress for ten years.

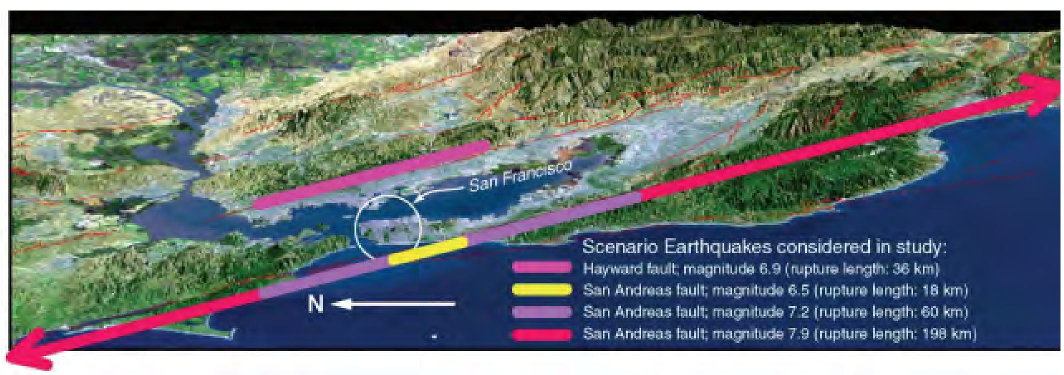

Figure 15.4 The four scenario earthquakes examined by the CAPSS study [ATC 2010a].

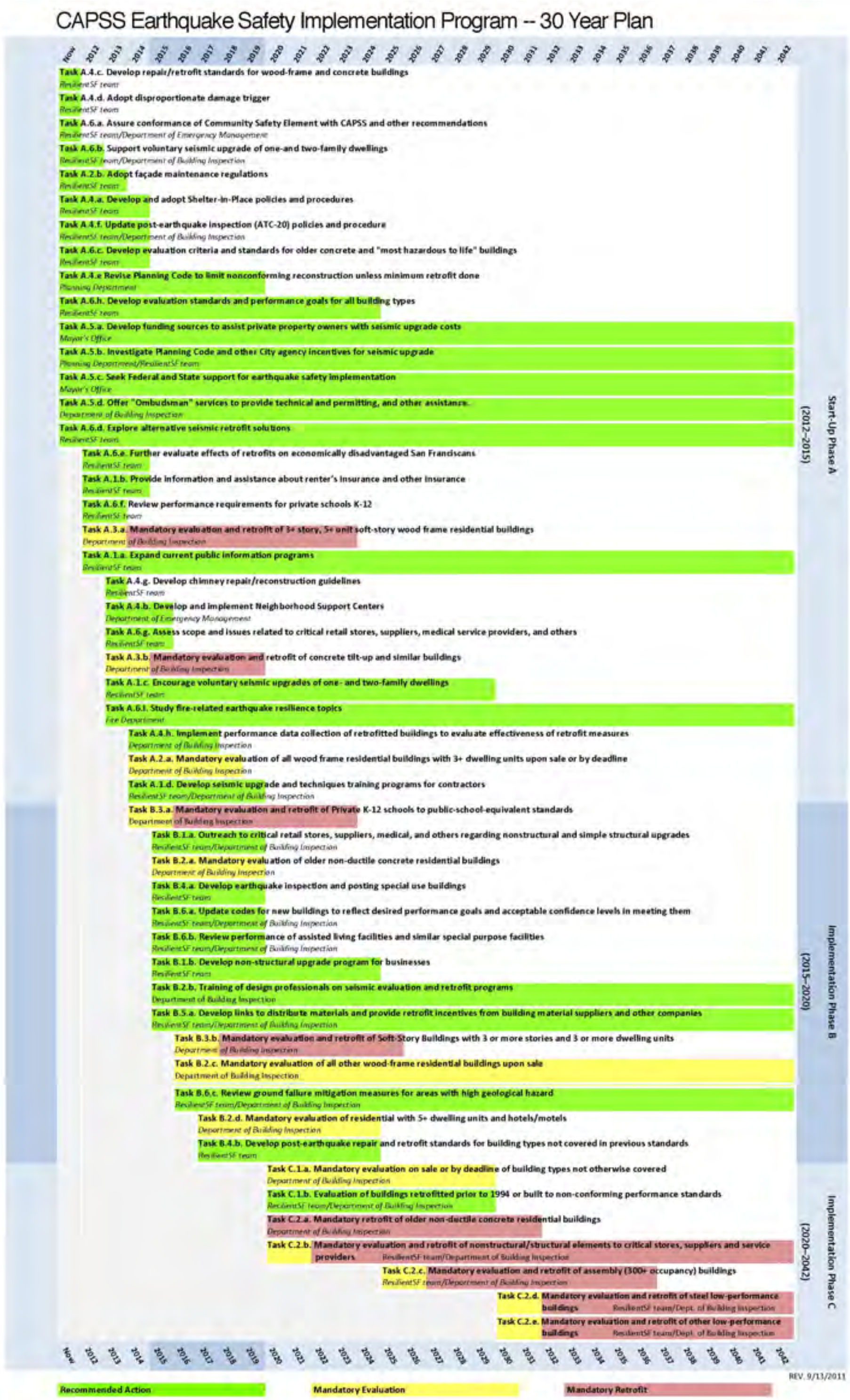

Figure 15.5 **The thirty-year ESIP, broken into three phases. Green rows denote an action that the city should perform, yellow rows denote the implementation of a mandatory evaluation, and red rows denote the implementation of a mandatory retrofit [City and County of San Francisco 2011].**

15.2 RESEARCH GOALS

The purpose of this project is to contribute to the completion of tasks outlined in ESIP. The overlapping tasks and long timelines means working on several projects with the knowledge that the fruits of one's labors will not be apparent immediately. One of the tasks that this project focused on is Task A.6.b: support voluntary upgrade of one- and two-family dwellings. Since ESIP is still in its early stages, mandatory evaluation of smaller homes is not yet on the agenda. Because ESIP prioritizes building weakness and the number of affected residents, mandatory evaluation and retrofit of multi-family homes that are especially weak are of higher priority, such as residential structures that fall under the Mandatory Soft-Story Retrofit Ordinance. This foot-in-the-door process seems to be the best method for success, while ESIP works its way down the priority list. By encouraging voluntary seismic upgrades, the eventual mandatory evaluation and retrofit may not face stubborn opposition.

15.3 RESEARCH METHODS

The completion of the ESIP task involves three parts: identifying the type of structure that needs seismic upgrades, devising ways to encourage retrofit, and providing homeowners with a retrofit strategy. It is important to first identify a single type of structure to target because different structure types have different upgrade needs. In this way, we can target the lowest performance structure for one- and two-family dwellings. Past experience has shown that simply informing a homeowner that their home is a low seismic-performing building is not enough to encourage retrofit. Many homeowners need to have additional incentives beyond the knowledge of the fact that their homes are low performing homes. For this reason, it is valuable to investigate incentive programs that have been used by other cities, the extent of their effectiveness, and develop our own program that would encourage homeowners to voluntarily perform their own retrofit. [ABAG 2011] Lastly, informing homeowners exactly how to perform their upgrade is especially important because it simplifies the complex step for the homeowner and makes voluntary retrofit more likely. This stresses the importance of identifying a type a single type of structure to target[ABAG 2009].

15.3.1 Identifying a Structure Type

There are a number of structure types to choose from. The structure that we targeted for our project is seismically weak and can be retrofitted relatively easily. After examining various building types (unreinforced masonry, soft stories, houses over garages), we decided our target structure type would be homes with cripple walls. Homes with cripple walls fit our criteria exactly: they are very seismically weak, but a set of standards exist that details how to retrofit the structure without having to hire an engineer. This standard as referred to herein as Plan Set A.

15.3.1.1 The Cripple Wall Home

Cripple walls are weak wood studs that generally form the perimeter of a crawl space, which is the empty space between the foundation and first floor of a home (see Figure 15.6). They are less than a full story height, are common in pre-1970s home, and are problematic because they lack resistance to shear forces, and in older homes are likely to not have been bolted in correctly. Cripple walls are generally the weakest part of a building.

Furthermore, in addition to often being the weakest part of a structure, cripple walls also generally bear the brunt of the shear forces in the event of an earthquake. This is because of the way that forces are distributed during an earthquake. When an earthquake causes sudden forces in the ground, Newton's third law of motion states that there are equal and opposite reactions. Newton's second law of motion states that force is equal to the product of the mass and acceleration, and thus the heaviest part of the building will feel the greatest force. The heaviest parts of a structure are the portions that support the most weight, which are the lowest portions: the foundation and the cripple wall. Figure 15.7 shows a basic depiction of the way forces are distributed in an earthquake. For this reason, cripple walls are a major weak point: they are generally the weakest part of a structure but bear some of the greatest forces.

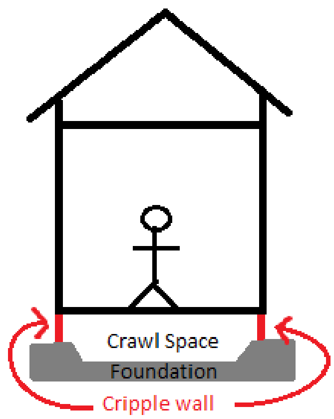

Figure 15.6 Basic diagram depicting cripple walls.

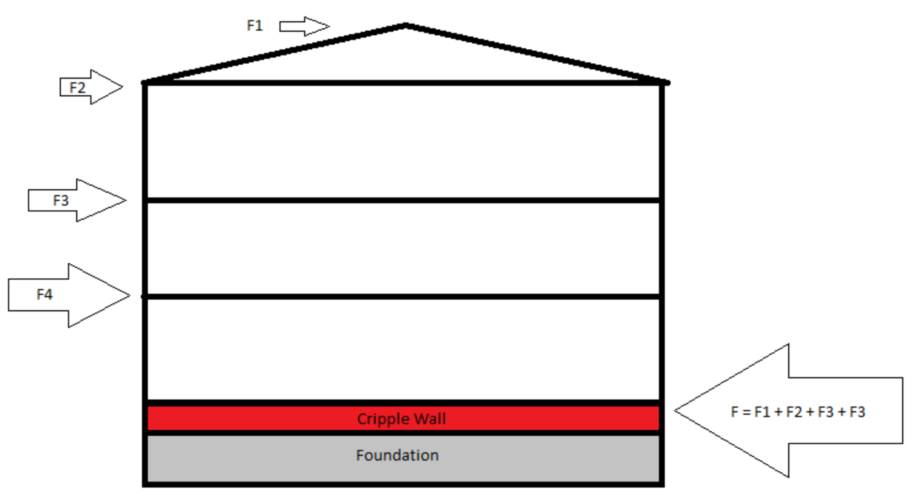

Figure 15.7 Basic depiction of how shear forces are distributed on a typical building. The forces decrease further away from the ground.

Cripple wall failures are not uncommon during earthquakes. In the Loma Prieta earthquake, there were countless cases of cripple wall failures (see Figures 15.8 and 15.9). Cripple wall failures are frustrating because they are so costly to repair. A home whose cripple wall has failed is generally uninhabitable unless repairs are made. This is due to the nature of cripple wall failure. In cripple wall failures, the wood studs that connect the foundation to the first story of a home begin to shift due to shear forces caused by an earthquake. Since they are the connection between foundation and home, this means that the entire home also begins to be displaced and leans toward its side with the wood studs. Figure 15.10 summarizes the mechanism of by which a home collapses during an earthquake. Repairs generally involve lifting a house, repairing the cripple wall, and placing the house back in its original position. This is a very costly procedure, especially when compared to cripple wall retrofits.

Figure 15.8 Cripple wall collapse in Watsonville, California, during the Loma Prieta earthquake. The house was displaced 2.5 ft [Nakata 1989].

Figure 15.9 Cripple wall failure in Watsonville, California, during the Loma Prieta earthquake. The house leans towards its side due to the weak cripple wall. This homeowner installed wood planks to prevent further displacements that can lead to collapse [Nakata 1989].

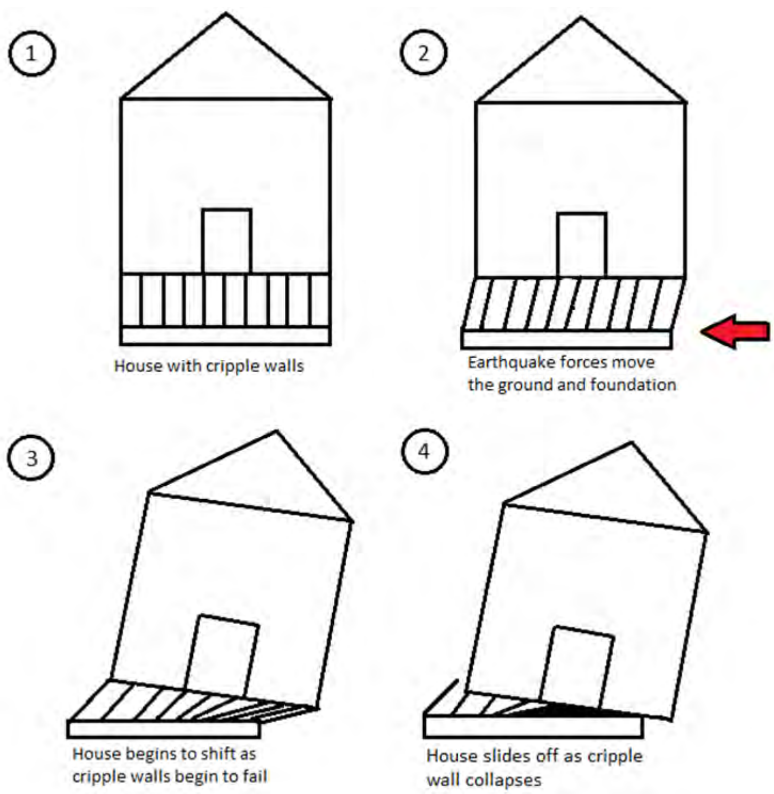

Figure 15.10 Basic depiction of the typical process of cripple wall collapse.

15.3.2 Incentive Programs

It is important to investigate retrofit programs that have been in place to compare the differences and effectiveness in existing or past programs. An ideal retrofit program for this project is one that doesn't mandate seismic upgrades, since the aim of this project is to encourage voluntary seismic upgrades. From examining other incentive programs, we were able to draw ideas and develop a program that will work well with our own cripple wall program. [EERI 2011]

15.3.2.1 San Leandro

Plan Set A was developed by the city of San Leandro as a set of prescriptive retrofit solutions. In addition to providing a set of standard procedures that do not require an engineer, the city also offers workshops that walk residents through the Plan Set A procedure. Upon completion of the workshop, residents can receive a permit from the building department for a reduced fee. There is also a tool-lending library where residents can borrow the necessary tools to perform their own retrofits. As a final incentive, city inspectors will also make trips to the homes during the retrofit process at no cost to ensure that the retrofits are being done properly. The city also offers grants and loans for low-income residents.

15.3.2.2 Oakland

In 2008, the city of Oakland set aside $1 million, raised from real estate transfer taxes, to fund an incentive program to encourage voluntary seismic upgrades by new homebuyers. Buyers could receive up to $5000 in rebates if they completed retrofit that met the city's seismic upgrade standards within 18 months of purchase. The program was extremely effective: before the program, there were only six permits issued for retrofits. Two years later, at the end of the program, that number had increased to 360. Unfortunately, the program ended due to the depletion of the money initially set aside for it, but the city hopes to implement this program again once the economy improves. To target low-income homeowners, the city offered a grant of up to $5000 to provide half the cost of retrofitting and low-interest loans to cover the second half. However, this program was not very effective, as only 33 permits have been issued so far.

15.3.2.3 Berkeley

In 2007, the city of Berkeley began a transfer tax refund program to encourage voluntary seismic upgrades. A transfer tax of 1.5% is imposed on transfers of ownerships of homes. The incentive program that the city of Berkeley implemented allowed for up to one-third of the tax to be refunded if seismic upgrades were made within a year of sale. Four years after its implementation, an estimated 600–800 seismic upgrades have been performed, making it the most effective retrofit program in the East Bay. There are three times as many retrofitted buildings in Berkeley as there are in adjacent cities. Although this program probably doesn't provide enough money to address all seismic issues, the seismic resistance of the home improves over time as it is bought and sold.

15.3.2.4 An Incentive Program for San Francisco's Cripple Wall Homes

What can we learn from the previous three incentive programs, which are among the most successful programs in the nation? It can be concluded that information and education alone is not enough to push voluntary seismic upgrades and that money is the major driving force for voluntary retrofits. Unfortunately, seismic upgrades costs can be quite burdensome for many homeowners. Providing funds to cover a portion of the costs spurs voluntary retrofit efforts. The homeowners that are most difficult to target are, unsurprisingly, low-income homeowners. For them, it seems that providing only a portion of the costs may not be enough.

Although the Berkeley and Oakland transfer tax programs appear to be the most successful, implementing a transfer tax program may not be the right fit for this project for two reasons. First, doing so requires a change in policy, which means that the transfer tax would not be in effect for some time. Our goal was to create incentive program that can be implemented sooner, while plans for a transfer tax program are being worked on. Second, the problem with the transfer tax program is that it only goes into effect when a home is purchased. For our project, we would like something more similar to San Leandro's program, where residents are free to perform retrofits at any given time. However, we recognized the importance of financial incentive, exemplified in the Berkeley and Oakland examples, and saw the benefit of providing financial incentives to all homeowners rather than just low-income homeowners (as is the case in San Leandro). Unfortunately, the task of providing financial incentive is incredibly difficult. Where does the money come from? If it is provided for directly by the City of San Francisco, it means that some other program would have to be compromised under current budget restrictions. The best solution seemed to be collaborating with other organizations with similar goals of financially incentivizing retrofits.

The California Earthquake Authority (CEA), an earthquake insurance company, is currently working on a project called California Residential Mitigation Program (CRMP) [CEA 2013]. The goal of CRMP is to provide California homeowners of wood-frame homes with incentives for seismic upgrades. The program's vision is very much in line with our own in that it seeks to provide education, outreach, and financial incentives. Talks with the CEA led to a joint collaboration where San Francisco would serve as testing grounds for CRMP. The CEA would provide a $3000 rebate for residents who can show that they have properly retrofitted their cripple wall homes. Plan Set A, a standardized solution for retrofitting homes with cripple walls that meet a certain criteria, allows for performing cheap retrofits. Because they are standardized, residents do not need to hire an engineer to assess and design a retrofit solution for their homes. Instead, residents can either perform the retrofit themselves or hire a contractor.

15.3.3 Locating the Right Cripple Wall Homes

In order to carry out our cripple wall retrofit program required identifying the location of our target buildings for two reasons: (1) we needed to determine if there were a significant enough number of qualified cripple wall homes to pursue this project any further; and (2) we needed an inventory of qualified cripple wall homes so that they can be notified of the existence of this incentive program. The set of criteria that a home must meet in order to qualify for Plan Set A retrofits is as follows:

1. The home must be a one- or two-family home.
2. The home must be under three stories.
3. The home must be wood framed.
4. There must be a continuous perimeter concrete foundation.
5. There must be a crawl space.
6. The cripple walls must be less than 4 ft tall. If the building is one story, more than 40% per side of the building must have cripple walls that are less than 4 ft. If the building is two stories tall, more than 50% per side of the building must have cripple walls that are less than 4 ft.
7. If there is stone or brick veneer along the exterior wall (excluding chimneys), they cannot be more than 4 ft above the foundation.
8. If the roof of the home is clay tile, there must not be mortar along the tile edges.

From our neighborhood surveys, we noticed that cripple wall homes generally have a few characteristics that make them easy to identify. A typical cripple wall home is basic in structure, has steps leading up to the entrance, and has ventilation where the crawl space is (see Figure 15.11). Generally, it is safe to say that if there are more than seven steps leading up to the first floor, the cripple wall is greater than 4 ft.

Figure 15.11 A typical cripple wall home (Google Maps).

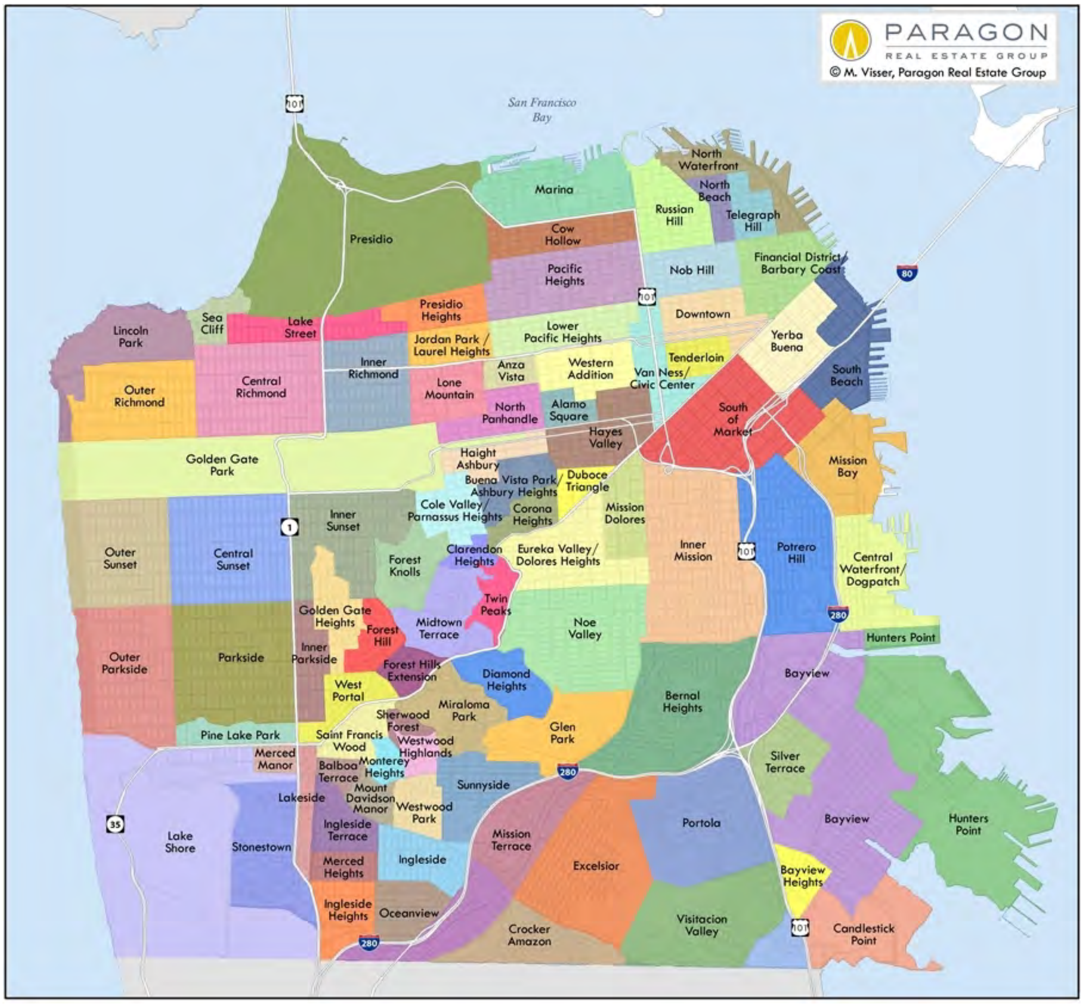

Figure 15.12 Map of San Francisco, broken up into neighborhoods [Paragon Real Estate Group 2013].

With 330,000 housing units, San Francisco is an incredibly dense city. Trying to identify all of the cripple wall homes without a cohesive plan would be reckless and inefficient. We had to devise ways to narrow down the 330,000 to a small enough number so that it would be feasible to perform walking surveys. First, we broke up the city of San Francisco into its constituent neighborhoods (see Figure 15.12). Based on this map, we eliminated Golden Gate Park and Presidio since there are no residential homes in those neighborhoods. We also eliminated Downtown and Civic Center neighborhoods, which do not have one- or two-family homes). To give us a better idea of the density of cripple wall homes, we categorized the neighborhoods into rankings: no cripple walls homes, few cripple wall homes, some cripple wall homes, and many cripple wall homes.

We decided to use the geography of San Francisco to further help us hone-in on areas likely to contain cripple wall homes. Given that San Francisco is an incredibly hilly city, cripple walls are often used to level out a home so that the first story sits flat despite being on a hill (see

Figure 15.13). The cripple walls used for this purpose are often higher than typical cripple walls due to the slope, disqualifying these homes for the Plan Set A Prescriptive solutions since they may be over 4 ft tall. Although homes vary by size, we were able to estimate on the upper limits of gradations that would make a cripple wall home greater than 4 ft. Gradation can be calculated as follows:

$$\text{Gradation} = \frac{\text{Height}}{\text{Length}} * 100\% \tag{15.1}$$

Since our target cripple walls cannot be greater than 4 ft, we modified the above equation to:

$$\text{Gradation} = \frac{4 \text{ ft}}{\text{Length}} * 100\% \tag{15.2}$$

Table 15.1 shows the maximum gradations that different sized homes can sit on and still have cripple walls that are under 4 ft, which gives a very high upper range. We can see that as houses decrease in size, they can sit on steeper ground and still have qualifying cripple walls. Most houses, however, are greater than 20 ft wide, so a gradation of 20% is probably too high to have qualifying cripple walls. With this information and paired with a gradation map (see Figure 15.14), we developed a better picture of where qualifying cripple wall homes are unlikely.

Table 15.1 Gradations of various house widths

House Width (Ft.)	Gradation (%)
20	20
30	13.3
40	10
50	8
60	6.67

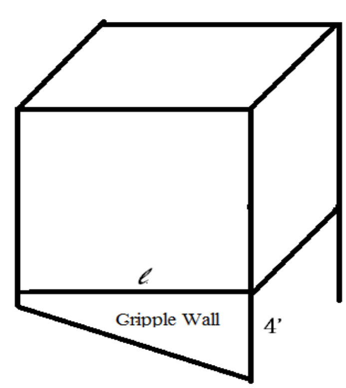

Figure 15.13 Simple schematic displaying the way a typical cripple wall sits on a hill.

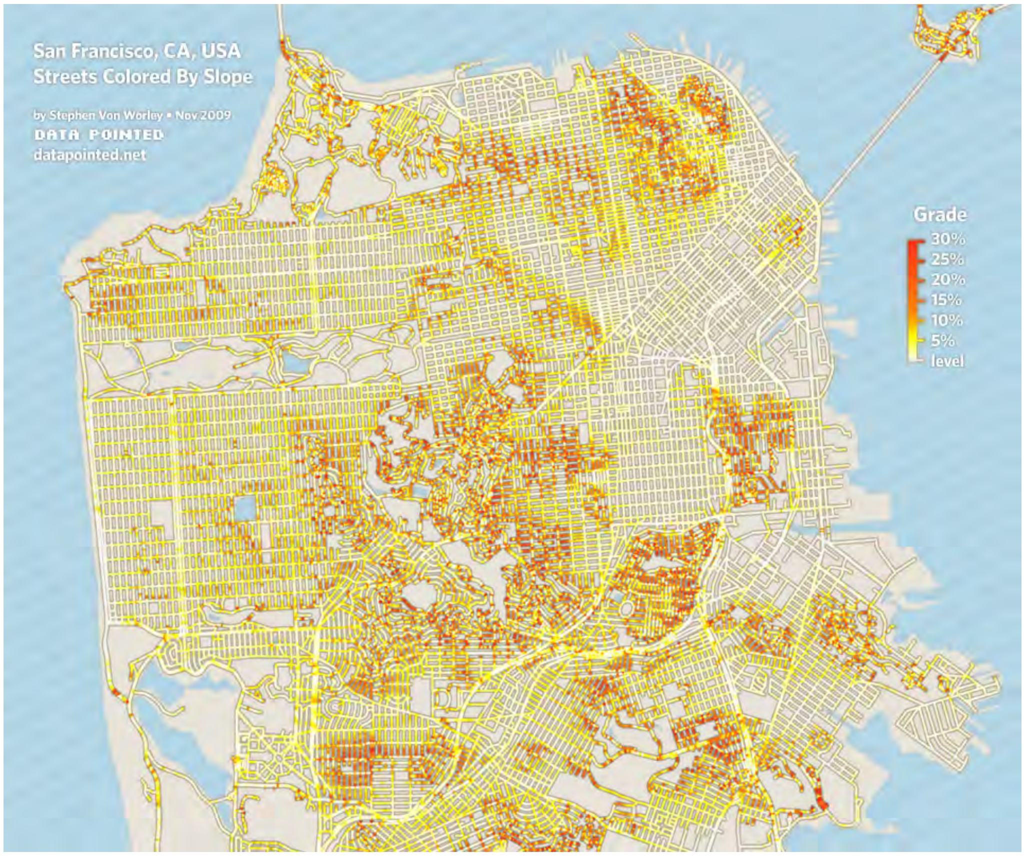

Figure 15.14 Slope map of San Francisco [Van Worley 2009].

From the gradation map, we can see that there are several areas that incredibly hilly and probably will not have cripple walls that fit our criteria. However, it was still too early to blindly eliminate neighborhoods that we are not fully certain of. This map simply served as a guide when we started investigating neighborhoods.

With the neighborhood and gradation maps, we began investigating individual areas, paying extra attention to flatter neighborhoods. We decided to use Google Maps Street View to examine some streets in each neighborhood. From looking at a fair number of streets per neighborhood, we were able to extrapolate the density of cripple walls in a given neighborhood and categorize each neighborhood. The categories are as follows: no cripple walls homes, few cripple wall homes (< 1%), some cripple wall homes (<10%), and many cripple wall homes (> 10%). Although these percentages may seem on the small side, it is important to remember that San Francisco has a housing stock of 330,000. Even if only 10% of those qualified, it would still be a whopping 33,000 cripple wall homes. Google Maps provided fairly good views of homes (see Figure 15.15). The major drawback of Google Maps is that it does not provide a back view of homes. At best, we could only examine the front and about half of each side wall. In order for a home to meet the criteria, at least 40% of each wall (assuming they were single-story homes) must have cripple walls that are less than 4 ft. Since San Francisco is so hilly, it is very possible that some of these houses may dip backwards, making their back cripple walls much larger than the rest.

After examining all of the neighborhoods in San Francisco and assigning them to a category, we had a much better idea of where the cripple wall homes were located (see Figure 15.16). However, we still needed to address the issue of the elusive back wall. Since we now know which areas are of extra interest, we can perform walking surveys of the neighborhoods with high cripple wall densities and begin building our inventory of cripple wall homes. On our survey, we examined homes from the front and made note of which addresses had qualifying cripple walls. We then took back views of the homes that have qualifying cripple walls from the front and noted which ones also qualified (see Figure 15.17). If a home fits the criteria in both the front and back views, it meant that it met the criteria of Plan Set A and would be added to our inventory of qualifying cripple wall homes in San Francisco.

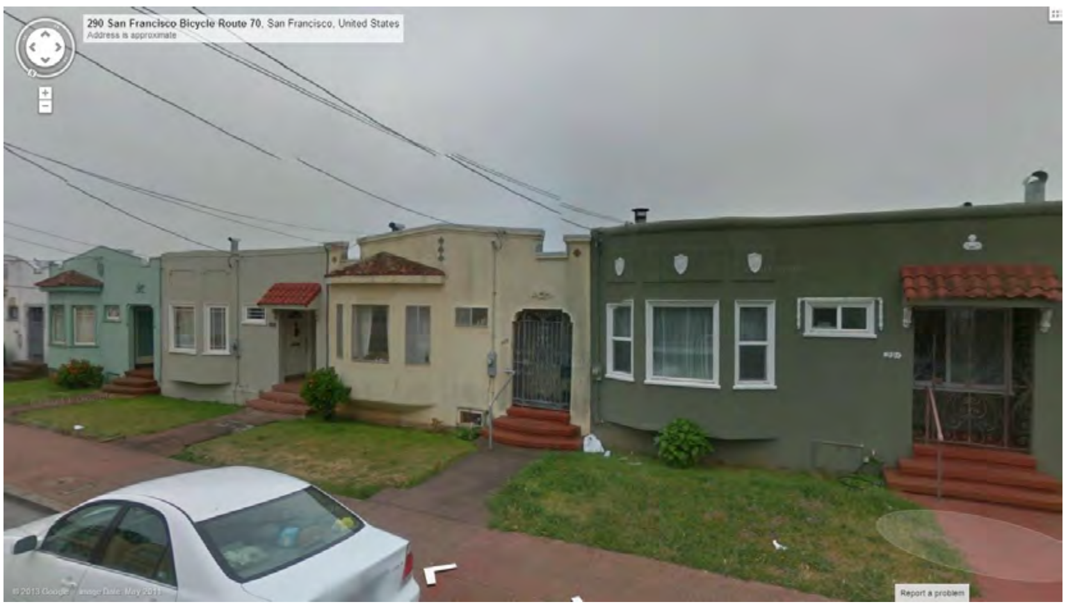

Figure 15.15 Google Map Street View of homes that may have qualifying cripple walls as indicated by the existence of vents and stairs fewer than seven steps leading up to the first floor. However, it is impossible to examine the back walls of these homes using Google Maps.

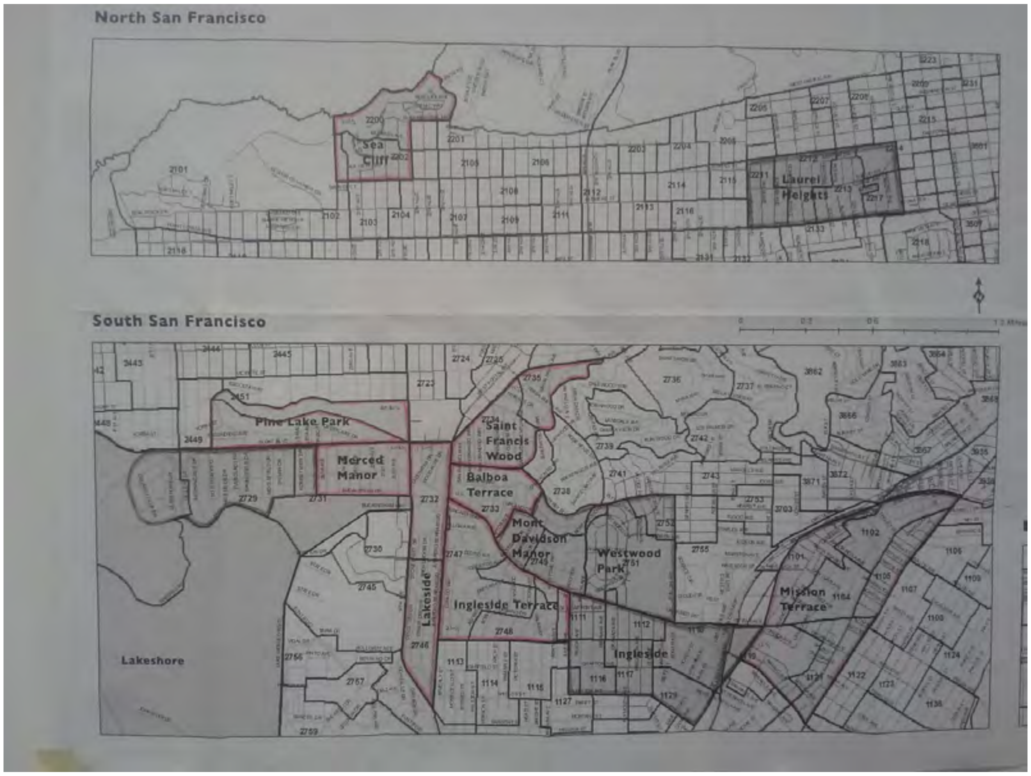

Figure 15.16 Zoomed in view of the neighborhoods that were estimated to have either many cripple wall homes or some cripple wall homes.

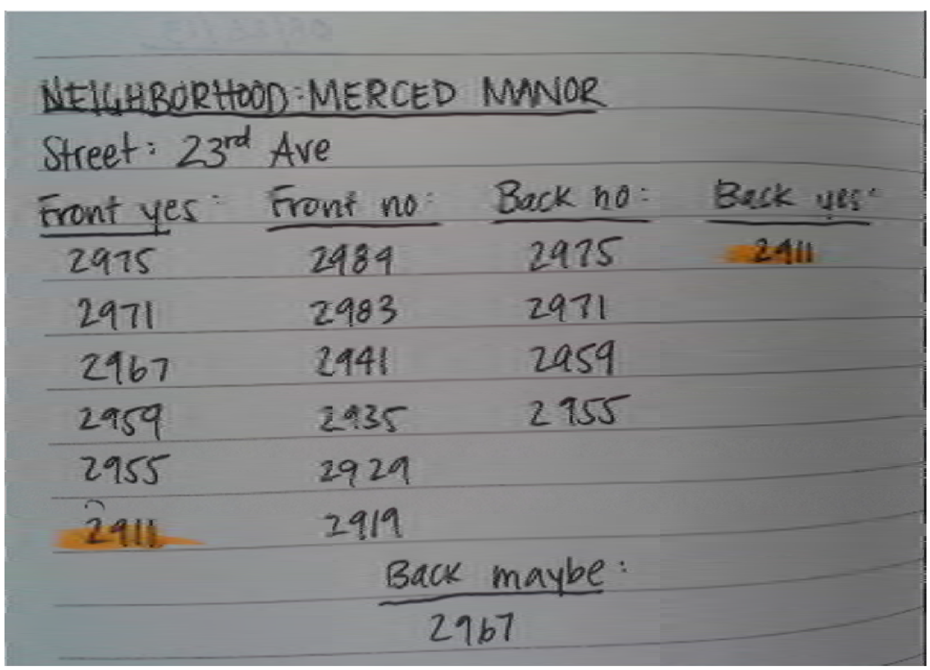

Figure 15.17 An example of the notes taken during the walking survey. Highlighted addresses mean that a home met the Plan Set A criteria and would be included in our cripple wall inventory.

15.4 RESULTS

From reviewing case studies of incentive programs in other cities, the plan with the CEA seems like a very sound plan. In conjunction with our own outreach efforts, the $3000 retrofit refunds provided for by the CEA would allow our program to include the two major factors that should be in a voluntary retrofit program: education and financial incentive.

From our preliminary Google Maps Street View search, we produced a map (see Figure 15.18) depicting where it seemed the cripple were most concentrated. The regions that are colored blue had no cripple wall homes, purple had few cripple wall homes, brown had some cripple wall homes, and red had many cripple wall homes. It turned out that this map looks very similar to the gradation map in terms of patterns. Where the areas are steepest (such as Diamond Heights, Westwood Highlands, and Twin Peaks), we estimated that there were no cripple walls. The areas with the highest estimated cripple wall home concentration (such as Ingleside Terrace, Balboa Terrace, and Lakeside) were in the flatter parts of San Francisco.

During our walking survey, we made the disappointing discovery that many of the homes that we thought fit the criteria of Plan Set A turned out to be disqualified due to the nature of their back walls. Many homes either sloped backwards, making their cripple walls larger than 4 ft or had garages in the back, causing the house to be disqualified since a home had to have qualifying cripple walls on at least 40% per side of the home for a one story home (see Figure 15.19). This fact was impossible to discern on Google Maps, which only provides a frontal view and sometimes some side views of homes. Once we were able to examine the whole perimeter of many homes, we found that those that did have cripple walls less than 4 ft were very complex in structure, which would make retrofit much more difficult and costly than average. Furthermore, many of those homes had very small crawl spaces, which adds to the difficulty and therefore cost of the retrofit.

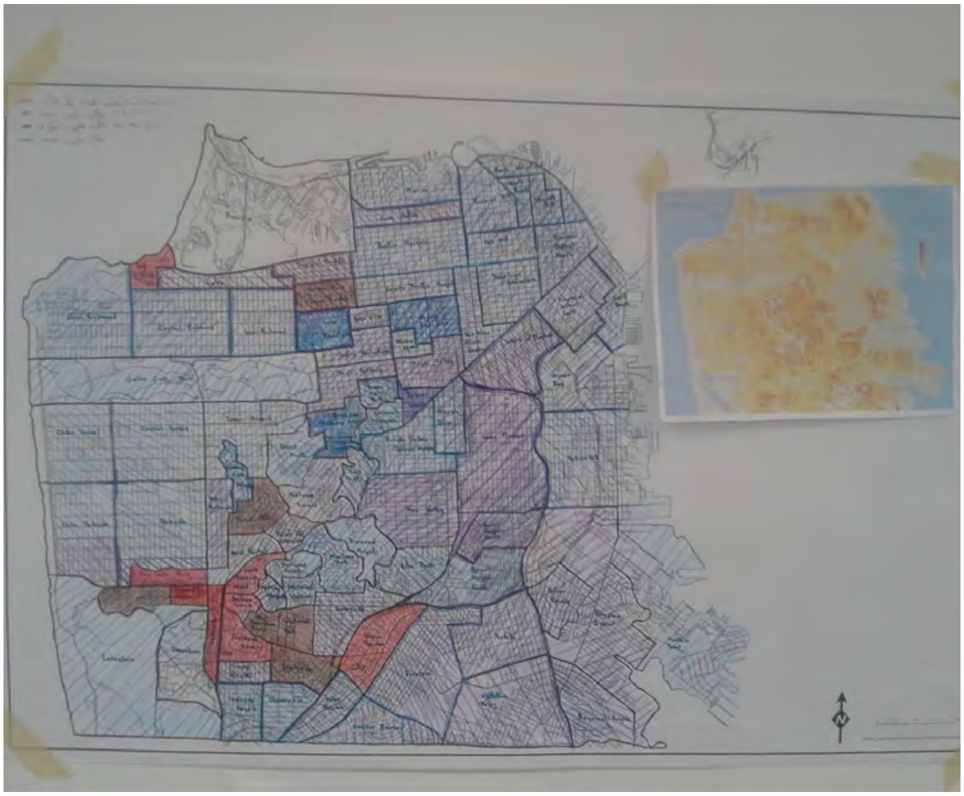

Figure 15.18 Map depicting categorized cripple wall density. Blue denotes no cripple wall homes, purple denotes few cripple wall homes, brown denotes some cripple walls homes, and red denotes many cripple wall homes. The map has patterns similar to those on the gradation map, pictured at right. Cripple wall concentrations appear to have some correlation with steepness.

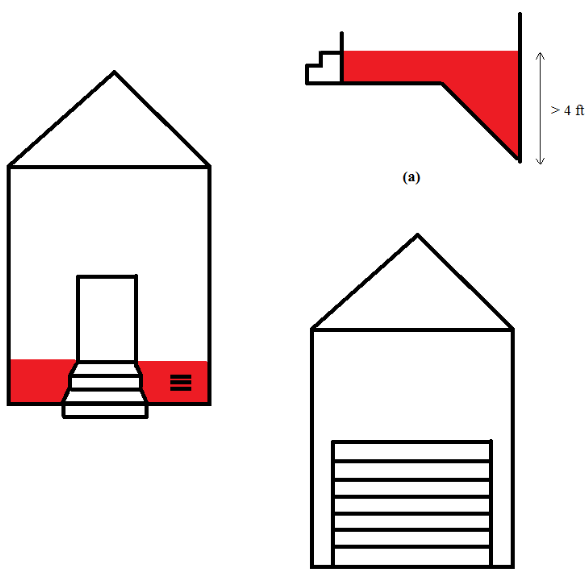

Figure 15.19 Many homes either (a) sloped backwards, making their cripple walls larger than 4 ft or (b) had large garages connected to their back wall.

15.5 CONCLUSIONS AND FURTHER WORK

Although it initially seemed like a promising endeavor, further investigation revealed that a cripple wall retrofit program using Plan Set A is not a viable strategy because a good percentage of San Francisco homes are unable to meet the Plan Set A criteria. Many of the cripple wall homes observed in San Francisco seemed to qualify until the back wall was examined. Then it was discovered that there was a large garage door (and therefore no cripple wall) or a backwards dip, making the cripple wall larger than 4 ft tall. The cripple wall buildings that did qualify had very complex structures or small crawl spaces (and sometimes both), making retrofit difficult and therefore, much more expensive.

Performing this investigation brought to our attention the surprising amount of buildings with cripple walls that are over 4 ft tall in San Francisco. Currently, a set of standardized solutions for cripple walls over 4 ft tall doesn't exist. Unfortunately, a lot of research today is focused on high-rise buildings rather than single or double family residential structures. The CEA is pursing prescriptive retrofit options for cripple wall homes that are over 4 ft and plans to issue them as guidelines. In the meantime, it is important to develop a database of the types of buildings and their locations in San Francisco. This way, once the prescriptive guidelines for cripple walls larger than 4 ft (or even guidelines for other structures) are available, we can encourage seismic upgrades immediately after. This database is also useful in that it would simply add to the general knowledge of the building stock in San Francisco.

Although this cripple wall retrofit program is not a good fit for San Francisco, we are fairly certain that it is a good program for other cities in the Bay Area. There are many cripple wall homes throughout the Bay Area that would fit the criteria of Plan Set A. We would like to encourage other cities to pursue programs that encourage retrofit programs, particularly ones that use Plan Set A. Because there is no need for an engineer it is relatively inexpensive. The CEA would like this refund to be available statewide after its pilot program with Oakland and Los Angeles in Fall 2013.

15.6 ACKNOWLEDGMENTS

This project was a summer research project as part of a joint PEER/City and County of San Francisco program and was made possible through funding from the National Science Foundation. Many thanks to Heidi Tremayne for her continued support and encouragement, Laurence Kornfield for his oversight and mentorship in research and beyond, and fellow PEER intern Julia Pavicic, and all of the summer CAPSS interns for their lively and supportive partnership.

15.7 REFERENCES

ATC (2010a). *Potential Earthquake Impacts, ATC 52-1*, Applied Technology Council, Redwood City, CA

ATC (2010b). *A Community Action Plan for Seismic Safety*, *ATC 52-2*, Applied Technology Council, Redwood City, CA.

ABAG (2009). *Training Material for Seismic Retrofit of Wood-Framed Homes,* Association of Bay Area Governments, retrieved August 2013 from: http://www.abag.ca.gov/bayarea/eqmaps/fixit/ch2/sld017.htm

ABAG (2011). *Shaken Awake!*, Association of Bay Area Governments, retrieved August 2013 from: http://quake.abag.ca.gov/wp-content/documents/Shaken-Awake-conference-summary.pdf

Brocher T. (2008). *The Hayward Fault: Is It America's Most Dangerous \Fault?,* retrieved August 2013 from: https://www.eeri.org/wp-content/uploads/2011/05/haywardfaultcatrisk2008.pdf.

City and County of San Francisco (2011). CAPSS Earthquake Safety Implementation Program, Workplan 2012-2042, draft, San Francisco, CA.

CEA (2013). *CEA Mitigation Program,* California Earthquake Authority, retrieved August 2013, from: http://www.earthquakeauthority.com/index.aspx?id=27&pid=5

Earthquake Engineering Research Institute. *Incentives for Retrofitting Vulnerable Privately-owned Buildings*, retrieved August 2013, from http://eerinc.org/old/quake06/best_practices/IRVPOP.pdf.

Meyer C.E (1989). Aerial view of roadbed collapse near the interface of the cantilever and truss sections of the San Francisco-Oakland Bay Bridge. View northwestward, photograph, U.S. Geological Survey, http://pubs.usgs.gov/dds/dds-29/web_pages/bay_bridge.html.

National Research Council (2011). *National Earthquake Resilience Research, Implementation, and Outreach*, The National Academies Press, Washington, D.C.

Nakata J.K. (1994). [Untitled photograph of collapsed cripple wall home], retrieved August 2013, from : http://pubs.usgs.gov/dds/dds-29/screens/089sr.jpeg.

Nakata J.K. (1994). [Untitled photograph of supported home], retrieved August 2013, from: http://pubs.usgs.gov/dds/dds-29/screens/090sr.jpeg.

San Francisco Museum. *Panorama of the Destroyed City* [Photograph] (1906), retrieved August 2013 from http://www.sfmuseum.org/hist/pix49.html.

Paragon Real Estate Group. (2013). *San Francisco neighborhood map* [Image], retrieved July 2013, from: http://www.paragon-re.com/San_Francisco_Neighborhood_Map/.

SPUR (2004). *Earthquakes: San Francisco at risk*. San Francisco, CA, San Francisco Planning and Urban Research Association, retrieved from http://www.spur.org/publications/library/article/earthquakessfatrisk08012004.

SPUR (2010). Transportation and Rebuilding, San Francisco Planning and Urban Research Association, *The Urbanist, 494, r*etrieved from http://www.spur.org/publications/library/article/transportation-and-rebuilding.

SPUR (2012). *Safe Enough to Stay,* San Francisco Planning and Urban Research Association, San Francisco, CA.

San Francisco Business Times (2013, March 28). *Tourist Industry on a Roll: SF Travel,* retrieved August 2013 from: http://www.bizjournals.com/sanfrancisco/news/2013/03/28/touristindustry-on-a-roll-sf-travel.html.

Field E.H., Milner K.R. et al. (2008). Forecasting California's earthquakes—what can we expect in the next 30 years?, U.S. Geological Survey, *USGS Fact Sheet 2008–3027*, Ver. 1.0, Menlo Park, CA.

Von Worley S. (2009). *Streets colored by slope* [Image], retrieved July 2013, from: http://www.datapointed.net/visualizations/maps/san-francisco/streets-slope/.

Wilshire, H.G. (1995). Side view of support-column failure and collapsed upper deck, Cypress viaduct, US Geological Survey, http://wrgis.wr.usgs.gov/docs/geologic/ca/dds-29/oakland.html.

16. Torsion-Induced Sliding Displacement in Isolated Light-Frame Structures

Curtis Fong

ABSTRACT

This paper examines the potential sources and effects of torsion in friction-based sliding isolation systems for light-frame structures. The primary motivation of this project is to provide earthquake-resistant housing by developing an affordable and effective base isolation system. Therefore, it is necessary to determine the extent of sliding displacement induced by torsion in order to keep the designed displacement tolerance of the isolators down and the system cost-low. Two potential sources of torsion are investigated in this paper, including (1) the frictional properties, namely, pressure dependence, of the materials used; and (2) the torsional stiffness parameter used in the OpenSees analysis model. To test the effects of torsion, numerous studies are performed, including: (1) a study of the isolator bearing element's torsional stiffness parameter in OpenSees; (2) torsion case studies under real load distribution; (3) two cases of altered load distribution for exaggerated center-of-stiffness and center-of-mass separation, (4) sliding interface locking; and (5) a study on the reduction of torsional displacement and other displacements in a dish-sliding isolation system. The paper concludes the pressure dependence of the material used is not the primary contributor to additional sliding displacement due to considering torsion in the isolation diaphragm.

16.1 INTRODUCTION

The 1994 Northridge earthquake displaced 60,000 people and caused $12.7 billion in direct economic loss as a result of damages to residential structures. In addition, when considering indirect economic losses due to insurance payouts, the total cost of damages rises to over $20 billion [Kircher et al. 1997]. The seismic resilience of conventional light-frame buildings needs to be improved in order to prevent the recurrence of severe yet avoidable consequences. Although light-framed residential buildings have traditionally not posed a significant collapse risk, associated damage is both extensive and expensive to repair [Symans et al. 2002]. An investigation into enhanced seismic resistance systems for light-framed structures with the potential for broad commercial implementation is needed.

Seismic isolation and supplemental damping systems are potentially the solution for reducing damage to light-frame structures. Although there has been extensive research examining the application of these systems in multi-story steel structures, not much research has occurred on seismic resistance systems for wood-framed one-to-two-story structures. In addition, the integration of enhanced seismic performance systems into multistory projects is both necessary and feasible since, on average, base isolation and damping systems only represent around 3% of the total construction cost [Devine 2012]. Unfortunately, commercially available isolation systems have not been shown to be financially viable for residential structures. For example, implementing an isolation system in a house would cost $50,000, which is far above an acceptable amount for a majority of homeowners. Affordability is an equal priority to effectiveness when considering a design for commercial implementation.

16.1.1 Lead Rubber Bearings vs Friction-based sliding isolators

When considering a low-cost base isolation system, the friction-based sliding isolation systems and the lead rubber bearing (LRB) isolation systems represent the simplest and most obvious choices for light-frame structures. However, sliding isolation systems do offer distinct advantages over the traditional LRB system.

1. The frictional forces developed at the sliding interface are directly proportional to the mass supported by that bearing in friction-based sliding isolation systems. This implies that there is no eccentricity between the superstructure's center of mass (COM)and center of stiffness (COS). Therefore, if the mass distribution varies from the original design, torsion within the superstructure is less of an issue. In contrast, LRB systems are more prone to torsional effects because fluctuations in vertical load induce different transferrable forces and local displacements.
2. A friction-based sliding isolator with no restoring component has no fundamental period, meaning that the response is governed entirely by the coefficient of friction and the content of the ground motion.
3. The maximum force and therefore acceleration of the friction-based sliding isolation system transferred to the building is exactly equal to the coefficient of friction at the interface in cases where there is no supplemental damping or restoring forces [Jangid 2000] [Constantinou et al. 1987]. In LRBs, there is substantially stiffening of the bearings at large displacements, leading to much higher base shear than is often needed to keep the structure above the isolation behaving linear-elastic.

To keep a sliding base isolation system affordable, the size of the sliding interfaces and cost of the isolation material need to be minimized. The frictional properties of the material-steel interface become paramount in reducing costs. Using polymers for the material-steel interface is worth exploring, due to their low cost, versatility, and availability.

16.1.2 Use of Polymers for Sliding Surfaces

Polymers generally behave viscoelastically. The frictional force that occurs in viscoelastic materials can be explained by the existence of two main mechanisms: adhesion and deformation. In adhesion, the junctions that are formed as a result of the two materials adhering to one another at the regions of intimate contact are sheared. Within the second mechanism, the asperities on the harder body drag through the surface of the softer, resulting in the deformation of the interface [Ludema and Tabor 1966]. Combined, these two mechanisms give rise to various factors influencing the frictional properties of the sliding interface such as time, pressure, velocity, and temperature.

Experimentation has proven that one polymer called polytetrafluoroethylene or PTFE (more commonly known as Teflon) exhibits the following characteristics when it slides against polished steel:

1. Friction increases with the acceleration of excitation as well as with sliding velocity. Friction also appears to be insensitive to variations in the frequency of sliding across tests with similar amplitudes of acceleration.
2. Friction decreases with increases in the bearing pressure.
3. Friction is particularly pressure dependent at low pressures, which is the range of pressures that can be expected in light-frame construction.
4. Teflon-steel interfaces do not behave according to Coulomb's law of friction (constant friction) but instead demonstrate phenomena such as breakaway or initial friction, and varying dynamic coefficients of friction [Constantinou et al. 1987; Constantinou et al. 1990; Mohka et al. 1990; Constantinou 1992; Tsopelas 1996; Dolce et al. 2005].

High density polyethylene (HDPE) is another viscoelastic polymer that could potentially be used as a sliding isolation material. Durometer comparison rates HDPE as a harder material than PTFE; therefore, it is suspected that the friction of HDPE demonstrates less pressure dependence than PTFE.

The influence of pressure on coefficient of friction is a particularly interesting property of viscoelastic plastics such as PTFE and HDPE. Generally, higher pressure translates to lower coefficient of friction. Low coefficients of friction will result in larger sliding displacements, and thus larger surfaces are required for the isolation system. Therefore, higher friction isolators with less pressure are desired, which deviates from past research goals and industry practice. In the lower pressure range, normal pressure on the isolator exerts greater influence on coefficient of friction. If there is a different amount of pressure at each isolator, torsion could be induced in the isolator's response. Dissimilarity in pressure at each support could cause an eccentricity between the COM and COS for a material with friction that is highly pressure dependent, which provides the necessary conditions for torsion. Additional sliding displacement due to torsion needs to be investigated: if the contribution of torsion due to low isolation pressure sources is significant, then the benefit of lowering the isolation pressure to raise the coefficient of friction may be negated. Discussed below is a study to investigate (1) the impact pressure dependent friction has on torsion, and (2) the extent of rotational sliding displacement that can occur relative to translational sliding displacement.

A secondary consideration in sliding isolation design is the residual displacement. Isolation systems such as the Friction-Pendulum System (FPS), which consists of an articulated slider on a spherical, concave chrome surface, uses gravity as a natural restoring force to reducing residual displacement after an earthquake to near zero [Zayas et al. 1990]. This not only slightly decreases the maximum sliding displacement the house experiences during an earthquake, but it also decreases maintenance costs associated with realigning a home if there is a large residual displacement. It will be investigated if an FPS type system can also reduce potential torsional displacement induced by pressure-dependent friction.

Events like the 1994 Northridge earthquake and future earthquakes underscore the need for earthquake-resistant housing. However, in order for an effective base isolation system to be implemented on a large scale, it has to be affordable: the steel plates at each bearing need to be small and the materials being used need to be readily available commercially. In an effort to limit the amount of sliding displacement while maintaining the effectiveness of the isolation system in reducing base shear, all sources of displacement need to be investigated. The friction coefficient of the interface primarily determines the amount of translational sliding displacement allowed, but additional sources of rotational displacement due to torsion may have a significant contribution and should be investigated. This report examines sources of torsional displacement, such as pressure dependent friction, and tests those cases for torsion contributions. A comparison between flat and dish slider bearings is also performed to examine reductions in residual displacement, peak displacement and torsional displacement.

16.2 PRESSURE-DEPENDENT MATERIALS

One possible source of torsional displacement is the use of pressure-dependent materials such as PTFE. The following friction curves were generated by testing unfilled PTFE on #8 mirror finish stainless steel at five sliding velocities (quasi-static, 1 in./sec, 2 in./sec, 4 in./sec, and 6 in./sec) for four different normal pressures (250 psi, 500 psi, 1000 psi, and 2000 psi) [Jampole et al. 2012]. As shown in Figure 16.1, the results of this experiment confirms previous findings that the coefficient of friction between PTFE and #8 mirror finish stainless steel rises as pressure decreases, and demonstrates that PTFE is more pressure dependent at lower pressures (which is the case for light-frame construction) [Constantinou et al. 1987; Jampole, et al. 2012].

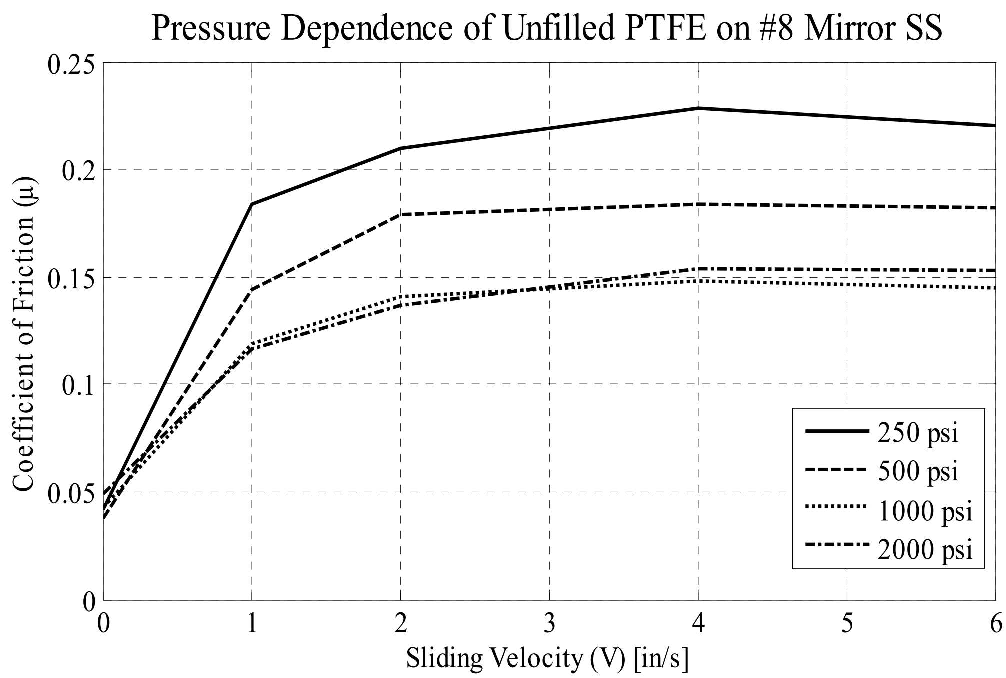

Figure 16.1 Friction curves of unfilled PTFE on #8 mirror-polished stainless steel.

To explain the various dependences that influence the frictional properties of sliding base isolators, Takahashi et al. [2004] developed a numerical model. Equations (16.1) and (16.2) predict the frictional force under different normal pressures and sliding velocities.

$$F = A\left[s'^{\left(1-e^{-nV}\right)\left(1-e^{-kV}\right)} + \alpha P\right] \tag{16.1}$$

$$\mu = s'\left[\left(1-e^{-nV}\right)\frac{\left(1-e^{-kV}\right)}{P} + \alpha\right] \tag{16.2}$$

where F is the frictional force at the interface, A is the area of the sliding interface, μ is the coefficient of friction at the interface, s' and n are constants relating to the change in friction at different sliding velocities, V, and k and α are constants that define the change in friction at different pressures, P. This numerical model is calibrated to the trends that (1) as normal pressure increases, the coefficient of friction decreases, and (2) as sliding velocity increases, the coefficient of friction increases and eventually converging to a limit.

In the case of a house, the superstructure is constructed on top of a rigid isolation diaphragm that bears on numerous sliding isolation bearings, as illustrated in Figure 16.2. As shown in Figure 16.3 of real isolator loads from a two-story house, when using PTFE on #8 mirror finish stainless steel or another pressure dependent material interface, the unbalanced distribution of gravity loads and pressure at each isolator-causes a *disproportional* frictional force to act at each isolator, which in turn causes different coefficients of friction at each isolator. This creates a differential between the COM and COS of the house, thereby creating a precondition for torsion. The larger the distance between the COM and COS, the larger the expected torsional response. By contrast, if a non-pressure dependent material were used, the coefficient of friction at each isolator would be equal, therefore it would take the same *proportional* frictional force to move each isolator. This creates no eccentricity between the COS and the COM, thus likely limiting additional sliding displacement due to torsion.

To demonstrate the concept of torsion in a sliding system, an exaggerated example of COM and COS separation is discussed here and illustrated in Figure 16.4. Since the COS is the centroid of the different frictional forces required to move the isolation diaphragm, pulling or laterally loading the COM in any one direction accurately describes, theoretically, the diaphragm's response to an earthquake at any point in time. If a rope attached to the COM were theoretically pulled a large distance directly in the z-direction, eventually the diaphragm will realign itself so that both the COM and the COS will reside on the $x = +50$ in. axis, since rotation will occur about the COS. The diaphragm and the house would then have rotated 90°, representing a very severe case of torsion. Since a majority of houses will not have even pressure at each isolator unit and will have some separation between their COM and COS, the investigation of additional sliding displacement due to pressure dependent friction is necessary.

Figure 16.2 House, isolation diaphragm, and slider bearings.

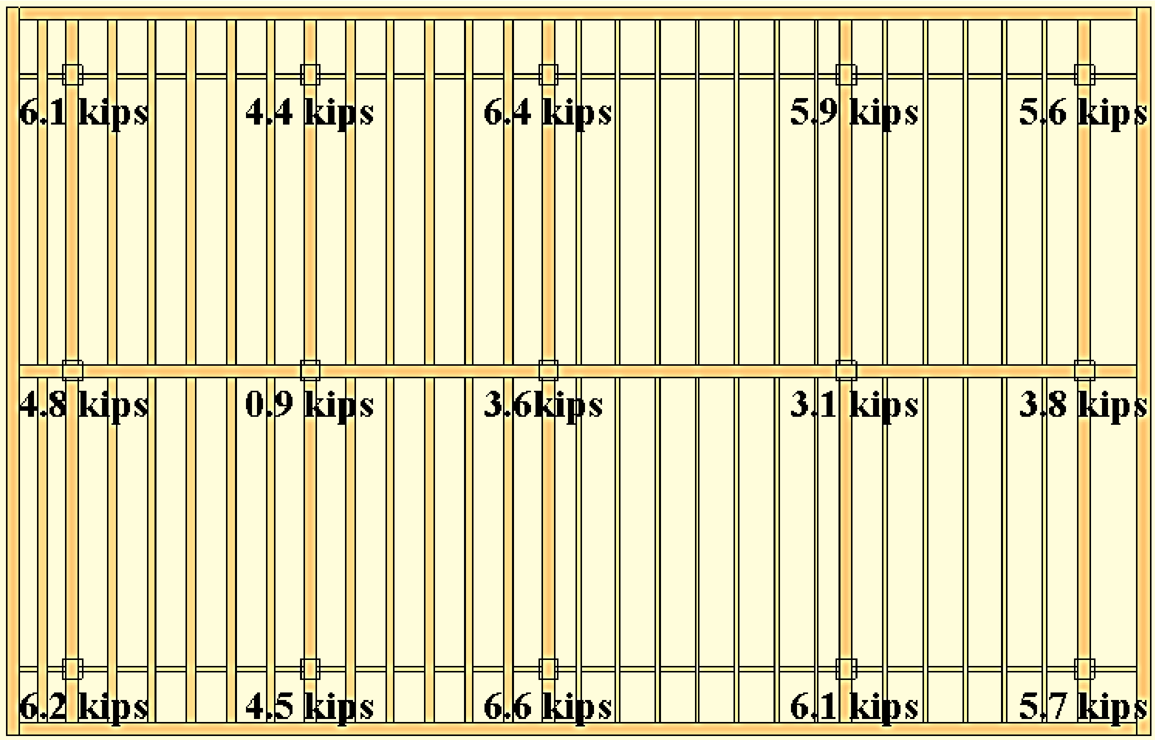

Figure 16.3 **Isolation diaphragm plan view, with a normal load at each isolator represented by the squares.**

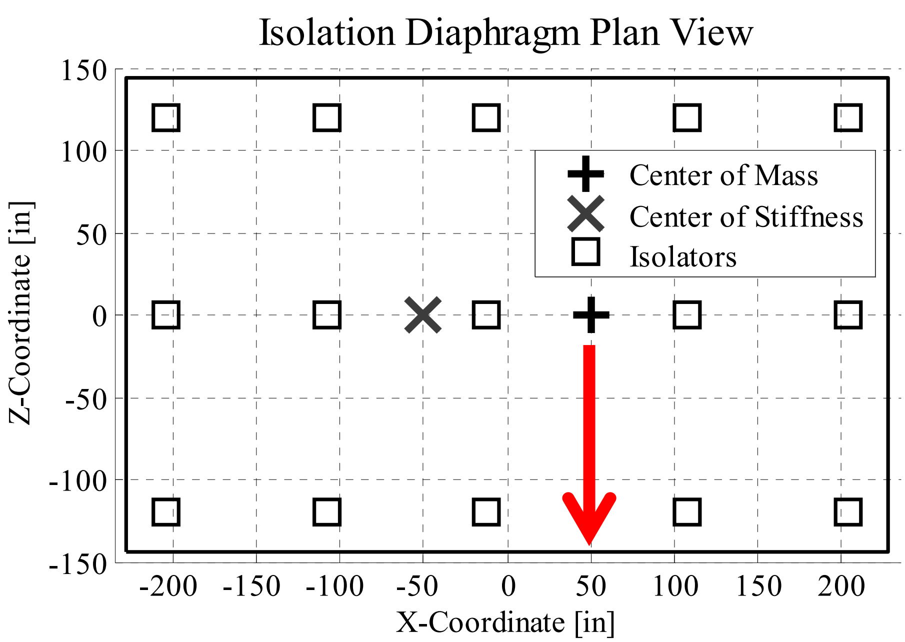

Figure 16.4 **Pressure dependence; center-of-mass and center-of stiffness separation.**

16.3 OPENSEES MODEL

Two models were developed using OpenSees [McKenna et al. 2000] and were run with 40 ground motion record pairs from the PEER Transportation Set 1a scaled to maximum considered earthquake (MCE) level event for a Site Class D structure in Los Angeles, California [Baker et al. 2011]. The first model included 15 isolation bearings and exactly replicated of the flexibility of the isolation diaphragm as shown in the Revit model in Figure 16.3. Because attempting to run all 40 ground motion record pairs became too cumbersome to run efficiently, a simplified model was created with a rigid diaphragm.

The simplified model consisted of 15 connected nodes to represent the isolation diaphragm with an isolator unit below each node. These nodes were connected together by a grid of rigid beams. Each isolator node was then loaded with the real load distribution as shown in Figure 16.3 (determined through SAP2000 linear-elastic analysis), whose values were determined by applying realistic line and area loads to simulate the weight of the superstructure to the full explicit model. To check the validity of this simplified model, displacement histories were compared to a more simplified single-node isolator model, the 15-node model, and the full explicit model. Running multiple simple analyses determined that the displacements predicted by the 15-node isolator model represent the response expected in the full explicit model. The impact of superstructure stiffness on dynamic sliding response was not considered.

16.3.1 Model Parameters

The *VelDependent* and *VelPressureDep* friction models were used to model velocity dependent and velocity and pressure dependent friction, respectively. Parameters for these friction models were calibrated to fit both the experimental data of PTFE shown in Figure 16.1 and hypothetical friction values at various pressures for exaggerated pressure dependence.

The *flatSliderBearing* element was used to model the isolator units. The area of each isolator bearing is the same and was calculated by dividing the total gravity load on the isolation diaphragm by 500 psi so that the average pressure across all the isolators would be 500 psi.

16.4 STUDY OF TORSIONAL STIFFNESS PARAMETER *J*

Among all the parameters used in the OpenSees model, the torsional stiffness (J) exerted particular influence over the amount of torsion seen in analyses results. Therefore, due to lack of resources providing an appropriate value for this parameter, a study was done, cycling through the 40 ground motions record pairs and nine values of torsional stiffness (J): 100, 250, 500, 750, 1000, 1500, 2000, 4000, and 6000 kip-in./rad, as shown in Figure 16.5.

Rotating an individual isolator bearing does not take significant force, thus low torsional stiffness should be assigned to each isolator unit for the velocity and pressure dependent model where some torsional response is expected. From Figure 16.5, it is seen that low values of individual isolator rotational stiffness result in mean and median ratios of torsional displacement (rotational) to diaphragm displacement (translational) are 0.1800 and 0.1659, respectively. This means that a ground motion that induces a peak sliding displacement of 16.5 in. when torsion is not accounted for will produce a peak sliding displacement of 20 in. on average, a substantial increase in required isolator size.

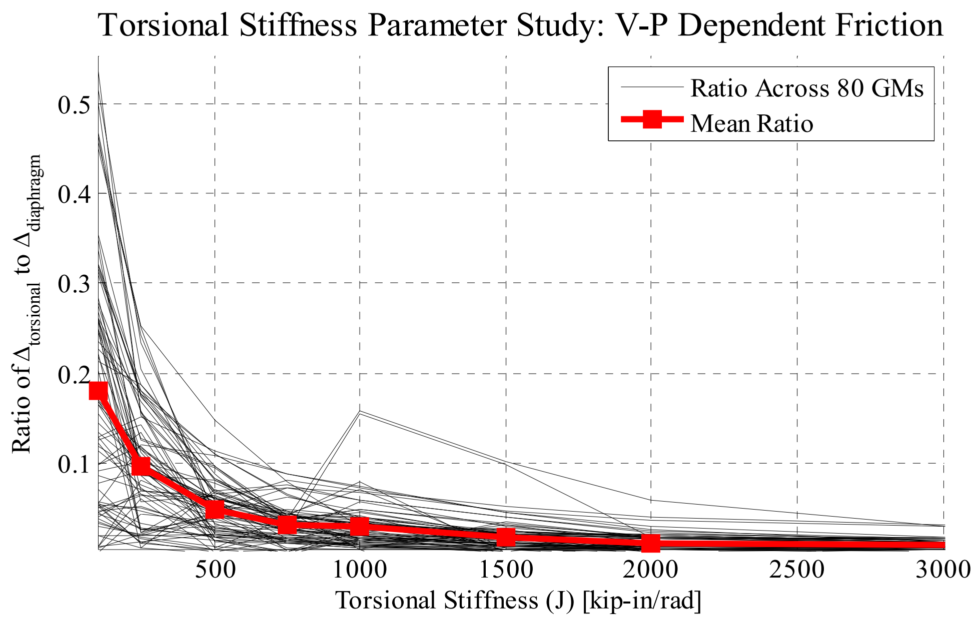

Figure 16.5 ***J* parameter study to measure how much additional rotational displacement there is due to torsion. Higher ratio means more torsion.**

As shown in Figure 16.11, running the full set of 40 ground motion record pairs results in some unrealistically high sliding displacements of up to 150 in. These unrealistically high displacements are due to the mismatch between linear ground motion scaling based on the linear-elastic period-dependent response spectrum and nonlinear period-independent sliding response. Since such displacements are not in the range one might realistically expect for higher friction isolators even near a fault, the cases yielding 10 to 20 in. of $\Delta_{diaphragm}$ will be our focus.

Figure 16.6 shows the records that induce a peak sliding displacement between 10 and 20 in. The influence of the torsional stiffness parameter on additional torsional displacement is clearly demonstrated in C99tcu060 and LP89g04, as the peak displacement is decreased by more than an inch when displacement due to torsion is included in the analysis. The pressure dependent friction represents low values of *J* while non-pressure dependent friction represents infinitely high values of *J*, the difference between which represents the amount of $\Delta_{torsional}$ observed in each case.

To illustrate the design implications, if a 30 in.×30 in. steel plate and 3 in.×3 in. polymer were used for the isolator, the maximum displacement tolerance would be 13.5 in. in any one direction to maintain full sliding contact. Then, if a 12 in. sliding displacement was induced by a severe ground motion using a non-pressure dependent material, a pressure-dependent material may provide the additional 1–2 in. of $\Delta_{torsional}$ that will cause the house to slide off the isolator units. Therefore, if a pressure-dependent polymer were used, then the steel plate size at each isolator would have to be larger, which is a major limiting factor in system affordability.

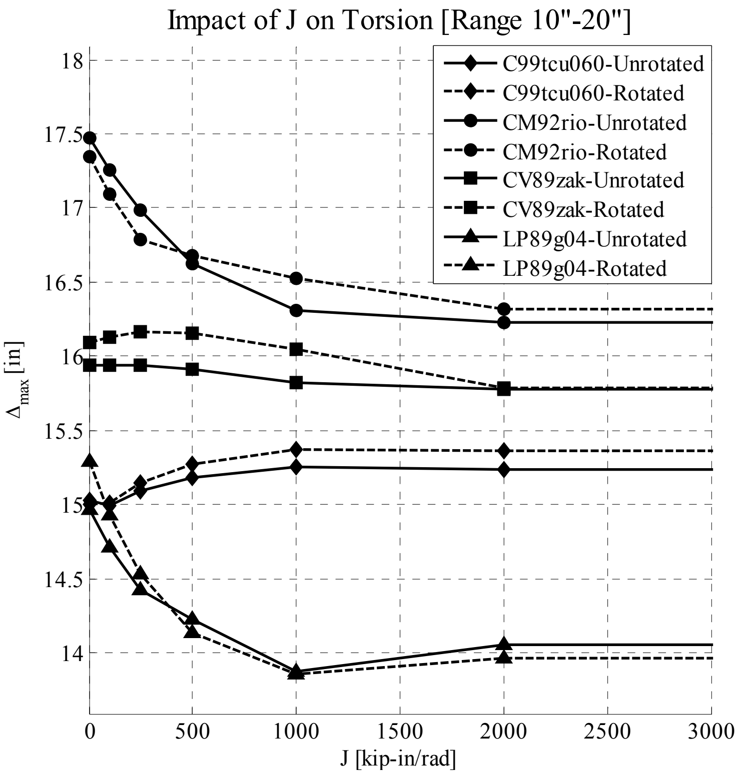

Figure 16.6 ***J* study, with additional $\Delta_{torsional}$ in 10–20 in. $\Delta_{diaphragm}$ cases.**

16.5 CASE STUDIES OF PRESSURE-DEPENDENT FRICTION

The simplified OpenSees model was used to conduct a series of torsion case analyses described in this section. The purpose of these case studies was to further investigate the impact of differences in the coefficient of friction at each isolator support on sliding response, and to assess the influence of added restoring stiffness in the system on mitigating induced torsional response.

16.5.1 Real Load Distribution Study

Under the real load distribution (from calculated line and area loads acting on the diaphragm) as shown by the loads in Figure 16.3, the distance between the COS and the COM is 8.27 in., a relatively small distance compared to the 456 in.×288 in. (38 ft×24 ft) isolation diaphragm modeled. Using this load distribution, analyses were performed testing for additional $\Delta_{torsional}$, first using the friction model calibrated to match the experimental results of PTFE, and second using a friction model with exaggerated pressure dependence at low pressures to determine the extent to which pressure dependence in friction has an impact on added sliding displacement due to torsion.

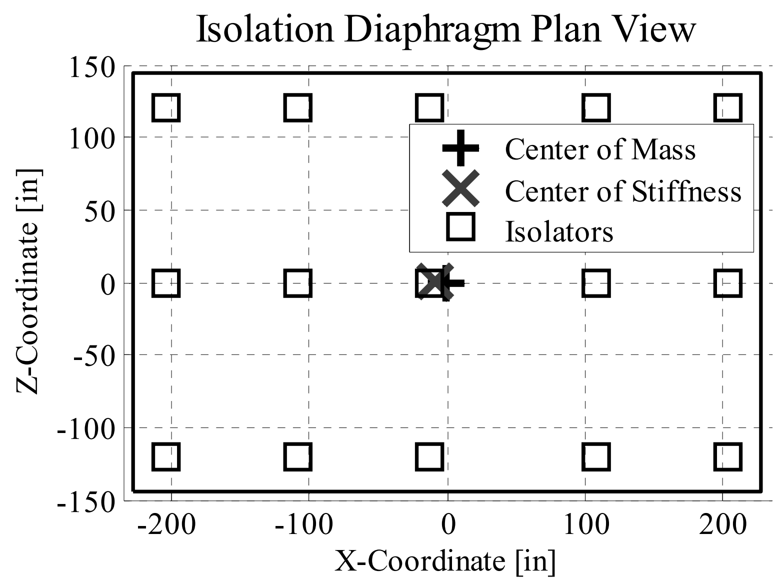

Figure 16.7 Real load distribution; COS and COM locations.

16.5.2 Friction Model Calibrated to Match Experimental Results of PTFE–MSS

Calibrated to match the experimental results of PTFE, this friction model returns a μ of 0.22 at 250 psi and a μ of 0.195 at 500 psi. Figures 16.8 and 16.9 illustrate the torsional effects of using a material with this amount of pressure dependence. The two ground motions shown in Figure 16.9 yield around the expected 10 to 20 in. expected peak displacement range and, as illustrated, yield 1 to 5 in. of $\Delta_{torsional}$. Across 80 ground motions, the mean and median additional $\Delta_{torsional}$ of the pressure dependent model are 6.96 in. and 1.76 in. respectively. Looking at Δ_{max}, the pressure dependent model yields a mean of 39.17 in. and a median of 24.15 in., whereas the non-pressure dependent model yields a mean of 32.20 in. and a median of 20.57 in. Therefore, it can be concluded that given the difference in Δ_{max} between the two friction models, the effect of torsion in sliding isolation is not insignificant.

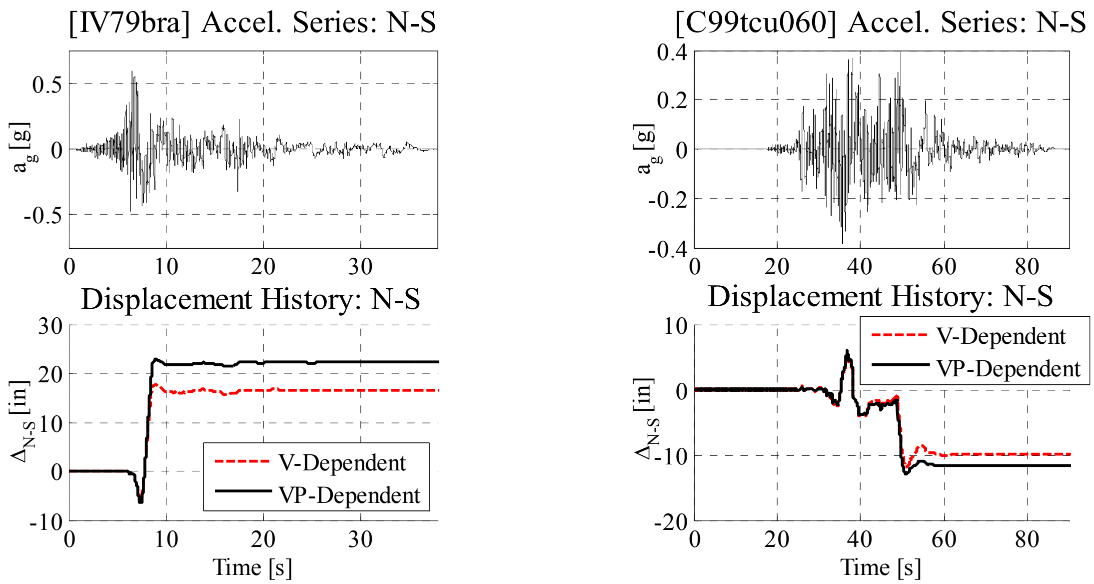

Figure 16.8 ***μ* = 0.22 @ 250 psi and *μ* = 0.195 @ 500 psi; additional $\Delta_{torsional}$ in one direction.**

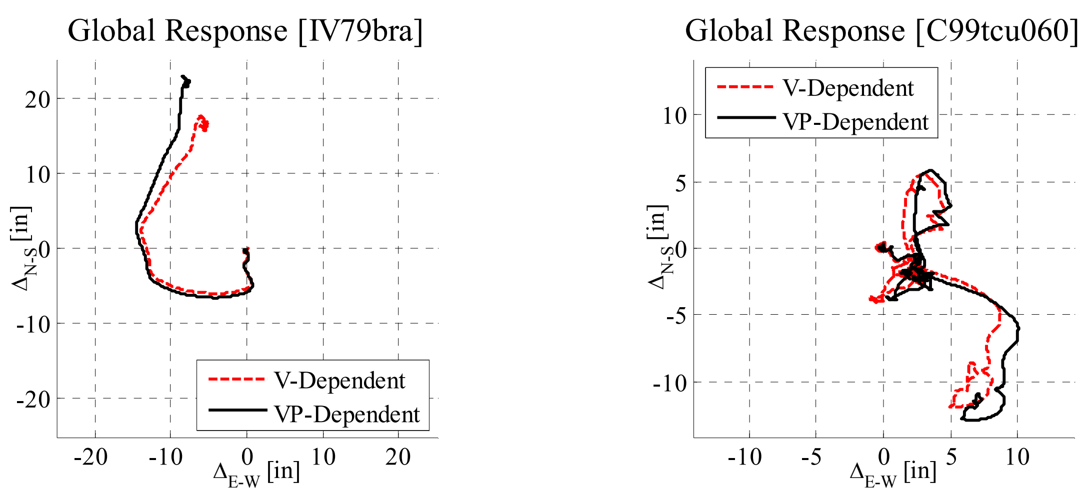

Figure 16.9 ***μ* = 0.22 @ 250 psi and *μ* = 0.195 @ 500 psi; additional $\Delta_{torsional}$ in two directions.**

16.5.3 Friction Model Calibrated for Exaggerated Pressure Dependence

Calibrated for exaggerated pressure dependence, this friction model returns a μ of 0.25 at 250 psi and a μ of 0.20 at 500 psi. However, the results for additional $\Delta_{torsional}$ did not differ much from the results obtained with the experimentally calibrated pressure dependent friction model. Figure 16.10 shows the difference in maximum displacement experienced across all 80 ground motions. Since the maximum difference is less than one, it can be hypothesized that pressure dependence may be a secondary contributing factor to additional $\Delta_{torsional}$ seen in the results, with including torsional response as the main factor.

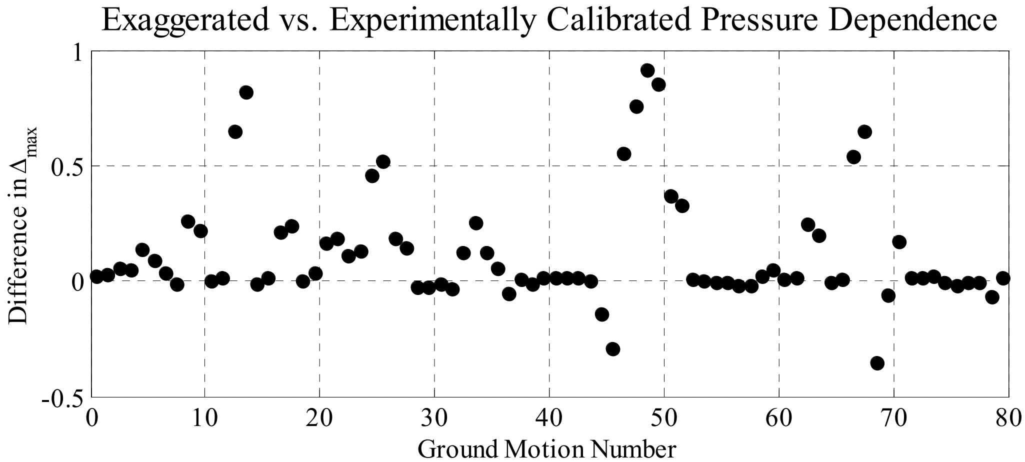

Figure 16.10 Difference in Δ_{max} between the exaggerated pressure dependent model and the pressure dependent model calibrated to experimental results.

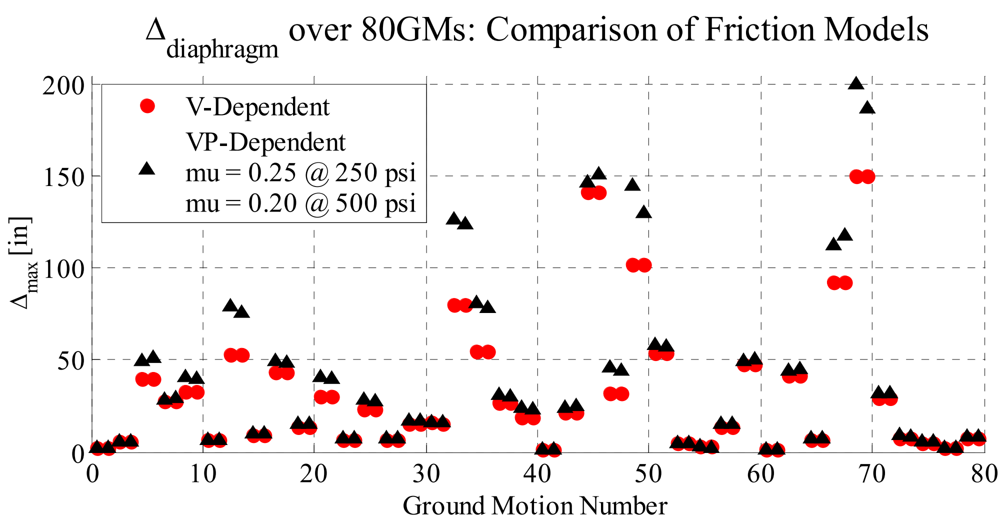

Figure 16.11 Real load distribution; exaggerated pressure dependence.

16.5.4 Altered Load Distribution Study

Keeping the line loads constant on the isolation diaphragm, the area loads are altered in this study from the uniform 10 psf area load in the real load distribution in order to create two cases of altered load distribution. Case 1 is generated by a 5/15 psf split with 5 psf on the left half of the diaphragm and 15 psf on the right half. This results in a COS and COM separation of 23.53 in, as illustrated in Figure 16.12. Case 2 is generated by a 0/20 psf split with 0 psf on the left half of the diaphragm and 20 psf on the right half. This results in a COS and COM separation of 70.32 in. as illustrated in Figure 16.13.

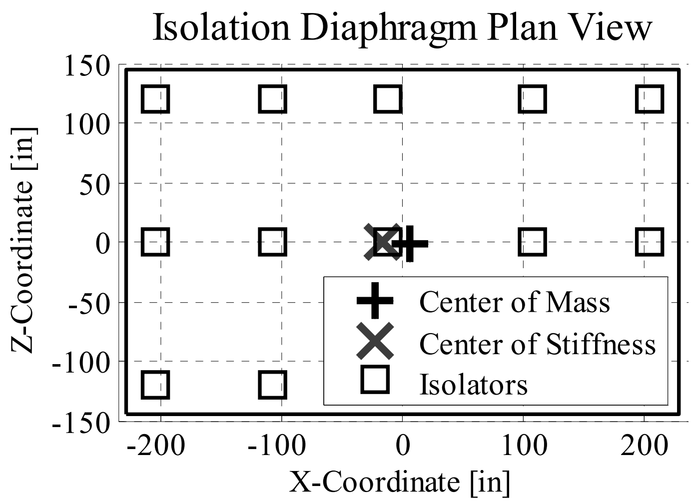

Figure 16.12 Altered load distribution Case 1: center-of-stiffness and center-of-mass locations.

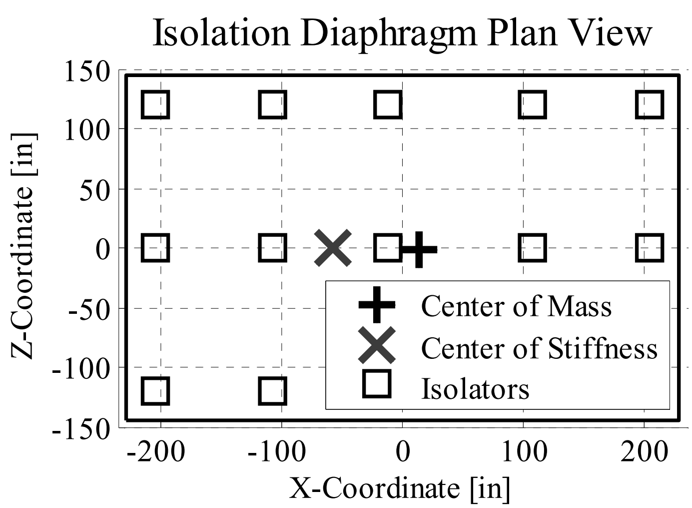

Figure 16.13 Altered load distribution Case 2: center-of-stiffness and center-of-mass locations.

The objective of this altered load distribution study is to develop scenarios in home construction that result in a substantial distance between the COS and COM. Theoretically, as exemplified through the rope-pull analogy, the home's torsional response to the COS-COM separation should be amplified as a result of the heightened distance between the COS and COM. However, having run through the altered load distribution cases, there is little change in the amount of $\Delta_{torsional}$ observed compared to the amount of $\Delta_{torsional}$ observed in the real load distribution case. Comparing the maximum displacements from the real load distribution study and Case 1 of the altered load distribution study, the mean and median differences between these two cases across 80 ground motions is 0.19 in. and 0.003 in., respectively. Comparing the maximum displacements from the real load distribution study and Case 2 of the altered load distribution (greater COS-COM eccentricity), the mean and median differences between these two cases across 80 ground motions is 0.52 in. and 0.11 in., respectively. That is almost a negligible difference between these scenarios. Although it does seem that a higher the COS-COM separation translates to higher $\Delta_{torsional}$, the pressure dependence of the material used does not have a large impact on the differences in displacement observed between the velocity and velocity and pressure dependent friction model outputs shown in Figures 16.8 and 16.9.

16.5.5 Interface Locking Study

Investigating other scenarios where torsion may be induced in a sliding isolation system includes scenarios where the sliding interface of an isolator unit becomes stuck and cannot move or when one isolator slides with more resistance in the event of abnormally high friction caused by dirt or other residue. To study these scenarios, six models were analyzed using both the pressure and non-pressure dependent model for the amount of $\Delta_{torsional}$ seen:

- the center isolator node of the isolation diaphragm is fixed
- the middle isolator node on a short side of the diaphragm is fixed
- a corner isolator node is fixed
- the center isolator node has a $\underline{\mu}$ of 0.70 (measured at high velocity and 500 psi)
- the middle isolator node on a short side has a μ of 0.70 (same conditions)
- a corner isolator node has a μ of 0.70 (same conditions)

The results of this study are as follows:

1. The pressure dependent friction model on average yields higher peak displacement than the non-pressure dependent friction model across all six scenarios.
2. The mean and median Δ_{max} at any isolator among the three high-friction single isolator models does not vary much with all three yielding a mean Δ_{max} of around 35 in. and a median Δ_{max} of around 19 in.
3. Among the three fixed isolator node models, fixing a corner isolator node yields the highest Δ_{max} with a mean Δ_{max} of 28.15 in. and a median Δ_{max} of 16.02 in.
4. Among the same three fixed isolator node models, fixing the center isolator node yields the lowest Δ_{max} with a mean Δ_{max} of 11.69 in. and a median Δ_{max} of 7.87 in.
5. All six models yield smaller mean and median Δ_{max} compared to the real load distribution pressure dependent friction model outputs.

Therefore, these torsion cases are not of concern in terms of displacement induced. However, to qualify these results, the Δ_{max} variable describes the maximum magnitude of displacement observed among all the isolator units. Since this study does not see much translational displacement of the diaphragm, with much of the response going into rotational displacement, the comparison is still valid since the maximum magnitude of displacement is the primary concern that dictates the necessary design size of the sliding interface. Figures 16.14 and 16.15 illustrate the response of the isolator that experiences the highest magnitude of displacement in this study. The scenario shown is the fixed-corner isolator node.

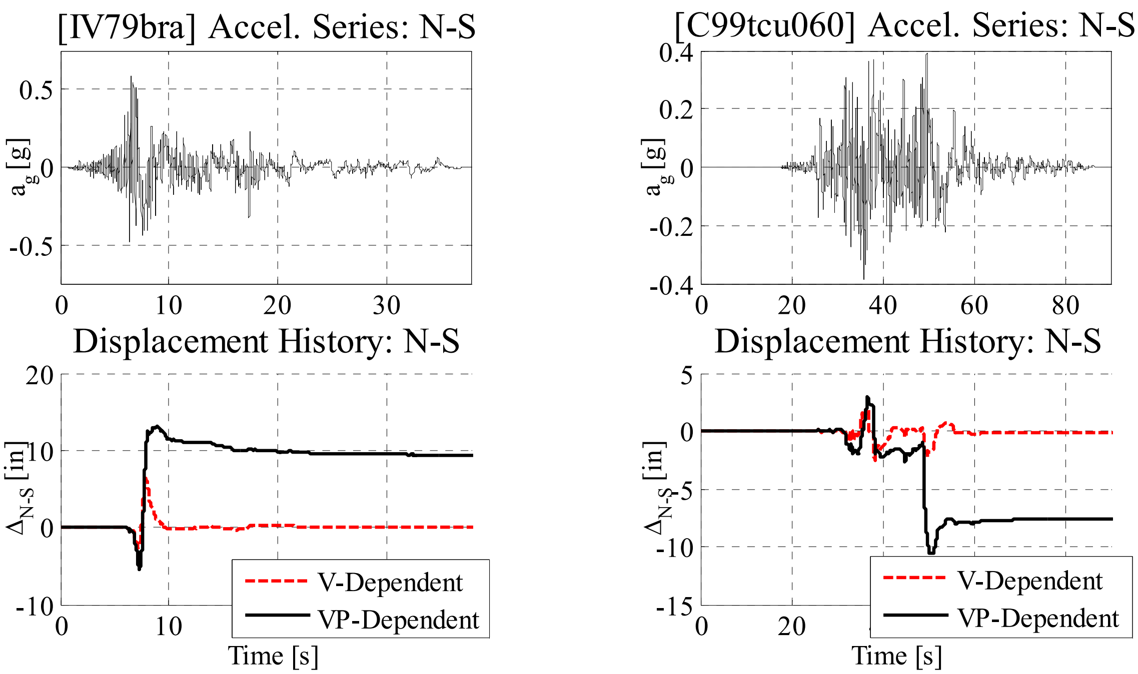

Figure 16.14 **Fixed-corner isolator node; comparison of friction models in one direction.**

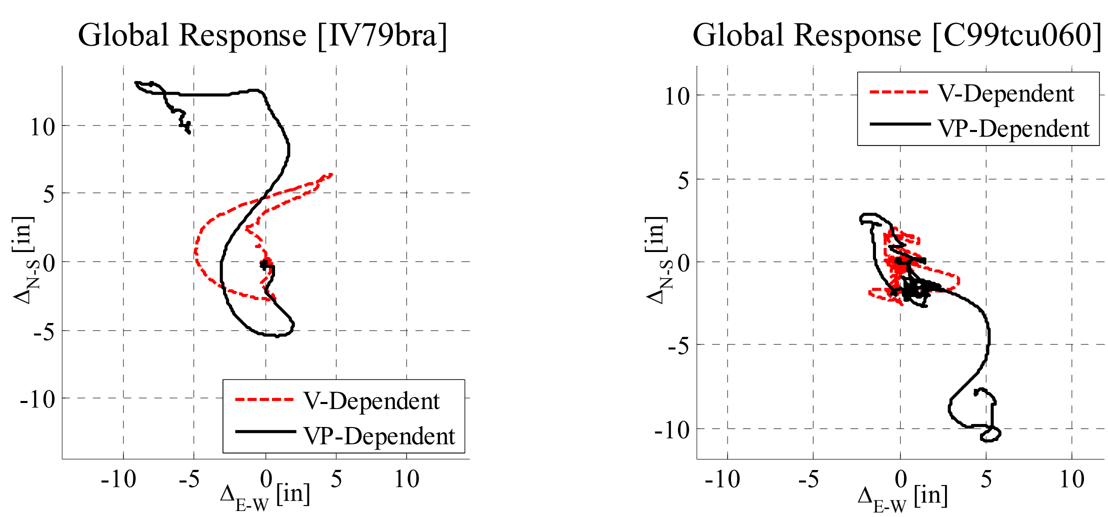

Figure 16.15 **Fixed-corner isolator node; comparison of friction models in two directions.**

16.6 COMPARISON OF FLAT- VERSUS DISH-SLIDING ISOLATION

Figures 16.16 and 16.17 investigate $\Delta_{torsional}$ in dish-sliding isolators, and Figures 16.18 and 16.19 compare the pressure dependent flat- and dish isolator responses with low torsional stiffness at each isolator.

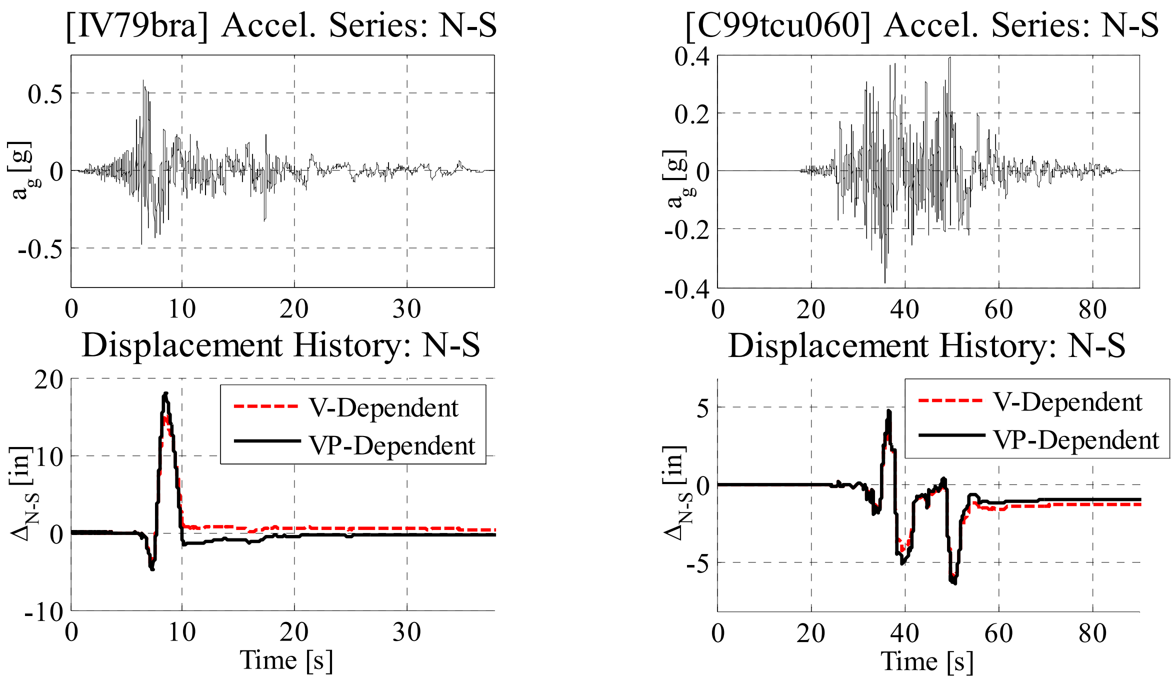

Figure 16.16 Dish-sliding isolators; additional $\Delta_{torsional}$ in one direction.

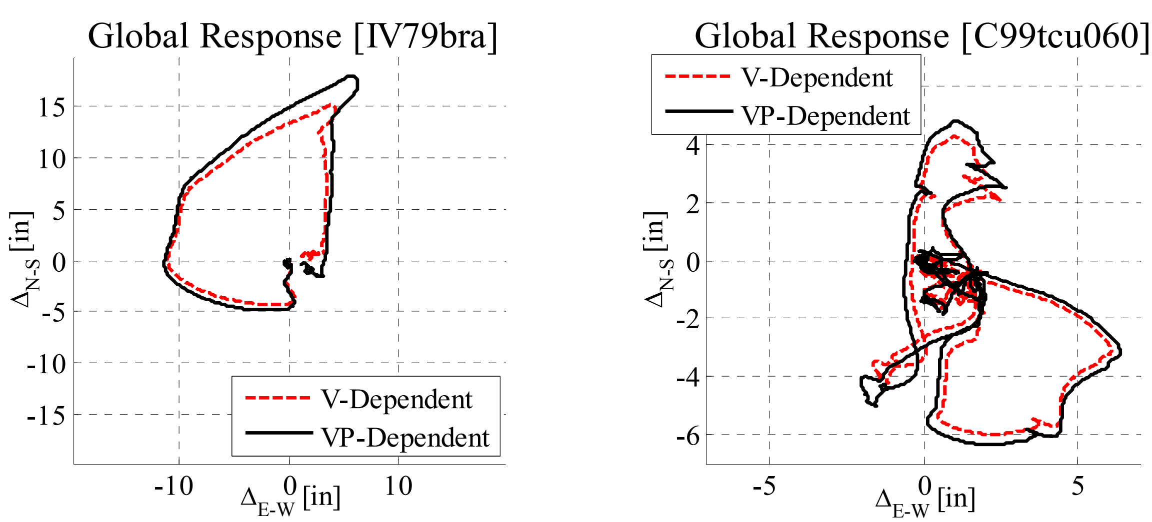

Figure 16.17 Dish-sliding isolators; additional $\Delta_{torsional}$ in two directions.

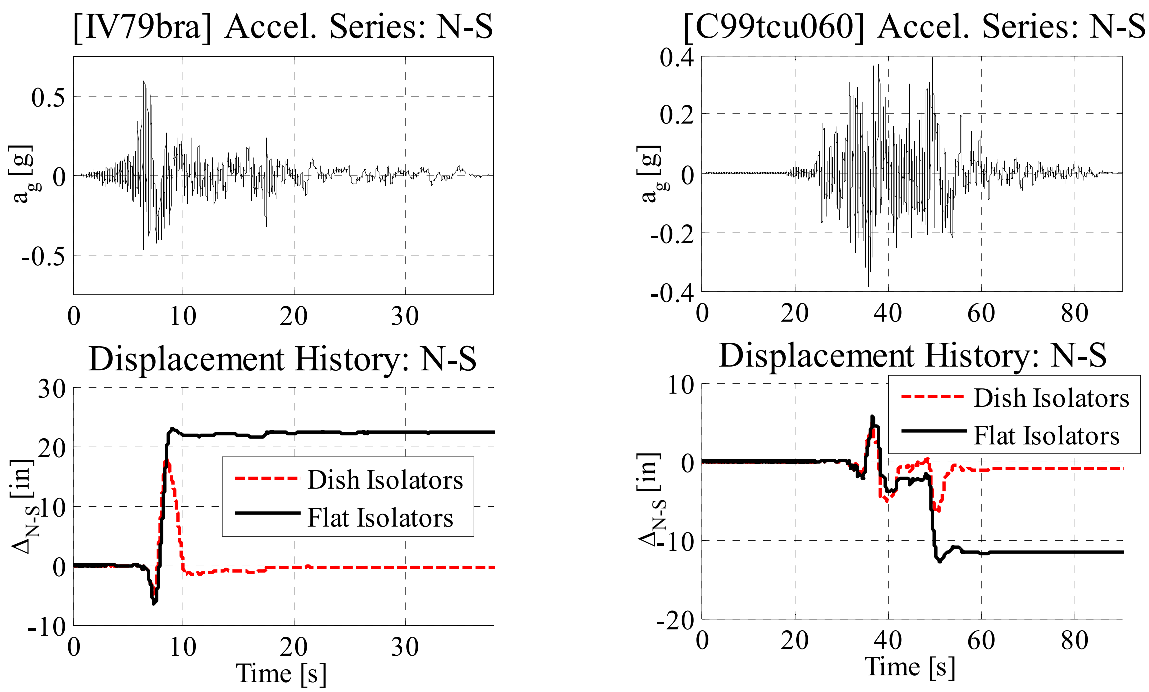

Figure 16.18 **Flat- versus dish-sliding isolators; difference in peak and residual displacement.**

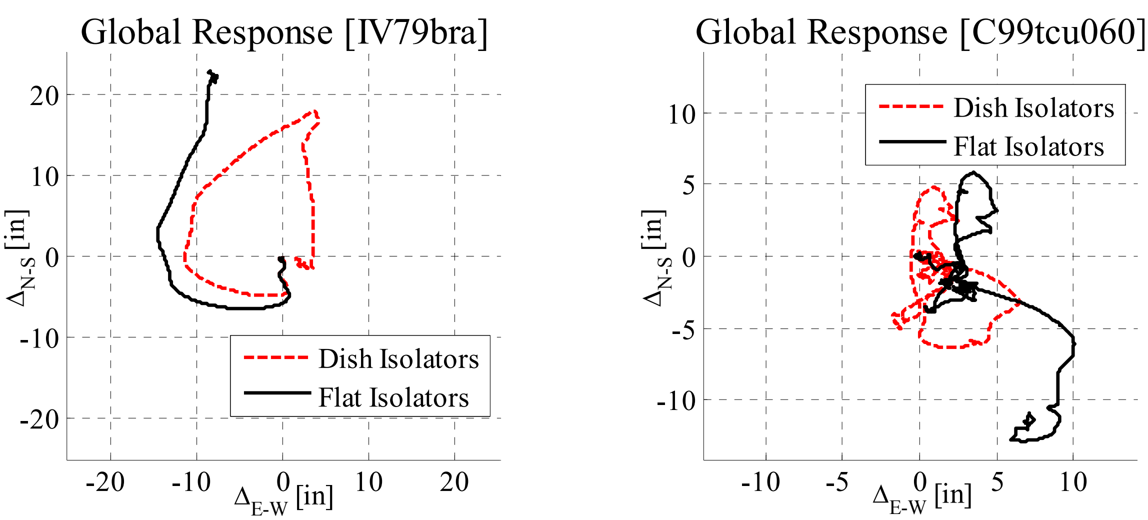

Figure 16.19 **Flat- versus dish-sliding isolators; difference in peak and residual displacement.**

For these studies, the dish-sliding isolators were modeled in OpenSees using the *singleFPBearing* element, with a radius of curvature parameter of 80 in. The results are as follows:

1. Fourteen out of the 80 ground motions failed to converge in OpenSees for the dish-sliding isolators once the magnitude of displacement reached around 32 in. or an elevation up the side of the dish of around 6.4 in.
2. The pressure dependent friction model for the dish isolator yielded additional $\Delta_{torsional}$ with a mean of 0.95 in. and a median of 0.61 in. compared to the non-pressure dependent model (these values exclude the 14 ground motions that yield diaphragm displacements above 32 in.).
3. Directly compared to the flat-sliding isolator model excluding the same 14 high displacement ground motions, the pressure dependent friction model yielded a mean of 3.13 in. and a median of 1.38 in. of additional torsion-induced displacement than did the dish isolators, indicating that dish-sliding isolators have a lower sensitivity to torsion-induced sliding displacement than do the flat-sliding isolators.
4. Comparing the Δ_{max} of the pressure dependent models for both the flat- and dish-sliding isolators, the mean and median Δ_{max} for the flat-sliding isolation were 21.73 in. and 15.16 in. respectively, while the mean and median Δ_{max} for the dish-sliding isolator was 12.94 in. and 11.39 in. respectively. This comes out to a mean and median difference of Δ_{max} between the two models of 8.89 in. and 2.97 in. respectively, a significant reduction.
5. The same can be said for comparing the two velocity dependent models with the mean and median difference of Δ_{max} of 6.71 in. and 1.73 in., respectively (the flat-sliding isolation yielded higher Δ_{max}).
6. The dish-sliding isolators consistently produced near-zero residual displacements compared to higher residual displacements produced by the flat-sliding isolators due to the lack of a restoring force.
7. The mean of $\Delta_{residual}$ of the pressure dependent models is 14.10 in. higher for the flat-sliding isolators then for the dish-sliding isolators.

The dish-sliding isolators are less sensitive to torsion-induced sliding displacement compared to the flat isolators, yield significantly less peak displacement (Δ_{max}), and yield less than an inch on average of residual displacement ($\Delta_{residual}$). Figure 16.20 illustrates the difference in peak displacement between the pressure and non-pressure dependent models for both the flat- and the dish-sliding isolation systems.

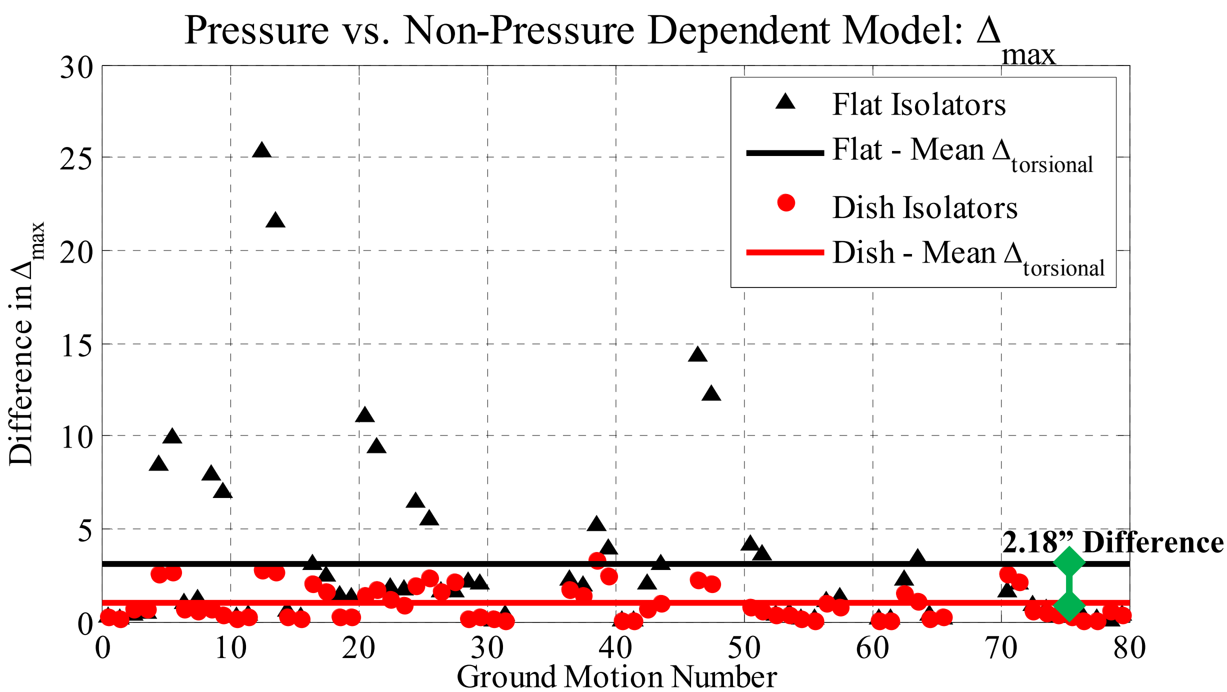

Figure 16.20 **Flat- versus dish-sliding isolators; comparison of additional torsional displacement.**

16.7 CONCLUSIONS

Identifying all possible sources of sliding displacement is necessary when designing an affordable sliding base isolation system for large-scale implementation. Beyond the basic principle that a higher coefficient of friction at the sliding interfaces translates to lower displacement, additional sources of displacement have to be examined in order to avoid the scenario where a house slides beyond the intended boundaries of the isolator sliding surface. This paper investigated the effects of torsion that adds a rotational component to sliding displacement, thereby increasing the magnitude of displacement a house would experience. Narrowing down the causes of torsion and testing the extent of additional induced torsional displacement is necessary in order to design an effective sliding base isolation system for light-frame construction.

Two primary sources of torsion were analyzed in this project. The first was the OpenSees torsional stiffness parameter, *J*. Due to a lack of literature or resources revealing the appropriate parameter value that should be assigned to the *flatSliderBearing* element model in OpenSees, a study was performed to investigate its influence on sliding displacement. The results showed that the parameter had a significant impact on how much torsion was recorded. By physical speculation, it was decided that low torsional stiffness is appropriate for the sliding interface and should be used for analyses. The second suspected source of torsion was the pressure dependence of the material used, namely, the polymer used to slide on top of a steel plate at each isolator unit. It was hypothesized that the pressure dependence of the material would create a separation between the center of mass and center of stiffness of the structure due to an unbalanced distribution of friction coefficients across the isolators, thereby leading to torsion. However, even when the center of stiffness to center of mass distance was exaggerated, the resulting increase in torsional displacement was minimal. Therefore, it was concluded that the pressure dependent friction of the material's effect on separating the center of stiffness and center of mass was not responsible for the amount of torsion observed when comparing the two OpenSees friction models: the torsional stiffness parameter, *J*, in OpenSees and the frequency content of the ground motion are responsible for additional induced sliding displacement. The impact of induced torsional displacement on dish isolator units was also investigated. Dish isolators consistently reduce peak, residual, and torsional displacements.

The analyses performed in OpenSees demonstrated that torsion contributed an additional 1 to 2 in. in sliding displacement on average for 10–20 in. in diaphragm displacement cases. The mechanism that causes that extent of torsion is still unknown, and more studies are required to understand what induced the torsion in the OpenSees model. The additional 1–2 in. contribution to sliding displacement from torsion does not compare to the amount of inches of steel plate saved by using a higher friction material (μ = 0.20 versus μ = 0.10 currently used in industry) [Jampole et al. 2013]. For a flat-sliding system, the median sliding displacement for a system with a coefficient of friction of 0.10 is 21 in., whereas the median sliding displacement for a system with a coefficient of friction of 0.20 is 10 in. This two-fold reduction in sliding displacement is far more significant than removing the 1–2 in. contribution of torsion, since that amount of displacement savings effectively reduces both the steel plate size and system cost four-fold. Therefore, although torsion may contribute an additional 10–20% of sliding displacement, the reduction in peak sliding displacement by using higher coefficient, though pressure-dependent, materials is not outweighed by that additional increase in sliding displacement due to torsional response.

16.8 ACKNOWLEDGMENTS

I would like to first thank Professors Gregory Deierlein and Eduardo Miranda, my faculty advisors, for giving me this opportunity, supervising this project and providing me with helpful insight throughout. I would also like to thank my graduate mentor, Ezra Jampole, for his full attention and guidance through the entire learning process and development of this project. Also, many thanks to PEER and Heidi Tremayne for organizing the internship program, for exposing all the interns to such great research projects, and for assisting me with all my questions throughout. Finally, I thank all my fellow interns for sharing with me all the work they have done in their respective research projects and for all the support they have given me as well. This project would not have been possible without the generous funding of the National Science Foundation through a grant made through the Network for Earthquake Engineering Simulation (award NEESR-1135029).

16.9 REFERENCES

Baker J.W., Shahi S., Jayaram, N. (2011). New ground motion selection procedures and selected motions for the PEER Transportation Research Program, *PEER Report 2011/03*, Pacific Earthquake Engineering Research Center, University of California, Berkeley, CA.

Constantinou M.C., Caccese J., Harris H.G. (1987). Frictional characteristics of Teflon–steel interfaces under dynamic conditions, *Earthq. Eng. Struct. Dyn.*,15 (6): 751–759.

Constantinou, M. (1992). Sliding isolation systems for bridges: Experimental study. *Earthquake Spectra 8.3*, 321-344.

Constantinou M.C., Mohka, A., Reinhorn A.M. (1990). Teflon bearings in base isolation II: Modeling. *J. Struct. Eng*, 116(2): 455–474.

Devine M. (2012). *Costs and Benefits of Seismic/Base Isolation*, Robinson Seismic Limited, Presentation to Canterbury Earthquake Royal Commission, Wellington, New Zealand.

Dolce M., Cardone D., Croatto F. (2005). Frictional behavior of steel-PTFE interfaces for seismic isolation, *Bull. Earthq. Eng.*, 3(1): 75–99.

Jampole E.A., Miranda E., Deierlein G.G. (2012). Friction characterization tests for viscoelastic plastics under varying pressures and velocities, unpublished raw data, Department of Civil and Environmental Engineering, Stanford University, Stanford, CA.

Jampole E.A., Swensen S., Fell B., Miranda E., Deierlein G.G. (2013). Parametric study of seismic isolation parameters: friction, restoring, and damping, unpublished raw data, Department of Civil and Environmental Engineering, Stanford University, Stanford, CA.

Jangid R.S. (2000). Optimum frictional elements in sliding isolation systems, *Computers & Structures*, 76(5): 651–661.

Kircher C.A., Reitherman R.K., Whitman R.V., Arnold C. (1997). Estimation of earthquake losses to buildings, *Earthq. Spectra*, 13(4): 703–720.

Ludema K.C., Tabor D. (1966). The friction and visco-elastic properties of polymeric solids, *Wear*, 9(5): 329–348.

McKenna F., Fenves G.L., Scott M.H., Jeremic B. (2000). Open System for Earthquake Engineering Simulation (OpenSees), Pacific Earthquake Engineering Research Center, University of California, Berkeley, CA.

Mohka A., Constantinou, M.C., Reinhorn A.M/ (1990). Teflon bearings in base isolation I: Testing, *J. Struct. Eng.,* 116(2): 438–454.

Symans M.D., Cofer W.F., Fridley K.J. (2002). Base isolation and supplemental damping systems for seismic protection of wood structures: Literature review, *Earthq. Spectra*, 18(3): 549–572.

Takahashi Y., Iemura H., Yanagawa S., Hibi M. (2004). Shaking table test for frictional isolated bridges and tribological numerical model of frictional isolator, *Proceedings, 13th World Conference on Earthquake Engineering,* Paper No. 1531, Vancouver, Canada.

Tsopelas P. (1996). Experimental study of bridge seismic sliding isolation systems, *Eng. Struct.,* 18(4): 301–310.

Zayas V.A., Low S.S., Bozzo L.M., Mahin S.A. (1989). Feasibility and performance studies on improving the earthquake resistance of new and existing buildings using the friction pendulum system, *UCB/EERC-89-09*, Earthquake Engineering Research Center, University of California, Berkeley, CA.

17. Sliding Base Isolation for Light-Frame Residential Housing

Katherine deLaveaga

ABSTRACT

Tests were conducted to determine the friction-model characteristics of several viscoelastic plastics on different type of steel for use as a sliding isolation system for light-frame structures. The plastics tested include glass-filled and unfilled PTFE, HDPE, and Kevlar filled nylon. The steel surfaces tested include mirror finish stainless steel and zinc galvanized steel. Cyclic tests developed a friction-velocity relationship for the material, which was used to develop a model for predicting dynamic sliding behavior to a system subjected to ground motions. Those predictions were then compared to experiments. Based on the data and results presented, a sliding isolator interface consisting of HDPE or glass-filled PTFE sliding on a galvanized steel surface is recommended. The influence of model variability was also assessed. Finally, the effect of restoring stiffness on sliding behavior was tested.

17.1 INTRODUCTION

Historically, the performance goals for earthquake engineered structures have been life safety and collapse prevention. A design was deemed successful if it emerged from an earthquake with no or minimal physical injury or loss of human life. The post-earthquake damage from the 1994 Northridge earthquake in Los Angeles, California, began to change this standard. Losses totaled around \$44 billion, and damages to light-frame houses comprised \$25.7 billion of that cost, resulting in the temporary or permanent displacement of over 80,000 people [Todd et al. 1994].

Increasing the capacity of a structure does not consistently lead to a reduction in structural damage; therefore, an alternative approach is to decouple the structure from its foundations. This approach is called “base isolation” (or seismic isolation). Separating the building from its foundation allows the building to move independently, thereby “isolating” it from the structurally damaging effects of ground motions that cause deformations in the superstructure. Currently, the main applications of base and story isolation in structures has been limited to large civil projects such as bridges, raised roadways, and hospitals; these applications are expensive and difficult to construct. A single isolator may cost upwards of five thousand dollars. This kind of investment is not feasible to implement for the majority of light-frame residential buildings. Researchers at Stanford University and California State University Sacramento seek to minimize potential damages to housing by combining two affordable and easily constructible isolation strategies:

- Combine structural with the non-structural components to form rigid wall diaphragms, termed the *unibody* concept
- Reduce the peak base shear in the structure by developing a seismic isolation system

17.1.1 Motivation of Research

Several researchers, including Taylor and Aiken [2012], have argued that factors such as high up-front costs, complicated isolator design procedures, and cultural belief in the protection of the building codes retard the use of seismic isolation in the U.S. This report presents research conducted to develop a low-cost sliding isolation system suitable for residential construction using exclusively off-the-shelf parts. Research was conducted by Stanford University at the nees@berkeley Laboratory in Richmond, California.

The frictional coefficient of an isolator is influenced by ambient temperature, confining pressure, sliding velocity, and surface roughness, as well as many other factors. These factors will determine the size and shape of the material sliding surface. Sliding isolation was chosen over other forms of isolation such as pendulum or rubber bearings because sliding systems are (a) designed for easy installation, (b) do not require a large mass to be effective, and (c) are more affordable and materially accessible for average homeowners.

This research seeks to encourage the use of seismic isolation in residential areas by reducing the up-front costs of isolators. This can be done by reducing the required size of the sliding surfaces in the interface, thus reducing installation and material costs for the homeowner. The effects of higher friction on structural displacements are examined to assess the implication on the primary isolation design parameters: peak and residual sliding displacement. Figure 17.1 illustrates the effect of friction on sliding displacement by showing the peak, residual, and minimum displacements of several time histories on a sliding isolation system for friction values between 0.04 and 0.25. It is apparent from this figure that as the friction increases, the overall displacements begin to decrease. An increase in coefficient of friction can come from lower pressures that are present in light-frame structures or from different isolation materials than are traditionally used. A high-friction level is desired for a light-frame isolator for several reasons:

1. Higher friction typically means smaller displacements, which enables a reduction in the size of the necessary foundations, thus saving time and construction costs.
2. If the wind coefficient in windy regions exceeds the breakaway friction, an additional breakaway device will be required to prevent ambient motion.
3. Higher friction is easier to achieve with the comparatively low pressures seen in light-frame housing. This places less stress on the connections to the structural diaphragm.

Therefore, it is more cost efficient to design for higher friction levels in the material interfaces of a sliding isolation system for light-frame houses.

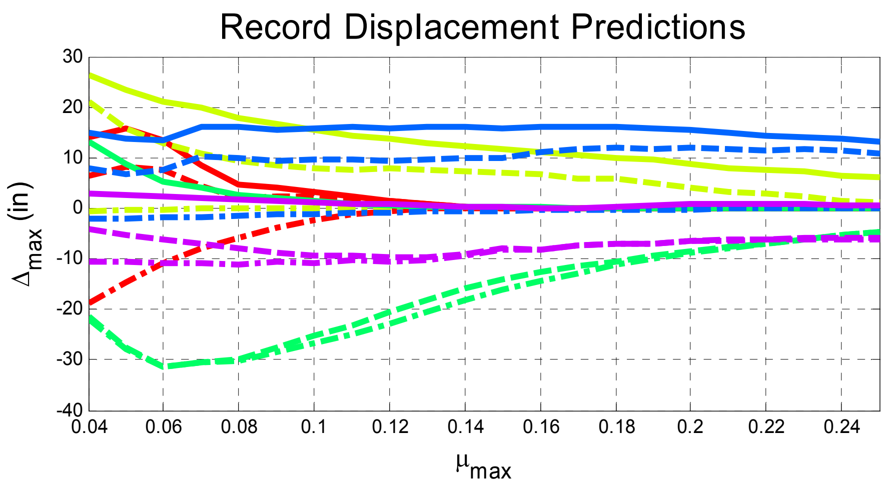

Figure 17.1 **Sensitivity of peak, residual, and minimum displacements by varying friction levels. Five records are shown in varying colors. Solid lines indicate the peak sliding displacement for the record, the dot-dashed line indicates the peak negative sliding displacement, and the dashed line indicates the residual displacement after sliding ceases.**

17.2 RESEARCH METHODS

Developing a sliding isolation system requires several steps, the first two of which are completed to date and are covered in this report:

1. *Structural Analysis*: Determine ideal friction coefficient, restoring force, and supplemental damping properties using parametric studies of system response [Jampole et al. 2013].
2. *Material and design testing*: Test potential sliders and sliding surface materials to achieve target friction properties, and evaluate potential restoring forces.
3. *Implementation:* Design a means to implement the sliding isolation system into residential construction in a cost effective manner.

17.3 MATERIAL TESTING PROCEDURE

Based on preliminary component tests conducted at Stanford University [Jampole et al. 2013], material interfaces were chosen to be tested as potential sliders and sliding surfaces in the isolator design to try to achieve a coefficient of friction = 0.2. The tested interfaces included:

- Kevlar filled nylon on zinc-galvanized steel
- Unfilled PTFE on zinc-galvanized steel

- Glass-filled PTFE by ConServ on zinc-galvanized steel
- HDPE on zinc-galvanized steel
- Glass-filled PTFE by ConServ on mirror finish stainless steel
- Unfilled PTFE on mirror finish stainless steel

Testing of the materials was conducted in two laboratories: small-scale tests were conducted at Stanford University; and high velocity cyclical testing and dynamic testing on a hybrid simulation platform (HSP) was conducted at the nees@berkeley laboratory in Richmond, California. The following describes the test set-up for the nees@berkeley tests.

Four plastic slider units (4.5 in.^{2} each) were attached to load cells on a guided sleigh resting on steel sliding surfaces. Concrete masses (2 at 4 kips each) were added to create a nominal pressure of 570 psi across all isolator supports. Past studies have indicated that friction for viscoelastic plastics is pressure dependent, with the coefficient of friction increasing with decreasing pressure. This low pressure was chosen to achieve the high desired friction levels needed in light-frame isolation, as has previously been seen by other researchers [Constantinou 1987; Jampole et al. 2012]. Zinc-galvanized steel was chosen as an alternative material interface to mirror finish stainless steel as it is less expensive. Figure 17.2 illustrates the testing set-up on the hybrid simulation platform in the nees@berkeley Laboratory.

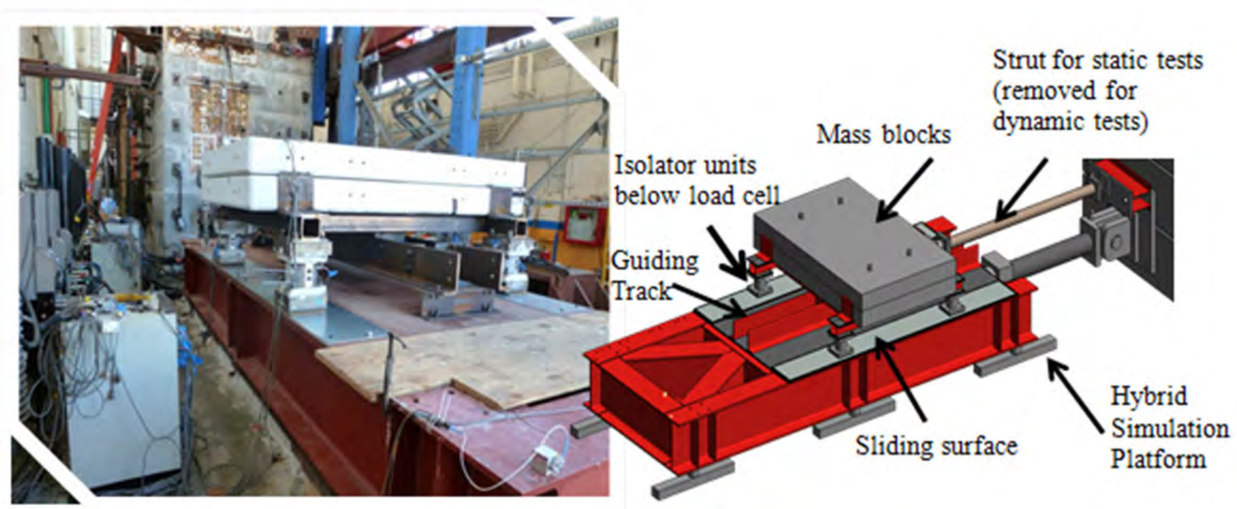

Figure 17.2 Test set-up on hybrid simulation platform (red table). Four plastic slider units were placed on a steel sliding surface under each load cell (left). A Revit model of the test set-up shown to the right. The guiding track is used to limit any out of plane displacements. The strut is removed after cyclical testing for dynamic testing.

Each material interface was tested in two types of motion; cyclical testing at varying velocities of quasi-static, 1, 2, 4, 8, 12, and 16 in./sec at +/- 12 in. displacements, followed by five full-scale ground motions chosen to cause large sliding displacements in the analytical model with 20% friction and high and similar peak ground velocities. Accelerometers and string displacement transducers tracked the acceleration and relative displacement of the sleigh on the platform. All records were un-scaled so as to most accurately reflect recorded time histories. The records selected and their properties are listed in Table 17.1.

After the flat-sliding tests were completed, the steel sliding surfaces were replaced with a galvanized steel dish with a radius of curvature of 80 in. The same process of cyclical and dynamic testing described previously was conducted for two interface combinations: HDPE and glass-filled PTFE on the galvanized steel dish, chosen after all the flat slider tests had been completed.

Table 17.1 Dynamic time histories run on each material interface.

Record	PGA	PGV	Anticipated Peak Displacement	Anticipated Residual Displacement
Chi Chi, Taiwan 1999 TCU 102 (NGA 1529)	0.169*g*	30 in./sec	0.3 in.	0.2 in.
Northridge, CA 1994 Newhall Fire Station (NGA 1044)	0.59*g*	38 in./sec	8 in.	4.5 in.
Northridge, CA 1994 West Pico Canyon Road (NGA 1045)	0.455*g*	36 in./sec	12.5 in.	11.5 in.
Kobe, Japan 1995 KJMA FN (NGA 1106)	0.821*g*	32 in./sec	13.5 in.	9.5 in.
Kobe, Japan 1995 KJMA FP (NGA 1106)	0.599*g*	29 in./sec	8 in.	8 in.

17.4 RESULTS AND FINDINGS

17.4.1 Initial Predictive Modeling Considering Properties of Viscoelastic Materials

Past research on the properties of viscoelastic material interfaces is worth reviewing to determine anticipated friction coefficients for predictive analytical models. Extensive research has been put into the interfacial properties of steel and a commercially available form of polytetraflouroethelyne (PTFE), commercially known as Teflon. This has been historically reported to have the desired frictional range for heavy construction isolation. Table 17.2 relays some common building code standards for sliding Teflon bearings taken from a study done by Mokha et al. [1990]. The AASHTO code [1999] calls for a friction range between 0.04 and 0.12; however, California standards allow for a friction based off of empirical evidence. This research has taken advantage of this empirical evidence as higher friction levels are desired for light-frame housing than the AASHTO code provides.

Table 17.2 Specifications for sliding teflon bearings. [Mokha et al. 1990].

Specification	Type of Teflon	Type of Stainless Steel	Max Bearing Pressure [psi]	Max Coeff of Friction
AASHTO	Unfilled, filled, woven	ASTM A240 type 304	2000-3000	0.04-0.12
CA Standard Special Provision	Unfilled	ASTM A240 type 304	Not Specified	Based on experiment

Friction between viscoelastic plastics and metals is typically dependent on the relative velocity between the two materials. Studies conducted by Constantinou et al. [1987], Mokha et al. [1988], and Bozzo and Barbat [1995] all suggest that the lowest value of friction is obtained at quasi-static motions, and peak levels are obtained at high sliding velocites.

Open System for Earthquake Engineering Simulation (OpenSees), a dynamic structural modeling program [McKenna et al. 2000], was used to construct an analysis model to predict the sliding displacement history of the sleigh subjected to each ground motion. The model numerically determines the displacement history of a structure given an acceleration series, friction model, weight, and restoring force. Without supplemental damping or restoring forces, the peak base shear the house experiences is equal to coefficient of sliding friction, so the base shear controlled. Particular interest is placed on determining peak displacements, with secondary importance placed on residual displacements, as these determine the necessary size of the sliding surfaces in the foundations. The friction-velocity curve is defined by Equation (17.1):

$$\mu = \mu_{\max} - \left(\mu_{\max} - \mu_{\min}\right)^{-va} \tag{17.1}$$

where v is velocity (in./sec), $\mu_{\max}$ is the maximum friction, $\mu_{\min}$ in the minimum friction, and a is the transition rate between the minimum and maximum friction. These parameters must be determined though cyclic testing of each material interface.

17.4.2 Cyclical Testing Results

Cyclic tests were run with four full cycles of +/- 12 in. Total load cell shear was measured and divided by the total weight of the sleigh and block to develop the hysteresis for sliding behavior; see sample hysteresis loop in Figure 17.3. Tests are repeated for each peak velocity. The coefficient off friction for each velocity is then extracted from each hysteresis loop. There are two methods of extracting this information. The first uses the measured friction values at the point of zero displacement during each cyclical trial. Due to the nature of sinusoidal excitations, they reach the peak velocity at exactly the point of zero displacement. Thus values reported at this location should most accurately reflect the coefficient of friction for that velocity test. The second—and empirically less accurate—model uses the peak coefficient of friction of each test, which does not necessarily occur at the moment of peak velocity (or zero displacement) during each test due to data acquisition noise.

The sample friction curve in Figure 17.3 shows a typical response for all tested materials where the peak friction coefficient and the friction coefficient of each interface are measured at zero displacement and are within 1–2% of each other at all velocities. Sliding displacement history predictions should thus be similar when using either model. Studies using each model are reported in a later section of this report, so as to make an assessment of which method of determining coefficient of friction values during cyclical tests most accurately characterizes the velocity-dependent friction model of the material. Velocity-dependent friction curves for each material interface are compared in Figure 17.4, demonstrating that glass-filled PTFE on galvanized steel and unfilled PTFE on mirror-finish stainless steel reported the highest levels of friction.

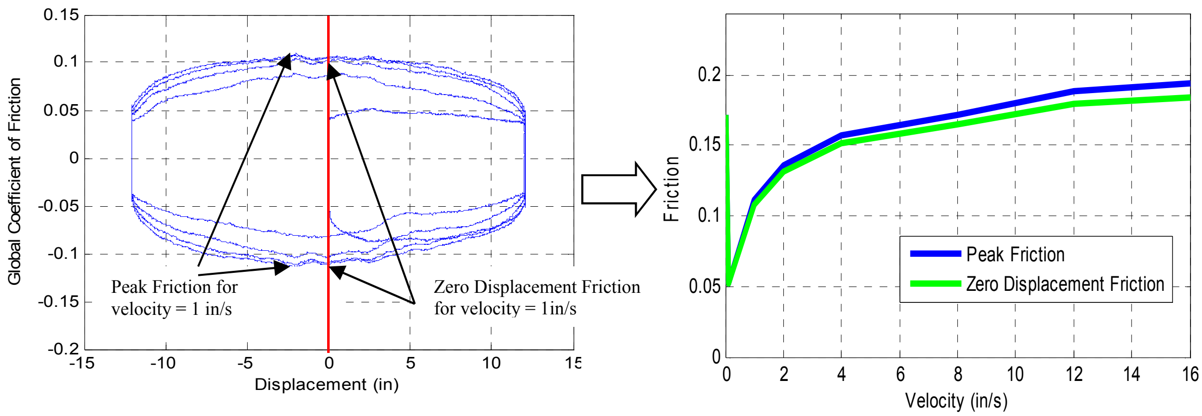

Figure 17.3 **A sample hysteresis loop of friction versus displacement for a cyclical test of unfilled PTFE on galvanized steel at 1 in/sec is pictured to the left. Each test consists of several of these tests at velocities varying from quasi-static to 16 in./sec. The peak and zero-displacement friction is extracted from each of these and used to create the velocity dependent friction curve pictured to the right.**

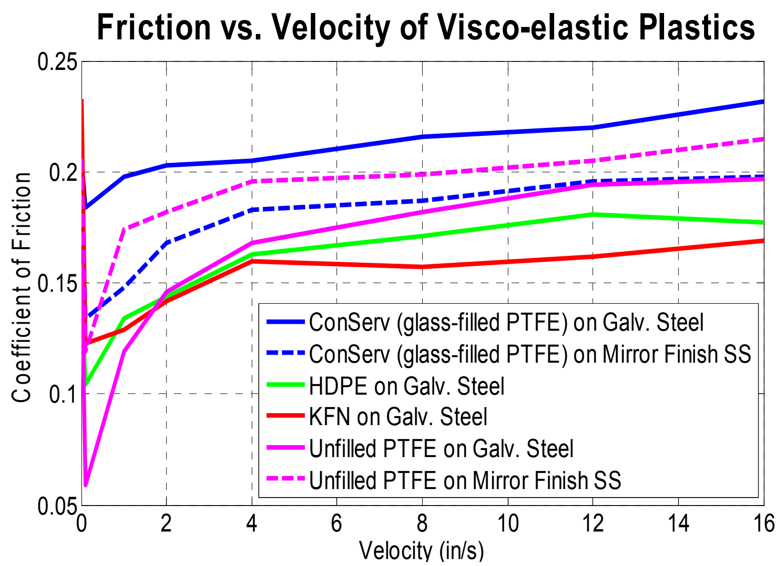

Figure 17.4 Comparison of velocity dependent friction curves for all materials. All curves are taken at zero displacement. Breakaway friction is noted for all curves, and definite velocity dependence is noted for all curves until around 6 in./sec.

17.4.3 Dynamic Testing Results

This section compares the measured displacement history of the sleigh to the analytical prediction of sliding displacement computed via OpenSees using velocity-dependent friction models calibrated using data from cyclical tests on the same slider units. For the sake of brevity, only one material interface, unfilled PTFE on galvanized steel, will be analyzed in detail for this report. Most frictional results of these interfaces are similar to those found in the case of unfilled PTFE. Any variances in successive interface tests will be noted.

Acceleration and displacement of the sleigh was recorded during each of the trials, as well as information on the shear and axial load in individual sliders. Peak and residual displacements were of particular interest because these are the two most important parameters in designing a sliding surface for use in a residence. Figure 17.5 shows the measured sliding displacement history of the record compared to the analytical prediction of sliding displacement history using the friction properties determined during cyclical testing for one of the dynamic time histories run.

It is apparent that the analytical model predicted the measured displacement very accurately. This was typical of all the records and the interfaces runs. The following summarizes the performance of the analytical model over all interfaces given friction parameters developed in the cyclical testing:

- < 10% error in peak displacements
- < 15% error in residual displacement predictions
- Analysis usually slightly underestimates displacements

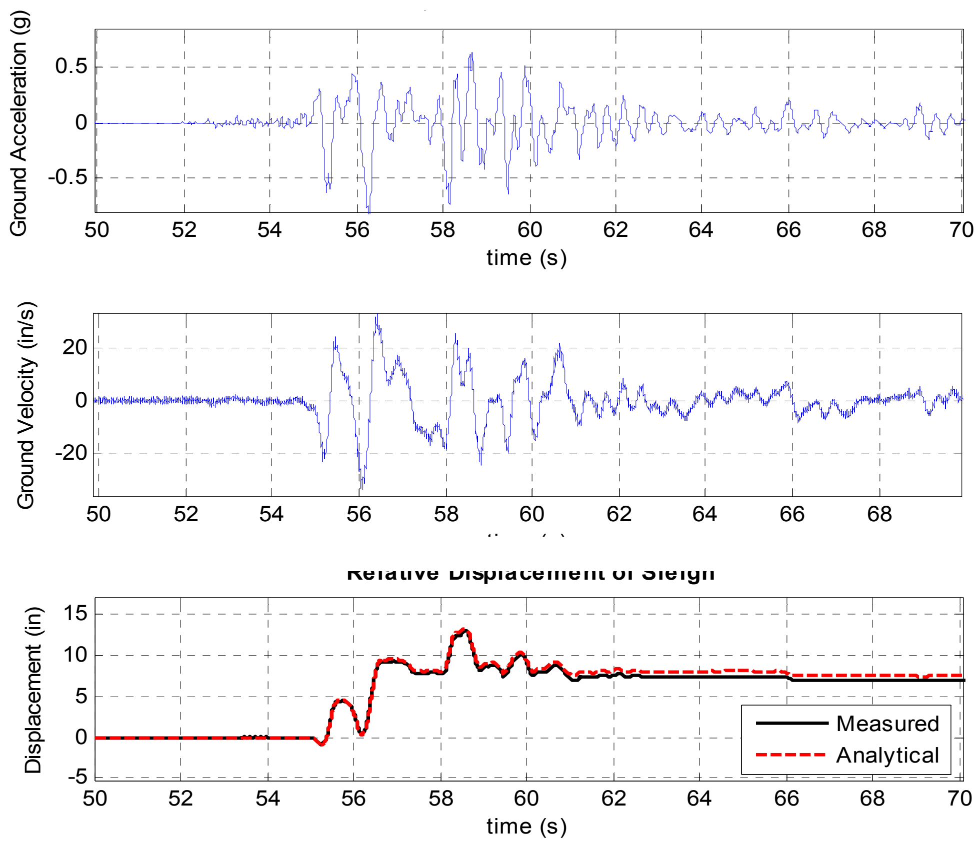

Figure 17.5 **Displacement history for KJM-000 compared to the ground acceleration and ground velocity.**

17.4.4 Friction Optimization to Create Idealized Friction Curves

To determine the apparent dynamic friction characteristics of the various material interfaces during the time histories, optimization codes were run to develop the following parameters that describe the velocity-dependent friction model:

- Maximum friction (μ_{max})
- Minimum friction (μ_{min})
- Transition rate (a)

Mean square errors of the analysis versus measured sliding predictions are minimized for the following response parameters:

- Peak sliding displacement
- Total record sliding displacement history

Optimizing the velocity-dependent friction parameters to minimize the total recorded sliding displacement history is biased towards matching the residual displacement due to the long period at the end of the most records when the earthquake is ongoing but at low amplitudes, so sliding has ceased. Optimization of parameters for each interface is done to minimize error for individual records and repeated to minimize the total error across all record.

In theory, the friction properties of the interface should not change from one time history to another, especially when considering that ample time is given between ground motion runs for the surface to cool if it had heated. The sleigh does not begin each run in the same location, thus there may be small differences in coefficient of friction from one time history to potential polishing of previously slid-over locations, but these are not expected to be significant since cyclical testing should have equally warmed all surfaces where sliding occurs. Optimizing the friction properties for each individual ground motion will no doubt yield very accurate results for determining the friction properties within an individual test; however, in order to assess the friction properties in a more general sense, the parameters μ_{max}, μ_{min}, and the transition rate are optimized to best match simultaneously all five of the time histories. Properties are again determined by separately optimizing based on peak, residual, and total record sliding displacement history. This section reports the analysis results and optimized parameters based on peak, residual, and total record sliding displacement history matching.

Table 17.3 summarizes data collected from post processing of the Kobe, Japan, 1995 KJM-000 record, with unfilled PTFE on galvanized steel, In addition to the measured peak and residual displacements and the velocity-dependent friction model parameters developed from cyclical testing, friction properties and peak and residual displacements are shown using the optimization schemes previously outlined.

The results are typical for most of the records in the following ways:

- Friction taken at zero displacement estimates the measured peak and residual displacements more accurately than friction pulled at peak values in the cyclical tests.
- The multiple ground motion optimization estimates measured displacements better than individual records optimization overall. Therefore, multiple ground motions will be used to create an idealized friction curve for each material.

A velocity-dependent friction model like the one shown in Figure 17.6 was developed for each material interface using Equation (17.1) and the parameters chosen from the optimization of multiple records, as shown in Table 17.3. These models can be effectively used as the friction models, which describe each material interface. Note that breakaway friction is not considered in this model as it is variable dependent on site and time factors. Breakaway friction will not have a significant effect on the overall dynamic response of the system, but could initiate local effects. Breakaway friction must be examined very carefully when designing the isolation to diaphragm connection for a light-frame structure.

Table 17.3 **Analytical optimization of friction parameters and effects on peak and residual displacements for unfilled PTFE on galvanized steel for KJM-000. Analysis considers an optimization of friction model of each ground motion record individually (single ground motion) and all records combined (multiple ground motions).**

Analysis type	Friction	Friction parameters			Displacements (in. or % divergent)	
		μ_{max}	μ_{min}	Trans rate	Peak	Residual
Measured					13.26 in	7.05 in
Analysis Based on Cyclical Data	@ zero displacement	0.189	0.055	0.420	0.15%	15.6%
	@ peak	0.193	0.059	0.440	0.82%	18.0%
Optimized Parameters Single Ground Motion	Peak Match	0.209	0.056	0.453	-4.7%	18.3%
	Entire Record	0.163	0.057	0.485	2.2%	0%
Optimized Parameters Multiple Ground Motions	Peak Match	0.191	0.059	0.451	2.2%	14.5%
	Entire Record	0.192	0.062	0.307	-2.7%	2.3%

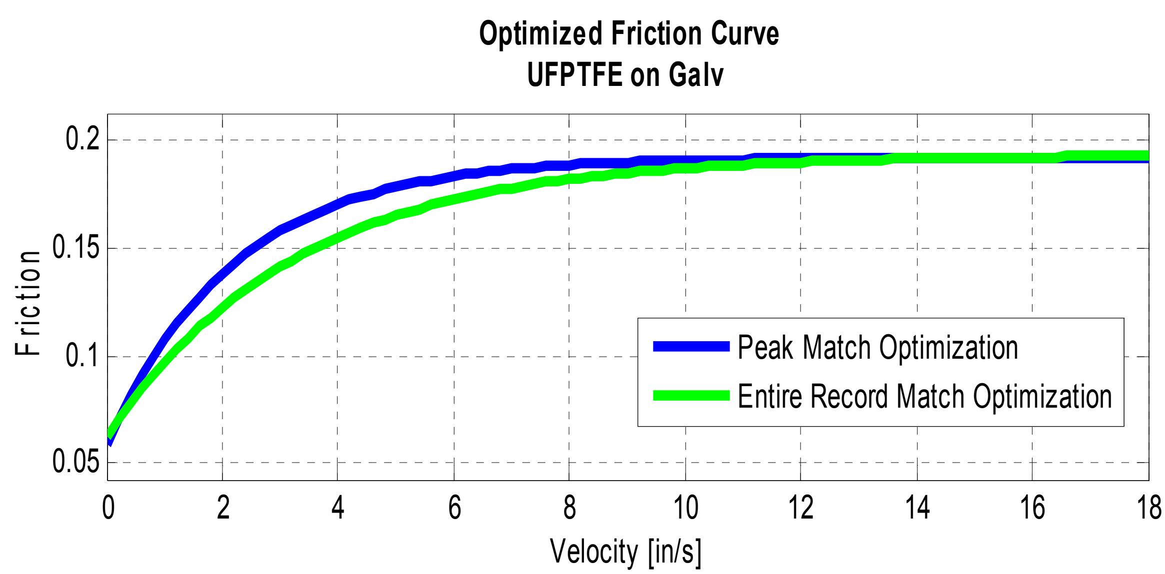

Figure17.6 **Optimized friction curve for unfilled PTFE on galvanized steel based on optimized parameters μ_{max}, μ_{min}, and transition rate *a*.**

Although the harmonic curve predicts friction to be higher than the dynamic tests measured, assuming a higher friction than reality in the isolator design has the potential to benefit the behavior initially. If left still for long periods of time, some viscoelastic polymers (such as unfilled PTFE) have the potential to creep and fill in the grooves of the steel, which causes an initial higher friction level than at the onset of sliding. In these cases, a higher predicted friction level would compensate this higher initial friction due to time-sensitive creep.

17.4.5 Expected Sliding Displacements

During a typical ground motion, it is hard to predict values of peak and residual displacements, regardless of the frictional model. The uncertainty due to friction coefficient of anticipated displacements can be assessed by using a Monte Carlo simulation to determine an adequate range of expected displacements.

A Coulomb frictional model is used to determine the spread of expected peak and residual displacements for computational simplicity. A variable maximum friction value was chosen based on the results obtained from the cyclical testing. The mean peak friction coefficient used in these distributions was 0.20, an idealistic friction level, with a standard deviation of 0.02. Both a normal and lognormal distribution were used for the coefficient of friction. One thousand simulations of each probability distribution give an idea of how uncertainty in coefficient of friction (modeling uncertainty) can impact anticipated peak and residual sliding displacements. The average and standard deviation of the peak and residual displacements are summarized into Table 17.4.

Table 17.4 Summary of the Monte Carlo simulation results for Newhall-360, Newhall-WPC-046, and KJM-000.

Record	No. of Analyses run	Distribution of Friction Parameters	Analytical Peak Displacement (in.)		Analytical Residual Displacement (in.)	
			Mean	Standard Deviation	Mean	Standard Deviation
Northridge, CA 1994 Newhall Fire Station (NGA 1044)	1000	Normal	8.17	1.13	3.71	1.24
		Lognormal	8.13	1.14	3.67	1.26
Northridge, CA 1994 West Pico Canyon Road (NGA 1045)	1000	Normal	9.47	2.46	8.85	1.98
		Lognormal	9.45	2.38	8.87	1.93
Kobe, Japan 1995 KJMA FN (NGA 1106)	1000	Normal	15.56	0.69	11.49	0.46
		Lognormal	15.53	0.76	11.47	0.43

It is apparent that the probability distribution chosen to describe maximum friction has only a minimal effect on the distribution of peak and residual displacements. The largest uncertainty of peak and residual displacement appears in Newhall-WPC-046, where the record induces a large sliding excursion due to one strong pulse. With these given ground motions, it is possible to predict residual displacements to within 3 in. for peak displacements and 2 in. for residual displacements, even in the presence of friction coefficient uncertainty. If small ground motions are expected, this interval can be reduced even further.

The next section determines how these expected displacements behave to determine if the peak and residual values have a normal distribution. Figure 17.7 compares the peak and residual displacements of the Monte Carlo simulation to a normal distribution to various records with normal distributions of friction parameters. An R^2 value close to 1 indicates a normal distribution. The pink dots in Figure 17.7 are the simulation using the standard friction value of 0.20 found in the materials testing. It is best to look at each record individually to determine normality of displacements. Newhall-WPC-046 follows a normal distribution to a high degree of accuracy, as indicated by the high R^2 values of 0.97. The only points of deviation arise when the displacements become larger than a standard deviation above the mean. These large displacements can be thought of as extreme events, and the rising tail indicates that these extreme events are becoming more likely. KJM-000, on the other hand, most likely does not have a normal distribution of peak displacement, and tends to a high range of 15.5 to 16.5 in peak and 11 to 12 in residual displacement. This suggests that a normal distribution of friction does not consistently result in a normal distribution of response, with the mean equal to the displacement predicted by the mean friction. Instead, the mean of displacement tends higher than the displacements using mean friction. Hence, it may be best to use a slightly lower coefficient of friction to predict displacement to account for this variability.

Figure 17.7 also gives an idea of the range of possible displacements that contribute to the expected displacements. The typical standard deviation from the mean anticipated peak displacement is 1 to 2.5 in., indicating that a standard deviation greater than 3 to 4 in. would notably influence the mean peak displacement. These types of records will dictate how big of a standard deviation would be needed in order to make a significant difference in the mean anticipated peak displacement. Each record reports slightly lower standard deviations for the mean anticipated residuals than the mean peak displacements, typically 1 to 2 in. A standard deviation of three or more inches would begin to significantly influence the mean residual displacement.

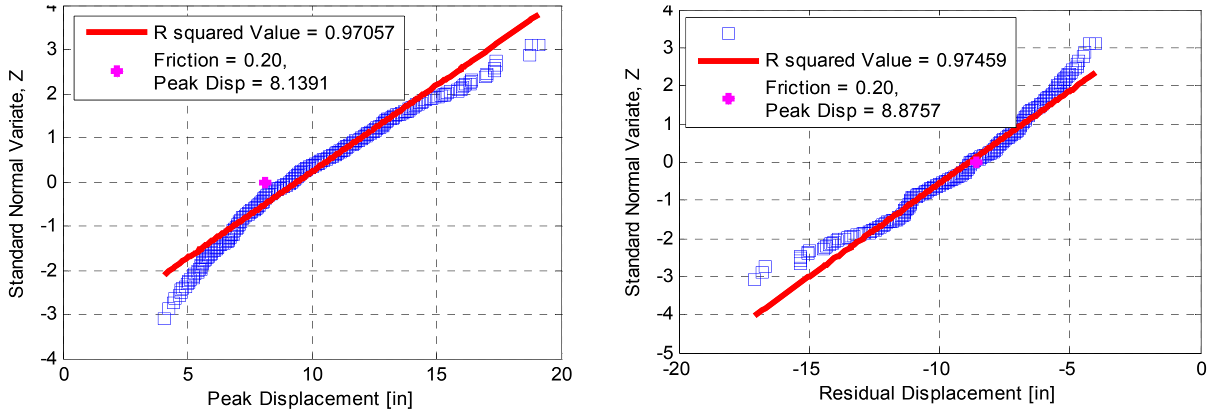

(a) Newhall-WPC-046

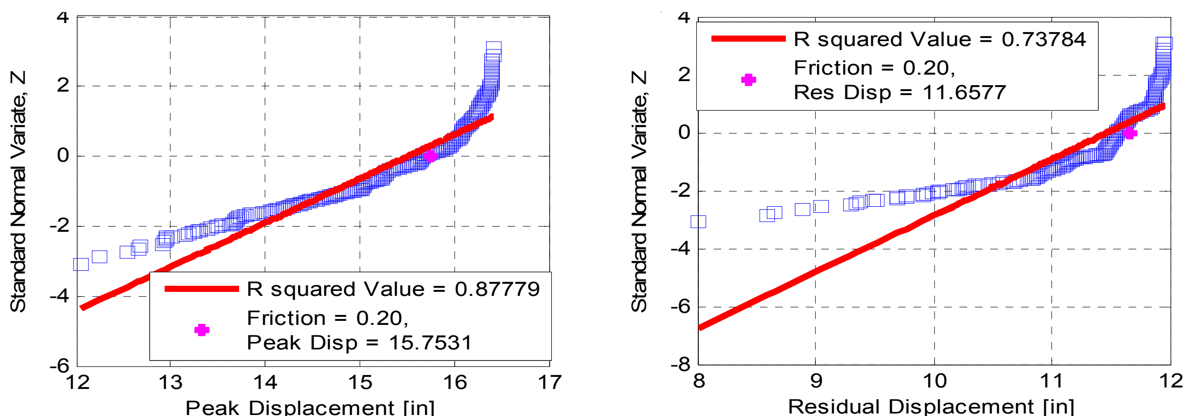

(b) KJM-000

Figure 17.7 Determining normality of peak and residual displacements. The red line indicates a normal distribution of displacements given uncertain friction. The pink dot indicates a typical frictional value of 0.20 pulled from the materials test. Deviation of the test values from the red line indicates a non-normal distribution of displacements. (a) Newhall-WPC-046, which adheres to normal distributions well; and (b) KJM-000, which does not adhere to normal distributions.

17.4.6 Restoring Forces – Dish Testing

An analysis was conducted to establish the factors that would lead to a recommendation for the use of a dish system versus the simpler flat-sliding isolator system. The dish system is recommended in the case where an additional restoring force is desired to reduce peak and residual displacements. There are several pros and cons to the implementation of a dish system.

The advantages of a dish system are as follows:

- Expected to moderately reduce peak sliding displacements that can cause foundational or utilities damages in a residence.

- Resists displacements due to small earthquakes or high wind loads greater than the breakaway friction that could potentially displace the superstructure, which may require re-centering efforts on a flat-sliding isolator.
- A flat-sliding system may need to be re-centered after an event that causes large displacements, which is a difficult and complex process.

The disadvantages of a dish system are as follows:

- A dish system causes greater base shear than a flat-sliding system. In the most extreme dynamic test, KJM-000, the peak normalized base shear in the dish system approached 0.4. This is double that of the coefficient for the flat-sliding system, which is equal to the peak friction, or 0.2.
- A dish systems is more expensive and harder to construct and install than a flat-sliding system.

Two isolator material interfaces were chosen to be examined to compare the behaviors of flat- and dish-sliding isolators: glass-filled PTFE by ConServ on zinc galvanized steel and HDPE on zinc galvanized steel. The restoring stiffness can be calculated using the following equation, [Zayas et al. 1990]:

$$K = w / R \tag{17.2}$$

where K is the effective restoring stiffness of the dish, w is that weight above the dish, and R is the radius of curvature of the dish. Using Equation (17.2), the restoring stiffness of the test rig for the dish with a radius curvature of 80 in. can be calculated to be 0.129 kip/in.

Figure 17.8 shows the peak and residual displacements of both the flat and dish-sliding isolator tests for glass-filled PTFE on galvanized steel. The results seen here are typical of both material interfaces tested on the dish. Both peak and residual displacements are reduced with the addition of a dish. Most often the residual displacements are reduced to greater extents than the peak displacements. It is important to look at the effects of a restoring force on all records. The reduction of the peak and residual displacements for HDPE and glass-filled PTFE on galvanized steel are summarized in Table 17.5.

In general, the dish restoring force tends to have a greater effect on the peak and residual displacements for the HDPE–steel interface than the glass-filled PTFE-steel interface due to the lower coefficient of friction. The largest reduction occurred in Newhall-WPC-046, with a residual displacement reduction of 11.62 in., which almost completely eliminates the residual displacement. The residual displacement of the sleigh was measured to be less than 1 in. for each record with HDPE on galvanized steel and less than 2 in. for each glass-filled PTFE record. These analyses demonstrate that there is around a 30–40% reduction in peak displacement and almost complete elimination of the residual displacements for every record, suggesting that even the minor restoring stiffness provided by a dish system or by any supplemental means, can be very effective in limiting displacements. Note that these results may only apply to the records selected for testing.

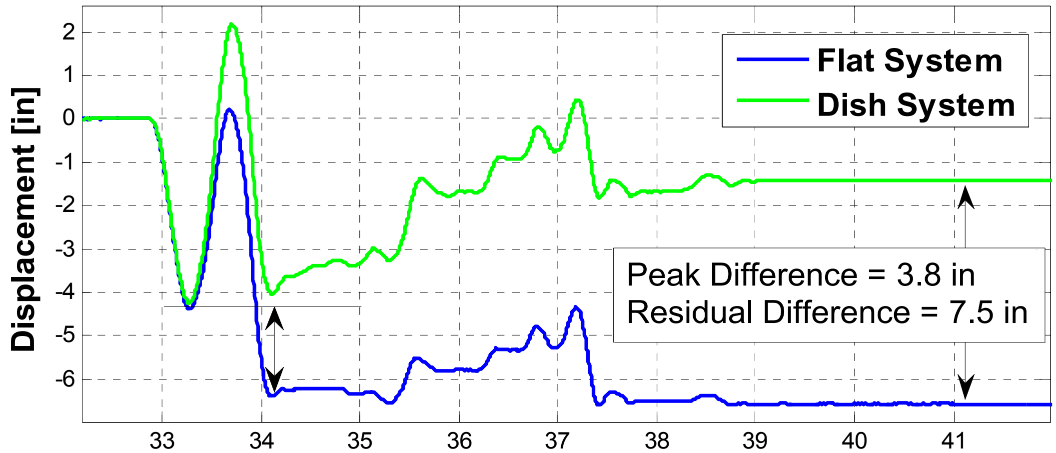

Figure 17.8 **A comparison of the flat- and dish-sliding isolator displacement histories of KJM-090 for glass-filled PTFE on galvanized steel.**

Table 17.5 **Displacement histories of dish- and flat-sliding systems; HDPE (galvanized steel) and GF PTFE (galvanized steel).**

Material Interface	**Record**	**Dish System Displacement (in.)**		**Flat System Displacement (in.)**		**Displacement Reduction by Use of a Dish (%)**	
		Peak	Residual	Peak	Residual	Peak	Residual
HDPE on Galvanized Steel	TCU102-N	0.68	0.54	0.74	0.63	NA	NA
	Newhall-360	6.35	0.79	9.40	3.91	32.4%	79.8%
	Newhall-WPC-046	9.50	0.43	14.37	12.05	33.9%	96.4%
	KJM-000	7.25	0.14	13.30	6.75	45.5%	97.9%
	KJM-090	5.15	0.47	8.48	7.79	39.3%	94.0%
Glass-filled PTFE on Galvanized Steel	TCU102-N	0.01	0.01	0.01	0.00	NA	NA
	Newhall-360	7.23	0.32	7.59	2.86	4.7%	88.8%
	Newhall-WPC-046	6.98	1.95	8.19	7.41	14.8%	73.7%
	KJM-000	8.54	0.75	14.34	9.82	40.4%	92.4%
	KJM-090	4.30	1.43	6.43	6.57	33.1%	78.2%

A dish system provides several advantages and disadvantages when used in an isolation system. The main advantage stems from the reduction of sliding displacements, which results in smaller required sliding plates. Even a few inches of reduction in peak displacement can be equivalent to several square feet of area in saved steel of the circular dish; a 30% reduction of peak displacement in an event like KJM-000 could potentially cut back 2.5 ft^2 of steel per isolator. On the other hand, a dish system is much more complicated and expensive to construct compared to a simple flat-sliding surface as required in a flat system, and can result in larger base shears. Therefore a dish system in a light-frame house is only recommended in the case where no or little residual displacement is required, or a re-centering effort on a flat system is undesirable.

17.4.7 Material Recommendations

There are several factors that must be taken into consideration when choosing an interface. These include friction level, effects of wear and tear, time sensitivity, and cost. With these factors in mind, a recommendation is given for the use of either HDPE or glass-filled PTFE on galvanized steel in an isolator with a nominal pressure around 500–700 psi:

The advantages to using galvanized steel:

- An inexpensive alternative to mirror finish stainless steel and readily available in sheets
- Due to its roughened surface, exhibits highly desired friction when combined with softer slider materials such as glass-filled PTFE or HDPE

The advantages to HDPE:

- Very common and inexpensive material
- Stiff material allows may reduce pressure dependence
- No material rub-off or change in frictional behavior due to large travel

Advantages to glass-filled PTFE:

- Highest friction available when combined with a galvanized steel interface
- Common and commercially available material
- Less material rub-off damage than unfilled PTFE with excessive sliding

17.5 CONCLUSIONS

Inexpensive and common materials like HDPE and galvanized steel can achieve higher coefficients of friction than are traditionally used in sliding isolation, thus reducing deformation demands. This facilitates the necessary reduction in isolation costs for widespread implementation of this damage-reducing technique for light-frame structures. The effects of sliding distance and wear and tear on friction level are also less significant for the low pressures inherent in light-frame construction; therefore, little maintenance is required. Additionally, uncertainty in interface friction model suggests that a designer does not tend to have a significant impact of peak sliding displacement. The promising results of this research show that isolation systems are possible for use in mitigating earthquake-risk in light-frame structures.

17.6 ACKNOWLEDGMENTS

Many thanks to student mentor Ezra Jampole and faculty supervisors Eduardo Miranda and Gregory Deierlein for all their advice and guidance through this research. This research is funded by the National Science Foundation (NSF) through a grant made through the Network for Earthquake Engineering Simulation (award NEESR-1135029). Student funding is thanks to Pacific Earthquake Engineering Research Center (PEER) summer internship program. Advice and guidance from David Mar and Barry Ralphs, (Tipping-Mar) were critical. Heartfelt appreciation goes out to Heidi Tremayne (PEER Outreach Director) for her organization and professional guidance of the internship program, and to Claire Johnson for her wonderful editorial skills.

17.7 REFERENCES

AASHTO (1999). *Guide Specifications for Seismic Isolation Design*, 2nd Edition with 2000 Interim Revisions, American Association of State Highway and Transportation Officials, Washington, DC.

Bozzo L., Barnbat A.H. (1995). Nonlinear response of structures with sliding base isolation, *J. Struct. Control*, 2(2): 59–77.

Constantinou M.C., Caccese J., Harris H.G. (1987). Frictional characteristics of Teflon-steel interfaces under dynamic conditions, *Earthq. Eng. Struct. Dyn*., 15: 751–759.

Constantinou M.C., Papageorgiou A.S. (1990). Stochastic response of practical sliding isolation systems, *Probabilistic Eng. Mech.*, 5(1): 27–34.

Jampole E.A., Miranda E. Deierlein G.G. (2012). Friction characterization tests for viscoleastic properties under varying pressures and velocities, unpublished data, Department of Civil and Environmental Engineering, Stanford University, Stanford, CA.

Jampole E.A., Swensen S., Fell B., Miranda E., Deierlein G.G. (2013). Parametric study of seismic isolation parameters: friction, restoring, and damping, unpublished data, Department of Civil and Environmental Engineering, Stanford University, Stanford, CA.

McKenna F. Fenves G.L., Scott M.H., Jeremic B. (2000). *Open System for Earthquake Engineering Simulation (OpenSees)*, Pacific Earthquake Engineering Research Center, University of California, Berkeley, CA.

Mokha A. Michalakis C., Constantinou M.C., Reinhorn A.M. (1988). Teflon bearings in asismic base isolation: Experimental studies and mathematrical modeling, *Report NCEER-88-0038*, National Center for Earthquake Engineering Research, Buffalo, NY.

Mokha A., Constantinou M.C., Reinhorn A. (1990). Teflon bearings in base isolation I: Testing, *J. Struct. Eng.*, 116(2): 438–454.

Taylor A., Aiken I. (2012). What's happened to seismic isolation of buildings in the US? *Structure*, pp. 10–13.

Todd D.R., Carino N.J., Chung R.M., Lew H.-S., Taylor A.W., Walton, W.D., Cooper J.D., Nimis R. (1994). 1994 Northridge earthquake: Performance of structures, lifelines, and fire protection systems, National Institute of Standards and Technology, *NIST SP 862; ICSSC TR-14*, 186 pgs. Gaithersburg, MD.

Zayas V.A., Low S.S., Mahin S.A. (1990). A simple pendulum technique for achieving seismic isolation, *Earthq. Spectra*, 6(2): 317–333.

18. Evaluation of the Bonding Properties of Various Construction Adhesives to Determine the Best Overall Product for the Light-Frame Unibody System

Rakeeb Khan

ABSTRACT

Current building codes ensure adequate life safety for residential structures, but these structures are vulnerable to costly seismic damage. If an earthquake occurs, most residents would be able to exit their home safely; however, the damage and the residual displacements caused by the earthquake can be devastating for homeowners. With significant damage to residential structures, homes are rendered uninhabitable, thereby causing households to be displaced and increasing the economic losses for the community. With such losses, it is obvious the design of residential structures must be adjusted to improve their seismic resiliency. A new strategy is being investigated whereby adhesive is utilized in combination with mechanical fasteners to make architectural and structural components work together as a unit to resist the lateral forces induced by an earthquake. As a result, the structure becomes stronger, stiffer, and more damage resistant. This paper investigates the properties of various adhesives when used to bond architectural components such as gypsum board to a 2×4 lumber structural element. Furthermore, this research aims to determine the best off-the-shelf adhesive based on its properties, cost, and availability.

18.1 INTRODUCTION

Current seismic building code provisions use response modification coefficients, or *R* factors ($R > 1$), to reduce the required strength of the lateral force resisting system below the elastic force demand in a design-level event thereby allowing for inelastic structural response and an increase in the ductility capacity of the components [ASCE 2010]. Although the exchange of an increased ductility for a reduction in strength may be acceptable for commercial buildings, this exchange may not be appropriate for residential structures. Residential structures must be treated individually because many aspects are different when compared to commercial buildings, e.g., the low mass of residential structures.

Much has been learned from previous earthquakes. For example, in the 1994 Northridge earthquake, 24 out of 25 fatalities caused by building damage occurred in wood-frame buildings, half or more of the $40 billion in property damage was due to damage to wood-frame construction, and 48,000 housing units, almost all of them in wood frame buildings, were rendered uninhabitable by the earthquake [Krawinkler et al. 2000]. Wood-framed structures are one of the common residential homes and may be a homeowner's largest asset. With the loss of homes or expensive seismic-related repairs, communities are faced with the difficulties of being displaced. The 1994 Northridge earthquake showed that wood-frame homes are vulnerable to damage and necessary improvements must be made in order to improve their seismic resilience.

Debris from architectural features contributes to one of the biggest dangers caused by an earthquake. Although architectural features are not considered in design, they can contribute significantly in the lateral resisting system. Recent experimental tests have shown that the influence of stucco and gypsum wallboard increase peak strength and initial stiffness and decrease deformation capacity of shear walls compared to bare wall [Gatto and Uang 2001; Pardoen et al. 2003]. By creating a more damage resistant light-frame structure, economic losses and displaced households are significantly reduced, creating more resilient communities. The new strategy aims to increase the durability of the house by addressing the damages caused by earthquake or wind loads.

The motivation of the overall research is to understand the behavior of a light-frame unibody structure. The research project consisted of four phases. The first phase was conducted at Stanford University, where small scale shear walls were tested. The second phase was conducted at California State University, Sacramento, where full-scale shear walls were tested. The third phase is currently on-going, where full-scale rooms are being tested in the nees@berkeley Laboratory at UC Berkeley, Richmond Field Station. The final phase of the research project will be conducted in San Diego, where a full-scale home will be tested on a shake table.

This research reported herein was motivated by the lack of information on adhesive bonding between architectural and structural components, particularly gypsum and wood studs. There are also many different brands of adhesives and within each brand many different types of adhesives. The research reported herein investigated if there were advantages to using one adhesive over another. The results presented herein can be implemented in modeling and design, allowing the engineer to model and design with appropriate values for the additional strength added if adhesive is included in the design process of a home.

18.2 BACKGROUND

Many common architectural features, such as wall finishes found in residential structures, are susceptible to damage at small deformations and can be costly to replace. Currently for light-frame structures, the force capacity is achieved at large drift levels, exposing the walls to large amounts of inelasticity. This inelasticity causes deformations and non-structural damages that can render a structure uninhabitable. For example, during the 1994 Northridge earthquake, nonstructural damage caused hospitals, schools, businesses, and industrial facilities to be inoperative even though structural damage was minimal or non-existent [Lew 1994]. Even though a structure may not have any structural damage, non-structural damage can cause operational problems, increasing the economic loss of a community. These damages can be costly and devastating for homeowners.

A Holmes and Somers report describes damage to a two-story wood frame single family dwellings (WFSFD) constructed in 1958 and located within 0.8 km (1/2 mile) of a strong-motion seismograph. Damage to this structure was non-structural and the WFSFD was considered suitable for immediate occupancy. Notably, the cost of repairing the damage to the structure was actually so great that it was considered a total loss [Kirkham 2013]. Even though the structure might be suitable for occupancy after the earthquake, the total loss may put a burden on the owner which may lead the owner to surrender the home.

To reduce the seismic damage to light-frame residential structures, the deformation needed to achieve the peak strength must be decreased. Through the use of construction adhesive in combination with mechanical fasteners to connect the sheathing and wood framing, a stiffer "unibody" system is created by a cost-effective method.

By the use of adhesive in combination with mechanical fasteners, the light-frame unibody system integrates the architectural features with the exterior walls of the home. This integration makes the architectural and structural components work together to improve the lateral force resisting system by creating stronger, stiffer walls. By increasing the stiffness of the walls, the deformation needed to achieve the peak strength is significantly decreased.

The effect on the deformation by increasing the stiffness is shown in Equation (18.1):

$$T = 2\pi\sqrt{\frac{m}{k}} \tag{18.1}$$

where T is the period, m is the mass, and k is the stiffness. Since the new strategy of the unibody system increases the stiffness, the period is decreased as a result. The following figure shows the effects of increasing the stiffness. With an increase in stiffness (k), the period (T), is reduced, therefore decreasing the displacement (S_a) as shown in Figure 18.1. With a decrease in displacement and period, the force capacity is achieved at smaller drift levels as shown in Figure 18.2.

The increase in strength and stiffness is provided with the addition of adhesive working in combination with the mechanical fasteners. Adhesives are used to hold substrates together under the desired end use conditions. This means that a bond needs sufficient strength and durability to hold the substrates together under a defined set of conditions [Frihart 2005a]. The key step in using adhesive is the settling of the adhesive. While the adhesive settles, the adhesive solidifies and the bond gains strength over time. The advantage of using mechanical fasteners in combination with adhesive is that the force holding and compressing the drywall together with the wood by screws, allows for the adhesive to set. With this method, the adhesive does not need to set rapidly. It is generally preferred that the adhesive bond be stronger than the substrate so that the failure mechanism is one of substrate fracture [Frihart 2005b]. This being said, it is important to determine if an adhesive is adequate for the design of a light-frame unibody system.

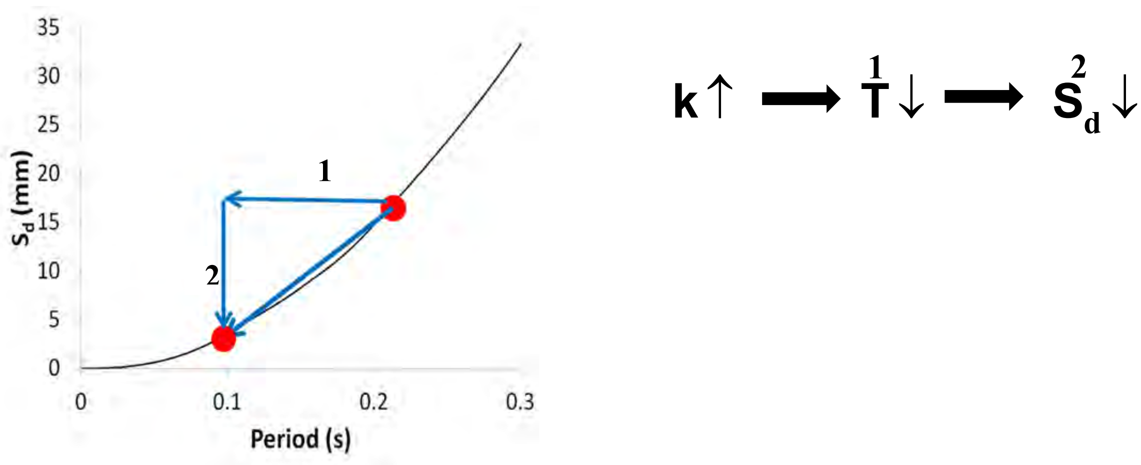

Figure 18.1: Effects on the displacement by increasing the stiffness.

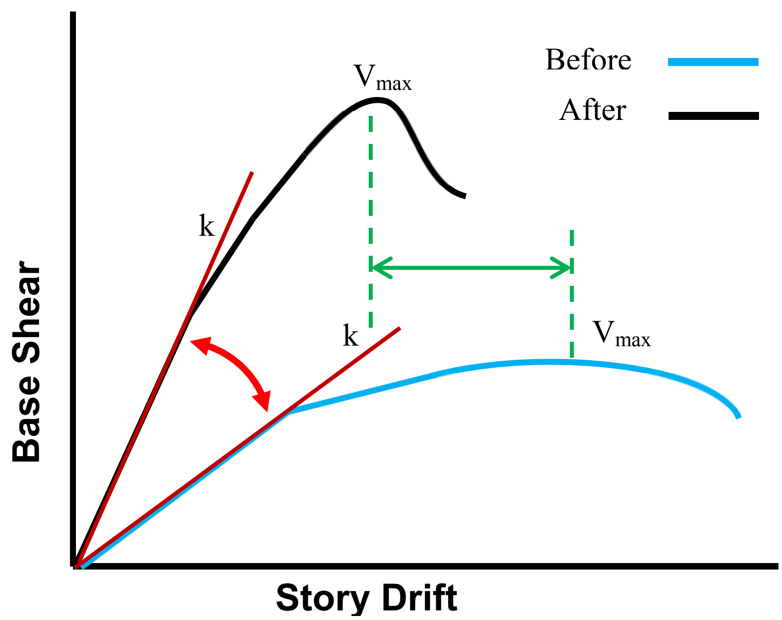

Figure 18.2 Effects on the force capacity by increasing the stiffness.

18.3 OBJECTIVES

The research presented in this paper will investigate the behavior of the adhesive connection between the gypsum and the wood stud. Through experimental and analytical results, the best adhesive will be determined. The evaluation criteria is not only strength-based but also takes into account the combined effects of stiffness, deformability, cost, and availability.

- There are many different brands of adhesives and within each brand many different types. This research addresses any possible advantages of a certain adhesive versus another.
- Six adhesives will be tested with the use of a push through test set-up.
- A model representing the results found from testing will be developed, which can be used in other design calculations or modeling, such as shear walls. The model will consist of the discovered results of strength, stiffness, and deformability.

18.4 ORGANIZATION AND OUTLINE

The research consisted of two test phases. The inconsistency in the results of the first phase resulted in a second phase in hopes of obtaining better results. Section 18.5 will discuss the Phase 1 testing and construction of the specimens, followed by the results for the adhesives, which is discussed in Section 18.6. Phase 2 testing and test set-up will be discussed in Section 18.7, followed by the results for each adhesive in Section 18.8. The analytical model and results are explained in Section 18.9, and key observations and conclusions drawn from the experiments along with future test recommendations are discussed in Section 18.10.

18.5 PHASE 1 TESTING

18.5.1 Introduction

To investigate the adhesive connection of wood stud to drywall, twenty specimens consisting of five different adhesives were constructed and tested. The various adhesives are shown in the test matrix with appropriate details in Table 18.1. Different brands and types of adhesives were tested. The adhesives being investigated were Liquid Nails Projects Adhesive, Liquid Nails Heavy Duty Adhesive, Loctite PL 375 VOC Heavy Duty Construction Adhesive, Loctite PL 200 Construction Adhesive, and OSI Green Series Drywall & Panel Adhesive. Specimens were allowed to cure for twenty-eight days before testing. Reported shear strength values were provided from the developers of the product. Liquid Nails Products were determined using ASTM D905 *Standard Test Method in Shear by Compression Loading* [ASTM 2013]; while all other products were determined using ASTM C557 [2009] Shear Strength test method with plywood to drywall paper backing connection.

Table 18.1 Phase 1 test matrix.

Specimen	Description	Reported Shear Strength	Price	Visual
P1	Liquid Nails Project Adhesive with 28 days of cure time.	400 psi after 28 days	\$1.65 for a 10 oz. tube \$0.165/oz	
P2				
P3				
P4				
HD1	Liquid Nails Heavy Duty Adhesive with 28 days of cure time.	Unknown after 28 days	\$2.33 for 10 oz. tube \$0.233/oz	
HD2				
HD3				
HD4				
LHD1	Loctite PL 375 VOC Heavy Duty Construction Adhesive with 28 days of cure time.	Unknown after 28 days 42 psi after 14 days	\$1.29 for a 10 oz. tube \$.129/oz	
LHD2				
LHD3				
LHD4				
L1	Loctite PL 200 Construction Adhesive with 28 days of cure time.	Unknown after 28 days 42.3 psi after 14 days	\$5.49 for a 28 oz. tube \$0.196/oz	
L2				
L3				
L4				
OSI1	OSI Green Series Drywall and Panel Adhesive with 28 days of cure time.	Unknown after 28 days 60 psi after 14 days	\$4.96 for a 28 oz. tube \$0.177/oz	
OSI2				
OSI3				
OSI4				

18.5.2 Construction Details

The simple idea of a push through test set-up was designed for investigating the adhesive connection. The specimens consisted of three 2×4s with a length of 4 in. and two 3.5 in.×4 in.×5/8 in. gypsum sheathing material. The configuration of the specimens is shown in Figure 18.3.

The first step was to cut the 2×4s and gypsum board to the correct length. Once the material was cut and prepared, the gypsum was attached to the 2×4s with the use of Gorilla Glue Epoxy, as shown in Figure 18.4. Epoxy was used to prevent any type of failure with this connection. A 1/8 in. offset between the gypsum and the 2×4 was set to prevent any type of crushing. Once the gypsum was attached to the 2×4, the gypsum was compressed. Painters tape was applied to the edges of the middle 2×4 to assure a 1.5 in. ×1.5 in. bonded area of adhesive, as shown in Figure 18.5. A spreader was attached to the caulking gun to distribute the adhesive evenly on the 2×4.

Figure 18.3 Test 1 specimen.

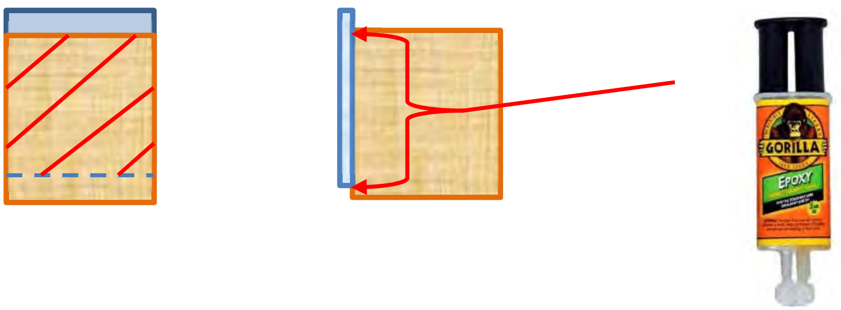

Side View **Front View**

Figure 18.4 Application of the epoxy.

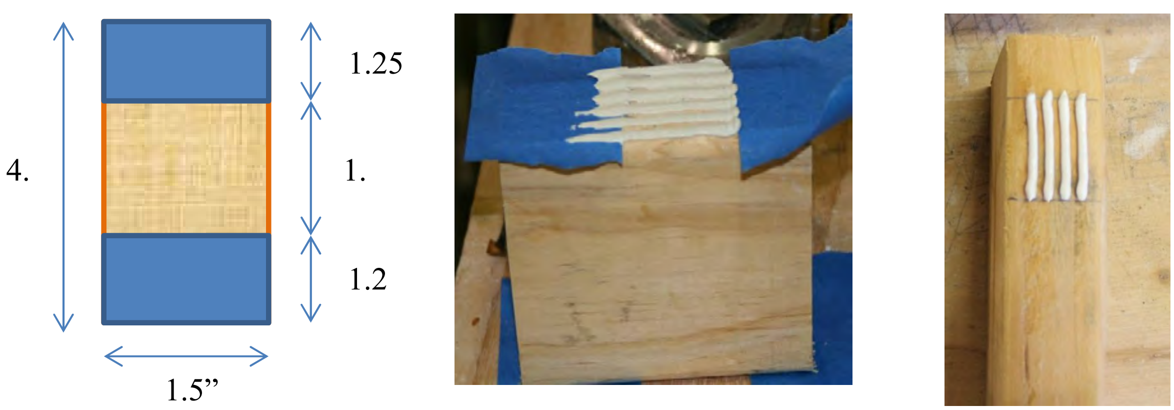

Figure 18.5 Painter’s tape alignment.

Once the adhesive was applied, the tape was removed and the 2×4 was quickly attached to the gypsum. After the middle 2×4 was attached, a clamp was used to compress the 2×4s together for about five minutes. While the clamp was attached, the excess adhesive was removed using a piece of cardboard as seen in Figure 18.6. The clamp was then removed, and the same process is completed for the opposite edge of the middle 2×4. The bottom edges of the 2×4s were sanded down to ensure a flat bottom. Once the construction process was completed, the specimens were allowed to cure for 28 days. After curing, specimens were set into the T-slot machine and loaded at a rate of 0.025 in./min and were displaced 0.5 in. The specimen set-up is shown in Figure 18.7.

Figure 18.6 Removal of excess adhesive.

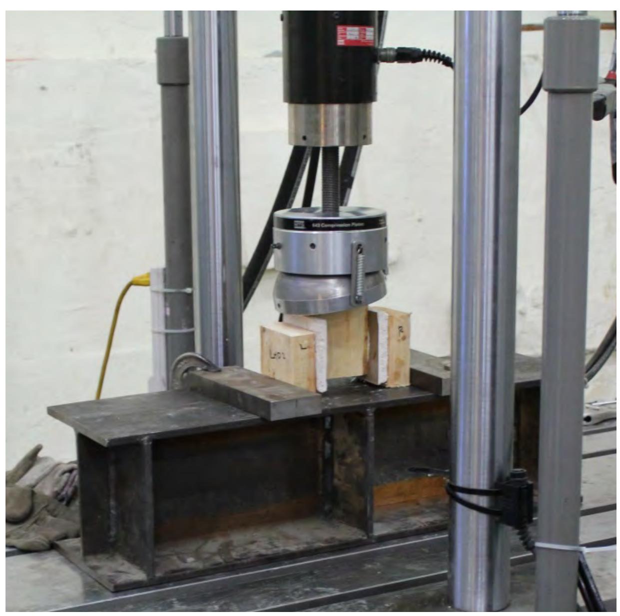

Figure 18.7 Set-up of Test 1 specimens.

18.6 RESULTS OF PHASE 1 TESTING

18.6.1 Introduction

Each specimen tested produced data consisting of force and displacement. The results for the five adhesives tested are described individually. For each specimen the maximum load and failure mode is discussed below.

18.6.2 Liquid Nails Heavy-Duty Construction Adhesive

The maximum load and maximum displacement before failure for the Liquid Nails Heavy Duty Construction Adhesive occurred in Specimen 1, HD1, valued at 396 lbf and 0.278 in. The results for the Liquid Nails Heavy Duty Construction Adhesive are shown in Figure 18.8, where it can be seen that a double peak occurs in the results for specimen HD1. The reasoning behind the double peak is the two adhesive connections failing during separate periods of the tests. While one side failed at 0.017 in, the opposite connection remained intact and continued to resist the load until the second failure at 0.278 in.

The failure mode for all specimens occurred in the paper backing of the drywall with the exception of specimen HD3, where the failure occurred in the adhesive. The failure mode in HD3 may have been due to the smaller amount of adhesive applied. Although the adhesive bondage area remained the same for all specimens, the amount of adhesive applied varied. Figure 18.9 displays the failure of HD3 and a lack of adhesive can be noticed. Both edges failed in a similar manner, with the adhesive failing rather than the paper backing of the drywall.

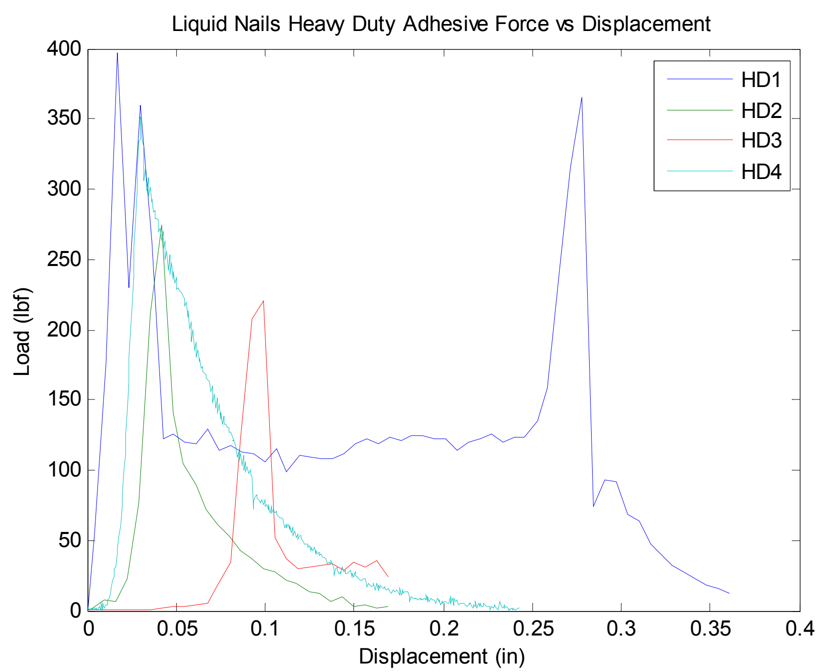

Figure 18.8 Test 1 results: Liquid Nails Heavy Duty Construction Adhesive.

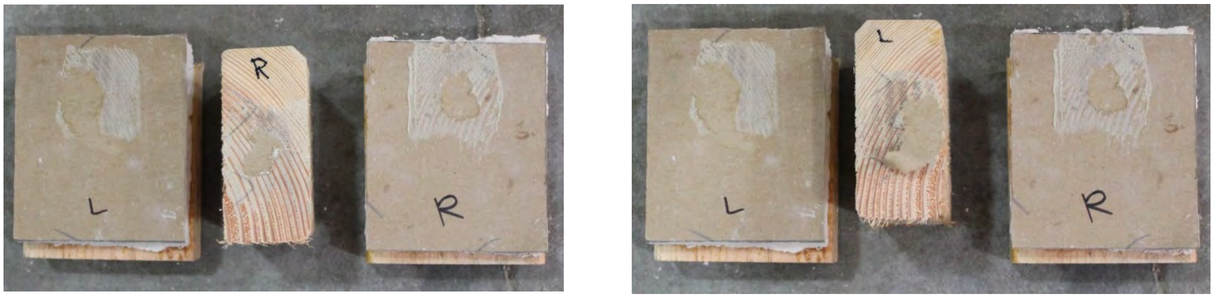

Figure 18.9 Specimen HD3 failure mode.

18.6.3 Liquid Nails Projects Adhesive

The maximum load and maximum displacement before failure for the Liquid Nails Projects Adhesive occurred in Specimen 1, P1, valued at 401 lbf with a displacement of 0.045 in. The set-up of P1 is shown in Figure 18.10. As seen in the figure, the outside 2×x4s displaced, which caused issues in the test results. The full strength was not achieved due to the outside 2×4s displacing, resulting in a premature connection failure.

During the construction process, two specimens were damaged during the process of sanding of the edges, leaving only two specimens for testing. Figure 18.11 displays the results for the Liquid Nails Projects Adhesive. The failure mode is shown in Figure 18.12. Both edges failed in a similar manner, with the paper backing of the drywall failing rather than the adhesive.

During the test, one adhesive connection failing occurred, as shown in Figure 18.13 which displays Specimen P2 at the completion of testing. The effects of this failure can be seen in the results as P2 valued at a maximum load of 92 lbf. A comparison of the specimens shows a large difference, but with only two specimens, not much can be said from the results and further testing must be completed to reach any conclusions.

Figure 18.10 Specimen P1 after completion of test.

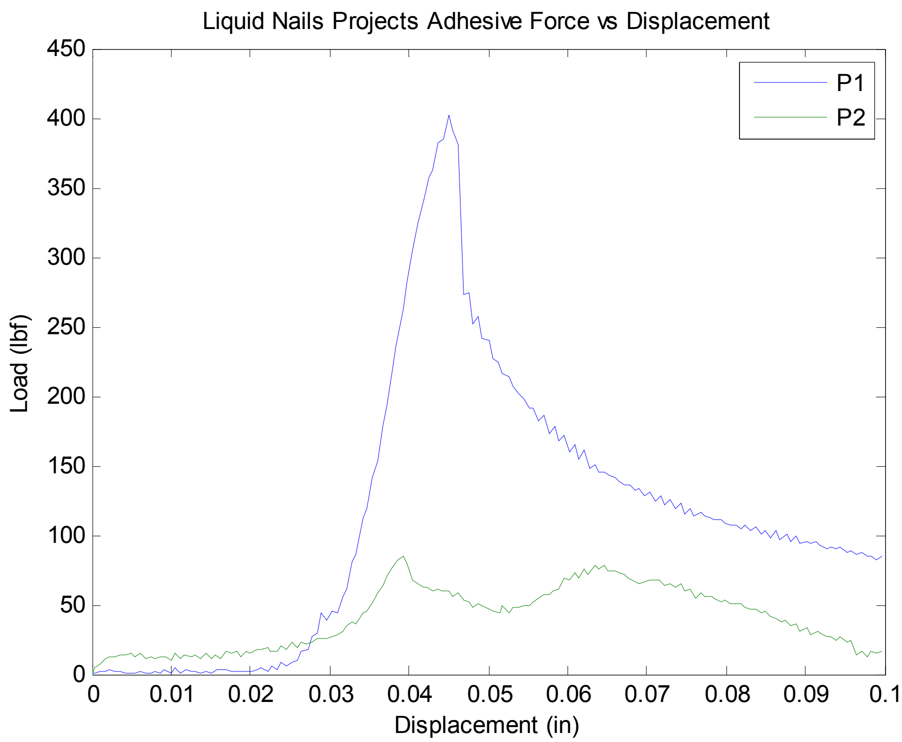

Figure 18.11 Test 1 results: Liquid Nails Projects Adhesive.

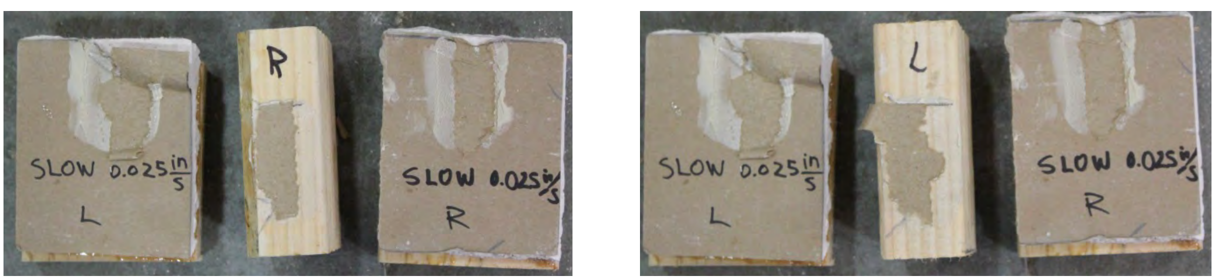

Figure 18.12 Specimen P1 failure mode.

Figure 18.13 Specimen P2 failure.

18.6.4 Loctite PL 375 VOC Heavy Duty Construction Adhesive

This test set-up was adjusted to eliminate the displacement of the outside 2×4s by clamping blocks on the outside of the 2×4s; see Figure 18.7. The maximum load for the Loctite VOC PL 375 Heavy Duty Construction Adhesive occurred in Specimen 3, LHD3, valued at 902 lbf. The maximum displacement before failure occurred in Specimen 2, LHD2 valuing at 0.10412 in. Figure 18.14 shows the results for the Loctite VOC PL375 Heavy Duty Construction Adhesive.

The failure mode of all specimens occurred in the paper backing of the drywall. In Figure 18.14, double peaks occurred in the results for all specimens with the exception of LHD3. The double peak did not occur in Specimen LHD3 because both adhesive connections failed simultaneously, which explains the higher maximum load.

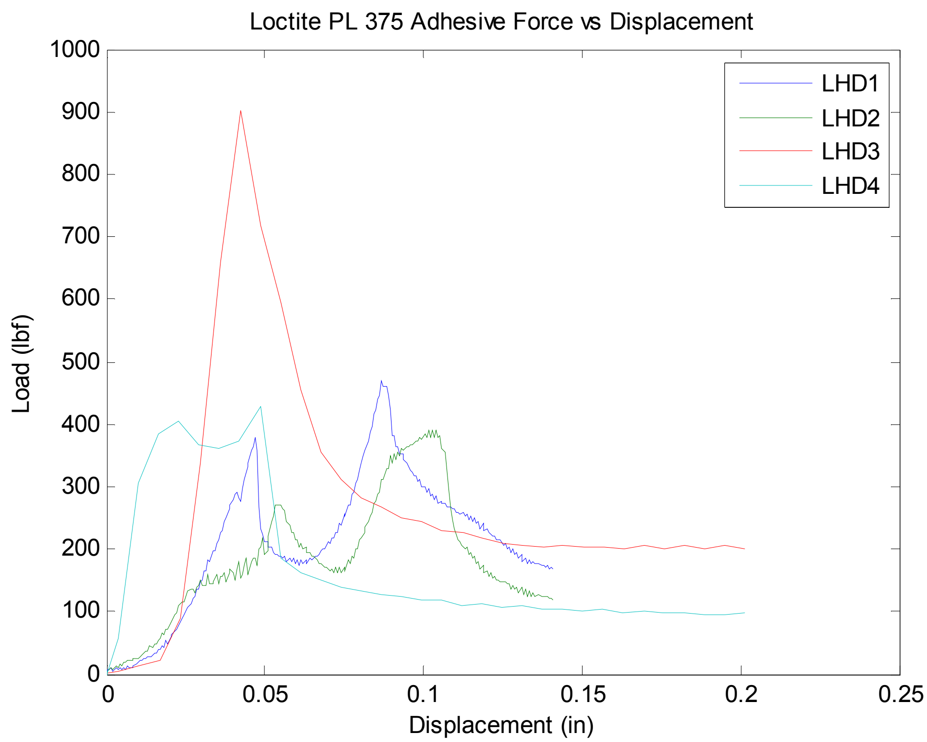

Figure 18.14 Test 1 results: Loctite VOC PL 375 Heavy Duty Construction Adhesive.

18.6.5 Loctite PL 200 Construction Adhesive

The maximum load for the Loctite PL 200 Construction Adhesive occurred in Specimen 1, L1, valued at 726 lbf. The maximum displacement before failure occurred in Specimen 3, L3 valuing at 0.0997 in. Figure 18.15 shows the results for the Loctite VOC PL375 Heavy Duty Construction Adhesive.

The failure mode for all specimens occurred in the paper backing of the drywall. As shown in Figure 18.15, double peaks occurred in the results for all specimens with the exception of L1 and L2. The double peaks did not occur in Specimens L1 and L2 because both adhesive connections failed simultaneously, which explains the higher maximum load.

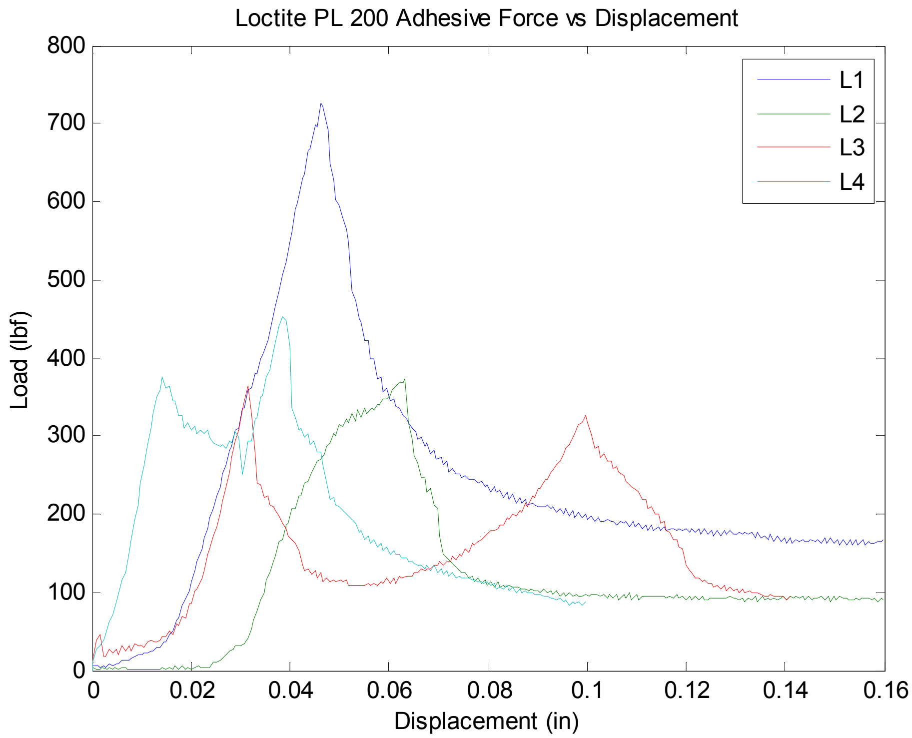

Figure 18.15 Test 1 results: Loctite PL 200 Construction Adhesive.

18.6.6 OSI Green Series Drywall and panel Adhesive

The maximum load for the OSI Green Series Drywall and Panel Adhesive occurred in Specimen 2, OSI2, valued at 592.37 lbf. The maximum displacement before failure occurred in Specimen 4, OSI4 valuing at 0.0698 in. Figure 18.16 displays the results for the OSI Green Series Drywall and Panel Adhesive.

During the construction process, an error occurred with the adhesive area because adhesive was applied to a 1.5 in.×2 in. area to all specimens. All specimens failure mode occurred in the paper backing of the drywall with the exception of Specimen 4, OSI4, where the failure mode was a half paper backing and half adhesive failure as shown Figure 18.17. As shown in Figure 18.16, double peaks only occurred in OSI4.

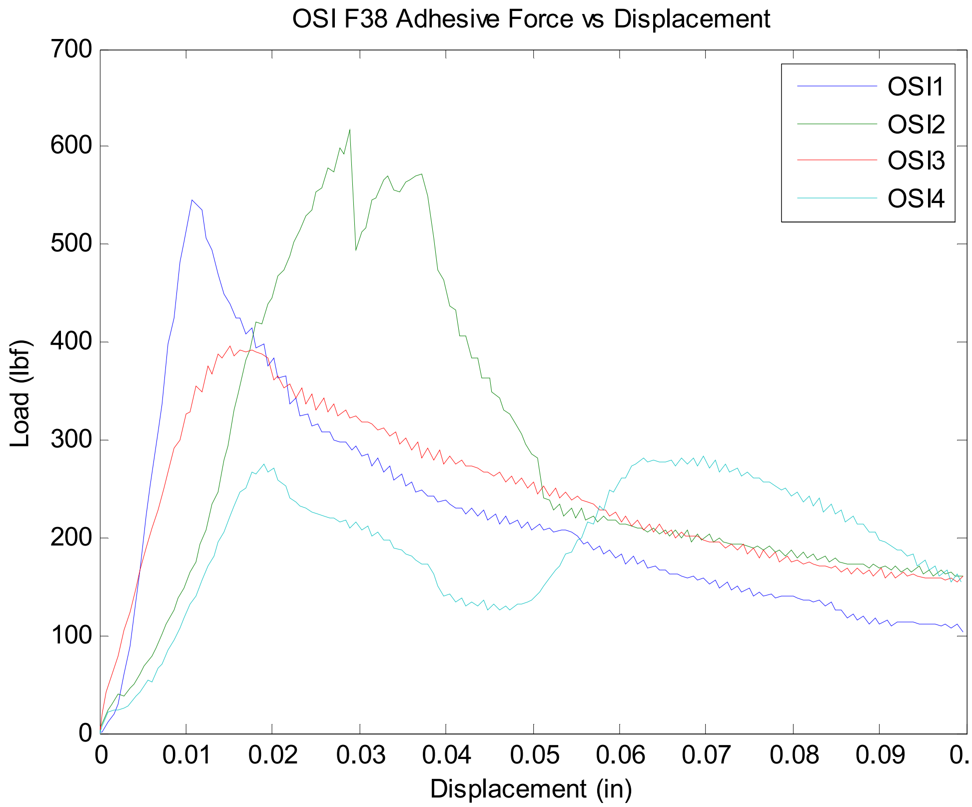

Figure 18.16 Test 1 results: OSI Green Series Drywall and Panel Adhesive.

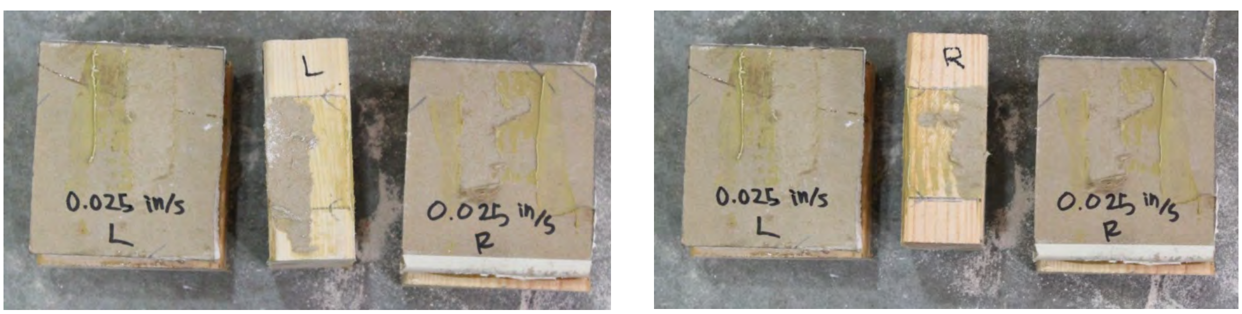

Figure 18.17 OSI4 failure mode.

18.6.7 Summary of Test 1

Given the inconsistency and odd behavior of specimens, a best adhesive could not be chosen; therefore, a new set-up must be designed for further testing. The following errors occurred in the original test set-up: (1) the displacement of the outside 2×4s; (2) tncluding two adhesive connections caused double peaks in the maximum load; (3) the irregularity of wood and cuts caused major issues in that specimens that were not completely flat prior to loading; and (4) the specimens were not identical. These adjustments must be made to ensure accurate test results.

18.7 PHASE 2 TESTING

Given the variability in results from test one; a new set-up was designed in hopes of improving the accuracy of the test results. The same adhesives were used as the previous test, but a sixth adhesive was added. The various adhesives are shown in the test matrix with appropriate details in Table 18.2. The sixth adhesive included in this test was Liquid Nails Drywall Adhesive. To eliminate the double peaks seen from first test results, only one sheathing connection was tested. All specimens in this test were left to cure for only seven days rather than the twenty-eight from the previous explained test.

Table 18.2 Phase 2 test matrix.

Specimen	Description	Reported Shear Strength	Price	Visual
L1	Loctite PL 200 Construction Adhesive with 7 days of cure time.	42.3 psi after 14 days	\$5.49 for a 28 oz. tube \$0.196/oz	
L2				
L3				
L4				
OSI1	OSI Green Series Drywall and Panel Adhesive with 7 days of cure time.	60 psi after 14 days	\$4.96 for a 28 oz. tube \$0.177/oz	
OSI2				
OSI3				
OSI4				
DW1	Liquid Nails Drywall Adhesive with 7 days of cure time.	400 psi after 28 days	\$3.99 for a 28 oz. tube \$0.143/oz	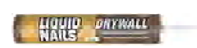
DW2				
DW3				
DW4				
LHD1	Loctite PL 375 VOC Heavy Duty Construction Adhesive with 7 days of cure time.	42 psi after 14 days	\$1.29 for a 10 oz. tube \$.129/oz	
LHD2				
LHD3				
LHD4				
HD1	Liquid Nails Heavy Duty Adhesive with 7 days of cure time.	240 psi after 7 days	\$2.33 for 10 oz. tube \$0.233/oz	
HD2				
HD3				
HD4				
P1	Liquid Nails Project Adhesive with 7 days of cure time.	400 psi after 28 days	\$1.65 for a 10 oz. tube \$0.165/oz	
P2				
P3				
P4				

18.7.1 Set-Up of Phase 2 Testing

The specimens were built using the same construction process as the first test. The second round of tests allowed us to address the issue of rotation of the 2×4s. A set-up was developed in which the edge of the 2×4 would slide down a set of wheels. The new instrument, shown in figure 18.18, was clamped down to prevent any movement; the new test set-up is shown in Figure 18.19. Additional changes were made: (1) the lengths of the 2×4s were adjusted so that the fixed 2×4 had a length of 8 in. in order to apply clamps to prevent any movement, while the moving 2×4 had a length of 7 in. in order to have enough space to attach the yolk; (2) the yolk was attached before testing by predrilling holes followed by drilling of the bolts; and (3) three bolts on both sides of the yolk were installed to ensure no slippage between the yolk and the 2×4.

Figure 18.18 Rotation prevention instrument.

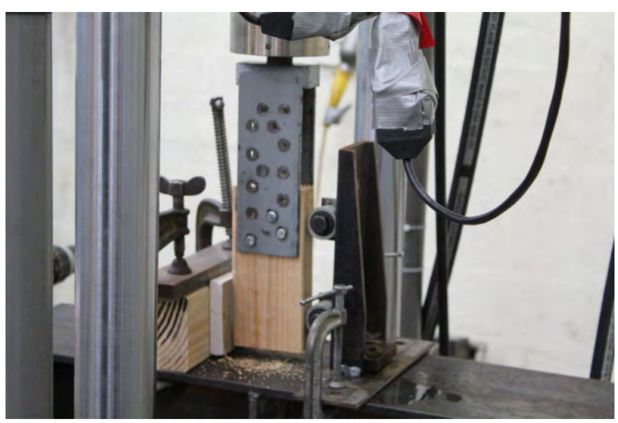

Figure 18.19 New test set-up of specimens for Phase 2.

18.8 RESULTS OF PHASE 2 TESTING

18.8.1 Introduction

Force and displacement data was recorded for each test specimen. The results for the six adhesives tested are described individually. For each specimen the failure mode, stiffness, and shear strength are discussed. The shear strength was calculated using Equation (18.2), and stiffness of the adhesive was calculated using Equation (18.3). The overall results for each adhesive are displayed in Figure 18.20.

$$\sigma = F/A \tag{18.2}$$

where σ is the shear stress (psi), F is the maximum force (lbf), and A is the area of the adhesive (in^2).

$$k = F/d \tag{18.3}$$

where k is the stiffness (k/in.), F is the force (lbf), and d is the displacement (in.).

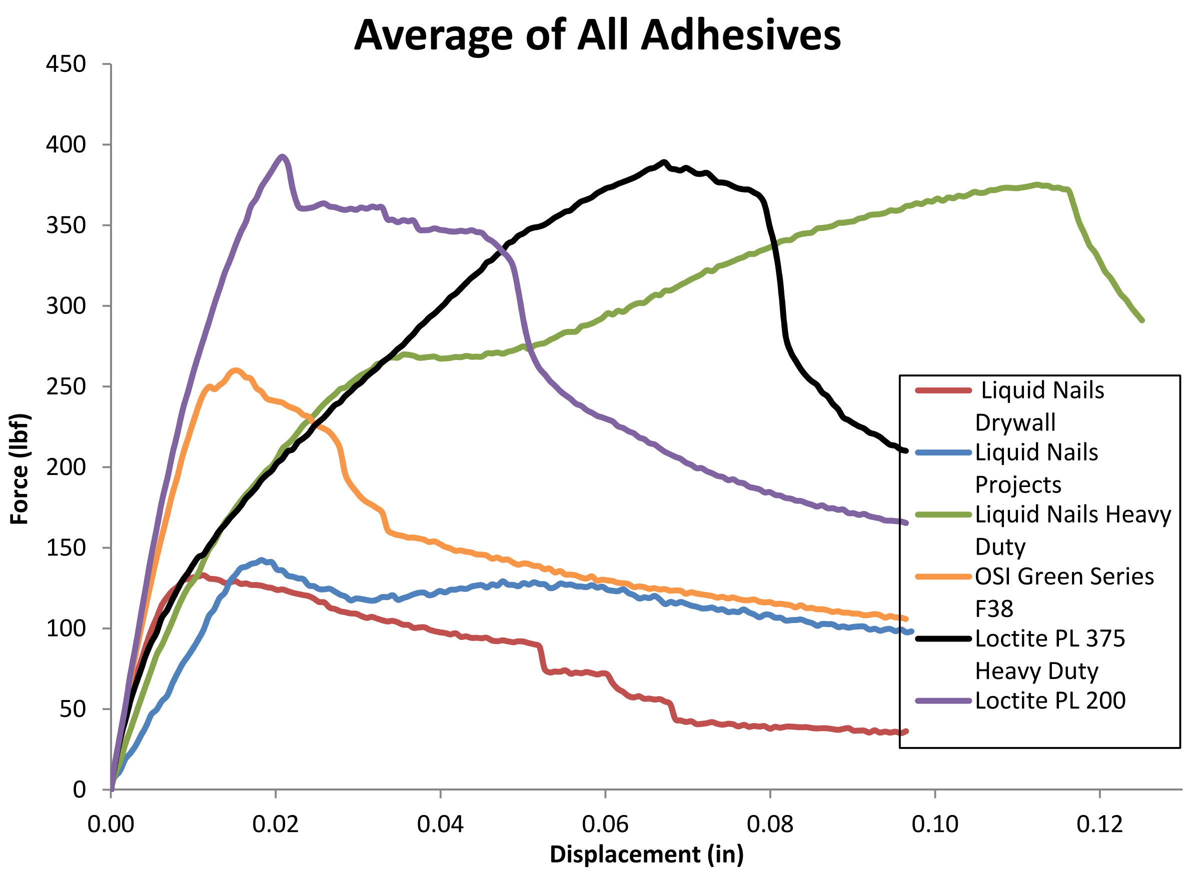

Figure 18.20 Phase 2 testing average of all adhesives.

18.8.2 Loctite PL 200 Construction Adhesive

The first adhesive tested was the Loctite PL 200 Construction Adhesive. Figure 18.21 displays the results for all four specimens using the Loctite PL 200 Adhesive. It can be seen that the double peaks from the first test were eliminated. The maximum load and maximum displacement before failure occurred with specimen 4, L4, which valued at 637 lbf and 0.0443 in. The failure mode of L1 was within the gypsum itself, while all other specimens had a failure occur in the paper backing of the drywall. Failure modes of L1 and L2 are shown in Figure 18.22.

After the test, the length of the adhesive area was measured and recorded in order to calculate the shear strength. With the recorded data, the stiffness and shear strength for each adhesive was calculated. Table 18.3 shows the results for the Loctite PL 200 Construction Adhesive. Specimen L1 has no calculated shear strength due to the failure mode being within the gypsum. The average maximum load, deformation at peak load, stiffness, and shear strength were calculated to be 454.21 lbf, 0.0292 in, 28.90 kips/in, and 114.74 psi, respectively. The coefficient of variance is shown in the table and the values are noticeably inconsistent.

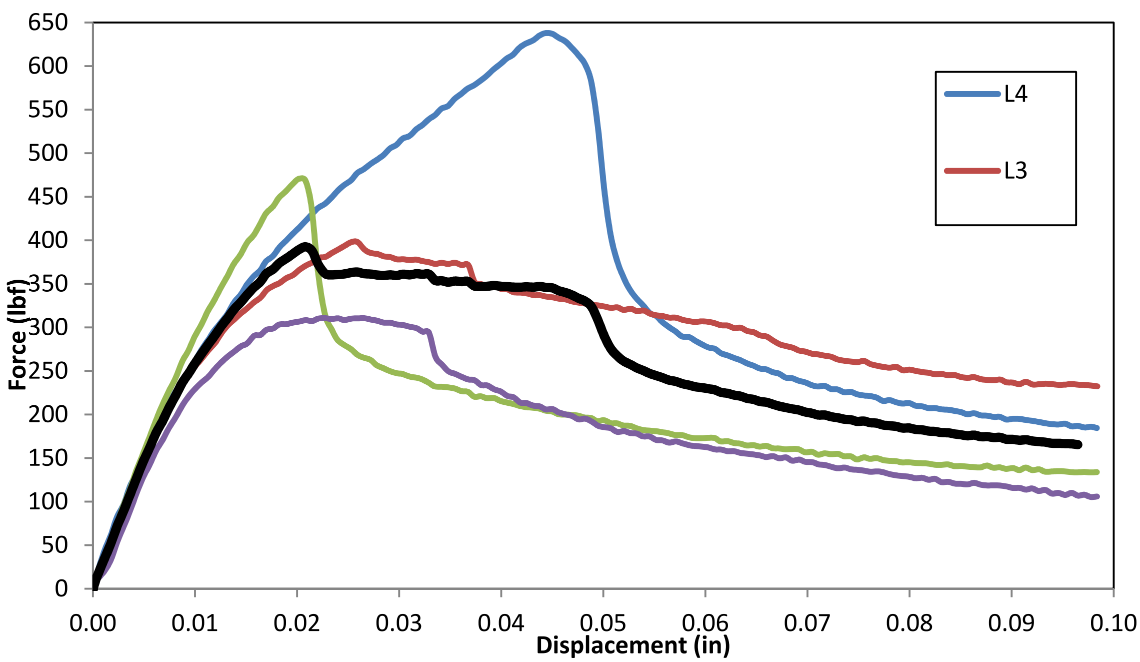

Figure 18.21 Test 2 results: Loctite PL 200 Construction Adhesive.

Table 18.3 Test 2 results: Loctite PL 200 Construction Adhesive.

Specimen	Maximum Load (lbf)	Deformation at Peak Load (in.)	Area of Adhesive (in^2)	Stiffness Calculation			Shear Strength (psi)
				Load (lbf)	Deformation at load (in.)	Stiffness (kips/in.)	
L1	310.58	0.0266		158.73	0.0062	25.59	
L2	470.46	0.0202	4.13	194.16	0.0062	31.28	114.05
L3	398.01	0.0259	4.50	181.06	0.0062	29.11	88.45
L4	637.80	0.0443	4.50	182.64	0.0062	29.62	141.73
Average	454.21	0.0292				28.90	114.74
COV	30.55%						23.23%

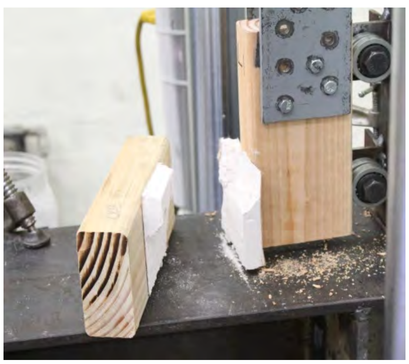

(a)

(b)

Figure 18.22 Failure modes: (a) L1 and (b) L2.

18.8.3 OSI Green Series Drywall and Panel Adhesive

Figure 18.23 displays the results for the four specimens and the average of the OSI Green Series Drywall and Panel Adhesive. The maximum load occurred in specimen 2, OSI2, with a value of 346 lbf. The maximum displacement before failure of the adhesive connection occurred in OSI3 at a value of 0.0704 in. During this test series, specimens OSI3 and OSI4 were damaged during the setup process of drilling the bolts. The damage can be seen in Figure 18.24 and while these specimens were damaged prior to testing, specimens were still tested and variability in maximum load is noticed. All OSI specimens failed in the paper backing of the drywall.

The stiffness and shear strength for each adhesive was calculated and results are shown in Table 18.4. The average maximum load, deformation at peak load, stiffness, and shear strength were calculated to be 280.15 lbf, 0.0208 in, 26.68 kips/in, and 57.47 psi, respectively. Since OSI3 and OSI4 were damaged prior to testing, they were not considered in the average results and are marked with a gray fill in the table.

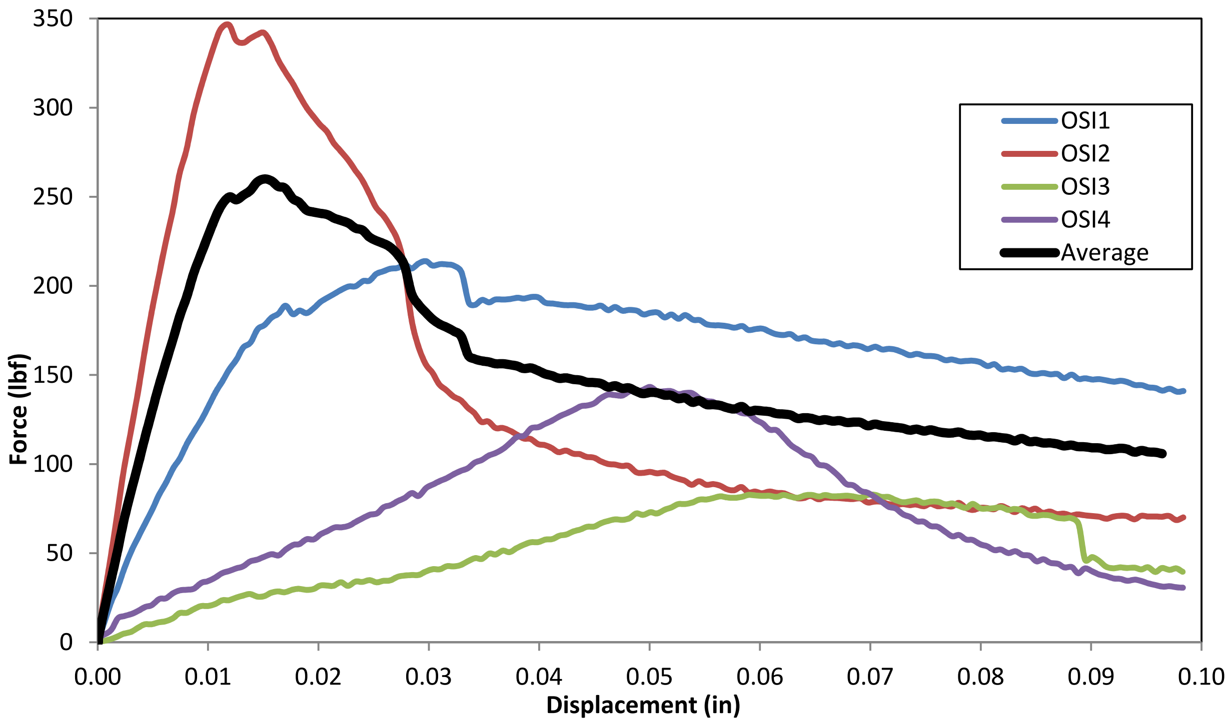

Figure 18.23 Test 2 results: OSI Green Series Drywall and Panel Adhesive.

Table 18.4: Test 2 results: OSI Green Series Drywall and Panel Adhesive.

Specimen	Maximum Load (lbf)	Deformation at Peak Load (in.)	Area of Adhesive (in^2)	Stiffness Calculation			Shear Strength (psi)
				Load (lbf)	Deformation at load (in.)	Stiffness (kips/in.)	
OSI1	213.89	0.0297	4.88	82.57	0.0055	14.90	43.87
OSI2	346.42	0.0119	4.88	139.71	0.0036	38.45	71.06
OSI3	82.75	0.0704	4.50	16.56	0.0081	2.05	18.39
OSI4	143.28	0.0501	4.59	36.39	0.0107	3.41	31.19
Average	280.15	0.0208				26.68	57.47
COV	33.45%						33.45

Figure 18.24 Damage prior to testing.

18.8.4 Liquid Nails Drywall Adhesive

Figure 18.25 displays the results for the three specimens and the average of the Liquid Nails Drywall Adhesive. The maximum load and maximum displacement before failure occurred in specimen 1, DW1, with a value of 156 lbf and 0.0183 in. During this test series, specimens DW2 and DW4 were damaged during the setup process of drilling the bolts. After DW2, a different size yolk was used due to difficulties with the original yolk. The adhesive connection for DW4 failed prior to testing and was not tested. All other DW specimens failed in the paper backing of the drywall.

The stiffness and shear strength for each adhesive was calculated and results are shown in Table 18.5. The average maximum load, deformation at peak load, stiffness, and shear strength were calculated to be 142.19 lbf, 0.0136 in, 28.60 kips/in, and 37.52 psi, respectively. Since DW2 was damaged prior to testing, it was not considered in the average results and is marked with a gray fill in the table.

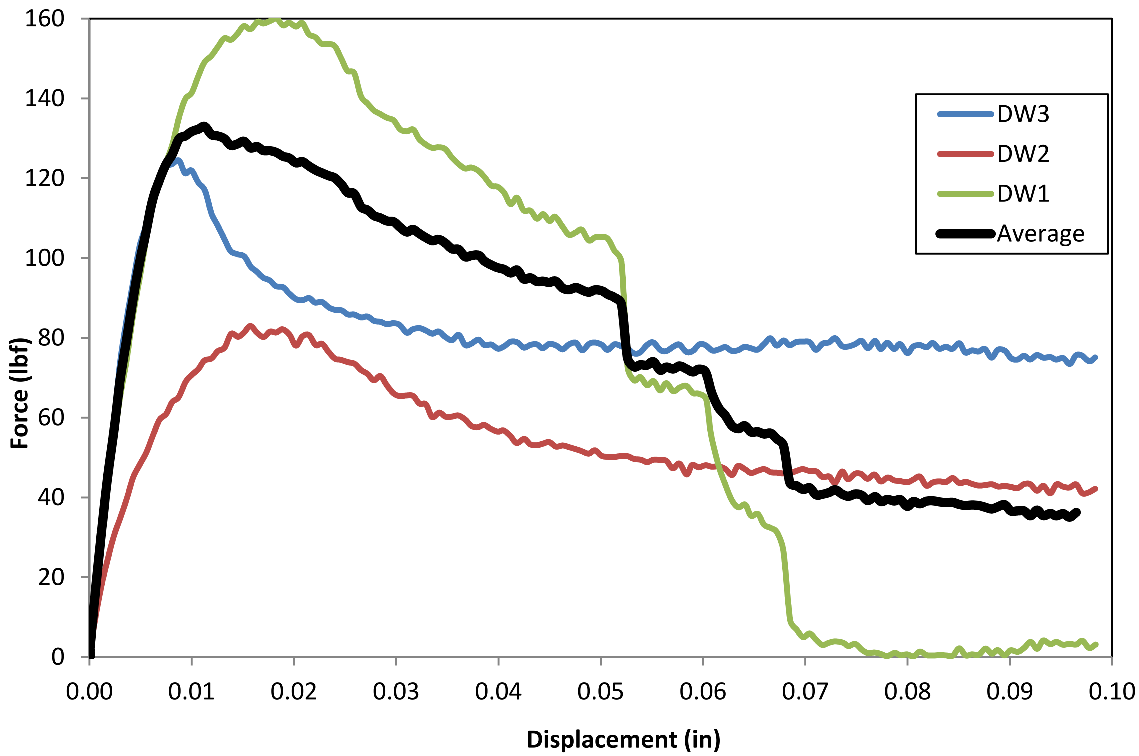

Figure 18.25 Test 2 results. Liquid Nails Drywall Adhesive.

Table 18.5 Test 2 results: Liquid Nails Drywall Adhesive.

Specimen	Maximum Load (lbf)	Deformation at Peak Load (in.)	Area of Adhesive (in.^{2})	Stiffness Calculation			Shear Strength (psi)
				Load (lbf)	Deformation at load (in.)	Stiffness (kips/in.)	
DW1	159.97	0.0183	4.59	42.36	0.0017	24.32	34.82
DW2	82.95	0.0157	4.59	17.33	0.0011	15.25	18.06
DW3	124.41	0.0088	3.09	14.19	0.0004	32.87	40.21
DW4	N/A						
Average	142.19	0.01355				28.595	37.52
COV	17.68%						10.16%

18.8.5 Loctite PL 375 VOC Heavy Duty Construction Adhesive

Figure 18.26 displays the results for the four specimens and the average of the Loctite PL 375 VOC Heavy Duty Construction Adhesive. The maximum load and maximum displacement before failure occurred in specimen 4, LHD4, with a value of 497 lbf and 0.0780 in. During this test series, specimens LHD2 was damaged during the setup process of drilling the bolts. After LHD1, only two bolts, one on each side, were installed to prevent or minimize damage to specimens. All LHD specimens failed in the paper backing of the drywall.

The stiffness and shear strength for each adhesive was calculated and results are shown in Table 18.6. The average maximum load, deformation at peak load, stiffness, and shear strength were calculated to be 425 lbf, 0.0676 in, 20.93 kips/in, and 90.20 psi, respectively. Since LHD2 was damaged prior to testing, it was not considered in the average results and is marked with a gray fill in the table.

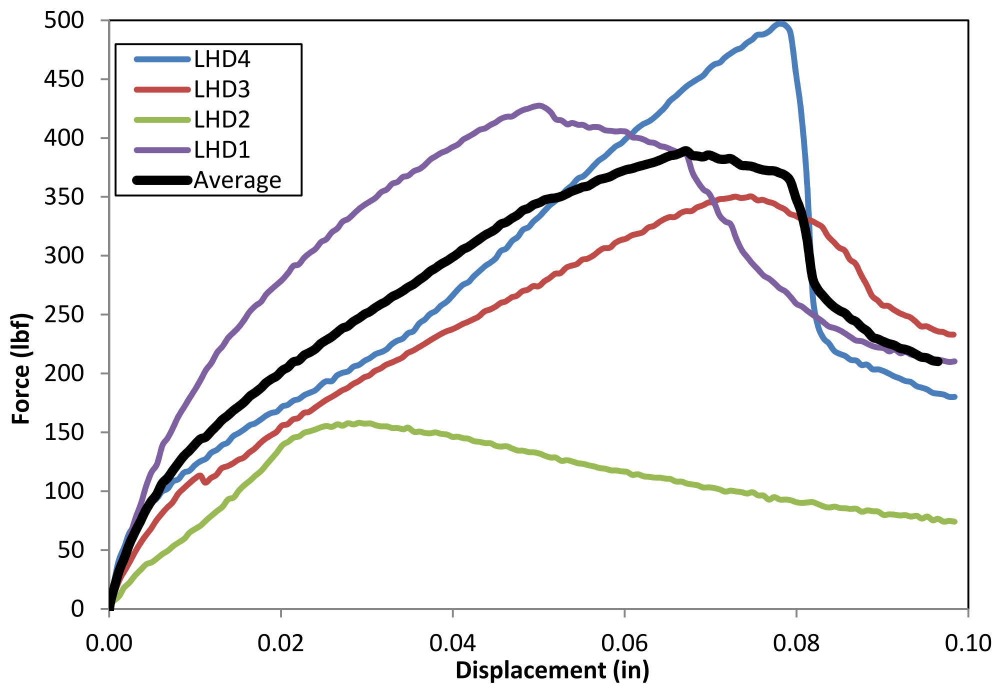

Figure 18.26 Test 2 results: Loctite PL 375 VOC Heavy Duty Construction Adhesive.

Table 18.6 Test 2 results: Loctite PL 375 VOC Heavy Duty Construction Adhesive.

Specimen	Max Load (lbf)	Deformation at Peak Load (in.)	Area of Adhesive (in.^{2})	Stiffness Calculation			Shear Strength (psi)
				Load (lbf)	Deformation at load (in.)	Stiffness (kips/in.)	
LHD1	427.46	0.0501	4.88	76.24	0.0030	25.09	87.68
LHD2	158.06	0.0291	4.69	56.49	0.0081	6.97	33.72
LHD3	350.32	0.0748	4.69	47.44	0.0029	16.09	74.74
LHD4	496.99	0.0780	4.59	78.15	0.0036	21.60	108.19
Average	424.92	0.0676				20.93	90.20
COV	17.27%						18.70%

18.8.6 Liquid Nails Heavy Duty Construction Adhesive

Figure 18.27 displays the results for the four specimens and the average of the Liquid Nails Heavy Duty Construction Adhesive. The maximum load and maximum displacement before failure occurred in Specimen 4, HD4, with a value of 580 lbf and 0.1137 in. During this test series, specimens HD1 and HD2 were damaged during the setup process of drilling the bolts. All HD specimens failed in the paper backing of the drywall.

The stiffness and shear strength for each adhesive was calculated and results are shown in Table 18.7. The average maximum load, deformation at peak load, stiffness, and shear strength were calculated to be 443 lbf, 0.0736 in, 13.75 kips/in., and 107.32 psi, respectively. Since HD1 and HD2 were damaged prior to testing, they were not considered in the average results and are marked with a gray fill in the table.

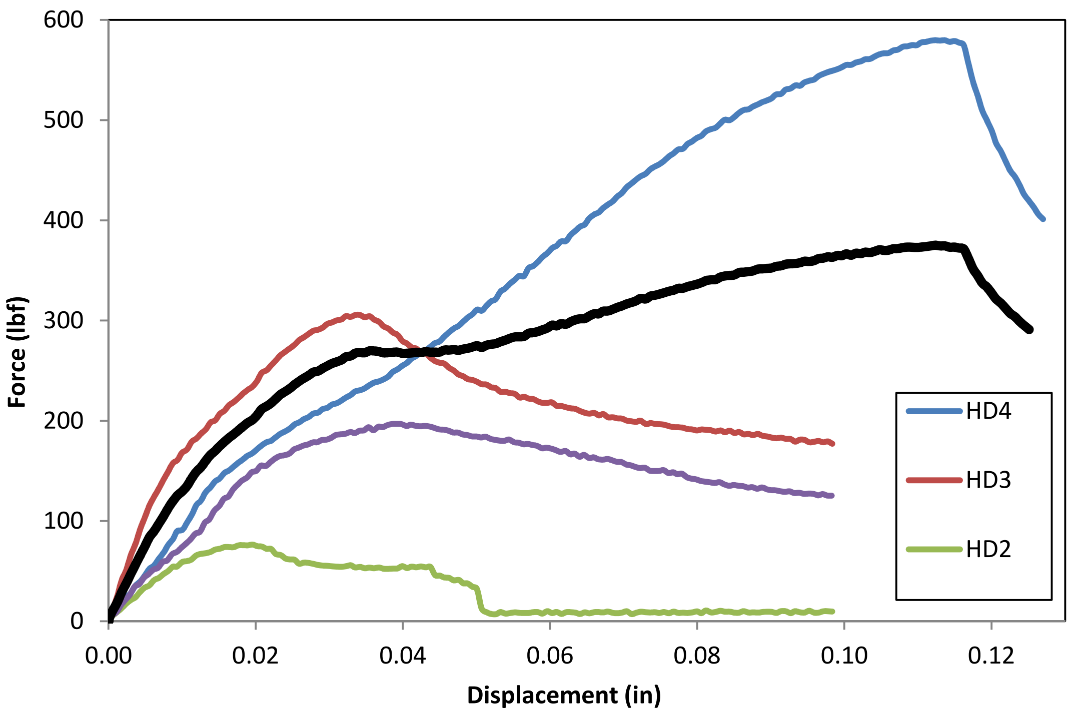

Figure 18.27 Test 2 results: Liquid Nails Heavy Duty Construction Adhesive.

Table 18.7 Test 2 results: Liquid Nails Heavy Duty Construction Adhesive.

Specimen	Maximum Load (lbf)	Deformation at Peak Load (in.)	Area of Adhesive (in.^{2})	Stiffness Calculation			Shear Strength (psi)
				Load (lbf)	Deformation at load (in.)	Stiffness (kips/in.)	
HD1	196.98	0.0392	4.69	77.70	0.0106	7.35	42.02
HD2	76.46	0.0196	4.78	40.88	0.0062	6.61	15.99
HD3	305.62	0.0336	4.13	148.93	0.0081	18.43	74.09
HD4	579.77	0.1137	4.13	91.21	0.0101	9.07	140.55
Average	442.70	0.0736				13.75	107.32
COV	43.79%						43.79%

18.8.7 Liquid Nails Projects Construction Adhesive

Figure 18.28 displays the results for the four specimens and the average of the Liquid Nails Projects Construction Adhesive. The maximum load and maximum displacement before failure occurred in Specimen 3, P3, with a value of 186 lbf and 0.0552 in. During this test series, specimen P2 was damaged during the setup process of drilling the bolts. Specimen P1 was disregarded because of an error in testing. The T-slot machine was not reset to the original position and the specimen did not displace enough to fail. All P specimens, with the exception of P1, failed in the paper backing of the drywall.

The stiffness and shear strength for each adhesive was calculated and results are shown in Table 18.8. The average maximum load, deformation at peak load, stiffness, and shear strength were calculated to be 174.29 lbf, 0.0361 in, 11.28 kips/in., and 38.78 psi, respectively. Due to the error in P1 and P2 being damaged prior to testing, they were not considered in the average results and are marked with a gray fill in the table.

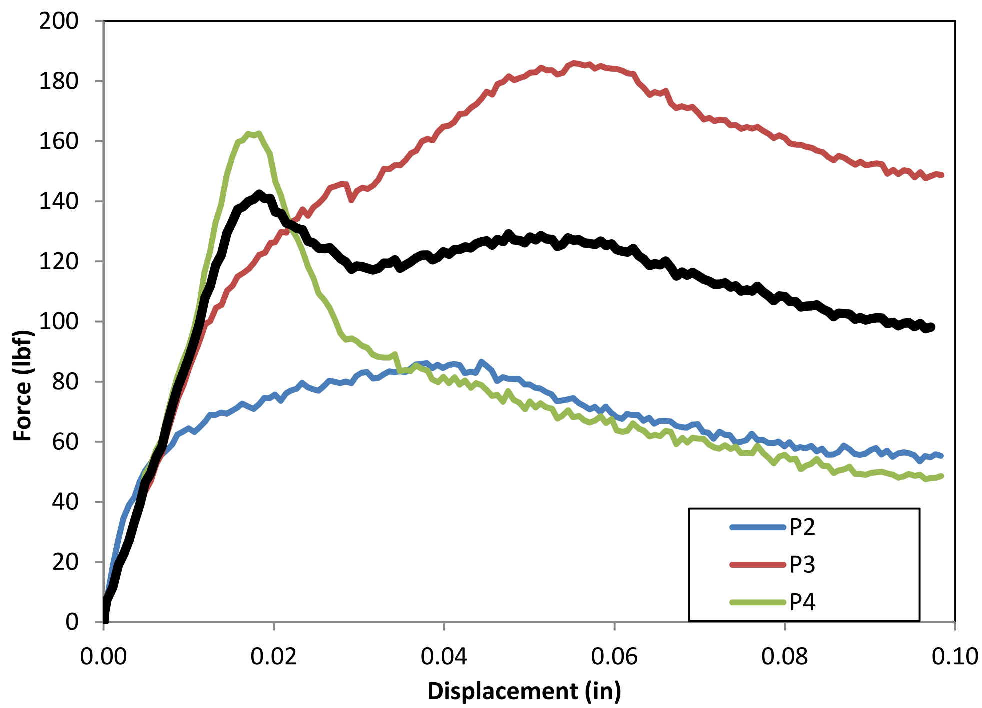

Figure 18.28 Test 2 results: Liquid Nails Projects Construction Adhesive.

Table 18.8 Test 2 results: Liquid Nails Projects Construction Adhesive.

Specimen	Max Load (lbf)	Deformation at Peak Load (in.)	Area of Adhesive (in.^{2})	Stiffness Calculation			Shear Strength (psi)
				Load (lbf)	Deformation at load (in.)	Stiffness (kips/in.)	
P1	N/A						
P2	86.59	0.0380	4.59	27.21	0.0017	15.81	18.85
P3	185.98	0.0552	4.88	12.85	0.0011	11.68	38.15
P4	162.59	0.0170	4.13	18.78	0.0017	10.89	39.42
Average	174.29	0.0361				11.28	38.78
COV	9.49%						2.31%

18.9 ANALYSIS

An analytical model was created with the properties found from the results by use of OpenSees, a dynamic structural modeling program [McKenna et al 2000]. Figure 18.29 displays the results from the model. The model uses *uniaxialMaterial MultiLinear* to represent the adhesive connection. This uniaxial material uses the force and displacement of the multiple points of the force versus displacement envelope to create a plot to represent the phase two test results. The model and test values can be applied to the design of a shear wall if a certain adhesive is implemented in the construction; however, more testing must be completed to achieve results with higher accuracy.

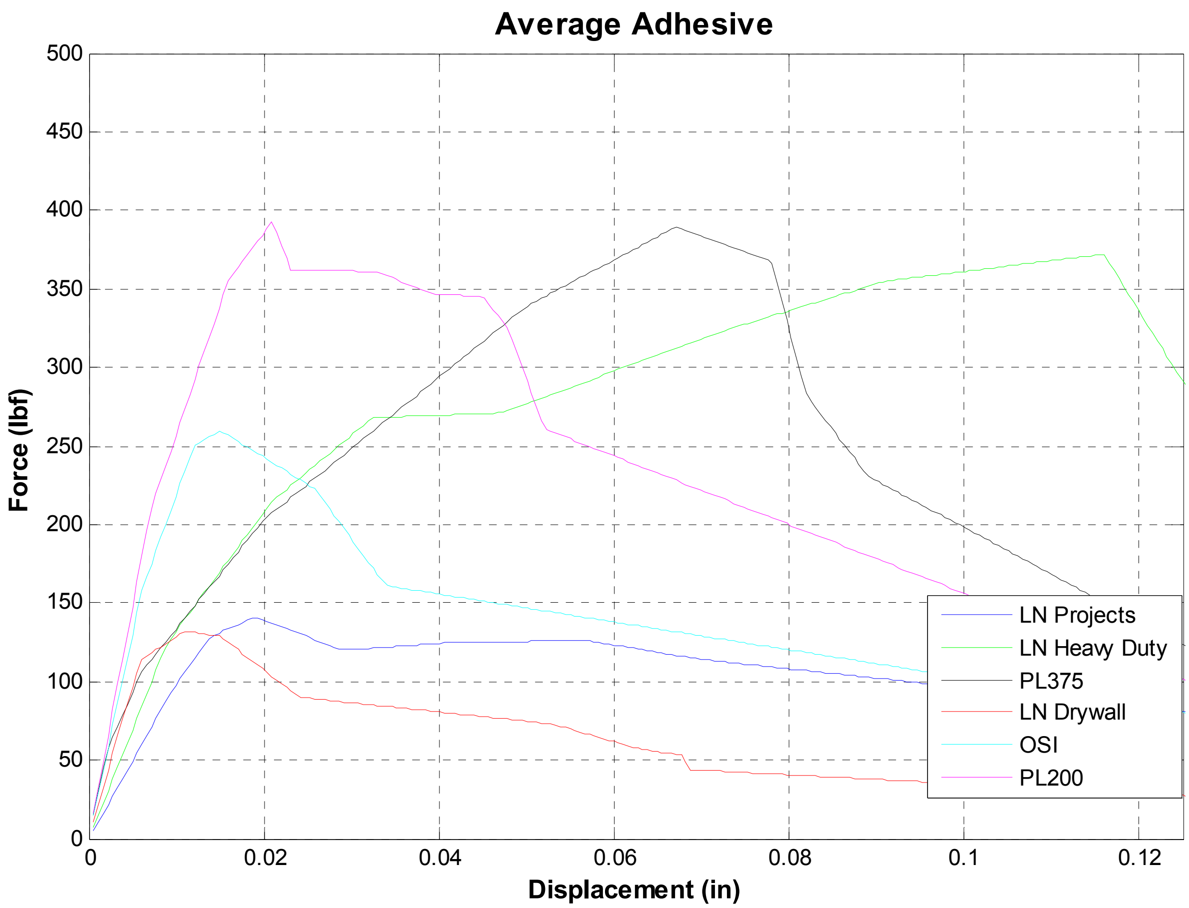

Figure 18.29 Model of average adhesive results.

18.10 CONCLUSIONS

The research conducted shows that Loctite PL 200 Construction Adhesive is the strongest and has the greatest shear strength capacity; however, does not have the greatest deformability. Liquid Nails Heavy Duty Construction Adhesive had an average deformability greater than any other adhesive. Although Loctite PL 375 VOC Heavy Duty Construction Adhesive did not obtain the greatest strength or deformability, it is the cheapest out of all the adhesives and performed well when compared to other adhesives. The average maximum load for Loctite PL 200 was calculated at around 453 lbf, while Liquid Nails Heavy Duty and Loctite PL 375were calculated at 443 and 425 lbf, respectively. The average deformability before failure for Loctite PL 200, Liquid Nails Heavy Duty, and Loctite PL 375 was calculated to be 0.0293, 0.0736, and 0.0676 in., respectively. These three adhesives are within about 30 lbf of each other in maximum load but Loctite PL 200 differs greatly when comparing the deformability of the adhesives. Liquid Nails Heavy Duty and Loctite PL 375 only differ by about 0.01 in. when comparing the deformability of these adhesives. When comparing the price of Liquid Nails Heavy Duty and Loctite PL 375, a difference of about $0.10/oz. is calculated between the two adhesives with Loctite PL 375 being the cheaper of the two. The availability of the adhesives must also be considered, because certain adhesives are not available at local stores and must be purchased online. For example, Liquid Nails Drywall Adhesive is not available at any local Home Depot or Lowes stores in the San Francisco Bay Area. Many parameters need to be considered before deciding the best adhesive.

Crucial data was lost with the damaged specimens, and due to insufficient and inconsistent data selecting a "best" adhesive proved difficult without further testing. Inconsistency in test results is still seen after disregarding the damaged specimens. The test results; however, did show the common failure mode being in the paper backing of the drywall and not the adhesive, which shows the drywall paper backing being the weak link. The results show two potential "best" adhesives being the Liquid Nails Heavy Duty Adhesive and Loctite PL 375. With the available data, a model was created with OPENSEES. The model represents the properties of the adhesives, which can be applied to design; however, more testing must be completed to achieve results with higher accuracy.

The new test set-up for the second phase was not efficient and improvement is necessary for future testing. The test set-up was time consuming due to the drilling process and should not be used in future testing. Using a more efficient attachment method to attach the displacing 2×4 will eliminate the damage to specimens caused by the drilling procedure. Another concerning issue is the development of identical specimens, which is extremely difficult because of the imperfections of wood and the amount of adhesive used. The adhesive area used causes statistical uncertainty issues because the area of adhesive cannot be controlled. After compressing the specimen, the adhesive spreads and the adhesive area used cannot be fixed. Due to imperfection in wood, proper adjustments must be made to ensure a proper set-up. Edges making contact with the base of test area and the edges making contact with the wheels of the instrument should be flat as possible. A mold of the specimen is recommended to help create identical specimens.

18.11 ACKNOWLEDGMENTS

I would like to thank my faculty supervisors Gregory Deierlein, Ben Fell, and Eduardo Miranda for all the support and guidance through the entire research project. Special thanks to Cristian Acevedo, who offered constant assistance, support, advice, and guidance. Deepest gratitude is due to the entire faculty at the Richmond Field Station Laboratory. I would like to give thanks to Scott Swensen and Ezra Jampole for aiding and guiding me through the modeling process. Thank you to all my fellow interns for the great experience. In addition, thank you to Heidi Tremayne for her assistance and organizing of the PEER program. Lastly, I would like to express my love and gratitude to my family for their understanding and endless love throughout the research.

18.12 REFERENCES

ASCE (2010). *Minimum Design Loads for Buildings and Other Structures (ASCE/SEI 7-10).* American Society of Civil Engineers, Reston, VA.

ASTM (2009). *Standard Specification for Adhesives for Fastening Gypsum Wallboard to Wood Framing, C557*, American Society for Testing and Material, West Conshojocken, PA

ASTM (2013). *Standard Test Method for Strength Properties of Adhesive Bonds in Shear by Compression Loading, D905-08,* American Society for Testing and Material, West Conshojocken, PA.

Frihart C.R. (2005a). Adhesive Bonding and Performance Testing of Bonded Wood Products, ASTM International, 2(7).

Frihart C.R. (2005b). Wood adhesion and adhesives, in *Handbook of Wood Chemistry and Wood Composites*, CRC Press: Florida.

Gatto K., Uang C.-M. (2001). Cyclic response of woodframe shearwalls: Loading protocol and rate of loading effects, *Report No. SSRP-2001/06*, Dept., of Structural Engineering, University of California, San Diego, La Jolla, CA.

Henkel (2012). *Technical Data Sheet.* Loctite PL 200 Construction Adhesive.

Henkel (2013). *Technical Data Sheet.* Loctite PL 375 VOC Heavy Duty Construction Adhesive.

Henkel (2012). *Technical Data Sheet.* OSI Green Series F-38 Drywall and Panel Adhesive.

Kirkham W. (2013). *State-of-the-Art: Seismic Behavior of Wood-Frame Residential Structures*, American Society of Civil Engineers, Reston, VA.

Krawinkler H., Parisi F., Ibarra L., Ayoub A., Medina, R (2000). Development of a testing protocol for woodframe structures*, CUREE Publication No. W-02*, Consortium of Universities for Research in Earthquake Engineering,, Richmond, CA.

Lew K.S. (1994). *The January 17, 1994, Northridge earthquake, California*, *NIST SP 871*, National Institute of Standards and Technology, Noel J. Raufaste, Jr., Ed., pp. 375–426, Gaithersburg, MD.

Liquid Nails (2009). *Technical Information*. Liquid Nails Drywall Construction Adhesive.

Liquid Nails (2009). *Technical Information*. Liquid Nails Drywall Construction Adhesive.

Liquid Nails (2011). *Technical Information.* Liquid Nails Heavy Duty Construction Adhesive.

Liquid Nails (2011). *Technical Information*. Liquid Nails Projects Construction Adhesive.

McKenna F. Fenves G.L., Scott M.H., Jeremic B. (2000). *Open System for Earthquake Engineering Simulation (OpenSees)*, Pacific Earthquake Engineering Research Center, University of California, Berkeley, CA.

Pardoen G.C., Waltman A., Kazanjv R., Freund E., Hamilton C. (2003). Testing and analysis of one-story and two-story shearwalls under cyclic loading, *CUREE Report W-25,* Task 1.4.4, Consortium of Universities for Research in Earthquake Engineering,, Richmond, CA.

19. Modeling of Light-Frame Unibody Residential Buildings

Geffen Oren

ABSTRACT

In an effort to enhance the resiliency of light-frame residential buildings so that large economic losses due to damage can be avoided in the event of a major earthquake, researchers have begun to explore the unibody approach. This method attempts to unify structural and architectural components so that they both work to resist earthquake loads. Specifically, it calls for the addition of hold-downs, anchorages, and adhesive between framing elements and gypsum wallboard in light-frame partition walls as a way to strengthen and stiffen the connection between these components and thereby a residential building as a whole. To further examine this approach to seismic design, this paper proposes a simplified OpenSees hysteretic model for light-frame unibody residential buildings. It makes use of existing experimental and analytical data to better represent the overall behavior of such structures. The model is constructed for two wall specimens and one room specimen, which is then verified against cyclic loading tests for the these specimens. Good correlation to the structural data is achieved.

19.1 INTRODUCTION

In the U.S., light-frame structures provide a large percentage of housing and thereby comprise a major part of our built environment. Constructed from wood or cold-formed steel framing elements and sheathing such as gypsum and plywood, these types of buildings have been demonstrated to be generally safe and resilient against collapse in the event of a major earthquake. However, the damage afflicted to these structures tends to be significant and can result in large economic losses for a region. For example, the 1994 M_w 6.7 Northridge earthquake, in the Los Angeles area created $20 billion in losses to light-frame residential buildings, forming more than half of the total losses engendered by the earthquake [Sinha and Gupta 2009]. Figure 19.1 shows clearly the level of damage done by the earthquake to a house in Santa Monica, California. Moreover, events like this one have the potential to displace large segments of the population for long periods of time, exacerbating economic losses for an area. It was predicted that 160,000 to 250,000 households would need to relocate if the 1906 San Francisco earthquake were to repeat itself in the present-day city [Jones et al. 2008]. In order to prevent such natural disasters from turning into economic and social catastrophes, efforts must be made to strengthen and enhance light-frame construction. National earthquake resiliency depends on research in earthquake engineering of light-frame structures to guide and inform emergency planning and prevention programs to ensure safer cities and buildings.

Figure 19.1 A close up of a house in Santa Monica damaged heavily by the 1994 Northridge Earthquake and in need of costly reparations [FEMA 1994].

Fortunately, new developments in this field have provided a few simple and cost-effective ways to increase the lateral strength and stiffness of light-frame residential buildings. One emerging method, referred herein as the unibody approach, involves strengthening and stiffening partition walls so they too can provide a house with greater resistance to lateral forces. Typically, the contribution of partition or architectural walls in light-frame residential buildings is highly penalized or neglected. Such structures are designed by sizing plywood or oriented strand board (OSB) sheathed shear walls to handle all of the lateral force during the lifetime of the building. This design methodology, however, creates structures that reach lateral strength at large story shears, leading to considerable damage. The conventional methodology does not take advantage of the abundant partition wall space in a residential building that can be used to stiffen and strengthen the house.

The unibody approach seeks to amend this design flaw by taking architectural components—such as partition walls—and making them structural components through the use of adhesives as well as anchorages and hold-downs, which are rarely present in partition walls. In addition to fasteners, adhesives possess the ability to strengthen and stiffen the bond between framing elements and sheathing in the construction of light-frame structures. In a study conducted at Stanford University, the contribution of adhesive towards the gypsum-to-framing connection was measured through a series of small wall tests. Test results comparing specimens with and without adhesive demonstrated that the additive was capable of increasing a wood-frame gypsum wall's strength by 86% and stiffness by more than twofold [Swensen et al. 2011]. This study demonstrated incorporating adhesive can significantly augment a house's earthquake resilience.

As walls and larger structural systems that incorporate adhesive start to be tested monotonically and cyclically in research facilities, it is vital to also develop computer models that accurately characterize this enhanced light-frame construction. Earthquake engineering strives for performance-based design and thus needs simplified computer models to dictate the design of these new types of buildings. As such, this paper will discuss a simplified OpenSees model [McKenna et al. 2000] that accounts for the addition of adhesive between gypsum wallboard and wood framing elements for light-frame residential buildings. The model is verified by comparing the force-displacement data obtained from two wall specimens tested at California State University, Sacramento, and a room specimen tested at the nees@berkeley Laboratory at the UC Berkeley's Richmond Field Station.

19.2 BACKGROUND

The testing and modeling of light-frame structures began in the 1940s when researchers took interest in the racking strength of wood-frame shear walls [van de Lindt 2004]. Since then a few highly sophisticated modeling techniques have been developed that accurately characterize the behavior of light-frame residential buildings. Earthquake engineers have developed both detailed models for smaller structural assemblies such as walls, as well as simplified models for larger systems including entire houses. While detailed finite element analysis models with discreet fasteners in a framed shear wall exist, other models make use of simplifications and assumptions that stem from existing experimental or analytical data to avoid being computationally heavy. The model proposed in this paper follows the latter style, namely, matching behavior to that of tested unibody light-frame walls. Relevant research is displayed below to provide some context into this type of modeling.

Generally, the three-dimensional detailed finite element modeling of light-frame wood structures breaks larger structures into subassemblies and joints. These subassemblies consist of shear walls, floor/roof diaphragms, and inter-component connections that tie these components together [Kasal et al. 1994; Tarabia and Itani 1997; Collins et al. 2005]. The structural systems tend to be modeled with shell elements to represent the sheathing, beam elements to model framing, and nonlinear hysteretic springs to account for the nonlinearity of the sheathing-to-framing connections as well as the inter-components, i.e., wall-to-wall, connections [Collins et al. 2005; He et al. 2001]. Depending on how detailed the model is, the amount of structural components considered may increase. For example, Tarabia and Itani [1997] incorporated sheathing interface elements meant to represent the interaction between adjacent sheathing panels as well as frame connector elements designed to account for the rotation and bending in stud-to-stud connections in addition to the framing, sheathing, and fastener elements described. Along similar lines, certain diaphragms in a three-dimensional representation of a house tend to require more modeling than others. In most cases, floor and roof diaphragms are assumed to act linear elastically, and therefore do not include as many modeling components as wall systems [Kasal et al. 1994; Xu and Dolan 2000; Collins et al. 2005]. Schmidt and Moody (1989) and many others modeled these floor and roof diaphragms as rigid shell elements to account for this simplification.

Most of the nonlinearity as well as the in-plane strength and stiffness of light-frame structures is assumed to develop in the framing-to-sheathing connection made by fasteners, i.e., nails and screws [Tarabia and Itani 1997]. Because fasteners are ubiquitous in light-frame structures, the simplified models tend to sidestep modeling every fastener by lumping them together in the form of one or two diagonal hysteretic springs that span between beam (framing) elements. The framing elements providing the axial stiffness of the model are commonly modeled as linear-elastic rigid truss elements, made stable by the diagonal springs [Kasal et al., 1994; Xu and Dolan 2000; Collins et al. 2005]; Figure 19.2 is a graphical representation of this concept. The properties of these diagonal springs produce the governing hysteric behavior of the model and are manipulated to match either existing empirical tests or results from detailed finite element simulations by varying the values of certain parameters linked to strength and stiffness models and backbone curves.

Over time, such models have evolved and built off one another to become more sophisticated, making use of more parameters to better represent the complicated hysteretic patterns in light-frame residential buildings, such as pinching as well as stiffness and strength deterioration. For example, Foliente [1995] extended the Bouc-Wen-Baber-Noori model of light-frame hysteresis with more parameters to include pinching and linear strength and stiffness degradation. Folz and Filiatrault [2001] expanded upon this model when creating the ten-parameter CASHEW Model under the CUREE-Caltech Wood-frame Project, which includes a built-in shear wall parameter calculator, making the model very appealing for simple analysis. Finally, Pang et al. [2007] adding seven more parameters to the CASHEW model so that it could more effectively characterize the nonlinear unloading strength and stiffness degradation patterns in light-frame hysteresis.

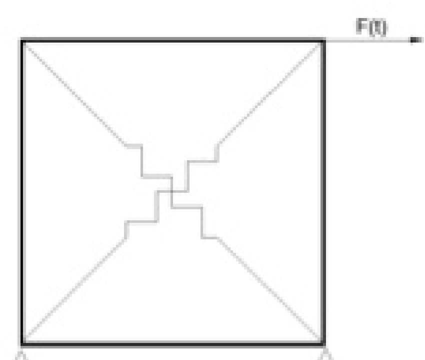

Figure 19.2 The Diagonal Hysteretic Spring Model.

Most of the models described follow the design principles and codes of current light-frame construction, namely that houses are built to withstand lateral force by the presence of plywood or OSB shear walls. A few of the models, such as the CASHEW model, can be used to predict the behavior of gypsum walls built with mechanical fasteners alone. Kavinde and Deierlein [2003] developed an analytical model for gypsum drywall partitions. Their parametric-mechanics based model incorporates a few supplementary parameters in addition to those for strength and stiffness degradation to represent overturning, wall strength, and wall panel end bearing influenced by the presence openings, such as doors or windows, in gypsum dry walls. Yet none of the previous research mentioned has provided a model for the contribution of adhesive in gypsum-to-sheathing connections. As such, this proposed model seeks to extend the research of unibody light-frame structures by accounting for the additional strength and stiffness adhesive provides to gypsum partition walls.

19.3 MODEL STRUCTURE

The proposed light-frame residential building model is constructed in the computer software OpenSees: Open System for Earthquake Engineering Simulation [McKenna et al. 2000]. By adhering to many of the general design principles discussed above, it (1) draws on existing experimental and analytical data; (2) employs diagonal nonlinear link elements to represent the behavior of the fasteners and adhesive; and (3) assumes all other components act linearly. Three specimens were constructed under this model: two wall specimens and one room specimen. The responses obtained from the model were later verified against responses obtained from testing. The details of the model are explained in this section.

19.3.1 Drawing on Existing Data

The proposed model attempts to match the behavior of the wall specimens tested cyclically by A. Hopkins [2013] at California State University, Sacramento. Constructed from gypsum, mechanical fasteners, adhesive, and steel or wood framing, the wall specimens were designed to measure the enhanced strength and stiffness of unibody partition walls. Twenty walls in total were tested, each one possessing a different configuration. A few of the walls had returns on their ends to model the additional stiffness of orthogonal walls framing into partition walls. Differences among walls specimens in terms of hysteresis, strength, and stiffness were measured.

Although the tests provided meaningful data in determining the effects of adhesive and/or returns in a partition wall, not enough walls were tested to develop the necessary relationship between the wall aspect ratio and the resultant stiffness of a unibody wall to assemble a simplified computer model of a light-frame structure. As a result, a highly detailed finite element model in ABAQUS was constructed to fill in the gaps in the testing data. This model simulated cyclic loading on unibody walls of various sizes without returns. The relationship between stiffness and length of wall, i.e., aspect ratio, for these simulations as well as for the tests conducted at California State University at Sacramento were measured and are plotted in Figure

19.3. This relationship provides a way to calculate the parameters in the model that control the shape of the hysteresis loops for a cyclic loading simulation.

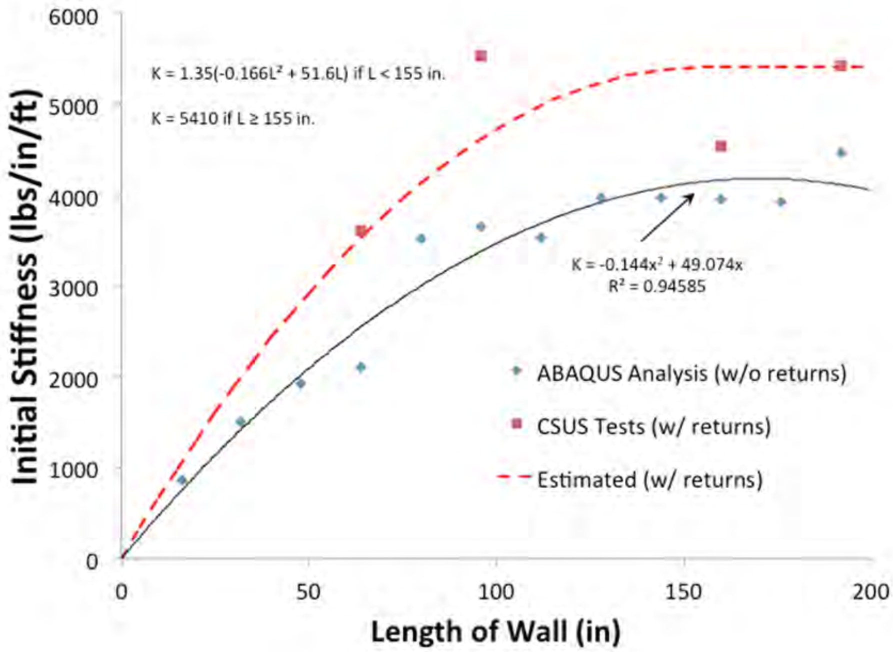

Figure 19.3 The effect of aspect ratio on initial stiffness for unibody walls.

19.3.2 OpenSees Framework

OpenSees was chosen as the software framework to design the model because of its wide variety of uniaxial material models. Users have access to sophisticated parametric models that can be assigned to elements and simulate high levels of nonlinearity. This feature is crucial in modeling light-frame residential buildings, as such structures display complicated hysteretic behavior. OpenSees tends to provide a less detail-oriented framework than ABAQUS, allowing for simplifications to be incorporated into the model. Thus, excessively detailed modeling could be avoided.

19.3.3 Assumptions

To construct the simplified model, the following assumptions were implemented: (1) the majority of the nonlinearity in the structure originated in the gypsum-to-sheathing connection; (2) all other elements and components act rigidly; (3) the walls have no out-of-plane stiffness; (4) inter-component connections, frame connector elements, and hold-downs are incorporated in the hysteretic wall model, and (5) the relationship between stiffness and aspect ratio in unibody walls without returns discovered through the ABAQUS analysis dictates the behavior assigned to each wall.

This last assumption influenced how the proposed model addresses openings in the wall. If openings are present in the specimen, the walls affected were broken down into subwalls, divided by where the openings lie as shown in Figure 19.4 with the hatched areas signifying openings and the number zones representing individual subwalls. Each subwall was assigned its own strength and stiffness through the relationship between stiffness and aspect ratio discussed.

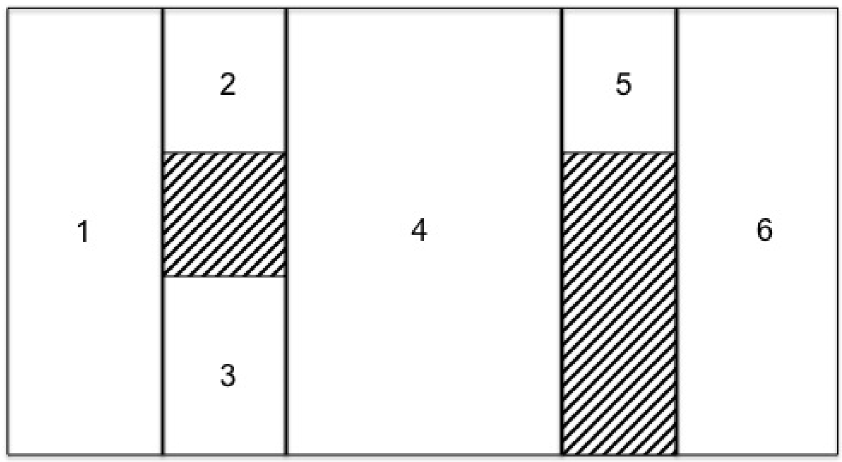

Figure 19.4 A wall broken into subwalls to account for the presence of openings in the model.

19.3.4 Model Composition

In keeping with these assumptions and following the logic of previous research, the model incorporated the following key features: diagonal nonlinear spring elements, pin-ended rigid framing elements, and a rigid floor/roof diaphragm if present.

The diagonal nonlinear spring elements account for the hysteretic behavior of the framing-to-sheathing connection made by fasteners and adhesive. In addition, they absorb the structural properties of the gypsum sheathing. These elements were modeled in OpenSees with *Two-Node Link Elements*. Because it is assumed that walls do not carry out-of-plane stiffness, no shell elements were included in the model. Pinned at their ends, the link elements span diagonally between vertical framing elements, providing stability to the model. To simplify the model, only one set of diagonal link elements was used above and below openings, meaning that a few of the vertical framing elements in these regions were not included in the model.

These elements were assigned two uniaxial material models available in OpenSees: the SAWS Model and the Modified Ibarra-Medina-Krawinkler Deterioration Model with Peak-Oriented Hysteretic Response. The first material model (see Figure 19.5) accounts for the hysteretic behavior of gypsum-to-framing screw fasteners; the second model (see Figure 19.6) represents the behavior of the adhesive. Both graphs provide a sense of the type and quantity of parameters used to manipulate the hysteresis loops under a cyclic loading simulation. These two material models were chosen out of the available models in OpenSees for their simplicity and great ability to capture the important behavior of the walls. Their accuracy can be seen in the next section where these models are verified against the response of the two wall specimens.

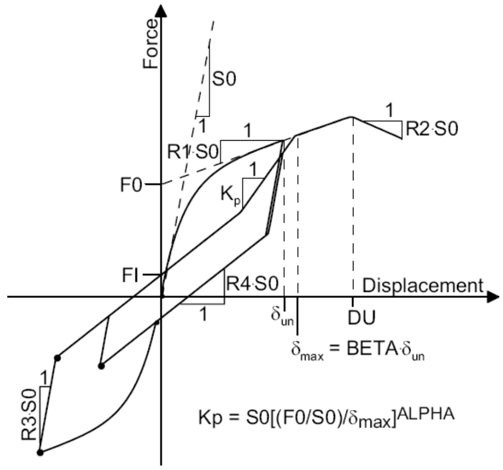

Figure 19.5 SAWS Material Model [OpenSees Wiki (a)].

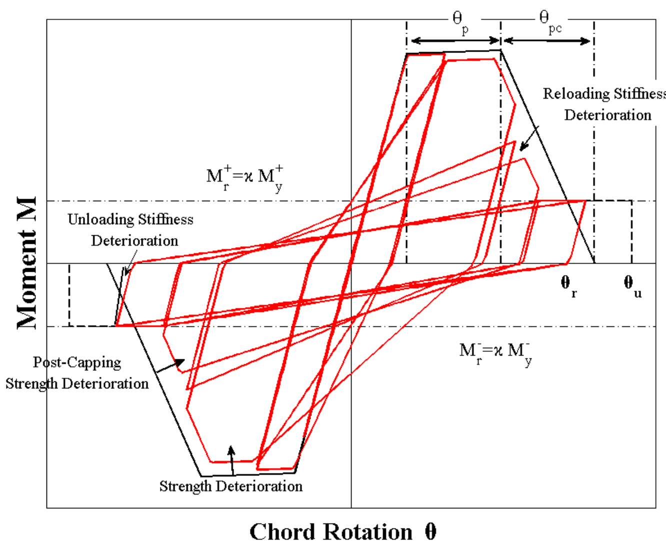

Figure 19.6 The modified Ibarra-Medina-Krawinkler Deterioration Model with Peak-Oriented Hysteretic Response [OpenSees Wiki (b)].

Truss elements were employed to model the majority of vertical framing elements. Each truss element was assigned the following parameters: square cross-sectional area of 400 in.^{2}; Young's Modulus of 29000; I_x of 13333 in.^{4}; and I_y of 13333 in.^{4} to act rigidly and to allow the diagonal link elements to govern the behavior of the model. However, in the event that a vertical framing element intersected with the boundary of an opening in a wall, an elastic beam column spanning from the bottom to the top of a wall was used instead to provide stability to the model. These elastic beam columns were assigned the same physical properties as the truss elements.

Horizontal framing elements were treated similarly. Elastic beam columns with the same proprieties were employed to model the horizontal elements denoting the top and bottom of a floor/roof diaphragm and the top of a parapet if present. On the other hand, truss elements with the same properties were used to model horizontal elements framing the openings.

Lastly, the floor/roof diaphragms were ensured to act rigidly with the *EqualDOF* command. This tool in OpenSees forces nodes to act in the same manner with regard to certain degrees-of-freedom. The nodes on the bottom and the top of these diaphragms were constrained to act the same way in six degrees-of-freedom, making the diaphragm infinity rigid. Although OpenSees does not have a graphical interface, a representation of what the model would like for a room specimen (without the detailing for the floor diaphragm) is exhibited in Figure 19.7

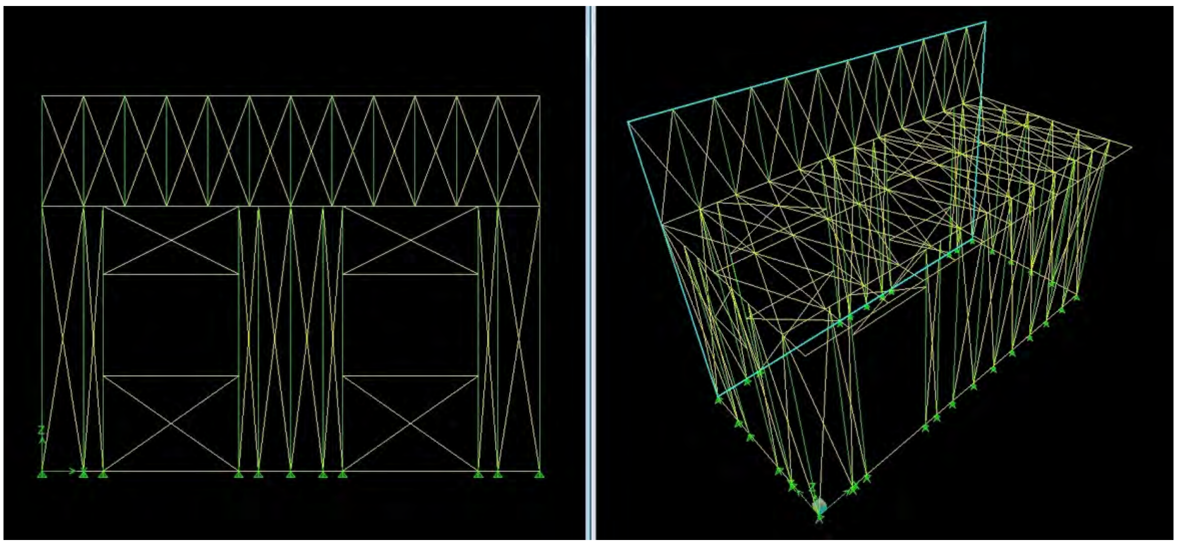

(a) (b)

Figure 19.7 A graphical representation of the OpenSees model: (a) with a wall elevation; and (b) a three-dimensional orthographic view.

19.4 MODEL VERIFICATION

To verify the proposed model, two wall specimens and one room specimen were constructed and were compared against the response obtained from structural tests. Good correlation was achieved between the analytical and empirical data for all three specimens. However, the correlation proved to be stronger for the wall tests than for the room test. Moreover, the model matched the hysteretic behavior of light-frame unibody structures better during the earlier stages of hysteresis than during the nonlinear stages.

19.4.1 Wall Models

Two walls specimens measuring 8 ft×8 ft were tested cyclically at California State University, Sacramento. Each specimen was built with a vertical stud every 16 in. and did not include openings. The first wall specimen was constructed to represent a conventional wall; namely, it only used mechanical fasteners to connect the gypsum sheathing to the framing elements. The second wall represented the unibody approach by adding adhesive to this connection. Both specimens were drawn up under the proposed model and simulated by running the same loading protocol. The first specimen only made use of the SAWS Material Model and the second employed both the SAWS Material Model and the Modified Ibarra-Medina-Krawinkler Deterioration Model with Peak-Oriented Hysteretic Response to include the effect of adhesive. These two tests are compared against the model simulations in Figures 19.8 and 19.9.

The comparison between the analytical and experiential data demonstrates that the SAWS Material Model and ModIMKPeakOriented Model work exceptionally well to model the behavior of gypsum walls built with both mechanical and adhesive fasteners. The force versus displacement graphs for Wall 1 match well until ±1.5 in. of displacement, revealing that the SAWS Model accurately predicts the nonlinear behavior of conventional wood-frame structures. The comparison for Wall 2 also shows great alignment between the model and the test data. Moreover, the pinching present in the experiential and analytical data seems to overlap completely. However, the two graphs for Wall 2 only match up to ±1 in. of displacement. Although it is assumed that a similar light-frame structure would not reach such a high level of displacement in a large earthquake event, it would still be beneficial to refine this model so that it aligns itself with such high levels of nonlinear deformation.

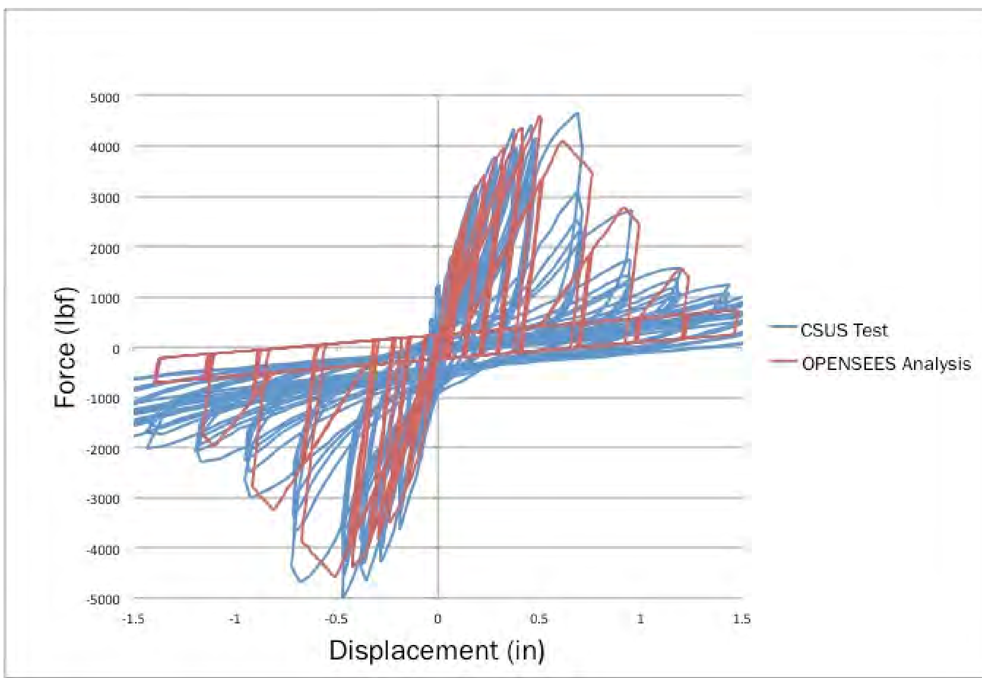

Figure 19.8 Wall 1: comparison of OpenSees analysis with the test data.

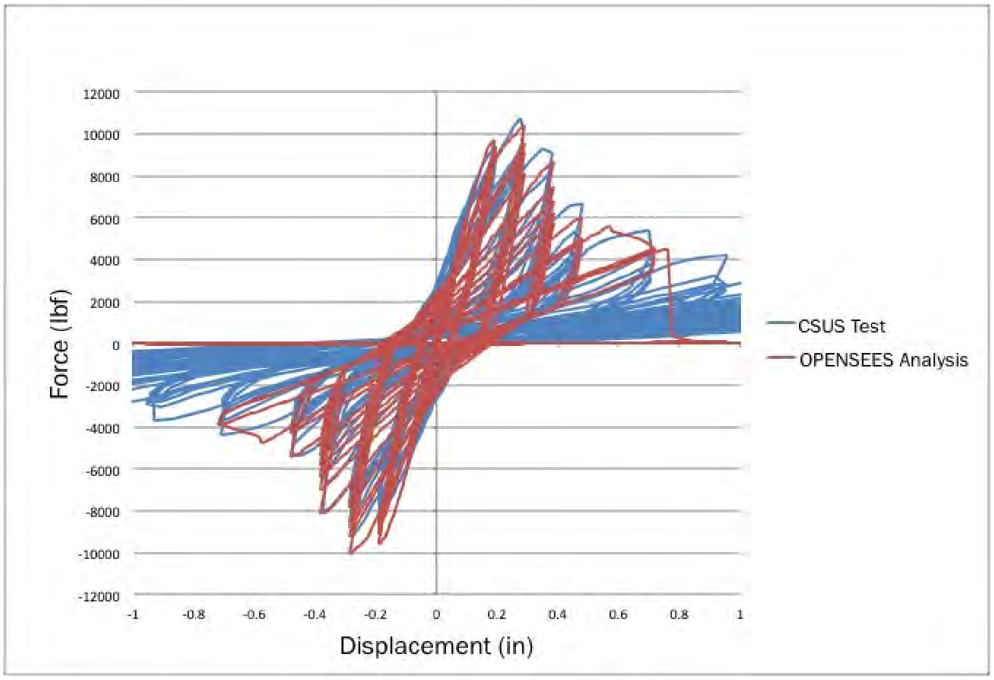

Figure 19.9 Wall 2: comparison of OpenSees analysis with the test data.

19.4.2 Room Model

Extending the research to larger structural systems, the model was verified against a room specimen tested cyclically at the NEES Laboratory at UC Berkeley's Richmond Field Station. The room specimen was built with adhesive, mechanical fasteners, framing elements, and gypsum wallboard to examine the behavior of light-frame unibody structures. Figure 19.10 displays the framing of the room specimen, which was tested by fixing the top diaphragm with an actuator and moving the floor of the specimen with a shake table. Following the design principles mentioned, a model was constructed with the same layout and loading protocol as that of the test. Figure 19.11 compares the analytical and empirical force versus the displacement data obtained from the test.

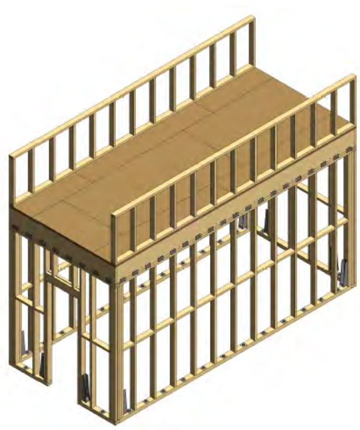

Figure 19.10 Room 1: framing details of test specimen.

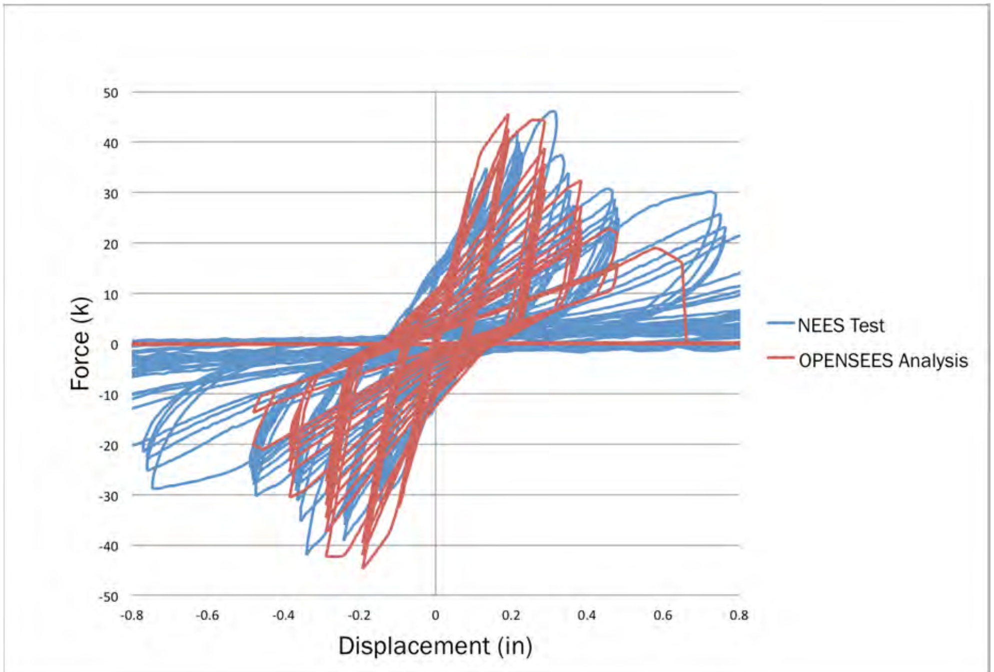

Figure 19.11 Room 1: comparison of OpenSees analysis with the test data.

Overall, the analytical results seem to match the test data fairly well, especially before the displacement reached ±0.4 in. or around ±0.4% drift, with pinching represented accurately in the model. In particular, at very low levels of deformation, the model seemed to match up perfectly. Figure 19.12 reveals the strong correlation between the initial stiffnesses of the model and of the test. Unfortunately, the model does not characterize the behavior of the light-frame unibody structures at large nonlinear deformations. That said, it is assumed that a unibody residential building would not reach such high levels of displacement under large earthquake loads. Therefore, the model appears to provide a good enough assessment of the light-frame unibody structure.

To gain addition insight into the performance of the model, Figure 19.13 compares the hysteretic energy dissipated during the model simulation and the testing protocol. The two graphs seem to run parallel, almost overlapping from a cumulative displacement of 0 to 25 in. Although the energy dissipated for the empirical data continued to increase after 25 in., the analytical data began to demonstrate asymptotic behavior. In this way, the model does not provide a very accurate representation of the light-frame unibody structure. However, it is possible that because many more data points were collected during the test than during the model simulation, high levels of data noise may have affected the dissipated energy measured during the testing protocol.

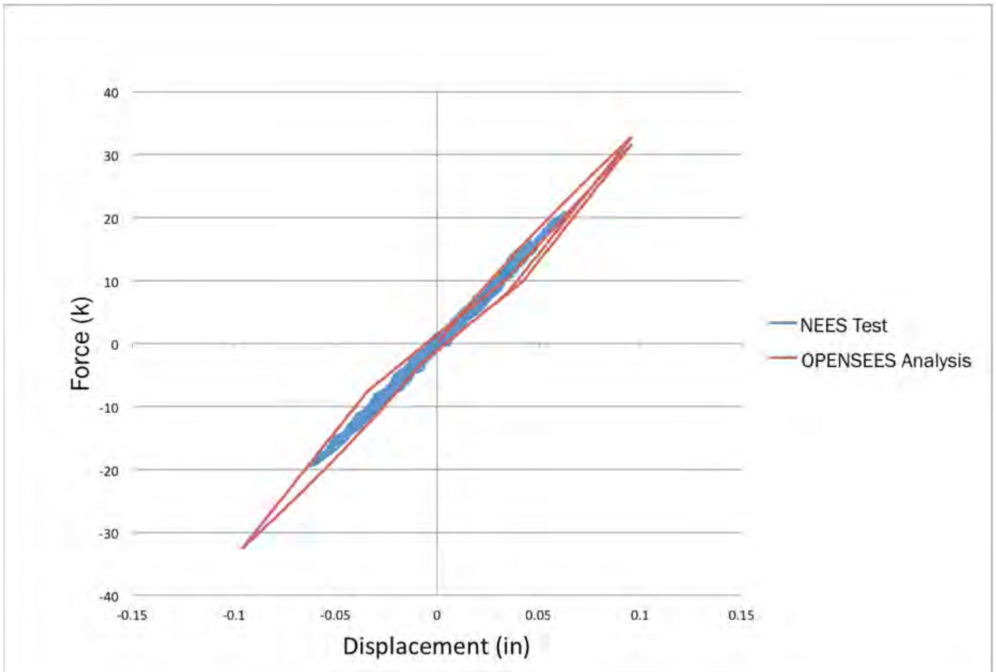

Figure 19.12 Room 1: Comparison between the initial stiffnesses derived from OpenSees analysis versus test data.

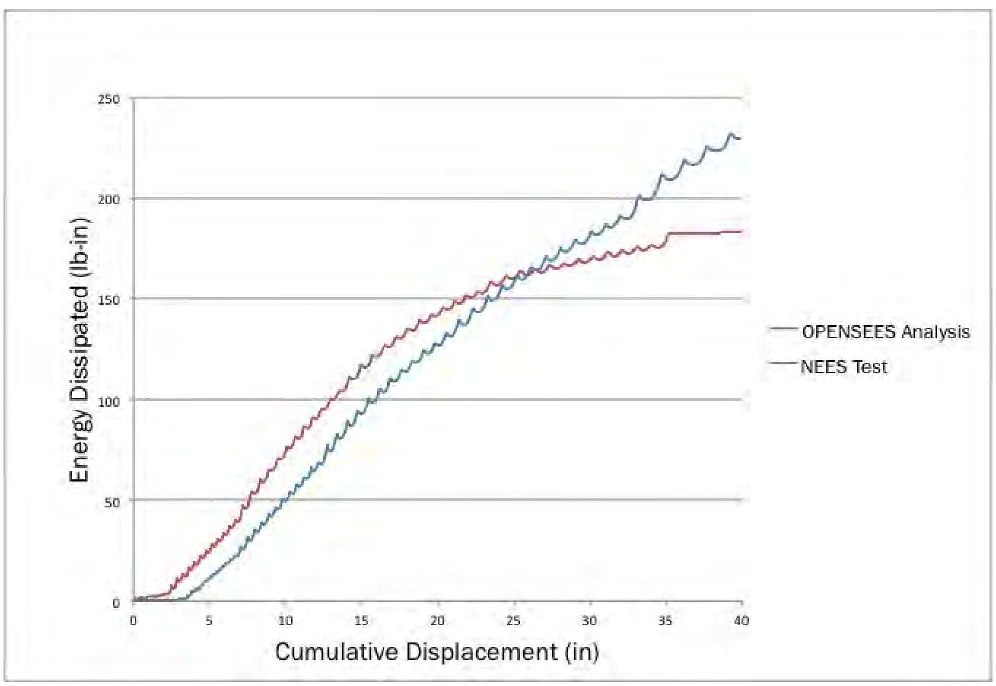

Figure 19.13 Room 1: Comparison between the hysteretic energy dissipation derived from OpenSees analysis versus test data.

19.5 SUMMARY AND CONCLUSIONS

Proposed herein is a simplified hysteretic model for light-frame unibody residential buildings. Aligning itself to existing data, the model made use of diagonal hysteretic spring elements to characterize effectively the nonlinear strength and stiffness deterioration of light-frame unibody structures under cyclic loading. The model was verified for two wall specimens and one room specimen tested cyclically. The model seemed to perform better under lower levels of displacement, indicated both by the force versus displacement data and by the energy dissipation data; overall, it correlated well with the empirical data.

Many more specimens including a house specimen were created and simulated under this model framework but have not been discussed in this paper due to the lack to empirical data available. Once more room tests as well as the house test are completed, this model can be further verified to better understand its performance. Such data would then increase the significance of the proposed model.

19.6 ACKNOWLEDGMENTS

I would like to thank PEER for this wonderful opportunity to engage in such meaningful research. In particular, I owe deep appreciation to Heidi Tremayne for organizing this research internship as well as the outreach events with the other PEER interns. Lastly, I would like to thank my mentors, Professors Gregory Deierlein and Eduardo Miranda, and graduate student Scott Swensen, for taking me on as an intern and making my experience educative and profoundly rewarding.

19.7 REFERENCES

Kavinde A.M., Deierlein G.G. (2006). Analytical models for the seismic performance of gypsum drywall partitions, *Earthq. Spectra*, 22(2): 391–411.

Collins M., Kasal B., Paevere P., Foliente G. (2005). Three-dimensional model of light frame wood buildings. I: Model description, *J. Struct. Eng*., 131(4): 676–683.

FEMA (1994). *Northridge Earthquake, California,* Photograph, Federal Emergency Management Agency, 1 Jan. 1994. 20 Sept. 2013.

Foliente G. (1995). Hysteresis modeling of wood joints and structural systems, *J. Struct. Eng*., 121(6): 1013–1022.

Folz B., Filiatrault A. (2001). Cyclic analysis of wood shear walls, *J. Struct. Eng*., 127(4): 433–441.

He M., Lam F., Foschi R. (2001). Modeling three-dimensional timber light-frame buildings, *J. Struct. Eng*., 127(8): 901–913.

Hopkins A. (2013). *Large-scale Tests of Seismically Enhanced Planar Walls for Residential Construction*, Master's Thesis, California State University, Sacramento, CA.

Jones L.M. et al. (2008). The ShakeOut scenario, U.S. Geological Survey, *Open File Report 2008–1150*. (available at http://pubs.usgs.gov/of/2008/1150/).

Kasal B., Leichti R., Itani R. (1994). Nonlinear finite-element model of complete light-frame wood structures, *J. Struct. Eng*., 120(1): 100–119.

McKenna F. Fenves G.L., Scott M.H., Jeremic B. (2000). *Open System for Earthquake Engineering Simulation (OpenSees)*, Pacific Earthquake Engineering Research Center, University of California, Berkeley, CA.

OpenSees Wiki (a). *"Folz Figure."* Graph. 2009. 20 Sept. 2013.

OpenSees Wiki (b). *"ModIMKPeakOriented Definition Figure."* Graph. 2012. 20 Sept. 2013.

Pang W., Rosowsky D., Pei S., van de Lindt J. (2007). Evolutionary parameter hysteretic model for wood shear walls. *J. Struct. Eng*., 133(8): 1118–1129.

Patton-Mallory M., Wolfe R., Soltis L., Gutkowski R. (1985). Light-frame shear wall length and opening effects, *J. Struct. Eng.,* 111(10): 2227–2239.

Schmidt R., Moody R. (1989). Modeling laterally loaded light-frame buildings, *J. Struct. Eng*., 115(1): 201–217.

Sinha A., Gupta R. (2009). Strain distribution in OSB and GWB in wood-frame shear walls. *J. Struct. Eng*., 135(6): 666–675.

Swensen S., Deierlein G., Miranda E. (2011). Monotonic and cyclic behavior of adhesive-gypsum to-framing connections and scaled light framed walls, Department of Civil and Environmental Engineering, Stanford University, Stanford, CA.

Tarabia A., Itani R. (1997a). Static and dynamic modeling of light-frame wood buildings, *Computers and Struct*., 63(2): 319–334.

Tarabia A., Itani R. (1997b). Seismic response of light-frame wood buildings, *J. Struct. Eng*., 135(8): 968–976.

van de Lindt J. (2004). Evolution of wood shear wall testing, modeling, and reliability analysis: Bibliography, *Pract. Period. Struct. Des. Constr.*, 9(1): 44–53.

Xu J., Dolan J. (2009). Development of a wood-frame shear wall model in ABAQUS, *J. Struct. Eng*., 135(8): 977–984.

PEER REPORTS

PEER reports are available as a free PDF download from http://peer.berkeley.edu/publications/peer_reports_complete.html. Printed hard copies of PEER reports can be ordered directly from our printer by following the instructions at http://peer.berkeley.edu/publications/peer_reports.html. For other related questions about the PEER Report Series, contact the Pacific Earthquake Engineering Research Center, 325 Davis Hall mail code 1792, Berkeley, CA 94720. Tel.: (510) 642-3437; Fax: (510) 665-1655; Email: peer_editor@berkeley.edu

PEER 2013/25 *Earthquake Engineering for Resilient Communities: 2013 PEER Internship Program Research Report Collection.* Heidi Tremayne (Editor), Stephen A. Mahin (Editor), Jorge Archbold Monterossa, Matt Brosman, Shelly Dean, Katherine deLaveaga, Curtis Fong, Donovan Holder, Elizabeth Jachens, Rakeeb Khan, David Lam, Daniela Martinez Lopez, Mara Minner, Geffen Oren, Julia Pavicic, Melissa Quinonez, Lorena Rodriguez, Sean Salazar, Kelli Slaven, Vivian Steyert, Jenny Taing, and Salvador Tena. December 2013.

PEER 2013/24 *NGA-West2 Ground Motion Prediction Equations for Vertical Ground Motions.* September 2013.

PEER 2013/23 *Coordinated Planning and Preparedness for Fire Following Major Earthquakes.* Charles Scawthorn. November 2013.

PEER 2013/22 *GEM-PEER Task 3 Project: Selection of a Global Set of Ground Motion Prediction Equations.* Jonathan P. Stewart, John Douglas, Mohammad B. Javanbarg, Carola Di Alessandro, Yousef Bozorgnia, Norman A. Abrahamson, David M. Boore, Kenneth W. Campbell, Elise Delavaud, Mustafa Erdik and Peter J. Stafford. December 2013.

PEER 2013/21 *Seismic Design and Performance of Bridges with Columns on Rocking Foundations.* Grigorios Antonellis and Marios Panagiotou. September 2013.

PEER 2013/20 *Experimental and Analytical Studies on the Seismic Behavior of Conventional and Hybrid Braced Frames.* Jiun-Wei Lai and Stephen A. Mahin. September 2013.

PEER 2013/19 *Toward Resilient Communities: A Performance-Based Engineering Framework for Design and Evaluation of the Built Environment.* Michael William Mieler, Bozidar Stojadinovic, Robert J. Budnitz, Stephen A. Mahin and Mary C. Comerio. September 2013.

PEER 2013/18 *Identification of Site Parameters that Improve Predictions of Site Amplification.* Ellen M. Rathje and Sara Navidi. July 2013.

PEER 2013/17 *Response Spectrum Analysis of Concrete Gravity Dams Including Dam-Water-Foundation Interaction.* Arnkjell Løkke and Anil K. Chopra. July 2013.

PEER 2013/16 *Effect of hoop reinforcement spacing on the cyclic response of large reinforced concrete special moment frame beams.* Marios Panagiotou, Tea Visnjic, Grigorios Antonellis, Panagiotis Galanis, and Jack P. Moehle. June 2013.

PEER 2013/15 *A Probabilistic Framework to Include the Effects of Near-Fault Directivity in Seismic Hazard Assessment.* Shrey Kumar Shahi, Jack W. Baker. October 2013.

PEER 2013/14 *Hanging-Wall Scaling using Finite-Fault Simulations.* Jennifer L. Donahue and Norman A. Abrahamson. September 2013.

PEER 2013/13 *Semi-Empirical Nonlinear Site Amplification and its Application in NEHRP Site Factors.* Jonathan P. Stewart and Emel Seyhan. November 2013.

PEER 2013/12 *Nonlinear Horizontal Site Response for the NGA-West2 Project.* Ronnie Kamai, Norman A. Abramson, Walter J. Silva. May 2013.

PEER 2013/11 *Epistemic Uncertainty for NGA-West2 Models.* Linda Al Atik and Robert R. Youngs. May 2013.

PEER 2013/10 *NGA-West 2 Models for Ground-Motion Directionality.* Shrey K. Shahi and Jack W. Baker. May 2013.

PEER 2013/09 *Final Report of the NGA-West2 Directivity Working Group.* Paul Spudich, Jeffrey R. Bayless, Jack W. Baker, Brian S.J. Chiou, Badie Rowshandel, Shrey Shahi, and Paul Somerville. May 2013.

PEER 2013/08 *NGA-West2 Model for Estimating Average Horizontal Values of Pseudo-Absolute Spectral Accelerations Generated by Crustal Earthquakes.* I. M. Idriss. May 2013.

PEER 2013/07 *Update of the Chiou and Youngs NGA Ground Motion Model for Average Horizontal Component of Peak Ground Motion and Response Spectra.* Brian Chiou and Robert Youngs. May 2013.

PEER 2013/06 *NGA-West2 Campbell-Bozorgnia Ground Motion Model for the Horizontal Components of PGA, PGV, and 5%-Damped Elastic Pseudo-Acceleration Response Spectra for Periods Ranging from 0.01 to 10 sec.* Kenneth W. Campbell and Yousef Bozorgnia. May 2013.

PEER 2013/05 *NGA-West 2 Equations for Predicting Response Spectral Accelerations for Shallow Crustal Earthquakes.* David M. Boore, Jonathan P. Stewart, Emel Seyhan, Gail M. Atkinson. May 2013.

PEER 2013/04 *Update of the AS08 Ground-Motion Prediction Equations Based on the NGA-West2 Data Set.* Norman Abrahamson, Walter Silva, and Ronnie Kamai. May 2013.

PEER 2013/03 *PEER NGA-West2 Database.* Timothy D. Ancheta, Robert B. Darragh, Jonathan P. Stewart, Emel Seyhan, Walter J. Silva, Brian S.J. Chiou, Katie E. Wooddell, Robert W. Graves, Albert R. Kottke, David M. Boore, Tadahiro Kishida, and Jennifer L. Donahue. May 2013.

PEER 2013/02 *Hybrid Simulation of the Seismic Response of Squat Reinforced Concrete Shear Walls.* Catherine A. Whyte and Bozidar Stojadinovic. May 2013.

PEER 2013/01 *Housing Recovery in Chile: A Qualitative Mid-program Review.* Mary C. Comerio. February 2013.

PEER 2012/08 *Guidelines for Estimation of Shear Wave Velocity.* Bernard R. Wair, Jason T. DeJong, and Thomas Shantz. December 2012.

PEER 2012/07 *Earthquake Engineering for Resilient Communities: 2012 PEER Internship Program Research Report Collection.* Heidi Tremayne (Editor), Stephen A. Mahin (Editor), Collin Anderson, Dustin Cook, Michael Erceg, Carlos Esparza, Jose Jimenez, Dorian Krausz, Andrew Lo, Stephanie Lopez, Nicole McCurdy, Paul Shipman, Alexander Strum, Eduardo Vega. December 2012.

PEER 2012/06 *Fragilities for Precarious Rocks at Yucca Mountain.* Matthew D. Purvance, Rasool Anooshehpoor, and James N. Brune. December 2012.

PEER 2012/05 *Development of Simplified Analysis Procedure for Piles in Laterally Spreading Layered Soils.* Christopher R. McGann, Pedro Arduino, and Peter Mackenzie–Helnwein. December 2012.

PEER 2012/04 *Unbonded Pre-Tensioned Columns for Bridges in Seismic Regions.* Phillip M. Davis, Todd M. Janes, Marc O. Eberhard, and John F. Stanton. December 2012.

PEER 2012/03 *Experimental and Analytical Studies on Reinforced Concrete Buildings with Seismically Vulnerable Beam-Column Joints.* Sangjoon Park and Khalid M. Mosalam. October 2012.

PEER 2012/02 *Seismic Performance of Reinforced Concrete Bridges Allowed to Uplift during Multi-Directional Excitation.* Andres Oscar Espinoza and Stephen A. Mahin. July 2012.

PEER 2012/01 *Spectral Damping Scaling Factors for Shallow Crustal Earthquakes in Active Tectonic Regions.* Sanaz Rezaeian, Yousef Bozorgnia, I. M. Idriss, Kenneth Campbell, Norman Abrahamson, and Walter Silva. July 2012.

PEER 2011/10 *Earthquake Engineering for Resilient Communities: 2011 PEER Internship Program Research Report Collection.* Eds. Heidi Faison and Stephen A. Mahin. December 2011.

PEER 2011/09 *Calibration of Semi-Stochastic Procedure for Simulating High-Frequency Ground Motions.* Jonathan P. Stewart, Emel Seyhan, and Robert W. Graves. December 2011.

PEER 2011/08 *Water Supply in regard to Fire Following Earthquake.* Charles Scawthorn. November 2011.

PEER 2011/07 *Seismic Risk Management in Urban Areas. Proceedings of a U.S.-Iran-Turkey Seismic Workshop*. September 2011.

PEER 2011/06 *The Use of Base Isolation Systems to Achieve Complex Seismic Performance Objectives.* Troy A. Morgan and Stephen A. Mahin. July 2011.

PEER 2011/05 *Case Studies of the Seismic Performance of Tall Buildings Designed by Alternative Means.* Task 12 Report for the Tall Buildings Initiative. Jack Moehle, Yousef Bozorgnia, Nirmal Jayaram, Pierson Jones, Mohsen Rahnama, Nilesh Shome, Zeynep Tuna, John Wallace, Tony Yang, and Farzin Zareian. July 2011.

PEER 2011/04 *Recommended Design Practice for Pile Foundations in Laterally Spreading Ground.* Scott A. Ashford, Ross W. Boulanger, and Scott J. Brandenberg. June 2011.

PEER 2011/03 *New Ground Motion Selection Procedures and Selected Motions for the PEER Transportation Research Program.* Jack W. Baker, Ting Lin, Shrey K. Shahi, and Nirmal Jayaram. March 2011.

PEER 2011/02 *A Bayesian Network Methodology for Infrastructure Seismic Risk Assessment and Decision Support.* Michelle T. Bensi, Armen Der Kiureghian, and Daniel Straub. March 2011.

PEER 2011/01 *Demand Fragility Surfaces for Bridges in Liquefied and Laterally Spreading Ground.* Scott J. Brandenberg, Jian Zhang, Pirooz Kashighandi, Yili Huo, and Minxing Zhao. March 2011.

PEER 2010/05 *Guidelines for Performance-Based Seismic Design of Tall Buildings.* Developed by the Tall Buildings Initiative. November 2010.

PEER 2010/04 *Application Guide for the Design of Flexible and Rigid Bus Connections between Substation Equipment Subjected to Earthquakes.* Jean-Bernard Dastous and Armen Der Kiureghian. September 2010.

PEER 2010/03 *Shear Wave Velocity as a Statistical Function of Standard Penetration Test Resistance and Vertical Effective Stress at Caltrans Bridge Sites.* Scott J. Brandenberg, Naresh Bellana, and Thomas Shantz. June 2010.

PEER 2010/02 *Stochastic Modeling and Simulation of Ground Motions for Performance-Based Earthquake Engineering.* Sanaz Rezaeian and Armen Der Kiureghian. June 2010.

PEER 2010/01 *Structural Response and Cost Characterization of Bridge Construction Using Seismic Performance Enhancement Strategies.* Ady Aviram, Božidar Stojadinović, Gustavo J. Parra-Montesinos, and Kevin R. Mackie. March 2010.

PEER 2009/03 *The Integration of Experimental and Simulation Data in the Study of Reinforced Concrete Bridge Systems Including Soil-Foundation-Structure Interaction.* Matthew Dryden and Gregory L. Fenves. November 2009.

PEER 2009/02 *Improving Earthquake Mitigation through Innovations and Applications in Seismic Science, Engineering, Communication, and Response. Proceedings of a U.S.-Iran Seismic Workshop.* October 2009.

PEER 2009/01 *Evaluation of Ground Motion Selection and Modification Methods: Predicting Median Interstory Drift Response of Buildings.* Curt B. Haselton, Ed. June 2009.

PEER 2008/10 *Technical Manual for Strata.* Albert R. Kottke and Ellen M. Rathje. February 2009.

PEER 2008/09 *NGA Model for Average Horizontal Component of Peak Ground Motion and Response Spectra.* Brian S.-J. Chiou and Robert R. Youngs. November 2008.

PEER 2008/08 *Toward Earthquake-Resistant Design of Concentrically Braced Steel Structures.* Patxi Uriz and Stephen A. Mahin. November 2008.

PEER 2008/07 *Using OpenSees for Performance-Based Evaluation of Bridges on Liquefiable Soils.* Stephen L. Kramer, Pedro Arduino, and HyungSuk Shin. November 2008.

PEER 2008/06 *Shaking Table Tests and Numerical Investigation of Self-Centering Reinforced Concrete Bridge Columns.* Hyung IL Jeong, Junichi Sakai, and Stephen A. Mahin. September 2008.

PEER 2008/05 *Performance-Based Earthquake Engineering Design Evaluation Procedure for Bridge Foundations Undergoing Liquefaction-Induced Lateral Ground Displacement.* Christian A. Ledezma and Jonathan D. Bray. August 2008.

PEER 2008/04 *Benchmarking of Nonlinear Geotechnical Ground Response Analysis Procedures.* Jonathan P. Stewart, Annie On-Lei Kwok, Yousseff M. A. Hashash, Neven Matasovic, Robert Pyke, Zhiliang Wang, and Zhaohui Yang. August 2008.

PEER 2008/03 *Guidelines for Nonlinear Analysis of Bridge Structures in California.* Ady Aviram, Kevin R. Mackie, and Božidar Stojadinović. August 2008.

PEER 2008/02 *Treatment of Uncertainties in Seismic-Risk Analysis of Transportation Systems.* Evangelos Stergiou and Anne S. Kiremidjian. July 2008.

PEER 2008/01 *Seismic Performance Objectives for Tall Buildings.* William T. Holmes, Charles Kircher, William Petak, and Nabih Youssef. August 2008.

PEER 2007/12 *An Assessment to Benchmark the Seismic Performance of a Code-Conforming Reinforced Concrete Moment-Frame Building.* Curt Haselton, Christine A. Goulet, Judith Mitrani-Reiser, James L. Beck, Gregory G. Deierlein, Keith A. Porter, Jonathan P. Stewart, and Ertugrul Taciroglu. August 2008.

PEER 2007/11 *Bar Buckling in Reinforced Concrete Bridge Columns.* Wayne A. Brown, Dawn E. Lehman, and John F. Stanton. February 2008.

PEER 2007/10 *Computational Modeling of Progressive Collapse in Reinforced Concrete Frame Structures.* Mohamed M. Talaat and Khalid M. Mosalam. May 2008.

PEER 2007/09 *Integrated Probabilistic Performance-Based Evaluation of Benchmark Reinforced Concrete Bridges.* Kevin R. Mackie, John-Michael Wong, and Božidar Stojadinović. January 2008.

PEER 2007/08 *Assessing Seismic Collapse Safety of Modern Reinforced Concrete Moment-Frame Buildings.* Curt B. Haselton and Gregory G. Deierlein. February 2008.

PEER 2007/07 *Performance Modeling Strategies for Modern Reinforced Concrete Bridge Columns.* Michael P. Berry and Marc O. Eberhard. April 2008.

PEER 2007/06 *Development of Improved Procedures for Seismic Design of Buried and Partially Buried Structures.* Linda Al Atik and Nicholas Sitar. June 2007.

PEER 2007/05 *Uncertainty and Correlation in Seismic Risk Assessment of Transportation Systems.* Renee G. Lee and Anne S. Kiremidjian. July 2007.

PEER 2007/04 *Numerical Models for Analysis and Performance-Based Design of Shallow Foundations Subjected to Seismic Loading.* Sivapalan Gajan, Tara C. Hutchinson, Bruce L. Kutter, Prishati Raychowdhury, José A. Ugalde, and Jonathan P. Stewart. May 2008.

PEER 2007/03 *Beam-Column Element Model Calibrated for Predicting Flexural Response Leading to Global Collapse of RC Frame Buildings.* Curt B. Haselton, Abbie B. Liel, Sarah Taylor Lange, and Gregory G. Deierlein. May 2008.

PEER 2007/02 *Campbell-Bozorgnia NGA Ground Motion Relations for the Geometric Mean Horizontal Component of Peak and Spectral Ground Motion Parameters.* Kenneth W. Campbell and Yousef Bozorgnia. May 2007.

PEER 2007/01 *Boore-Atkinson NGA Ground Motion Relations for the Geometric Mean Horizontal Component of Peak and Spectral Ground Motion Parameters.* David M. Boore and Gail M. Atkinson. May. May 2007.

PEER 2006/12 *Societal Implications of Performance-Based Earthquake Engineering.* Peter J. May. May 2007.

PEER 2006/11 *Probabilistic Seismic Demand Analysis Using Advanced Ground Motion Intensity Measures, Attenuation Relationships, and Near-Fault Effects.* Polsak Tothong and C. Allin Cornell. March 2007.

PEER 2006/10 *Application of the PEER PBEE Methodology to the I-880 Viaduct.* Sashi Kunnath. February 2007.

PEER 2006/09 *Quantifying Economic Losses from Travel Forgone Following a Large Metropolitan Earthquake.* James Moore, Sungbin Cho, Yue Yue Fan, and Stuart Werner. November 2006.

PEER 2006/08 *Vector-Valued Ground Motion Intensity Measures for Probabilistic Seismic Demand Analysis.* Jack W. Baker and C. Allin Cornell. October 2006.

PEER 2006/07 *Analytical Modeling of Reinforced Concrete Walls for Predicting Flexural and Coupled–Shear-Flexural Responses.* Kutay Orakcal, Leonardo M. Massone, and John W. Wallace. October 2006.

PEER 2006/06 *Nonlinear Analysis of a Soil-Drilled Pier System under Static and Dynamic Axial Loading.* Gang Wang and Nicholas Sitar. November 2006.

PEER 2006/05 *Advanced Seismic Assessment Guidelines.* Paolo Bazzurro, C. Allin Cornell, Charles Menun, Maziar Motahari, and Nicolas Luco. September 2006.

PEER 2006/04 *Probabilistic Seismic Evaluation of Reinforced Concrete Structural Components and Systems.* Tae Hyung Lee and Khalid M. Mosalam. August 2006.

PEER 2006/03 *Performance of Lifelines Subjected to Lateral Spreading.* Scott A. Ashford and Teerawut Juirnarongrit. July 2006.

PEER 2006/02 *Pacific Earthquake Engineering Research Center Highway Demonstration Project.* Anne Kiremidjian, James Moore, Yue Yue Fan, Nesrin Basoz, Ozgur Yazali, and Meredith Williams. April 2006.

PEER 2006/01 *Bracing Berkeley. A Guide to Seismic Safety on the UC Berkeley Campus.* Mary C. Comerio, Stephen Tobriner, and Ariane Fehrenkamp. January 2006.

PEER 2005/16 *Seismic Response and Reliability of Electrical Substation Equipment and Systems.* Junho Song, Armen Der Kiureghian, and Jerome L. Sackman. April 2006.

PEER 2005/15 *CPT-Based Probabilistic Assessment of Seismic Soil Liquefaction Initiation.* R. E. S. Moss, R. B. Seed, R. E. Kayen, J. P. Stewart, and A. Der Kiureghian. April 2006.

PEER 2005/14 *Workshop on Modeling of Nonlinear Cyclic Load-Deformation Behavior of Shallow Foundations.* Bruce L. Kutter, Geoffrey Martin, Tara Hutchinson, Chad Harden, Sivapalan Gajan, and Justin Phalen. March 2006.

PEER 2005/13 *Stochastic Characterization and Decision Bases under Time-Dependent Aftershock Risk in Performance-Based Earthquake Engineering.* Gee Liek Yeo and C. Allin Cornell. July 2005.

PEER 2005/12 *PEER Testbed Study on a Laboratory Building: Exercising Seismic Performance Assessment.* Mary C. Comerio, editor. November 2005.

PEER 2005/11 *Van Nuys Hotel Building Testbed Report: Exercising Seismic Performance Assessment.* Helmut Krawinkler, editor. October 2005.

PEER 2005/10 *First NEES/E-Defense Workshop on Collapse Simulation of Reinforced Concrete Building Structures.* September 2005.

PEER 2005/09 *Test Applications of Advanced Seismic Assessment Guidelines.* Joe Maffei, Karl Telleen, Danya Mohr, William Holmes, and Yuki Nakayama. August 2006.

PEER 2005/08 *Damage Accumulation in Lightly Confined Reinforced Concrete Bridge Columns.* R. Tyler Ranf, Jared M. Nelson, Zach Price, Marc O. Eberhard, and John F. Stanton. April 2006.

PEER 2005/07 *Experimental and Analytical Studies on the Seismic Response of Freestanding and Anchored Laboratory Equipment.* Dimitrios Konstantinidis and Nicos Makris. January 2005.

PEER 2005/06 *Global Collapse of Frame Structures under Seismic Excitations.* Luis F. Ibarra and Helmut Krawinkler. September 2005.

PEER 2005//05 *Performance Characterization of Bench- and Shelf-Mounted Equipment.* Samit Ray Chaudhuri and Tara C. Hutchinson. May 2006.

PEER 2005/04 *Numerical Modeling of the Nonlinear Cyclic Response of Shallow Foundations.* Chad Harden, Tara Hutchinson, Geoffrey R. Martin, and Bruce L. Kutter. August 2005.

PEER 2005/03 *A Taxonomy of Building Components for Performance-Based Earthquake Engineering.* Keith A. Porter. September 2005.

PEER 2005/02 *Fragility Basis for California Highway Overpass Bridge Seismic Decision Making*. Kevin R. Mackie and Božidar Stojadinović. June 2005.

PEER 2005/01 *Empirical Characterization of Site Conditions on Strong Ground Motion.* Jonathan P. Stewart, Yoojoong Choi, and Robert W. Graves. June 2005.

PEER 2004/09 *Electrical Substation Equipment Interaction: Experimental Rigid Conductor Studies.* Christopher Stearns and André Filiatrault. February 2005.

PEER 2004/08 *Seismic Qualification and Fragility Testing of Line Break 550-kV Disconnect Switches.* Shakhzod M. Takhirov, Gregory L. Fenves, and Eric Fujisaki. January 2005.

PEER 2004/07 *Ground Motions for Earthquake Simulator Qualification of Electrical Substation Equipment.* Shakhzod M. Takhirov, Gregory L. Fenves, Eric Fujisaki, and Don Clyde. January 2005.

PEER 2004/06 *Performance-Based Regulation and Regulatory Regimes.* Peter J. May and Chris Koski. September 2004.

PEER 2004/05 *Performance-Based Seismic Design Concepts and Implementation: Proceedings of an International Workshop.* Peter Fajfar and Helmut Krawinkler, editors. September 2004.

PEER 2004/04 *Seismic Performance of an Instrumented Tilt-up Wall Building.* James C. Anderson and Vitelmo V. Bertero. July 2004.

PEER 2004/03 *Evaluation and Application of Concrete Tilt-up Assessment Methodologies.* Timothy Graf and James O. Malley. October 2004.

PEER 2004/02 *Analytical Investigations of New Methods for Reducing Residual Displacements of Reinforced Concrete Bridge Columns.* Junichi Sakai and Stephen A. Mahin. August 2004.

PEER 2004/01 *Seismic Performance of Masonry Buildings and Design Implications.* Kerri Anne Taeko Tokoro, James C. Anderson, and Vitelmo V. Bertero. February 2004.

PEER 2003/18 *Performance Models for Flexural Damage in Reinforced Concrete Columns.* Michael Berry and Marc Eberhard. August 2003.

PEER 2003/17 *Predicting Earthquake Damage in Older Reinforced Concrete Beam-Column Joints.* Catherine Pagni and Laura Lowes. October 2004.

PEER 2003/16 *Seismic Demands for Performance-Based Design of Bridges.* Kevin Mackie and Božidar Stojadinović. August 2003.

PEER 2003/15 *Seismic Demands for Nondeteriorating Frame Structures and Their Dependence on Ground Motions.* Ricardo Antonio Medina and Helmut Krawinkler. May 2004.

PEER 2003/14 *Finite Element Reliability and Sensitivity Methods for Performance-Based Earthquake Engineering.* Terje Haukaas and Armen Der Kiureghian. April 2004.

PEER 2003/13 *Effects of Connection Hysteretic Degradation on the Seismic Behavior of Steel Moment-Resisting Frames.* Janise E. Rodgers and Stephen A. Mahin. March 2004.

PEER 2003/12 *Implementation Manual for the Seismic Protection of Laboratory Contents: Format and Case Studies.* William T. Holmes and Mary C. Comerio. October 2003.

PEER 2003/11 *Fifth U.S.-Japan Workshop on Performance-Based Earthquake Engineering Methodology for Reinforced Concrete Building Structures.* February 2004.

PEER 2003/10 *A Beam-Column Joint Model for Simulating the Earthquake Response of Reinforced Concrete Frames.* Laura N. Lowes, Nilanjan Mitra, and Arash Altoontash. February 2004.

PEER 2003/09 *Sequencing Repairs after an Earthquake: An Economic Approach.* Marco Casari and Simon J. Wilkie. April 2004.

PEER 2003/08 *A Technical Framework for Probability-Based Demand and Capacity Factor Design (DCFD) Seismic Formats.* Fatemeh Jalayer and C. Allin Cornell. November 2003.

PEER 2003/07 *Uncertainty Specification and Propagation for Loss Estimation Using FOSM Methods.* Jack W. Baker and C. Allin Cornell. September 2003.

PEER 2003/06 *Performance of Circular Reinforced Concrete Bridge Columns under Bidirectional Earthquake Loading.* Mahmoud M. Hachem, Stephen A. Mahin, and Jack P. Moehle. February 2003.

PEER 2003/05 *Response Assessment for Building-Specific Loss Estimation.* Eduardo Miranda and Shahram Taghavi. September 2003.

PEER 2003/04 *Experimental Assessment of Columns with Short Lap Splices Subjected to Cyclic Loads.* Murat Melek, John W. Wallace, and Joel Conte. April 2003.

PEER 2003/03 *Probabilistic Response Assessment for Building-Specific Loss Estimation.* Eduardo Miranda and Hesameddin Aslani. September 2003.

PEER 2003/02 *Software Framework for Collaborative Development of Nonlinear Dynamic Analysis Program.* Jun Peng and Kincho H. Law. September 2003.

PEER 2003/01 *Shake Table Tests and Analytical Studies on the Gravity Load Collapse of Reinforced Concrete Frames.* Kenneth John Elwood and Jack P. Moehle. November 2003.

PEER 2002/24 *Performance of Beam to Column Bridge Joints Subjected to a Large Velocity Pulse.* Natalie Gibson, André Filiatrault, and Scott A. Ashford. April 2002.

PEER 2002/23 *Effects of Large Velocity Pulses on Reinforced Concrete Bridge Columns.* Greg L. Orozco and Scott A. Ashford. April 2002.

PEER 2002/22 *Characterization of Large Velocity Pulses for Laboratory Testing.* Kenneth E. Cox and Scott A. Ashford. April 2002.

PEER 2002/21 *Fourth U.S.-Japan Workshop on Performance-Based Earthquake Engineering Methodology for Reinforced Concrete Building Structures.* December 2002.

PEER 2002/20 *Barriers to Adoption and Implementation of PBEE Innovations.* Peter J. May. August 2002.

PEER 2002/19 *Economic-Engineered Integrated Models for Earthquakes: Socioeconomic Impacts.* Peter Gordon, James E. Moore II, and Harry W. Richardson. July 2002.

PEER 2002/18 *Assessment of Reinforced Concrete Building Exterior Joints with Substandard Details.* Chris P. Pantelides, Jon Hansen, Justin Nadauld, and Lawrence D. Reaveley. May 2002.

PEER 2002/17 *Structural Characterization and Seismic Response Analysis of a Highway Overcrossing Equipped with Elastomeric Bearings and Fluid Dampers: A Case Study.* Nicos Makris and Jian Zhang. November 2002.

PEER 2002/16 *Estimation of Uncertainty in Geotechnical Properties for Performance-Based Earthquake Engineering.* Allen L. Jones, Steven L. Kramer, and Pedro Arduino. December 2002.

PEER 2002/15 *Seismic Behavior of Bridge Columns Subjected to Various Loading Patterns.* Asadollah Esmaeily-Gh. and Yan Xiao. December 2002.

PEER 2002/14 *Inelastic Seismic Response of Extended Pile Shaft Supported Bridge Structures.* T.C. Hutchinson, R.W. Boulanger, Y.H. Chai, and I.M. Idriss. December 2002.

PEER 2002/13 *Probabilistic Models and Fragility Estimates for Bridge Components and Systems.* Paolo Gardoni, Armen Der Kiureghian, and Khalid M. Mosalam. June 2002.

PEER 2002/12 *Effects of Fault Dip and Slip Rake on Near-Source Ground Motions: Why Chi-Chi Was a Relatively Mild M7.6 Earthquake.* Brad T. Aagaard, John F. Hall, and Thomas H. Heaton. December 2002.

PEER 2002/11 *Analytical and Experimental Study of Fiber-Reinforced Strip Isolators*. James M. Kelly and Shakhzod M. Takhirov. September 2002.

PEER 2002/10 *Centrifuge Modeling of Settlement and Lateral Spreading with Comparisons to Numerical Analyses***.** Sivapalan Gajan and Bruce L. Kutter. January 2003.

PEER 2002/09 *Documentation and Analysis of Field Case Histories of Seismic Compression during the 1994 Northridge, California, Earthquake.* Jonathan P. Stewart, Patrick M. Smith, Daniel H. Whang, and Jonathan D. Bray. October 2002.

PEER 2002/08 *Component Testing, Stability Analysis and Characterization of Buckling-Restrained Unbonded Braces™.* Cameron Black, Nicos Makris, and Ian Aiken. September 2002.

PEER 2002/07 *Seismic Performance of Pile-Wharf Connections.* Charles W. Roeder, Robert Graff, Jennifer Soderstrom, and Jun Han Yoo. December 2001.

PEER 2002/06 *The Use of Benefit-Cost Analysis for Evaluation of Performance-Based Earthquake Engineering Decisions*. Richard O. Zerbe and Anthony Falit-Baiamonte. September 2001.

PEER 2002/05 *Guidelines, Specifications, and Seismic Performance Characterization of Nonstructural Building Components and Equipment*. André Filiatrault, Constantin Christopoulos, and Christopher Stearns. September 2001.

PEER 2002/04 *Consortium of Organizations for Strong-Motion Observation Systems and the Pacific Earthquake Engineering Research Center Lifelines Program: Invited Workshop on Archiving and Web Dissemination of Geotechnical Data, 4–5 October 2001*. September 2002.

PEER 2002/03 *Investigation of Sensitivity of Building Loss Estimates to Major Uncertain Variables for the Van Nuys Testbed.* Keith A. Porter, James L. Beck, and Rustem V. Shaikhutdinov. August 2002.

PEER 2002/02 *The Third U.S.-Japan Workshop on Performance-Based Earthquake Engineering Methodology for Reinforced Concrete Building Structures*. July 2002.

PEER 2002/01 *Nonstructural Loss Estimation: The UC Berkeley Case Study.* Mary C. Comerio and John C. Stallmeyer. December 2001.

PEER 2001/16 *Statistics of SDF-System Estimate of Roof Displacement for Pushover Analysis of Buildings.* Anil K. Chopra, Rakesh K. Goel, and Chatpan Chintanapakdee. December 2001.

PEER 2001/15 *Damage to Bridges during the 2001 Nisqually Earthquake.* R. Tyler Ranf, Marc O. Eberhard, and Michael P. Berry. November 2001.

PEER 2001/14 *Rocking Response of Equipment Anchored to a Base Foundation.* Nicos Makris and Cameron J. Black. September 2001.

PEER 2001/13 *Modeling Soil Liquefaction Hazards for Performance-Based Earthquake Engineering.* Steven L. Kramer and Ahmed-W. Elgamal. February 2001.

PEER 2001/12 *Development of Geotechnical Capabilities in OpenSees.* Boris Jeremić. September 2001.

PEER 2001/11 *Analytical and Experimental Study of Fiber-Reinforced Elastomeric Isolators*. James M. Kelly and Shakhzod M. Takhirov. September 2001.

PEER 2001/10 *Amplification Factors for Spectral Acceleration in Active Regions.* Jonathan P. Stewart, Andrew H. Liu, Yoojoong Choi, and Mehmet B. Baturay. December 2001.

PEER 2001/09 *Ground Motion Evaluation Procedures for Performance-Based Design.* Jonathan P. Stewart, Shyh-Jeng Chiou, Jonathan D. Bray, Robert W. Graves, Paul G. Somerville, and Norman A. Abrahamson. September 2001.

PEER 2001/08 *Experimental and Computational Evaluation of Reinforced Concrete Bridge Beam-Column Connections for Seismic Performance*. Clay J. Naito, Jack P. Moehle, and Khalid M. Mosalam. November 2001.

PEER 2001/07 *The Rocking Spectrum and the Shortcomings of Design Guidelines.* Nicos Makris and Dimitrios Konstantinidis. August 2001.

PEER 2001/06 *Development of an Electrical Substation Equipment Performance Database for Evaluation of Equipment Fragilities*. Thalia Agnanos. April 1999.

PEER 2001/05 *Stiffness Analysis of Fiber-Reinforced Elastomeric Isolators.* Hsiang-Chuan Tsai and James M. Kelly. May 2001.

PEER 2001/04 *Organizational and Societal Considerations for Performance-Based Earthquake Engineering.* Peter J. May. April 2001.

PEER 2001/03 *A Modal Pushover Analysis Procedure to Estimate Seismic Demands for Buildings: Theory and Preliminary Evaluation.* Anil K. Chopra and Rakesh K. Goel. January 2001.

PEER 2001/02 *Seismic Response Analysis of Highway Overcrossings Including Soil-Structure Interaction.* Jian Zhang and Nicos Makris. March 2001.

PEER 2001/01 *Experimental Study of Large Seismic Steel Beam-to-Column Connections.* Egor P. Popov and Shakhzod M. Takhirov. November 2000.

PEER 2000/10 *The Second U.S.-Japan Workshop on Performance-Based Earthquake Engineering Methodology for Reinforced Concrete Building Structures.* March 2000.

PEER 2000/09 *Structural Engineering Reconnaissance of the August 17, 1999 Earthquake: Kocaeli (Izmit), Turkey.* Halil Sezen, Kenneth J. Elwood, Andrew S. Whittaker, Khalid Mosalam, John J. Wallace, and John F. Stanton. December 2000.

PEER 2000/08 *Behavior of Reinforced Concrete Bridge Columns Having Varying Aspect Ratios and Varying Lengths of Confinement.* Anthony J. Calderone, Dawn E. Lehman, and Jack P. Moehle. January 2001.

PEER 2000/07 *Cover-Plate and Flange-Plate Reinforced Steel Moment-Resisting Connections.* Taejin Kim, Andrew S. Whittaker, Amir S. Gilani, Vitelmo V. Bertero, and Shakhzod M. Takhirov. September 2000.

PEER 2000/06 *Seismic Evaluation and Analysis of 230-kV Disconnect Switches.* Amir S. J. Gilani, Andrew S. Whittaker, Gregory L. Fenves, Chun-Hao Chen, Henry Ho, and Eric Fujisaki. July 2000.

PEER 2000/05 *Performance-Based Evaluation of Exterior Reinforced Concrete Building Joints for Seismic Excitation.* Chandra Clyde, Chris P. Pantelides, and Lawrence D. Reaveley. July 2000.

PEER 2000/04 *An Evaluation of Seismic Energy Demand: An Attenuation Approach.* Chung-Che Chou and Chia-Ming Uang. July 1999.

PEER 2000/03 *Framing Earthquake Retrofitting Decisions: The Case of Hillside Homes in Los Angeles.* Detlof von Winterfeldt, Nels Roselund, and Alicia Kitsuse. March 2000.

PEER 2000/02 *U.S.-Japan Workshop on the Effects of Near-Field Earthquake Shaking.* Andrew Whittaker, ed. July 2000.

PEER 2000/01 *Further Studies on Seismic Interaction in Interconnected Electrical Substation Equipment.* Armen Der Kiureghian, Kee-Jeung Hong, and Jerome L. Sackman. November 1999.

PEER 1999/14 *Seismic Evaluation and Retrofit of 230-kV Porcelain Transformer Bushings.* Amir S. Gilani, Andrew S. Whittaker, Gregory L. Fenves, and Eric Fujisaki. December 1999.

PEER 1999/13 *Building Vulnerability Studies: Modeling and Evaluation of Tilt-up and Steel Reinforced Concrete Buildings.* John W. Wallace, Jonathan P. Stewart, and Andrew S. Whittaker, editors. December 1999.

PEER 1999/12 *Rehabilitation of Nonductile RC Frame Building Using Encasement Plates and Energy-Dissipating Devices.* Mehrdad Sasani, Vitelmo V. Bertero, James C. Anderson. December 1999.

PEER 1999/11 *Performance Evaluation Database for Concrete Bridge Components and Systems under Simulated Seismic Loads.* Yael D. Hose and Frieder Seible. November 1999.

PEER 1999/10 *U.S.-Japan Workshop on Performance-Based Earthquake Engineering Methodology for Reinforced Concrete Building Structures.* December 1999.

PEER 1999/09 *Performance Improvement of Long Period Building Structures Subjected to Severe Pulse-Type Ground Motions*. James C. Anderson, Vitelmo V. Bertero, and Raul Bertero. October 1999.

PEER 1999/08 *Envelopes for Seismic Response Vectors.* Charles Menun and Armen Der Kiureghian. July 1999.

PEER 1999/07 *Documentation of Strengths and Weaknesses of Current Computer Analysis Methods for Seismic Performance of Reinforced Concrete Members.* William F. Cofer. November 1999.

PEER 1999/06 *Rocking Response and Overturning of Anchored Equipment under Seismic Excitations.* Nicos Makris and Jian Zhang. November 1999.

PEER 1999/05 *Seismic Evaluation of 550 kV Porcelain Transformer Bushings.* Amir S. Gilani, Andrew S. Whittaker, Gregory L. Fenves, and Eric Fujisaki. October 1999.

PEER 1999/04 *Adoption and Enforcement of Earthquake Risk-Reduction Measures.* Peter J. May, Raymond J. Burby, T. Jens Feeley, and Robert Wood.

PEER 1999/03 *Task 3 Characterization of Site Response General Site Categories*. Adrian Rodriguez-Marek, Jonathan D. Bray, and Norman Abrahamson. February 1999.

PEER 1999/02 *Capacity-Demand-Diagram Methods for Estimating Seismic Deformation of Inelastic Structures: SDF Systems*. Anil K. Chopra and Rakesh Goel. April 1999.

PEER 1999/01 *Interaction in Interconnected Electrical Substation Equipment Subjected to Earthquake Ground Motions.* Armen Der Kiureghian, Jerome L. Sackman, and Kee-Jeung Hong. February 1999.

PEER 1998/08 *Behavior and Failure Analysis of a Multiple-Frame Highway Bridge in the 1994 Northridge Earthquake.* Gregory L. Fenves and Michael Ellery. December 1998.

PEER 1998/07 *Empirical Evaluation of Inertial Soil-Structure Interaction Effects.* Jonathan P. Stewart, Raymond B. Seed, and Gregory L. Fenves. November 1998.

PEER 1998/06 *Effect of Damping Mechanisms on the Response of Seismic Isolated Structures.* Nicos Makris and Shih-Po Chang. November 1998.

PEER 1998/05 *Rocking Response and Overturning of Equipment under Horizontal Pulse-Type Motions.* Nicos Makris and Yiannis Roussos. October 1998.

PEER 1998/04 *Pacific Earthquake Engineering Research Invitational Workshop Proceedings, May 14–15, 1998: Defining the Links between Planning, Policy Analysis, Economics and Earthquake Engineering.* Mary Comerio and Peter Gordon. September 1998.

PEER 1998/03 *Repair/Upgrade Procedures for Welded Beam to Column Connections.* James C. Anderson and Xiaojing Duan. May 1998.

PEER 1998/02 *Seismic Evaluation of 196 kV Porcelain Transformer Bushings.* Amir S. Gilani, Juan W. Chavez, Gregory L. Fenves, and Andrew S. Whittaker. May 1998.

PEER 1998/01 *Seismic Performance of Well-Confined Concrete Bridge Columns.* Dawn E. Lehman and Jack P. Moehle. December 2000.

ONLINE PEER REPORTS

The following PEER reports are available by Internet only at http://peer.berkeley.edu/publications/peer_reports_complete.html.

PEER 2012/103 *Performance-Based Seismic Demand Assessment of Concentrically Braced Steel Frame Buildings.* Chui-Hsin Chen and Stephen A. Mahin. December 2012.

PEER 2012/102 *Procedure to Restart an Interrupted Hybrid Simulation: Addendum to PEER Report 2010/103.* Vesna Terzic and Bozidar Stojadinovic. October 2012.

PEER 2012/101 *Mechanics of Fiber Reinforced Bearings.* James M. Kelly and Andrea Calabrese. February 2012.

PEER 2011/107 *Nonlinear Site Response and Seismic Compression at Vertical Array Strongly Shaken by 2007 Niigata-ken Chuetsu-oki Earthquake.* Eric Yee, Jonathan P. Stewart, and Kohji Tokimatsu. December 2011.

PEER 2011/106 *Self Compacting Hybrid Fiber Reinforced Concrete Composites for Bridge Columns.* Pardeep Kumar, Gabriel Jen, William Trono, Marios Panagiotou, and Claudia Ostertag. September 2011.

PEER 2011/105 *Stochastic Dynamic Analysis of Bridges Subjected to Spacially Varying Ground Motions.* Katerina Konakli and Armen Der Kiureghian. August 2011.

PEER 2011/104 *Design and Instrumentation of the 2010 E-Defense Four-Story Reinforced Concrete and Post-Tensioned Concrete Buildings.* Takuya Nagae, Kenichi Tahara, Taizo Matsumori, Hitoshi Shiohara, Toshimi Kabeyasawa, Susumu Kono, Minehiro Nishiyama (Japanese Research Team) and John Wallace, Wassim Ghannoum, Jack Moehle, Richard Sause, Wesley Keller, Zeynep Tuna (U.S. Research Team). June 2011.

PEER 2011/103 *In-Situ Monitoring of the Force Output of Fluid Dampers: Experimental Investigation.* Dimitrios Konstantinidis, James M. Kelly, and Nicos Makris. April 2011.

PEER 2011/102 *Ground-motion prediction equations 1964 - 2010.* John Douglas. April 2011.

PEER 2011/101 *Report of the Eighth Planning Meeting of NEES/E-Defense Collaborative Research on Earthquake Engineering.* Convened by the Hyogo Earthquake Engineering Research Center (NIED), NEES Consortium, Inc. February 2011.

PEER 2010/111 *Modeling and Acceptance Criteria for Seismic Design and Analysis of Tall Buildings.* Task 7 Report for the Tall Buildings Initiative - Published jointly by the Applied Technology Council. October 2010.

PEER 2010/110 *Seismic Performance Assessment and Probabilistic Repair Cost Analysis of Precast Concrete Cladding Systems for Multistory Buildlings.* Jeffrey P. Hunt and Božidar Stojadinovic. November 2010.

PEER 2010/109 *Report of the Seventh Joint Planning Meeting of NEES/E-Defense Collaboration on Earthquake Engineering. Held at the E-Defense, Miki, and Shin-Kobe, Japan, September 18–19, 2009.* August 2010.

PEER 2010/108 *Probabilistic Tsunami Hazard in California.* Hong Kie Thio, Paul Somerville, and Jascha Polet, preparers. October 2010.

PEER 2010/107 *Performance and Reliability of Exposed Column Base Plate Connections for Steel Moment-Resisting Frames.* Ady Aviram, Božidar Stojadinovic, and Armen Der Kiureghian. August 2010.

PEER 2010/106 *Verification of Probabilistic Seismic Hazard Analysis Computer Programs.* Patricia Thomas, Ivan Wong, and Norman Abrahamson. May 2010.

PEER 2010/105 *Structural Engineering Reconnaissance of the April 6, 2009, Abruzzo, Italy, Earthquake, and Lessons Learned.* M. Selim Günay and Khalid M. Mosalam. April 2010.

PEER 2010/104 *Simulating the Inelastic Seismic Behavior of Steel Braced Frames, Including the Effects of Low-Cycle Fatigue.* Yuli Huang and Stephen A. Mahin. April 2010.

PEER 2010/103 *Post-Earthquake Traffic Capacity of Modern Bridges in California.* Vesna Terzic and Božidar Stojadinović. March 2010.

PEER 2010/102 *Analysis of Cumulative Absolute Velocity (CAV) and JMA Instrumental Seismic Intensity (I_{JMA}) Using the PEER–NGA Strong Motion Database.* Kenneth W. Campbell and Yousef Bozorgnia. February 2010.

PEER 2010/101 *Rocking Response of Bridges on Shallow Foundations.* Jose A. Ugalde, Bruce L. Kutter, and Boris Jeremic. April 2010.

PEER 2009/109 *Simulation and Performance-Based Earthquake Engineering Assessment of Self-Centering Post-Tensioned Concrete Bridge Systems.* Won K. Lee and Sarah L. Billington. December 2009.

PEER 2009/108 *PEER Lifelines Geotechnical Virtual Data Center.* J. Carl Stepp, Daniel J. Ponti, Loren L. Turner, Jennifer N. Swift, Sean Devlin, Yang Zhu, Jean Benoit, and John Bobbitt. September 2009.

PEER 2009/107 *Experimental and Computational Evaluation of Current and Innovative In-Span Hinge Details in Reinforced Concrete Box-Girder Bridges: Part 2: Post-Test Analysis and Design Recommendations.* Matias A. Hube and Khalid M. Mosalam. December 2009.

PEER 2009/106 *Shear Strength Models of Exterior Beam-Column Joints without Transverse Reinforcement.* Sangjoon Park and Khalid M. Mosalam. November 2009.

PEER 2009/105 *Reduced Uncertainty of Ground Motion Prediction Equations through Bayesian Variance Analysis.* Robb Eric S. Moss. November 2009.

PEER 2009/104 *Advanced Implementation of Hybrid Simulation.* Andreas H. Schellenberg, Stephen A. Mahin, Gregory L. Fenves. November 2009.

PEER 2009/103 *Performance Evaluation of Innovative Steel Braced Frames.* T. Y. Yang, Jack P. Moehle, and Božidar Stojadinovic. August 2009.

PEER 2009/102 *Reinvestigation of Liquefaction and Nonliquefaction Case Histories from the 1976 Tangshan Earthquake.* Robb Eric Moss, Robert E. Kayen, Liyuan Tong, Songyu Liu, Guojun Cai, and Jiaer Wu. August 2009.

PEER 2009/101 *Report of the First Joint Planning Meeting for the Second Phase of NEES/E-Defense Collaborative Research on Earthquake Engineering.* Stephen A. Mahin et al. July 2009.

PEER 2008/104 *Experimental and Analytical Study of the Seismic Performance of Retaining Structures.* Linda Al Atik and Nicholas Sitar. January 2009.

PEER 2008/103 *Experimental and Computational Evaluation of Current and Innovative In-Span Hinge Details in Reinforced Concrete Box-Girder Bridges. Part 1: Experimental Findings and Pre-Test Analysis.* Matias A. Hube and Khalid M. Mosalam. January 2009.

PEER 2008/102 *Modeling of Unreinforced Masonry Infill Walls Considering In-Plane and Out-of-Plane Interaction.* Stephen Kadysiewski and Khalid M. Mosalam. January 2009.

PEER 2008/101 *Seismic Performance Objectives for Tall Buildings.* William T. Holmes, Charles Kircher, William Petak, and Nabih Youssef. August 2008.

PEER 2007/101 *Generalized Hybrid Simulation Framework for Structural Systems Subjected to Seismic Loading.* Tarek Elkhoraibi and Khalid M. Mosalam. July 2007.

PEER 2007/100 *Seismic Evaluation of Reinforced Concrete Buildings Including Effects of Masonry Infill Walls.* Alidad Hashemi and Khalid M. Mosalam. July 2007.

The Pacific Earthquake Engineering Research Center (PEER) is a multi-institutional research and education center with headquarters at the University of California, Berkeley. Investigators from over 20 universities, several consulting companies, and researchers at various state and federal government agencies contribute to research programs focused on performance-based earthquake engineering.

These research programs aim to identify and reduce the risks from major earthquakes to life safety and to the economy by including research in a wide variety of disciplines including structural and geotechnical engineering, geology/seismology, lifelines, transportation, architecture, economics, risk management, and public policy.

PEER is supported by federal, state, local, and regional agencies, together with industry partners.

PEER Core Institutions:
University of California, Berkeley (Lead Institution)
California Institute of Technology
Oregon State University
Stanford University
University of California, Davis
University of California, Irvine
University of California, Los Angeles
University of California, San Diego
University of Southern California
University of Washington

PEER reports can be ordered at http://peer.berkeley.edu/publications/peer_reports.html or by contacting

Pacific Earthquake Engineering Research Center
University of California, Berkeley
325 Davis Hall, mail code 1792
Berkeley, CA 94720-1792
Tel: 510-642-3437
Fax: 510-642-1655
Email: peer_editor@berkeley.edu

ISSN 1547-0587X